UNIVERSITY OF
JAN 9 1962
CHICAGO

JOURNAL OF APPLIED PHYSICS

Vol. 32, No. 12

December, 1961

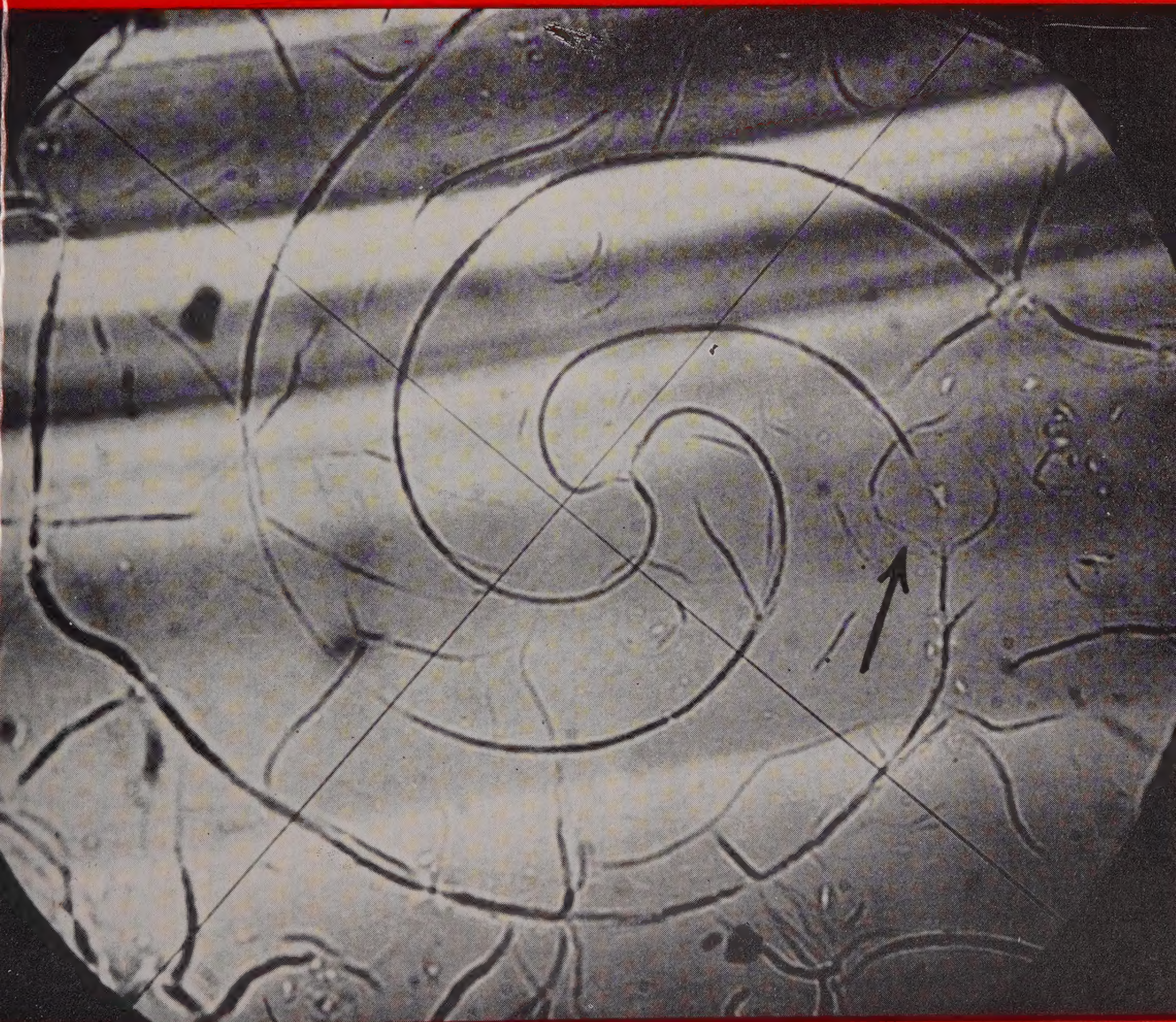

Spiral Source of Linear Flaws in Glass Containing 20% PbO.
See Page 2525.

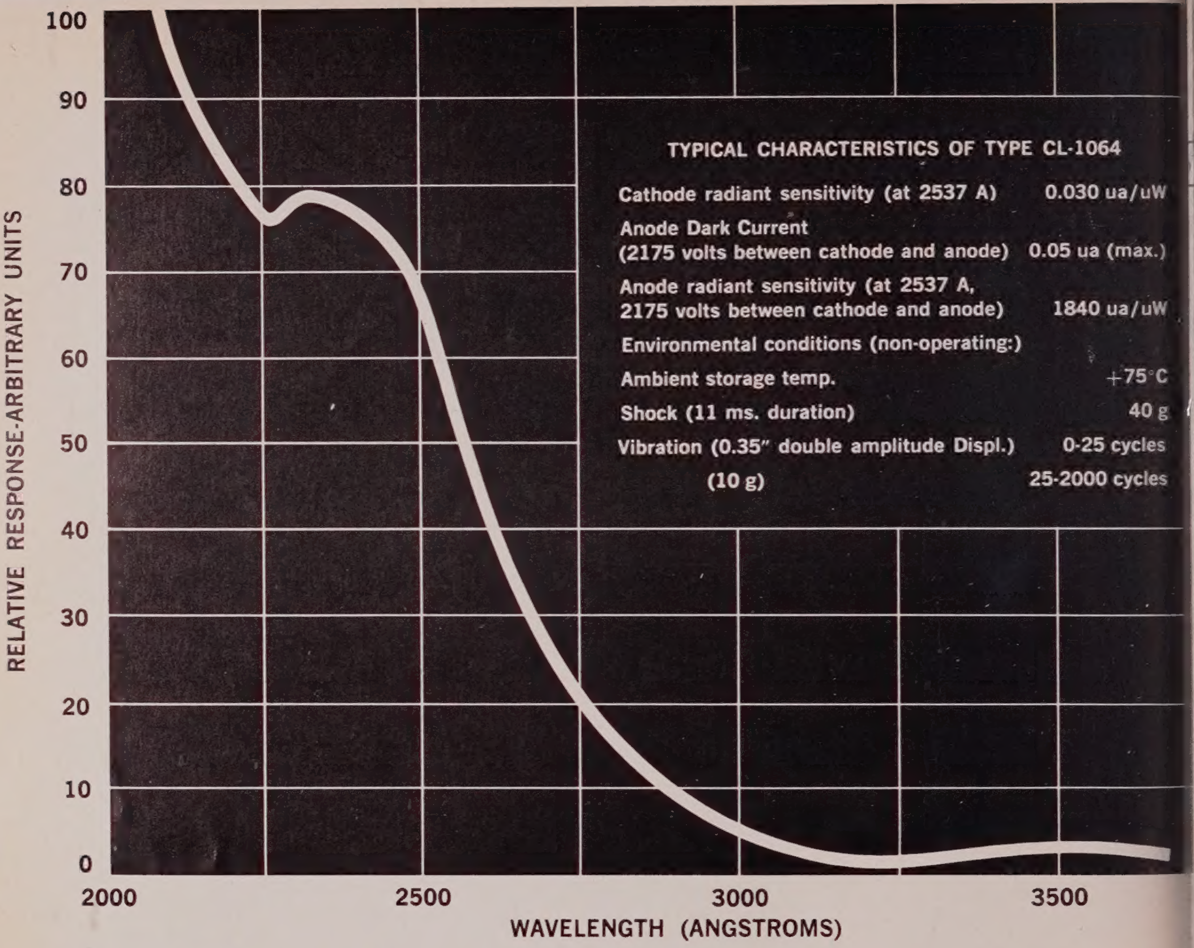

TYPICAL CHARACTERISTICS OF TYPE CL-1064

Cathode radiant sensitivity (at 2537 A)	0.030 ua/uW
Anode Dark Current (2175 volts between cathode and anode)	0.05 ua (max.)
Anode radiant sensitivity (at 2537 A, 2175 volts between cathode and anode)	1840 ua/uW
Environmental conditions (non-operating:)	
Ambient storage temp.	+75°C
Shock (11 ms. duration)	40 g
Vibration (0.35" double amplitude Displ.)	0-25 cycles
(10 g)	25-2000 cycles

FROM CBS LABORATORIES...
NEW SOLAR-BLIND PHOTOMULTIPLIE

Type CL-1064, the latest in CBS Laboratories' new line of photomultipliers, has a high-peak quantum efficiency heretofore unavailable in solar-blind photomultiplier tubes. It has a peak sensitivity to ultraviolet radiation and very low sensitivity to visible and infrared radiation. These characteristics result from its unique photocathode, a composite of rubidium and tellurium deposited on a solid metal surface. Peak quantum efficiency of the photocathode is approximately 25%.

The solar-blind CL-1064 is designed for detecting low-level ultraviolet radiation in the presence of visible and infrared radiation. It is specially constructed f use in rocket and other airborne instrumentati Current applications include star-tracking, measuri ultraviolet radiation from the stars, and ultravio vacuum spectroscopy. The tube, whose diameter 2 inches, employs an end-on photocathode and 13-stage multiplier.

A wide range of special purpose tubes is also availab (or can be readily designed) with cathode sensitiviti of from 10,000 Å (in the infrared region) to approx mately 1000 Å (in the vacuum ultraviolet region

CBS LABORATORIES

HIGH RIDGE ROAD, STAMFORD, CONNECTIC
A DIVISION OF COLUMBIA BROADCASTING SYSTEM, I

JOURNAL OF APPLIED PHYSICS

ol. 32, No. 12 DECEMBER, 1961

In This Issue

Electron Microscope Investigation on the Nature of Tracks of Fission Products in Mica . . . Guido Bonfiglioli, Andrea Ferro, and Adriana Mojoni 2499
Growth of Stannic Oxide Crystals from the Vapor Phase . . . J. A. Marley and T. C. MacAvoy 2504
Magnetic Investigation of Pure Manganese and of Several of its Alloys . . . H. W. Cooper, A. S. Arrott, and H. W. Paxton 2506
Theory of Electron Collection of Spherical Probes . . . G. Medicus 2512
Characteristic Electron Energy Loss Measurements at Low Temperatures . E. M. Hörl and J. A. Suddeth 2521
Defect Mechanisms in a Noncrystalline Solid . . . W. C. Levengood 2525
Growth of Refractory Crystals Using the Induction Plasma Torch . . . Thomas B. Reed 2534
Properties of Single-Domain Particles of Cobalt-Nickel . . . R. B. Falk and G. D. Hooper 2536
Improved Representation of Calculated Surface Mobilities in Semiconductors. I. Minority Carriers . . . N. B. Grover, Y. Goldstein, and A. Many 2538
Improved Representation of Calculated Surface Mobilities in Semiconductors. II. Majority Carriers . . . Y. Goldstein, N. B. Grover, A. Many, and R. F. Greene 2540
A cw Solid State, Push-Pull Maser in the 5 to 6 Millimeter Wavelength Region . . . David L. Carter 2541
Low-Temperature Thermoelectric Power of the Rare-Earth Metals . . . H. J. Born, Sam Legvold, and F. H. Spedding 2543
A Method for the Measurement of Short Minority Carrier Diffusion Lengths in Semiconductors . . . Alvin M. Goodman 2550
Theory of the Potential Well Produced by Multipacting Electrons. I. Very Low-Pressure Regime . . . R. L. Ingraham 2553
A Comparison of Theory and Experiment for a Thermoelectric Cooler . . . M. H. Norwood 2559
Hardening of Lithium Fluoride Crystals by Irradiation . . . J. S. Nadeau and W. G. Johnston 2563
Motion of c Domain Centers in BaTiO$_3$ . . . G. L. Link 2566
High-Temperature Kilocycle Internal Friction in Al$_2$O$_3$ Single Crystals . . . R. J. Huber, G. S. Baker, and P. Gibbs 2573
Momentum and Energy of Waves . . . J. R. Pierce 2580
Magnetic Domain Patterns in Cr-Modified Mn$_2$Sb . . . J. D. Wolf and J. E. Hanlon 2584
Growth from the Melt. III. Dendritic Growth . . . G. F. Bolling and W. A. Tiller 2587
High-Field Conductivity in Germanium and Silicon at Microwave Frequencies . . . J. Zucker, V. J. Fowler, and E. M. Conwell 2606
Space-Charge Instabilities in Electron Diodes and Plasma Converters . . . Charles K. Birdsall and William B. Bridges 2611
Magnetically Confined Cold-Cathode Gas Discharges at Low Pressures . . . R. L. Jepsen 2619
Harmonic Generation and Frequency Mixing in Ferromagnetic Insulators . . . R. L. Jepsen 2627
A Method for Measuring the Conductivity in a High Electron Density Plasma . . . K. B. Persson 2631
Effect of Residual Gases on the Properties of Indium Films . . . Hollis L. Caswell 2641
Voltage Dependence of Microplasma Density in p-n Junctions in Silicon . A. Goetzberger and C. Stephens 2646

Letters to the Editor:

Thermionic Properties of HfC . . . John H. Ingold 2651
Erratum: Man-Made Heating and Ionization of the Upper Atmosphere . . . P. A. Clavier 2651

Announcements:

Increase in Publication Charge . . . 2651
Author Index to Volume 32 . . . 2652
Subject Index to Volume 32 . . . 2668
Index to Advertisers . . . xxviii

JOURNAL OF APPLIED PHYSICS

A journal of general physics and its applications to other sciences and to industry

Published by the

American Institute of Physics

GOVERNING BOARD

Members

Ralph A. Sawyer, *Chairman*
James G. Baker
R. H. Bolt
Wallace R. Brode
Harvey Brooks
Dirk Brouwer
J. H. Elliott
Herbert A. Erf
N. S. Gingrich
S. A. Goudsmit
W. W. Havens, Jr.
W. V. Houston
Winston E. Kock
R. Bruce Lindsay
David L. MacAdam
H. Victor Neher
Leonard O. Olsen
C. J. Overbeck
Ray Pepinsky
S. L. Quimby
Ralph A. Sawyer
Francis W. Sears
Frederick Seitz
C. Guy Suits
Mary E. Warga
William R. Willets

ADMINISTRATION

Elmer Hutchisson
Director

Wallace Waterfall
Secretary and Treasurer

Henry A. Barton
Administrative Consultant

W. C. Kelly
Director of Education

Eugene H. Kone
Director of Public Relations

Hugh C. Wolfe
Director of Publications

Kathryn Setze
Assistant Treasurer

James E. Mills
Supervisor, Editorial Department

Sistina Greco
Circulation Manager

Edward Tober
Manager, Production and Distribution

Theodore Vorburger
Advertising Manager

Emily Wolf
Manager, Special Services

Editor
J. H. Crawford, Jr.

Assistant Editor
Ethel McMillan

Editorial Board

J. E. Goldman
J. L. Tuck
C. A. Wert
Herman A. Haus
C. Lester Hogan
R. S. Rivlin
Henry Hurwitz
James A. Krumhansl
C. P. Slichter

THE JOURNAL OF APPLIED PHYSICS is devoted to general physics and its applications to other sciences, to engineering, and to industry. Previous to 1937, this journal was called PHYSICS.

The JOURNAL OF APPLIED PHYSICS welcomes articles of two distinct kinds: (1) Descriptions of new results in experimental or theoretical physics which are of general interest to physicists. The author should explain his contribution in such a way that a physicist or engineer in another field of specialization can appreciate its objectives and essential features. (2) Critical reviews of particular areas of physics or surveys of extensive investigations at a single laboratory. Authors contemplating writing such should correspond with the Editor before they begin writing.

The JOURNAL OF APPLIED PHYSICS welcomes Letters to the Editor which are short [approximately four (4) typewritten pages] communications without abstracts. Timeliness, briefness, and degree of current importance of the subject matter will be of primary concern in the publication of Letters. Letters should not be looked upon as partial publication or announcement of more comprehensive work, but rather self-contained presentations in themselves.

Manuscripts should be submitted to the Editor, J. H. Crawford, Jr., Solid State Division, Oak Ridge National Laboratory, Oak Ridge, Tennessee. Authors should read the "Information for Contributors," facing page 1 of the January issue, before writing articles or letters. The *Style Manual* of the American Institute of Physics is also helpful to writers preparing manuscripts for journals published by the American Institute of Physics. It can be obtained for $1.00 from the American Institute of Physics, 335 East 45 Street, New York 17, New York.

Corrected proofs and all correspondence concerning papers in the process of publication should be addressed to the Supervisor, Editorial Department, American Institute of Physics, 335 East 45 Street, New York 17, New York.

Subscriptions, renewals, and orders for back numbers should be addressed to the American Institute of Physics, 335 East 45 Street, New York 17, New York.

Subscription Price	U.S. and Canada	Elsewhere
To members of member organizations of the American Institute of Physics and Affiliated Societies ..	$12.00	$13.00
To all others	14.00	16.00

Back Number Prices

Yearly back number rate when complete year is available: $17.00.
Single copies: $1.75 each (exception: March, 1958—$3.00 each).

Change of address: Allow at least six weeks' advance notice. Send both old and new addresses to the Circulation Department, American Institute of Physics, 335 East 45 Street, New York 17, New York. If possible, please include an address stencil imprint from the mailing envelope of a recent issue.

Advertising rates supplied on request. Orders, advertising copy, and cuts should be sent to the American Institute of Physics.

The Journal of Applied Physics is published monthly at Prince and Lemon Streets, Lancaster, Pennsylvania.
Second-class postage paid at Lancaster, Pa.

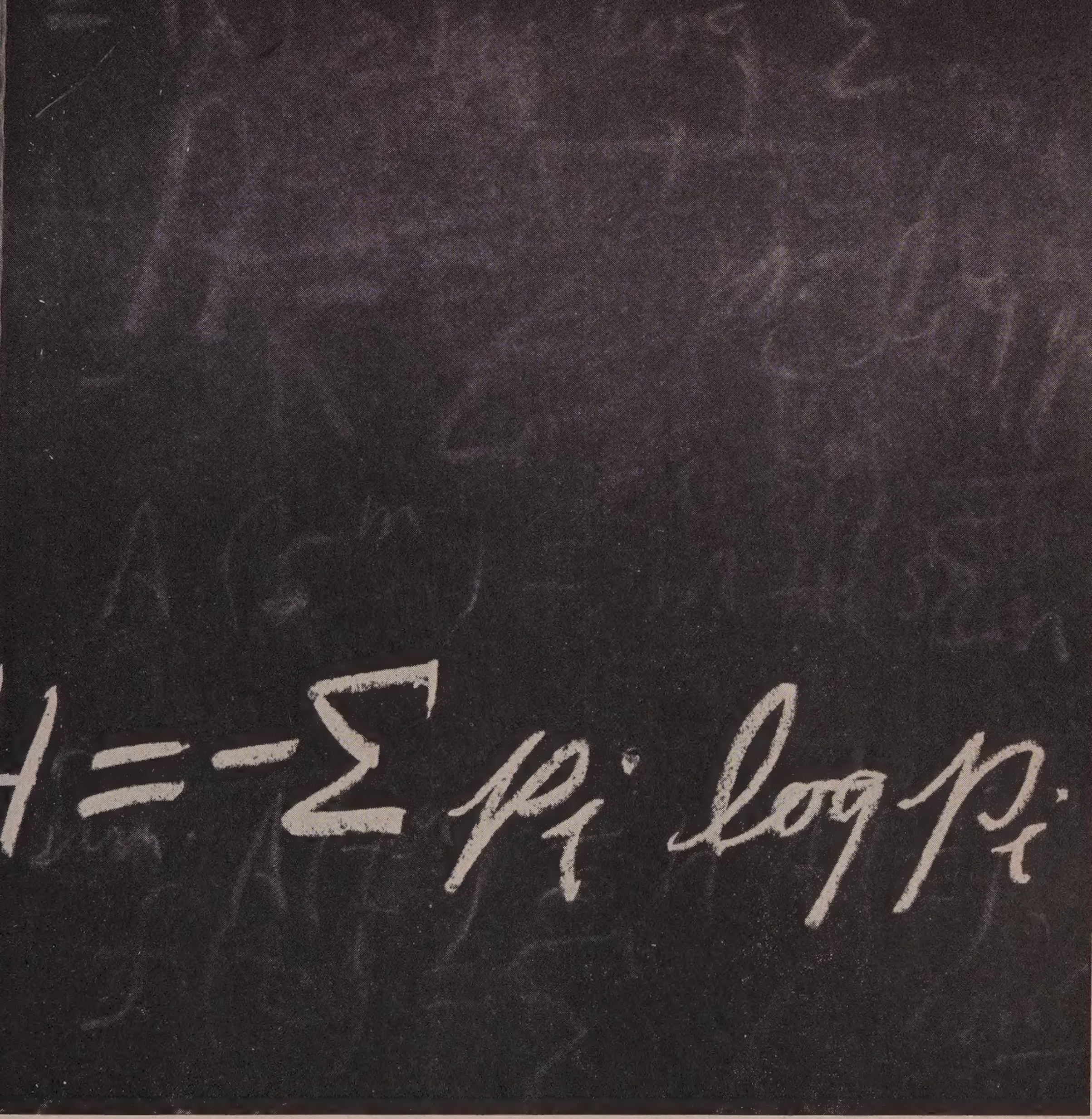

c formula from Information Theory . . . provides a measure of the amount of information in a particular type of message, such as TV . . . helps determine the frequency idth, for example, required to transmit the messages. Information Theory, pioneered at Bell Laboratories, guides the search for better communications systems.

ISCOVERY AT BELL TELEPHONE LABORATORIES

New knowledge comes in many forms. Sometimes it comes in a mathematical formula. Usually it comes after much thought and experiment and the fruitful interaction of different minds and abilities. Most often, too, a particular discovery is small. But many small discoveries have a way of leading to big advances at Bell Laboratories—advances like the transistor . . . or, more recently, the gaseous optical maser, forerunner of communications at optical frequencies. Opportunities for discovery are enhanced by the abilities of the scientists and engineers and the range of the facilities at Bell Laboratories, *world center of communications re-*

depth

The new Sperry Rand Research Center has been established to pursue a specific objective—the advancement of man's knowledge and understanding through basic research in the broad and diversified scientific fields that are of potential long-range interest to the many technical activities of the Sperry Rand Corporation.

To achieve this ambitious goal, many significant investigations must be pursued to great depths. Investigations in depth are vitally important to Sperry Rand in the following areas:

1. **Solid State Physics** including theoretical and experimental studies of magnetic, electrical, optical, chemical, and mechanical properties.
2. **Information Processing** including such areas as communication, information and coding theory; automatic control; modulation, generation and detection techniques; human factors.
3. **Plasma Physics** including electromagnetic wave interactions, reentry problems, propagation studies.
4. **Applied Mathematics** including probability and statistics, discrete mathematics, solid and fluid mechanics.
5. **Earth Sciences** including geophysics, physical oceanography, atmospheric physics, and special topics in Life Sciences.

At the present time professional openings are available to senior scientists with experience in:

- Semiconductor Physics
- Magnetic Resonance Phenomena
- Solid State Theory
- Physical Chemistry
- Communication Theory
- Signal Processing Theory & Application
- Automatic Control Theory
- Plasma Physics
- Wave Propagation
- Reentry Physics
- Stochastic Processes
- Game Theory
- Fluid & Solid Mechanics
- Operations Research
- Geophysics
- Oceanography
- Atmospheric Physics

Inquiries may be directed
in complete confidence to:
Mr. Frederick M. Swope, Jr.,
Sperry Rand Research Center,
North Road,
Sudbury, Massachusetts

an important
word
at the new

SPERRY RAND RESEARCH CENTER

SUDBURY, MASSACHUSETTS

NEW MEASUREMENT EFFICIENCY

WITH THIS TEKTRONIX DIGITAL READOUT OSCILLOSCOPE

DIGITAL READOUT
of time differences to
50 picoseconds.

DIGITAL READOUT
of pulse risetimes to
one-half nanosecond.

DIGITAL READOUT
of pulse amplitudes to
2 millivolts peak-to-peak.

TYPE 567

A Tektronix Readout Oscilloscope enables you to make precision measurements faster and easier—for simultaneously with the analog display on the 5-inch crt, you have a digital presentation on the automatic computing programmer.

u set the program *once* for all successive similar meas-
ents.

r each measurement, you merely read the up-to-4-digit
nal units of actual measurement.

dicators light to designate the readout status—whether
e preset-limit range, *below* it, or *above* it.

a typical application such as transistor-switching-time
urements, you can read directly such characteristics
e delay, rise, storage, and fall times; the total turn-on
urn-off times; the width of pulse A and pulse B; and
and amplitude between two selected points on either
th waveforms. You know immediately by the digital
ntation and indicator lights whether or not the item
d has met specifications.

achieve this faster and simpler approach to precision
urement, the Type 567 incorporates many features *new*
oscilloscope. In the automatic computing programmer,
xample, some of these new features include: positionable measurement-reference zones, automatic normalization, zone-intensity markers, automatic and manual start-timing and stop-timing systems, preset-limit selector and indicators, provision for external programming. These features—and others in the two sampling plug-in units and the oscilloscope itself—enable the new Type 567 to greatly increase your measurement proficiency.

On a production line, in a laboratory, or for sustained testing programs, the digital readout convenience of a Type 567 can speed-up and simplify measurement of pulse amplitudes and time increments between percentages of selected amplitude levels *on an absolute or relative basis.* In addition, you can also measure pulse amplitudes and time increments on differential signals between A and B inputs.

Type 567 Readout Oscilloscope (without plug-ins) . . . . . . $ 700

Plug-In Units include:

Type 3D1 Digital Unit (Automatic Computing Programmer) $2500
Type 3S76 Sampling Dual-Trace Unit $1100
Type 3T77 Sampling Sweep Unit . . . . $ 650

U.S. Sales Prices, f.o.b. Beaverton, Oregon

For complete information about the characteristics and capabilities of this new Digital Readout Oscilloscope, please call your Tektronix Field Engineer.

ktronix, Inc. *P. O. BOX 500 · BEAVERTON, OREGON / MItchell 4-0161 · TWX—BEAV 311 · Cable: TEKTRONIX*

ONIX FIELD OFFICES: Albuquerque, N. Mex. • Atlanta, Ga. • Baltimore (Towson) Md. • Boston (Lexington) Mass. • Buffalo, N.Y. • Chicago (Park Ridge) Ill. • Cleveland, Ohio • Dallas, Texas • Dayton, Ohio
Colo. • Detroit (Lathrup Village) Mich. • Endicott (Endwell) N.Y. • Greensboro, N.C. • Houston, Texas • Indianapolis, Ind. • Kansas City (Mission) Kan. • Los Angeles, Calif. Area (East Los Angeles
West Los Angeles) • Minneapolis, Minn. • Montreal, Quebec, Canada • New York City Area (Albertson, L.I., N.Y. • Stamford, Conn. • Union, N.J.) • Orlando, Fla. • Philadelphia, Pa. • Phoenix (Scottsdale) Ariz.
Oreg. • Poughkeepsie, N.Y. • San Diego, Calif. • San Francisco, Calif. Area (Lafayette, Palo Alto) • Seattle, Wash. • Syracuse, N.Y. • Toronto (Willowdale) Ont., Canada • Washington, D.C. (Annandale, Va.).

ERING REPRESENTATIVES: Kentron Hawaii Ltd., Honolulu, Hawaii. Tektronix is represented in twenty-five overseas countries by qualified engineering organizations.
and African countries, the countries of Lebanon and Turkey, please contact TEKTRONIX INTERNATIONAL A.G., Terrassenweg 1A, Zug, Switzerland, for the name of your local engineering representative.
rseas areas, please write or cable directly to Tektronix, Inc., International Marketing Department, P. O. Box 500, Beaverton, Oregon, U.S.A. Cable: TEKTRONIX.

Career Opportunities in

SEMICONDUCTOR TECHNOLOGIES

IBM THOMAS J. WATSON RESEARCH CENTER

The new IBM Thomas J. Watson Research Center in Yorktown, N.Y. is undertaking important new long-range projects requiring scientists and engineers with experience in, or relating to, various aspects of semiconductor research. Research projects under way are directed toward purely scientific goals . . . as well as toward developing technology for advanced information handling systems.

SEMICONDUCTOR COMPOUND CHEMISTRY

Several openings exist for Physical and Inorganic Chemists to conduct research on the preparation and purification of materials, and to study their physical properties. Experience is highly desirable, but not necessary.

SEMICONDUCTOR VAPOR GROWTH

Applicants should be familiar with studies of vapor growth reactions in general as well as vapor growth junction technologies. An advanced degree in Physical Chemistry, Metallurgy or Physics is desirable, but a B.S. with a strong background in related technology will be considered.

SEMICONDUCTOR CIRCUITS

The position involves the proposing, experimental exploration, and evaluation of circuits which have a high degree of probability of lending themselves to fabrication into integrated circuitry by means of advanced semiconductor technologies including expitaxial crystal growth from the vapor phase. This work will be done in close cooperation with device fabrication scientists. The ultimate aims of this activity include consideration of integrated or preconnected computer circuits wherein transmission lines are treated as integral parts. An advanced degree or equivalent in Electrical Engineering or Physics is desirable. We prefer experience in circuits using semiconductor devices as applied to large high-speed computers.

SEMICONDUCTOR CRYSTAL GROWTH

This is an outstanding opportunity for a person with an advanced degree or equivalent experience in Physical Metallurgy or Chemistry. The person who can fill this position must be able to take charge of a semiconductor crystal growing activity and carry out a program of research on related problems. Experience should include the preparation of solid state materials and a background in semiconductor physics.

The Thomas J. Watson Research Center at Yorktown, N.Y., is located in pleasant, rural Westchester County countryside, just 35 miles from New York City. The Research Center was designed to provide the best possible working environment for scientists and engineers engaged in advanced research studies. The location provides excellent schools and housing. IBM offers a fully paid benefits program. All qualified applicants will receive consideration for employment without regard to race, creed, color, or national origin.

Please write, outlining your education and experience to:

Mr. J. B. Farrington, Dept. 579M
Thomas J. Watson Research Center
P. O. Box 218
Yorktown Heights, New York

IBM®

INTERNATIONAL BUSINESS MACHINES CORPORATION

ENGINEERS, SCIENTISTS

THE SEARCH FOR NEW AND BETTER METHODS OF MEASUREMENT...

..the continuing challenge at Keuffel & Esser Company Optics and Metrology Division

om pre-history to the present and on into the future, man has sought better
d more precise methods of measurement. Each advance in metrology—
e science of measurement—has brought corresponding gains in other
chnologies—chemistry, metallurgy, electronics, physics, space/aeronautics,
chitecture, mechanics.

oday the bold technological dreams of yesterday are becoming realities. The
ptics and Metrology Division of Keuffel and Esser Company has made
d will continue to make important contributions to these achievements by
eeting the growing metrological needs of our scientific age.

MMEDIATE OPENINGS NOW EXIST FOR:

TICAL ENGINEERS
ould possess a B.S. or M.S. in Physics or
gineering with a minimum of 5 years'
perience in optics. A background in elec-
nics will be most helpful.

CHANICAL ENGINEER (BS, MS, Ph.D)
r design of specialized engineering
ipment and application of theoretical
nciples and fundamental physical and
mical properties of material to equip-
nt fabrication. Will require familiarity
h properties of materials, metal treat-
nts, die casting technique.

PHYSICIST
B.S. or graduate degree with a major in optics. Work involves research and development on optical systems, instruments, components, optical films, reticles and electronic-optical instruments.

ELECTRONICS ENGINEER (BSEE)
Will assist with circuit design and related work on newly developed instruments.

MATHEMATICIAN (BS or MS in Math)
Programming experience desirable.

Qualified applicants can arrange a convenient personal discussion by directing their inquiries in confidence to: Mr. R. W. Romberger

BLISHED 1867

KEUFFEL & ESSER CO.
300 ADAMS STREET, HOBOKEN, NEW JERSEY
An Equal Opportunity Employer

NEW KEITHLEY AC AMPLIFIER

can increase scope sensitivity 1000 times!

The Keithley Model 103 gives you the best attainable signal-to-noise ratio for source impedances from 3000 ohms to over 10 megohms. (The equivalent input noise resistance on the low noise position is only 3 k ohms.) Bandwidth of .1 cps to 100 kc covers a wide range of uses; eleven high and low frequency cuts permit restricted bandwidths for minimum noise.

Applications include Hall Effect studies, bridge null detection, and semi-conductor investigations, as well as such biophysical applications as recording nerve action potentials.

The usefulness of the Model 103 is enhanced by its versatility:

NOISE can be improved by changing input impedance with a "Normal" and "Low Noise" switch. Chart below indicates noise levels with input shorted, gain 1000x, 10 cps to indicated cutoff:

BANDWIDTH can be selected by using 11 high and low frequency cutoffs between .1 cps and 100 kc.

INPUT IMPEDANCE in the "Normal" mode is 10 megohms; in the "Low Noise" mode, 100 k ohms.

AMPLIFIER GAIN may be set at either 100 or 1000 and adjusted to precise values.

INPUT CONNECTIONS can be made single-ended or differential.

DIFFERENTIAL REJECTION is at least 80 db permitting increased signal-to-noise ratios in many applications.

POWER—from batteries or the Keithley Model 1031, a separate, solid state power supply with noise characteristics equivalent to batteries.

PRICES: Model 103, **$245;** rack, **$255**
1031 Power Supply, **$245;** rack, **$255**

Frequency of high cutoff point	Maximum noise, microvolts RMS referred to input	
	Normal (10 meg impedance)	Low Noise (100 k impedance)
100 kc	3.0	1.9
30 kc	1.9	1.1
10 kc	1.4	0.8
3 kc	0.9	0.6
1 kc	0.7	0.4
300 cps	0.5	0.3
100 cps	0.4	0.25

This oscillograph shows a 2 kc square wave of 5 microvolts peak-to-peak amplitude at input with the amplifier in "Low Noise" position. Horizontal calibration equals 200 μv per division; vertical equals 2 μv per division. Low cut is 10 cps, high cut 1 kc. The unusually low noise levels in the 103 are achieved through the use of ceramic tubes in cascode circuitry.

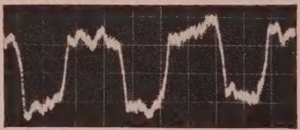

send for complete specifications in latest engineering note . . .

KEITHLEY INSTRUMENTS
12415 EUCLID AVENUE
CLEVELAND 6, OHIO

electrometers • micro-microammeters • microvoltmeters • milliohmmeters

Original painting by Louise Ganthiers, Taos, New Mexico

FROM DIVERSITY COMES UNITY

Diverse disciplines, approaches, and methods, interacting in an atmosphere of freedom, expand scientific knowledge.

Qualified applicants are invited to send resumes to: Director of Personnel, Division 61-108

los alamos
scientific laboratory
OF THE UNIVERSITY OF CALIFORNIA
LOS ALAMOS, NEW MEXICO

All qualified applicants will receive consideration for employment without regard to race, creed, color, or national origin. U.S. citizenship required.

THERE IS A BIG DIFFERENCE

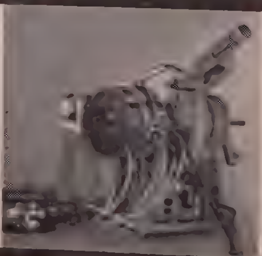

Norelco high temperature, high vacuum diffractometer attachment is available for all diffractometers including competitive makes.

Automatic recording of the diffraction spectr is achieved by the addition of a wide range go ometer and new electronic circuit panel to basic diffraction unit.

..in Norelco®

nalytical Instrumentation*

re have been obvious visual changes in the working tools of X-ray diffractometry and X-ray spectrog- hy – a science which we at Philips Electronic Instruments know best. These Norelco product nges are based on years of experience accumulated in our own research and in the field. As a result, ay instrumentation for elemental analyses and structure determinations is greatly facilitated by ening investigative areas while producing data faster and easier.

what about the physical differences? For one thing, the electronic circuit panel is top-to-bottom with a linear/log scaler, double power supply with variable output for detectors operating on erent voltages up to 3 KV. There is a time and fixed count operations feature also.

high-intensity X-ray tubes can now be loaded to double capacity up to 2000 watts. Constant ential high tension transformers now lengthen tube life while providing greater precision in any en time. Any unit in operation can be updated because the constant potential feature is also ilable in kit form for any existing transformer in the field.

new high-temperature furnace operates at temperatures over 2000° C with tantalum boats and in cryogenic area – down to minus 185° C. The furnace is adaptable to every Norelco wide-range iometer made.

re you have a quick, boiled-down version of usable news . . . news you can put to work . . . updating s from Norelco for years of dependable, expandable, top-quality performance.

* Incidentally, there are pronounced differences in all X-ray analytical instrumentation made by Philips. These differences are manifest in "know-how" and quality of apparatus designed from-the-ground-up for specific X-ray analytical work.

HILIPS
ECTRONIC
STRUMENTS
Norelco®

If you would like details about this news, ask your Philips Electronics dealer for your copy of the new Norelco X-ray Instrumentation Brochure or write today to:

PHILIPS ELECTRONIC INSTRUMENTS
A Division of Philips Electronics and Pharmaceutical Industries Corp.
750 South Fulton Avenue, Mount Vernon, N. Y.
In Canada: Research & Control Instruments • Philips Electronics Industries Ltd. • 116 Vanderhoof Ave. • Leaside, Toronto 17, Ont.

ANNOUNCING:

Appointments to the Aerophysics Staff of General Electric's Missile & Space Vehicle Dept.

Now part of MSVD's new,
multi-million dollar
Space Technology Center
near Valley Forge Park

The Space Sciences Laboratory of the Missile & Space Vehicle Department is a research-oriented organization probing the sciences related to extra atmospheric vehicle and advanced development. Currently a number of opportunities are available to join this highly qualified group of scientists in the superbly equipped, new Space Technology Center, 17 miles from Philadelphia.

THEORETICAL & EXPERIMENTAL PLASMA INVESTIGATIONS

Opening for Physicist with PhD degree or equivalent experience in physics or any of the related fields of electro-magnetic phenomena or gaseous electronics. These men will perform theoretical and experimental investigations associated with the generation and diagnosis of plasmas. And, he will be offered the opportunity to study the interactions of plasmas with magnetic fields and microwave radiation.

SPACE ENVIRONMENT RESEARCH

Meteorologists and geophysicists, are required for carrying out both basic and applied research on the physical properties of the earth's and other planetary atmospheres, the Van Allen radiation belts, solar flares, meteorological satellites, and other problems of space environment and exploration. PhD degree required. Both experimentalists and theoreticians can contribute in the investigations being conducted and planned in this expanding operation.

THEORETICAL GAS DYNAMICS

Scientists with PhD degree or equivalent in aerodynamics, gas dynamics, or the physics of fluids at high temperature and high altitude regimes are sought. These scientists will perform theoretical investigations of the following areas of gas dynamics: magnetogasdynamics, nonequilibrium effects in gas dynamics at high altitudes, mass transfer and heat transfer boundary layer theory and flow field analysis.

MAGNETOHYDRODYNAMIC POWER GENERATION

Experimental and theoretical physicist and research engineer to perform fundamental research on magnetogasdynamics in conjunction with direct energy conversion. Problems include: kinetic theory and statistical plasma mechanics / electron physics and ionization phenomena / plasma measurements and diagnostics / magnetogasdynamic flows / boundary layers in plasmas / magnetohydrodynamic power generation / systems study and applications. PhD or equivalent in physics, aerodynamics, fluid mechanics, or combustion is required.

Send a brief summary of your background to:

Mr. F. J. Wendt, Div. 447-L, Missile & Space Vehicle Department
General Electric Company, 3198 Chestnut Street, Philadelphia, Pa.

All qualified applicants will continue to receive consideration for employment without regard to race, creed, color or national origin.

GENERAL ELECTRIC

C TYPE MAGNETS in a wide range of sizes to meet your design needs in ★ Transverse Field Isolators ★ Differential Phase Shifters ★ Duplexers

Arnold C-type Alnico Magnets are available in a wide selection of gap densities ranging from 1,000 to over 7,500 gausses. There are six different basic configurations with a wide range of stock sizes in each group.

The over-all size and gap density requirements of many prototype designs can be met with stock sizes of Arnold C Magnets, or readily supplied in production quantities.

When used in transverse field isolators, Arnold C Magnets supply the magnetizing field to bias the ferrite into the egion of resonance, thus preventing interaction between microwave networks and isolating the receiver from the ransmitter. These magnets are also used in differential phase shifters and duplexers, and Arnold is prepared to design and supply tubular magnets to provide axial fields n circular wave guides.

A feature of all Arnold C Magnets is the excellent field uniformity along the length of the magnet. Versatility in design may be realized by using multiple lengths of the same size magnet stacked to accomplish the needs of your magnetic structure.

Let us work with you on any requirement for permanent magnets, tape cores or powder cores. ● For information on Arnold C Magnets, write for Bulletin PM-115. Address *The Arnold Engineering Company, Marengo, Illinois.*

ADDRESS DEPT. JA-12

7428 B

ARNOLD
SPECIALISTS in MAGNETIC MATERIALS

BRANCH OFFICES and REPRESENTATIVES in PRINCIPAL CITIES
Find them FAST in the YELLOW PAGES

Sames

ELECTROSTATIC GENERATORS

Utilized Worldwide for Applications in:
Nuclear Physics, Insulation Testing, Electron Microscopy, Mineral Separation, Electrostatic Precipitation

Provide High-Voltage Power Supplies in a Wide Range of Models...
Featuring:

- Essentially pure DC output
- Voltages to 600 KV, infinitely variable
- Current to 14 ma
- Medium or High Stability, to 0.1% hr. drift
- Easily adjustable, closely regulated output voltages to .001%
- Simplified maintenance, long life
- Extreme safety: Low output capacitance, Minimal short-circuit & overload currents, Remote adjustment & shut down

Write now for new Catalog 100 covering the complete line of Sames Electrostatic Generators.

SAMES

Sames

Dept. 312, 30 Broad St., New York 4, N.Y.

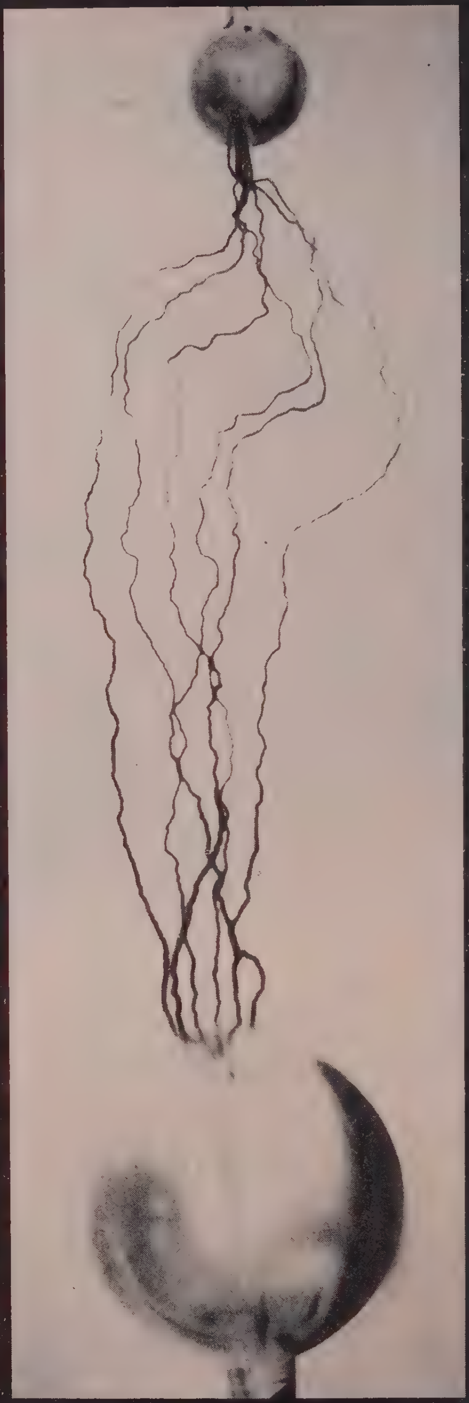

THE FIRST SUCCESSFUL MICROWAVE SOLID-STATE TRANSMITTER
WITH POWER CAPABILITY ADEQUATE FOR SATELLITE APPLICATION
A DEVELOPMENT BY THE SCIENTISTS AT AMHERST LABORATORIES

The objective assigned to the Amherst Laboratories' scientists was this: Advance the state-of-the-art of microwave space vehicle transmitters by increasing performance, reducing size, reducing weight and increasing reliability. The time was June 1960. One year later, these objectives had been reached *and exceeded by a wide margin.* The result: a solid-state transmitter applicable for satellite use, operating within the S-band, about half the size of a carton of cigarettes, and with a life expectancy of two years. This significant achievement is representative of many challenges currently being met by the scientists at Amherst Laboratories.

PAPER ON REQUEST: The paper which explains the new techniques employed in development of the new microwave Solid-State Transmitter authored by W. J. Maciag is available to engineers and scientists on request. Write for the paper entitled "Solid State, S-band Single Side Band Suppressed Carrier Transmitter"

AMHERST LABORATORIES • 1183 WEHRLE DRIVE • WILLIAMSVILLE, NEW YORK
AN EQUAL OPPORTUNITY EMPLOYER

SYLVANIA **ELECTRONIC SYSTEMS**
Government Systems Management
for ***GENERAL TELEPHONE & ELECTRONICS***

GENERAL SYSTEM

X-Ray Diffraction Equipment by RIGAKU

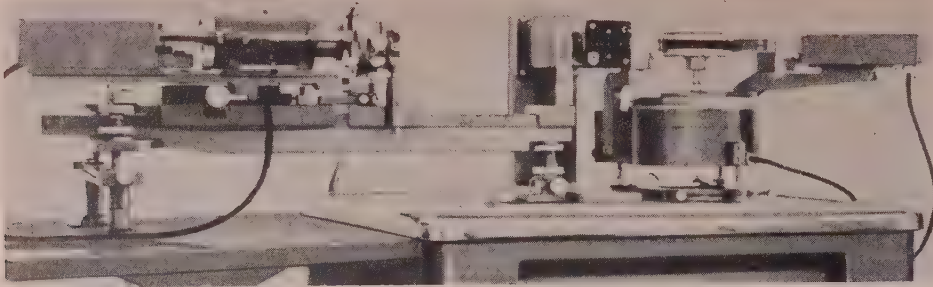

Shown above is the Rigaku Low Angle Scattering Goniometer, one of many fine instruments designed and built by Rigaku Ltd., pioneers in the x-ray diffraction equipment field since 1923. The Low Angle Scattering Goniometer has been designed for use with all standard x-ray diffraction units, to study the size, form, orientation and aggregate condition of fine individual particles os a sub stance. It is also used in studying the crystal periods o extra-long periodic substances, by either automatic recording or photographic techniques. It is useful in th study of organic and inorganic colloids, protein molecules, fiber micelles, resins, catalysts, clays, metals, etc

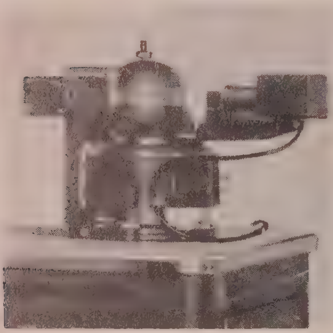

LEFT The Rigaku High Temperature Specimen Holder is used for investigations, at high temperatures, of solubility changes as well as structural changes in the test sample. This precision instrument maintains a temperature gradient of plus or minus 5% at temperatures up to 1500°C, in vacuum or with atmospheres such as air or inert gas.

RIGHT The Rigaku Continuous High Temperature Camera has been designed to make a continuous record of x-ray diffraction patterns of crystal specimens, in series, on film. The camera has a unique ability to capture ever-changing x-ray diffraction patterns, and features a high vacuum system, high maximum temperature and simplified operation.

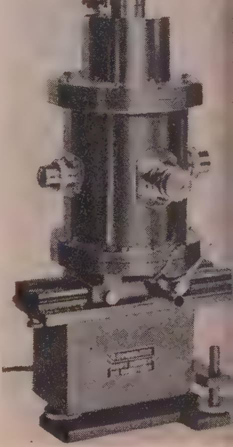

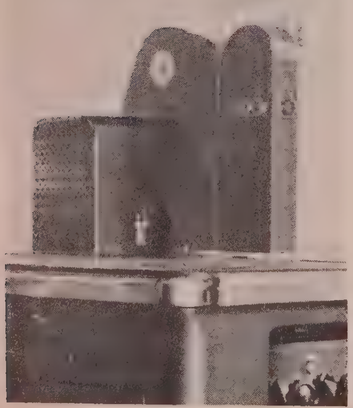

LEFT The Rigaku Rota Unit provides the high power required for rapid analyses. Current of 100 mA at 50 KV are available from various target materials. The water cooled rotating anode is positively sealed to preclude water leaking into the vacuum. This highly reliable research tool can be used with solids, liquids or gases.

RIGHT The Rigaku Low Temperature Specimen Holder is used to investigate, at low temperatures, solubility and crystal structure changes in the specimen under survey. The temperature of the specimen is lowered to −190°C, using liquid nitrogen as the refrigerant. The investigation can be made with the specimen in an atmosphere of air, inert gas, or a vacuum.

BELOW The Rigaku Microflex is a Microfocus X-ray Diffraction Unit, designed to provide a research tool for the analysis of minute areas of a crystal, as well as the crystal structure of micro substances in the specimen, etc. The versatile Microflex can be used as either a projection or reflection type instrument, depending on the specimen being analyzed.

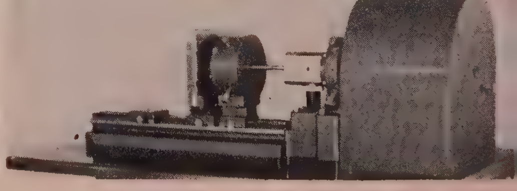

Call or write for more information at the most convenient of the three addresses shown below.

ERB & GRAY SCIENTIFIC, Inc.

Exclusive Rigaku distributors for the United States

5927 Riverdale Avenue,
New York 71, N. Y.

1103 Westgate Avenue,
Oak Park, Ill.

854 South Figueroa Street, Los Angeles 17, California

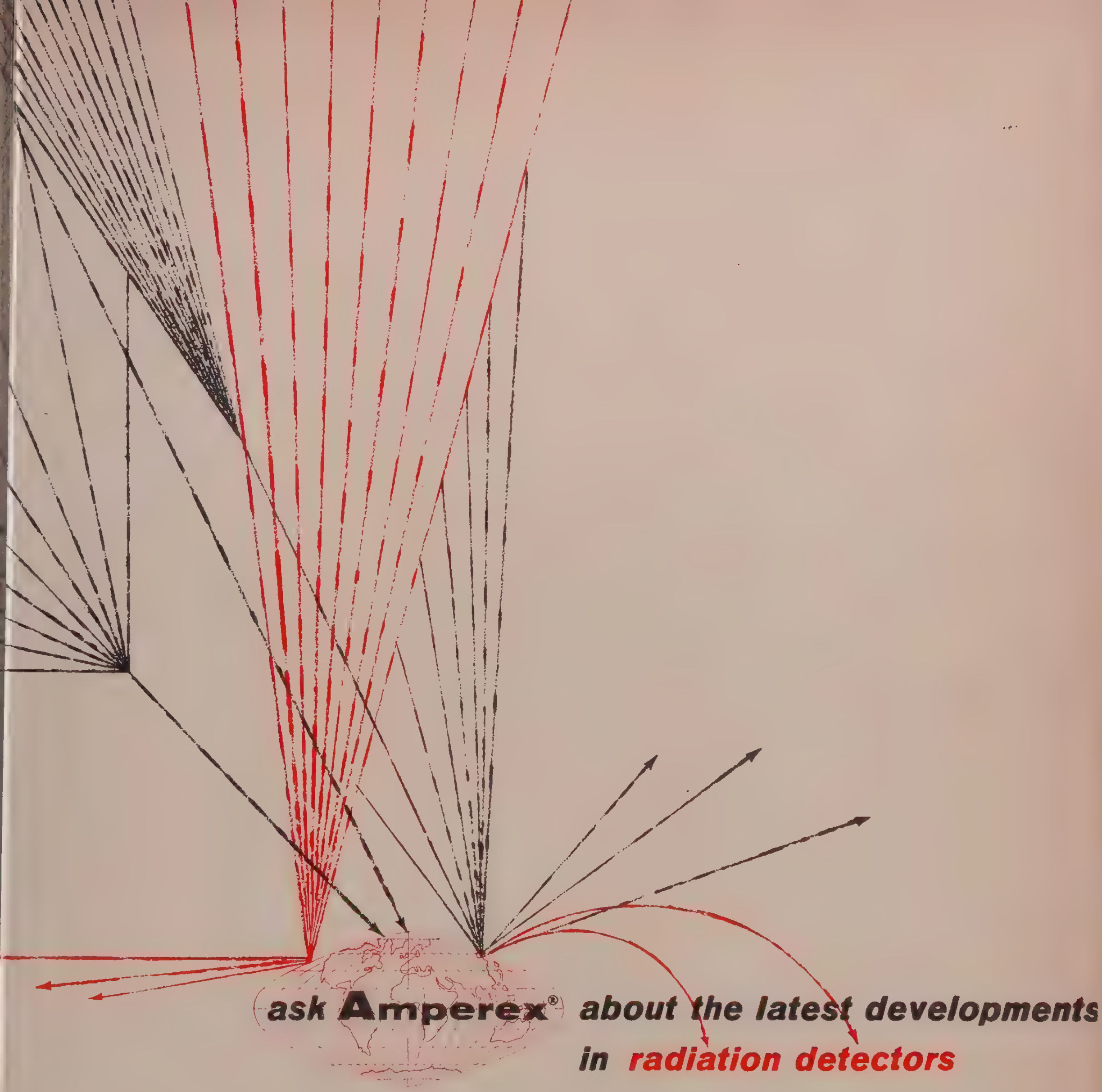

ask Amperex® about the latest developments in radiation detectors

Continual Research and Development of unique and specialized components for nuclear applications . . . close contact with laboratory and field organizations... development of new and improved manufacturing techniques for maximum uniformity, reliability and economy—these are the factors that make Amperex the nuclear industry's unrivaled source for all types of radiation detectors, electron tubes and semiconductors as well as other specialized components.

eutron detectors

3 ***PROPORTIONAL COUNTERS:*** excel-
t pulse height resolution characteristics
rugged construction utilizing ceramic-
metal seals and heliarc welding tech-
ues ... stainless steel and aluminum
hodes. ***FISSION COUNTERS:*** excellent
crimination between neutron and alpha
ticles...all-aluminum construction util-
ng heliarc welding...design versatility.

geiger tubes

Low operating voltage...infinite life, halogen quenched...but with the same plateau characteristics and detection efficiencies as short-lived organic quenched types. Plateau lengths of several hundred volts with slopes in the order of 2%/100V... large pulses...electrical and mechanical ruggedness...excellent reproducibility. Ideally suited for transistorized circuitry.

photomultipliers

Types 56 AVP and 58 AVP, already famed in high energy physics research. Unrivaled for time resolution characteristics ... low transit time fluctuations ... fast rise time ... extreme uniformity ... minimum guaranteed gain 10^8. Unquestioned superiority for fast coincidence counting, Cerenkov radiation, etc. Other types for low noise and good energy resolution characteristics.

d ask Amperex about flow and sealed proportional counters for alpha particles and low energy gamma and X-rays.

EREX ELECTRONIC CORPORATION, Nuclear Products Department, **230 Duffy Avenue, Hicksville, L. I., N.**

ada: Philips Electronics Industries, Ltd., Tube, Semiconductor and Components Departments, 116 Vanderhoof Avenue, Toronto 17, Ontario

Now 1 x 10^{-10} mm Hg
from
ILIKON CORPORATION

Ilikon's new metal ULTRAHIGH VACUUM CHAMBERS are the only complete systems available today that can reliably produce and maintain pressures as low as 1×10^{-10} mm Hg.

Designed specifically for advanced space simulation, vapor deposition and materials research applications. Literature on request.

ILIKON
NATICK INDUSTRIAL CENTRE
Natick, Mass. • Tel. CEdar 5-8220

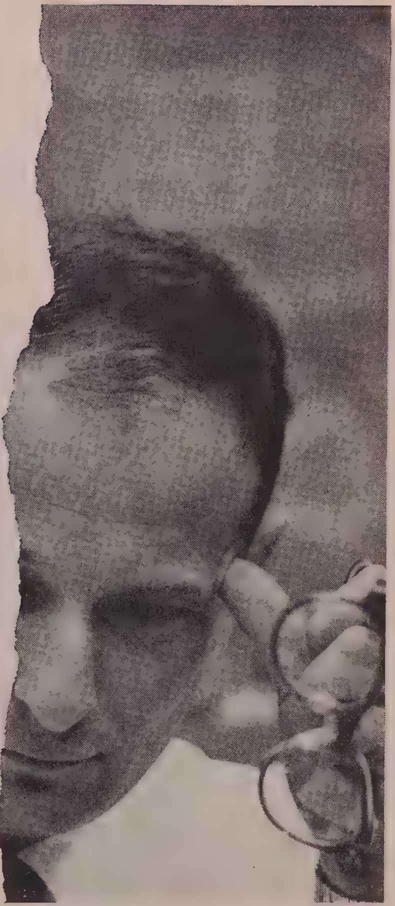

To the physicist who's realizing only part of his potential

Ampex can make your job picture complete. For at Ampex, you'll be given free reign to think up theories of your own. And see them come to life in the world's most advanced magnetic tape recorders. You'll have room to experiment. (And plenty of room to grow, for research has always played a major role at Ampex.) You'll be working in the finest climate and cultural environment anywhere: Redwood City, California — near Stanford, near U. C., near glittering San Francisco. If you have a PhD in Physics and up to 8 years experience leading theoretical and experimental studies in: magnetic materials, thin films, new storage media, fine particles, solid state materials or electron optics, write us for more details. Or simply send your resume today to: Mr. John I. Doolittle, Office of Scientific Placement, Ampex Corporation, 2406 Bay Road in Redwood City, California.

AMPEX

Welch

LARGE 12-INCH SCREEN

LECTURE-TABLE OSCILLOSCOPE

For all customary classroom demonstrations

New!

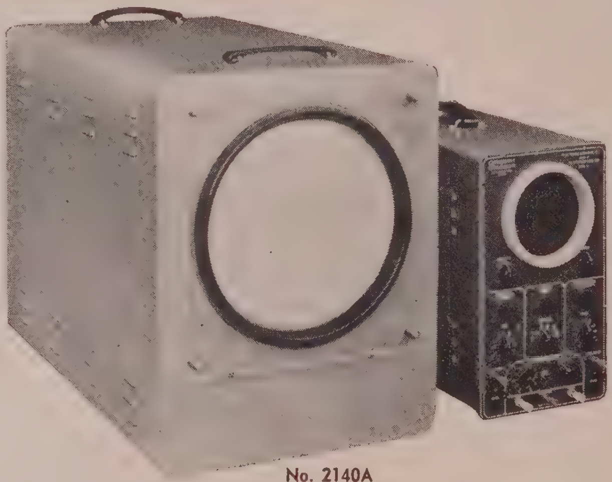

Patent pending

No. 2140A

Compare it with the standard 5-inch scope you've been using up to now!

12-inch screen faces class.

3-inch monitor screen and all controls on rear panel for instructor's convenience.

Controls operate 12-inch and 3-inch tube simultaneously.

Controls and operating characteristics comparable to that of average 5-inch oscilloscope.

All components chosen with generous ratings to insure reliability.

Net weight: 80 pounds.

Cat. No. 2140A Each, $390.00

Write for complete circular

THE WELCH SCIENTIFIC COMPANY
ESTABLISHED 1880
1515 Sedgwick Street, Dept. C-1 Chicago 10, Illinois

Journal
of
Applied Physics

Volume 32, Number 12 December, 1961

Electron Microscope Investigation on the Nature of Tracks of Fission Products in Mica*

Guido Bonfiglioli, Andrea Ferro, and Adriana Mojoni
Istituto Elettrotecnico Nazionale Galileo Ferraris, Torino, Italy

(Received May 22, 1961; revised manuscript received July 21, 1961)

Specimens of biotite, muscovite, artificial fluorophlogopite, and muscovite annealed at 900°C were examined using an electron microscope after having been covered with a uranium layer and irradiated in a reactor. Tracks due to fission products appeared on every specimen except biotite, and the respective diameters were put into correspondence with the resistance of the various micas to thermal decomposition. The tracks were larger in muscovite (240 A), thinner in fluorophlogopite (150 A), and still more in dehydrated muscovite (115 A). The writers believe that the mechanism of damage has its origin in the heat released by the heavy ionizing particles. Peculiar recovery effects were often observed.

1. INTRODUCTION

THE electron microscope is the most suitable means to obtain direct information on the defects produced by fast particles irradiation on solids. Recent work on metals bombarded with fast neutrons has been performed by Hirsch[1] and collaborators, on graphite by Bollman,[2] on fission tracks in mica by Silk and Barnes,[3] and on evaporated uranium oxide by Noggle and Stigler.[4] Unpublished work[5] on tracks of fission fragments in muscovite performed through the same technique of Silk and Barnes had led the writers to the view that such tracks are essentially caused by thermal effects.

However, the mechanism of production of the observed tracks did not appear to be clarified completely, and it seemed that further studies dealing with different materials would be worthwhile. In particular from this viewpoint, materials with very similar crystal structures, but having different thermal decomposition points, look very suitable.

2. EXPERIMENTAL

The materials chosen were biotite, muscovite, artificial fluorophlogopite, and muscovite which had been dehydrated by annealing one hour at 900°C.

The crystal structures of these micas are very similar. All are monoclinic and can be easily cleaved along the basal plane into extremely thin sheets.

However, they differ widely as to their resistance to thermal decomposition. Biotite loses crystallization water at about 500°C; muscovite does the same at 750°C, and fluorophlogopite does not decompose up to 1200°C. Muscovite dehydrated at 900°C decomposes further only at about 1400°C, where vitreous silicates are formed. In addition, at about 1100°C, some Al_2O_3 may be formed by prolonged annealing.[6]

Composite sandwiches of the micas and of natural uranium evaporated on high purity Al foils were prepared.[3] Micas were 30 μ thick, which corresponds roughly to the range of the fission fragments. A first series of specimens were irradiated in the swimming pool reactor of CENG (Grenoble, France) with an integrated flux of $1.1.10^{15}$ thermal neutrons/cm^2 and a second series in the swimming pool reactor of SORIN Corporation (Saluggia, Italy), with an almost identical flux.

A few hours after irradiation, the specimens were put

---

* The research reported in this paper has been sponsored by the Air Force Office of Scientific Research of the Air Research and Development Command, U. S. Air Force.

[1] P. B. Hirsch and J. Silcox, Phil. Mag. 4, 1356 (1959).

[2] W. Bollman, Phil. Mag. 5, 621 (1960).

[3] E. C. H. Silk and R. S. Barnes, Phil. Mag. 4, 970 (1959).

[4] T. S. Noggle and J. O. Stigler, J. Appl. Phys. 31, 2199 (1960). We thankfully acknowledge the kindness of these authors, who et us see their paper prior to publication.

[5] G. Bonfiglioli, A. Ferro, and A. Mojoni, Final Report of the ARDC (U. S. A. F.) March, 1960.

[6] Cf. R. Roy, J. Am. Chem. Soc. 32, 202 (1949); also W. Brindley, *X-ray Identification of Structure of Clay* (Miner Society, London, 1951).

Copyright © 1961 by the American Institute of Physics.

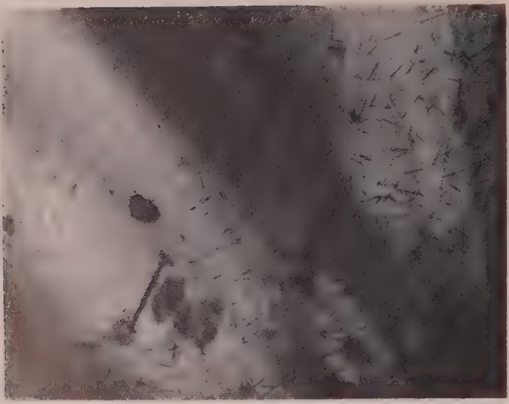

FIG. 1. Fission tracks in muscovite (virgin); (magnification: 15 000 ×).

in a liquid nitrogen bath, where they were kept until observation (that is, some weeks at most). For the electron microscope examination the specimens were thinned by repeated cleavage until transparent. The final thickness, checked by shadow-casting, were between 1000 and 2000 A. All the pictures considered here were made with an Hitachi microscope (HU 11).[7] Over 400 pictures of different specimens were taken and the most significant ones are reproduced in Figs. 1, 2, and 3 (respectively: virgin muscovite, annealed muscovite, fluorophlogopite).

The magnification was carefully checked several times each day by a diffraction grating replica; the reproducibility—which is of primary concern in this work—was definitely better than 5%, even though the accuracy in the absolute calibration cannot be assumed to be as good as this. The electron magnification was 20 000.

To avoid excessive heating the pictures were taken with very low illumination and long time exposures, unless otherwise desired.

3. TRACK WIDTHS

The point of main concern was the measurement of the diameter of the tracks. In fact, we already suggested in our preliminary report[5] that tracks could represent thermal spikes caused by heat generated by the intense ionization in the wake of the fission fragments. Different interpretations have been suggested by Silk and Barnes,[3] such as Rutherford collisions or direct ionization effects.

More recently and independently, thermal spikes have also been taken into consideration by Noggle and Stigler[4] to account for the observed diameters of the tracks in irradiated uranium oxide. The sizes of the tracks observed in our experiments can rather well be accounted for on these grounds.

As is well known, viewing crystalline specimens with suitable objective apertures, we obtain local contrast (diffraction contrast) through local differences in the intensity of the Bragg diffracted beams. These considerations apply, for instance, to the observation of dislocations, whose strain field distorts the lattice. In the case of a thermal spike, the situation should be rather similar; in particular with mica, we think that the wake of the particle should consist of material which has been thermally altered and which therefore has a crystalline structure different from the adjacent region.

As a consequence, for limited portions of the range, the image to be expected—at least in a densely packed crystal—would be that of a cylinder, with a strong contrast in respect to the surroundings, its diameter being close to the actual diameter of the altered region.

Actually, in an open structure like mica, it cannot be surely stated that the altered region is cylindrical, since sensible effects of anisotropicity in the thermal diffusion could have occurred. Nevertheless, if we are only aiming at a rough evaluation, we may speak of the "characteristic dimension" of the altered region as of a diameter. This diameter can be calculated approximately from the stopping power of the fission fragments, taking into account average values of the various quantities involved.[8]

The data quoted show that the energy of the particle is, almost along its whole path, far in excess of the critical energy for prevailing displacement production

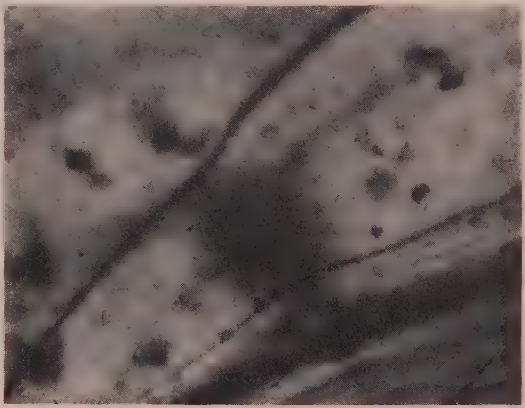

FIG. 2. Fission tracks in muscovite annealed (dehydrated) 1 hr at 900°C; (magnification: 15 000 ×).

---

[7] The examinations referred to in reference 5 were made with an old Siemens instrument. In addition to a great improvement of the resolving power, the presence of a double condenser strongly reduced heating.

[8] The average atomic weight of a typical mica is 20, its density 2.8 g/cm^3, its average atomic number 10. The mean value of the mass of a fission fragment is 117 and the mean initial energy about 78 Mev; hence its velocity is about 10^9 cm/sec. Accordingly, the particle is heavily ionized, with an initial charge of about $18e$ [A. H. Cottrell, Met. Rev. **1**, 479 (1956)]. The range of such a typical fragment in a typical mica can be estimated, from the data in argon [N. O. Larsen, Danske Videnskab. Selskab, Matt.-fys. Medd. **25**, 11 (1949); reproduced in Progr. Nuclear Phys. **2**, 146 (1952)] to be around 21 μ.

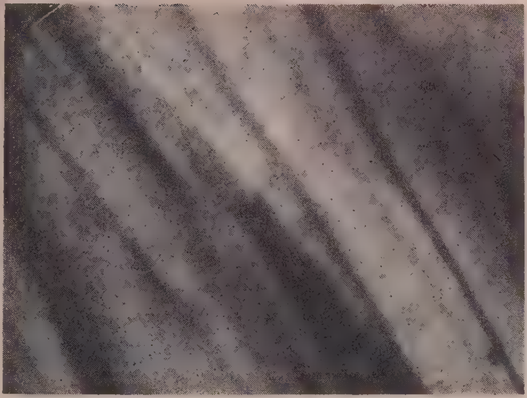

FIG. 3. Fission tracks in (artificial) fluorophlogopite; (magnification: 15 000 ×).

(cf. reference 10) (here less than 100 kev). The overwhelming majority of this energy is therefore spent in ionization. Of course in this order of approximation the energy lost per unit length in various micas can be considered the same—say 370 ev/A—the variation along the path being far greater in the same specimen.

Now, the diameter of a thermal spike which is assumed to be cylindrical can be easily evaluated, considering that the region where the energy is first released as ionization has a diameter which is small compared to that of the tracks.

Given a certain "critical temperature," let us call it T_c, it is easy to show that a cylinder of radius r exists, which marks the boundary between an external region which never reaches temperatures higher than T_c, and an internal region which at some instant is heated above T_c. This radius is

$$r=2e^{-\frac{1}{2}}(Q/4cT_c)^{\frac{1}{2}},$$

where Q stands for the heat released per unit length and c for the heat capacity of the material.

It is interesting to note that the radius is independent of transport parameters, such as heat conductivity, and only dependent on structure parameters.

If the values of T_c are taken to be the thermal decomposition points which have been observed for bulk specimens of the different micas and if a mean stopping power of 370 ev/A is assumed for every mica, then the theoretical estimates reported in Table I, column A are obtained. Needless to say, this approach using a "mean stopping power," is very rough. On the other hand, it would be practically impossible to make a calculation which would take into account the various statistical distributions of the quantities involved in such a way as to be capable of accounting for the fairly broad distribution of diameters which is found experimentally on every picture. The above calculation is then justified insofar as only an order-of-magnitude value of the thermal spike diameter is sought.

TABLE I. Comparison of the calculated diameters of the tracks to the experimental values.

Material	Decomposition point	Diameter of the tracks (A) Calculated (from mean energy loss)	Diameter of the tracks (B) Observed (mean)
Biotite	500° C	...	No tracks observed
Muscovite	700° C	120	240
Fluorophlogopite	1200° C	90	148
Muscovite heat treated 1 hr at 900° C	1400° C	80	115

As to the comparison with the experimental values, let us remark that the statistical distribution of the widths of the tracks shown by the pictures arises from different causes. The prominent cause is due to the spectrum of initial energies and to the fact that different unknown portions of the ranges of the particles are recorded. Other minor causes are to be found in differences among tracks crossing regions of strong contrast, such as wide extinction contours; here the tracks are wider, by roughly 15%, than in clear regions. Lastly, differences in focusing can perhaps bring a further

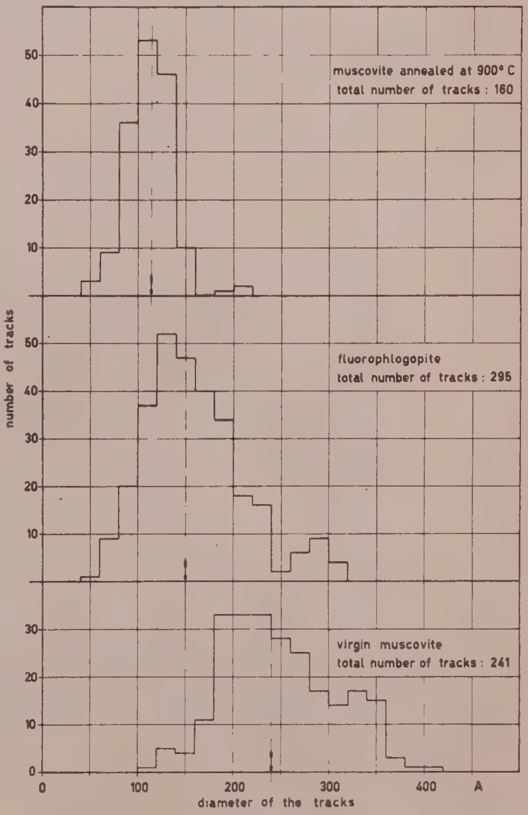

FIG. 4. Hystograms showing statistical distribution of the track diameters.

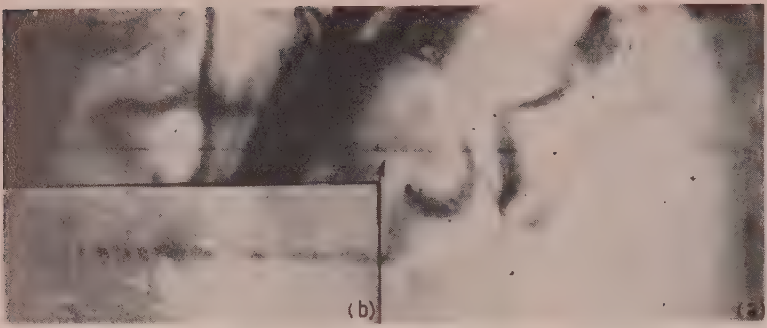

FIG. 5. (a) A long track (magnification 23 000 ×) in muscovite. (b) Enlarged detail of Fig. 5 (a), showing dotted region of the track (magnification 70 000 ×).

appreciable variation in the apparent diameter. To gather information about the effect of the significant variable alone (the nature of the material), we evaluated for each material a mean value of the tracks' widths obtained by averaging on the random variables, that is to say, by considering rather large groups of tracks on several pictures and for every material, whether in dark or in clear regions. The hystograms reproduced in Fig. 4 show that this procedure allows for a reasonable degree of confidence in the results. It can be seen that the mean values of the experimental distributions obtained by the indicated procedure are well separated for the three species of micas and are smaller the more resistant the mica is to thermal decomposition.

No doubt, the assumption of well-defined "critical temperatures" to account for thermal transients of some 10^{-11}-sec duration may appear objectionable. For a critical discussion of the theory of temperature spikes, the reader is referred to the article by Seitz and Koehler[9] and in particular to footnote 24, which precisely deals with the case of a fission fragment. In conclusion, the sensible differences in average width shown by tracks seen in different micas, and also the fact that the tracks are narrower in thermally more stable materials, strongly support the idea of their thermal origin.

4. OTHER EFFECTS

Some tracks (see Figs. 5 and 6) look dotted or dashed. We think this fact is essentially due to incipient recovery of the defects, as also indicated from the circumstance that fluorophlogopite and dehydrated mica do not show this phenomenon. Silk and Barnes[3] have interpreted the dots as due to Rutherford collisions which eject atoms from the mica lattice.

The effects indicating nuclear encounters may occasionally be detected. Moreover, it is indeed unquestionable that Rutherford collisions imparting to the struck nucleus an energy greater than the threshold for displacing it, occur roughly once every 100 atoms along the path of a fission particle.[10] However, the

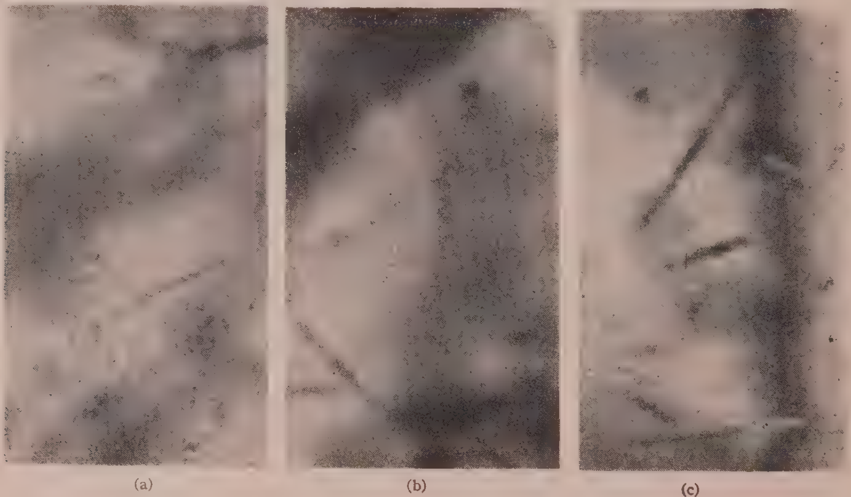
(a) (b) (c)

FIG. 6. Helices and dotted tracks due to recovery in virgin muscovite (magnification 47 500 ×).

---

[9] F. Seitz and J. S. Koehler, in *Solid-State Physics*, edited by F. Seitz and D. Turnbull (Academic Press, Inc., New York, 1956) Vol. 2, p. 351 ff.

[10] A. H. Cottrell, Met. Rev. 1, 479 (1956).

energy spent in ionization is a thousand times greater and the Rutherford displacement encounters are superimposed onto a far heavier continuous ionization process, and therefore they do not seem to participate in the formation of the tracks.

Another explanation of tracks which can reasonably be ruled out is that of direct ionization effects. An estimate of the so-called "maximum radius" of Bohr's equation[11] gives for it a value of a few angstroms, as compared with the more than 100-A diameters of the tracks.

As previously stated, apparent changes in the widths of tracks occur when the tracks cross extinction contours [see Fig. 7 (a)]. We are inclined to regard these alterations as optical effects, which can in this case be considered as artifacts. A further example of this effect is found in Fig. 7 (b), where a small needle-shaped crystalline inclusion (perhaps TiO_2) shows an apparent change in width as it crosses each of several extinction contours. However, intrinsic effects of a certain interest can be seen on some pictures.

Some tracks in virgin muscovite appear as distinctly resolved dots (see Figs. 5 (a) and (b) and Fig. 6); such tracks were not found in fluorophlogopite or in annealed mica, where the tracks always appeared as continuous thin black lines. We have interpreted the spottish aspect of these tracks as incipient recovery of the damaged region of the tracks under the electron beam of the microscope. Unfortunately, it has not been possible to check this by direct inspection, since all the pictures were taken with long exposure and low illumination in an effort to avoid excessive heating. It is interesting to note that the tracks shown in Figs. 6 (a), (b), and (c) look very much like the spiral dislocations which have been observed in quenched materials.[12] These features seem consistent with the fact that no tracks have been detected in biotite, which is the least heat-resistant mica examined. The preparation and irradiation of the biotite specimens was performed in exactly the same way as for other micas. It is therefore reasonable to suspect that in this material tracks have recovered during the irradiation or, more likely, under the microscope beam, even at the low illumination used.

CONCLUSION

The results of the investigation of fission fragment tracks in biotite, in muscovite dehydrated at 900°C, and in (artificial) fluorophlogopite indicate that the tracks are essentially thermal spikes whose widths are in rather good agreement with those calculated from the decomposition temperatures. The tracks are definitely thinner in fluorophlogopite and dehydrated muscovite than in virgin muscovite. Important recovery effects under the beam are observed in the latter. In biotite, where the recovery effects are likely to be more intense, no tracks have been observed.

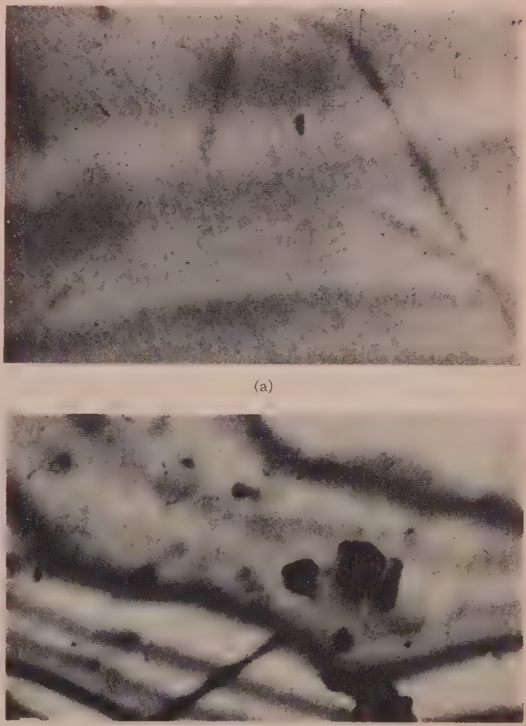

(a)

(b)

Fig. 7. (a) A clear effect of modulation of darkening at the crossing of an extinction contour (magnification 42 000 ×); (b) effect of darkening modulation of a spurious needle-shaped crystal (magnification 15 000 ×).

ACKNOWLEDGMENTS

It is a pleasure to acknowledge the help so generously obtained from the following persons and Institutions: Professor L. Néel, Director, and Dr. J. Rossillon of CENG of Grenoble for kindly performing the first irradiation; Dr. A. Cesoni and Dr. L. Orsoni, Directors, and Dr. A. Zimmer of SORIN Co. of Saluggia, for the second irradiation; the Micalex Company of America (Clifton, New Jersey), Electronic Mechanics, Inc. (Clifton, New Jersey), and General Telephone and Electronics Laboratories Inc. (New York) for generous supplies of specimens of artificial fluorophlogopite.

---

[11] E. Fermi, *Nuclear Physics* (University of Chicago Press, Chicago, Illinois, 1950) p. 27.

[12] See, for example, K. H. Westmacott, D. Hull, R. S. Barnes, and R. E. Smallman, Phil. Mag. 4, 1089 (1959).

JOURNAL OF APPLIED PHYSICS VOLUME 32, NUMBER 12 DECEMBER, 1961

Growth of Stannic Oxide Crystals from the Vapor Phase

J. A. MARLEY AND T. C. MACAVOY
Research and Development Division, Corning Glass Works, Corning, New York

(Received June 2, 1961)

Single crystals of stannic oxide up to 30×4×2 mm have been prepared by a high temperature vapor deposition technique. Using high purity SnO_2 powder, crystallization and growth were studied under both neutral and oxidizing conditions. Neutral carrier gases, with the exception of helium, encouraged the formation of voids and inclusions. However, the use of a helium-oxygen system was found to eliminate these defects. An explanation is offered for this behavior. Three distinct variations in the crystalline habit of SnO_2 have been observed, apparently dependent upon the temperature at which growth occurred.

As part of a program to explore and evaluate the electrical and optical properties of oxide single crystals, stannic oxide crystals suitable for such property measurements have been grown by a vapor deposition process. Basically, the method employed involves the high temperature vaporization of SnO_2 powder, via a decomposition process to SnO and O_2,[1] followed by subsequent reoxidation and deposition of SnO_2 crystals at lower temperatures. Thermodynamic calculations were used to indicate the theoretical decomposition pressure assuming vaporization of SnO_2 occurs as outlined above. Using $\Delta F°$ values available for SnO and SnO_2,[2,3] K_p and the total pressure were calculated. The resulting data may be represented by the equation

$$\log P(\text{mm}) = 11.23 - (1.822\text{X}10^4)/T.$$

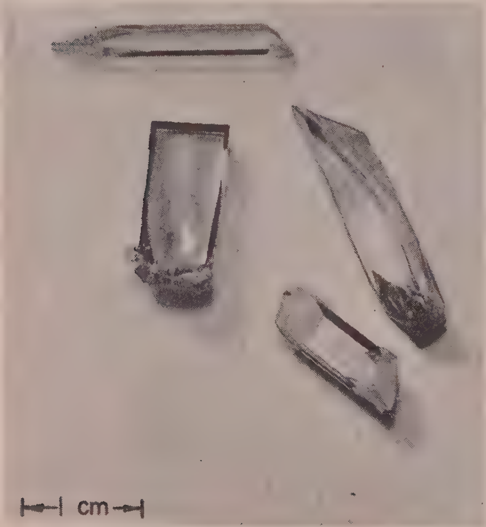

FIG. 1. Stannic oxide crystal rods.

The variation of crystal habit with temperature and the parameters affecting purity, size, and perfection have been studied.

DESCRIPTION OF THE PROCESS

Experiments were performed in a horizontal 2 zone Pt-20% Rh wound tube furnace, 1.5 in. i.d. by 36 in. long. Each zone was independently controlled to allow as flexible a temperature system as possible. The thermal profile consisted of a 3 in. constant temperature hot zone maintained at 1650°C, followed by an area 10 in. long containing a decreasing temperature gradient of approximately 20°C/in. Attached to the furnace was a gas entrainment apparatus which allowed accurate metering of carrier gases. Sintered alumina-ceramic muffle tubes (type AP30, McDanel Refractory Porcelain Company) were used throughout the furnace except where crystal deposition occurred; in this area a removable tube of high temperature mullite was substituted since it was found that at these temperatures the mullite provided a substrate plastic enough to firmly anchor the growing crystals. This tube also served as a convenient removable substrate. Ceramic materials other than alumina were found unsuitable because of their relatively high impurity content.

The furnace was charged with a 50-g sample of SnO_2 powder (99.999+%) which was positioned in the constant temperature vaporization zone. SnO_2 was prepared in this laboratory from zone refined tin (99.9999%) and transistor grade HNO_3. The resulting meta stannic acid was calcined in oxygen at 1450°C. Carrier gases were then passed over the charge, thereby transporting the vapor species into the growing zone where supersaturation and crystal growth took place.

A variety of carrier gases have been evaluated, including neutral gases, oxygen, and oxygen in combination with either argon, nitrogen, or helium. The flow rate of the carrier gases was generally maintained at from 100 to 250 cc/min. In the case of systems using both oxygen and a neutral gas, the proportion of oxygen amounted to approximately 25% of the total gas flow. Nitrogen or argon led to rapid growth, but the resulting crystals contained many voids and irregularities. Oxygen alone serves to suppress vaporization by shifting the equilibrium of the decomposition eaction in favor of undissociated SnO_2. It is also ikely that, if some disproportion of SnO to SnO_2 and Sn occurs on condensation, the excess of oxygen from he carrier gas will serve to maintain stoichiometry by eoxidizing free tin metal to stannic oxide. As expected, rowth is slow and crystals are small when oxygen is he carrier. This system does have the advantage, how-ver, of producing crystals which are free from voids nd inclusions.

---

[1] T. C. Platteeuw and G. Mayer, Trans. Faraday Soc. **52**, 1066 (1956).

[2] J. F. Elliott and M. Gleiser, *Thermochemistry for Steelmaking* (Addison-Wesley Publishing Company, Inc., Reading, Massachusetts, 1960), Vol. I.

[3] J. P. Coughlin, *Heats and Free Energies of Formation of Inorganic Oxides* (U. S. Bureau of Mines, Washington, D. C., 1954), Bull. 542.

Experiments in which two carrier gases were used vere conducted in such a manner that oxygen was dmitted to the system only in the crystal growing rea, vaporization having occurred in the presence of he neutral gas. This was accomplished by admitting he oxygen to the system through a small ceramic tube vhich extended just beyond the vaporization zone. Such an arrangement takes advantage of the increased rate of vaporization in a neutral atmosphere before the ddition of oxygen to the system.

Nitrogen or argon in combination with oxygen produced crystals up to 25×2×2 mm in 24 hr, although his rapid growth occurred at the expense of perfection. Large voids and growth marks are prevalent, particularly as crystal size increases, making such samples unsuitable for property measurements.

These limitations have been overcome, however, by substituting helium as the neutral gas, other experimental conditions being kept constant. Colorless single crystals 30×4×2 mm, free from gross imperfections, were grown in a period of 28 hr (Fig. 1). The structure of these crystals was identified as tetragonal, with the optic axis lying parallel to the length of the crystal. Spectrographic analysis indicated that total trace metal impurities, in the form of iron, vandium, manganese, chromium, copper, and titanium were below 20 ppm.

The explanation for this marked improvement in quality appears to be in the order of magnitude increase in the thermal conductivity of helium over the other gases used. Before crystallization can occur, the heat of crystallization must be given up to be dissipated by either the crystal or its surrounding medium. If the crystallizing substance has a high thermal conductivity, then it can dissipate this heat by conduction through the crystal itself. In the case of materials such as SnO_2, whose thermal conductivity is relatively low, it seems likely that an appreciable fraction of the heat of crystallization must be dissipated to the surroundings, in this case the carrier gas. Use of a carrier gas with a high thermal conductivity will contribute significantly to heat dissipation. This explanation also suggests that the crystal imperfections develop in the nitrogen and argon systems because the heat of crystallization is not efficiently removed, which in turn allows localized revaporization to occur resulting in the imperfections described.

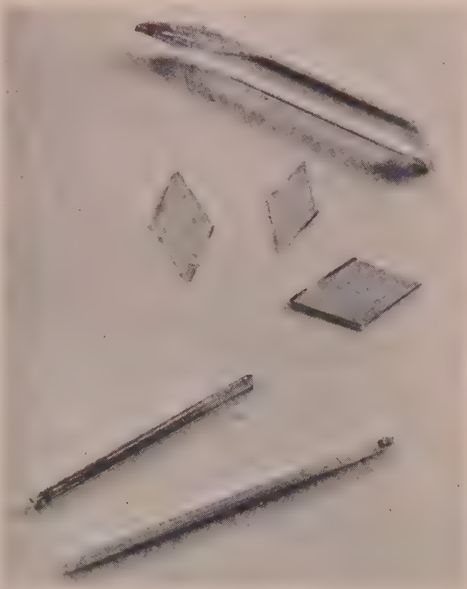

FIG. 2. Variations in the crystal habit of stannic oxide.

Three distinct variations in the crystalline habit of SnO_2 have been observed, apparently depending upon the temperature at which growth occurred. Figure 2 shows this variation with temperature. With the vaporizing site at 1650°C, rod formation is confined to an area between 1620° and 1570°C, twinned plates from 1570° to 1460°C, and needles from 1460° to 1300°C.

This general pattern of growth has been observed to occur despite variations in the temperature of the vapor source. Using a lower source temperature, for example, only twinned plates and needles were observed. It appears that the growth habit is a function of temperature alone. Similar observations have been made by Mason[4] in the growth of ice crystals from the vapor phase.

The degree of supersaturation in the growth of SnO_2 crystals is difficult to evaluate since a straightforward evaporation-condensation process is not involved. Rather, the process involves decomposition, evaporation, condensation, and reoxidation, the rate of each step being an independent function of temperature.

Property measurements on these crystals are currently under study.

---

[4] B. J. Mason, Sci. Am. **204**, No. 1, p. 120 (January, 1961).

JOURNAL OF APPLIED PHYSICS VOLUME 32, NUMBER 12 DECEMBER, 1961

Magnetic Investigation of Pure Manganese and of Several of its Alloys*

H. W. Cooper
Motorola Semiconductor Products Division, Phoenix, Arizona

A. S. Arrott
Ford Motor Company, Scientific Laboratory, Dearborn, Michigan

AND

H. W. Paxton
Carnegie Institute of Technology, Pittsburgh, Pennsylvania

(Received February 6, 1961)

Arrott, Coles, and Goldman have shown that a parasitic ferromagnetism can be induced at low temperatures in antiferromagnetic α manganese by pickling in nitric acid, and that this effect can be subsequently removed by a vacuum anneal. We have confirmed this result. Furthermore, we have eliminated as possible sources for this effect the presence of hydrogen or nitrogen in solid solution and the formation of nitrides or hydrides. However, strains arising upon transforming from the β phase to the α phase can induce this parasitic ferromagnetism. These results fit well with Li's hypothesis of antiferromagnetic domain boundaries giving rise to parasitic ferromagnetism. According to Li, strains should serve well to stabilize the domain boundaries.

I. INTRODUCTION

THE study of the magnetic properties of manganese was begun about half a century ago, but only with the work of recent investigators has an approach been made toward understanding the complex situation. Many of the early workers reported manganese to be weakly ferromagnetic under certain conditions.[1–3] Several compounds of manganese were found to be ferromagnetic, including one of the nitrides, the arsenide, the antimonide, and others. Contamination by nitrogen may well be suspected as a source of ferromagnetism in early measurements. Early workers were also hampered by the paucity of information concerning allotropy in manganese and the relevant phase diagrams.

The variation of magnetic susceptibility with temperature has been studied by Isobe,[4] showing clearly the effects of allotropy. Picon and Flahaut[5] found the magnetic susceptibility of α-Mn of high purity to be 9.24×10^{-6} emu/g at 20°C, a value which agrees well with the results of the present investigation. Shull and Wilkinson[6] studied the magnetic structure of α-Mn by means of neutron diffraction and detected an antiferromagnetic arrangement at low temperatures with a Néel temperature of 100°K. Measurements of the specific heat of α-Mn at liquid helium temperatures by Guthrie, Friedberg, and Goldman[7] yielded a value for the electronic term that is very large compared with those of other elements of the first transition series.

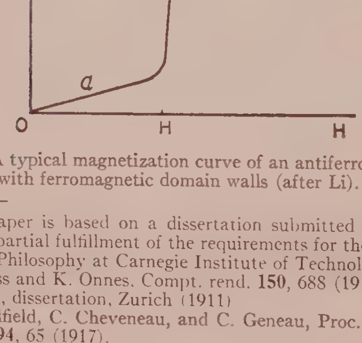

FIG. 1. A typical magnetization curve of an antiferromagnet with ferromagnetic domain walls (after Li).

Arrott, Coles, and Goldman[8] measured the magnetic susceptibility of α-Mn at low temperatures. An "as cast" ingot which was pickled in HNO_3 showed hysteresis effects at 4.2°K (with a remanence of 0.07 emu/g), while electrolytic flakes similar to those used by Shull and Wilkinson exhibited a remanence at 4.2°K of only 0.005 emu/g. Vacuum fusion analysis of their cast material revealed 0.4 atomic percent hydrogen, 0.11 atomic percent oxygen, and 0.09 atomic percent nitrogen, while analysis of the electrolytic flakes using the diffuse background in the neutron-diffraction pattern showed the hydrogen content not to be greater than 0.02 atomic percent. A vacuum anneal of their cast specimen reduced the remanence at 4.2°K to 0.003 emu/g. In the pickled specimen the hysteresis effect disappeared near 50°K, which is of the order of one-half the Néel temperature of α-Mn. The results of

---

[*] This paper is based on a dissertation submitted by H. W. Cooper in partial fulfillment of the requirements for the degree of Doctor of Philosophy at Carnegie Institute of Technology.

[1] P. Weiss and K. Onnes, Compt. rend. **150**, 688 (1910).

[2] E. Kuk, dissertation, Zurich (1911).

[3] R. Hadfield, C. Cheveneau, and C. Geneau, Proc. Roy. Soc. (London) **94**, 65 (1917).

[4] M. Isobe, Sci. Repts. Tôhoku Univ. **A3**, 78 (1951).

[5] M. Picon and J. Flahaut, Compt. rend. **237**, 569 (1953).

[6] C. G. Shull and M. K. Wilkinson, Revs. Modern Phys. **25**, 100 (1953).

[7] G. Guthrie, S. A. Friedberg, and J. E. Goldman, Bull. Am. Phys. Soc. **30**, 42 (1955).

[8] A. Arrott, B. R. Coles, and J. E. Goldman, Phys. Rev. **98**, 1864 (1955).

TABLE I. Analysis by weight % of manganese studied.

Impurity	Al	Si	Fe	Ni	Co	As	Sb	Bi	H	N	O
concentration	0.08	None	0.002	N.D.	N.D.	N.D.	Trace	Trace	0.002	0.002	0.04

riessman and McGuire[9] are in agreement with those Arrott, Coles, and Goldman, (hereafter referred to ACG), in that both sets of workers found a broad aximum in the susceptibility of Shull's electrolytic anganese at about 125°K.

Recently Kasper and Roberts[10] have studied α- and Mn by neutron diffraction and corroborated the data Shull and Wilkinson for α-Mn and, in addition, oposed a specific antiferromagnetic structure for Mn. The α-Mn has a complex cubic structure of 58 oms per unit cell with an a_0 of 8.91°A. Kasper and berts propose two alternative assignments of moents, each involving four types of atoms or spins.

II. PURPOSE OF THIS INVESTIGATION

Accepting the fact that α-Mn is basically antiferroagnetic, how does one account for the results of ACG at a hysteresis loop is induced by pickling α-Mn in NO_3? Four possible sources of the effect from pickling ave been suggested: (1) the inclusion of hydrogen,) the inclusion of nitrogen, (3) the introduction of rain, and (4) the preferential solution of Mn atoms om particular lattice sites.

The mechanism involving hydrogen or nitrogen might either the formation of a chemical compound (hyride or nitride) or the interaction of the gas atoms, ith some of the Mn atoms to upset the spin balance. The mechanism involving strain is due to Li,[11] who ses the concept of antiferromagnetic domain walls. e proposes that an antiphase domain structure in ntiferromagnetics is stabilized by the presence of ttice imperfections. An antiphase domain wall has net moment that can be inferred from the sequence. he direction of the net moment in the wall will depend pon the position of the wall. The moment of walls in a agnetic field can lead to walls preferring to sit with eir moments in the field direction. Such movement walls would give hysteresis effects. A prediction of i (Fig. 1) shows considerable resemblance to the Mn data of ACG.

The preferential solution argument is due to Goldan. The expectation is that such a system would be rrimagnetic. The large coercive forces result because the very small moment available for the field to use rotate the antiferromagnetically-coupled spin sysm. The remanence indicates that no more than 1 Mn om in 1000 is participating in either the domain wall echanism of Li or the defect mechanism of Goldman. This investigation includes a study of the solution of hydrogen in α-Mn, of the phase diagram of the Mn-N systems, of the effect of strain, and finally a repeat of the pickling experiment, all of which are carried out on Mn of higher purity than that used in the previous experiments of ACG.

III. APPARATUS AND METHODS

The manganese employed as the starting material in this study was 99.9% pure electrolytic flakes.[12] These were melted under argon, maintained at about 1 atm, with a slow gas flow rate so that a static closed condition could be approached to minimize pickup of impurities from the gas. The ingots prepared were about 1 in. in diameter and 1 in. long. The large grains of the cast structure were clearly visible on the bright ingot surface. From these ingots, specimens suitable for magnetic analysis were ground in the form of disks about $\frac{3}{4}$ in. in diameter and $\frac{1}{4}$ in. thick. Piping problems were severe, as expected on the basis of the 4.5% volume contraction on solidification. As a result of piping and extensive cracking, only about half the ingots yielded specimens suitable for magnetic analysis. Table I pre-

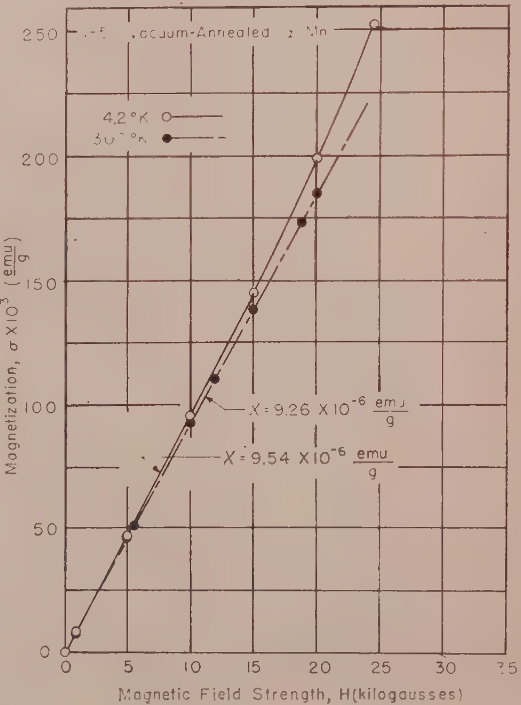

FIG. 2. Magnetization curve for vacuum α-annealed Mn.

---

[9] C. J. Kriessman and T. R. McGuire, Phys. Rev. **98**, 936 955).

[10] J. S. Kasper and B. W. Roberts, Phys. Rev. **101**, 537 (1956).

[11] Y. Y. Li, Phys. Rev. **101**, 1450 (1956).

[12] Kindly supplied by the Electro Metallurgical Company.

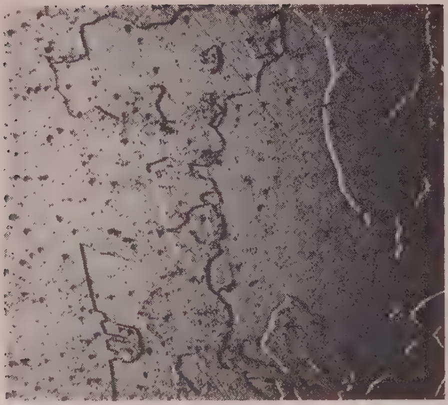

FIG. 3. The α-Mn microstructure viewed at 120× under oblique illumination.

sents the spectrographic and vacuum fusion analyses of a typical manganese ingot. The concentration of iron impurity was, in all cases, far less than the solubility limit of iron in α-manganese, and in no case could observed magnetic behavior be attributed to iron. The specimens were treated in Vycor at temperatures up to 950°C in a system which permitted measurement and control of gas content.

An inductive method of magnetic examination developed by Arrott and Goldman[13] was employed. It has an accuracy of about 1% in determining the susceptibility of manganese. The method uses a current in a coil wrapped about the cylindrical specimen to produce a balance between the moment of the coil and the sample. Any unbalance is detected by means of the voltage induced in coils (placed about the sample) when the sample is moved. The magnetizations of Mn were sufficiently large that a heavily damped ballistic galvanometer could be used as a detector, producing a signal linear in the magnetization. It was therefore convenient to use the null coil only to calibrate. The apparatus is mounted in a double Dewar. The temperatures employed in this study were 4.2°, 77°, and 300°K.

IV. PROCEDURES AND RESULTS

The investigation can be considered to be in 3 parts, namely, studies of "pure" α-Mn, of hydrogen-loaded α-Mn, and of the Mn rich end of the Mn-N phase diagram.

A. α-Manganese (Annealed)

A disk cut and ground from the "pure" manganese ingot was annealed for 47 hr at 600°C in a vacuum of 2×10^{-5} mm of Hg. It was then furnace-cooled. Magnetization isotherms for 300° and 4.2°K are shown in Fig. 2. The susceptibility is essentially the same at the two temperatures, but it can be judged from previous work[8,9] that this does not preclude a slight maximum in the susceptibility near 100°K. The curvature at 4.2°K is outside experimental error and can be attributed to the usual expectation for antiferromagnetic materials in fields which are low in comparison to the field necessary to rotate an antiferromagnetic spin system from parallel to perpendicular to the applied field. As the susceptibility is expected to be higher for the perpendicular alignment, the increase could be accounted for by rotation of the spin system of some of the antiferromagnetic domains.[14] The room temperature data are in excellent agreement with the result of Picon and Flahaut.

The microstructure of the α-Mn specimen is shown in Fig. 3. The grains are large and quite irregular. It was found difficult to produce a polished specimen entirely free of scratches. The final polish was with Linde "B" powder and kerosene on a microcloth wheel. The etch was 1% HCl in alcohol. There was no metallographic indication of a second phase, and x rays clearly indicated α-Mn with a lattice parameter of 8.912A, in agreement with the literature.[15,16]

Pickled α-Manganese

A similar specimen was subjected to a pickling treatment to attempt to reproduce the results of ACG. After a 24-hr anneal at 650°C in an evacuated Vycor capsule, the specimen was immersed for 15 sec in a 50-50 solution of H_2O and concentrated HNO_3. The weight decreased from 15.2 to 13.2 grams, and dark cracks on the specimen before pickling became deep open gorges. The sample dimensions changed from a thickness and diameter of 0.291 in. and 0.768 in. to 0.279 in. and 0.756 in., respectively. The magnetic isotherms for 300°, 77°, and 4.2°K are shown in Fig. 4. At 4.2°K the sample shows hysteresis, that is, a remanence and a coercive force. The curve shown for 4.2°K is the result for decreasing field from which a well-defined susceptibility can be obtained. This behavior is qualitatively the same as found by ACG.

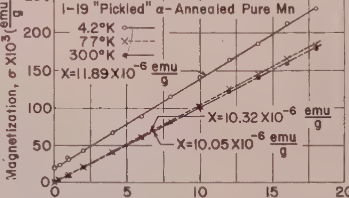

FIG. 4. Magnetization curves for α-annealed "pickled" manganese.

---

[13] A. Arrott, thesis, Carnegie Institute of Technology, Pittsburgh, Pennsylvania (1954), and J. E. Goldman, Rev. Sci. Instr. **28**, 99 (1957).

[14] L. Néel, Proc. Intern. Conf. Theoret. Phys., Kyoto and Tokyo, Japan, 1953, **1954**, 701.

[15] W. B. Pearson, *Handbook of Lattice Spacings and Structures of Metals* (Pergamon Press, New York, 1958), p. 735.

[16] Z. Basinski and J. W. Christian, Proc. Roy. Soc. (London) **A223**, 54 (1954).

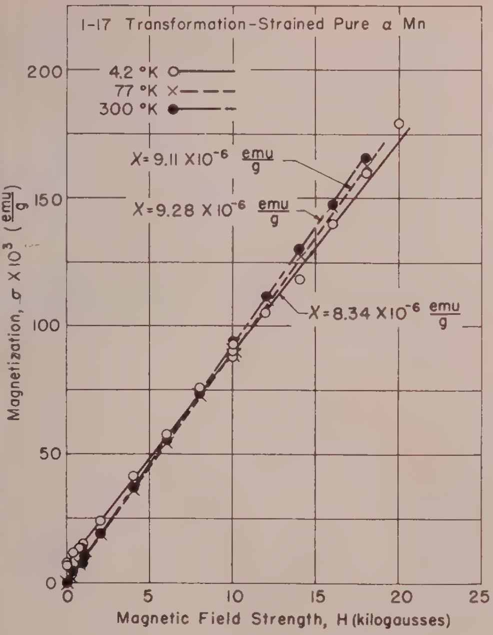

FIG. 5. Magnetization curves for transformation-strained pure α-Mn.

Vacuum fusion analysis was carried out for material extracted from both the center and the edge of the ingot. The nitrogen was not detected to 0.00 weight percent; hydrogen was 0.0053 and 0.0016 weight percent for the edge and center, respectively. The oxygen content was high at both the edge and center (0.34 and 0.22, respectively). The microstructure showed an abundance of MnO dendrites. From the magnetic susceptibility per gram of MnO as given by Bizette, Squire, and Tsai,[17] namely, 7×10^5 at 300° and 77°K and 6×10^5 at 4.2°K, it is possible to correct for the presence of the oxygen by assuming it all to be as MnO. This is sufficient to account for the increase of susceptibility on pickling as observed at 300° and 77°K, but not at 4.2°K. The behavior at 4.2°K will be discussed below.

Transformation-Strained α-Manganese

In an attempt to produce β-Mn, a specimen was heated for 24 hr at 950°C (the middle of the β range) while encapsulated in evacuated Vycor. The capsule was quenched in ice brine, but when the Vycor failed to break, the quench was moderated. The result as shown by x-ray and metallographic examination was α-Mn with some of the transformation strains retained. The magnetic isotherms at 300°, 77°, and 4.2°K are shown in Fig. 5. The 300°K result is in agreement with the unstrained material. However, below the antiferromagnetic Néel point the results are considerably different. At 77°K the susceptibility decreases instead of increasing with respect to 300°K. At 4.2°K hysteresis is observed, but there is no significant increase in susceptibility as in the pickled specimen. If anything, the susceptibility is decreased, particularly if the susceptibility is taken between 0 and 10 kg. It is apparent from this result that gaseous impurities are not essential to the production of hysteresis in antiferromagnetic α-Mn. The transformation-strained α-Mn showed no measurable change in lattice parameter.

B. Hydrogen-Loaded Mn

From previous literature it seemed possible that hydrogen was the major contributor to the hysteresis effect at low temperature. Thus, before the above experiments with transformation-strained α-Mn and the repeat of the pickling specimen were undertaken, a series of experiments were carried out which showed that hydrogen had no appreciable effect. By cathodically hydriding for 24 hr with a current density of 50 ma/cm² using a platinum anode and a neutral buffer solution maintained at 100°C, it was possible to bring a specimen of α-Mn to a point close to disintegration. No hydrides were observed either metallographically or by x rays. Vacuum fusion showed variations in hydrogen content of from 0.007 weight percent at the center of the sample to 0.014 weight percent at the surface. (The solubility limit[18] at 300°K is approximately 0.002 weight percent, and it decreases with increasing tem-

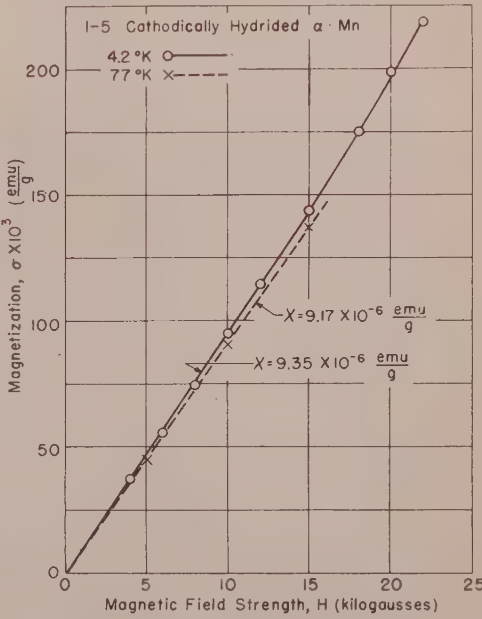

FIG. 6. Magnetization curves for cathodically hydrided α-Mn.

---

[17] H. Bizette, C. F. Squire, and B. Tsai, Compt. rend. **207**, 449 (1938).

[18] E. V. Potter and H. C. Lukens, Trans. Am. Inst. Mining, Met., Petrol., Engrs. **171**, 401 (1947).

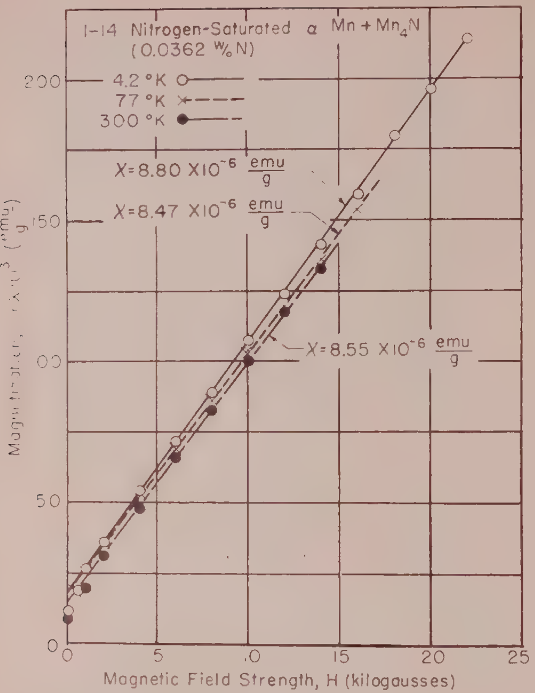

FIG. 7. Magnetization curves for nitrogen-saturated (at 450°C) α-Mn in equilibrium with a small amount of Mn_4N.

perature.) The magnetic isotherms at 77° and 4.2°K are shown in Fig. 6.

C. Manganese-Nitrogen System

It has been well established that the face-centered cubic compound Mn_4N is ferromagnetic with a Curie temperature of 465°C.[19] This is the only composition in the system known to show ferromagnetism. This investigation set out to determine if the small amount of N soluble in α-Mn could give rise to the effects observed by ACG. After metallographic studies showe that specimens with more than 0.036 weight percen nitrogen contained some Mn_4N when heat treated a 450°C, a specimen with 0.036 weight percent N wa studied magnetically. This specimen was prepared b dissolving nitrogen at 950°C for 24 hr, isothermall treating at 450°C for 51 hr, and then quenching in ic water. The results of the magnetic studies are show in Fig. 7. The low-field behavior at all temperatures i explained as the result of alignment of the magnetization of the regions of ferromagnetic Mn_4N. From th extrapolation of the high-field data to zero field, on obtains the spontaneous magnetization of this phase Its temperature dependence is reasonable, namely, som change between 300° and 77°K, but little between 77 and 4°K. The magnitude is explained by the presenc of 0.006 weight percent Mn_4N or less than 0.000 weight percent of N in the combined form. This indicates that the solubility limit of N in α Mn at 450° is very close to the composition of this specimen namely, 0.036 weight percent N. It may be conclude from the results obtained after correcting for the sma

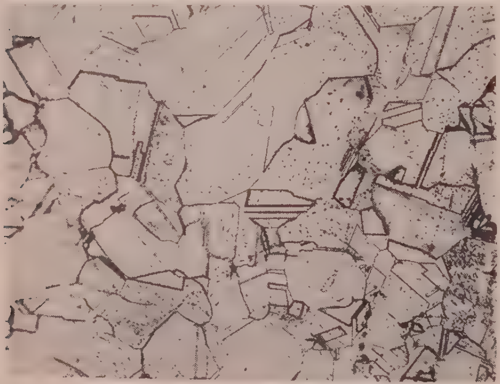

FIG. 8. Specimen containing 1.7% nitrogen water-quenched from 950°C. X rays show fc tetragonal structure.

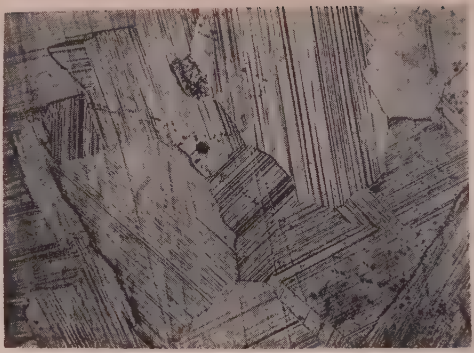

FIG. 9. Specimen containing 3% nitrogen quenched from 950°C. Very slight anisotropy under polarized light is observed. X-ra pattern shows a fcc structure.

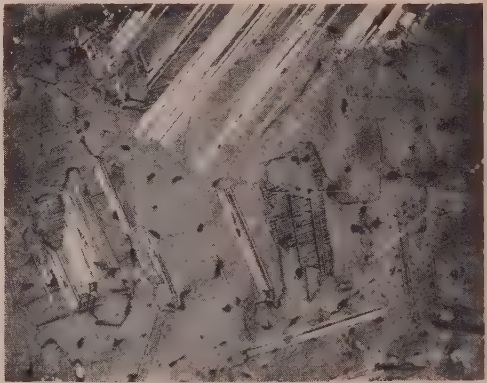

FIG. 10. Specimen containing 5.5% nitrogen viewed unde polarized light. Note relatively strong optical activity. This specimen is ferromagnetic; x rays show a fcc structure.

---

[19] C. Guillaud and J. Wyart, Rev. mét. 45, 271 (1948).

TABLE II. Summary of results—susceptibilities and remanences.

Ingot	Treatment	Susc. ×10⁶ emu/g 300°K	77°K	4.2°K	Rem. ×10³ emu/g 300°K	77°K	4.2°K	Vacuum fusion analysis Wt% H	Wt% N	Wt% O	Lattice parameters
I-5	vac. α-annealed	9.26	9.40	9.54	0	0	0	0.001	0.000	0.021	8.912
I-5	H_2 α-annealed	9.50		9.33	0		0	0.001	0.0009	0.105	
I-5	α-ann. +cath. hydr.	9.22	9.17	9.35	0	0	0	0.007–0.014	0.001	0.031	
I-14	sat'd α-Mn+Mn_4N	8.55	8.47	8.80	14	17.7	18.1		0.036		8.918
I-16	γ-Mn (1.5 wt% N)	7.66	7.66	7.00	20.4	33	29.7		1.510		
I-17	transf.-strained α	9.28	9.11	8.34	0	0	7		0.0014		8.912
I-12	0.01% N in strained α	8.68	8.76	9.30	0	0	1.1		0.011		8.9145
I-19	α-ann. and pickled	10.05	10.32	11.89	0	0	18.8	0.0016	0.00	0.23	8.915
								0.0053	0.00	0.341[a]	
rom ACG:											
N R C	N R C pickled Mn	8.8	9.4	15.0	0	0	70	0.0074	0.0231	0.0321	

[a] Along edge of I-19.

mount of Mn_4N that the solubility of nitrogen in -Mn does not account for the results of ACG. In many nanganese base systems, e.g., Mn-Cu,[20] Mn-Ga,[21] and In-Ge,[21] a diffusionless transformation from face-entered cubic γ to a face-centered tetragonal phase ccurs. The M_s temperature decreases with increasing mounts of alloying element, and the c/a ratio increases.

It seems very probable that Mn-N alloys behave imilarly, although a complete study was not made. lloys containing approximately 1.5, 3, and 5.5% itrogen were prepared and water-quenched to room emperature from 950°C. Neither the 1.5% or the 3% alloys were ferromagnetic at room temperature or −196°C, as measured qualitatively with a permanent magnet. The 5.5% alloy was markedly ferromagnetic. X-ray examination showed the 1.5% alloy to be face-centered tetragonal, and the 3 and 5.5% alloys were face-centered cubic. Typical micrographs are shown in Figs. 8–10.

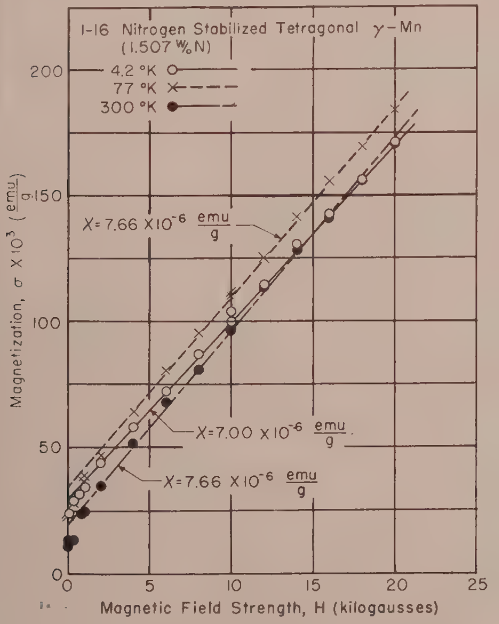

FIG. 11. Magnetization curves for nitrogen-stabilized, fc tetragonal γ Mn.

The heavily twinned structure of Fig. 9 is not unusual in diffusionless transformations. Examination of both 3 and 5.5% samples under polarized light showed some optical activity; Fig. 10 is in fact taken with polarized light since this sample is more anisotropic. It is not clear how this can be rationalized with the fcc x-ray pattern; conceivably, the magnetic field of the 5.5% alloy could be rotating the plane of polarization of the incident light (as in observation of Bitter patterns on iron single crystals), but this cannot explain the effect in the 3% alloy.

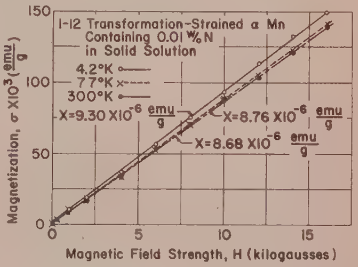

FIG. 12. Magnetization curves for transformation-strained α-Mn containing 0.01 weight percent N in solid solution.

A specimen of γ-manganese stabilized by 1.5 weight percent nitrogen also was examined magnetically. The results are shown in Fig. 11. The low-field data may possibly be due to the alignment of the magnetization of regions of Mn_4N, although none were observed microscopically or by x rays. Although the apparent decrease in susceptibility at 4.2°K is puzzling, there is no evidence in this system that γ-Mn contributes to the effect of ACG.

Results on a final specimen of Mn-N are given in Fig. 12. This specimen contained 0.01% N, was quenched rapidly from the β phase, but transformed to α-Mn with some resulting strain. This sample shows the decrease in susceptibility characteristic of nitrogen in solution, and yet it also shows a small hysteresis resulting from the transformation strain.

---

[20] Z. Basinski and J. W. Christian, J. Inst. Metals **80**, 659 1951–2).

[21] V. Zwicker, Z. Metallk. **42**, 246 (1951).

V. DISCUSSION

A summary of the results of this investigation is given in Table II. The pickling effect of ACG has been reproduced here on α-Mn of higher purity. In addition, it has been shown that, to a lesser extent, the hysteresis phenomena results from the strain produced in fast transformation. On the other hand, studies of hydrogen and nitrogen in α-Mn reveal no evidence for these gases being responsible for the effect of ACG. It is not easy to differentiate between the predictions of the antiphase domain wall model of Li and the preferential missing atom model of Goldman, in that either could account for hysteresis. Both defects could result from either rapid transformation or from pickling. Possibly the increased susceptibility of the pickled sample indicates that Goldman's mechanism plays an important role, inasmuch as this increase occurs even above the Néel temperature of α-Mn.

ACKNOWLEDGMENTS

Acknowledgment is due the U. S. Army Signal Corps, which supported most of this study, the Metals Research Laboratory, and the Office of Naval Research for further financial assistance. Thanks are given to Dr. G. Derge and Mr. J. R. Shegog for vacuum fusion analyses, to the U. S. Navy Metals Laboratory, Munhall, Pennsylvania, for spectrographic analyses, and to Mr. E. J. Pasierb for some laboratory assistance. The continued interest of Drs. J. E. Goldman and B. R. Coles has been of considerable value.

JOURNAL OF APPLIED PHYSICS VOLUME 32, NUMBER 12 DECEMBER, 1961

Theory of Electron Collection of Spherical Probes

G. Medicus
Advanced Techniques Branch, Wright-Patterson Air Force Base, Ohio

(Received March 20, 1961)

The theory of spherical probes based on the impact parameter of the carriers is given. Fields outside the sheath are neglected, which is justified for electron collection. The results are obtained more directly than by Mott-Smith and Langmuir. General results such as the transition from impact parameter limitation to sheath limitation for the spherical case, not previously treated in the literature, are derived. The case of a uniformly accelerated half-Maxwellian (as opposed to a Maxwellian with drift) is treated in detail; the case of a pure Maxwellian superimposed on the accelerated half-Maxwellian and the superposition of two different accelerated half-Maxwellians is discussed briefly.

INTRODUCTION

MOTT-SMITH and Langmuir,[1] after having derived their equations for carrier collection in a very general way, suggest an alternate treatment by subdividing the flow of carriers into infinitesimal monoenergetic swarms of parallel motion (p. 751), but do not carry out this suggestion. It turns out that such a treatment, in combination with the use of the impact parameter, simplifies greatly the derivations for the spherical case. Some of the more intricate aspects of the theory presented in reference 1, such as the transition from impact parameter limitation to sheath limitation become almost self-evident. Only the spherical case will be considered, because the advantages of the use of the impact parameter are most pronounced there and because the treatment of this case in reference 1 is incomplete.

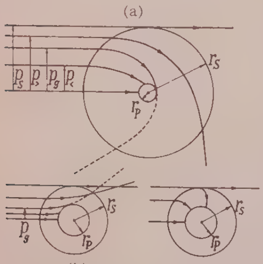

FIG. 1. Paths of monoenergetic electrons in vicinity of probe (schematic). Acceleration: (a), Retardation: (b). These two cases are p limited, the limiting $p=p_g$. Case (c) is sheath limited, with no grazing incidence on the probe. Impact parameter $=p$; subscript g: grazing; sheath radius $=r_S$; probe radius $=r_P$.

The results are considered to be valid only for electron collection because the penetration of the field into the plasma region adjacent to the "sheath" is neglected, which normally is not justified for ion collection.[2]

The following trivial fact is noteworthy: In a parallel beam of electrons which has a number density n and which flows with a uniform drift velocity v in a quasineutral plasma, a spherical probe at plasma potential will intercept a current $J=\pi r_P^2 env$, where r_P is the robe radius. If now the same density n has a random istribution of the directions of the same velocity v, the robe current arising from the random carriers is $=4\pi r_P^2 env/4$, which is the same as in the beam.

---

[1] H. M. Mott-Smith and I. Langmuir, Phys. Rev. **28**, 727 (1926).

[2] J. E. Allen, R. L. F. Boyd, and P. Reynolds, Proc. Phys. Soc. (London) **B70**, 297 (1957).

The usual assumptions are made, some of which are: No collisions in the sheath; no reflection of carriers at he probe surface; the velocity distribution of the arriers is constant in space and spherically symmetrical n velocity space (no preference direction); Langmuir's heath concept[1] is assumed to be applicable. Under uch conditions, the paths through the sheath of all arriers arriving at a spherical sheath edge with the ame velocity v and the same impact parameter p Fig. 1) have the same shape. In order to better isualize the geometry, one can assume the paths of all he carriers to be parallel outside the sheath. (For a eal parallel stream, of course, the sheath will not be niform.)

If p_g denotes the impact parameter for grazing incidence on the probe, the carriers can be divided into the ollowing classes (Fig. 1):

1. Carriers with $0<p<p_g$ reach the probe.
2. Carriers with $p_g<p<r_S$ fly through the sheath without reaching the probe.
3. Carriers with $p>r_S$ do not enter the sheath.
4. Carriers with imaginary p can have closed orbits within the sheath.

Class 4 must be expected to be populated by the action of collisions in the sheath, even if collisions are very are. Space charge and potential distribution are affected by such carriers. This class of carriers obviously is absent for retarding probe voltages [Fig. 1(b)]. There are cases in which grazing incidence on the probe does not occur, as will be discussed in detail. In such cases class 2 is absent and the maximum p for carriers to reach the probe is equal to r_S [Fig. 1(c)].

DERIVATIONS

The paths of the carriers in the sheath are governed by conservation of energy and angular momentum. The velocities at the sheath edge (subscript S) and at the probe surface (subscript P) are connected by the following equations which are independent of the potential distribution in the sheath (see, however, reference 1).

$$\tfrac{1}{2}m(v_{rP}^2+v_{tP}^2)=\tfrac{1}{2}m(v_{rS}^2+v_{tS}^2)+eV_{SP}, \qquad (1)$$

$$r_P v_{tP}=r_S v_{tS}=p v_S=\text{const}, \qquad (2)$$

where v=velocity, r=radius, p=impact parameter, V=voltage, subscript r=radial, subscript t=tangential, subscript S=sheath edge, and subscript P=probe surface.

Eliminate the tangential velocities from (1) and (2), set $v_{rP}^2=0$, remember that $v^2=v_r^2+v_t^2$, and obtain the impact parameter p_g for which the carriers graze the probe surface [Fig. 1(a)]:

$$p_g^2=r_P^2(1+2eV/mv^2)=r_P^2(1+V/U_v), \qquad (3)$$

with $V_{SP}\equiv V$, $v_S\equiv v$, and $\frac{1}{2}mv^2=eU_v$.

Actual voltages are denoted by V, voltage equivalents of energies are denoted by U throughout. As in reference 1, $V>0$ for acceleration.

For retarding potentials ($-U_v<V<0$), the impact parameter for grazing incidence p_g from (3) lies between 0 and r_P. For $V>0$, p_g in (3) formally can assume any value >0. For a given r_P and a given r_S, i.e., a given $V>0$, p_g will become greater than r_S for small enough carrier velocities $v=[(2e/m)U_v]^{\frac{1}{2}}$. Obviously [Fig. 1(a)], this is impossible. Certainly carriers with $p_g>r_S$ will not enter the sheath, much less graze the probe. Actually the upper limit of p_g in (3) for $V>0$ is $p_g=r_S$, i.e., $V=U_v[(r_S/r_P)^2-1]$. In this limiting case, the carriers which graze the sheath and enter it also graze the probe. The condition $p_g=r_S$ in (3) separates the region of "impact parameter limitation" from that of "sheath limitation" of the probe current. The transition between the two regions occurs at a critical carrier velocity v_k which follows from (3) with $p_g=r_S$ to be given by

$$\tfrac{1}{2}mv_k^2/e=U_k=V/[(r_S/r_P)^2-1]. \qquad (4)$$

So, at a given probe voltage $V>0$, and for a given sheath radius r_S, the probe current arising from carriers with $U_v>U_k$ will be p-limited with the maximum p, i.e., $p_g<r_S$, given by (3). For carriers with $U_v<U_k$ the probe current will be sheath limited, with the maximum $p=r_S$, and all carriers (even those which graze the sheath and enter it) arriving at the probe under a finite angle of incidence. For $U_v=U_k$ the carriers which graze the sheath and enter it also graze the probe.

The drastic difference between the p-limited case [Fig. 1(a)], with its gradual transition of the paths from sheath-grazing to probe-grazing, and the r_S-limited case [Fig. 1(c)], with the paths jumping from sheath-grazing to nongrazing incidence on the probe, is caused by the following circumstance: In the former case the (monoenergetic) particles which populate the intermediate paths [$p_>$ Fig. 1(a)] stem from a ring area of the beam $\pi(r_S^2-p_g^2)$; the current of these particles is proportional to this ring area. If now, other things being equal, the energy of the particles in the beam decreases, p_g increases because of the stronger deflection of the slower particles, and the ring area $\pi(r_S^2-p_g^2)$ decreases, so that the intermediate paths are less populated. A further decrease of the particle energy, down to the critical energy, $U_v=U_k$, i.e., $p_g=r_S$ makes the ring area disappear and leaves the intermediate paths unpopulated. A decrease of U_v below U_k leaves the intermediate paths between grazing incidence on the sheath and now nongrazing incidence on the probe unpopulated *a fortiori*.

The above considerations qualitatively do not depend on the nature of the potential distribution in the

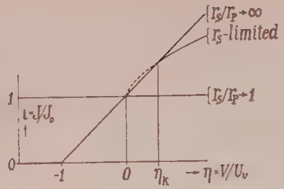

FIG. 2. Reduced probe current $\iota=J/J_0$ ($J_0=$ probe current for probe at space potential, $V=0$), as function of reduced probe voltage $\eta=V/U_v$ ($U_v=$voltage equivalent of electron energy). Monoenergetic electrons. (Curve for sheath limitation schematic.)

sheath (except that it must be monotonic[1]) as long as the microfields and collisions are neglected. Actually the degree of abruptness of the transition between p-limitation and r_S-limitation will depend strongly on the development of the potential inside the sheath edge, and will be affected by the microfields.

As long as it can be assumed that the field strength in the plasma outside the sheath is zero, the sheath edge is well defined as the surface within which the field strength is not zero. Then, for the case of sheath limitation, the sheath radius r_S is equal to the "absorption radius" r_A as used in reference 2. Under such conditions, $r_A=r_S$ is independent of the carrier velocity as long as $U_v<U_k$. Actually the field outside the sheath (in the "pre-sheath"[3]) can be neglected for electron collection without significant influence on the probe results. However the field in the pre-sheath must not be neglected for ion collection.[2,3] In this case the sheath edge becomes somewhat ill defined, but it may be identified with the absorption radius which remains well defined,[2] although it now depends on the velocity of the carriers because of the stronger influence of the weak pre-sheath field on the slower carriers. This paper is concerned only with electron collection for which the weak pre-sheath field is neglected; in other words, plasma density and plasma potential outside the sheath are assumed to be constant.

1. Monoenergetic Case

The probe current J caused by electrons with velocity v which is constant in value but random in direction is

$$J=\pi p_g^2 env \quad \text{for} \quad v>v_k$$

(p-limitation, no "absorption radius"[2]), (5)

$$J=\pi r_S^2 env \quad \text{for} \quad v<v_k$$

(r_S-limitation, absorption radius $r_A=r_S$). (6)

From (3) in (5) the probe current, now as a function of the probe potential V, becomes

$$J(V)=\pi r_P^2 env(1+V/U_v) \quad (p\text{-limitation}). \qquad (7)$$

Obviously for $V<-U_v$ none of the electrons with U_v can reach the probe against the retarding V, and the probe current is zero. The lower limit of (7) is $J=0$, i.e., $V=-U_v$. The probe current rises linearly with $V>-U_v$ through space potential $V=0$, into the electron accelerating region $V>0$, until sheath limitation is reached at $V=U_v((r_S/r_P)^2-1)$, according to (4) with $U_v=U_k$ (cf. Fig. 2). So the limits of (7) can be written as

$$-1<V/U_v<(r_S/r_P)^2-1. \qquad (8)$$

With decreasing sheath thickness, i.e., with r_S approaching r_P in (8), the upper limit is reached at probe voltages V approaching zero, i.e., at plasma potential. This extreme case is equivalent to the "plane probe" for which the probe current is saturated above plasma potential and is equal to $J(V=0)$ in (7). With increasing relative sheath thickness, i.e., $r_S/r_P\to\infty$, the upper limit in (8) also approaches infinity; that is, for the infinitely small probe the linear ascent with V in (7) has no r_S-limitation.[1] In practice, of course, not even the finite upper limit in (8) may be reached because of ionization in the sheath.

$J(V)$ for r_S-limitation, (6) is hard to express, because $r_S[n,V,r_P,F(v)]$ is a complicated function, but this part of the probe curve is of secondary interest here.

The transition between the linear ascent (7) and the sheath limited region (6) in the monoenergetic case is marked by a jump in the derivatives J', J'' . . . of the current with respect to the voltage, as becomes evident from an extension of (6) into the region below its actual validity (Fig. 2, dotted curve). The curve for sheath limitation intersects the straight line under a finite angle. However, there is no indication of $V=($ in $J(V)$.

2. General Velocity Distributions

General velocity distributions can now be treated by superposition of infinitesimal monoenergetic contributions as follows: If $dn_v=nF(v)dv$ denotes the density of carriers with absolute velocities between $v\to dv$ (short for v and $v+dv$), its contribution to the probe current will be $dJ_v=\pi p_{vg}^2 evdn_v$, with the maximum impact parameter p_{vg} for this specific velocity v being given by (3)

$$p_{vg}^2=r_P^2(1+V/U_v). \qquad (9)$$

For any particular probe voltage V there is a critical velocity v_k which corresponds to the transition from impact parameter limited to sheath limited conditions. The critical velocity v_k is given by (4). The total probe current $J(V)$ is obtained by replacing the total density n in (6) and (7) by the infinitesimal density dn_v for the velocity interval $v\to dv$, $dn_v=nF(v/v_c)dv/v_c$,[4] and integrating over dv/v_c. Then the total current $J(V)$ to the probe is composed of two integrals, the first one taken between $v=0$ and $v=v_k$, corresponding to the sheath limited contribution (6) (the slower carriers are more easily deflected in the sheath), and a second one, taken between $v=v_k$ and $v=\infty$, corresponding to the p-limited contribution (7). In order to facilitate writing the formulas, the following abbreviations are introduced:

---

[3] The term "pre-sheath" seems to have been originated by Allis and Buchsbaum in "Notes on Plasma Dynamics," Summer Session 1959, Massachusetts Institute of Technology, Cambridge, Massachusetts.

[4] Any velocity distribution can be written in dimensionless form by means of a characteristic velocity v_c. For the Maxwellian, for instance, the natural choice of v_c is $v_c^2=2kT/m$.

$$v/v_c=\alpha,\quad v_k/v_c=\alpha_k;\quad U_v/U_c=\eta,\quad V/U_c=\eta_V,$$

so that

$$\alpha^2=\eta,\quad V/U_v=\eta_V/\eta=\eta_V/\alpha^2.$$

Then the total probe current becomes

$$J(\eta_V)=\pi env_c\left\{r_S{}^2\int_0^{\alpha_k}\alpha F(\alpha)d\alpha\right.$$
$$\left.+r_P{}^2\int_{\alpha_k}^{\infty}\alpha(1+\eta_V/\alpha^2)F(\alpha)d\alpha\right\},\ \eta_V>0.\quad (10)$$

This equation with v_k from (4) holds for $V>0$, i.e., for carrier acceleration.

Since for carrier retardation there is no sheath limitation and the lower limit for integration is determined only by the lower limit in (8), $V/U_v=-1$, with the corresponding velocity $\alpha_V=v_V/v_c$ being given by

$$V/U_v=\eta_V/\alpha_V{}^2=-1,\quad\text{or}\quad \alpha_V{}^2=-\eta_V;\quad (11)$$

the probe current in the retarding voltage region becomes

$$J(\eta_V)=\pi env_cr_P{}^2\int_{\alpha_V}^{\infty}\alpha(1+\eta_V/\alpha^2)F(\alpha)d\alpha,\ \eta_V<0.\quad (12)$$

Equation (12) is the second integral in (10) with the lower limit α_k replaced by α_V so that it is independent of the sheath.

3. Maxwellian Velocity Distribution

For the Maxwellian velocity distribution, the distribution function $F(\alpha)$ is $F(\alpha)=(4/\pi^{\frac{1}{2}})\alpha^2\exp(-\alpha^2)$, with $v_c=v_T$, $\alpha=v/v_T$. With $\alpha^2=\eta=eU/kT$, $v_T{}^2=2kT/m$, and $\alpha_V{}^2=-\eta_V$ from (11), (12) becomes

$$J(\eta_V)=2\pi^{\frac{1}{2}}r_P{}^2env_T\exp(\eta_V),\quad\text{for}\quad V<0,\ \eta_V<0,\quad (13)$$

and (10) becomes

$$J(\eta_V)=2\pi^{\frac{1}{2}}r_S{}^2env_T(1-(1-r_P{}^2/r_S{}^2)$$
$$\times\exp\{-[r_P{}^2/(r_S{}^2-r_P{}^2)]\eta_V\})\quad (14)$$
$$\text{for}\quad V>0,\ \eta_V>0,$$

in agreement with reference 1.

4. General Conclusions

From (4), (10), and (12) the following general conclusions can be drawn:

(1). For $r_S\rightarrow r_P$ in (4), that is for infinitely thin sheaths $v_k\rightarrow\infty$, so that the second integral in (10) disappears. The first integral in (10), now taken between 0 and ∞, becomes unity so that the probe current is saturated above plasma potential. This is the extreme case of sheath limitation, equivalent to the plane probe.

(2). For $r_S\rightarrow\infty$ or $r_P\rightarrow 0$ in (4), that is for infinitely small probe, $v_k\rightarrow 0$, so that the first integral in (10) disappears. The second integral in (10), taken between 0 and ∞, always results in a form $a+bV/U_c$ (with U_c a characteristic voltage, $U_c=U_T=kT/e$, and $a=b=1$ for the Maxwellian case treated above). The integral in (12), taken between 0 and ∞ has the same form. That means a linear ascent of $J(V)$ for $V>0$, tangential to $J(V<0)$ at $V=0$, is a general feature of the small spherical probe for any velocity distribution.

(3). The transitional cases between the plane and the small spherical probe generally cover the area between saturation and the linear rise without major peculiarities. But if low-energy electrons are missing, i.e., if the distribution function starts from zero at finite energies U_0, as will be the case in the example treated later on, the linear rise of the probe current in the retarding region between $V=-U_0$ and $V=0$ will always continue through space potential into the accelerating range for finite spherical probes. The point of departure of $J(V)$ from this linear rise, marked by a discontinuity in the derivatives, is a function of r_S and U_0, as will be discussed.

(4). The second derivative of the probe current with respect to the probe voltage V, J'' is proportional to $F(U^{\frac{1}{2}})/U=2G(U)/U^{\frac{1}{2}}$ (see below), with $U/U_c=(v/v_c)^2$ $=-V/U_c$ in the retarding voltage region. The function $G(U)/U^{\frac{1}{2}}=S(U)$ may be called the "second derivative function," hereafter called the "SD function." The transformation from $F(U^{\frac{1}{2}})$ to $G(U)$ follows from

$$dn_v=nF(v/v_c)dv/v_c=\tfrac{1}{2}nF((U/U_c)^{\frac{1}{2}})(U/U_c)^{-\frac{1}{2}}dU/U_c$$
$$=nG(U/U_c)dU/U_c.$$

In the following proof of statement (3), the voltage is counted positive in the carrier repelling direction to avoid awkwardness in writing the equations. Then by setting $U/U_c=\eta$, $V/U_c=\eta_V$, Eq. (12) becomes

$$J=K\int_{\eta_V{}^{\frac{1}{2}}}^{\infty}\eta^{\frac{1}{2}}F(\eta^{\frac{1}{2}})[1-(\eta_V/\eta)]d(\eta^{\frac{1}{2}})$$

$$=\tfrac{1}{2}K\int_{\eta_V}^{\infty}F(\eta^{\frac{1}{2}})[1-(\eta_V/\eta)]d\eta,\ K=\pi enr_P{}^2v_c$$

$$\frac{\partial J}{\partial\eta_V}=-\tfrac{1}{2}K\int_{\eta_V}^{\infty}\left[\frac{F(\eta^{\frac{1}{2}})}{\eta}\right]d\eta,$$

$$\partial^2J/\partial\eta_V{}^2=\tfrac{1}{2}KF(\eta_V{}^{\frac{1}{2}})/\eta_V=KG(\eta_V)/\eta_V{}^{\frac{1}{2}}=KS(\eta_V),$$

which is a general derivation of what is known as Druyvesteyn's second derivative method for the spherical probe (and which results in an exponential for a Maxwellian).

5. Nonuniform Sheaths

The above derivations are valid for spherical sheaths, i.e., for velocities random in direction. For the extreme cases of infinitely thin sheaths on the one hand and of infinitely small probes on the other, the influence of the sheath disappears, so that the theory should hold for large directed velocities. But one can expect that even finite nonspherical sheaths do not cause excessive deviations from the spherical case, at least in the electron retarding region; this region is sheath independent in the spherical case and the dependence on the sheath in the nonspherical cases will not be strong. Experimental results to be published seem to bear out this expectation. Actually the applicability of the spherical probe to cases with large directed velocities is its most important advantage. In the example to be treated below there will normally be a large directed velocity which produces a nonuniform sheath. The influence of this nonuniformity is neglected.

6. Accelerated Half-Maxwellian

a. General Conditions

Many experimental cases will approximate the following idealized situation: The (saturated) emission current of a homogeneous plane cathode at T°K is accelerated in an electrical field perpendicular to the cathode. The mean free path of the electrons is so large that collisions of any kind can be neglected. The distribution function of the electrons is "half-Maxwellian" at the cathode surface,[5] i.e., all velocity components into the cathode are missing from the full-Maxwellian.

Practical examples for conditions approaching this idealized situation are, for instance, the emission from a hot cathode into a plasma through a cathode fall sheath, or the emission from one plasma into another through a double layer. Although these practical cases will differ from the ideal one by the presence of the "background plasma" into which the half-Maxwellian is shot, it is reasonable to treat the ideal case without background plasma, because it is easy to superimpose the latter, as will be discussed, and because situations which are practically free of background plasma do occur.

The results of the treatment of the ideal case are expected to hold outside the accelerating sheaths or layers, disregarding the background plasma. To what extent they apply inside the accelerating regions will depend on the geometry of the probes and their sheaths and of the accelerating regions. Inside accelerating sheaths or layers a closer approach to the pure case without background plasma can be expected, because the electrons of the background plasma may not penetrate appreciably into the accelerating region. Experimental results to be published indicate that a close approach to the pure case without background is possible inside accelerating regions.

b. Mean Velocities and Densities

If $\mathrm{u}(>0)$ is the velocity component perpendicular to the cathode, and v, w are the components parallel to the cathode, the density differential of the electrons with $\mathrm{u}\rightarrow d\mathrm{u}$, $\mathrm{v}\rightarrow d\mathrm{v}$, $\mathrm{w}\rightarrow d\mathrm{w}$ before acceleration, i.e., at the cathode, is

$$d^3n_{\mathrm{uvw}}=(2/\pi^{\frac32})n_c\exp[-(\mathrm{u}^2+\mathrm{v}^2+\mathrm{w}^2)/t^2]d(\mathrm{u}/t)\times d(\mathrm{v}/t)d(\mathrm{w}/t), \quad (15)$$

with n_c = density at the cathode surface, $t=(2kT/m)^{\frac12}$ = thermal velocity. The integral over (15), taken for u between 0 and ∞, and v and w between $-\infty$ and ∞ is equal to n_c. The density differential for $\mathrm{u}\rightarrow d\mathrm{u}$ integrated over v and w, therefore, is

$$dn_{\mathrm{u}}=(2/\pi^{\frac12})n_c\exp[-(\mathrm{u}/t)^2]d\mathrm{u}/t,\ \mathrm{u}\geq 0. \quad (16)$$

The mean velocity in direction perpendicular to the cathode is

$$\bar{\mathrm{u}}=\int_0^\infty \mathrm{u}dn_{\mathrm{u}}\bigg/\int_0^\infty dn_{\mathrm{u}}=t/\pi^{\frac12}. \quad (17)$$

The velocities after acceleration by the voltage V_0 are denoted by u, v, w. Obviously $\mathrm{v}=v$, $\mathrm{w}=w$. The kinetic energy connected with the velocity component perpendicular to the cathode is

$$\tfrac12 mu^2=\tfrac12 m\mathrm{u}^2+eV_0=eU,$$

or

$$u^2=\mathrm{u}^2+\kappa V_0=\kappa U,\quad \kappa=2e/m, \quad (18)$$

with the accelerating voltage V_0 counted positive in the direction of acceleration, so that

$$du^2=d\mathrm{u}^2,\quad du=(\mathrm{u}/u)d\mathrm{u}=(\mathrm{u}^2+\kappa V_0)^{-\frac12}\mathrm{u}d\mathrm{u}. \quad (19)$$

According to Liouville's theorm the particle current differential di before and after acceleration is the same:

$$di=\mathrm{u}dn_{\mathrm{u}}=udn_u=(\mathrm{u}^2+\kappa V_0)^{\frac12}dn_u, \quad (20)$$

so that the density differential of electrons with velocity components $u\rightarrow du$ becomes

$$dn_u=[\mathrm{u}/(\mathrm{u}^2+\kappa V_0)^{\frac12}]dn_u \quad (21)$$

which, according to (16) becomes

$$dn_u=(2/\pi^{\frac12})n_c\mathrm{u}(\mathrm{u}^2+\kappa V_0)^{-\frac12}\exp[-(\mathrm{u}/t)^2]d\mathrm{u}/t$$
$$=(1/\pi^{\frac12})n_ct(\mathrm{u}^2+\kappa V_0)^{-\frac12}\exp[-(\mathrm{u}/t)^2]d(\mathrm{u}/t)^2. \quad (22)$$

Then the mean value of the velocity components perpendicular to the cathode becomes

$$\bar{u}=\int_0^\infty udn_u\bigg/\int_0^\infty dn_u$$
$$=\int_0^\infty \exp[-(\mathrm{u}/t)^2]d(\mathrm{u}/t)^2\bigg/\int_0^\infty(\mathrm{u}^2+\kappa V_0)^{-\frac12}\times\exp[-(\mathrm{u}/t)^2]d(\mathrm{u}/t)^2, \quad (23)$$

---

[5] H. Shelton, Phys. Rev. **107**, 1553 (1957).

hich results in

$$\bar{u}=\frac{\frac{1}{2}t\exp(-\kappa V_0/t^2)}{E((\kappa V_0)^{\frac{1}{2}}/t)}, \tag{24}$$

ith

$$E(\;)=\int_{x=(\kappa V_0)^{\frac{1}{2}}/t}^{\infty}\exp(-x^2)dx.$$

The density after acceleration by V_0, n, because of $n_c\bar{\mathrm{u}}=n\bar{u}$, becomes

$$n=(2/\pi^{\frac{1}{2}})n_c\exp(\kappa V_0/t^2)E((\kappa V_0)^{\frac{1}{2}}/t). \tag{25}$$

Velocity and Energy Distribution after Acceleration

According to Liouville's theorem, the differentials of the particle current density i before and after acceleration must be equal

$$d^3i_{\mathrm{uvw}}=d^3i_{uvw}=\mathrm{u}d^3n_{\mathrm{uvw}}=ud^3n_{uvw}; \tag{26}$$

so that according to (15) and (18)

$$d^3n_{uvw}=(2/\pi^{\frac{3}{2}})n_c\mathrm{u}(\mathrm{u}^2+\kappa V_0)^{-\frac{1}{2}}\exp[-(\mathrm{u}^2+\mathrm{v}^2+\mathrm{w}^2)/t^2]$$
$$\times d(\mathrm{u}/t)d(\mathrm{v}/t)d(\mathrm{w}/t). \tag{27}$$

By setting $\mathrm{v}^2+\mathrm{w}^2=v^2+w^2=r^2$, $dvdw=rdrd\varphi$, and by integration over $d\varphi$, $\mathrm{u}^2=u^2-\kappa V_0$ from (18) and $d\mathrm{u}=[(\mathrm{u}^2+\kappa V_0)^{\frac{1}{2}}/\mathrm{u}]du$ from (19)

$$d^2n_{ur}=(4/\pi^{\frac{1}{2}})n_c\exp[-(u^2-\kappa V_0+r^2)/t^2]$$
$$\times(r/t)d(r/t)d(u/t). \tag{28}$$

By setting $dudr=adad\theta$, $a^2=u^2+r^2=$absolute velocity, $u=a\cos\theta$, $r=a\sin\theta$, and by keeping $a=$const (c.f. Fig. 3), the density differential of electrons with absolute velocities $a\rightarrow da$ becomes

$$\begin{aligned}dn_a=&(4/\pi^{\frac{1}{2}})n_c(a^2/t^2)d(a/t)\int_{\theta=0}^{\theta_{\max}}\\&\times\exp[-(a^2\cos^2\theta-\kappa V_0+a^2\sin^2\theta)/t^2]\sin\theta d\theta\\=&(4/\pi^{\frac{1}{2}})n_c(a^2/t^2)\\&\times\exp[-(a^2-\kappa V_0)/t^2]d(a/t)\int_0^{\theta_{\max}}\sin\theta d\theta,\end{aligned} \tag{29}$$

with the upper limit $\theta_{\max}$ given by

$$u^2{}_{\min}=\kappa V_0=a^2\cos^2\theta_{\max}. \tag{30}$$

By integration

$$dn_a=(4/\pi^{\frac{1}{2}})n_c(a/t)^2[1-(\kappa V_0/a^2)^{\frac{1}{2}}]$$
$$\times\exp[-(a^2-\kappa V_0)/t^2]da/t. \tag{31}$$

From this, with $a/t=\alpha$, $(\kappa V_0)^{\frac{1}{2}}/t=\alpha_0$, $\kappa V_0/a^2=(\alpha_0/\alpha)^2$, the velocity distribution function $F_c(\alpha)$, with n_c as reference density, becomes

$$\begin{aligned}F_c(\alpha)&=dn_a/n_cd\alpha\\&=(4/\pi^{\frac{1}{2}})\alpha^2(1-\alpha_0/\alpha)\exp[-(\alpha^2-\alpha_0^2)],\quad\alpha\geq\alpha_0.\end{aligned} \tag{32}$$

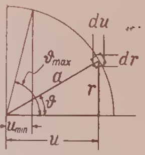

FIG. 3. Axial and radial components u and r of total velocity a after acceleration of half-Maxwellian by a voltage $U_0=u_{\min}{}^2\,m/2e$.

The corresponding energy distribution function, with $\alpha^2=\eta=U/U_T$, $\alpha_0^2=\eta_0=V_0/U_T$, $eU_T=kT$, and by means of $d\eta=d\alpha^2$, or $d\alpha=(1/2\eta^{\frac{1}{2}})d\eta$ (also with n_c as reference density) becomes

$$G_c(\eta)=dn_a/n_cd\eta=(2/\pi^{\frac{1}{2}})\alpha[1-(\alpha_0/\alpha)]e^{-(\eta-\eta_0)}, \tag{33}$$
$$\eta\geq\eta_0.$$

The corresponding functions with n as reference density, by means of (25) and $nF=n_cF_c$, $nG=n_cG_c$ become

$$\left.\begin{aligned}F(\alpha)&=dn_\alpha/nd\alpha=[2/E(\alpha_0)]\alpha(\alpha-\alpha_0)e^{-\eta} && (34)\\G(\eta)&=dn_\eta/nd\eta=[1/E(\alpha_0)](\alpha-\alpha_0)e^{-\eta} && (35)\\S(\eta)&=G(\eta)/\alpha=[1/E(\alpha_0)][1-(\alpha_0/\alpha)]e^{-\eta} && (36)\end{aligned}\right\}\begin{aligned}&\alpha\geq\alpha_0\\&\eta\geq\eta_0.\end{aligned}$$

$S(\eta)$ is the SD-function. $E(\alpha_0)=\int_{\alpha_0}^{\infty}\exp(-x^2)dx$, $\alpha^2=\eta$. Of course, all these functions are zero for

$$0<\eta=\alpha^2<\eta_0=\alpha_0^2,$$

(compare, for instance, Figs. 6, 7, and 8).

d. Probe Current

The probe current is given by (12) in the decelerating and by (10) in the accelerating range of the probe voltage. If again the decelerating normalized probe voltage $\eta_V=V/U_T$ is counted positive, (12), with the sign of V changed, becomes

$$J(\eta_V)=C\int_{\alpha_V}^{\infty}\alpha(1-\eta_V/\alpha^2)F(\alpha)d\alpha, \tag{37a}$$
$$\eta_V=\alpha_V{}^2\geq\eta_0=\alpha_0^2.$$

In the probe voltage interval $0<\eta_V<\eta_0$ or $0<V<V_0$ the integration covers only the range of $F(\alpha)\neq0$:

$$J(\eta_V)=C\int_{\alpha_0}^{\infty}\alpha(1-\eta_V/\alpha^2)F(\alpha)d\alpha,\ 0<\eta_V\leq\eta_0. \tag{37b}$$

The constant C in (37a) and (37b) is $C=\pi r_P{}^2ent$. Integration of (37a, b) with $F(\alpha)$ from (34), with $\eta_V\equiv\eta$, results in

$$J(\eta)=[C/E(\alpha_0)][(1-\alpha_0\alpha)e^{-\eta}+(2\eta-1)\alpha_0E(\alpha)], \tag{38a}$$
$$\eta\geq\eta_0,$$

$$J(\eta)=C[(1-\eta)/e^{\eta_0}E(\alpha_0)+(2\eta-1)\alpha_0], \tag{38b}$$
$$0\leq\eta\leq\eta_0.$$

The latter equation is a straight line, tangential to J(38a) at $\eta=\eta_0$ (see Fig. 4).

In the accelerating region of the probe voltage, Eq. (10), with the original signs and with $F(\alpha)=0$ for

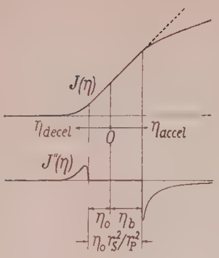

FIG. 4. Probe current J and its second derivative J'' as functions of normalized probe voltage $\eta=V/U_T$ for accelerated half-Maxwellian. Normalized acceleration voltage $\eta_0=V_0/U_T$. Normalized critical probe voltage η_b for transition from impact parameter limitation to sheath limitation. Temperature equivalent of original half-Maxwellian $=U_T$; sheath radius $=r_S$; probe radius $=r_P$.

$0<\eta_V\leq\eta_0$ being considered, becomes

$$J(\eta_V)=C_1\left\{r_S^2\int_{\alpha_0}^{\alpha_k}\alpha F(\alpha)d\alpha\right.$$

$$\left.+r_P^2\int_{\alpha_k}^{\infty}\alpha(1+\eta_V/\alpha^2)F(\alpha)d\alpha\right\},\quad(39a)$$

$$\eta_k\geq\eta_0,\quad\text{or}\quad\eta_V\geq\eta_0[(r_S/r_P)^2-1]$$

with $\eta_k=\alpha_k^2$ from (4), by normalization:

$$\eta_k=\alpha_k^2=\eta_V/[(r_S/r_P)^2-1].\qquad(40)$$

The limit for the validity of (39a) is given by $\eta_k=\eta_0$ in (40) or

$$\eta_V\geq\eta_0[(r_S/r_P)^2-1].\qquad(41)$$

For $\eta_V\leq\eta_0[(r_S/r_P)^2-1]$, i.e., $\eta_k\leq\eta_0$, $\alpha_k\leq\alpha_0$, the first integral in (39a) disappears and the lower limit in the second one becomes α_0:

$$J(\eta_V)=C_1r_P^2\int_{\alpha_0}^{\infty}\alpha(1+\eta_V/\alpha^2)F(\alpha)d\alpha,\quad(39b)$$

$$0<\eta_V\leq\eta_0[(r_S/r_P)^2-1],$$

which is independent of the sheath and is identical with (37b) except for the opposite sign of η_V. Thus (39b) is the continuation of the linear ascent of J from the decelerating region through space potential into the accelerating region of the probe voltage.

Integration of (39a), (39b) again with $\eta_V\equiv\eta$, results in

$$\begin{aligned}J(\eta)=&[C_1/E(\alpha_0)]\\&\times(r_S^2\{e^{-\eta_0}-(1+\eta_k-\alpha_0\alpha_k)e^{-\eta_k}\\&-\alpha_0[E(\alpha_0)-E(\alpha_k)]\}\\&+r_P^2[(1+\eta_k-\alpha_0\alpha_k+\eta)e^{-\eta_k}\\&-\alpha_0(1+2\eta)E(\alpha_k)]),\quad(42a)\end{aligned}$$

with

$$\eta_k=\alpha_k^2=\eta/[(r_S/r_P)^2-1]\geq\eta_0$$

or

$$\eta\geq\eta_0[(r_S/r_P)^2-1],\quad C_1=\pi ent,$$

which for $\eta_0\rightarrow0$ approaches (14) for the unaccelerated Maxwellian, and

$$J(\eta)=C\{[(1+\eta)/e^{\eta_0}E(\alpha_0)]-\alpha_0(1+2\eta)\}\quad(42b)$$

with

$$\eta_k=\eta/[(r_S/r_P)^2-1]\leq\eta_0,$$

or

$$0\leq\eta\leq\eta_0[(r_S/r_P)^2-1],\quad C=\pi r_P^2ent,$$

which, of course, disappears for $\eta_0\rightarrow0$.

e. Discussion of Development of Probe Current

The probe current according to (38a), (38b) and (42a), (42b) and its second derivative are plotted over the reduced probe voltage η schematically in Fig. 4. In the decelerating range of the probe voltage, J'' of course is proportional to the SD function (36). The negative portion of J'' in the accelerating range, namely J'' (42a), is a very complicated function with a general character as shown (according to some preliminary experimental results).

The behavior of the probe current according to Fig. 4 offers an interesting relationship between r_S/r_P at the breakoff point at $\eta_b=\eta_0[(r_S/r_P)^2-1]$ of J from the linear rise in the accelerating range and η_0 and the width δ of the linear range of the probe current, which follows from the limits of (38a), (38b) and (42a), (42b).

$$\delta=\eta_0+\eta_b=\eta_0r_S^2/r_P^2,\quad\text{or}\quad r_S^2/r_P^2=\delta/\eta_0.\qquad(43)$$

Unfortunately, there is no indication of η_0 in the probe curve. A possibility for the determination of η_0, at least in theory, is a comparison of $J''(\eta)$ in the decelerating region with the theoretical development of $S(\eta)$ in Fig. 7 (which must be done in any case in order to determine the density and the asymtotic temperature). This possibility to measure r_S should be mentioned, even though conditions for the sheath are the peculiar ones of the accelerated half-Maxwellian and only a crude average r_S will result, because of the nonuniformity of the sheath.

It is evident from (37a), (37b) and (39a), (39b) that the possibility of a linear rise for finite probes in the accelerating region is common to all distribution functions which start from zero at a finite velocity, i.e., in which slow electrons are missing.

f. Normalization for Graphical Presentation

In order to obtain a concise graphical picture of the results in the decelerating probe voltage range and also for evaluation purposes, the results are normalized in the following way: As far as the temperature of the original half-Maxwellian is concerned, the results are normalized already ($\alpha=a/t$, $\eta=U/U_T=\alpha^2$, etc.). In addition, the probe current is normalized by dividing by the probe current at space potential J_0, so that $\iota(\eta)=J(\eta)/J_0$. Furthermore, the tangent of the normalized current at zero potential is made constant and equal to that of the pure exponential for zero acceleration $V_0=0$, by compression of the abscissa scale, i.e., by multiplication of η by $-\iota_0'$. From (42b)

$$J_0=C\{[1/e^{\eta_0}E(\alpha_0)]-\alpha_0\}\qquad(44)$$

$$\iota_0' = -J_0'/J_0 = (1-2F)/(1-F), \qquad F = \alpha_0 e^{\eta_0} E(\alpha_0) \tag{45}$$

$$-1/\iota_0' \rightarrow \alpha_0 + 2 \quad \text{for} \quad \alpha_0 \gg 1, \tag{45a}$$

.f. Fig. 9). Finally, the area under the normalized D-function is made equal to the area under $S(\eta)$ by ompressing the abscissa scale as in ι, and at the same me expanding the ordinate scale by the same factor. he results are shown in Figs. 5 and 6.

In Fig. 7 the SD function (36) is plotted semilogaithmically, [disregarding the factor $1/E(\alpha_0)$], which ives a clear picture of the development of the energy ectrum of the electrons. The corresponding electron nergy spectrum itself, $G(\eta) = S(\eta)\alpha$, also disregarding he factor $1/E(\alpha)$, is shown in Fig. 8. The advantage of he SD function $S(\eta)$ over the distribution function $(\eta) = S(\eta)\alpha$, namely the exponential behavior for $=0$, is evident. In Fig. 9 the reciprocal of the reducon factor (45) is plotted.

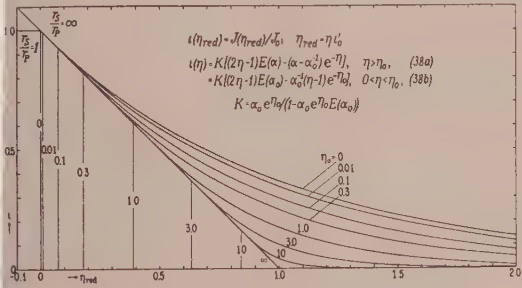

FIG. 5. Reduced probe current $\iota = J/J_0$ as function of reduced robe voltage $\eta_{red} = \eta\iota_0'$, with normalized acceleration voltage $= V_0/U_T$ as parameter [Eqs. (38a), (38b), (44), (45) disregardg the − sign].

g. Discussion of the SD Function

(1). As Fig. 7 shows, the SD function approaches the xponential asymptotically. That means the electron emperature from the asymptotic slope corresponds to he original temperature of the half-Maxwellian before cceleration. In a semilog plot of the probe current the eviations from the asymptotic straight line are scarcely isible for smaller values of the acceleration voltage.

(2). The deviations of the energy spectrum from the riginal half-Maxwellian are drastic; electrons with nergies smaller than the equivalent of the accelerating oltage are absent, and the maximum of the SD funcion becomes progressively flatter with increasing aceleration voltage $\eta_0 = V_0/U_T$. Even small η_0's cause arked rounding of the sharp top of the original xponential, in contrast to the behavior of the fullMaxwellian with superimposed drift where small drift elocities cause only minute deviations from the Maxellian. This behavior is essential for the questions oncerning the "rounding of the knee" of the probe urves.

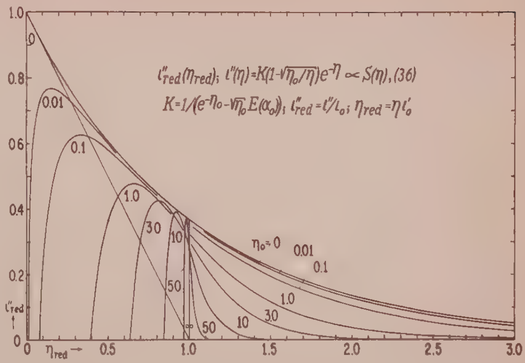

FIG. 6. Reduced second derivative $\iota_{red}'' = \iota''/\iota_0'$ as function of reduced probe voltage $\eta_{red} = \eta\iota_0'$, with normalized acceleration voltage $\eta_0 = V_0/U_T$ as parameter [Eqs. (36), (45) disregarding the − sign].

(3). The approach to the monoenergetic case with increasing η_0 is rapid compared to the corresponding Maxwellian with superimposed drift, as a quantitative comparison shows. (Originally the latter case had been treated in this paper, but because of its highly academic character it has been replaced by the accelerated half-Maxwellian.)

(4). A large number of experimental results seem to indicate that the importance of the case of the accelerated half-Maxwellian has been underestimated thus far. Although a pure form of the nature assumed here may never be observed, it probably describes many experimental conditions in which small deviations from a pure Maxwellian are observed at least in principle. Probably a superposition of the contributions of a distributed V_0 will give an even better approximation to many experimental conditions.

h. Superimposed Background Plasma

As mentioned previously, in most cases one of the main deviations from the ideal case treated thus far is

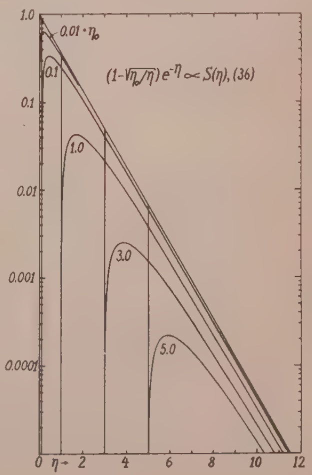

FIG. 7. Semilog plot of the second derivative function $S \propto \iota''$ over normalized probe voltage $\eta = V/U_T$, [Eq. (36)], with the normalized acceleration voltage $\alpha_0^2 = \eta_0 = V_0/U_T$ as parameter, disregarding the factor $1/E(\alpha_0)$.

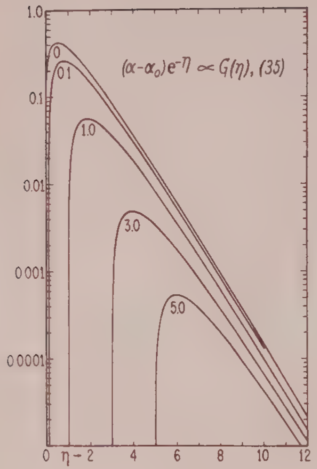

FIG. 8. Same as Fig. 7 for distribution function $G(\eta)=\alpha S(\eta)$, also disregarding the factor $1/E(\alpha_0)$.

the presence of a background plasma into which the accelerated half-Maxwellian is shot. Such a situation amounts to a superposition, for example, of two different cases of the nature treated above, one with a large accelerating voltage V_{01} and another one with a small V_{02}, and normally with different temperatures of the respective original Maxwellians and, of course, different densities. Often V_{02} will be negligibly small, which amounts to Maxwellian character of the background plasma. It should be stressed that in the background plasma the directed velocity which corresponds to V_{02} [$\bar{u}$ from (24)] may have been almost entirely randomized and, in spite of that, the distribution function may closely resemble the non-thermal-equilibrium state, (34) to (36), because elastic collisions with heavy neutrals, and especially reflections from boundary layers, may quickly randomize the original beam, but the interaction among the random electrons may be too weak to establish thermal equilibrium among the background electrons within their lifetime.

Without going into a detailed treatment, the main characteristics of a case with $V_{02}\approx 0$ shall be briefly discussed by means of the semi-schematic diagram, Fig. 10. Fortunately, the development in the retarding probe voltage range is nothing but a linear superposition of the two cases, because there everything is independent of the probe sheath. Therefore, the probe current first rises according to (38a), then it rises linearly according to (38b), until the slow electrons of the background-Maxwellian cause an exponential rise above the linear rise, according to (13), which continues up to plasma potential. From there on, of course, the development is complicated because it depends on the sheath radius r_S which is a complicated function of the combination of the accelerated half-Maxwellian and the background plasma. But, fortunately, the presence of the latter now gives a precise indication of space potential in that there J'' jumps from the positive exponential in the decelerating range to strongly negative values in the accelerating range of the probe voltage. Normally, ionization in the probe sheath at large enough accelerating probe voltages is indicated by a positive J'' (dotted curve in Fig. 10), with the distance between the end of $J''\propto S(\eta)$ and the dotted rise being close to the ionization voltage of the gas.

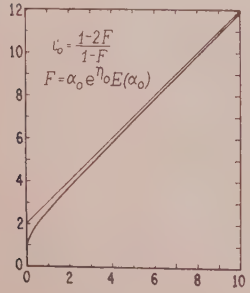

FIG. 9. Reciprocal reduction factor $|1/\iota_0'|$ [Eq. (45)] as function of the normalized acceleration voltage $\eta_0=V_0/U_T$.

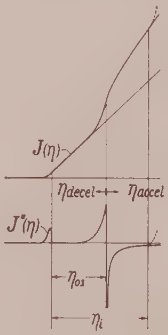

FIG. 10. Probe current J and its second derivative J'' as functions of normalized probe voltage $\eta=V/U_{T1}$ for Maxwellian superimposed on accelerated half-Maxwellian. Normalized acceleration voltage

$$\eta_{01}=V_{01}/U_{T1};\ (\eta_{02}=0),$$

η_i = normalized ionization voltage.

It should be noted that in the experimental curve all the abrupt transitions in J'' are smoothed out by the inherent nonuniformity of the work function of th probe surface, and also by the inherent nonuniformity of the probe sheath.

The influence of the ion current on the second derivatives, fortunately, as a rule is negligible in the electron repelling range. However, under certain condition peculiarities in the experimental SD curves near spac potential are caused by the ion current (as will be discussed in a paper to be published). In discharges in th lightest gases the nonlinearity of the ion current ma have some influence even throughout the electro repelling range.

ACKNOWLEDGMENT

I want to thank Dr. P. Parzen, Republic Aviation Corporation, for my conversion from an academi drifting Maxwellian to a hopefully less academic accelerated Maxwellian.

JOURNAL OF APPLIED PHYSICS VOLUME 32, NUMBER 12 DECEMBER, 1961

Characteristic Electron Energy Loss Measurements at Low Temperatures

E. M. Hörl and J. A. Suddeth
National Bureau of Standards, Washington 25, D. C.

(Received April 28, 1961)

A method is described for the investigation of characteristic energy losses of electrons in solids at temperatures in the liquid helium and liquid hydrogen temperature range. This method had been primarily developed for the investigation of thin films of solidified permanent gases, but it is also very suitable for the study at low temperatures of any substance, which is obtainable as a thin film. For the measurement of the energy losses itself, a very versatile electrostatic analyzer lens has been constructed which allows the observation of electron diffraction patterns of the samples before and after energy loss measurements. First results are reported on thin films of solid oxygen and solid xenon.

INTRODUCTION

ELECTRON characteristic energy losses in gases and solids have been studied by different methods during the last thirty years. Most of the measurements have been carried out at room temperature until the interesting question of the temperature dependence of the energy loss values in metals arose from theoretical considerations. First studies on the metal aluminum in the liquid helium temperature range were undertaken by Leder and Marton[1] and compared with the theoretically expected values.

Our interests have been focused on the investigation of the characteristic energy loss spectra of solidified permanent gases for which the molecular or atomic energy levels are well known in the gas phase and for which some optical data are available, or at least can be expected to be available in the near future, for the solid phase.

Our aim was to investigate the density effect which is due to the agglomeration of the molecules or atoms into a solid and which can cause a departure of the dielectric constant from unity.[2] In the case that the dielectric constant departs only very slightly from unity, it would be possible with sufficient resolution to study the effects of the crystalline fields as in the usual optical investigations. However, such a resolution is for most of the crystalline materials very far from being obtainable with today's electron energy analyzers. This fact constitutes a rather strong limitation of the method, but we may still expect detectable effects in cases where there exists a fairly strong binding between neighboring molecules. This argument made the study of solid oxygen particularly attractive for which there are indications for the existence of $(O_2)_2$ complexes in the solid.[3] Further, there are also some optical data available for solid oxygen in the visible, infrared, and ultraviolet spectral region.[4,5] Unfortunately the crystal structure of solid oxygen is still unknown, which again complicates the situation. In addition to oxygen, we also made measurements on solid xenon as a representative of the rare gases.

For the measurement of the electron energy losses itself, a very versatile electrostatic analyzer lens[6] was constructed, which allowed rotation and translation of the entrance slit as well as change of slit width during operation. Entire electron diffraction patterns of the samples could be observed and photographed before and after energy loss measurements by shifting the complete lens assembly off the electron beam path, whereas in previous work[7,8] observation of only a slice of the diffraction pattern was possible by opening up the slit of the analyzer lens.

EXPERIMENTAL TECHNIQUE

A schematic vertical cross section of our experimental arrangement for the measurement of characteristic electron energy losses at very low temperatures is presented in Fig. 1. A thin supporting foil (collodion, Formvar, or Al) is mounted over a hole in a target block of oxygen-free high-conductivity copper which is soldered to the bottom of a cylindrical container filled with liquid helium or liquid hydrogen. The tempera-

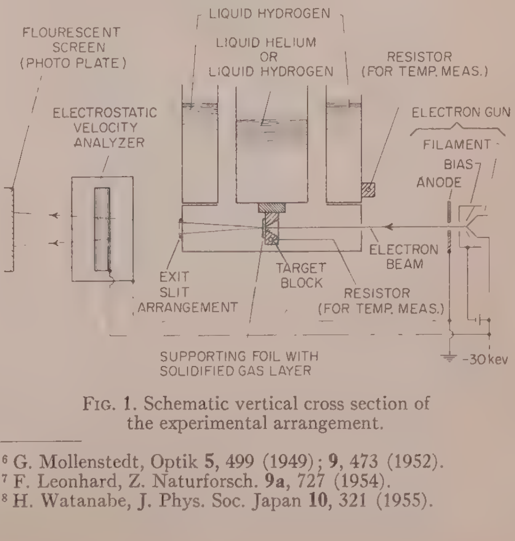
LIQUID HYDROGEN
FLOURESCENT SCREEN (PHOTO PLATE)
LIQUID HELIUM OR LIQUID HYDROGEN
RESISTOR (FOR TEMP. MEAS.)
ELECTROSTATIC VELOCITY ANALYZER
ELECTRON GUN
FILAMENT
BIAS
ANODE
ELECTRON BEAM
EXIT SLIT ARRANGEMENT
TARGET BLOCK
RESISTOR (FOR TEMP. MEAS.)
SUPPORTING FOIL WITH SOLIDIFIED GAS LAYER
-30kev

FIG. 1. Schematic vertical cross section of the experimental arrangement.

---

[1] L. B. Leder and L. Marton, Phys. Rev. **112**, 341 (1958).

[2] L. Marton, L. B. Leder, and H. Mendlowitz, Advances in Electronics **7**, 83 (1955); J. Hubbard, Proc. Phys. Soc. (London) **A68**, 441 (1955); H. Frohlich, and H. Pelzer, *ibid.* **A68**, 525 (1955).

[3] W. Finkelnberg, *Kontinuierliche Spectren* (J. Springer, Berlin, 1938), p. 227.

[4] A. Prikhotko, M. Ruheman, and A. Federitenko, Physik. Z. Sowjet-union **7**, 410 (1935).

[5] M. J. Romand and J. Granier-Mayence, J. phys. radium **15**, 62 (1954).

[6] G. Mollenstedt, Optik **5**, 499 (1949); **9**, 473 (1952).

[7] F. Leonhard, Z. Naturforsch. **9a**, 727 (1954).

[8] H. Watanabe, J. Phys. Soc. Japan **10**, 321 (1955).

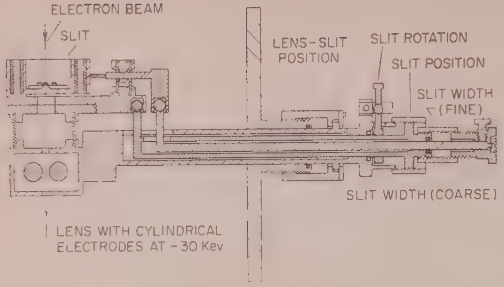

FIG. 2. Horizontal cross section through the analyzer lens and its control mechanism.

ture of the target block can be measured by means of a carbon resistance thermometer. On the supporting foil, thin layers of gases can be formed by condensation and investigated by means of an electron beam of 30-kev energy. The electron beam is produced by a Steigerwald type electron gun[9] and passes through the conical bore of the target block which is coated with a fluorescent substance for proper beam alignment. The target is completely surrounded by a radiation shield at a temperature of 20°K, which has only three openings: a circular opening for the entrance, a rectangular opening for the exit of the electron beam, and a circular opening for the molecular beam necessary for the formation of solidified gas layers on the substrate. A detailed discussion of the cryostat is given in an earlier publication.[10]

After passing through the specimen film, the electron beam enters a cylindrical analyzer lens.[6] The entrance slit of this lens "cuts out" of the cone of diffracted electrons a thin vertical slice. The electrostatic field of the lens acts on two electrons with an equal scattering angle but with different energy so that they will hit a photographic plate behind the lens at two different positions on a horizontal line. Electrons of equal energy but different scattering angle will hit the plate on a vertical line. One thus obtains on the photographic plate a two dimensional plot of electron intensity (represented by the density of the plate) as a function of scattering angle (vertical coordinate) and energy loss (horizontal coordinate). Patterns of this ideal kind will be obtained only if very small angles of scattering are permitted and only if the very central region of the lens is used. If one studies electrons scattered at large angles (up to 0.06 rad), one encounters a bending of the vertical lines of equal electron energy. With increasing scattering angles the bending effect increases.

Figure 2 shows the essential features of the lens design. "Outside the vacuum" controls are provided for positioning the slit-lens assembly with respect to the electron beam, positioning of the slit with reference to the lens for optimizing resolution and dispersion, rotation of slit to the lens, and fine and coarse adjustments of slit width. All the controls are provided on concentric shafts for ease of operation in a darkened room. "In-vacuum" friction is essentially eliminated by the use of phosphor bronze deformation members.[11]

The slit edges used are of a new design suggested by L. Marton as shown in Figs. 2 and 3(a). Instead of the usual knife edge slits used in light optics, the slit edges are made of stretched 10 mil Nichrome wire. This eliminates a major machining operation and provides for easy replacement of the slit edges. Parallelism of the slit edge is maintained throughout the slit width range of 1 μ to 2 mm by means of the parallel spring movements.[11] The slit is very stable in that no subsequent adjustments have been made over a nine month period since the original tightening and alignment of the slit wires.

The dimensional data for the "cylindrical" electrostatic lens are the same as for the lens discussed by Leder,[12] except for the dimensions along the cylindrical axis. To allow for transmission and analysis of the undiffracted and diffracted beams, the openings along the cylindrical axis are 50 mm or more. Figure 3(b) shows the construction of the center electrode and its supports. The re-entry design[13] of the end pieces was found necessary to prevent electrical breakdown on the

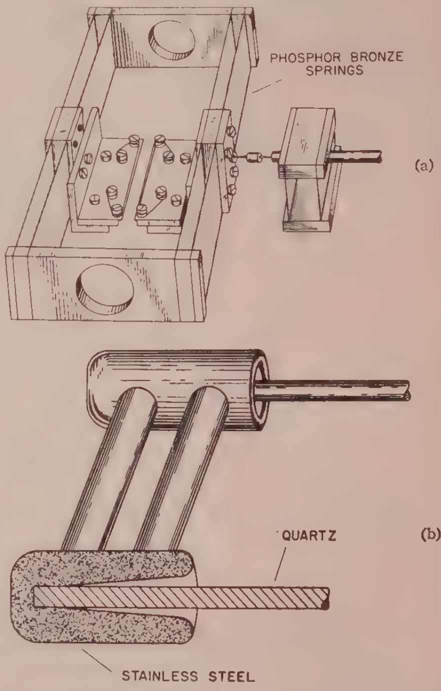

FIG. 3. (a) Entrance slit assembly. (b) Cylindrical electrodes of the analyzer lens mounted on cylindrical quartz insulators.

---

[9] K. H. Steigerwald, Optik 5, 469 (1949).

[10] E. M. Hörl and L. Marton, Rev. Sci. Instr. 29, 859 (1958).

[11] R. V. Jones, J. Sci. Instr. 28, 38 (1951).

[12] L. B. Leder, Phys. Rev. 103, 1721 (1956).

[13] J. D. Trimmer and H. Pearlman, "High voltage problems," ORNL Report TID 5211 (1951).

surface of the quartz rods due to the field gradient building up at the negative high voltage end of the quartz rods.

The usual procedure of investigating thin films of solidified gases is the following. First the analyzer is moved off the electron beam path and an electron diffraction pattern of the foil is taken. Rotation of the target also allows the observation and registration of diffraction patterns at different angles of electron incidence. The analyzer lens is then moved into the electron beam path and is properly aligned. A calibration spectrum is now taken by changing the potential of the gun-filament with respect to the center electrode of the analyzer lens in steps of approximately 6 v. This potential difference is obtained from batteries which were very carefully measured by means of a potentiometer. An example of such a calibration spectrum is given in Fig. 4(b). Now the actual electron energy loss spectrum of the specimen is taken followed by another calibration spectrum. The photographic patterns of loss and calibration spectra are traced by a densitometer.

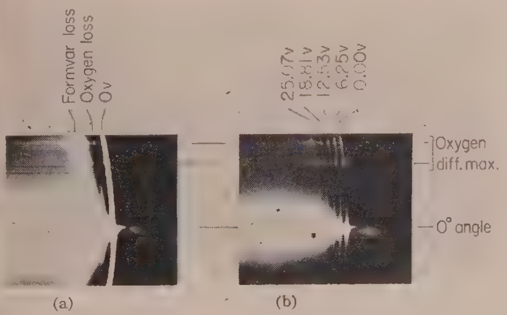

FIG. 4. (a) Electron energy loss pattern obtained from a thin layer of solid oxygen on a Formvar substrate at a temperature of 20°K. The 9.5-ev energy loss of solid oxygen as well as the broad energy loss of the Formvar substrate at approximately 23 ev are indicated. (b). Calibration for pattern shown in (a).

One encounters two major experimental difficulties in extending electron characteristic energy loss measurements to temperatures in the liquid helium and liquid hydrogen temperature range. These difficulties are the same as those which occur in extending the electron diffraction technique to temperatures in the abovementioned range. They consist of (1) the condensation of the residual gases of the high vacuum system on the surface of the cold specimen and (2) electrical charging effects due to the high electrical resistance of solidified permanent gases. These difficulties and methods of correcting them were discussed in more detail in a previous paper.[14]

EXPERIMENTAL RESULTS

(a) Thin Films of Solid Oxygen at 20°K

Our first experiments were carried out on thin films of solid oxygen on Formvar substrates at a temperature of 20°K. The electron diffraction patterns obtained from these solid oxygen layers will be discussed in another publication. We only want to note that the diffraction patterns of the films studied with the technique described in this paper indicated an approximately random orientation of the microcrystallites with a size on the order of 100 A. An electron energy loss pattern obtained is given in Fig. 4(a). Besides the energy loss of the Formvar substrate, an energy loss at 9.5 ev (±0.6 ev)[15] is visible. Its intensity decreases somewhat with scattering angle, but is still pronounced at very large angles. A discussion of this loss will follow in a later section.

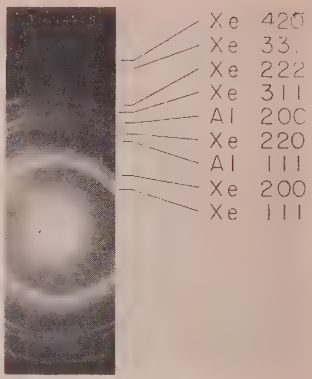

FIG. 5. Electron diffraction pattern of a thin layer of solid xenon on an aluminum supporting foil at a temperature of 20°K. The Laue indices of the Debye-Scherrer rings are indicated.

(b) Thin Films of Solid Xenon at 20°K

In one series of experiments xenon gas was condensed on a thin Al foil of a thickness on the order of 100 A and at a temperature of 20°K. A diffraction pattern taken from this xenon layer is shown in Fig. 5.

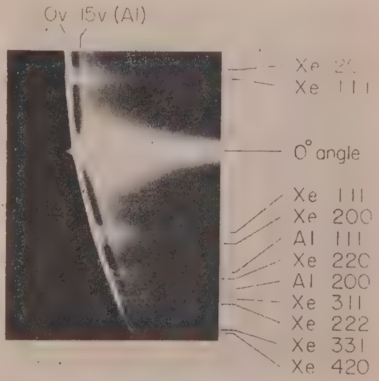

FIG. 6. Electron energy loss pattern of a thin layer of solid xenon on an aluminum supporting foil at a temperature of 20°K. It is the same foil for which the diffraction pattern is shown in Fig. 5. The 15-ev aluminum energy loss is distinctively visible; an energy loss at approximately 8–9 ev, which barely can be seen on this picture but better on the plate, is discussed in the text.

---

[14] E. M. Hörl and L. Marton, Acta Cryst. 14, 11 (1961).

[15] The error of ±0.6 ev quoted throughout this paper indicates the maximum value of the probable errors in our measurements of energy loss values.

It indicates the formation of xenon microcrystallites oriented randomly with a size comparable to those of the aluminum microcrystallites making up the substrate foil. The size of the aluminum crystallites are in the order of magnitude of 100 A. Spacings and intensities of the xenon diffraction rings are in good agreement with the known crystal structure for solid xenon[16] (structure type Al, fcc). The electron energy loss pattern taken from the same foil is presented in Fig. 6. The electrons which were diffracted by the Xe crystals and which also suffered inelastic collisions form the distinct white horizontal lines marked with the corresponding net plane indices. The 15-ev energy loss line of the aluminum supporting foil is clearly visible. There is also an indication of an energy loss line at approximately 8 to 9 ev. As an interpretation of this loss we would have to consider two possibilities. We could attribute it to aluminum (so called "low lying" loss) or to xenon. No other energy loss lines were detectable.

In a second series of experiments a xenon layer three times as thick as the one discussed above was investigated on a collodion substrate. These experiments were carried out in order to decide whether the observed weak energy loss at 8 to 9 ev is due to aluminum or due to xenon. Collodion has only one broad energy loss around 23 ev, like Formvar, and, therefore, does not affect the 10 ev region. The observed energy loss pattern was carefully traced at scattering angles of 0 rad and 0.018 rad. The result is shown in Fig. 7. The 0-rad trace shows an absorption of energy starting at 7 ev with a peak at 7.9 ev (±0.6 ev) in addition to the absorption due to collodion. This peak, not very distinct on the densitometer tracing in Fig. 7, is easily measurable on the original photographic plate by means of a traveling microscope. This absorption decreases with increasing scattering angle and is completely missing at a scattering angle of 0.018 rad where only the energy absorption due to the substrate is left over.

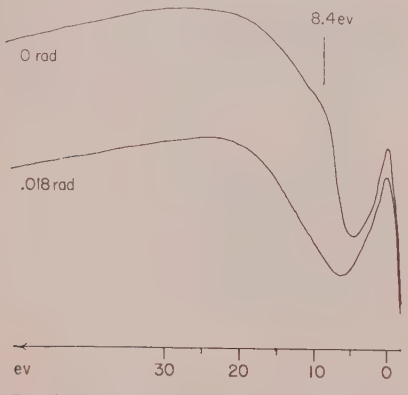

FIG. 7. Density traces of an energy loss pattern of a solid xenon layer on a collodion substrate. Traces taken at the scattering angles of 0 rad and 0.018 rad show the decreasing absorption of electron energy ≧8.4 ev with angle. The position of the Xe-resonance line at 8.4 ev is indicated.

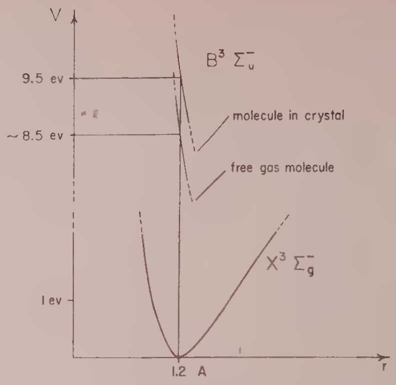

FIG. 8. Shift of potential curve of $B^3\Sigma_u^-$ state of O_2 molecule due to crystal-field perturbation (schematically).

DISCUSSION OF EXPERIMENTAL RESULTS

(a) Experiments on Solid Oxygen

The observed electron energy loss at 9.5 ev may be interpreted as the $X^3\,\Sigma_g^- \rightarrow B^3\,\Sigma_u^-$ transition of the perturbed O_2 molecules comprising the oxygen crystals. In the case of the free gas molecule the above transition gives rise to the well-known Schuman-Runge band system in the ultraviolet spectral range. Measurements of the excitation energy carried out on the free O_2 molecule with the electron impact method using low and medium energy electrons have given values of 7.9 ev,[17] 8.5 ev,[18] 9.0 ev,[19] 8.0±0.3 ev,[20] and 8.43±0.1 ev[21] in the energy range where one would expect the $X^3\,\Sigma_g^- \rightarrow B^3\,\Sigma_u$ transition.

An interpretation of the 9.5-ev energy loss in solid oxygen at 20°K in terms of a perturbed transition of the above kind would require the assumption of a dielectric constant ≈1 and a shift of the left side of the potential curve of the upper state to higher energies and/or to larger r values as illustrated in Fig. 8. For this shift a small change of the equilibrium internuclear distance, the dissociation energy, and the vibrational constant of the upper state, individually or in some combination, would follow.

A less probable alternative transition would be the perturbed $X^3\,\Sigma_g^- \rightarrow A^3\,\Sigma_u^+$ transition, which gives rise to the Herzberg bands in the case of the free O_2 molecule. In this case also the assumption of a shift or change of shape of the potential curve of the upper state would be necessary.

---

[16] Strukturbericht **II**, 203 (1928–1932).

[17] R. H. Dalton, J. Am. Chem. Soc. **51**, 2366 (1929).

[18] J. E. Roberts and R. Widdington, Proc. Leeds Phil. Lit. Soc., Sci. Sect. **2**, 12 (1929).

[19] L. A. M. Henry, Bull. Soc. chim. Belges **40**, 339 (1931).

[20] G. Mollenstedt, Z. Naturforsch. **7a**, 465 (1952).

[21] W. Dietrich, Z. Physik **152**, 87 (1958).

(b) Experiments on Solid Xenon

The value of the absorption peak (7.9±0.6 ev) in hin solid xenon layers agrees within the error of measurement with the excitation energy of the strongest of he two resonance transitions of the free and neutral Xe atom observed by electron impact experiments at 8.4 ev,[22] 8.3 ev,[23] and 8.25±0.15 ev.[21] The wavelengths of the resonance lines are: 1469.621 A (≈8.4 ev) and 1295.560 A (≈9.6 ev).[24] This observation would indicate that the dielectric constant of solid xenon is approximately unity and that there are no density effects $\gtrsim 3000\ \text{cm}^{-1}$.

ACKNOWLEDGMENTS

The authors would like to thank Dr. L. Marton and Dr. J. A. Simpson for their help in the design of the analyzer lens and discussions on various aspects of the problem. Our thanks are also extended to L. E. Mann and A. B. Dauses for their excellent care and precision in the construction of the apparatus.

[22] G. Deljardin, Compt. rend. **178**, 1069 (1924).

[23] G. Hertz and R. K. Kloppers, Z. Physik **31**, 463 (1925).

[24] J. C. Boyce, Phys. Rev. **49**, 730 (1936).

JOURNAL OF APPLIED PHYSICS VOLUME 32, NUMBER 12 DECEMBER, 1961

Defect Mechanisms in a Noncrystalline Solid

W. C. Levengood*
Ball Brothers Research Corporation, Muncie, Indiana

(Received April 27, 1961)

It is proposed that spiral defects originate at torque stress fields in glass and represent variations in localized bond energy. By postulating shear stress couples across flaw lines, extension and annihilation of flaws from neighboring spiral sources were tentatively explained. Distortion or movement within a spiral was indicated on samples subjected to localized stress before etching. Experimentally it was shown that substitution of lead and bismuth for silica in a nonspiral glass produced a rigid, brittle network which ultimately disclosed spirals originating at minute nuclei. Details of structure were quantitatively studied by using the dynamic spherical indenter. Flaw loops were also discovered which originated at random etch pit sources and increased in diameter with applied stress. Rows of etch pits were observed on samples stressed in torque. The conjecture was introduced that the torsion stress caused collapse of flaws into point defect rows. The etch pit rows appeared to be more stable than linear flaws. The minimum length of stability of a void derived from dislocation theory was in agreement with experimental measurements from the point defect rows.

I. INTRODUCTION

FLAW loops originating at minute sources in glass and formation of etch pit rows under applied stress are new phenomena presented in this paper. The significance of these will be discussed in relation to recent findings of spiral defect patterns in glass. Also included are studies of spiral sources and their formation mechanisms. Hypothetical stress vectors were found useful for qualitatively explaining the morphology of interacting spiral sources. Annihilation of flaws indicated opposing shear vectors, whereas reinforcement and extension indicated parallel vectors. It was originally suggested that spiral formation took place primarily by localized bond readjustment. The present experimental observations support, at least qualitatively, this original hypothesis. A major difference between defects in glass and dislocations in crystals appears to be their extension through the lattice. In glass, defect formation is limited, whereas in crystals, because of long range order, dislocation networks may become more extensive.

Spiral defects were also observed in glasses containing lead and bismuth. Associated with spiral formation were apparent changes in structure. These structural variations were quantitatively studied by using a dynamic spherical indenter technique, described in an earlier paper.[1] This method of loading, combined with the etching technique, was recently utilized in a study of subtle defect variations in commercial glasses.[2] In this case it was found feasible to consider both average length and number of flaws nucleated in order to obtain information regarding relative bond breakage under the given load conditions. The problem of bond strength versus the factor of brittleness or rigidity of a network may be delineated at least on a relative basis.

II. DYNAMIC SPHERICAL INDENTER TECHNIQUE

A diagram of the dynamic spherical indenter apparatus is shown in Fig. 1. The $\frac{5}{16}$ in. ball was drawn horizontally over the glass at a velocity of about 0.5 cm/sec.

---

* Present address: University of Michigan, Institute of Science and Technology, Willow Run Laboratories, Ann Arbor, Michigan.

[1] W. C. Levengood and T. S. Vong, J. Appl. Phys. **31**, 1416 (1960).

[2] W. C. Levengood and T. S. Vong, Phys. and Chem. of Glasses **1**, 189 (1960).

The ball trace was made on both halves of freshly broken surfaces. Flaw lengths and numbers were microscopically determined using about 100× magnification and a calibrated ocular micrometer. The lengths were measured to ±0.001 mm and flaw counts were made over a 3 to 4 cm trace length. Flaw numbers are given as number nucleated per millimeter of trace line. The flaws produced by the indenter are not the same as "cracks" in glass. It has been previously pointed out[2] that the etching characteristics of flaws are radically different than a microscopic crack. The flaws discussed here also move and reform under applied stress, whereas cracks, once formed, remain stationary.

In all of the glasses studied, between 50 and 100 flaws were measured on each sample. The experimental composition glasses, as in the previous study, were all made from reagent material and melting was carried out in platinum at a temperature of 1430°C, with a melting time of approximately one-half hour. The glass was then annealed with a final internal tension of about 20 lb per in.^{2}

The product of the average flaw length (F_1) and flaw number (F_n) was taken to be a relative measure of the bonds broken under the applied load given as

$$N_b=(F_1)(F_n). \tag{1}$$

When approximating the stress field around the indenter, static loading conditions were assumed.[2] The critical yield stress (σ_c) occurs at the point where the radial flaws terminate. This stress is given by

$$\sigma_c=K/(F_1)^2, \tag{2}$$

where

$$K=P(1-2\nu)/2\pi, \tag{3}$$

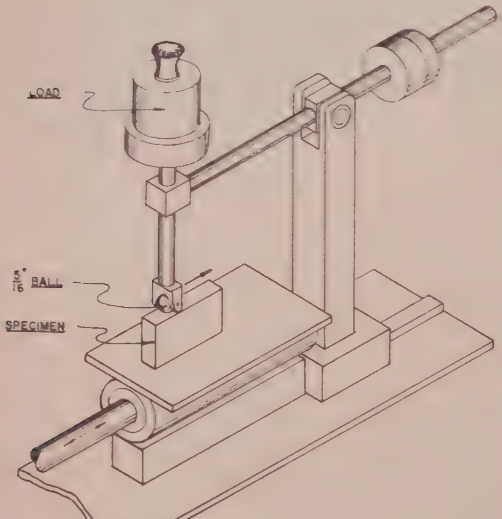

Fig. 1. Schematic drawing of dynamic spherical indenter apparatus.

with P being the load and ν Poisson's ratio. The load P was kept constant at 500 g. In these studies, the parameters of flaw length and number will be discussed, as well as the N_b product. Flaw length (F_1) is associated with relative bond strength or the ease with which a flaw region forms. Flaw number (F_n) is believed to indicate the brittleness or rigidity of the network. A large number of flaws nucleated suggests a high rigidity with localized bond rupture replacing a yield or bending of bonds. The N_b product takes into account both the bond strength and rigidity and is believed to provide an over-all indication of strength changes occurring in the network.

III. RESULTS

Dislocation terminology applied to spiral defects in glass has recently been criticized with an alternative explanation being offered. It was suggested by Hillig and Charles[3] that this effect is due to deviations in a crack front which passes close to an inhomogeneous region within the glass network. This, however, does not appear to be a valid explanation for two reasons; first, as was originally pointed out by Levengood and Vong,[1] these spiral formations occur on a free melt surface. They are found on a glass (of proper composition) which has been poured out, cooled, and etched. In this case, no crack front is involved.

A second factor which casts doubt on their proposed mechanism is seen by examining the flaw patterns on opposing breakage surfaces. Flaws appear to be created by localized stress release or readjustment in the surface after the crack front has passed. The spiral patterns do not match on opposite surfaces, even in regions of very localized stress. An example of flaws located at the terminus of macroscopic rib marks is shown in Fig. 2(a) (on a spiral composition glass). In this case, the rib mark appears to act as an origin or focal point for a shock wave type of stress release effect. Matching rib marks on the opposite breakage surface are shown in Fig. 2(b), and here it may be seen that there is a suggestion of radiating lines at the tips of these rib marks; however, the pattern does not match the flaw grouping in Fig. 2(a). This nonmatching effect would certainly suggest that the flaw patterns were formed after passage of the rapidly moving crack front. Only the large rib marks show a matching or mirror image pattern. It was found by Levengood[4] that if an internal crack is stopped and after a period of time is again extended, matching flaws are formed on opposite cleavage surfaces. These matching flaw patterns were found only in the region where the initial crack tip remained static for a period of several hours or days.

Perhaps, it should also be pointed out that etching time does not influence number of flaws, only their microscopic contrast. With very short times, the flaws are faint and sensitive methods of observation must be

---

[3] W. B. Hillig and R. J. Charles, J. Appl. Phys. **32**, 123 (1961).
[4] W. C. Levengood, J. Appl. Phys. **30**, 378 (1959).

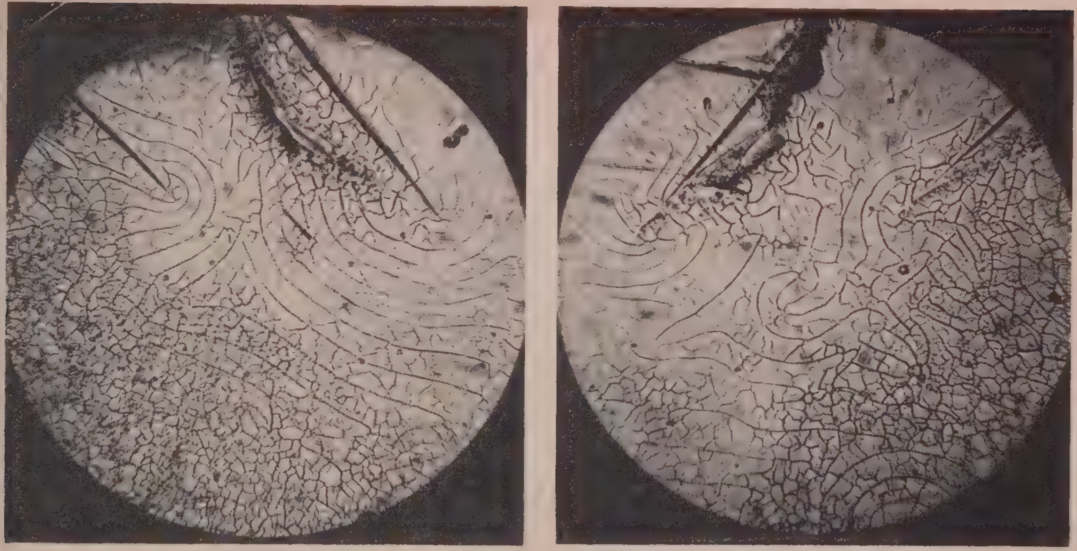
(a) (b)

FIG. 2. Opposite breakage surfaces on a spiral composition glass (22.1×). (a) Flaw interaction around rib marks; (b) nonmatching flaw pattern on opposite surface.

sed, such as phase contrast, whereas at very long tching times, the nucleation crystals become proounced. A point was also brought out in the discussion f the spiral effect[3] regarding the etching time effecting he number of spiral rotations. Within a range of 2 to 0 minutes etching time, the number of spiral rotations vas not significantly different.

A. Detailed Examination of Spiral Stress Fields

Since the spirals do not appear to form as the result f undulations in a breakage plane, one may gain a etter understanding of the mechanisms involved by etailed examination of spiral regions. In the original ublication, mutual interaction effects were shown vhere the flaws from one spiral source encircled an djacent spiral region. In this example the flaw lines rom both sources appeared to spiral or "rotate" the ame. It is instructive to consider this case in greater etail, as well as other patterns.

It has been shown[1] that spirals may be reproduced vith a mechanical torsion stress. The direction of torque etermines whether the flaws spiral clockwise or counterlockwise. From this mechanical analog, it may be seen hat the torque field would be as shown by the arrows at he central region of the spirals in Fig. 3(a). [Figure 3(a) a portion of the interacting spirals given as Fig. 2 in eference 1.] The assumption of a torque field is reasonble from a more theoretical point of view. It has also een demonstrated[1] that the spiral patterns may be erived mathematically by assuming a torque stress at e spiral origin. This torque stress field is believed to be artially relieved by the formation of the flaw lines. elease of this stress may conceivably produce a shear across individual flaw lines or a stress couple which may be represented diagramatically by the arrows in Fig. 3. The two spiral regions shown in Fig. 3(a), disclose parallel rotation and when a flaw line originating at one spiral enters the stress field around a line originating at the adjacent spiral region, the shear vectors are additive, since the hypothetical stress couples are all in counterclockwise rotation. Because of this localized stress reinforcement, the flaw lines continue around the neighboring spiral. This encircling mechanism appears to continue until the stress energy has decreased below the critical value for flaw formation. In the region between parallel rotating sources, more widely separated than those in Fig. 3(a), the flaws indicated at regions (x) and (y) have been observed to join and become one continuous line.

In the case where there is opposing rotation of spirals, the stress vectors would also be in opposition, as shown in Fig. 3(b). In the central region between the two spiral sources, flaws originating from each spiral are seen to approach one another and the process of stress cancellation is indicated by an annihilation or termination of the two flaw lines at the point just above the cross hair in the field. Here we have, in effect, a stress cancellation by the encounter of opposing shear couples. It is noteworthy that there are no encircling effects by the flaws in the outer turns of the spiral in Fig. 3(b).

Variations in the effects shown here have been observed; that is, adjacent sources of different size as well as varying distances between sources. In every case, the observed effects could be explained by considering shear vectors and subsequently analyzing their interactions.

B. Distortion of Spirals by Localized Indenter Stresses

When producing the dynamic spherical indenter traces on breakage surfaces showing the spiral effect, it was observed that when the trace line was near a spiral defect pattern, the influence of the stress could be seen. In many cases, the indenter trace was observed to alter a major part of the spiral pattern. Occasionally, however, the stresses from the trace line caused a distortion of the spiral without complete flaw rearrangement.

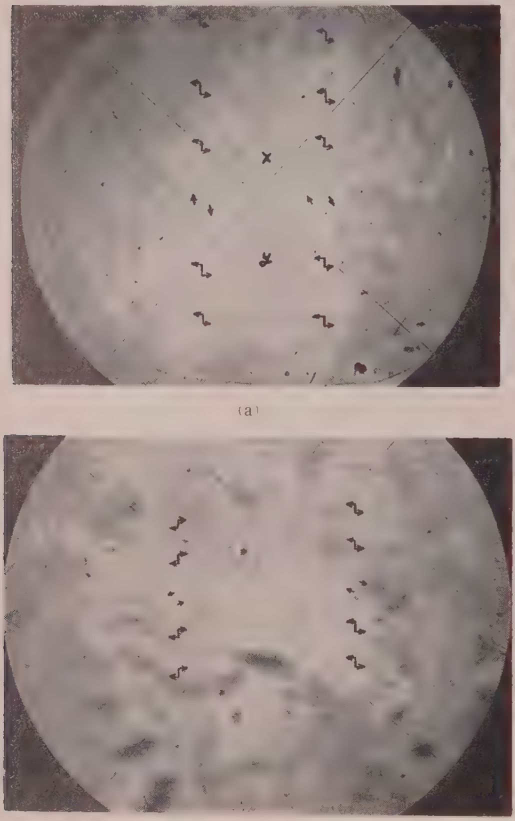
(a)

(b)

FIG. 3. Interacting spiral regions showing proposed shear stress couples (75×). (a) Encircling effect with parallel "rotating" spiral sources; (b) opposite "rotating" sources showing flaw cancellation effect.

In Fig. 4, the trace line passed fortuitously through the center of a spiral region producing an apparent flaw movement or an elongation of the spiral. The trace line is shown by the faint band of etch crystals extending horizontally through the center of the field. The origin of the spiral is immediately at the left of the cross hair. At the right of the origin, the spiral turns are elongated in an elliptical pattern indicating a movement effect. At the left of the spiral origin, there appears to be a more complete destruction of the spiral turns. This sample provides additional evidence of flaw movement produced by localized stresses, without crack front involvement.

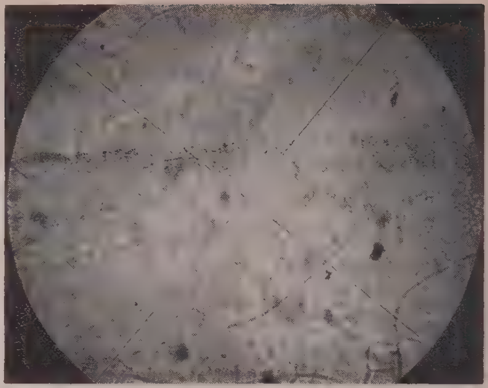
FIG. 4. Distortion of spiral region by a dynamic spherical indenter trace (70×).

In glasses showing spiral patterns, flaw movement appears to be more localized than the extensive cyclic patterns found between diamond scratches on commercial glasses.[5] From the type of structure possessed by the spiral containing glasses, one would expect the distortion effects to be localized. That the spiral glasses are characterized by a more rigid network will be subsequently shown.

C. The Addition of Lead and Bismuth Ions to a Nonspiral Glass

Lead, a common network forming ion in glass, and bismuth oxide were substituted for silica in a base glass containing 70% SiO_2, 16% Na_2O, and 14% CaO. After

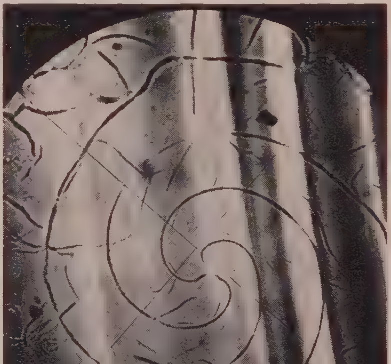
FIG. 5. Spiral source in glass containing 20% PbO (70×).

---

[5] W. C. Levengood and T. S. Vong, J. Chem. Phys. 31, 1104 (1959).

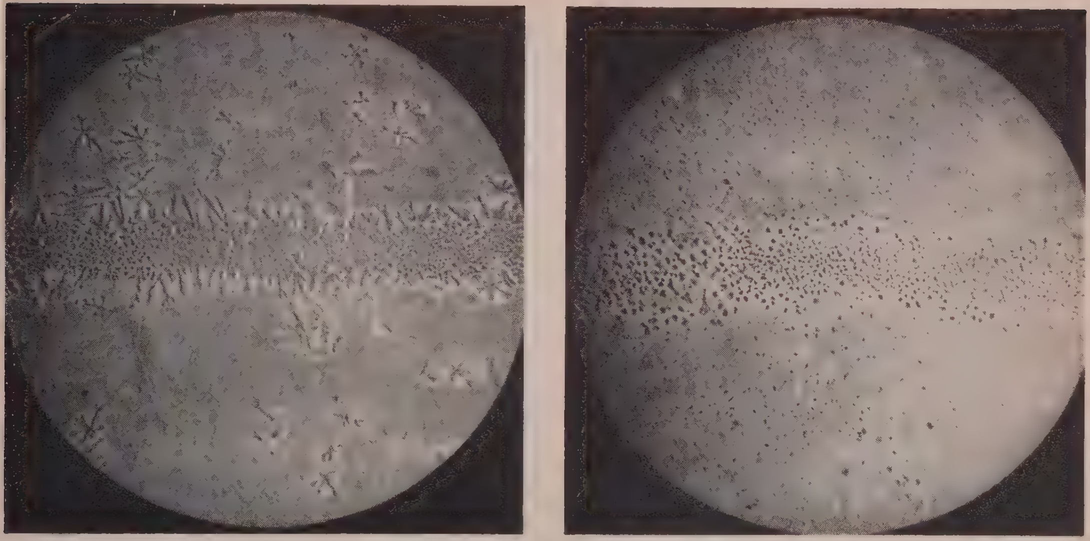
(a) (b)

FIG. 6. Changes in flaw characteristics produced by bismuth (46×). (a) 15% Bi_2O_3; (b) 20% Bi_2O_3.

nnealing, the dynamic spherical indenter technique as applied to fresh breakage surfaces as previously escribed.

The changes in the flaw parameters in the lead oxide eries are shown in Table I. In glasses with 5 and 10% bO additions, the flaws were very pronounced and nger, as may be seen in the F_1 values. With 15% added, here was a very decided decrease in flaw length and ronounced increases in flaw number; also, the flaws xtended in a very irregular manner from the trace line. the glass containing 20% PbO, the spiral type defect atterns were observed.

In many cases, spirals appeared to originate at minute uclei in the structure as shown in Fig. 5. The interrup- on of one of these spiral flaws by a localized stress gion in the structure is indicated by the arrow below e cross hair. Many of the nuclei did not form spirals, ut instead disclosed this circular flaw effect. This rcular or "loop" type of flaw formation will be dis- ussed in more detail in the following section.

The bismuth ion, with greater number of screening ectrons and higher ionic polarizability was expected to ave a somewhat more pronounced weakening effect the glass structure. The Bi_2O_3 glasses became black appearance and it was necessary to make replicas of the trace lines in order to measure flaw parameters. Figure 6(a) shows the 15% Bi_2O_3 glass with a few irregular flaws originating at the trace line which extends horizontally through the field. In Fig. 6(b), the 20% Bi_2O_3 discloses a much greater number of flaws nucleated and they are much shorter in length. The flaw parameter data in Table II show, as predicted, that the bismuth does produce a greater weakening effect (higher N_b product) compared with the lead ion. This weakening by the bismuth becomes even more apparent when the

TABLE I. Flaw parameters in a glass with lead substituted for silica (70% SiO_2; 14% CaO; 16% Na_2O).

PbO (%)	F_1	F_n	N_b
0	0.792	0.760	0.602
5	1.128	0.687	0.776
10	0.910	0.759	0.691
15	0.436	2.300	1.003
20	0.239	6.210	1.485

TABLE II. Substitutions of Bi_2O_3 for SiO_2 in a three-component system (70% SiO_2; 14% CaO; 16% Na_2O).

Bi_2O_3 (%)	F_1	F_n	N_b
0	0.792	0.760	0.602
5	1.016	0.522	0.530
10	0.867	0.964	0.836
15	0.222	5.083	1.129
20	0.120	13.334	1.600

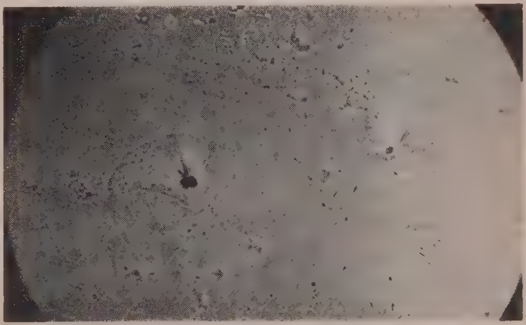

FIG. 7. Spiral formations in 20% Bi_2O_3 glass.

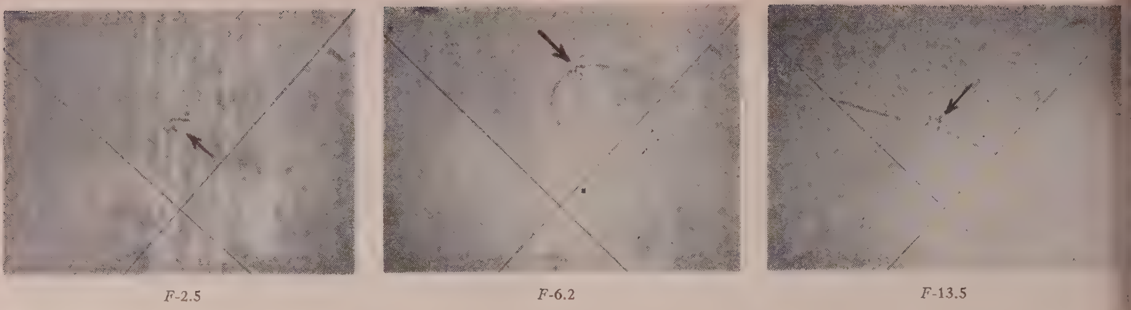

FIG. 8. Growth of loop flaws with applied force on rectangular load sections. Areas shown are normal to maximum tension and compression surfaces. F is applied force in pounds (45×).

ratio of the ionic concentrations of Pb^{2+} to Bi^{3+} is taken into consideration.

It was also observed that the 20% Bi_2O_3 glass contained spiral patterns but they were not as well formed as in the lead series. These spirals also were observed to originate at minute crystal nuclei in the glass, as shown in Fig. 7. In both the lead and bismuth containing glasses, it should be noted that the spirals occur when the flaw number is large, indicating a rigid network.

D. Flaw Loop Sources

Examination of etched surfaces on regular commercial soda-lime-silica glasses generally discloses random pits, which seemingly have no relation to linear flaw patterns. A more detailed study disclosed that these pits are nucleation sites for an etch deposit crystal (pseudomorph of sodium silico-fluoride) and a very short flaw loop. Microscopically, these etch pits and associated flaw patterns may be readily distinguished from the lighter, random crystal deposits.

Application of shear stress, before etching, caused growth of the loop type flaw patterns originating at the etch pits. The flaw growth was not, however, uniform at each pit source. An example of typical loop growth under stress is shown in Fig. 8 (the arrows indicate the pit sources associated with the loops). These loops were produced on the fresh breakage surface of a rectangular section stressed by simple beam loading. The end supports were $1\frac{1}{2}$ in. apart and the load was centrally applied by means of a $\frac{1}{2}$ in. aluminum rod placed across the sample. The test samples were approximately 1 in. wide and 0.22 in. thick. The loading time was one minute per sample.

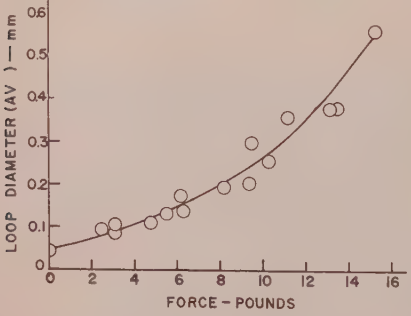

FIG. 9. Effect of applied force on flaw loop diameter. Each point is the average of approximately 30 sources in a 1.5 in.×0.22 in. rectangular region located normal to the tension and compression surfaces.

The loops shown in Fig. 8, were near the center of the fresh breakage surface located normal to the maximum tension and compression surfaces. A number of samples (all cut from the same type of bottle glass) were loaded in this manner and the loop diameters measured in the load region between the end supports (1.5 in.×0.22 in. area). The results of these measurements are summarized in Fig. 9, with each point representing an average loop diameter of approximately 30 pit sources. This stressing occasionally caused the flaws, originating at the etch pits, to become extensive, and interesting loop interaction effects were observed in the flaw patterns as shown in Fig. 10. The pseudomorph crystals, located at the nucleus of these loops, are observed at an earlier stage in the etching process than the random, background deposit crystals. The early appearance of the crystal and associated pit region suggests that the loop source is a high energy stress region.

On regular breakage surfaces, loop sources have an average diameter of approximately 50 μ, as shown by the low load point on the curve in Fig. 9. The loops vary in size with glasses of different composition. In commercial sheet glass, for example, the loops were about the same size and shape as in bottle glass, but not as numerous. In the 20% PbO glass, shown in Fig. 5, the loops appear to be more numerous with a larger initial diameter ($\sim$100 μ).

E. Etch Pit Rows

An interesting effect was occasionally observed on the surfaces of glass after being subjected to cyclic stresses. It was found that flaw interactions may, under certain conditions, produce rows of etch pits. Association of these defect rows with applied load was demonstrated by producing a fresh breakage surface at the longitudinal edge of a strip of glass, then applying a torsion stress.

An example of the type of defect pattern observed on e torsion samples is presented in Fig. 11. The region own is at the center of a 0.25-in.-thick edge of a strip proximately 2 in. long and 1 in. wide. The ends were amped and the sample was given seven complete cles of approximately 35 in. lb torque.

From the pattern in Fig. 11, and our previous obser- ations of flaw movement under applied stress,[5] it is ggested that the cyclic torsion loading created flaws the central region which on the reverse cycle began "move out" of the stress region or disappear because the opposing stress field. The collapse of the flaws or islocated regions is only partially complete and the eries of etch pit rows were produced by stress interac- on. This partial collapse may result from the transitory ature of the stress fields. These etch pit rows have also een observed on regular commercial containers and in is case rapidly varying thermal stresses may have used flaw collapse.

Several lines of crossing etch pit rows are shown in ig. 11. These crossing lines indicate a greater degree of ability than exhibited by the continuous line type of aw. The line flaws are rarely found to cross one another ut instead usually terminate at a 90° angle of inter- ction. Some of these pit rows form parallel lines which ay have occurred on different stress cycles. It is teresting to note that several of these pit rows form ngles very close to 45°, which is consistent with the eneral direction of the shear stress field created by this ype of torsion load.

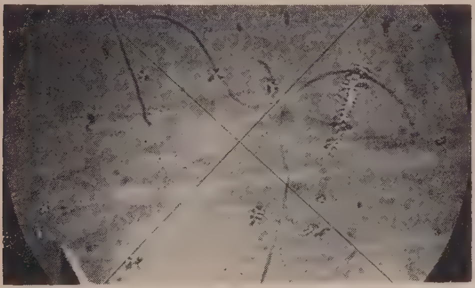

FIG. 10. Large flaw loop formation around an extensive source (32.5×).

F. Morphology of Line Flaws

In an earlier work[5] it was pointed out that flaw depth as indicated by examination of cross sections. This was one by splitting so that the plane of a fresh surface was cated normal to flaw lines. In many cases flaws were und to terminate at a minute pit located from 5 to 20 μ elow the original surface. These experiments were re- eated in an attempt to photographically demonstrate flaw line with its terminus below the surface.

The etching time was reduced to about 7½ minutes to educe the number of nucleation crystals and increase e clarity of the flaws. Although they were very difficult to photograph, some of the most severe flaws clearly disclosed an etch effect on the freshly broken surface. The photomicrograph in Fig. 12, was taken with the corner tilted so that both the freshly broken and the lehr surface could be viewed simultaneously. The sharp corner edge is shown extending horizontally through the center of the photograph and above this line is the lehr surface. A flaw, severed by the breakage plane, is shown just to the left of the cross hair and extends to the left edge and out of focus. The resulting pit, on the fresh broken edge where the flaw terminates, is indicated by the arrow. If this pit represents the actual terminal point, the flaws do not extend deep into the structure of the glass. The average depth, as previously indicated, is about 12 μ.

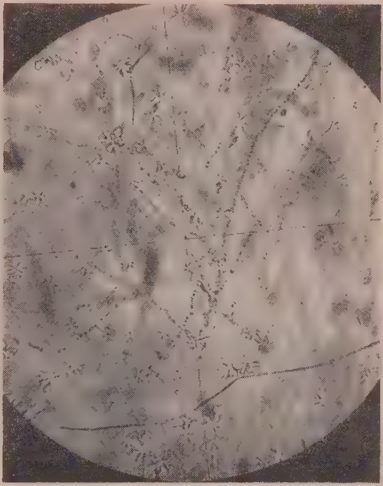

FIG. 11. Etch pit rows on the fresh breakage surface of a sample given torsion stress cycling (32.5×).

IV. DISCUSSION OF RESULTS

It has been argued[3] that in glasses there is no apparent mechanism for dislocation extension compared with a crystal lattice which permits movement known as glide. In the crystal, however, this movement is restricted to certain crystalline planes and in some directions the glide or dislocation formation is inhibited. In glass,

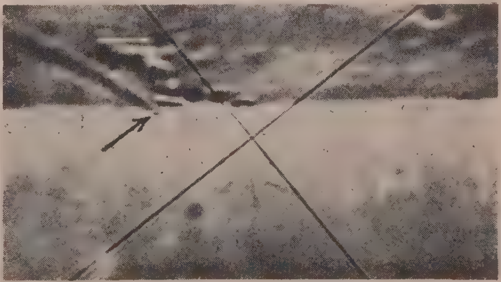

FIG. 12. Termination of flaw on a fresh breakage surface (240×).

because of relative short range order, a dislocation torus may form without regard for particular orientation planes in the structure.

It has been previously suggested that the line defects found on the surfaces of glass are the edges of slip planes with the source of the slip region being indicated by the etch pit shown in Fig. 12. Conceivably, this etch pit is the center or "core" of the hypothetical torus surrounding the dislocated region. The slip plane extends from this core to the surface. It is proposed that at the surface the strain is partially relieved by slip; however, localized strained bonds exist which act as high energy regions. During the etching, the chemical reaction is more rapid at the strain area. Because of the very localized or short range separations in these strained regions, bonds may reform and the slip line may move under low applied stress. The critical shear stress (τ_F) for the formation of flaws was previously found to be 6×10^7 dynes per cm^2 which is far below the rupture strength of ordinary glasses.

One does not have to search very far to find both mechanical and thermal influences which may create sufficient stress to produce these flaw patterns or slipped regions. On the fresh breakage surfaces, discussed in the preceding sections, mechanical forces account for the flaw effects. Flaws, however, are found on regular commercial glasses, or as previously mentioned in Sec. III on the surfaces of experimental melts which have not been subjected to applied mechanical stresses. In this case one looks toward thermal stresses as being the energy source for the flaw formation. For example, we may consider thermal effects by using an approach similar to that previously employed.[6] The possibility of tension stresses developing on a cooling sphere of hot glass of volume V_1 is shown in a qualitative manner. As the outermost layers cool and contract, a resulting compression is produced on the interior of the sphere and the work done by the surface layer is

$$W=\int_{V_1}^{V_2} Pdv, \tag{4}$$

where P is the pressure on the interior. The work done is comparable to stretching the surface over an incompressible sphere. Assuming Hooke's law to hold, we have from the laws of elasticity,

$$dP=\frac{dV}{V_1}K', \tag{5}$$

where K' is the bulk modulus. By substitution for dV in Eq. (4) this gives

$$W=\int_0^P \frac{V_1P}{K'}dP=\frac{V_1P^2}{2K'}. \tag{6}$$

Here an initial zero pressure is assumed. As the surface shrinks, the increase to the equilibrium pressure P results in a balance of forces between the surface energy and the internal pressure. If the surface layer of thickness t is small compared to r the radius of this sphere, the resultant of this surface stress σ_s is given by

$$\sigma_s=rP/2t. \tag{7}$$

From Eq. (6) this gives

$$\sigma_s=(WK'/2V_1)^{\frac{1}{2}}r/t. \tag{8}$$

It is thus seen, in Eq. (8), that in a thin layer (t) the stresses may become large and exceed the critical value (τ_F) of flaw formation. When the flaws are produced in the surface of the cooling glass, part of the potential energy stored in the surface is released as energy of flaw formation (W_F) and is given by

$$W_F=2\gamma Lt, \tag{9}$$

where γ is the surface energy and L the length of the flaw. This length L in Eq. (9) may have a minimum value and any flaw less than this length could collapse, possibly forming the etch pit rows occasionally observed on the etch surface of regular commercial glasses (as mentioned in Sec. III E).

It was also suggested that flaw collapse may, with stress interaction, result in the formation of the more stable etch pit rows (Fig. 11). Fujita[7] gives a relationship for the critical energy (W_V) of a collapsing void as,

$$W_V=\frac{Gh^2}{2\pi(1-\nu)}\left[\log\frac{t}{r_0}+\frac{1}{2}\right], \tag{10}$$

where h is the width of the void, ν is Poisson's ratio, t the depth of the void, and r_0 the radius of the core of the dislocation. By equating the energy of flaw formation given in Eq. (9) with the critical collapse of a flaw of minimum length we may, by simple substitution, solve for this length of minimum stability as

$$L=\frac{Gh^2}{4\pi\gamma t(1-\nu)}\left[\log\frac{t}{r_0}+\frac{1}{2}\right]. \tag{11}$$

By using the values $\gamma=300$ dynes per cm, $r_0=2.3\times10^{-8}$ cm, $h=10^{-7}$ cm, $G=2.8\times10^{11}$ dynes per cm^2, and the determined flaw depth of 12 μ for t, we obtain for this critical length of flaw

$$L=4.3\times10^{-3}\text{ cm}. \tag{12}$$

The etch pit rows shown in Fig. 11 may represent the collapse of flaws and the maximum distance between pairs of etch pits should, therefore, agree with the minimum length of flaw stability. Measurements made from numerous samples showing the etch pit rows gave a value around 50 μ which agrees very well with the theoretical value in Eq. (12). It appears that flaws less than 50 μ in length will collapse into individual point defects.

---

[6] W. C. Levengood and E. B. Butler, J. Am. Ceram. Soc. **36**, 257 (1953).

[7] F. E. Fujita, Acta. Met. **6**, 543 (1958).

On the breakage surfaces of commercial glasses, sources were found which produced minute flaw loops also around 50 μ in diameter. As indicated in Figs. 8 and 9, an applied stress caused these flaw loops to grow outward from a central point. If we assume these sources produce dislocations, as the load experiments indicated, the stress conditions at the defects may be approximately determined. It is not necessary to know the exact characteristics of these loop sources to examine the stress field. In the case of crystals, as pointed out by Van Bueren,[8] dislocation elements on application of a stress may act as Frank-Read sources if their end points are fixed. This author also points out that "other structures the nature of which is yet unknown," produce dislocation loops and are believed to be "connected with the surface." For these sources in glass the resolved shear stress along the Burgers vector (b) of the source must exceed the critical value

$$\tau_{\mathrm{crit}}=Gb/L_s, \tag{13}$$

where L_s is the length of the source. By using the critical shear stress (τ_F) found to produce flaws and 50 μ for L_s, the Burgers vector b of the flaw loops may be calculated by

$$b=\tau_F L_s/G. \tag{14}$$

This gives a value for b of 1.1×10^{-7} cm, which agrees with the previously assumed value of 10 A. If this value of the Burgers vector is used in Eq. (13) to determine the critical stress at the sources, the value obtained is approximately a factor of 10 less than the critical stress (τ_F) to produce or move flaws on the glass surface. This order of magnitude between these two values may indicate an existing stress field at the loop source which decreases the amount of additional energy necessary for flaw formation.

V. CONCLUSIONS

A detailed examination of stress fields around interacting spiral defect regions in glass disclosed that their morphology may be described by considering the mutual influences of hypothetical shear stress couples. Adjacent spiral sources with shear couples showing twin or parallel rotation disclosed possible reinforcement and encircling effects. In cases showing opposing rotation of spirals, the proposed stress couples were also in opposition and a cancellation or annihilation of defects was indicated. Localized distortion effects were observed in defect spirals which were located on or near dynamic spherical indenter traces. A case is discussed where the spiral was elongated into an eliptical shape by the stress field created by the indenter.

The dynamic spherical indenter was also utilized to study structure variations in systems with lead and bismuth substituted for silica. A simple three-component base glass was used and the substitution of both lead and bismuth was found to create the spiral defect sources. Quantitative changes in structure were shown by considering both the average flaw length (F_1) and flaw number (F_n). The product of these parameters (N_b), gave a relative indication of the total bond breakage with the applied indenter load. In both series it was observed that as the flaw length decreased the number of flaws nucleated became very large indicating an increase in the rigidity of the lattice network. The bismuth ion, with the higher polarizability, appeared to have the greater weakening effect in the glass structure.

A series of etch pit rows were created by torsion stress. These patterns indicated the collapse of flaw lines into more stable point defects. The measured distance between the etch pits was in agreement with a theoretical derivation of the minimum length of stability of a flaw.

Also observed, were random pits in the glass which under applied stress acted as sources for flaw loop formation. Increasing stress produced an increase in loop diameter. From the dimensional characteristics of these defect sources the Burgers vector of the shear stress was calculated to be around 10 A. The dimensional characteristics and stress fields associated with the sources appear to be markedly influenced by compositional variations.

---

[8] H. G. Van Bueren, *Imperfections in Crystals* (Interscience Publishers, Inc., New York, 1960), p. 151.

JOURNAL OF APPLIED PHYSICS VOLUME 32, NUMBER 12 DECEMBER, 1961

Growth of Refractory Crystals Using the Induction Plasma Torch

THOMAS B. REED
Lincoln Laboratory, Massachusetts Institute of Technology, Lexington 73, Massachusetts*

(Received April 24, 1961)

Apparatus is described for growing refractory crystals using the induction plasma torch in a Verneuil-type geometry. The plasma torch makes possible crystal growth at higher temperatures than can be achieved with flames and in inert or reactive atmospheres. Conditions are given for growth of sapphire, stabilized zirconia, and niobium crystals.

IN a recent[1] article an induction-coupled plasma torch has been described which is used for heating gases to 10 000–20 000°K using a standard radio-frequency power source. Such a torch exhibits a number of desirable features for growing crystals. We will describe here the further steps that have been taken to grow crystals in the Verneuil-type geometry using this torch.

Since there are no electrodes, this torch has been operated in inert, reducing, and oxidizing gases; thus, the atmospheres for crystal growth are not limited as they are in conventional Verneuil crystal growth. The high temperatures which exist in the plasma make possible the growth of very refractory materials. The lack of an electrode at the axis of the plasma makes the introduction of powder much simpler than it would be with dc plasma torches. Finally the resulting plasma flame has a large cross section and low velocity so that it completely envelops the growing crystal, and has no tendency to blow the molten cap away.

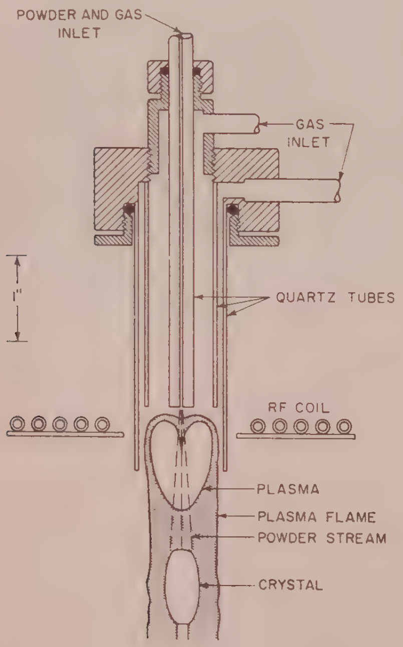

FIG. 1. Modification of induction-coupled plasma torch for crystal growth.

Figures 1 and 2 are drawings and Fig. 3 is a photograph of the induction-coupled plasma torch modified for Verneuil-type crystal growth. Basically it consists of three concentric quartz tubes with three independent gas flows. A concentrator type rf coil surrounds the bottom of the outer tube which forms a nozzle to shape the heated gas into a long laminar flame. Gas flows at high velocity between this tube and the intermediate tube to keep the outer tube from melting and to create recirculation in the plasma region. Gas which flows at low velocity through the intermediate tube forms the main body of the plasma. Finally, gas flowing at high velocity through the center tube carries powder through the highest temperature region to the molten cap of the crystal.

The torch is started in argon gas by coupling the rf coils to a grounded carbon or tungsten rod inserted into the high-rf field from above or below. The heated tip lowers the breakdown potential and allows formation of a thermal plasma which is maintained by the rf energy. Once started, the rod is removed and oxygen,

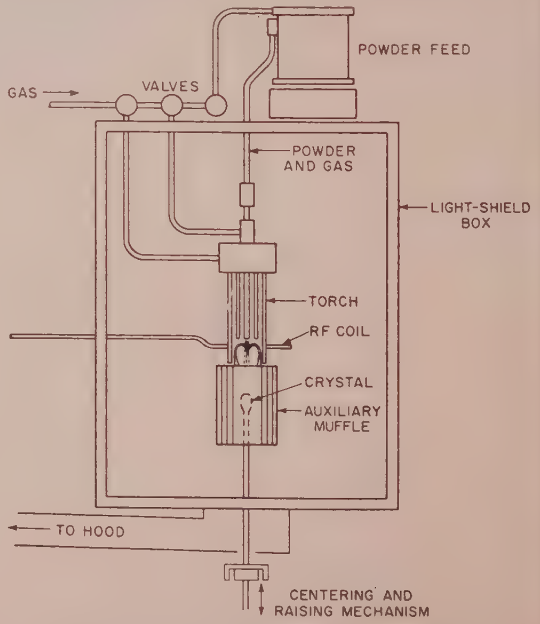

FIG. 2. Apparatus for plasma crystal growth.

---

* Operated with support from the U. S. Army, Navy and Air Force.

[1] T. B. Reed, J. Appl. Phys. 32, 821 (1961).

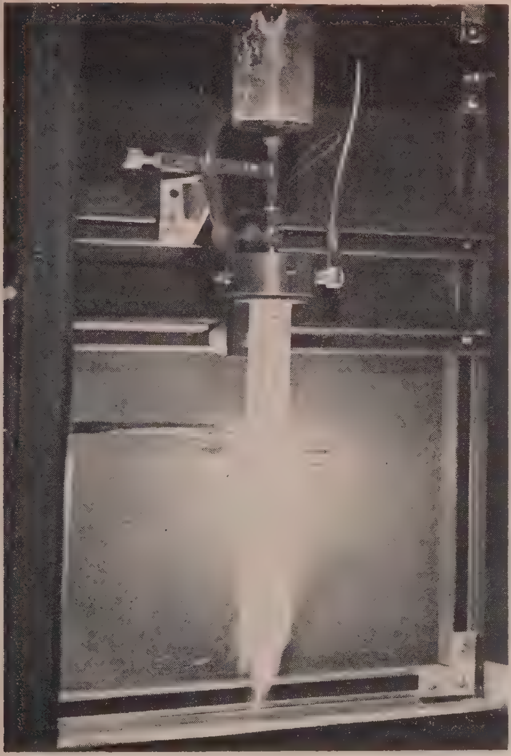

FIG. 3. Crystal of stabilized zirconium oxide being grown in induction plasma torch.

itrogen, hydrogen, or helium can be added to the rgon depending on the crystal being grown. The liatomic gases and helium provide more heat transfer o the crystals. Typical total flows of 10–20 liters NTP er min are used in conjunction with a power input of –10 kw.

Figure 2 shows the complete assembly for crystal rowth. The torch is mounted in a water cooled sheet netal box, open at the top, with dark grey Plexiglas vindows for observation and protection of personnel rom ultra-violet and infrared radiation. The enclosure s attached to an exhaust vent to remove heat and owder, and ozone and nitric oxide formed in the lasma. In some cases a refractory muffle is placed round the growing crystal to decrease radiation heat osses and to minimize temperature gradients and conequent thermal strain in the crystal. For growing netal and other crystals sensitive to oxygen, an exension of the outer tube with a larger diameter surounds the boule to prevent aspiration of air into the lasma flame. Powder is fed through the center tube sing either a vibratory spiral-ramp feeder or a vibratng-screen method somewhat similar to the tap type sed with the classical Verneuil crystal growth. Figure is a photograph of a zirconium oxide crystal being rown.

The boules grown in this apparatus (Figure 4) have ranged in size from 5- to 15-mm diam and 30 to 90 mm long, and were grown at rates of 20 to 50 mm/hr. The top crystal is a sapphire crystal grown in an argon atmosphere and it appears to be similar to the sapphire crystals grown with the classical Verneuil method, using the oxyhydrogen flame. The middle crystal is a stabilized zirconium oxide crystal containing about 10% calcia; its melting point is in the range of 2600 to 2700°C. It was grown using 50% oxygen in the argon. This boule has some cracks but shows large single crystal regions. To the best of the author's knowledge, no single crystals of stabilized zirconia have been previously grown. The bottom boule is a niobium crystal, melting at 2420°C, grown in an argon-15% helium atmosphere. These crystals represent the types of material which can be grown in the rf plasma torch and exhibit the versatility of the device.

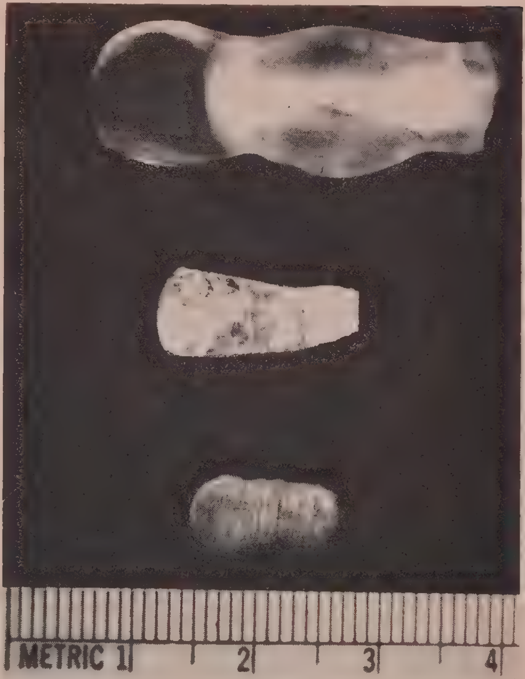

FIG. 4. Boules grown in induction plasma torch; (top) sapphire, (center) stabilized zirconia, (bottom) niobium.

Two areas for future improvement have been noted. Whereas very small particle size is desirable in flame-Verneuil crystal growth, the high temperature of the rf plasma tends to vaporize small particles, making them unavailable for molten crystal growth (though sometimes resulting in small needle growth on the side of the boule) and causing a considerable increase in radiation. On the other hand a coarse, nondense powder can bring small bubbles into the crystal giving a milky appearance to the final crystal. Therefore the proper choice of feed powder is important. Also at the highest power levels, some form of water cooling on the outer quartz nozzle would be desirable.

JOURNAL OF APPLIED PHYSICS VOLUME 32, NUMBER 12 DECEMBER, 1961

Properties of Single-Domain Particles of Cobalt-Nickel*

R. B. Falk and G. D. Hooper
Metallurgical Products Department, General Electric Company, Edmore, Michigan

(Received March 22, 1961)

Single-domain particles of cobalt-nickel have been prepared by electrodeposition into mercury, and the intrinsic coercive force observed as a function of particle composition. A marked increase in coercive force occurred in particles having a composition of 87.5% cobalt–12.5% nickel. On the basis of the spherical structure of the particles observed in electron micrographs and from the constancy of the coercive force with packing, crystal anisotropy was assumed to be the principal factor contributing to the coercivity of the cobalt-nickel particles. An intrinsic coercive force of 1750 oe was achieved, and a minimum crystal anisotropy of -2.4×10^6 ergs/cc calculated at -196°C for the above composition. Magnets were prepared with a maximum magnetic energy of 1.3×10^6 gauss-oe.

I. INTRODUCTION

CONTINUING research in fine particle permanent magnet technology has logically lead to the exploration of materials other than the extensively reported elongated single-domain iron and iron-cobalt systems.[1–2] Using the experience and techniques acquired in preparing and evaluating these particle systems, a survey of the cobalt-nickel system has been completed. It is the purpose of this paper to report the magnetic properties of single-domain particles of cobalt-nickel as a function of both composition and preparation.

II. PREPARATION

The single-domain particles of cobalt-nickel were prepared by electrodeposition into a mercury cathode. The electrolyte consisted of the bivalent sulfates of cobalt and nickel. The composition of the particles was varied over the range 12% cobalt–88% nickel to 99% cobalt–1% nickel by increasing the Co^{++}/Ni^{++} ion ratio in the electrolyte. An anode of electrolytic cobalt, spaced 0.75 in. from the mercury cathode, was used throughout. Cobalt-nickel particles were prepared over this composition range at current densities of 25 amp/sq ft, 50 amp/sq ft, 75 amp/sq ft, and 85 amp/sq ft. The duration of plating was 1 hr for each run.

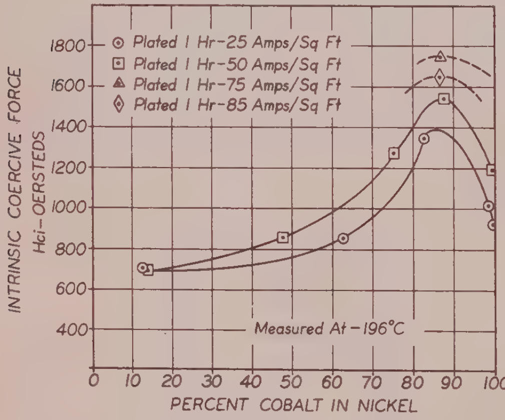

Fig. 1. Intrinsic coercive force measurements of heat-treated particles.

The particles were removed from the plating cell as a putty-like mass and magnetically concentrated to contain 3% by volume of cobalt-nickel in a matrix of mercury. The particle compositions were then brought to their optimum coercive force by heat treating the particle-mercury mixture at 175°C for 7 min and washing with an amalgam of tin. Magnetic measurements were made on this dilute material by freezing specimens in liquid nitrogen and measuring at -196 °C. Solid specimens of higher packing fractions (0.27–0.42) were prepared by compacting the particle-mercury mixture in a magnetic field and expelling excess mercury under pressure. Magnetic measurements were made at 20°C on the compacted specimens.

Particles were removed from the mercury by exposing the particle-mercury mixture to an oxidizing atmosphere (moist air). The mercury-free, oxide-coated particles were then washed from the mercury surface with acetone and dried to obtain electron micrographs and electron diffraction results.

III. RESULTS

Figure 1 represents intrinsic coercive force measurements of the heat-treated particles of nickel-cobalt taken at -196°C and at a magnetic packing fraction of 0.03. The curves are plotted as a function of particle composition and electroplating current density. It should be pointed out that the particle composition was determined quantitatively by a wet analysis of the total particle-mercury mixture, and the composition of the ferromagnetic, single-domain, cobalt-nickel particles could be slightly in error due to the formation of such compounds as $NiHg_4$ and $NiHg_3$.[3–4] This also could account for our inability to obtain a ferromagnetic deposit at nickel contents higher than 87%. At constant current density plating conditions, a marked crease in particle coercive force was observed at a omposition of approximately 85% cobalt. The coercive rce was found to increase at this composition as the lating current density was raised from 25 amp/sq ft 75 amp/sq ft. A subsequent increase in current ensity from 75 amp/sq ft to 85 amp/sq ft resulted in decrease in intrinsic coercive force of 100 oe from he peak value of 1750 oe.

---

* Presented at 1959 Conference on Magnetism and Magnetic Materials, November 16–19, 1959, Detroit, Michigan.

[1] L. I. Mendelsohn, F. E. Luborsky, and T. O. Paine, J. Appl. Phys. **26**, 1274 (1955).

[2] F. E. Luborsky, L. I. Mendelsohn, and T. O. Paine, J. Appl. Phys. **28**, 344 (1957).

[3] F. Lihl, Z. Metallk. **44**, 160–166 (1953).

[4] F. Lish and H. Nowotny, Z. Metallk. **44**, 359 (1953).

In order to determine the magnetic anisotropy forces ontributing to the coercive force of the cobalt-nickel articles, samples were removed from the mercury and sed for electron micrographs. Pictures were taken of hese particles at all compositions and current density arameters. From the electron micrographs it was irtually impossible to distinguish differences in particle omposition or plating parameters. All particles appeared to be essentially round having a median diameter of approximately 250 angstrom units, and ranging diameter from 50 to 500 angstrom units. Since the lectron micrographs indicated neither a definite particle elongation nor change in particle shape with omposition, it was assumed that the changes in corcive force with composition were due to changes in he crystal anisotropy constant and saturation induction.

Kittel[5] has pointed out that particles deriving their oercive force from shape anisotropy should have the ntrinsic coercive force of individual particles reduced y the factor (1-p), where p is the packing fraction of he particles, while particles deriving their coercive orce from crystal anisotropy should have a coercive orce independent of packing. Both of these types of ehavior have been observed. For example, elongated ingle-domain iron particles exhibit an intrinsic coercive orce proportional to (1-p), while barium iron oxide, as well as pure cobalt particles, exhibit an intrinsic corcive force independent of packing. Single-domain articles having a composition of approximately 87% obalt–13% nickel and an intrinsic coercive force of 750 oe (at −196°C) were compacted in a mercury matrix and measured at 20°C with the results shown in able I. It is apparent that the particles compacted t packing fractions from 0.27 to 0.42 exhibit no change in intrinsic coercive force. The decrease in coercive force from 1750 oe at a packing fraction of 0.03 to 955 oe at a packing fraction of 0.27 can be accounted for by the temperature coefficient of coercive force. The value of the intrinsic coercive force of the dilute sample was obtained by a linear extrapolation. Since the intrinsic coercive force is constant with packing, the maximum magnetic energy increases in direct proportion to the packing fraction.

ABLE I. Intrinsic coercive force due to magnetic packing fraction of single-domain cobalt-nickel particles (87% cobalt).

Magnetic packing fraction	Hci (oe)	Br/Bis	(BH) max $\times 10^{-6}$ G.O.	Br (gauss)	Temp. (°C)
0.03	1750	0.58	...	...	−196
0.03	1375	0.58	...	...	−90
0.03	980[a]	...	...	...	20
0.27	955	0.60	0.75	2600	20
0.31	950	0.61	0.81	3000	20
0.38	955	0.64	1.15	3950	20
0.39	945	0.65	1.20	4100	20
0.42	950	0.67	1.30	4600	20

[a] Extrapolated.

Preliminary electron diffraction analysis indicated that the particles are not cubic but appear to be a complex structure, possibly hexagonal. However, the particles could not be aligned in a magnetic field as evidenced by the Br/Bis of 0.58 as shown in Table I, and by the transverse coercive force of 1750 oe for the dilute sample. Similar behavior is observed for pure cobalt particles. Some alignment of the cobalt-nickel particles can be achieved by the compacting process as shown in Table I.

A rough estimate of the anisotropy constant of the cobalt-nickel particles can be made by assuming that the maximum coercive force corresponds to

$$H_{ci},\ \text{random} = 0.96\ K/I_s,$$

as derived for a random assembly of uniaxial crystallites by Néel,[6] where K is the crystal anisotropy constant and I_s is the saturation magnetization. This assumes that, at this particle size (just above the size where superparamagnetism starts to reduce the intrinsic coercive force), the intrinsic coercive force has reached its maximum value of $2K/I_s$ for each particle. Thus the K calculated in this manner is only a lower limit. The results of this calculation compared to literature values from measurements on bulk crystals are shown in Table II.

TABLE II. Crystal anisotropy constants.

Composition (%)		Crystal anisotropy constant K ergs/cc$\times 10^{-6}$	
Cobalt	Nickel	Calc., −196°C	Literature, 20°C
100 (cu)			−0.94[a]
100 (hex)			−4.2 −8.0 (−196°C)
99.1	0.9	−1.7	
87.5	12.5	−2.4 −1.3 (20°C)	
50 (hex)	50		−0.108[b]
47.5	52.5	−0.6	
20 (hex)	80		−0.004[b]
13.5	86.5	−0.45	
3 (hex)	97		−0.010[b]

[a] C. P. Bean, J. D. Livingston, and D. S. Rodbell, J. phys. radium **20**, 298 (1959).
[b] L. W. McKeehan, Phys. Rev. **51**, 136 (1937).

IV. CONCLUSIONS

Single-domain particles of cobalt-nickel have been prepared by electrodeposition into mercury, and the intrinsic coercive force has been observed as a function of particle composition. A marked increase in coercive force occurred in particles having a composition of 87.5% cobalt–12.5% nickel. From the lack of any observable elongation in electron micrographs of the particles, and from the independence of the intrinsic coercive force on packing, crystal anisotropy energy is assumed to be the major factor contributing to the coercivity of the cobalt-nickel particles. An intrinsic coercive force of 1750 oe was achieved, and a minimum crystal anisotropy constant of -2.4×10^6 ergs/cc calculated at −196°C for the above composition. Compacts of these particles resulted in magnets with energie only up to 1.3×10^6 gauss-oe at 20°C because the particles could not be aligned.

---

[5] C. Kittel, Revs. Modern Phys. **21**, 541 (1949).

[6] L. Néel, Compt. rend. **224**, 1488 (1947).

ACKNOWLEDGMENTS

The authors deeply appreciate the contributions o R. B. Downs, R. C. Nichols, J. A. Hussey, and J. E Foy in preparing specimens and performing magneti measurements, as well as the work of K. H. McKe in preparing electron micrographs. The criticism an help of F. E. Luborsky is gratefully acknowledged.

JOURNAL OF APPLIED PHYSICS VOLUME 32, NUMBER 12 DECEMBER, 196

Improved Representation of Calculated Surface Mobilities in Semiconductors. I. Minority Carriers

N. B. Grover, Y. Goldstein, and A. Many
Department of Physics, The Hebrew University, Jerusalem, Israel

(Received June 19, 1961)

A simple and convenient representation is given of calculated values of minority carrier surface mobility over the range of practical interest of surface potential from depletion to strong inversion layers for an extended range of material resistivity and temperature.

RECENTLY, Greene, Frankl, and Zemel[1] have published a surface transport theory following Schrieffer's original treatment[2] while taking into account the exact form of the Poisson potential. These new calculations involve three variables: $u_S\equiv q\phi_S/kT$, $u_B\equiv q\phi_B/kT$ (where ϕ_S and ϕ_B are the surface and bulk potentials, respectively), and the ratio L_D/λ. Here $\lambda\equiv(kT/2\pi m^*)^{\frac{1}{2}}$ is the unilateral mean free path and L_D is the so-called[3] Debye length given by $(\epsilon kT/8\pi q^2 n_i)^{\frac{1}{2}}$. This ratio is extremely temperature sensitive due to the exponential dependence of the intrinsic carrier density n_i on temperature. As such, it is an inconvenient quantity whenever results of calculations at different temperatures are required. This is illustrated[4] by values computed for a typical germanium sample ($N_D-N_A=6.6\times10^{13}$ cm^{-3}), where the ratio L_D/λ is seen to vary over eight orders of magnitude between 250° and 80°K.

The attendant inconvenience can be overcome by the introduction[4] of the parameter $L\equiv L_D/(\cosh u_B)^{\frac{1}{2}}=[\epsilon kT/4\pi q^2(n_B+p_B)]^{\frac{1}{2}}$ which is comparatively insensitive to temperature in most cases of interest. (Here n_B and p_B are the bulk electron and hole concentrations, respectively.) With such a parameter, it is possible to represent the calculated values of surfac mobility as families of nearly equidistant curves ove an extensive range of carrier density and temperature It should be pointed out that, from physical arguments L must be the pertinent parameter over the entir range of surface potential. This follows from the fac that the dominant factor governing the surface mobility is the effective barrier thickness, and this in tur is characterized by the length L and not by L_D. Suc can be seen to be the case by the following considerations: Given any barrier height V_s, Poisson's equatio for the tail end of the barrier at $|V|\ll kT/q$ can b approximated[5] by

$$\partial^2 v/\partial x^2=L^{-2}v, \qquad (1$$

where $v\equiv u-u_B\equiv qV/kT$. The solution to this is obviously exponential with characteristic length L. Because $|dV/dx|$ is a monotonically decreasing functio of x, the distance between the surface and the poin where $|V|=kT/q$ must be less than $L|v_s|e/(e-1)$. I other words, the characteristic length in this regio will always be less than $L|v_s|$. More detailed calculations[6] show, in fact, that in accumulation and inversio layers the characteristic length is a fraction of L whereas in depletion layers it is several times L.

In this paper we shall present in convenient form exact calculations of minority carrier mobility. Her

---

[1] R. F. Greene, D. R. Frankl, and Jay Zemel, Phys. Rev. **118**, 967 (1960).

[2] J. R. Schrieffer, Phys. Rev. **97**, 641 (1955).

[3] E. Spenke, *Electronic Semiconductors* (McGraw-Hill Book Company Inc., New York, 1958), English ed., footnote on p. 102.

[4] A. Many, N. B. Grover, Y. Goldstein, and E. Harnik, J. Phys. Chem. Solids **14**, JD5 (facing p. 298) (1960).

[5] W. Shockley, Bell System Tech. J. **28**, 435 (1949).

[6] H. Flietner, Ann. phys. **3**, 396 (1959).

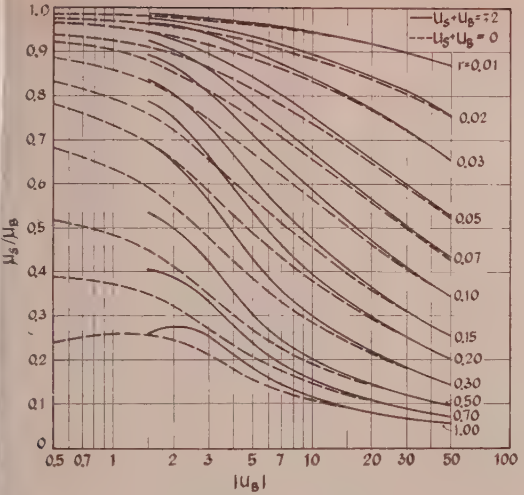

FIG. 1. Values of the ratio μ_S/μ_B of the *minority* carrier surface-o-bulk mobility plotted as a function of $|u_B|=q|\phi_B|/kT$ (where $_B$ is the bulk potential) for various values of the parameter $=\mu_B(2m^*/\epsilon)^{\frac{1}{2}}(n_B+p_B)^{\frac{1}{2}}$. Two families of curves are given: u_S+u_B $=\mp2$ and $u_S+u_B=0$ ($u_S=q\phi_S/kT$, where ϕ_S is the surface potential). The upper sign refers to electrons in p-type material nd the lower sign to holes in n-type material. The solid curves $u_S+u_B=\mp2$) are terminated at $|u_B|=1.5$. For $|u_B|=1$ (i.e., lat bands), the value of μ_S/μ_B is simply $1-r$ [see Eq. (4.5) of eference 1].

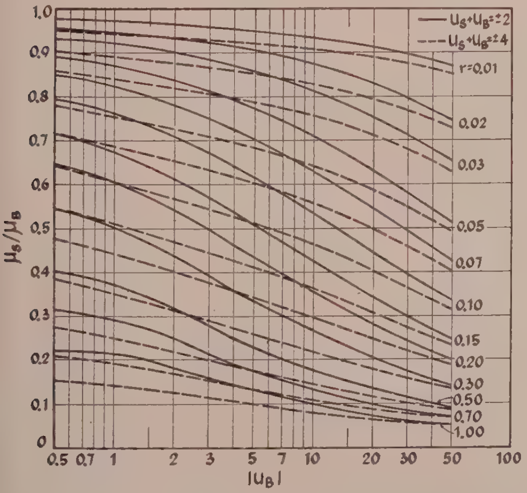

FIG. 2. Ratio μ_S/μ_B plotted as a function of $|u_B|$ for various alues of r with $u_S+u_B=\pm2$ and $u_S+u_B=\pm4$. The upper signs efer to electrons in p-type material and the lower signs to holes n-type material.

$_S+u_B$ proves to be a more suitable variable than ither u_S or v_s; the mobility depends strongly on u_S+u_B nd weakly on u_B. This is more so the stronger the nversion layer. This too can be seen from physical rguments. (An n-type sample will be considered.) For xtrinsic samples ($u_B\gtrsim1$) under inversion layer conditions ($u_S+u_B<0$), Poisson's equation can be approximated by

$$\partial^2(u+u_B)/\partial x^2=-L^{-2}[1+e^{-(u+u_B)}] \qquad (u+u_B<0;\ u_B\gtrsim1), \qquad (2)$$

thus involving only $u+u_B$. Despite the fact that the equation holds for $u+u_B<0$ only, this is the range of u in which most of the minority carriers are found. The exact shape of the barrier outside this range (away from the surface), which is governed by u_B, is of secondary importance—hence the weak dependence of the surface mobility on u_B.

In Figs. 1–3 values are shown of the ratio μ_S/μ_B of *minority* carrier surface-to-bulk mobility as a function of u_B for various values of the parameter $r\equiv\lambda/L$ at six values of u_S+u_B. These six values cover the range of practical interest, which extends from depletion layers where minority carrier concentrations are negligible to the strongest inversion layers normally attainable. The weak dependence of μ_S/μ_B on $|u_B|$ (approximately logarithmic) is obvious from the semilogarithmic plot used. Values of μ_S/μ_B at $u_B=0$ (intrinsic samples) may be obtained from the plot of μ_S/μ_B for majority carriers given in the following paper.[7]

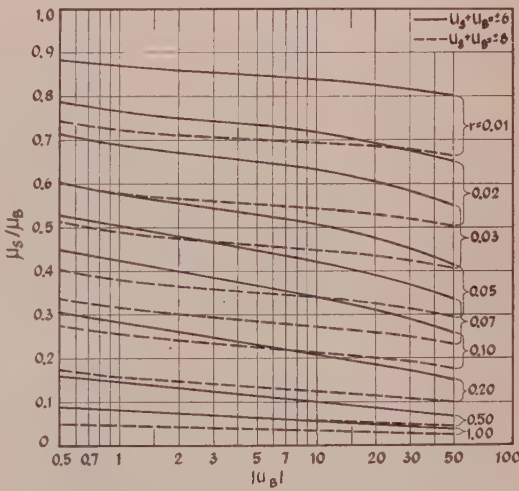

FIG. 3. Ratio μ_S/μ_B plotted as a function of $|u_B|$ for various values of r with $u_S+u_B=\pm6$ and $u_S+u_B=\pm8$. The upper signs refer to electrons in p-type material and the lower signs to holes in n-type material.

ACKNOWLEDGMENT

The authors would like to thank Y. Accad for programming the numerical calculations for the WEIZAC of the Weizmann Institute, Rehovoth.

---

[7] Y. Goldstein, N. B. Grover, A. Many, and R. F. Greene, J. Appl. Phys. **32**, 2540 (1961), following paper.

Improved Representation of Calculated Surface Mobilities in Semiconductors. II. Majority Carriers

Y. Goldstein, N. B. Grover, and A. Many
Department of Physics, The Hebrew University, Jerusalem, Israel

AND

R. F. Greene
U. S. Naval Ordnance Laboratory, White Oak, Silver Spring, Maryland

(Received June 19, 1961)

Improved representation is given of calculated values of majority carrier surface mobility. For extrinsic material the semiconductor effectively constitutes a single-carrier system. The surface mobility is then independent of the bulk potential and can be expressed as a function of the potential barrier V_s by a single family of curves over the entire range of interest of surface potential, material resistivity, and temperature.

In this paper approximate expressions for majority carrier surface mobilities are given for extrinsic samples based on the calculations of Greene, Frankl, and Zemel.[1] Here a very simple representation is possible,[2] which is much more convenient than that for minority carriers.[3] The only parameter[3] now is $r\equiv\lambda/L$, the results being independent of the bulk potential $(kT/q)u_B$. This follows from the fact that for extrinsic samples ($|u_B|\gtrsim 2$) in the region of accumulation and depletion layers considered ($v_s\equiv u_S-u_B>-2\mu_B+2$ for n type), the semiconductor constitutes essentially a single-carrier system and Poisson's equation reduces to the simple form

$$\partial^2 v/\partial x^2=L^{-2}(e^v-1) \tag{1}$$

to a very good approximation over the entire range of x from the surface to the bulk. Thus, in terms of the variable $v\equiv u-u_B$, the barrier shape is independent of u_B, so that the mobility reduction is expected to depend on r and v_s only. With these physical considerations in mind, the theoretical results of Greene, Frankl, and Zemel[1] were examined. It was found that their equations (2.13) could be rewritten for *majority* carriers to within an accuracy of better than 1% in the simpler forms:

$$\frac{\mu_S}{\mu_B}=1-\frac{r}{\sqrt{2}}\frac{1-e^{-|v_s|}}{(e^{-|v_s|}+|v_s|-1)^{\frac{1}{2}}}$$

$$\begin{cases} n \text{ type } (u_B\gtrsim 2)\colon -2u_B+2\lesssim v_s\leq 0 \\ p \text{ type } (u_B\lesssim -2)\colon 2u_B-2\gtrsim v_s\geq 0 \end{cases} \tag{2}$$

$$\frac{\mu_S}{\mu_B}=1-\frac{r}{\sqrt{2}}(e^{|v_s|}-|v_s|-1)^{-\frac{1}{2}}\int_{-|v_s|}^{0} e^{-x}(1-e^{-f(x)/r})dx$$

$$\begin{cases} n \text{ type } (u_B\gtrsim 2)\colon v_s\geq 0 \\ p \text{ type } (u_B\lesssim -2)\colon v_s\leq 0, \end{cases} \tag{3}$$

where

$$f(x)\equiv(2\pi)^{-\frac{1}{2}}\int_{-x}^{|v_s|}(x+y)^{-\frac{1}{2}}(e^y-y-1)^{-\frac{1}{2}}dy$$

and

$$r\equiv\lambda/L=\mu_B(2m^*/\epsilon)^{\frac{1}{2}}(n_B+p_B)^{\frac{1}{2}},\quad v_s\equiv u_S-u_B.$$

The value of μ_S/μ_B at flat bands ($v_s=0$) is just $1-r$.

It is thus seen that μ_S/μ_B is indeed independent of u_B and involves a single parameter r whose only temperature dependence is that of the majority carrier bulk mobility μ_B. Equation (2), which applies to depletion layers, gives the surface mobility in closed form. For accumulation layers, the values of μ_S/μ_B were evaluated numerically from Eq. (3) by computer and are presented in Fig. 1 as a function of the barrier height v_s for various values of the parameter r. Also shown are the corresponding plots (dashed lines) for $u_B=0$, which are seen to lie quite close to the solid

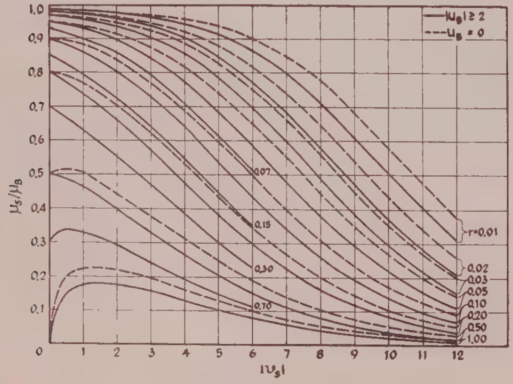

FIG. 1. Values of the ratio μ_S/μ_B of the *majority* carrier surface-to-bulk mobility in accumulation layers plotted as a function of $|v_s|=q|V_s|/kT$ (where $V_s\equiv\phi_S-\phi_B$ is the potential barrier at the surface) for various values of the parameter $r=\mu_B(2m^*/\epsilon)^{\frac{1}{2}}\times(n_B+p_B)^{\frac{1}{2}}$. The solid curves cover the region where the mobility is independent of u_B, i.e., for $|u_B|\gtrsim 2$ (extrinsic material). For comparison purposes, the curves for $u_B=0$ (intrinsic material) are also shown (dashed lines).

---

[1] R. F. Greene, D. R. Frankl, and Jay Zemel, Phys. Rev. **118**, 967 (1960).

[2] A. Many, N. B. Grover, Y. Goldstein, and E. Harnik, J. Phys. Chem. Solids 14, JD5 (facing p. 298) (1960).

[3] N. B. Grover, Y. Goldstein, and A. Many, J. Appl. Phys. **32**, 2538 (1961), preceding paper.

rves ($|u_B|\gtrsim 2$). The values for $|u_B|=0.4$ fall ap- oximately midway between the two sets of curves.

The simplified calculations presented here serve as illustration of the effectiveness of the single carrier proximation approach. This method can be advan- geously employed in any problems pertaining to ace-charge layers in extrinsic materials. In fact, this approach is being used in studies of surface thermoelectric power.[4]

ACKNOWLEDGMENT

The authors would like to thank Miss Ann Penn of the Naval Ordnance Laboratory for programming the numerical calculations for the IBM 704.

---

[4] R. F. Greene (private communication, 1961).

OURNAL OF APPLIED PHYSICS VOLUME 32, NUMBER 12 DECEMBER, 1961

A cw Solid State, Push-Pull Maser in the 5 to 6 Millimeter Wavelength Region*

DAVID L. CARTER
Department of Physics, Columbia University, New York, New York

(Received May 1, 1961)

Cw maser oscillation from 49 to 57 kMc was achieved with 0.12% Fe^{3+}-doped rutile, using push-pull pumping at 78.2 kMc. A short experiment on cross-relaxation effects was also performed.

TO operate a cw solid-state maser at signal frequencies from 49 to 57 kMc with a pump frequency ear 78.2 kMc, Fe^{3+}-doped TiO_2 (rutile) has been sed. The maser was operated in the push-pull mode.[1] his operation is indicated in Fig. 1. Pumping radiation applied simultaneously to transitions 3–5 and 4–6 hich are adjusted to the same frequency, and population inversion is obtained in transition 5–4.

For equal relaxation rates between all energy levels his mode of operation has one advantage over ordinary hree-level[2] systems in that the pump frequency need ot be greater than twice the signal frequency in order o obtain population inversion.

Fe^{3+} in TiO_2 is particularly well suited for millimeter ave masers because it has large zero-field splittings 43.3 and 81.3 kMc), and reasonable relaxation times nd linewidths.[3] These zero-field splittings allow one to se moderate values of magnetic field strength to obtain splittings suitable for maser operation in the mm avelength region. Maser action in Fe-doped rutile at requencies both higher and lower than those reported ere has been achieved by Foner *et al.*[4,5]

In our experiments the signal frequency varied line- rly with dc magnetic field strength from 49 to 57 Mc, as the field strength was changed from 7200 to 5500 gauss. The orientation of the magnetic field was held fixed and was 73° from the [110] direction in the (001) plane of the crystal. Figure 1 is a plot of allowed energy as a function of field strength for Fe-doped rutile at the above orientation computed from from the spin Hamiltonian of reference 3. These energy levels predicted the maser operating points to within the paramagnetic resonance linewidth ($\simeq$200 Mc). Also listed in the figure are the maximum values of the computed magnetic dipole moment matrix elements in units of μ_B, the Bohr magneton. From 5500 to 7200 gauss the transitions 3–5 and 4–6 both have the same splittings to within $\frac{1}{2}\%$ of the average theoretical value of 78.4 kMc. In the experiment it was necessary only to change the field *strength* to obtain maser action over the range of signal frequencies when the pump frequency was held fixed. If the pump frequency was changed by two or three hundred Mc it was necessary to change the magnetic field orientation by a few tenths of a degree to obtain the same range of signal frequen-

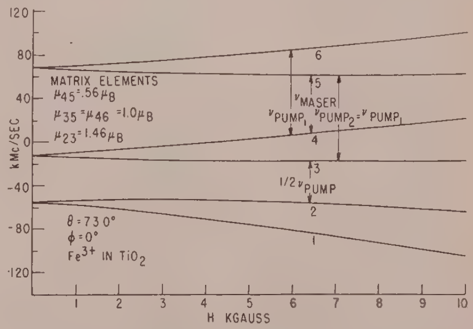

FIG. 1. Energy levels of Fe^{3+} in TiO_2 as a function of magnetic field for the field pointing 73° from the [110] direction in the (001) plane. The matrix elements are the maximum values and μ_B is the Bohr magneton.

---

* This research was supported in part by the U. S. Air Force nd monitored by the Air Force Office of Scientific Research of he Air Research and Development Command.

[1] C. Kikuchi, J. Lambe, G. Makhov, and R. W. Terhune, J. ppl. Phys. **30**, 1061 (1959).

[2] Some three-level masers use idler doping or cross relaxation o improve inversion, and in these cases the restriction of the ump frequency to be greater than twice the signal frequency is emoved. See, for example, P. A. Forrester and W. B. Mims, J. ppl. Phys. **32**, 317 (1961).

[3] D. Carter and A. Okaya, Phys. Rev. **118**, 1485 (1960).

[4] S. Foner and L. R. Momo, J. Appl. Phys. **31**, 742 (1960).

[5] S. Foner, L. R. Momo, J. B. Thaxter, G. S. Heller, and R. M. hite, *Second International Conference on Quantum Electronics, arch, 1961* (to be published).

cies. The range of pump frequencies over which maser action was observed was approximately 78.1 to 78.8 kMc.

Maser action was detected by observing the swept-frequency signal power reflected from the Fe-doped rutile when cw pump power was applied. The rutile was mounted in a cubic copper box 0.6 in., on a side which terminated the two waveguide transmission lines. The rutile was held in position in the box by paraffin or polyfoam. The floor of the box was movable to change microwave coupling and was controlled from outside the cryostat. Both pump and signal guides were 0.074 by 0.148 in. in cross-sectional dimensions. The Fe-doped rutile piece thus mounted provided its own dielectric resonant cavity, as described in reference 3 and by Okaya.[6] The rutile samples used were large enough to accommodate a density of dielectric modes of the order of one every 5 to 20 Mc, dependent upon sample size. These modes had Q's of the order of 10^4 at the pump and signal frequencies when the temperature was below 4.2°K. The doping of the rutile used in the experiments was 0.12% Fe to TiO_2 by weight.[7] Pump power was supplied by a Raytheon QKK 866 reflex klystron which had an available power output of approximately 50 mw at 78.2 kMc. For crystals with a volume of 0.15 cm^3 this power was insufficient to obtain signal gain at 4.2°K, although a decrease in absorption was seen. However, lowering the temperature to 1.6°K increased the spin-lattice relaxation time to give enough saturation of the pump transitions for both maser gain and oscillation. For crystals smaller than $\frac{1}{4}$ of the above volume, the required saturation was easily obtained at both 4.2°K and 1.6°K.

Cw oscillation was observed throughout the signal frequency region. By adjusting coupling parameters, amplitude modulation of the oscillation was produced. It was found that it was very difficult to obtain large enough microwave coupling in the signal resonances to obtain gain stable enough for root-gain-bandwidth measurements. Early measurements were made using video detection with signal power levels of approximately -30 db below a mw. This power was high enough to saturate oscillation and to give the appearance of stable, linear gain. When superheterodyne detection with 10 Mc bandwidth was employed and lower power levels were used, cw oscillation was found at all the frequencies where apparent gain was measured at the higher power levels.

The transition 2–3 has a resonance frequency of $\frac{1}{2}$ the pump frequency over a large range of magnetic fields. Therefore, one might expect cross relaxation[8] to occur between the pump levels and the 2–3 transition; then saturation of levels 2 and 3 would result in saturation of the pump transitions with subsequent inversion of levels 4 and 5. An experiment to test this hypothesis was tried, with a negative result. The magnet was adjusted so that the pump levels and levels 2 and 3 were resonant at the same field for a two-to-one frequency ratio. Then high power was applied to one frequency resonance while the other frequency resonance was monitored for saturation. Other transitions with frequencies equal to $\frac{1}{2}$ pump frequency and which were also coincident in field with the pump transitions were tried without success. It is believed that the negative result was due to the unfavorable ratio of the spin-lattice relaxation time to the cross-relaxation time.

Mims and McGee[9] find three-spin-flip cross-relaxation times of a few milliseconds in ruby with the same spin concentration as the Fe-doped rutile used in our experiment. The nearest neighbor distances in rutile are of the same order as those in ruby and we might therefore conclude that the cross times are of the same order. Pulse-decay measurements, with superheterodyne detection, of the spin-lattice relaxation times at 9680 Mc and 1.4°K for 0.12% Fe-doped rutile yielded values which ranged from 2 msec to somewhat less than 1 msec, dependent upon the transition. From theory[10] and some experiments on various crystals it is to be expected that the spin-lattice time will be the same[11] or shorter[12,13] at millimeter wavelengths than it is at centimeter wavelengths. To this date no experimenters have found an increasing relaxation time with increasing frequency. Therefore, at X band the threefold cross-relaxation effects on a particular resonance line will be greatly reduced by the competing spin-lattice relaxation. At the higher frequencies it is then expected that the spin-lattice process is even more dominant than at X band and that the amount of cross saturation is extremely small.

ACKNOWLEDGMENT

The author would like to thank F. R. Nash for making the X band relaxation measurements and for several illuminating discussions on relaxation phenomena.

---

[6] A. Okaya, Proc. Inst. Radio Engrs. **48**, 1921 (1960).

[7] These Linde crystals were kindly lent to us by H. Lewis, H. Gerritsen, and E. Sebisky of RCA.

[8] N. Bloembergen, S. Shapiro, P. S. Pershan, and J. O. Artman Phys. Rev. **114**, 445 (1959).

[9] W. Mims and J. McGee, Phys. Rev. **119**, 1233 (1960).

[10] See, for example, R. D. Mattuck and M. W. P. Strandberg, Phys. Rev. **119**, 1204 (1960). This theory, however, does not apply to S state ions.

[11] S. Foner, L. R. Momo, A. Mayer, and R. A. Myers, *Quantum Electronics* (Columbia University Press, New York, 1960), pp. 487–498. This work shows that the relaxation time in ruby is approximately independent of frequency.

[12] J. Castle, P. Chester, and P. Wagner, Phys. Rev. **119**, 953 (1960).

[13] J. Pace, D. Sampson, and J. Thorp, Royal Radar Establishment Memorandum No. 1752 (August, 1960) (unpublished). A comparison of the work of references 12 and 13 shows a decreasing relaxation time with increasing frequency for $K_3Cr(CN)_6$.

JOURNAL OF APPLIED PHYSICS VOLUME 32, NUMBER 12 DECEMBER, 1961

Low-Temperature Thermoelectric Power of the Rare-Earth Metals*

H. J. Born,† Sam Legvold, and F. H. Spedding
Institute for Atomic Research and Department of Physics, Iowa State University, Ames, Iowa

(Received May 10, 1961; revised manuscript received July 7, 1961)

The Seebeck coefficients (thermoelectric powers) of yttrium, lanthanum, and 11 of the rare earths have been measured for the temperature range 7° to 300°K. The transitions reported by other investigators on specific heat, magnetic moment, and resistivity at the magnetic ordering temperatures are, in many instances, visible also in the curves of thermoelectric power (TEP) vs temperature. The Néel temperature is evidenced by a change in slope in the TEP vs T curve. The ferro-antiferro transition temperature is obvious only in the case of dysprosium and appears as a sharp drop in the curve. With the exception of samarium and ytterbium, the TEP's of the metals are negative throughout most of the temperature range covered, and, with the same exceptions, the TEP curves have about the same slope near room temperature.

INTRODUCTION

THE electronic configurations of the rare-earth metals differ from each other, in most cases, only in the number of electrons in the $4f$ shell. However, the lanthanide contraction may well influence the Brillouin zone boundaries and thus somewhat influence the conduction process. Studies of the physical properties of these metals should, in the long-range view, provide a better understanding of metals in terms of their electronic structure.

The measurements reported here are concerned with the thermoelectric properties of the rare earths and, in most instances, provide a confirmation of the anomalous behavior noted in heat capacity, resistivity, thermal expansion, and magnetic moment measurements at the magnetic transition temperatures. These temperatures, with the exception of the Curie point of gadolinium, all fall below room temperature. Because thermoelectric effects depend strongly on impurities in metals, the reported curves of thermoelectric power vs temperature must be viewed with caution. However, the curves may be regarded as representative of the general shape expected for the pure metals.

EXPERIMENTAL PROCEDURE

The metals used were of the highest purity available at the present time. The samples were cast slightly larger than the size required and then turned to shape on a lathe. Measurements were made on samples $\frac{3}{16}$-in. in diameter and 2-in. long. Lathe turnings and/or small pieces from the end of the castings were analyzed spectroscopically for other rare earths and common metals and, in addition, some metals were analyzed for carbon and nitrogen. Results of the analyses are shown in Table I. As an additional indication of the purity of the samples, the residual resistivity (taken at 4.2°K) is given.

The sample chamber used for this investigation is shown in Fig. 1. The chamber was immersed in liquid helium for sample temperatures between 4.2° and 77.5°K and in liquid nitrogen for temperatures between 77.5°K and room temperature. The sample was clamped securely to the bottom of a copper housing, which was fastened in turn to an outer copper container (shown cross-hatched in Fig. 1) immersed in the liquid. The two copper containers were separated by a length of thin-wall stainless steel tubing which served as a heat path, and the entire sample chamber was evacuated to a pressure of less than 10^{-5} mm Hg. Thus by supplying an appropriate amount of Joule heat to a heater wrapped and glued securely around the periphery of the lower section of the inner container, the sample could be maintained at any temperature above that of the liquid surrounding the outer container. Because of the great difficulty in ascertaining the equilibrium amount of heat for any given temperature

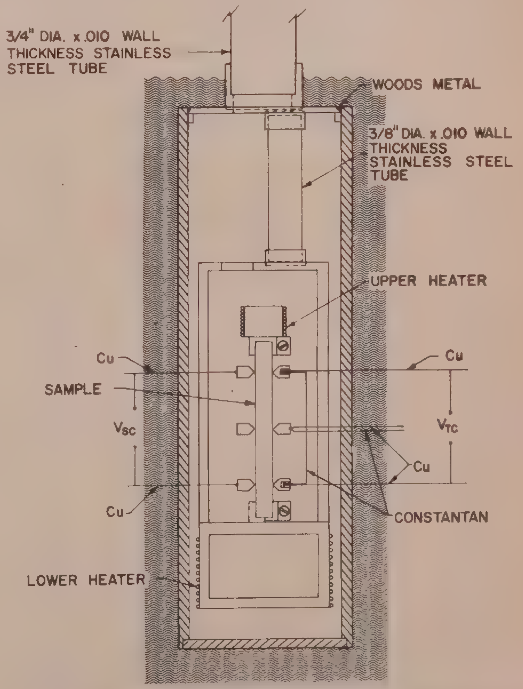
3/4" DIA. x .010 WALL THICKNESS STAINLESS STEEL TUBE
WOODS METAL
3/8" DIA. x .010 WALL THICKNESS STAINLESS STEEL TUBE
UPPER HEATER
Cu
Cu
SAMPLE
V_{SC}
V_{TC}
Cu
Cu
CONSTANTAN
LOWER HEATER

Fig. 1. Sample chamber for thermoelectric power measurement.

---

* Contribution No. 927. Work was performed in the Ames Laboratory of the U. S. Atomic Energy Commission.

† Now at Illinois State Normal University, Normal, Illinois.

Table I. Analyses of samples.

Yttrium	Ca, <0.02; Fe, 0.05; Mg, <0.01; Si, 0.5; Ta, <0.1; Cr, 0.1; Ti, trace; Dy≤0.005; Gd, ≤0.01; Ho, ≤0.05; Er, ≤0.005; Sm, ≤0.05; Tb, ≤0.04; Si, weak; Zr, faint trace Residual resistivity, 5.2×10^{-6} ohm-cm Estimated purity, >99.2%
Lanthanum	Nd, ≤0.02; Ce, ≤0.03; Ca, <0.01; Fe, 0.15; Mg, <0.01; Si, <0.01; Ta, 0.2; Cu, trace; Pr, ≤0.03; Ni, very weak; Sm, faint trace. Al, B, Co, Dy, Er, Eu, Gd, Lu, Pb, Sc, Si, Tb, Tm, Y, and Yb, not detected Residual resistivity, 1.0×10^{-6} ohm-cm Estimated purity, >99.5%
Praseodymium	Nd, ≤0.02; Ce, ≤0.1; La, ≤0.005; Ca,0.1; Fe, 0.02; Mg, ≤0.01; Si, <0.025; Ta, 0.2; Cr, 0.01; Cu, trace; Mn, faint trace; Ni, trace; Ti, weak; Y, trace. Ag, Al, As, Ar, B, Be, Bi, Cd, Co, Dy, Er, Eu, Fe, Gd, Ge, Hf, Hg, Ho, In, Ir, Li, Lu, Mo, Na, Nb, P, Pb, Pt, Rh, Sc, Sm, Sn, Sr, Tb, Te, Tm, V, W, Yb, Zn, and Zr, not detected Residual resistivity 0.7×10^{-6} ohm-cm Estimated purity, >99.5%
Neodymium	Ca, <0.05; Fe, <0.005; Mg, <0.01; Si, <0.025; Ta, <0.1; Cr, <0.01; Cu, trace; Mn, very weak; Ni, trace; Pr, ≤0.08; B, trace; Sm, ≤0.06; C, 333 ppm; N, 48 ppm; 0, 350 ppm; As, Au, Be, Bi, Cd, Co, Ga, Ge, Hg, In, Mo, Nb, P, Pb, Ru, Sb, Sn, Ta, Te, Ti, Tl, V, W, and Zr, not detected Residual resistivity, 7.35×10^{-6} ohm-cm Estimated purity, >99.7%
Samarium	Nd, ≤0.02; Ca, <0.03; Fe, 0.005; Mg, <0.01; Si, <0.01; Cu, 0.05; Gd, ≤0.02; Eu, ≤0.005 Residual resistivity, 6.3×10^{-6} ohm-cm Estimated purity, 99.8%
Gadolinium	Nd, <0.05; Ca, 0.06; Fe, 0.02; Mg, ≤0.01; Si, 0.025; Ta, <0.1; Y, ≤0.05; Dy, ≤0.01; Eu, ≤0.01; Sm, ≤0.05; Tb, ≤0.01; Au, B, Be, Bi, Co, Cr, Cu, Ga, Ge, Hg, Ir, Mn, Mo, Na, Pb, P, Pd, Rh, Ru, Sm, Sr, Ti, Tl, V, W Zn, and Zr, not detected. C, 210 ppm; N, 130 ppm Residual resistivity, 4.4×10^{-6} ohm-cm Estimated purity, >99.6%
Terbium	Ca, 0.04; Dy, 0.05; Gd, 0.05. Eu, Fe, Ho, Si, Ta, Y, Yb, Tm, La, Lu, Nd, Pr, and Er, not detected Residual resistivity, 3.5×10^{-6} ohm-cm Estimated purity, >99.8%
Dysprosium I	Ca, very faint trace; Mg, very faint trace; Ta, 0.2; Y, <0.01; Er, <0.02; Ho, <0.02; Tb, ≤0.1; Si, <0.03; C, 100 ppm; N, 15 ppm; Fe, Al not detected Residual resistivity, 2.4×10^{-6} ohm-cm Estimated purity, 99.7%
Dysprosium II	Yb, ≤0.0005; Er, 0.6; Ho, ≤0.02; Y, ≤0.007; Tb, ≤0.1; Al, faint trace; Ca, trace; Cu, trace; Fe, faint trace; Mg, trace; Si, trace; Yb, faint trace; B, Co, Ni, Pb, and Y, not detected Residual resistivity, 9.0×10^{-6} ohm-cm Estimated purity, >99.2%
Holmium	Tm, ≤0.01; Ta, 0.2; Cu, trace; Ni, trace; Y, <0.01; Dy, ≤0.04; Er, ≤0.02; Tb, <0.01; C, 75 ppm; N, 94 ppm; Si, 0.02. Mo, Cr. Al, and Sc, not detected Residual resistivity, 7.0×10^{-6} ohm-cm Estimated purity, >99.6%
Erbium	La, trace; Ca, <0.01; Fe, 0.02; Mg, <0.01; Si, <0.01, Y, <0.01, Dy, ≤0.005; Ho, ≤0.08; Tm, ≤0.002; Yb, ≤0.0002. Al, B, Ce, Eu, Gd, Lu, Nd, Ni, Pb, Pr, Sc, Si, Sm, Tb, Y, and Yb, not detected Residual resistivity, 4.7×10^{-6} ohm-cm Estimated purity, >99.8%
Thulium	Lu, ≤0.003; Yb, <0.01, Er, ≤0.004; Ho, ≤0.02; Y, ≤0.006; Ca, trace; Fe, very weak; Mg, faint trace; Si, faint trace; Al, B, Ce, Co, Cu, Dy, Eu, Gd, La, Lu, Nd, Ni, Pb, Pr, Sc, Sm, and Tb, not detected Residual resistivity, 8.8×10^{-6} ohm-cm Estimated purity, >99.8%
Ytterbium	Ca, weak; Fe, medium; Mg, very weak; Si, trace; Ta, weak; Cr, faint trace; Cu, weak; Mn, faint trace; Ti, very weak; Y, trace; Al, trace; Ho, trace; Pb, very weak. Be, Ce, Dy, Er, Eu, F, Ho, La, Lu, Nd, Pr, Sc, Ta, Tm, Y, Yb not detected Residual resistivity, 2.3×10^{-6} ohm-cm
Lutetium	Ce, <0.05; Ca, <0.05; Fe, <0.01; Mg, <0.03; Si, <0.03; Ta, medium; Cr, <0.01; Cu, <0.02; Mn, very weak; Y, 0.05; B, very weak; Ni, trace; Pb, trace; Sc, <0.02; Sm, <0.002, Yb, <0.005. C, 66 ppm; N, 720 ppm; As, Au, Ba, Be, Cd, Co, Cr, Ga, Hf, Hg, In, Na, P, Pt, Ru, Te, Ti, Tl, V, Zr not detected Residual resistivity, 4.5×10^{-6} ohm-cm Estimated purity, 99.6%

and the attendant temperature drift which accompanied this ignorance, an automatic temperature control system was incorporated. A standard continuous-balance Wheatstone bridge resistance circuit was used; the sensing device was a copper wire wound on the inner container underneath the heater and the amplified error signal from the bridge was fed to a servomotor connected mechanically to an adjustable resistance in series with the heater.

A temperature gradient along the sample length was maintained by a heater clamped to the upper end of the sample. Ordinarily, a temperature difference of some 2–5°K was established between the two ends of the sample.

Copper thermocouple holders were clamped to the sample near the upper and lower ends and in the center. Thermally connected to the upper and lower thermocouple holders but electrically insulated from them was a copper-Constantan difference thermocouple. Soldered directly to the upper and lower holders were copper wires used to measure the thermoelectric voltage. Thus we have

$$V_{SC}=S_{SC}\Delta T+\delta_{SC}, \qquad (1)$$

$$V_{TC}=S_{TC}\Delta T+\delta_{TC}, \qquad (2)$$

here V_{SC} is the voltage between the two copper wires ldered to the holders, V_{TC} is the voltage between e two ends of the difference thermocouple, S_{SC} is the EP between the sample and copper, S_{TC} is the sensivity of the copper-Constantan thermocouple at the mperature measured by an additional thermocouple ldered to the center thermocouple holder, ΔT is the mperature difference between the upper and lower ermocouple holders, and δ_{SC} and δ_{TC} are extraneous oltages caused by large temperature gradients in homogeneous sections of the wires, or thermals in e measuring circuit.

By careful construction and the use of a thermofree ubicon microvolt potentiometer, the extraneous volt- ges δ_{SC} and δ_{TC} were virtually eliminated. Then from) and (2) we obtain

$$S_{SC}=\frac{V_{SC}}{V_{TC}}S_{TC}.$$

${}_{TC}$ was read from a curve constructed from tables iven by Powell and Bunch.[1] The average sample temerature was read from a thermocouple calibrated by he usual method, using corrections from a calibration f Powell and Bunch.[1]

Thus by a measurement of V_{SC} and V_{TC} at various mperatures between 4.2°K and room temperature, nd knowing S_{TC} for the same temperature region, ${}_{SC}$ can be obtained as a function of temperature. To nd the absolute TEP of a sample, the relative TEP etween the copper wires in the apparatus and a ample of 99.999+% pure lead obtained from the merican Smelting and Refining Corporation was easured. This was done in two different ways. First, piece of the 99.999+% pure lead was extruded into $\frac{1}{8}$-in.-diam wire. This was used together with a iece of copper wire, from the same spool as the copper sed in the apparatus, to form a thermocouple. By eans of a heat leak chamber, one junction of this hermocouple could be held at any desired temperature rom 4.2° to 300°K. A plot of emf versus temperature as made and S_{SC} was calculated from this. From this ead wire a 2-in. long piece was cut which was then laced in the conventional sample chamber. Again this ave us S_{SC} as a function of temperature. These two eterminations agreed within experimental error. The verage gives very good agreement on the high-temerature end, where impurities have a negligible effect, ith an independent determination by Gold *et al.*[2] hen, using the absolute TEP data of Christian *et al.*[3] for lead, the absolute TEP of the copper was obtained. The more obvious plan of merely correcting S_{SC} for the absolute TEP of copper from published data is valueless because of the great dependence of the TEP of copper on impurities.[4–6]

By the definition $S_S=S_C-S_{SC}$, all the data needed to find S_S were then available.

The measurements reported are internally consistent as evidenced by the lack of scatter in most of the resulting curves. Systematic errors, however, are difficult to evaluate. Because of the difficulty of establishing equilibrium conditions at the lower temperatures (say, below 20°K), and also because errors resulting from lack of reproducibility of the thermocouples and deviations of S_{TC} of the thermocouple from the published curves are larger at low temperatures, the data below about 20°K should be considered as only semiquantitatively correct. Above 20°K, S_S is estimated to be accurate within $\pm 0.1\ \mu\text{v}/°\text{K}$ and the temperature to be accurate within ±0.3°K.

RESULTS AND DISCUSSION

The thermoelectric powers of the measured metals are plotted versus temperature in Figs. 4–9.

Anomalous behavior of TEP near the ferromagnetic Curie point has been known for a long time.[7–9] Theoretical treatments of the thermoelectric power of the ferromagnetic iron group elements (*s* and *d* electrons) have been reported by Samoilovich and Korenblit[10] and by Rezanov.[11] The former give an approximation for the discontinuity in Thomson's coefficient at the Curie temperature. This is related to the change in slope of S with T at the Curie point. The value they derive for the discontinuity, $|\Delta\rho|\cong 10^{-5}$ v/°K, is found to be in agreement with the calculated values from the experimental data.

Rezanov[11] gives a formula which is quadratic in temperature and which describes the thermoelectric power below θ, the magnetic ordering temperature

$$-dE/dT=CT-\lambda T(\theta-T),$$

where C and λ are temperature-independent constants depending on the electronic structure of the metal. His results give fair agreement with our data for the rare-earth metals in the temperature range immediately below the ordering temperature. In Fig. 2 we give a comparison of Rezanov's predictions with experimental results for gadolinium and holmium. The theory

---

[1] R. L. Powell and M. D. Bunch, in *International Institute for efrigeration, Problems of Low Temperature Physics and Thermoynamics* (Pergamon Press, London, 1959), pp. 129–135.

[2] A. V. Gold, D. K. C. MacDonald, W. B. Pearson, and I. M. empleton, Phil. Mag. **5**, 765 (1960).

[3] J. W. Christian, J. P. Jan, W. B. Pearson, and I. M. Templeon, Proc. Roy. Soc. (London) **A245**, 213 (1958).

[4] G. Borelius, Physica **19**, 807 (1953).

[5] D. K. C. MacDonald, Physica **19**, 841 (1953).

[6] D. K. C. MacDonald and W. B. Pearson, Acta Met. **3**, 392 (1955).

[7] L. F. Bates, Phil. Mag. **13**, 393 (1932).

[8] A. Hammer, Ann. Physik **30**, 728 (1937).

[9] A. Krupkowski and W. J. de Haas, Proc. Acad. Sci.–Amsterdam **32**, 912 (1929).

[10] A. G. Samoilovich and L. L. Korenblit, Zhur. Eksptl. i Teoret. Fiz. **22**, 360 (1952).

[11] A. I. Rezanov, Doklady Akad. Nauk S.S.S.R. **82**, 885 (1952).

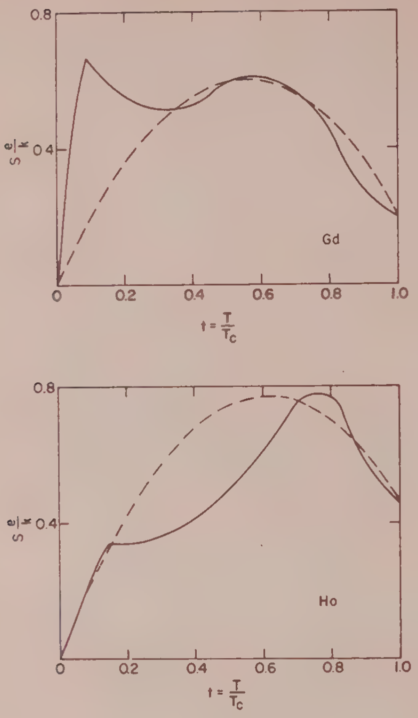

FIG. 2. Comparison of Rezanov's prediction (dashed curve) with experimental results.

Rezanov presents is not intended to describe the low temperature impurity and/or phonon drag anomalies.

More recently, Kasuya[12] has derived some equations for the TEP of ferromagnetic materials, using a molecular field approximation for sufficiently low temperatures. Using these equations, he predicted the TEP of gadolinium and drew a set of three curves, one for the normal part of the TEP, the other two for the anomalous part, using the molecular field approximation for one curve and the spin-wave approximation for the other. His prediction, together with the experimental results, is shown in Fig. 3. Except for the maximum in the experimental curve near 20°K ($t=0.07$), his prediction gives qualitative agreement.

The unusual behavior of the TEP of most metals near 20°K is not well understood. Many investigators[4,13–15] have reported anomalous behavior at low temperatures, the maximum or minimum in TEP sometimes decreasing and other times increasing with percentage of impurity. Even lead, now accepted as the standard[16,17] reference metal for measuring absolute TEP, shows a pronounced bump in its TEP curve near 20°K. According to Jan *et al.*,[17] however, the TEP of lead is not much affected by small amounts of Cd, In, Sn, or Bi, so that it is difficult in the case of lead to attribute the anomaly to impurity scattering. It is also possible to blame the low-temperature anomaly on phonon drag, a phenomenon whereby the electrons are carried along by the lattice vibrational waves, contributing to a larger TEP at low temperatures where the effect is more pronounced.

With the exception of samarium and ytterbium, the TEP's of the metals measured are negative throughout most of the temperature range covered. The transition from paramagnetism to either ferromagnetism or antiferromagnetism makes itself evident on the curves as a change in slope. The transition from ferromagnetism to antiferromagnetism shows up on the curve as a step in the one case (dysprosium) where it is unmistakably evident.

Yttrium

The TEP of yttrium at high temperatures (0–1000°C) has recently been measured by Johansen and Miller[18] who give their results as TEP between platinum and yttrium. Using the values of Cusack and Kendall[19] for the absolute TEP of platinum, a value of the TEP of yttrium at 0°C of $-1.35\ \mu v/°K$ was calculated. This is to be compared with a value of $-1.48\ \mu v/°K$ at 0°C in the present study. Part of the results of Johansen and Miller are shown as an insert in Fig. 4.

The electrical resistivity of yttrium has been measured by Hall *et al.*[20] on single crystals and by Colvin[21]

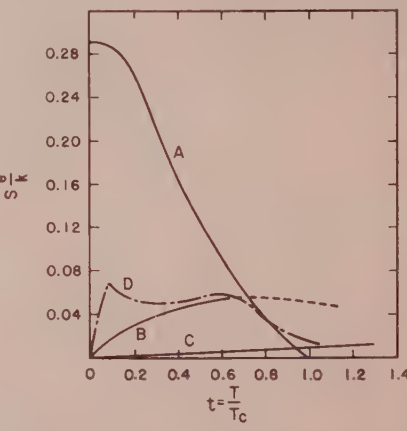

FIG. 3. Comparison of Kasuya's predictions with experimental results: A, Se/k as predicted by molecular field approximation; B, Se/k as predicted by spin-wave approximation; C, Se/k from free electron theory; and D, experimental Se/k from present study.

---

[12] T. Kasuya, Progr. Theoret. Phys. (Kyoto) **22**, 227 (1959).

[13] G. Borelius, W. H. Keesom, C. H. Johansson, and J. O. Linde, Proc. Acad. Sci.–Amsterdam **35**, 10 (1932).

[14] C. Crussard and F. Aubertin, Compt. rend. **226**, 1003 (1948).

[15] C. A. Domenicali and F. A. Potter, J. Appl. Phys. **26**, 377 (1955).

[16] J. W. Christian, J. P. Jan, W. B. Pearson, and I. M. Templeton, Proc. Roy. Soc. (London) **A245**, 213 (1958).

[17] J. P. Jan, W. B. Pearson, and I. M. Templeton, Can. J. Phys. **36**, 627 (1958).

[18] H. A. Johansen and R. C. Miller, J. Less-Common Metals **1**, 331 (1959).

[19] N. Cusack and P. Kendall, Proc. Phys. Soc. (London) **72**, 898 (1958).

[20] P. M. Hall, S. Legvold, and F. H. Spedding, Phys. Rev. **117**, 971 (1960).

[21] R. V. Colvin (private communication).

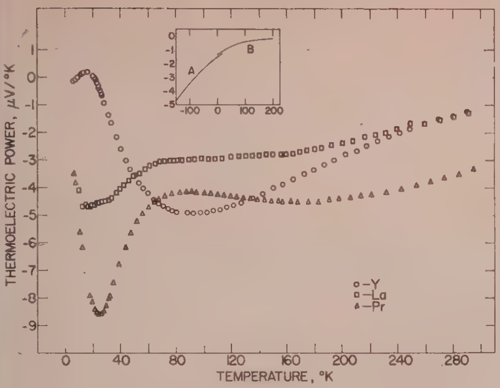

FIG. 4. Thermoelectric power of yttrium, lanthanum, and pradseoymium vs temperature.

on a polycrystalline sample. They report the resistivity o have the normal behavior for metals.

Lanthanum

Lanthanum has been reported by several investigaors[22,23] as having a mixture of both the face-centeredubic structure and a close-packed hexagonal structure vith a stacking sequence *ABAC*. Since no attempt was nade to anneal the sample in the present study, it is quite probable that both crystal structures existed. The curve of the TEP of lanthanum is shown in Fig. 4. Other attempts to duplicate this curve were unsuccessul. The general temperature dependence was about he same, but the magnitude varied from one run to he next. Much more scatter in experimental points about a smoothed curve than exists for the curves of he rest of the metals can also be noted. Kevane *et al.*,[24] while measuring the Hall effect in lanthanum, reported he same difficulty with varying magnitude during different runs, even after attempts to get the pure fcc orm by annealing and quenching. Since the magnitude of the TEP depends quite strongly on the relative shape of the Fermi surface and the Brillouin zone boundaries, it is quite likely that scatter in the data and lack of reproducibility of the curves are caused by some transformations taking place between the two crystal structures, even below room temperature.

Lanthanum, with an empty $4f$ shell, has no lowying electrons with unpaired spin, and thus exhibits no ferromagnetic properties. This is exhibited also in he TEP curve, which has no pronounced maxima or minima or changes in slope except at about 20°K where a minimum occurs.

Praseodymium

The TEP of praseodymium as a function of temperature is displayed in Fig. 4. Only one minimum is noted, appearing at about 25°K. With two electrons in the $4f$ shell, praseodymium exhibits the double c-axis hexagonal structure[23] as does lanthanum in its hexagonal close-packed form. The TEP curves of the two metals are somewhat similar. The resistivity curve of Alstad *et al.*[25] showed an abrupt slope increase at 61°K and a slope decrease at 95°K. This corresponds to a broad peak covering the 60° to 100°K temperature region for the thermoelectric data.

Neodymium

Neodymium, like lanthanum and praseodymium, has the modified hexagonal close-packed structure,[23] and its TEP (shown in Fig. 5) follows the same general temperature dependence as do those of lanthanum and praseodymium. Behrendt *et al.*[26] report that neodymium is probably ferromagnetic at 4.2°K. Parkinson *et al.*[27] have measured the heat capacity of neodymium and found two maxima, at 7° and at 19°K. The electrical resistivity of neodymium also indicates anomalous properties near liquid hydrogen temperatures.[25] No indications of these transitions were observed in the TEP. However, the TEP is changing very rapidly at these temperatures and any transition would be difficult to detect with the present experimental equipment.

Samarium

The TEP of samarium, plotted as a function of temperature, is shown in Fig. 5. There is a barely discernible "dip" in the curve at about 106°K, the temperature of a large peak in the heat capacity curve as reported by Jennings *et al.*[28] Alstad *et al.*,[25] in resistivity

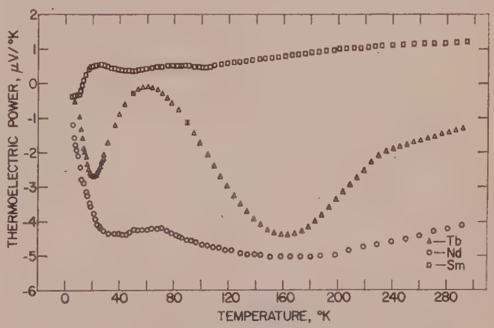

FIG. 5. Thermoelectric power of neodymium, samarium, and terbium vs temperature.

---

[22] G. S. Anderson, S. Legvold, and F. H. Spedding, Phys. Rev. 109, 243 (1958).

[23] F. H. Spedding, A. H. Daane, and K. W. Herrmann, Acta Cryst. 9, 559 (1956).

[24] C. J. Kevane, S. Legvold, and F. H. Spedding, Phys. Rev. 91, 1372 (1953).

[25] J. K. Alstad, R. V. Colvin, S. Legvold, and F. H. Spedding, Phys. Rev. 121, 1637 (1961).

[26] D. R. Behrendt, S. Legvold, and F. H. Spedding, Phys. Rev. 109, 1544 (1958).

[27] D. H. Parkinson, F. E. Simon, and F. H. Spedding, Proc. Roy. Soc. (London) A207, 137 (1951).

[28] L. D. Jennings, E. Hill, and F. H. Spedding, J. Chem. Phys. 31, 1240 (1959).

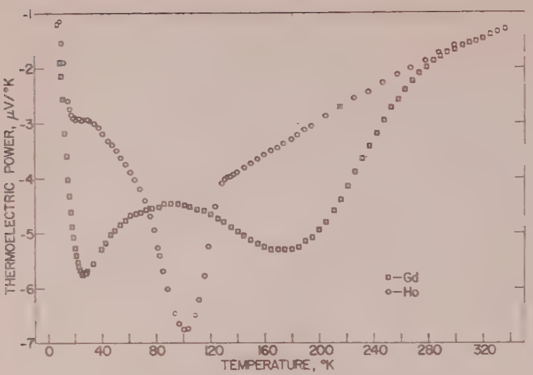

FIG. 6. Thermoelectric power of gadolinium and holmium vs temperature.

measurements on samarium, report an anomaly in the resistivity vs temperature curve, also at about 106°K, which indicates some sort of magnetic ordering. The TEP of samarium is positive throughout almost the entire temperature range covered. This is true for only samarium and ytterbium of all the rare earths covered in the present study. Also samarium has a strange atom stacking[29] of hexagonal layers *ababcbcac*···, and ytterbium is face-centered-cubic.

Gadolinium

Gadolinium has a ferromagnetic Curie point of 289°K.[30–32] Anomalous behavior at or near this temperature has been noted in the thermal expansion,[33] heat capacity,[34] and resistivity[35] for gadolinium. A change in slope of the TEP curve of gadolinium was observed at about 290°K, as may be seen in Fig. 6. The change in slope is not at all abrupt as it is for some of the heavier rare earths.

Terbium

Terbium is believed to have weakly bound antiferromagnetic ordering for temperatures between 218° and 230°K, and to be ferromagnetic below 218°K.[36] Barson *et al.*[33] found a region of negative coefficient of expansion from about 175° to about 235°K, a region including the Néel point and ferromagnetic Curie points mentioned above. Anomalous behavior has also been noted in specific heat studies[37] and in resistivity measurements[35] near both 220° and 230°K. A change in slope of the curve of TEP of terbium (Fig. 5) was found at about 232°K but no transition could be detected by this method near 220°K.

Dysprosium

As was discovered by Trombe,[38] and confirmed by later investigators,[26,39] dysprosium is paramagnetic above 179°K, antiferromagnetic between 179° and 85°K and ferromagnetic below 85°K. These transitions are easily recognizable in the curves of heat capacity[40] and resistivity[35,41] of dysprosium. The TEP of dysprosium was measured on two different samples, labeled Dy I and Dy II. Curves of TEP vs temperature for the two samples are shown in Fig. 7. It is obvious from the figure that the magnetic transitions are more pronounced on Dy I, the sample with the higher purity. (Dy I has a residual resistivity of 2.4×10^{-6} ohm-cm compared to 9.0×10^{-6} ohm-cm for Dy II.)

Holmium

Holmium, paramagnetic above 133°K, appears to be antiferromagnetic between 20° and 133°K, and ferromagnetic below 20°K.[42] The same temperatures are evident as transition points in heat capacity[43] and resistivity[35] measurements. As may be seen in Fig. 6, there is a sharp change in slope of the curve of TEP vs temperature of holmium near 130°K. Also, the

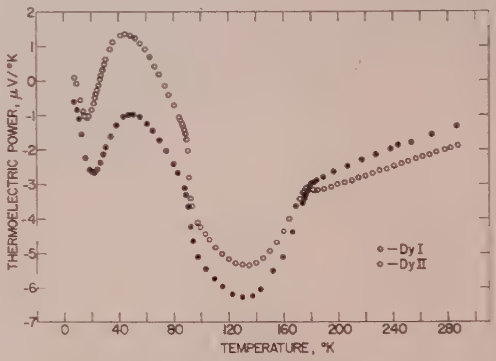

FIG. 7. Thermoelectric power of dysprosium I and dysprosium II vs temperature.

---

[29] A. H. Daane, R. E. Rundle, H. G. Smith, and F. H. Spedding, Acta Cryst. **7**, 532 (1954).

[30] S. Legvold, F. H. Spedding, F. Barson, and J. F. Elliott, Revs. Modern Phys. **25**, 129 (1953).

[31] F. Trombe, Ann. phys. **7**, 385 (1937).

[32] G. Urbain, P. Weiss, and F. Trombe, Compt. rend. **200**, 2132 (1935).

[33] F. Barson, S. Legvold, and F. H. Spedding, Phys. Rev. **105**, 418 (1957).

[34] M. Griffel, R. E. Skochdopole, and F. H. Spedding, Phys. Rev. **93**, 657 (1954).

[35] R. V. Colvin, S. Legvold, and F. H. Spedding, Phys. Rev. **120**, 741 (1960).

[36] W. C. Thoburn, S. Legvold, and F. H. Spedding, Phys. Rev. **112**, 56 (1958).

[37] L. D. Jennings, R. M. Stanton, and F. H. Spedding, J. Chem. Phys. **27**, 909 (1957).

[38] F. Trombe, Compt. rend. **221**, 19 (1945).

[39] J. F. Elliott, S. Legvold, and F. H. Spedding, Phys. Rev. **94**, 1143 (1954).

[40] M. Griffel, R. E. Skochdopole, and F. H. Spedding, J. Chem. Phys. **25**, 75 (1956).

[41] P. M. Hall, S. Legvold, and F. H. Spedding, Phys. Rev. **117**, 971 (1960).

[42] B. L. Rhodes, S. Legvold, and F. H. Spedding, Phys. Rev. **109**, 1547 (1958).

[43] B. C. Gerstein, M. Griffel, L. D. Jennings, R. E. Miller, R. E. Skochdopole, and F. H. Spedding, J. Chem. Phys. **27**, 394 (1957).

ransition at 20°K as reported in other properties is vident on the TEP curve.

Ytterbium

The 4*f* shell is filled prematurely in ytterbium, leaving only two electrons for conduction processes. This gives it properties entirely different from the other rare earths. Also, its crystal structure is face-centered-cubic,[23] which alone might account for its thermoelectric properties being different from the other rare earths.

The TEP of ytterbium is shown in Fig. 8. Near 80°K, where the change was made from the use of liquid helium for the bath liquid to the use of liquid nitrogen, the two sections of the curve do not meet. As the procedure that was followed consisted of measuring the TEP from nitrogen temperature up to room temperature, followed by a measurement from helium temperature up to nitrogen temperature, the lack of joining of the two sections of the curve is believed to be a hysteresis effect. This effect did not occur in any of the other metals measured.

It will be noted also that the TEP of ytterbium is somewhat larger than that for the other rare earths. Most of the others have TEP of about -1 or -2 μv/°K at room temperature, while that of ytterbium is about 27 μv/°K.

Lutetium

The absolute TEP of lutetium is shown in Fig. 9. As would be expected because lutetium has a filled 4*f* shell, no magnetic transitions are indicated. The temperature dependence of the TEP of lutetium is very close to that of yttrium.

Erbium

It is believed that erbium is ferromagnetic below 20°K, antiferromagnetic from 20° to about 80°K and paramagnetic above 80°K.[44,45] The heat capacity curve[46] shows, in addition to the maxima at 19.9° and 84°K, an additional maximum at 53.5°K. On a single crystal, with current parallel to the *c* axis, Green[45] reported a large jump in resistance at 20.4°K, a peak in ρ vs T at 53.5°K, and a sharp change in slope at 84°K. He found only the 84°K transition in the resistivity of an *a*-axis crystal. The curve of the TEP of erbium as a function of temperature (Fig. 9) clearly shows the magnetic transition at about 85°K as a change of slope. However, below about 80°K there is a considerable amount of scatter in the data. An attempt to repeat the curve in this same temperature region resulted in the same type of scatter and same general temperature dependence.

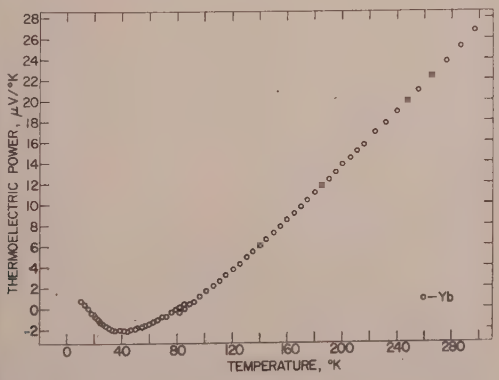

FIG. 8. Thermoelectric power of ytterbium vs temperature.

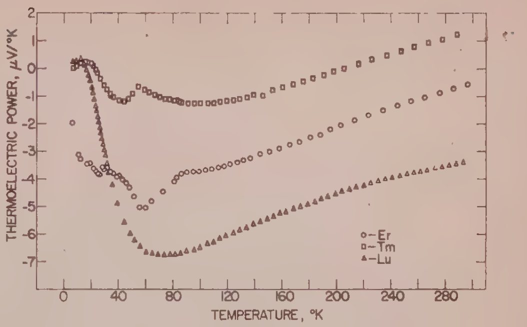

FIG. 9. Thermoelectric power of erbium, thulium, and lutetium vs temperature.

Thulium

The TEP of thulium is shown in Fig. 9. There is a sharp maximum and discontinuous change in slope at 55°K, a temperature corresponding to the 54.5°K reported by Colvin *et al.*[35] for a peak in the resistivity curve. Measurements of the magnetic properties of thulium by Rhodes *et al.*[42] indicate that in addition to the Néel point near 51°K there is a magnetic transition somewhere between 20.4° and 4.2°K. In some recent measurements, Davis and Bozorth[47] found thulium to be antiferromagnetic between 22° and 60°K and ferromagnetic below 22°K. There is no indication of unusual behavior near 22°K in this study of TEP.

ACKNOWLEDGMENTS

We wish to thank R. Colvin and J. Alstad for measuring the residual resistivities given in Table I. We also wish to thank Dr. C. Swenson and R. Colvin for helpful suggestions concerning the design of the experimental equipment and L. Sill for revising the manuscript.

---

[44] J. F. Elliott, S. Legvold, and F. H. Spedding, Phys. Rev. **100**, 1595 (1955).

[45] R. W. Green, S. Legvold, and F. H. Spedding, Phys. Rev. **122**, 827 (1961).

[46] R. E. Skochdopole, M. Griffel, and F. H. Spedding, J. Chem. Phys. **23**, 2258 (1955).

[47] D. D. Davis and R. M. Bozorth, Phys. Rev. **118**, 1543 (1960).

JOURNAL OF APPLIED PHYSICS VOLUME 32, NUMBER 12 DECEMBER, 1961

A Method for the Measurement of Short Minority Carrier Diffusion Lengths in Semiconductors*

ALVIN M. GOODMAN
RCA Laboratories, Princeton, New Jersey

(Received May 31, 1961)

A method is presented whereby short minority carrier diffusion lengths in semiconductors may be determined by measuring the variation of surface photovoltage as a function of optical absorption coefficient. The method does not depend upon the specific form of the relationship between the surface photovoltage and the density of the excess minority carriers injected at the bulk edge of the surface space charge region. Only capacitive contacts to the sample are needed for the measurement. The method has been used to determine the minority carrier diffusion length in both *n* and *p* type gallium arsenide.

I. INTRODUCTION

THE most commonly used method for determining the minority carrier diffusion length L in a semiconductor employs a measurement of the minority carrier lifetime τ and the relationship $L=(D\tau)^{\frac{1}{2}}$, where D is the minority carrier diffusion constant.[1,2] This method may be difficult to apply if (1) the minority carrier lifetime is too short to measure conveniently, (2) trapping effects give misleading results for lifetimes determined by photoconductive decay or similar techniques, or (3) D is not known. A method for determining L from the spectral dependence of the surface photovoltage has been developed. This method has been modified to permit the determination of the value of L in each region of a solar cell (plane *p-n* junction) from the spectral dependence of the open circuit junction voltage.[3] In this paper a simplified formulation of the original method is presented. The method is similar to that reported by Quilliet and Gosar[4] but is less restrictive in that the surface photovoltage may be *any* monotonic function of light intensity. Preliminary results of the application of the method to the measurement[5] of L in gallium arsenide are presented.

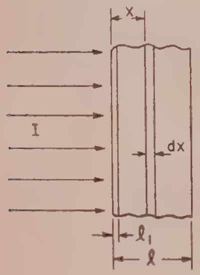

FIG. 1. Sample geometry. ℓ_1=depth of the surface space-charge layer at the illuminated surface; ℓ=sample thickness; and I=incident photon flux.

II. THEORY

The measured quantity is the surface photovoltage of the semiconductor.[6–8] The surface photovoltage ΔV developed at the illuminated surface is a function of the excess minority carrier density Δp injected into the surface space charge region. The density Δp is in turn dependent upon the incident light intensity I, the optical absorption coefficient k, and the diffusion length L. The diffusion length may then be determined by measuring the variation of ΔV with k (i.e., with wavelength λ). An accurate knowledge of k as a function of λ is required.

It can be shown[9] that a steady state solution of the one dimensional diffusion equation for the sample geometry illustrated in Fig. 1 is

$$\Delta p=\frac{\alpha I(1-\rho_1)}{(D/L)+s}\cdot\frac{kL}{1+kL}, \tag{1}$$

assuming that

$$k\ell\gg 1, \tag{2a}$$

$$k\ell_1\ll 1, \tag{2b}$$

$$\ell\gg L, \tag{2c}$$

$$\ell_1\ll L, \tag{2d}$$

$$\Delta p\ll n_0, \tag{2e}$$

where α is the photon quantum efficiency for hole-electron pair creation, ρ_1 is the optical reflection coefficient at the illuminated surface, s is the surface recombination velocity at the illuminated surface, ℓ is the sample thickness, ℓ_1 is the depth of the space charge layer[10] at the illuminated surface, and n_0 is the majority carrier density.

---

[*] The research reported in this paper has been sponsored in whole or in part by the Air Force Cambridge Research Laboratories, U. S. Air Force.

[1] E. M. Pell, Phys. Rev. **90**, 278 (1953).

[2] J. R. Haynes and J. Hornbeck, Phys. Rev. **90**, 152 (1953).

[3] J. J. Loferski and J. J. Wysocki, Bull. Am. Phys. Soc. Ser. II, **5**, 265 (1960).

[4] A. Quilliet and M. P. Gosar, J. phys. radium **21**, 575 (1960).

[5] I. Kudman (personal communication).

[6] W. H. Brattain and J. Bardeen, Bell System Tech. J. **32**, 1 (1953).

[7] C. G. B. Garrett and W. H. Brattain, Phys. Rev. **99**, 376 (1955).

[8] E. O. Johnson, Phys. Rev. **111**, 153 (1958).

[9] T. S. Moss, J. Electronics and Control **1**, 126 (1955).

[10] A simple method of estimating the maximum value of ℓ_1 for a semiconductor in which both the bulk and surface are nondegenerate is given in the Appendix.

The surface photovoltage[11] may be written as

$$\Delta V = f[\Delta p] = f\left[\frac{\alpha I(1-\rho_1)}{(D/L)+s}\cdot\frac{kL}{1+kL}\right], \qquad (3)$$

here the form of the functional dependence need not e known explicitly. It will, in fact, vary from one ample to another depending on the type of semi-onductor, doping, surface treatment, etc. If ρ_1 and α re essentially constant over the k region of interest, q. (3) may be rewritten as

$$\Delta V = f[CIk/(1+kL)], \qquad (4)$$

here C is a constant. Although the specific form of this elationship may not be known, it is a monotonic function[12] and may therefore be inverted to give

$$Ik/(1+kL) = F(\Delta V). \qquad (5)$$

The same value of ΔV may be obtained for two lifferent values of I (perhaps I_1 and I_2) provided that he corresponding values of λ and hence k (k_1 and k_2) re properly chosen. It follows in this case from Eq. 5) that

$$I_1k_1/(1+k_1L) = I_2k_2/(1+k_2L). \qquad (6)$$

Thus L may be obtained as

$$L = [I_2k_2 - I_1k_1]/[k_1k_2(I_1-I_2)]. \qquad (7)$$

III. EXPERIMENTAL TECHNIQUE

The experimental arrangement is shown in Fig. 2. Chopped light from a monochromator uniformly illuminates an area on the front surface slightly larger than the pickup probe area to eliminate edge effects. With the 10-cps chopping rate, the recombination and trapping processes in the semiconductor reach a steady state in a time which is short in comparison with the "light on" portion of the chopping cycle. It is important to prevent incoming light from reaching the semiconductor surface adjacent to the reference electrode to eliminate the possibility of a photovoltage being developed there. Further experimental details are given in reference 8. The fact that only capacitive pickup probe "contacts" are used in the measurement is an advantage over other methods for measuring lifetime (photoconductivity decay method) and diffusion length (PEM method)[14] which require conducting electrical contacts to be made to the sample.

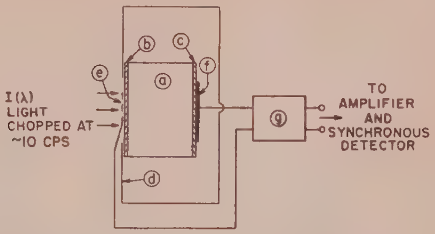

FIG. 2. Experimental arrangement for measurement of surface photovoltage. (a) Semiconductor sample; (b) thin transparent insulator on illuminated surface; (c) thin insulator on dark surface; (d) shield to prevent light from reaching the unilluminated (dark) surface; (e) transparent conducting coating (pickup probe) (area 10^{-3} to 10^{-1} cm); (f) conducting coating (reference probe); and (g) preamplifier with electrometer tube input.

In the measurement described, the surface photovoltage is not the only one which will be detected by the capacitive probe. A Dember potential[15] will also be developed in the bulk semiconductor between the probe at the illuminated surface and the reference probe at the unilluminated surface. It can be shown that the Dember potential is[16]

$$V_D = \frac{kT}{e}\cdot\frac{b-1}{b+1}\ln\left[\frac{(b+1)\Delta p + bn_0 + p_0}{(b+1)\Delta p_r + bn_0 + p_0}\right],$$

where kT/e is the thermal energy, b is the ratio of electron mobility to hole mobility, n_0 and p_0 are the thermal equilibrium values of the electron and hole densities and Δp_r is the excess minority carrier density at the unilluminated surface adjacent to the reference probe. If $(b+1)\Delta p_r \ll bn_0 + p_0$, V_D will vary only with Δp; thus, in any given case, the total voltage observed between the probes will depend only upon Δp. The condition $(b+1)\Delta p_r \ll bn_0 + p_0$ is actually much less restrictive than Eq. (2e). The presence of the Dember potential does not violate any of the conditions previously assumed, and it is therefore clear that it will introduce no error into the measurements.

IV. EXPERIMENTAL RESULTS

The minority carrier diffusion length in both n and p type gallium arsenide samples has been determined by the method described.[5] A brief summary of the preliminary results is given in Table I. The wavelengths used in the measurements corresponded to k values between 10^3 and 10^4 cm^{-1} and were in the range where α and ρ_1 are essentially constant. The experimental conditions were such that Eqs. (2) were satisfied [see the Appendix for a check on Eqs. (2b) and (2d)]. One of the samples (M-43-6) was later used to make a

---

[11] ΔV is actually measured between a capacitive probe at the illuminated surface and one at the unilluminated surface. It is therefore necessary that the surface photovoltage developed at the unilluminated surface be negligible. Equations (2a) and (2c) assure that this may be achieved in any practical case.

[12] This is shown in reference 8 for Ge provided that significant changes in the "slow" surface state charge density do not occur during the measurement. This behavior is also observed in GaAs.[13] On the basis of the physical reasoning employed in references 7 and 8 one would expect the same behavior to be observed in other semiconductors as well.

[13] A. M. Goodman (unpublished work).

[14] A. Amith, Phys. Rev. **116**, 793 (1959).

[15] W. van Roosbroeck, Phys. Rev. **101**, 1713 (1956).

[16] This is equivalent to Eq. (20) of T. S. Moss, L. Pincherle, and A. M. Woodward, Proc. Phys. Soc. (London) **66**, 743 (1953).

TABLE I.

Sample	Majority carrier concentration, cm^{-3}	Diffusion length L, microns Surface photovoltage measurement	Transistor measurement
RCA-105 3	$n_0 = 7.2\times 10^{16}$	1.4	
M-43-4	$p_0 = 10^{18}$	6.6	
M-43-6	$p_0 = 10^{18}$	8.8	7
M-43-9	$p_0 = 10^{18}$	6.9	
M-43-11	$p_0 = 10^{18}$	7.2	
M-43-13	$p_0 = 10^{18}$	7.5	

transistor and an estimate of L obtained from current gain measurements is in good agreement with the value obtained from the surface photovoltage measurement. A more comprehensive account of the experimental studies will be published at a later date.

ACKNOWLEDGMENTS

It is a pleasure to acknowledge the helpful suggestions and encouragement of E. O. Johnson. The author is indebted to I. Kudman for permission to quote his unpublished data and to A. Amith for his critical reading of the manuscript. Several helpful discussions with R. Braunstein are also gratefully acknowledged.

APPENDIX

It is important to estimate the maximum value of the space charge layer depth ℓ_1 in order to insure the validity of Eqs. (2b) and (2d). We consider here only material in which both the bulk and surface are nondegenerate. It is clear from the work of Kingston and Neustadter[17] that for a given doping and magnitude of space charge potential, the maximum space charge layer depth occurs for an inversion layer rather than for an accumulation layer. If then we compute the value of ℓ_1 for an inversion layer assuming a particular doping and the largest possible space charge potential (assuming the surface remains nondegenerate), we obtain the maximum value of ℓ_1 for that doping. An exact computation of $(\ell_1)_{\max}$ may be accomplished using the method of reference 17; however, a much simpler method (which tends to overestimate ℓ_1) is to obtain $(\ell_1)_{\max}$ from a solution of Poisson's equation, assuming that the uncompensated charge concentration in the space charge region is constant and equal to the bulk doping density. This gives[18]

$$(\ell_1)_{\max} = [2\epsilon\Delta V_{\max}/ne]^{\frac{1}{2}},$$

where n is the uncompensated ion density, ϵ is the dielectric coefficient, e is the electronic charge, and $\Delta V_{\max}$ is the maximum value of the potential difference across the space charge layer, all in mks units. $\Delta V_{\max}$ is the energy difference between the Fermi level and the furthest band edge. It follows that

$$(\ell_1)_{\max} = \left[\frac{2\epsilon\{E_g/2 + (kT/e)\ln(n/n_i)\}}{ne}\right]^{\frac{1}{2}},$$

where E_g is the energy bandgap and n_i is the intrinsic carrier density. Only a slight error is incurred if $\Delta V_{\max}$ is set equal to E_g.

$$(\ell_1)_{\max} = [2\epsilon E_g/ne]^{\frac{1}{2}}.$$

Both approximations for $(\ell_1)_{\max}$ are shown in Fig. 3 for doping densities from 10^{13} to $10^{18}/\mathrm{cm}^3$. A comparison of this graph with the data of Table I shows that Eqs. (2b) and (2d) are indeed satisfied.

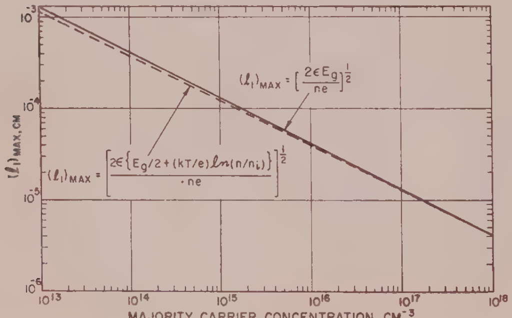

FIG. 3. Maximum depth of the surface space charge layer in nondegenerate gallium arsenide.

---

[17] R. H. Kingston and S. F. Neustadter, Lincoln Laboratory Quart. Progr. Rept. on Solid State Research, p. 10 (August 1, 1954).

[18] For a derivation of this expression, see A. Van der Ziel, *Solid State Physical Electronics* (Prentice-Hall, Inc., Englewood Cliffs, New Jersey, 1957), p. 252.

JOURNAL OF APPLIED PHYSICS VOLUME 32, NUMBER 12 DECEMBER, 1961

Theory of the Potential Well Produced by Multipacting Electrons. I. Very Low-Pressure Regime*

R. L. Ingraham
Research Center, New Mexico State University, University Park, New Mexico

(Received May 31, 1961)

Electrons multipacting in an evacuated discharge tube produce an effective static potential well in which the positive ions can be contained. The theory of the positive ion behavior in this "electron well" in the very low pressure regime ($\mathcal{P} \lesssim 10^{-5}$ mm Hg) is developed here. The electron potential well is expressed finally as a double numerical integral of complete elliptic integrals for the general field point; for on-axis points it reduces to a single numerical integral of irrational expressions. With the "short tube" and "constant sheet velocity" approximations, the well is parabolic; the corresponding ion harmonic vibration frequencies are calculated. For the rigorous well these parabolas are flattened in the central parts and steepened near the electrodes. A self-consistent calculation of the ion density is made using an individual particle description of the ion gas (appropriate to very low densities) which results in an inhomogeneous integral equation. The solutions describe ion distributions peaked in the middle of the tube. For comparison with experiment the deflection of an ion beam fired across the tube is worked out.

I. INTRODUCTION

MULTIPACTING electrons in an evacuated discharge tube simulate a static negative space charge as far as positive ions are concerned, which, because of their much greater masses, cannot follow the high frequency rf electric field. This effective negative space charge creates a potential well in which positive ions can be contained, oscillating at some much lower frequency.[1]

This paper and one to follow develop a theory of the ion behavior in such an "electron well." This situation has several special features which set it apart from the phenomena usually investigated in the theory of ionized gases interacting with an electromagnetic field: (1) one of the components has a highly non-Maxwellian distribution, the multipacting electrons, whose velocities are parallel to the tube axis and far exceed their thermal velocities; (2) the ionized gas is far from plasma conditions because the electrons created by the ionization are removed by the rf field from the gas in a half-cycle or so (they join the multipacting electrons), leaving a net positive space charge.

In Part II of this paper the time-averaged potential due to the oscillating electron "sheet" is rigorously derived. The rigor is justified here since the motion and other parameters characterizing this electron sheet are known with relative exactness. The electrons of the sheet will then be represented in the ion equations by this potential well, taken as an unvarying "external field." In the very low-pressure regime, with practically unshielded positive ions, this is well justified; for higher pressures, and thus partial shielding, this electron-ion interaction has to be supplemented by a collision term. With a *uniform* effective negative charge distribution (the multipacting electron charge density averaged over an rf cycle) the electron well would be parabolic[2] in both dimensions, neglecting effects due to the finite size of the tube. This follows from the simple argument that the force on an ion in any direction is proportional to the difference of the total charges it sees on either side of it, and this is proportional (with a negative sign) to its displacement from the equilibrium position of equal total charge on both sides. This ideal parabolic shape is modified in our solution by two factors. One is that of "surface effects" (finite size of the tube). The other is the fact that the effective negative charge distribution is not uniform, but peaked toward the electrodes: the discharge electrons spend more of their time at the ends than in the middle of the tube. Peaking of a charge distribution at the ends tends to flatten the central part and steepen the outer parts of the parabolic well by the same simple argument given above. Similarly, as will happen for the ion "hill," peaking of the charge in the center tends to do just the opposite to a parabolic well (see Fig. 1). A correction (which has

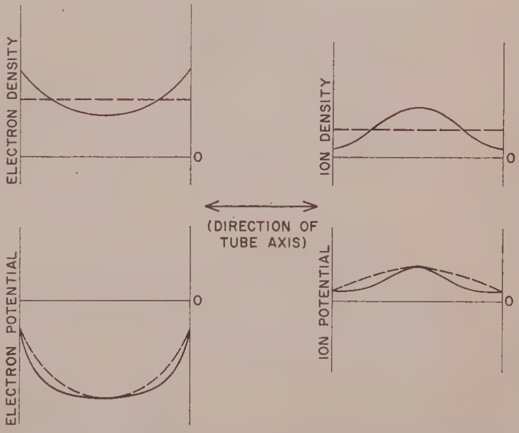

Fig. 1. General shapes of the potentials within the discharge tube along any straight line parallel to the tube axis for the indicated electron and ion density distributions. Dashed lines represent uniform densities and the corresponding approximately parabolic potentials; solid lines indicate the actual densities and the corresponding distorted parabolic potentials.

---

* Supported by the Office of Ordnance Research.

[1] H. B. Williams, Phys. Rev. 107, 1451 (1957).

[2] Here and hereafter we mean "parabolic" at points within the discharge tube.

been neglected in this theory) would have to be made if there were an appreciable amount of conducting material in the vicinity of the tube.

Although one cannot in general use the time-averaged charge density to compute a rigorous time-averaged potential (since this neglects retardation effects), it is interesting that here this procedure is correct. The reason is that our idealized time-dependent electron distribution (the oscillating electron sheet) is rigid. The electron potential well is obtained in the final form of a double integral over dimensionless time and cylindrical radius coordinates of Legendre functions of the second kind of order $-\frac{1}{2}$. It is regrettable that these functions are apparently not tabulated since they arise in *every* problem of the potential of a finite cylindrically symmetric distribution. They can be expressed however in terms of complete elliptic integrals. The potential at on-axis points reduces to a single integral (over dimensionless time) of irrational expressions. Incidentally, because the prescribed motion of the electron sheet enters these formulas, the potential does not simply "scale" under changes of the dimensional parameters.

In this first paper the very low pressure regime ($\mathcal{P} \lesssim 10^{-5}$ mm Hg) is treated, so that the "microscopic," i.e., individual particle, description of the ions suffices. Since the well is approximately parabolic in both dimensions, the ion motion will be roughly harmonic. Theoretical expressions for these effective spring constants are derived. An equation is also derived which allows the spring constant for motion parallel to the axis to be read off from the angular deflection of an ion beam fired across the tube.

The total potential an ion finds itself in is the sum of the electron well and the ion "hill" due to all the other ions (provided the phases of the ions' harmonic motions are distributed at random). One can get an idea of the ion number density n_i on the microscopic picture by the following self-consistent calculation. Suppose the ions are created by collisions of gas molecules with the electron sheet at the constant rate αn_a per unit volume ($n_a \equiv$ number density of the neutrals) and are annihilated by recombination after all having lived a common lifetime. Approximate the electron well as parabolic: then the ions near the axis perform harmonic motion parallel to it with some angular frequency ω. The electron sheet motion is prescribed, hence the coefficient α above is supposed a known function of position; and $n_a = \mathcal{P}/kT - n_i$. Then adding up the contributions of the individual harmonically moving ions to the ion density at a point and time, one can derive an integral equation for n_i at points near the axis. The solutions are peaked in the middle of the tube. They involve ω parametrically. Self-consistency requires that the ion potential hill, calculated with this solution, when added to the electron well give a sum well in which the ions vibrate with the frequency ω assumed at the outset. Strictly speaking this would require the ion hill to be parabolic, thus n_i to be uniform (neglecting finite size effects). Practically, one would require only that the ion hill not perturb the parabolic electron well too much. For convenience, the potential hill for a uniform ion density is calculated. It is again a double numerical integral, but for on-axis points it can be completely integrated.

The following paper will investigate the ion gas in the higher pressure regime ($10^{-4} \lesssim \mathcal{P} \lesssim 10^{-2}$ mm Hg). Stationary solutions of the coupled transport equations for the ion gas and Maxwell equations for its electric field can be taken to describe these phenomena since the ions are insensitive to the rapidly varying applied rf field. The sheet electrons are taken into account first, by inserting the force term for (slightly shielded) ions in the given electron well electric field and second, by an ion-sheet electron collision term.

Our method is to eliminate fields successively between these equations, finally getting an approximate nonlinear second order ordinary differential equation for the ion density. This can be solved approximately in closed form or numerically. The quantitative features of the solution are the following. The ion velocity field is negligible and the ion density near the axis is roughly Gaussian, peaked of course at the center of the tube. The sum well then shows two troughs on either side of a central hill. If this hill is high enough, the positive ions will no longer be contained but can be ejected through holes in the electrodes. This central hill also provides a well to trap gas electrons, thus inhibiting the departure from electrical neutrality. Our principal aim is to understand the shape and size of this sum well quantitatively so as to be able to predict the onset of "organized" phenomena. This onset appears to be very discontinuous and probably occurs at the resonance between the frequencies of certain electron or ion plasma oscillation modes and other frequencies occurring in our problem, namely the oscillator frequencies in the net potential wells or the applied radio frequency. It is believed that the sharply defined "plasmoids"[3] which appear suddenly in this regime and the sudden drop in radio frequency noise emitted from the tube are evidence for a collective mode of motion of some kind. We will postpone further discussion of our theoretical results on the high-pressure regime to the second paper.

II. THEORY OF THE VERY LOW-PRESSURE REGIME

A. Electron Sheet Potential Well

Let the multipacting electrons be idealized to a perfectly thin sheet with uniform negative surface charge density $-\sigma$. Let its known equation of motion be[4]

---

[3] R. W. Wood, Phys. Rev. **35**, 673 (1930).

[4] The function $f(t)$ has the form $f(t) = z(t)$, $(0 \leq t \leq \tau/2)$; $= -z(t-\tau/2)$, $(\tau/2 \leq t \leq \tau)$, where τ is the period of the rf field and $z(t)$, defined only for the range $0 \leq t \leq \tau/2$, is of the form $a + bt + c\sin(2\pi t/\tau + \epsilon)$ and $z(0) = -L/2$. The condition of multipacting resonance determines the constants in terms of the length of the tube, the phase and amplitude of the rf field, and the secondary emission characteristics of the electrodes.

$=f(t)$. The function $f(t)$ is periodic, of course, with period τ, the period of the rf field. We take cylindrical coordinates z, r, ϕ with origin at the center of the cylindrical discharge tube of length L and radius R. The exact electric potential at any point and time is then

$$\phi_e(z,r,t)=-\frac{\sigma}{4\pi\epsilon_0}\int_{\text{tube}}\frac{\delta[z'-f\{t-R(P,P')/c\}]}{R(P,P')}\times r'dr'd\phi'dz', \quad (2.1)$$

where

$$R(P,P')\equiv[(z-z')^2+r^2+r'^2-2rr'\cos(\phi-\phi')]^{\frac{1}{2}},$$

since the time-dependent charge density is

$$\rho(z,t)=-\sigma\delta[z-f(t)]. \quad (2.2)$$

By cylindrical symmetry all quantities will be independent of ϕ, the azimuth. This Green's function is appropriate to a potential normalized to zero at infinity—thus this simplest theory neglects the presence of conductors in the vicinity of the tube. Write

$$\delta[z'-f\{t-R(P,P')/c\}]=\frac{\delta[t-t_1(z')-R(P,P')/c]}{v_1(z')}+\frac{\delta[t-t_2(z')-R(P,P')/c]}{v_2(z')},$$
$$(0<t<\tau). \quad (2.3)$$

Here $t_1(z)\leqslant\tau/2$, $t_2(z)\geqslant\tau/2$ are the two times during one rf cycle at which the sheet passes the point z on its way up and on its way down, respectively. They are determined by inverting the motion equation $z=f(t)$.[4] Also $v_1(z)\equiv v[t_1(z)]$ and $v_2(z)\equiv v[t_2(z)]$ are the speeds of the sheet as it passes z going up and going down, respectively. Equation (2.3) can be justified by noting that the argument of the δ function on the left has exactly two zeroes $(t_0)_1$, $(t_0)_2$ in one rf cycle, and these are given by

$$(t_0)_1=t_1(z)+R(P,P')/c, \quad (t_0)_2=t_2(z)+R(P,P')/c.$$

Now the positive ions find themselves in an effective static potential well[5] given by the time-average

$$\bar{\phi}_e(z,r)\equiv\lim_{T\to\infty}\frac{1}{2T}\int_{-T}^{T}\phi_e(z,r,t)dt$$

of this potential. Doing the time integration with the aid of (2.3), we come out with

$$\bar{\phi}_e(z,r)=-\frac{\sigma}{4\pi\epsilon_0\tau}\int_{\text{tube}}\left\{\frac{1}{v_1(z')}+\frac{1}{v_2(z')}\right\}\frac{1}{R(P,P')}\times r'dr'd\phi'dz'. \quad (2.4)$$

The τ appears since for any pair of points P, P', the time interval over which we must integrate to get the contribution from both δ functions in (2.3) is of length exactly τ. Expand $1/R(P,P')$ in the manner convenient for cylindrical symmetry,[6]

$$\frac{1}{R(P,P')}=\sum_{m=-\infty}^{\infty}\exp[im(\phi-\phi')]\int_0^{\infty}d\lambda\times J_m(\lambda r)J_n(\lambda r')\exp(-\lambda|z-z'|);$$

the angle integration collapses the infinite sum to $2\pi\times$term $m=0$. The remaining expression can be identified[7] with the Legendre function of the second kind of order $-\frac{1}{2}$

$$\int_0^{\infty}d\lambda J_0(\lambda r)J_0(\lambda r')\exp(-\lambda|z-z'|)=\frac{1}{\pi}(rr')^{-\frac{1}{2}}Q_{-\frac{1}{2}}\left[\frac{r^2+r'^2+(z-z')^2}{2rr'}\right].$$

Hence we get

$$\bar{\phi}_e(z,r)=-\frac{\sigma}{2\pi\epsilon_0\tau}\int\left\{\frac{1}{v_1(z')}+\frac{1}{v_2(z')}\right\}\left(\frac{r'}{r}\right)^{\frac{1}{2}}\times Q_{-\frac{1}{2}}\left[\frac{r^2+r'^2+(z-z')^2}{2rr'}\right]dr'dz'.$$

It is perhaps slightly more convenient for numerical integration to use the position $f(t)$ of the sheet rather than the speeds $v_1(z)$, $v_2(z)$. We change the z' integration to a time integration via the formulas

$$t_1(z)=\int_0^z\frac{dz'}{v_1(z')},$$

which is the inverse of $z=f(t)$ in $0\leqslant t\leqslant\tau/2$, and

$$\int_{-L/2}^{L/2}dz'\frac{F(z')}{v_2(z')}=\int_{-L/2}^{L/2}dz'\frac{F(-z')}{v_1(z')}$$

which holds for any function $F(z)$ since $v_1(z)=v_2(-z)$. This gives

$$\bar{\phi}_e(z,r)=-\frac{\sigma}{2\pi\epsilon_0\tau}r^{-\frac{1}{2}}\int_0^R(r')^{\frac{1}{2}}\times dr'\int_0^{\tau/2}dt\left\{Q_{-\frac{1}{2}}\left[\frac{r^2+r'^2+(z-z(t))^2}{2rr'}\right]+Q_{-\frac{1}{2}}\left[\frac{r^2+r'^2+(z+z(t))^2}{2rr'}\right]\right\},$$

---

[5] One can show that the time-averaged vector potential vanishes.

[6] P. Morse and H. Feshbach, *Methods of Theoretical Physics* (McGraw-Hill Book Company, Inc., New York, 1953), Part II, Eq. (10.3.23).

[7] G. N. Watson, *Theory of Bessel Functions* (Cambridge University Press, Cambridge, 1922), p. 389, Eq. (2).

where $z(t)$ is the function defined in footnote 4. Introduce the dimensionless time $\theta \equiv t/\tau$, radius $\rho \equiv r/R$, and height $\zeta \equiv 2z/L$, and write

$$z(t) \equiv \tfrac{1}{2} L \zeta(\theta).$$

Then finally

$$\bar{\phi}_e(\zeta,\rho) = -\frac{\sigma R}{2\pi\epsilon_0}\rho^{-\frac{1}{2}} \int_0^1 (\rho')^{\frac{1}{2}} d\rho' \int_0^{\frac{1}{2}} d\theta \times \left\{ Q_{-\frac{1}{2}}\left[\frac{\rho^2+\rho'^2+\beta^2(\zeta-\zeta(\theta))^2}{2\rho\rho'}\right] + Q_{-\frac{1}{2}}\left[\frac{\rho^2+\rho'^2+\beta^2(\zeta+\zeta(\theta))^2}{2\rho\rho'}\right]\right\}. \quad (2.5)$$

Here the single parameter

$$\beta \equiv L/2R$$

characterizes the geometry of the tube. Under a change of the external parameters $\bar{\phi}_e$ does *not* scale since not only β but also in general the form of the dimensionless function $\zeta(\theta)$ will change.

The Legendre function may be expressed in terms of the complete elliptic integral of the first kind $K(k)$ via

$$Q_{-\frac{1}{2}}(\cosh x) = kK, \quad k = \operatorname{sech} \tfrac{1}{2} x$$

and tables of the $K(k)$ used in numerical integration.

For on-axis points $r=0$, $R(P,P')$ simplifies so that the r' integration can be done explicitly. Hence going back to Eq. (2.4) and doing the ϕ' and r' integrals in this case, we get finally

$$\bar{\phi}_e(\zeta,0) = -\frac{\sigma R}{2\epsilon_0}\int_0^{\frac{1}{2}} d\theta \{[1+\beta^2(\zeta-\zeta(\theta))^2]^{\frac{1}{2}} + [1+\beta^2(\zeta+\zeta(\theta))^2]^{\frac{1}{2}} - \beta|\zeta-\zeta(\theta)| - \beta|\zeta+\zeta(\theta)|\}. \quad (2.6)$$

Formulas (2.5) and (2.6) are our final theoretical results for the electron sheet potential well.

A measure of the net depth of the well, i.e., the depth relative to its level at the electrodes ($\zeta = 1, -1$), is given by

$$\Delta\bar{\phi}_e \equiv \bar{\phi}_e(1,0) - \bar{\phi}_e(0,0) \equiv \gamma\sigma R/2\epsilon_0. \quad (2.7)$$

For a typical set of parameters[8] the "fiducial potential" $\sigma R/2\epsilon_0$ comes out to be ≈ 875 v while the dimensionless integral factor $\gamma \approx 0.079$.

The well $\bar{\phi}_e$ is parabolic in both r and z with certain approximations—this "doubly parabolic" approximation, because of its analytical simplicity, will be useful in the investigation of the ion behavior by means of the transport equations. The parameters involved, for the z-dependent part, can be calculated from the exact on-axis form (2.6) by employing the approximations

$$\frac{1}{v_1(z)} + \frac{1}{v_2(z)} \equiv \frac{2}{\bar{v}} = \text{const} \quad (\text{“constant sheet velocity approximation”})$$

and

$$O(\beta^2) = 0 \quad (\text{“short tube approximation”}).$$

Then $d\theta = (L/2\tau\bar{v})d\zeta'$ and

$$\bar{\phi}_e(\zeta,0) \approx -\frac{\sigma R}{2\epsilon_0}\cdot\frac{L}{2\bar{v}\tau}\int_{-1}^{1} d\zeta' \{2-\beta|\zeta-\zeta'|-\beta|\zeta+\zeta'|\}$$

$$= -\frac{\sigma RL}{2\epsilon_0\bar{v}\tau}[2-\beta(\zeta^2+1)] \quad (-1 \le \zeta \le 1),$$

so that if we represent the on-axis well by $\bar{\phi}_e(z,0) = \frac{1}{2}(K_z)_e z^2 + \text{const}$, the spring constant is given by

$$(K_z)_e = 2\sigma/\epsilon_0\bar{v}\tau.$$

In this approximation the net well depth, defined by (2.7), has dimensionless factor γ given by

$$\gamma \approx L^2/2R\bar{v}\tau.$$

Note that since $\bar{v}\tau \approx 2L$, $(K_z)_e \approx \sigma/\epsilon_0$ and $\gamma \approx \beta/2$ Graphs of the exact potential well (2.5) plotted against ζ for various values of ρ are given in Fig. 2, while equipotentials are plotted in Fig. 3.

B. Ion Density and Ion Potential Hill

If the positive ion gas had some constant *uniform* number density n_i, then the associated potential ϕ_i would be given by the formula (2.1) with the density ρ (2.2) replaced by Zqn_i ($q \equiv$ magnitude of the electron charge). The time average is unnecessary, the space integrations are carried through as before, and one comes out with

$$\phi_i(\zeta,\rho) = \frac{Zqn_iLR}{4\pi\epsilon_0}\rho^{-\frac{1}{2}}\int_0^1 (\rho')^{\frac{1}{2}} d\rho' \int_{-1}^{1} d\zeta' \times Q_{-\frac{1}{2}}\left[\frac{\rho^2+\rho'^2+\beta^2(\zeta-\zeta')^2}{2\rho\rho'}\right]. \quad (2.8)$$

The corresponding on-axis form can be completely integrated and is

$$\phi_i(\zeta,0) = \frac{Zqn_iLR}{4\epsilon_0}\Big[\tfrac{1}{2}(1-\zeta)[1+\beta^2(1-\zeta)^2]^{\frac{1}{2}} + \tfrac{1}{2}(1+\zeta)[1+\beta^2(1+\zeta)^2]^{\frac{1}{2}} + \frac{1}{2\beta}\log\left\{\frac{[1+\beta^2(1-\zeta)^2]^{\frac{1}{2}}+\beta(1-\zeta)}{[1+\beta^2(1+\zeta)^2]^{\frac{1}{2}}-\beta(1+\zeta)}\right\} - \beta(\zeta^2+1)\Big]. \quad (2.9)$$

---

[8] $L=3$ cm, $R=3.5$ cm, E (peak rf voltage) $=59.5$ v cm^{-1}, $2\pi/\tau = 3\times10^8$ sec^{-1}, ϵ (entrance phase of the rf field,[4]) $= -30°$, v_i (mean secondary electron emission velocity) $\approx 10^8$ cm sec^{-1}, $\sigma \approx 4.4\times10^{-11}$ coul cm^{-2}, $\mathcal{P} \approx 10^{-5}$ mm Hg.

hen the total field seen by a positive ion (provided of course that the individual ion phases are incoherent) is ${}_e+\phi_i$. With the "short tube approximation" $O(\beta^2)=0$ he on-axis ion potential hill is purely parabolic, so that ith both this approximation and the "constant sheet elocity approximation" the on-axis sum well $\bar{\phi}_e(\zeta,0)$ $\phi_i(\zeta,0)$ is also purely parabolic with the smaller pring constant

$$K_z\equiv(K_z)_e+(K_z)_i=\frac{2\sigma}{\epsilon_0\bar{v}\tau}-\frac{Zqn_i}{2\epsilon_0}$$

nd associated ion vibration frequency

$$\omega\equiv\left(\frac{ZqK_z}{M}\right)^{\frac{1}{2}}=\left[\frac{Zq}{M}\left(\frac{2\sigma}{\epsilon_0\bar{v}\tau}-\frac{Zqn_i}{2\epsilon_0}\right)\right]^{\frac{1}{2}}. \qquad (2.10)$$

To get an idea of how good the assumption of uniorm ion density really is, one can perform the selfonsistent calculation described in the Introduction. ssume that there is some cylindrical region around the ube's axis in which the positive ions' motions are urely axial and harmonic with some angular frequency ω. Let the ions be created (at rest) at the constant ate αn_a per unit volume and all live some common mean lifetime T. $n_a\equiv\mathcal{P}/kT-n_i$ is the number density of the neutrals. The ionization rate coefficient α is ome known function of position, depending on the charge density and motion of the multipacting electron sheet, which we shall take to be a constant for simplicity. Then the contribution of the ion created at $\mathbf{r}_0$ at time t_0 to the number density[9] $n_i(z)$ at $z>0$ is

$$\Delta n_i(z;\mathbf{r}_0,t_0)=r_0^{-1}\delta[z-z_0\cos\omega(t-t_0)] \times\delta(r-r_0)\delta(\phi-\phi_0)h(t,t_0),$$

where $h(t,t_0)$ is the characteristic function on the time interval (t_0, t_0+T)

$$h(t,t_0)=1,\ t_0<t<t_0+T;\quad h(t,t_0)=0 \text{ otherwise.}$$

Now we add up all the contributions Δn_i for a given point $\mathbf{r}$ and time t, which amounts to multiplying $\Delta n_i(z;\mathbf{r}_0,t_0)$ by $\alpha[\mathcal{P}/kT-n_i(z_0)]d^3x_0dt_0$ and integrating with respect to $\mathbf{r}_0$ over the tube and with respect to t_0 from $-\infty$ to ∞. The factor $h(t,t_0)$ reduces the t_0 integration range to the interval $(t-T, t)$ and equals unity on this range. We consequently get

$$n_i(z)=\alpha\int_{t-T}^{t}dt_0 \times\frac{\{\mathcal{P}/kT-n_i[z/\cos\omega(t-t_0)]\}\theta[\frac{1}{2}L\cos\omega(t-t_0)-z]}{|\cos\omega(t-t_0)|},$$

where $\theta(x)$ is the step function $\theta(x)=0$, $x<0$; $\theta(x)=1$, $x>0$. Make the change of integration variable $x=t-t_0$; then the factor $\theta(\ )$ is nonzero only in the interval $0<x<t^*(z)$ where the time $t^*(z)$ is defined

$$(L/2)\cos\omega t^*=z \quad (0\leqslant t^*\leqslant\pi/2\omega).$$

Hence

$$n_i(z)=\alpha\frac{\mathcal{P}}{kT}\int_0^{t_m}\frac{dx}{\cos\omega x}-\alpha\int_0^{t_m}dx\frac{n_i(z/\cos\omega x)}{\cos\omega x},$$

where $t_m=t_m(z)\equiv\min[t^*(z),T]$. Finally we can make the change of integration variable $y=z/\cos\omega x$, whence the equation becomes

$$n_i(z)=\alpha\frac{\mathcal{P}}{kT}\log\left\{\frac{[1+\cos\omega t_m]^{\frac{1}{2}}+[1-\cos\omega t_m]^{\frac{1}{2}}}{[1+\cos\omega t_m]^{\frac{1}{2}}-[1-\cos\omega t_m]^{\frac{1}{2}}}\right\} -\frac{\alpha}{\omega}\int_z^{z/\cos\omega t_m}dyn_i(y)(y^2-z^2)^{-\frac{1}{2}}, \quad (z>0). \qquad (2.11)$$

This is an inhomogeneous integral equation for the ion number density. Normally the ion's lifetime T will

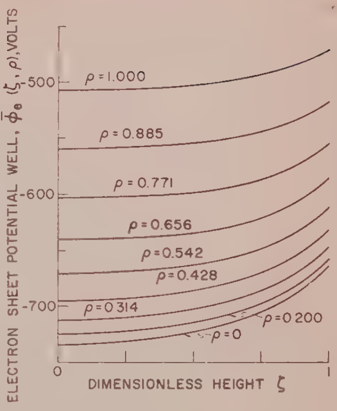

FIG. 2. The electron sheet potential well $\bar{\phi}_e(\zeta,\rho)$ plotted against dimensionless height $\zeta\equiv 2z/L$ for various values of the dimensionless radius $\rho\equiv r/R$. The parameters are those of reference 8.

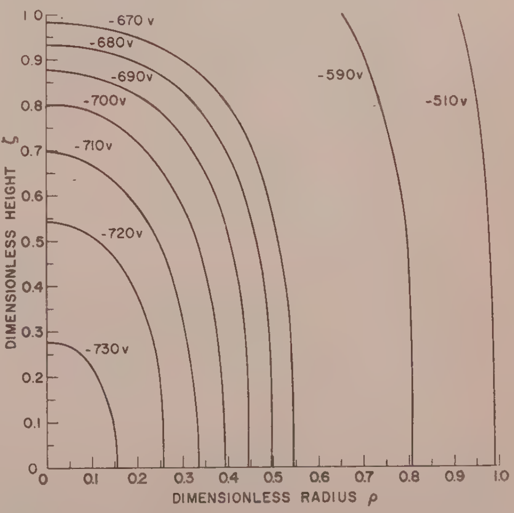

FIG. 3. Equipotential curves in any azimuthal plane ϕ = const. of the electron well $\bar{\phi}_e(\zeta,\rho)$. The parameters are those of reference 8.

---

[9] We assume n_i to be time-independent and an even function of z on-axis which is self-consistent; see Eq. (2.11).

exceed a quarter period of its harmonic motion, hence $t_m(z)$ will be $t^*(z)$, $\cos\omega t_m$ in the logarithm term will be $2z/L\equiv\zeta$, and the upper limit in the integral becomes the constant $L/2$. In the other case, for small enough z, $t_m(z)=T$, hence the logarithm term is truncated at its value with $\cos\omega t_m\rightarrow\cos\omega T$ and the upper limit in the integral becomes $z/\cos\omega T$, proportional to z. The defining Eq. (2.11) is to be supplemented by the requirement that $n_i(z)$ be even.

From Eq. (2.11) we infer qualitatively that $n_i(z)$ is a decreasing function of z, i.e., that the ion density is peaked in the center of the tube. The constant ω plays the role of an eigenvalue in (2.11) for which the corresponding eigensolution is $n_i(z;\omega)$, say. Then self-consistency requires that when we calculate the ion potential hill ϕ_i with this nonuniform density, it can be sufficiently well approximated by Eq. (2.9) with some *uniform* density, call it $\bar{n}_i(\omega)$. If this is so, then ω is determined from the implicit equation (2.10) with $n_i\rightarrow\bar{n}_i(\omega)$.

C. Effective Static Electron Density, Experimental Checks, Etc.

It is interesting to note what is the effective static negative charge distribution seen by the ions. Time-averaging $\rho(z,t)$, Eq. (2.2), over an rf period τ, we get

$$\bar{\rho}(z)=-\frac{\sigma}{\tau}\left[\frac{1}{v_1(z)}+\frac{1}{v_2(z)}\right].$$

But this is just the static charge density which appears in the time-averaged electron sheet potential, Eq. (2.4), which is exact, i.e., includes retardation effects. This is because the contribution to the field $\bar{\phi}_e(P)$ at a point P coming from the volume element d^3x' around any other point P' is proportional to $(1/\tau)[1/v_1(z')+1/v_2(z')]$ regardless of whether the transit time of this signal is considered to be zero or the finite time $R(P,P')/c$.

To a good approximation the electron sheet velocity is linear in the height,

$$v_1(\zeta)\approx v_i+\tfrac{1}{2}(v_f-v_i)(1+\zeta),\quad v_2(\zeta)\approx v_i+\tfrac{1}{2}(v_f-v_i)(1-\zeta),$$

where v_i and v_f are the initial and arrival velocities of the sheet. Hence in this approximation

$$\bar{\rho}(\zeta)=-\frac{\sigma}{\tau}\frac{2\langle\bar{v}\rangle}{\langle\bar{v}\rangle^2-\frac{1}{4}(\Delta v)^2\zeta^2},$$

with $\langle\bar{v}\rangle\equiv\frac{1}{2}(v_f+v_i)$, $\Delta v\equiv v_f-v_i$. Thus the effective negative charge distribution is peaked at the electrodes, the peaking increasing for increasing v_f/v_i.

To check the theory of the sum well in the extreme low-pressure range developed here one can send an ion beam across the tube and measure its deflection. The (small) angular deflection in the vertical plane is predicted to be proportional to the height of the ion gun. The details are as follows. First, to derive a somewhat more general theory, let $\omega_z(r)$ and $\omega_r(z)$ be the harmonic frequencies of the ion vibrations in the z direction (at radius$=r$) and r direction (at height$=z$). They are determined from the spring constants K_z and K_r of the sum well according to (2.10), where the spring constants are those of best fit parabolas, determined graphically or otherwise. As the notation indicates, they are (at most weakly varying) functions of r and z, respectively. The transit time of an ion fired horizontally through the axis of the tube at height z_0 with velocity V will then be given by solving

$$t_{\text{tr}}=(R/V)\{1+\cos[(\omega_r)_0t_{\text{tr}}]\},\qquad(2.12)$$

where $(\omega_r)_0\equiv\omega_r(z_0)$. During transit, assuming the deflection small, its z motion will be determined by

$$dz\approx-z_0\omega_z(t)\sin[\omega_z(t)t]dt$$
$$\omega_z(t)\equiv\omega_z[r(t)],\quad r(t)=-Vt+R\cos[(\omega_r)_0t].$$

(Negative values of $r(t)$ are to be interpreted in the obvious way.) Hence the z deflection will be

$$\Delta z\approx-z_0\int_0^{t_{\text{tr}}}\omega_z(t)\sin[\omega_z(t)t]dt.\qquad(2.13)$$

Formula (2.13) *cum* (2.12) determines the desired deflection.

If we further assume a doubly parabolic well (ω_z, ω_r constants) and periods of vibration long compared to the time R/V:

$$(\omega_rR/V)^2\ll1,\quad(\omega_zR/V)^2\ll1,$$

these simplify to

$$t_{\text{tr}}\approx2R/V,\quad\Delta z\approx-2z_0(\omega_zR/V)^2.\qquad(2.14)$$

If the deflection of the beam is not measured directly at the tube wall, it may be more convenient to have an expression for the angular deflection. This is, to the same approximation,

$$\Delta\theta\equiv(v_z/v_r)_{t=t_{\text{tr}}}\approx-2z_0(\omega_z^2R/V^2).\qquad(2.15)$$

JOURNAL OF APPLIED PHYSICS VOLUME 32, NUMBER 12 DECEMBER, 1961

A Comparison of Theory and Experiment for a Thermoelectric Cooler

M. H. Norwood
Central Research Laboratories, Texas Instruments Incorporated, Dallas, Texas

(Received May 22, 1961)

The performance of single-stage Peltier thermocouples was calculated using the experimentally measured values of thermoelectric power, electrical resistivity, and thermal conductivity as functions of temperature. These calculations were made by solving numerically the differential equation for the temperature distributions in the thermoelements. The boundary conditions were the hot junction temperature and the heat flow at the cold junction. The calculated behavior of the thermocouples agreed well with the measured performance in the three cases studied. The measured thermocouple figure of merit agreed with that calculated from the material properties.

The effect of temperature variations of the material properties on thermocouple performance was studied by comparing exact calculations with calculations involving one temperature-averaged constant material property. This type of calculation showed that the Thomson effect caused about 4°K of the maximum ΔT of 66°K for one couple studied. The temperature variation of resistivity was found to be the major cause of disagreement between exact calculations and the simpler theory (Ioffe equations).

INTRODUCTION

IN the past few years interest in thermoelectric power generation and thermoelectric refrigeration has grown. Perhaps the best known treatise describing the behavior of semiconducting thermocouples was written by A. F. Ioffe.[1] Ioffe derives equations which describe operation of the thermocouples, assuming that the material properties do not change with temperature. These equations proved useful in designing thermoelectric devices because of their simplicity and ease of use.

Recently, several workers investigated the dependence of device performance on temperature variation of: (1) the thermoelectric power, (2) the electrical resistivity, and (3) the thermal conductivity. These investigations were made possible by the derivation[2] of a differential equation governing the steady state temperature distribution in a thermoelectric material with a dc current flowing through it. Sherman, Heikes, and Ure[3] have studied generators and coolers using numerical solutions of this equation, and they showed greater differences between the simple and exact theories for Peltier coolers. Brandt[4] studied generator performance, considering radiation heat loss, electrical contact resistance, and variable cross-sectional area of the thermocouple legs; however, he assumed identical material properties for the n- and p-type elements. Lyon and Bustard[5] also studied generators considering electrical contact resistance, variable area, and different material properties for each leg. Moore[6] and Swanson, Somers, and Heikes[7] made extensive computations on segmented-leg thermoelectric generators.

From the papers listed, it is apparent that more work has been done for generators than for coolers, and little has been reported comparing the exact theory and experimental measurements. This paper reports such a comparison for the simple and exact calculations. After a description of the method of calculation, the experimental and theoretical performance of three couples are presented. The theoretical performance is calculated using experimental values of the material properties. The effects of the temperature dependence of thermoelectric power and resistivity are then shown by comparing a calculation using temperature dependent properties with a calculation using a constant value of thermoelectric power and one using a constant resistivity. Finally, the figures of merit obtained from thermocouple properties and material properties are compared.

DESCRIPTION OF CALCULATION

The differential equation for the temperature distribution in a thermoelectric material was derived by Domenicali.[2] Applied to a one-dimensional case such as a thermoelectric cooler leg, it can be written

$$\frac{d}{dx}\left(\kappa\frac{dT}{dx}\right)-J\tau\frac{dT}{dx}+J^2\rho=0, \qquad (1)$$

where κ is the thermal conductivity, τ the Thomson coefficient, and ρ the electrical resistivity. By using the Kelvin relation between the Thomson coefficient and the thermoelectric power α, the equation may be expressed entirely in terms of easily measured quantities

$$\kappa\frac{d^2T}{dx^2}+\frac{d\kappa}{dT}\left(\frac{dT}{dx}\right)^2-J\frac{d\alpha}{dT}T\frac{dT}{dx}+J^2\rho=0. \qquad (2)$$

---

[1] A. F. Ioffe, *Semiconductor Thermoelements and Thermoelectric Cooling* (Infosearch, Ltd., London, England, 1957).

[2] C. A. Domenicali, J. Appl. Phys. **25**, 1310 (1954).

[3] B. Sherman, R. R. Heikes, and R. W. Ure, Jr., J. Appl. Phys. **31**, 1 (1960).

[4] J. A. Brandt, Paper given at Symposium on Thermoelectric Energy Conversion, Dallas, Texas, January 9–12, 1961 [to be published in *Advanced Energy Conversion* (Pergamon Press, New York)].

[5] W. C. Lyon and T. C. Bustard, paper given at Symposium on Thermoelectric Energy Conversion, Dallas, Texas, January 9–12, 1961 [to be published in *Advanced Energy Conversion* (Pergamon Press, New York)].

[6] R. G. Moore, paper given at Symposium on Thermoelectric Energy Conversion, Dallas, Texas, January 9–12, 1961 [to be published in *Advanced Energy Conversion* (Pergamon Press, New York)].

[7] B. W. Swanson, E. V. Somers, and R. R. Heikes, Trans. Am. Soc. Mech. Engrs., Series C **83**, 77 (1961).

This equation is nonlinear and has not been solved in closed form. Several authors[8–10] have obtained solutions to this equation, or to variations of this equation, when κ is considered constant, thus omitting the second term.

To apply this differential equation to a thermocouple made of n-type and p-type semiconductors, a solution must be obtained for each leg separately. These solutions are not independent, however, since they must satisfy certain boundary conditions. The computer code used in this work was designed to solve the equation with any of three sets of boundary conditions:

(a) Hot junction temperature (T_H) and cold junction heat load (Q),
(b) Cold junction temperature (T_C) and cold junction heat load (Q),
(c) Hot junction temperature (T_H) and cold junction temperature (T_C).

The equation for the heat load at the cold junction is written

$$Q=[\alpha_p(T_C)-\alpha_n(T_C)]IT_C+\kappa_p(T_C)A_pT_p'(L)+\kappa_n(T_C)A_nT_n'(L)\cdots, \qquad (3)$$

where the junction at temperature T_H is arbitrarily taken to be $x=0$, and the junction at temperature T_C is at $x=L$. If the current, material properties, heat load Q, and areas of the legs are known, then a relationship is established between the slopes of the temperature distributions at $x=L$ [Eq. (3)]. To solve the problem using set (a) of the boundary conditions, the IBM 704 computer starts the numerical integration procedure from an estimated value of T_C supplied in the input data. It calculates solutions to the differential equation for each leg by the Adams method of integration. These solutions will usually end at different temperatures at $x=0$; therefore, a new guess is made on one of the slopes at $x=L$, and the other slope is determined by Eq. (3). The machine iterates until the solutions for both legs have the same temperature at $x=0$. This temperature is not the value specified for the hot junction (T_H), however, so a new guess is made for the cold junction temperature (T_C). The process is repeated until the solutions have the value T_H at $x=0$ and slopes $T_p'(L)$ and $T_n'(L)$ which satisfy Eq. (3). This process requires an iteration within an iteration, and usually between 2 and 3 min per problem on the computer. Problems with boundary conditions (b) and (c) require only one iteration and involve much less time.

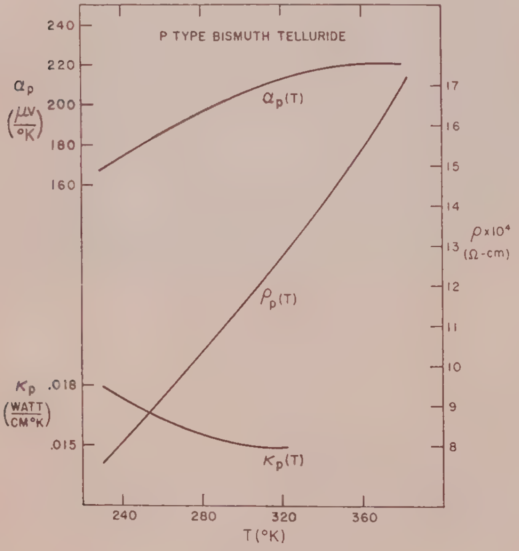

FIG. 1. Material properties of p-type bismuth telluride alloy as a function of temperature.

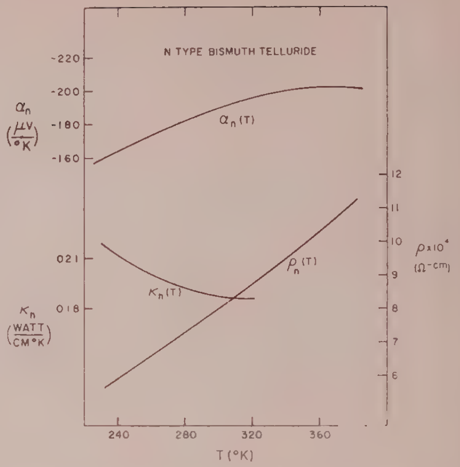

FIG. 2. Material properties of n-type bismuth telluride alloy as a function of temperature.

COMPARISON WITH EXPERIMENT

The thermoelectric properties of two different n-type and two different p-type alloys of bismuth telluride were measured in this laboratory. One set of material properties is shown in Figs. 1 and 2. Figs. 3 and 4 show two comparisons between the calculated and measured values of the temperature difference across each couple, ΔT, as a function of the currents through the couples. The quantity ΔT was measured in a vacuum with essentially zero heat load. The couple represented in Fig. 4 was made from the material whose properties are shown in Figs. 1 and 2. Since six experimentally measured quantities were used in calculating a seventh measured quantity, ΔT, the agreement of points and curves in Figs. 3 and 4 is quite good. Figure 5 shows the performance of another couple made from the same ingot

---

[8] J. E. Parrott, Solid State Electronics **1**, 135 (1960).

[9] A. D. Reich and J. R. Madigan, Bull. Am. Phys. Soc. **5**, 280 (1960).

[10] E. B. Penrod and Cho Yen Ho, J. phys. radium **21**, 97A (1960).

f material as couple II. This couple (III) was subected to a heat load of various values, and the correponding ΔT was measured. The agreement with the alculations from the exact theory is within experinental error. Figures 3–5 show that the experimental ehavior of thermocouples can be calculated with a fair legree of accuracy if careful measurements are availble for the thermoelectric power, resistivity, and thernal conductivity as functions of temperature. Such alculations should be of value for designing coolers of ny variety.

EFFECT OF TEMPERATURE DEPENDENCE OF THERMOELECTRIC POWER AND RESISTIVITY

It is interesting to see the results of the Thomson effect and the temperature variation of resistivity in a Peltier cooler. Figure 6 shows the result of the exact calculation (curve C) compared with calculations using various constant values of the parameters. Also shown is a result from the simple theory (curve D), where all parameters have been averaged.

In each case the constant values were obtained by averaging the material properties over the temperature range between the hot and cold junction temperatures at maximum ΔT ($T_H=300°\text{K}$; $T_C=233°\text{K}$). Curve B shows the result of an exact type calculation where the thermoelectric power was held constant. Curve A shows the result of a calculation where the slope of the thermoelectric power vs temperature was reversed (Thomson heating) while the average value remained the same. Curve E was obtained when the resistivity was held constant.

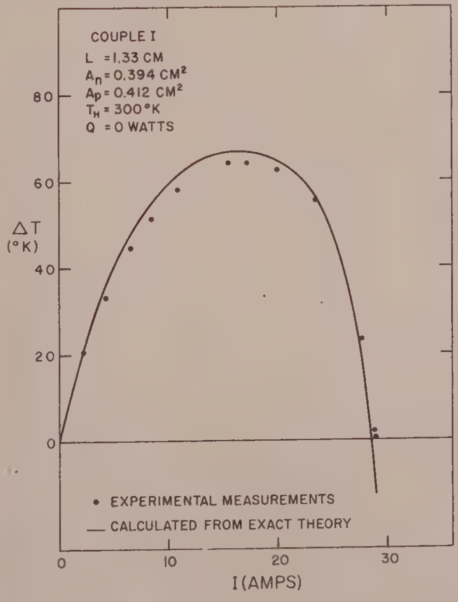

FIG. 3. Comparison of theoretical and experimental performance of couple I in a vacuum with no external heat load.

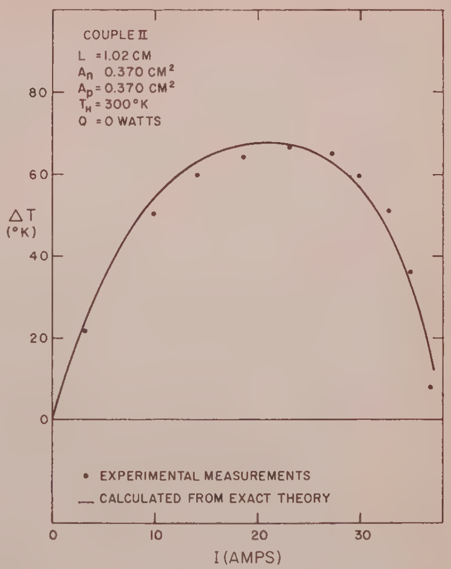

FIG. 4. Comparison of theoretical and experimental performance of couple II in a vacuum with no external heat load.

The poor agreement between simple and exact theories at high currents results from the fact that the average values of the parameters over the temperature range between T_H and T_C are not the same as the average values over the length of the couple. This is true because at high currents the temperature distribution over the couple goes through a maximum which is higher than T_H. The resistance, in particular, is higher when integrated over the length of the couple using the temperature distributions of the exact theory. The resistivity increases rapidly with temperature. Thus, since the centers of the legs are at a higher temperature than T_H or T_C, the simple theory fails if the average resistivity between temperatures T_H and T_C is used. In one case the integrated resistance along the couple was 60% higher than the value obtained from the average resistivity between 233° and 300°K. The curve shown in Fig. 6 using a constant value of ρ falls very slowly with increasing current (curve E). This shows that the sharp decrease in ΔT at high currents can be attributed mainly to the rapid increase of resistivity with temperature.

The difference between curves B and C shows that the Thomson effect causes about 4°K of the maximum ΔT. If a new function of temperature is used for $\alpha(T)$ where the average value between 233° and 300°K is the same but the sign of the slope is changed (Thomson heating), the maximum ΔT drops approximately another 4°K. The optimum current also decreases when the Thomson effect is reduced. Goldschmid,[11] among others, has shown that the simple theory takes into account the Thomson effect to some extent if the average value of α between T_C and T_H is used to compute the Peltier effect at the cold junction, rather than the value of α at temperature T_C. Using an alternate procedure, the equation for the heat load in the simple theory may be written

---

[11] H. J. Goldschmid, *Applications of Thermoelectricity* (Methuen & Company, Ltd., London, England, 1960).

$$Q=\alpha_C I T_C+\tfrac{1}{2}I\tau\Delta T-K\Delta T-\tfrac{1}{2}I^2R, \qquad (4)$$

where $\alpha_C=\alpha_p(T_C)-\alpha_n(T_C)$ and τ is an average Thomson coefficient. This equation assumes that half the Thomson cooling flows to each end. If Q is zero and ΔT is maximized with respect to I, it can be shown to a reasonable approximation that

$$I_0=\frac{\alpha_C T_C}{R}+\frac{\tau Z' T_C^2}{4R} \qquad \Delta T_{\max}=\frac{Z'T_C^2}{2[1-(\tau Z'T_C/2\alpha_C)]}, \qquad (5)$$

$$Z'=\alpha_C^2/RK.$$

The approximation $(1-x)^{\frac{1}{2}}=1-x/2-x^2/8$ has been used where $x=Z'T_C$. Equation (5) shows that the optimum current and the maximum ΔT increase as the Thomson coefficient increases in the positive direction. These results are clearly seen in the exact calculations shown in Fig. 6 where τ is positive, zero, and negative (curves C, B, and A, respectively).

RELATION BETWEEN MATERIAL AND THERMOCOUPLE FIGURE OF MERIT

Table I shows the figures of merit obtained for couples I and II. The first values are the average values of Z of the materials between 300° and 233°K. The properties of the two legs are so nearly the same that a single Z value can be considered. The second row gives the Z values based on the experimental $\Delta T_{\max}$ measurement. These values of the figure of merit agree within experimental error. Thus, $\Delta T_{\max}$ is a good measure of the material properties of thermoelements having similar properties. This measure of Z is a preferred criterion of the quality of any material, rather than the Z obtained from material properties. There is much more room for error in the latter determination of Z. Also there seems to be no reason to expect Z values from material properties to differ significantly from the Z of the thermocouple.

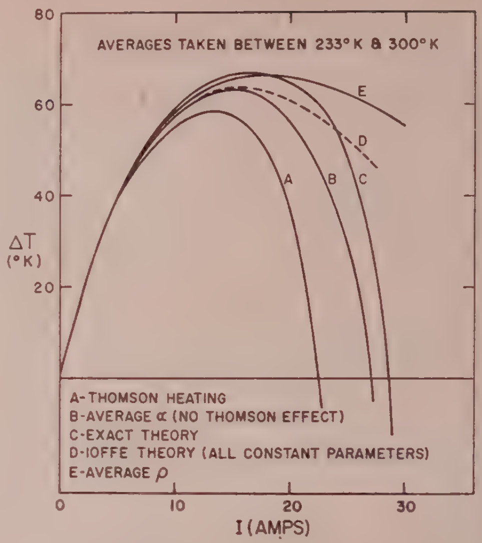

FIG. 6. Calculated values of ΔT as a function of current using all parameters variable with temperature (C), none variable with temperature (D), constant thermoelectric power (B), constant resistivity (E), and reversed Thomson coefficient (A).

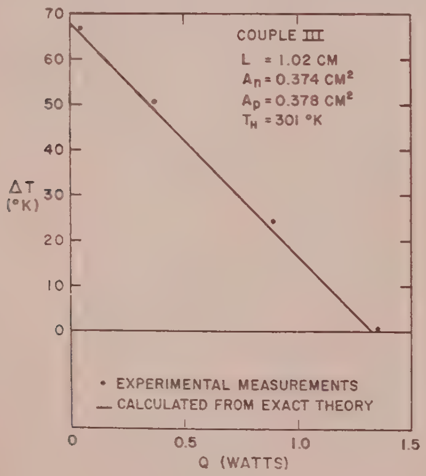

FIG. 5. Experimental and theoretical heat pumping performance for couple III.

TABLE I. Values of Z in $(°\mathrm{K})^{-1}$ from couples and materials.

	Couple I	Couple II
Temperature average material Z (233° to 300°K)	2.32×10^{-3}	2.35×10^{-3}
Z from experimental $\Delta T_{\max}$	2.33×10^{-3}	2.43×10^{-3}

CONCLUSIONS

It was shown that the performance of a single Peltier thermocouple can be calculated for any operating condition using exact theory if the properties of the semiconducting materials are known as a function of temperature. This type of calculation should prove useful in designing Peltier coolers.

The averaged material figure of merit between the hot and cold junction temperatures agrees with the figure of merit obtained from a $\Delta T_{\max}$ measurement. There is no reason to expect the Z determined from material properties to differ from that deduced from thermocouple performance measurements.

Calculations showed that the Thomson effect accounts for about 4°K cooling in the couples studied.

lso it was shown by calculation that temperature ariation of the resistivity is the main cause for disgreement between the Ioffe theory and the exact heory.

ACKNOWLEDGMENTS

The author wishes to thank Paul Carnahan for writing the computer code used in this problem and John Stamper for material property measurements.

OURNAL OF APPLIED PHYSICS VOLUME 32, NUMBER 12 DECEMBER, 1961

Hardening of Lithium Fluoride Crystals by Irradiation

J. S. Nadeau and W. G. Johnston
General Electric Research Laboratory, Schenectady, New York

(Received June 19, 1961)

The very soft, pure crystals of LiF that are now commercially available are unsuitable for some experimental work because they suffer accidental plastic deformation during cleavage and tend to split on (110) planes. Irradiation with gamma rays produces harder crystals that can be cleaved and handled without much damage. The radiation-induced hardening and the color centers produced by moderate irradiation can be completely removed by annealing for several hours at 450°C. This method for handling very soft crystals may be useful for other types of crystals, and various types of irradiation can be employed.

I. INTRODUCTION

THE usefulness of a particular material for studying dislocation behavior and plastic deformation lepends to a large extent upon the availability of single rystals that can be shaped to produce test specimens vith a low dislocation content. For example, in recent vears it has been possible to study dislocations in lithium fluoride in some detail,[1–9] because large, hard, single crystals with relatively few dislocations in them could be obtained commercially from the Harshaw Chemical Company. The crystals were sufficiently hard that they could be easily cleaved into small test specimens without increasing the dislocation content.

In the past two or three years, however, the hardness of LiF crystals available from the Harshaw Chemical Company has gradually decreased to the extent that those presently available cannot be cleaved without being severely damaged. Some of the softer large crystals already contain accidentally introduced glide bands as received. It has been found that the hardness of the earlier LiF was due to the presence of small amounts of divalent impurities.[10] The striking difference between the early crystals and the pure, soft ones now produced is shown by the deformation curves of Fig. 1. The soft crystal did not contain any impurities that were spectroscopically detectable, while the hard crystal contained about eighty parts per million of magnesium.

When the soft crystals are cleaved, they deform plastically, and many dislocations are introduced. Often the cleaved crystals are visibly bent. A further disadvantage of the soft crystals is that fracture very often tends to occur along (110) planes in addition to the normal (100) cleavage planes, making it difficult to obtain specimens free of cracks.

We have investigated radiation hardening as a means

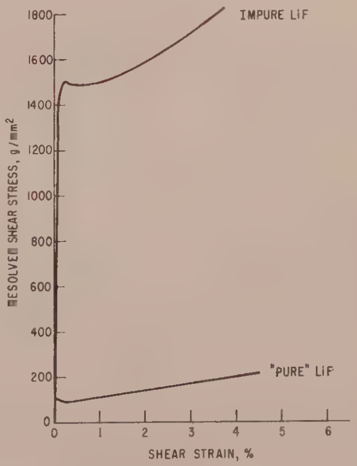

Fig. 1. Stress strain curves obtained in compression for pure and impure LiF single crystals. The strain rate was $\sim 10^{-4}$ sec^{-1}.

---

[1] J. J. Gilman and W. G. Johnston, *Dislocations and Mechanical Properties of Crystals* (John Wiley and Sons, Inc., New York, 1957), p. 116.

[2] J. J. Gilman, Trans. Am. Inst. Mining, Met., Petrol. Engrs. **209**, 449 (1957).

[3] J. J. Gilman, C. Knudsen, and W. Walsh, J. Appl. Phys. **29**, 601 (1958).

[4] J. J. Gilman, Trans. Am. Inst. Mining, Met., Petrol. Engrs. **212**, 310 (1958).

[5] W. G. Johnston and J. J. Gilman, J. Appl. Phys. **30**, 129 (1959).

[6] J. J. Gilman, J. Appl. Phys. **30**, 1584 (1959).

[7] W. G. Johnston and J. J. Gilman, J. Appl. Phys. **31**, 632 (1960).

[8] J. J. Gilman and W. G. Johnston, J. Appl. Phys. **31**, 687 (1960).

[9] A review of the work in references 1–8, written by J. J. Gilman and W. G. Johnston, will appear in Vol. 13 of *Solid State Physics*, edited by F. Seitz and D. Turnbull.

[10] W. G. Johnston, "Effect of impurities on the flow stress of LiF crystals" (to be published).

of obtaining crystals that can be cleaved without damage. When the radiation effects are annealed out, a soft, highly pure crystal with low dislocation content is obtained. The technique developed here can be useful in hardening crystals preparatory to almost any mechanical operation such as cleaving, cutting, or grinding in order to minimize accidental damage.

II. RADIATION HARDENING

Lithium fluoride crystals were hardened by irradiating them at room temperature with gamma rays from a 10 000-curie cobalt-60 source. The flux was 4×10^5 r/hr. The critical resolved shear stress as a function of irradiation time is shown in Fig. 2.

An irradiation of four hours duration produced sufficient hardening so that large crystals could be cleaved into small specimens without producing deformation during the cleavage. In Fig. 3 are compared the etched cleavage faces of a soft, pure crystal and a radiation hardened crystal that had been irradiated for four hours. The radiation hardened crystals show very little tendency to fracture on (110) planes, compared to the soft crystals, and the cleaved specimens are free of cracked corners.

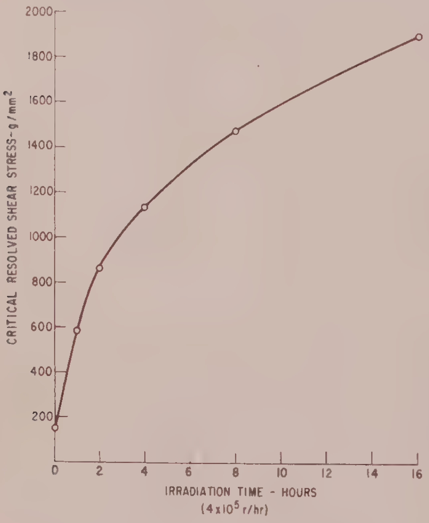

Fig. 2. Hardening effect of gamma radiation. The critical resolved shear stress was measured in compression at a strain rate of $\sim10^{-4}$ sec^{-1}. The flux of gamma rays from the cobalt 60 source was $\sim4\times10^5$ r/hr.

It is also possible to determine whether glide bands were present in the soft crystals as received, without actually handling them in the soft condition. The fact that the density of dislocations in a glide band depends upon the flow stress[5] can be employed to determine at what stage in the processing a particular glide band was formed. Glide bands formed in the soft crystal are sparsely populated with dislocations and those formed in the radiation hardened crystal are densely populated. Figure 4 shows both types of glide bands in a crystal; the two sparse bands were present prior to irradiation, and the two dense bands were deliberately introduced by deforming the hardened crystal.

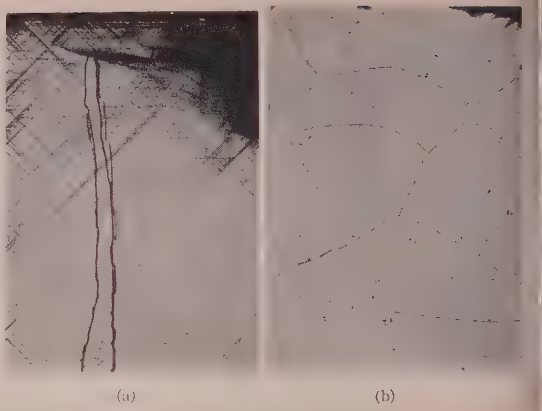
(a) (b)

Fig. 3. Cleavage face of an unirradiated crystal (a) and an irradiated crystal (b) etched to reveal the dislocation structure. Large glide bands are visible in the soft crystal, and the corner is badly split where it was penetrated by the chisel.

The formation of color centers in LiF by gamma radiation has been studied and the most prominent optical absorption bands have been identified. A very strong band in the ultraviolet (242 mμ) is attributed to F centers and a smaller band at 445 mμ is probably due to M centers.[11] The latter band results in a pale yellowish coloration in lightly irradiated crystals which can be deepened through amber to black with very extended irradiations. It appears that the 445-mμ band forms by clustering of other centers both during and after irradiation at room temperature because the

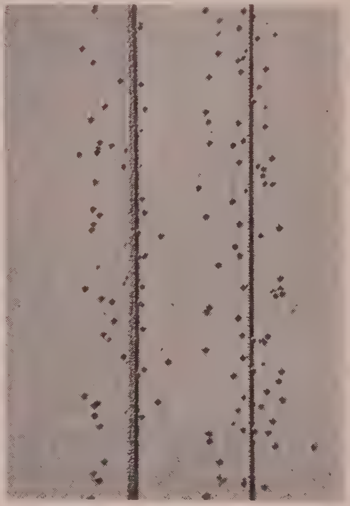

Fig. 4. Two sparse glide bands and two dense glide bands formed while the crystal was in the soft condition and the radiation hardened condition, respectively.

---

[11] C. J. Delbecq and P. Pringsheim, J. Chem. Phys. **21**, 794 (1953).

coloration can be seen to change from green-yellow to yellow during storage.

III. ANNEALING OF RADIATION DAMAGE

Radiation hardening as a step in the processing of test specimens can be useful only if the effects of irradiation can be subsequently removed. Therefore, the annealing of mechanical and optical changes due to irradiation were investigated.

The pulse annealing of hardening produced by four hours irradiation at room temperature is shown in Fig. 5. A large number of irradiated specimens were heated for a half hour at the lowest annealing temperature and air cooled to room temperature. Three specimens were removed and tested in compression, while the remainder were heated to the next higher annealing temperature for a half hour, cooled to room temperature, etc. Each data point therefore indicates the cumulative effect of annealing up to that temperature. Resoftening is complete at about 450°C. A longer (~2 hr) isothermal anneal at 450°C will produce the same recovery as the treatment described above.

Optical absorption measurements were made on crystals subjected to the same annealing treatment as in Fig. 5. The annealing of the 242-mμ and 445-mμ bands is shown in Fig. 6. After annealing to 450°C the absorption spectrum of an irradiated crystal is indistinguishable from that of an unirradiated crystal. It, therefore, appears that the mechanical and optical effects of the moderate radiation damage can be completely annealed out at 450°C.

Radiation damage can also be produced with neutrons,[12] x rays,[13] and high energy electrons.[14] The penetration of soft x rays and electrons is insufficient to harden large crystals uniformly, but higher energy x rays ($\geq$70 kv) and neutrons are suitable.

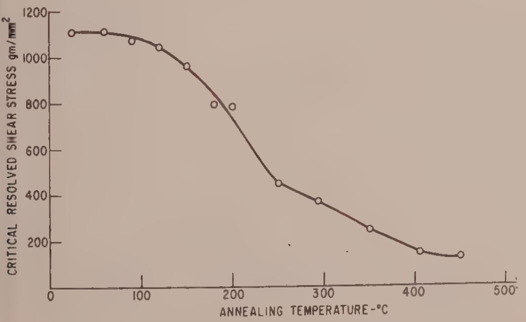

FIG. 5. Pulse annealing of critical resolved shear stress after a four hour irradiation. Specimens were annealed for half-hour periods at successively higher temperatures and then tested in compression at room temperature.

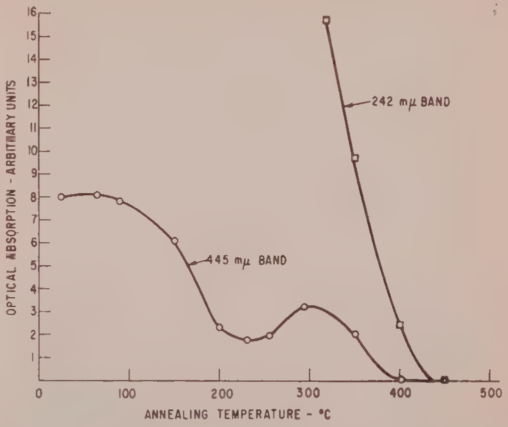

FIG. 6. Pulse annealing of the two most prominent absorption bands produced during four hours of irradiation. Specimens were annealed for half-hour periods at successively higher temperatures, and absorption measurements were made at room temperature.

In the present experiments we have shown that the effects of 1.6×10^6 r of cobalt-60 gamma radiation can apparently be completely annealed out. We have not determined whether the effects of much longer irradiations can also be removed, but there is some evidence that it cannot be removed. Severe neutron irradiation ($\geq10^{16}$ nvt), followed by annealing, results in the formation of numerous cavities.[11] It is reasonable to assume that very severe exposure to any of the other types of radiation would also result in irreversible damage.

The application of this method to other crystals depends to some extent upon the stability of radiation damage in them. If substantial diffusion occurs at the temperature of irradiation, it is possible that little hardening would result from moderate dosages. The prolonged irradiation necessary to produce a desired hardness might then cause damage that would not readily anneal out.

IV. SUMMARY

It is possible to harden the presently available, soft lithium fluoride crystals by exposing them to cobalt-60 gamma irradiation. An exposure of 1.6×10^6 r at room temperature increases the critical resolved shear stress to about 1000 g/mm^2 so that crystals can be handled without accidentally damaging them and introducing new dislocations. Annealing for about two hours at 450°C removes all optical and mechanical effects of the irradiation and apparently returns the crystals to their original condition.

---

[12] J. J. Gilman and W. G. Johnston, J. Appl. Phys. **29**, 877 (1958).

[13] W. H. Vaughan and J. W. Davisson, Acta Met. **6**, 554 (1958).

[14] A. D. Whapham, Phil. Mag. **3**, 103 (1958).

JOURNAL OF APPLIED PHYSICS VOLUME 32, NUMBER 12 DECEMBER, 1961

Motion of *c* Domain Centers in $BaTiO_3$

G. L. LINK
Bell Telephone Laboratories, Inc., Murray Hill, New Jersey
(Received March 24, 1961; in final form August 4, 1961)

A novel effect has been observed in $BaTiO_3$. By applying a biased alternating field to a $BaTiO_3$ crystal which contains an *a* domain, one can observe a large number of small dots which move in straight lines. The dots are shown to be small *c* domains, and their motion can be accounted for by the electric field perturbation caused by the *a* domain.

INTRODUCTION

In the course of studying ferroelectric $BaTiO_3$ by electrical and optical techniques, a novel effect was discovered. This paper describes the effect and proposes an explanation for it. Succinctly, this effect is the appearance of a large number of small "dots" which appear when a biased, alternating potential is applied to a $BaTiO_3$ crystal which contains *a* domains. The dots move in parallel straight-line paths, the position and direction of their motion being determined by an underlying *a* domain, and the magnitude of the dots' velocity being determined by the magnitude and frequency of the applied potential. The dots are shown to be small *c* domains, and their motion can be attributed to a perturbation of the electric field near the *a* domain.

EXPERIMENTAL

To observe the motion of *c* domain centers ("dots") a suitable[1] $BaTiO_3$ crystal containing *a* domains[2] is selected and etched with H_3PO_4 to clean the surface. The crystal is then mounted in a liquid electrode device so that a selected region can be observed with a polarizing microscope. Observation is made with the polaroids crossed and with the polarizing direction parallel to the *a* domains, as this makes the dots most clearly visible. Magnification is typically in the range of 50–100×.

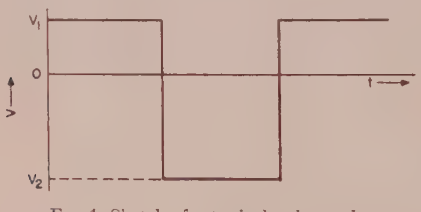

FIG. 1. Sketch of a typical pulse cycle.

A voltage is applied in the form of a biased squarewave, with frequency varying from 20–10^6 cps. A typical waveform is illustrated in Fig. 1. For ease in discussion, each half-cycle will be referred to as a "pulse." Typical applied fields are +400 and −600 v/cm on alternate pulses. A schematic representation of the motion of a typical dot is given in Fig. 2.

RESULTS

Microscopic observation of the crystal, while being pulsed, shows the appearance of a large number of small dots. These dots move within bands, and their motion is along straight paths which are perpendicular to the band edges. Figure 3 is a photograph of a typical microscope image.

Nature of Dots

The nature of the dots was ascertained by an experiment in which dots were formed, as above, and then all fields were removed. A small dc field was then applied, and it was observed that each dot acted as the origin of a *c* domain which visibly grew under the influence of the field in a manner like that described by Miller and Savage.[4] It was thus concluded that each dot is a small *c* domain of polarization direction opposite to that of its immediate environment. Stroboscopic observation of the dots as they move showed that the dots expand and contract in phase with the field, suggesting that the same process as above occurs during their horizontal motion.

A plot of switching current vs time over a complete cycle of the applied field is shown in Fig. 4. It shows that the crystal continues to switch up to the very end of the application of the low-field pulse, i.e., the crystal as a whole is only partially switched. On the high-field pulse, however, the crystal stops switching before the

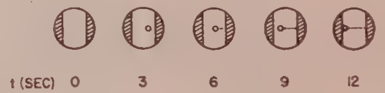

FIG. 2. A schematic representation of the motion of a dot, moving from right to left, as it might appear in a microscope image. Actually, there are a multitude of such dots moving simultaneously, both in the same track (dotted line) and in parallel tracks. (The field frequency could be, e.g., 10^2 cps).

---

[1] Suitable crystals are those which facilitate observations in two ways: First, thick crystals (ca $3–5\times10^{-2}$ cm) are chosen for long "track" lengths; second, Fe doping (ca 0.2%) seems to make the dots more easily visible.

[2] $BaTiO_3$ in its ferroelectric state has a tetragonal crystal structure with the polarization direction along the tetragonal (*c*) axis. The butterfly-wing habit crystals grown by the Remeika method[3] have the ferroelectric axis perpendicular to the large flat surfaces of the crystal. Such a crystal is termed a "*c* domain." There are, however, regions of the crystal in which the polarization direction is parallel to the crystal surface. These regions are called "*a* domains" and, under a polarizing microscope, appear as colored slabs at 45° to the crystal surface.

[3] J. P. Remeika, J. Am. Chem. Soc. **76**, 940 (1954).

[4] R. C. Miller and A. Savage, Phys. Rev. Letters **2**, 294 (1959).

pulse is complete. A graphical integration of the switching current shows that the charges switched on each pulse are equal, and hence the high-field pulse brings the crystal back to some constant state; the low field takes it away from that state to an extent that depends only on the magnitude of the low field and the time during which it is applied. Henceforth, the low-field pulse will be referred to as the "growth" pulse and the high-field pulse as the "collapse" pulse.

Motion of Dots

The velocity of the dots is observed to depend on the field. The dependence is through the growth pulse. This was demonstrated by varying the magnitude of the collapse pulse, keeping the magnitude of the growth pulse constant and observing that the velocity is constant. Changing the growth field pulse changes the velocity, even if the collapse field is kept constant. The dot velocity u depends on the growth field E_1 as

$$u=Ae^{-B/E_1}.$$

A plot of $\log u$ vs $1/E_1$ data is given in Fig. 5. E is calculated as simply the applied voltage divided by the crystal thickness.

Although no quantitative investigation was made, it was also observed that the velocity increases with pulse frequency at constant field.

The most striking aspect of the motion is its geometric relation to the crystal. The motion is only observed along tracks lying within bands. These bands correspond to the projection of a domains onto the crystal surface (Fig. 6). Further, the direction is uniquely determined by the direction of polarization of the a domain, the dots moving in the direction opposite to the conventional polarization direction of the underlying a domain. At the top of Fig. 6 is a schematic diagram of a typical image observed in the microscope. The two vertical bands are the images of two a domains in the crystal, and the horizontal lines within these bands indicate the positions of tracks along which motion occurs. The direction of flow within each band is indicated by arrows on the tracks. At the bottom of Fig. 6, a cross section of the crystal is portrayed. The two pairs of slanted lines represent the ends of the two a domains, which happen to be slanted in opposite directions. The vectors P_s indicate the polarization directions of the various domains which would result if the crystal were completely switched in the direction of the collapse-field pulse. When the polarity of the pulses is reversed, the polarization directions also reverse and so does the direction of dot motion.

In summary, then, the experimental results have shown that the dots are small c domains which are being expanded and contracted by the applied field during the motion. It was also shown that the motion only occurs in the region of a domains and that the direction of the motion is opposite to the conventional polarization direction in the underlying a domain. The velocity depends on the magnitude of the growth-field pulse, and its relation to that field E_1 is given by the equation $u=Ae^{-B/E_1}$. The velocity also increases with increasing pulse frequency.

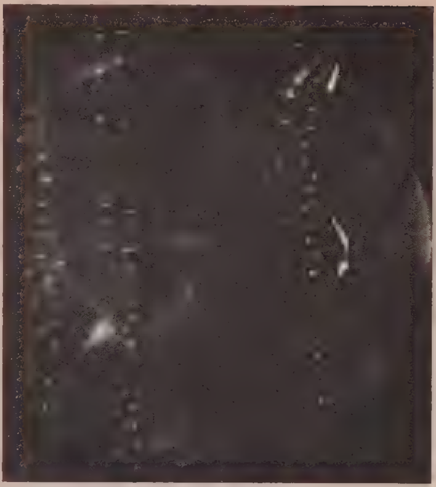

FIG. 3. Photograph of a microscope image showing regions where dots move. The horizontal streaks within the vertical bands are dot tracks (time exposure).

DISCUSSION

Perturbation of the Applied Field

In order to understand these observations, it is first necessary to recognize that an a domain perturbs the electric field in the crystal. For a $BaTiO_3$ crystal which is a single c domain, application of a voltage across the crystal gives rise to a uniform field normal to the surface. However, since $BaTiO_3$ is anisotropic in its dielectric properties, the insertion of an a domain into the c domain alters this surface field. To determine the nature

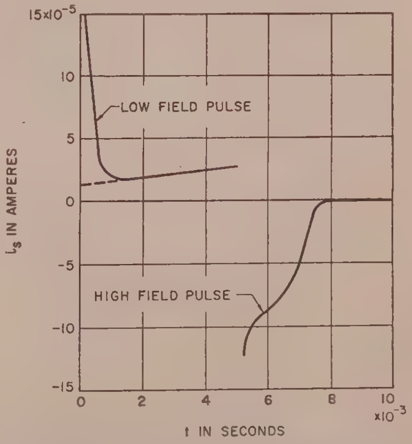

FIG. 4. Typical plot of switching current i_s vs time for a complete pulse cycle.

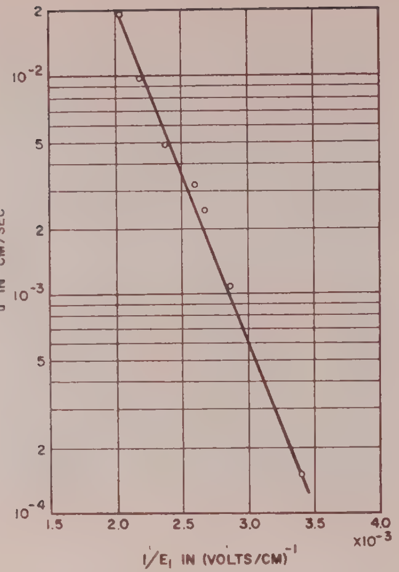

FIG. 5. Plot of log dot velocity $\log u$ vs reciprocal of the applied field on the growth-field pulse $1/E_1$.

of the field variation, a wire analog of the dielectric $BaTiO_3$ was constructed. In this analog the anisotropic dielectric constant was represented by wires of different conductivities arranged in a square network so as to represent an a domain in a c domain matrix. (The a domain width was taken as $\frac{1}{5}$ the crystal thickness.) Appropriate resistors were inserted at the sides of the model so as to represent a single a domain in an infinitely long c domain matrix. Figure 7 is a schematic representation of the analog and defines the coordinates used in Table I. Table I gives some of the potential values as a function of position, the potential having been adjusted to make the total potential drop 20 units across the crystal. (An Appendix indicates the salient features of the analog.)

From the data in Table I, the normal component of the electric field was determined by fitting the $V_{n,m}$ to a quadratic equation. Treating $V_{n,m}$ as continuous $V(x,y)$, the $V(x,y)$ were differentiated to find $(E_y)_{y=0^+}$. [Tabular data of $(E_y)_{y=0^+}$ are included in Table II.] A plot of $E(x)$ is shown in Fig. 8.

Growth of a Small c Domain

Consider a small, cylindrical c domain which has its spontaneous polarization direction opposite to that of its immediate environment. Depending on the polarity, an applied field will cause this domain either to expand or to contract. The velocity of the cylinder's wall is described by the equation for *wall* velocity v,[5]

$$v = v_\infty e^{-\delta/E},$$

where v_∞ and δ are constants for a particular crystal at

TABLE I. $V_{n\,m}$.

$m \backslash n$	1	2	3	4	5	6	7	8	9	10
0	10	10	10	10	10	10	10	10	10	10
1	6.98	7.14	7.22	7.32	7.38	7.46	7.50	7.54	7.57	7.
2	6.67	4.55	4.72	4.82	4.91	5.00	5.09	5.16	5.22	5.

a fixed temperature with fixed electrodes. Miller an Weinreich have derived an equation of this form o the basis of a nucleation model (i.e., domain growt proceeds by the nucleation of new steps at the domai wall).[6] In their derivation, E is the normal field nea the crystal's surface.

In a crystal without a domains, this field is uniform and hence a sufficiently small c domain should expan or contract symmetrically when a field is applied.[7] Fo a crystal that does contain a domains, however, th field is not uniform along the surface, and the expansio or contraction will not be symmetric. If the domain growing, e.g., from the bottom surface in Fig. 8, the the c domain will grow faster toward the lower acu region than away from it since the field is higher in th acute region, as shown in Fig. 8. Thus, the expansio process shifts the center of the domain toward the le in this example.

Motion of c Domain Centers

Miller[8] has observed that c domain polarization r versal proceeds by the initial formation of a cone-shape reversed domain ("spike") followed by a growt through the crystal, to become a truncated cone, fo

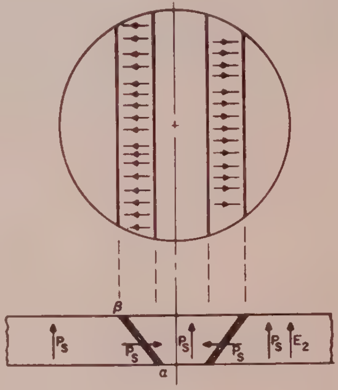

FIG. 6. Top: Schematic diagram of a microscope image showi two (vertical) bands where dot motion occurs. The horizon streaks are the tracks for dot motion. The arrowheads on th streaks indicate the direction of motion of the dots. Bottom: Cr section of the crystal showing the slant of the two a domains a the polarization directions corresponding to the direction of d motion above. These polarization directions are those that prev during the high-field pulse.

---

[5] R. C. Miller and A. Savage, Phys. Rev. 112, 755 (1958).

[6] R. C. Miller and G. Weinreich, Phys. Rev. 117, 1460 (1960).

[7] For sufficiently small c domains, the depolarizing fields can neglected.

[8] R. C. Miller, Phys. Rev. 111, 736 (1958).

ved by a sidewise expansion of the domain. He also ted "a very strong preference for the [cone's] base appear on the side of the [crystal] sample facing negative electrode." Taken with the above statement (that the field important in domain polarization versal is the normal component of the field at, or near, surface), these observations indicate the field reonsible for the formation of a *c* domain is that which present at the negative electrode, i.e., the internal d positive electrode fields can be ignored. Assuming at this surface field is also the only important field termining the growth of the domain, then over a mplete pulse cycle the changes in the domain would as indicated in Fig. 9. At time t_0 the field causes the versed *c* domain to start growing. During the time terval t_0 to t_1, the higher field at the left dot wall uses that wall to move farther than the right wall uring the same time interval. At time t_1 another field opposite polarity is applied, making the top surface e negative electrode. The domain walls are now conained to move inward, but since the field (at the gative electrode) acting on the *right* wall is now higher an that on the left, the right wall must move farther ward the left than the left wall does toward the right. hus, at time t_2 the walls have moved so as to make the sition of the domain at the end of the pulse cycle to e left of the original position, i.e., over a complete cle of the field, the position of the domain has ifted. The direction of this shift is, by this argument, posite to the polarization direction in the *a* domain.

Since a shrinking domain can be expected to leave a all residual domain, the last part of the field cycle, om t_2 to t_3, is not effective in changing the size of the main. Hence, this residue provides a continuity of e domain's existence over many cycles. Thus, since ch cycle shifts the domain, then continued application f an alternating field should cause a net horizontal otion of the *c* domain.

Correlation of the Model with Observations

The most interesting property of the model is that t provides an explanation for the fact that *c* domain nters do, in fact, move. In addition, the model also orrectly accounts for the direction of motion, the locaion where motion occurs, and the field dependence of he motion. Justification for these statements follows.

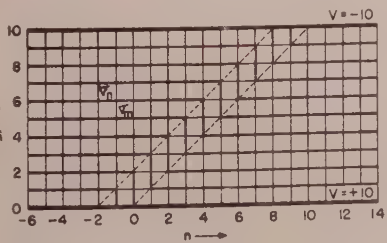

FIG. 7. Schematic diagram of the wire analog. The conductivity the heavy lines (wires) is σ_n, that of the light lines (wires) σ_m.

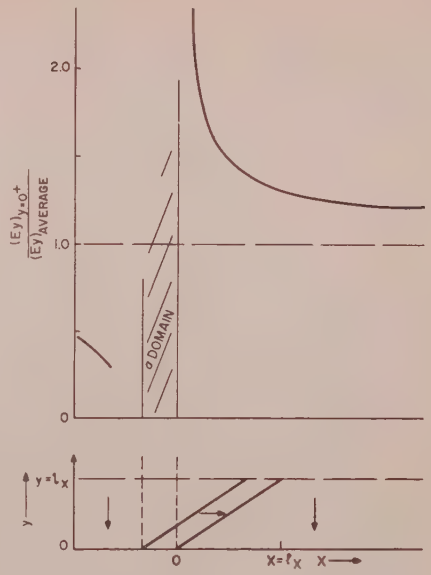

FIG. 8. Sketch of the normal component of the (bottom) surface field as a function of distance from the *a* domain.

The direction of motion is observed to be opposite to the polarization direction in the underlying *a* domain. The consistency of the model with this observation was demonstrated in the last section.

The tracks for dot motion are observed to lie in the normal projection of the *a* domain onto the crystal surface (as illustrated in Fig. 6). Prior discussion has shown that dot motion should occur *within* the bands (*a* domains), and it remains to be shown that motion should not be continued *outside* those bands. Consider first the band edge at the *origin* of the tracks (e.g., position α in Fig. 6). A dot just outside the band edge might be expected to move slightly and in the same direction as those inside the band until the dot touches the *a* domain. When the dot crosses the *a* domain on the growth pulse, it is being acted upon by the least asymmetric field of the growth pulse. After penetrating the *a* domain, that portion of the dot inside the band will, on the subsequent collapse pulse, be opposed by the maximum collapse field, and hence the dot should collapse asymmetrically so as to end outside the *a* domain where it started. Since the collapse field in this region is minimal, the dot should grow to a relatively large dot with stationary center and steady-state size. Large stationary dots are indeed observed at the origin side of the band (Fig. 3).

At the terminal side of the band (i.e., at position β in Fig. 6), the question to be answered is, "Why do not the dots continue beyond the band edge?" The reason is similar to the previous answer: There is a very small growth field just beyond the terminal side of the band edge; hence, if any dot were to cross that edge, it would not expand appreciably, and its con-

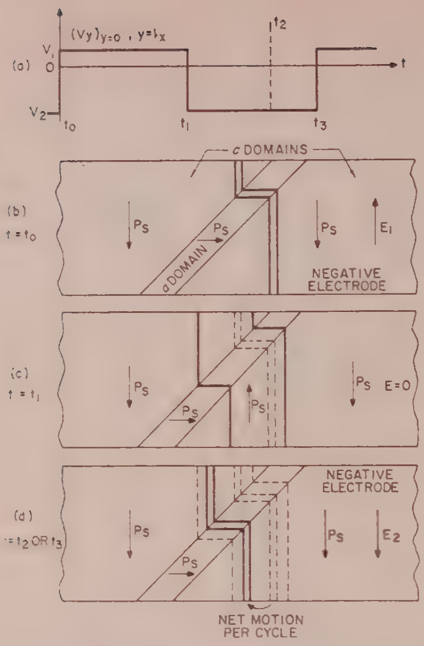

FIG. 9. Diagrams illustrating the nature of the c domain (dot) displacement during one pulse cycle. (a) Sketch of the pulse cycle. (b) Cross section of the crystal at the beginning of the pulse cycle. (c) Cross section of the crystal halfway through the pulse cycle. (d) Cross section of the crystal at the end of the pulse cycle.

traction would be almost completely symmetrical, i.e., the dot velocity should be reduced very much compared to that within the band and therefore not be observable. Furthermore, its small size would accentuate its invisibility, Finally, the low-growth field would probably allow it eventually to be annihilated.

Analytic Form of *u*

An expression for dot velocity u as a function of the experimental parameters can be obtained as follows: Consider the dot in Fig. 9. When the growth field E_1 is applied, each side of the dot has the same time in which to expand. However, the expansion field depends on the position of the dot wall (Fig. 8) so that each wall will move a different distance during the expansion time, $\frac{1}{2}\nu$ (where ν is the field's frequency). Calling the initial position of the dot x_0 and the position of the right and left walls after expansion x_r and x_l, respectively, then ignoring the small size of the initial residue, the following equations imply the maximum dot size x_r-x_l:

$$\frac{1}{2\nu}=\int_{x_l}^{x_0}\frac{dx}{v_1(x)}=\int_{x_0}^{x_r}\frac{dx}{v_1(x)},$$

where $v_1(x)$ is the wall velocity on the growth pulse. The step distance per cycle $l_s=x_f-x_0$, where x_f is the center of the subsequently collapsed dot, is then determined by the additional requirement that

TABLE II. $v_0/v(x)$.

x	1	2	3	4	5	6	7	8	9	10
$E(x)$	4.38	3.00	2.92	2.77	2.69	2.58	2.54	2.50	2.47	2.4
$\varphi(x)$	2.19	1.50	1.46	1.38	1.34	1.29	1.27	1.25	1.23	1.2
$10^2 v_0/v(x)$	0.44	3.60	4.30	6.40	7.90	10.50	11.90	13.50	15.40	16.4

$$\frac{1}{2\nu}\geq\tau=\int_{x_l}^{x_f}\frac{dx}{v_2(x)}=\int_{x_f}^{x_r}\frac{dx}{v_2(x)},$$

where $v_2(x)$ is the wall velocity on the collapse pulse These integrals could be evaluated numerically, but a sufficiently good approximation is obtained by taking $1/v_1\propto x$ and $1/v_2\propto(x-l_x)$, where l_x is the crysta thickness (see Fig. 11). This approximation can b justified as follows:

The equation for wall velocity v is

$$v(x)=v_\infty e^{-\delta/E(x)}.$$

Taking as a reference velocity v_0 that v which woul result from the applied macroscopic field, the rati $v_0/v(x)$ can be expressed as

$$\frac{v_0}{v(x)}=\exp\left\{-\delta\left[\frac{1}{E_0}-\frac{1}{E(x)}\right]\right\}.$$

Hence,

$$\ln\frac{v_0}{v(x)}=+\delta\frac{E_0-E(x)}{E_0E(x)}.$$

Defining the function $\varphi(x)$ as:

$$\varphi(x)\equiv E(x)/E_0,$$

then

$$\ln\left[\frac{v_0}{v(x)}\right]=-\left[\frac{\varphi(x)-1}{\varphi(x)}\right]\left(\frac{\delta}{E_0}\right).$$

The quantity $(\varphi(x)-1)/\varphi(x)$ can be evaluated from the data obtained from the analog. Table II lists the $\varphi(x)$ so obtained. Taking the typical value $\delta/E_0=10$

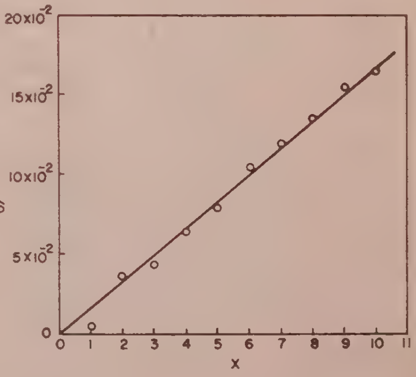

FIG. 10. Plot of $v_0/v(x)$ vs x from the data of Table II.

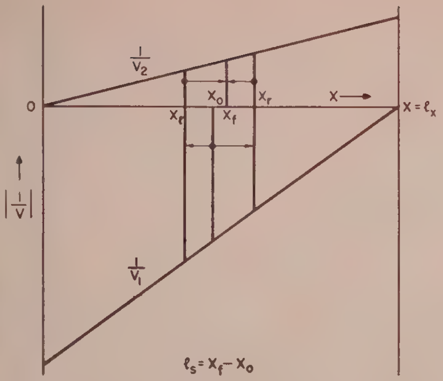

FIG. 11. Plot of reciprocal wall velocity $1/v$ as a function of distance along the track, using the approximation in the text. The lower curve $(1/v_1)$ corresponds to the growth pulse, the upper $(1/v_2)$ to the collapse pulse. The area of the trapezoid between $(1/v_1)$ and the abscissa (x_0 to x_f) equals the time of the low-field pulse, as does the trapezoid beside it (x_l to x_0). The boundaries of the trapezoids above the abscissa are determined by the lower boundaries, and the position of x_f is determined by requiring the upper trapezoids to have equal areas. For a dot starting at x_0, then, the step distance per cycle is $x_f - x_0$.

the resulting ratio of $v_0/v(x)$ is also indicated. A plot of $v_0/v(x)$ versus x is shown in Fig. 10. Thus, for x not too close to the acute region formed by the a domain with the surface, a good approximation of $1/v$ is obtained by taking $1/v_1 \propto x$ and $1/v_2 \propto (x - l_x)$. Using this approximation to evaluate the integrals (Fig. 11), one obtains

$$\frac{1}{2\nu} = \frac{1}{v_1}(x_r - x_0) + \frac{m_1}{2}(x_r - x_0)^2$$

$$= \frac{1}{v_1}(x_0 - x_l) - \frac{m_1}{2}(x_0 - x_l)^2$$

$$\tau = -\frac{1}{v_2}(x_f - x_l) + \frac{m_2}{2}(x_f - x_l)^2$$

$$= -\frac{1}{v_2}(x_r - x_f) - \frac{m_2}{2}(x_r - x_f)^2,$$

where

$$m_1 = \frac{d\,1/v_1}{dx},$$

and

$$m_2 = \frac{d\,1/v_2}{dx}.$$

On solving for x_r and x_l,

$$x_r = x_0(1+y)^{\frac{1}{2}} = l_x - (l_x - x_f)(1-z)^{\frac{1}{2}},$$

$$x_l = x_0(1-y)^{\frac{1}{2}} = l_x - (l_x - x_f)(1+z)^{\frac{1}{2}},$$

where

$$y = 1/m_1 \nu x_0^2,$$

and

$$z = 2\tau/m_2(x_f - l_x)^2.$$

The contribution to l_s on the growth pulse l_g is $x_0 - (x_r + x_l)/2$ and on the collapse pulse l_c is $(x_r - x_l)/2 - x_f$. Using the above x_r, x_l,

$$l_g = (x_0/2)[2 - (1+y)^{\frac{1}{2}} - (1-y)^{\frac{1}{2}}]$$
$$= (x_0/2)(y^2/4 + \cdots)$$
$$= 1/8m_1^2\nu^2 x_0^3 + \cdots.$$
$$l_c = \tfrac{1}{2}(l_x - x_f)[2 - (1+z)^{\frac{1}{2}} - (1-z)^{\frac{1}{2}}]$$
$$= \tfrac{1}{2}(l_x - x_f)(z^2/4 + \cdots)$$
$$= 4\tau^2/8m_2^2(l_x - x_f)^3 + \cdots.$$

For x not too close to 0 or l_x, y and z are small, and only the first term need be taken in the above expressions for l_g and l_c. The time actually spent collapsing τ is approximately given (for $l_s \ll l_x$) by

$$\tau = (x_r - x_l)/v_2 = (x_r - x_l)m_2(l_x - x_f),$$

while

$$1/2\nu = (x_r - x_l)/v_1,$$

i.e.,

$$x_r - x_f = v_1/2\nu = 1/2\nu m_1 x_f;$$

hence,

$$\tau = m_2(l_x - x_f)/2\nu m_1 x_f,$$

and thus

$$l_c = \frac{4}{8m_2^2(l_x - x_f)} \cdot \frac{m_2^2(l_x - x_f)^2}{4\nu^2 m_1^2 x_f^2} = \frac{1}{8m_1^2\nu^2 x_f^2(l_x - x_f)}.$$

The step distance per cycle $l_s = l_g + l_c$ or

$$l_s = \frac{1}{8m_1^2\nu^2}\left[\frac{1}{x_0^3} + \frac{1}{x_f^2(l_x - x_f)}\right].$$

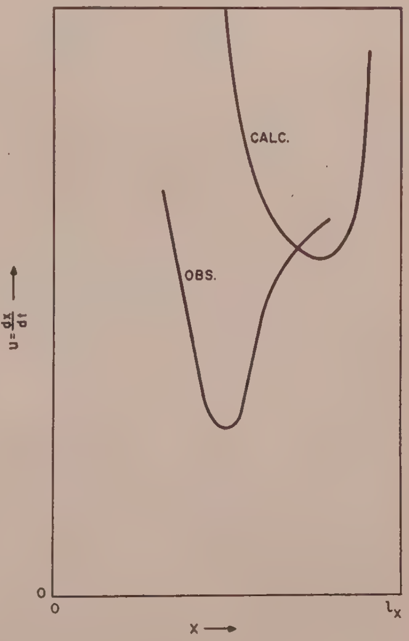

FIG. 12. Plot of dot velocity u vs distance along the track x. The upper curve is calculated, the lower observed.

The dot velocity u is then

$$u = \nu l_s = \frac{1}{8}\left(\frac{1}{\nu}\right)\left(\frac{1}{m_1^2}\right)\left[\frac{1}{x_0^3} + \frac{1}{x_f^2(l_x - x_f)}\right],$$

where the term in square brackets is an asymmetry factor $\alpha(x)$ which depends on the position x of the dot in its track, and the $1/m_1^2$ term expresses the field dependence.

The asymmetry term $\alpha(x)$ was an unexpected result of the calculation. The step distance per cycle l_s depends on the extent of dot expansion expressed in the $1/\nu m_1^2$ term and the asymmetry of that expansion expressed in the $\alpha(x)$ term. The form of $\alpha(x)$ indicates that the dot should decelerate to about the middle of its track and then accelerate beyond that point. Since the u data were obtained by measuring an average u over a large portion of the track, the $u(x)$ had not been detected. To check the form of $u(x)$, the position of a dot was measured in successive frames of a movie film of dot motion. In the region where the approximations used in deriving $\alpha(x)$ are best, i.e., toward the center of the track, the expected change in velocity was found, as illustrated in Fig. 12.

The field factor $1/m_1^2 \equiv [dx/d(1/v_1)]^2$ has been shown to be independent of position in the track. Hence $1/m_1^2$ must vary as v_1^2. Since $v_1^2 = v_\infty^2 \exp(-2\delta/E_1)$, then $1/m_1^2 \propto \exp(-A/E_1)$ and $\ln u \propto 1/E_1$, as observed.

It is observed that the dot velocity increases with increasing pulse frequency. The model, as it stands, predicts the opposite ($u(\nu) \propto 1/\nu$). The requirement for consistency between model and observation is that $l_s \propto v^{-1+\delta}$(vs $\langle l_s \rangle \propto \nu^{-2}$), where $\delta > 0$. This requirement can be written as $v \propto \nu^\delta$, i.e., *wall* velocity increasing with increasing pulse frequency. This is precisely the effect reported by Miller,[8] viz., that recently switched regions exhibit a higher wall velocity than those not recently switched. In the present case, the trailing edge of the expanding dot lies in the region where the leading edge lay in the previous growth pulse, i.e., in a region that has been recently switched. Thus, the expansion of the dot is slightly less asymmetric than previously indicated, resulting in the observed frequency dependence without substantially altering the prior arguments.

CONCLUSION

The motion of c domain centers ("dots") in $BaTiO_3$ occurs only in the presence of an a domain. The effect of the a domain is to alter the normal component of the surface field when a field is applied to a $BaTiO_3$ crystal. Since the dielectric constant is higher in the a domain than in the c domain, one expects and finds a field enhancement near the a domain. A quantitative description of the surface field variation, coupled with previously published observations, is sufficient to explain the dependence of the dot velocity on the experimental variables studied in this investigation. The crux of that argument lies in recognizing that the variation of surface field causes asymmetric growth and collapse of small c domains, the result being a net translational motion of the c domain when an alternating field is applied to the crystal. The proposed model, then, accounts for all of the observed features of the motion of c domain centers.

ACKNOWLEDGMENT

The author appreciates the assistance of his colleagues in this work; in particular that of Robert C. Miller and A. Savage for prepublication techniques on optical observation of c domains and general experimental expedition; L. R. Walker for his help with the analog; and J. F. Dewald for valuable discussions of the model.

APPENDIX

A straightforward solution of $\nabla \cdot \mathbf{D} = 0$ with the present boundary conditions is not possible since the coefficients of the formal solution cannot be obtained. In a wire analog however, current can be made to satisfy the analogous difference equation $\mathbf{\Delta} \cdot \mathbf{i} = 0$. Hence it is possible to use this analog to find the desired potential $V_{n,m}$. Since the analog is to represent a lattice that is infinite in one direction, the current necessary to produce $V_{n,m}$ would be infinite also. To avoid this, only the *deviation* U from a linear potential φ was used ($V_{n,m} = \varphi_m + U_{n,m}$). As current is conserved at a point, it follows that the deviation potential results from the application of equal currents to each point on one side of the "a domain" and extracting currents of equal magnitude from each point on the other side.

The method of determining the values of the appropriate resistors, to be inserted so as to simulate an infinite grid, is indicated as follows. Since the potential V in the difference equation $\mathbf{\Delta} \cdot \mathbf{i}(V) = 0$ is to have a *linear* potential φ subtracted from it, the difference equation $\mathbf{\Delta} \cdot \mathbf{i}(U) = 0$ must also be valid for the same boundary conditions. A formal solution of this latter equation is

$$U_{n,m} = \sum_r^{M-1} c_r e^{-n\lambda_r} \sin m\mu_r,$$

where $\mu_r = \pi r/M$, M = total number of horizontal wires, and the λ_r are given in

$$\sinh^2 \frac{\lambda_r}{2} = \frac{\sigma_m}{\sigma_n} \sin^2 \frac{\mu_r}{2}.$$

The current in the mth wire is then

$$i_m = \sigma_n \sum_r^{M-1} U_{r;m,n}(e^{\lambda_r} - 1),$$

nd since the origin of n is arbitrary, and the period f U is $2M$, then

$$c_r=\frac{1}{M}\sum_{m'}^{M-1} U_{0,m'}\sin m'\mu_r,$$

hus

$$i_m=\frac{\sigma_n}{M}\sum_{m'}^{M-1} U_{0,m'}\sum_{r}^{M-1}\sin m\mu_r\cdot\sin m'\mu_r(e^{\lambda_r}-1).$$

Calling the sum over r $a_{m,m'}$, the a's can be tabulated nd permit i_m to be written

$$\begin{aligned}{}_{m}=(\sigma_n/M)[(a_{m,1}+a_{m,2}+\cdots+a_{m,M-1})U_m\\ +a_{m,1}(U_1-U_m)+a_{m,2}(U_2-U_m)+\cdots\\ +a_{m,M-1}(U_{M-1}-U_m)].\end{aligned}$$

The i_m can also be written in terms of the required resistors, where these resistors have conductivities $\sigma_{m,m'}$

$$\begin{aligned}i_m=\sigma_{m,0}(U_0-U_m)+\sigma_{m,1}(U_1-U_m)+\cdots\\ +\sigma_{m,n}(U_M-U_m).\end{aligned}$$

Equating coefficients of like potentials in these two expressions for i_m

$$\begin{aligned}\sigma_{m,m'}&=(\sigma_n/M)a_{m,m'} \qquad (m'\neq 0,M),\\ \sigma_{m,0}=\sigma_{m,M}&=-\frac{\sigma_n}{2M}\sum_{m'}^{M-1} a_{m,m'}(m'=0,M).\end{aligned}$$

The resistances required to simulate a semi-infinite lattice are thereby determined.

JOURNAL OF APPLIED PHYSICS VOLUME 32, NUMBER 12 DECEMBER, 1961

High-Temperature Kilocycle Internal Friction in Al_2O_3 Single Crystals*†

R. J. Huber, G. S. Baker, and P. Gibbs
University of Utah, Salt Lake City, Utah

(Received May 8, 1961)

Dislocation damping in Al_2O_3 single crystals has been measured to 1850°C. Undeformed specimens show no damping greater than $\delta=10^{-5}$. Deformed specimens have an exponentially rising damping above 1450°C with an activation energy of 100–120 kcal/mole. The damping is amplitude independent at least to 10^{-5} strain amplitude. Dislocation densities and distributions for the specimens were determined by surface etching.

I. INTRODUCTION

THE internal friction of aluminum oxide single crystals has been studied by a few investigators. Wachtman[1] reported measurements of this property between room temperature and about 100°C. Chang[2] has made low frequency measurements to more than 1500°C. He used flexural vibrations at frequencies between 10 and 50 cps.

In this paper we report measurements of the internal friction of aluminum oxide single crystals at frequencies near 50 kc/sec as a function of temperature to 1840°C and as a function of prior plastic deformation. The dislocation density and distribution were determined by etch pit counts. The resolution was such that changes in the log decrement of about 10^{-5} or greater could be observed.

II. EXPERIMENTAL METHOD

The samples used in this experiment were single crystals of artificial white sapphire obtained from the Linde Company. The crystals were in the form of rods $\frac{1}{10}$ in. in diameter and up to 16 in. long.

The log decrement of the samples was measured using a modified version of the composite piezoelectric oscillator described by Marx.[3] High temperatures were provided by a small resistance heated furnace mounted in a manner similar to that used by Marx and Sivertsen,[4] so as to enclose the sample portion of the sapphire crystal. The apparatus was enclosed in a vacuum chamber to eliminate air losses and to protect the furnace winding. Figure 1 shows a sketch of the appa-

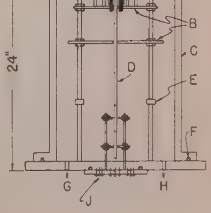

FIG. 1. Experimental apparatus. (A) thermal insulators, (B) steel plates, (C) vacuum chamber, (D) composite oscillator, (E) electrical insulators, (F) O-ring seal, (G) vacuum pump line, (H) vacuum gauge, (J) covar seals.

---

* This work was sponsored by the Office of Naval Research.

† This is an essential portion of a thesis done for a Ph.D. at the University of Utah.

[1] J. B. Wachtman, WADC Tech. Rept. 59-278 (May, 1959).

[2] R. Chang, J. Appl. Phys. 32, 1127 (1961).

[3] J. Marx, Rev. Sci. Instr. 22, 503–509 (1951).

[4] J. Marx and J. Sivertsen, J. Appl. Phys. 24, 81–87 (1953).

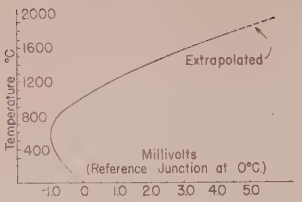

FIG. 2. emf vs temperature for tungsten/molybdenum thermocouple.

ratus. The driver gauge part of the composite oscillator was two $\frac{1}{8}$-in. square x-cut quartz crystals cut for longitudinal resonance at 50 kc/sec. The sample section of the oscillator was a $\frac{1}{10}$-in.-diam sapphire rod one and one-half wavelengths long at the frequency of measurement. The first wavelength above the quartz driver-gauge combination served as a thermal buffer, and the top one-half wavelength formed the actual sample. When deformed crystals were used, they were cut so that only the sample portion had been plastically deformed.

Occasionally the sapphire rod from which the sample was to be cut was too short to allow the cutting of a one piece one and one-half wavelength sample with the deformed portion properly located. In these cases the sample was cut one wavelength long and an additional half wavelength rod was cemented to it using silver chloride as a cement.

The heating element consisted of about 60 turns of 0.020-in. tungsten wire wound on a recrystallized alumina tube $\frac{3}{8}$ in. o.d. and $\frac{1}{4}$ in. i.d., about $4\frac{1}{2}$ in. long. A thin overlay of castable alumina served to hold the windings in place. This element was mounted on a stainless steel plate and surrounded by two thermal insulation pieces, one of recrystallized alumina and the other of fused quartz.

Temperature measurements were made with a tungsten-molybdenum[5] thermocouple placed inside the furnace as near the sample as possible. Figure 2 is a plot of the thermal emf vs temperature of the thermocouple used. It is nearly linear in the high temperature region of interest of this experiment. The calibration curve of this W/Mo thermocouple was obtained by mounting the W/Mo thermocouple and a Pt/Pt+13% Rh thermocouple as close together as possible in the furnace and comparing readings. The calibration curve is believed to be accurate to about ±2% of the temperature above 1000°C. The plot in the region above 1650°C was obtained by extrapolation. This is felt to be reliable because the curve is linear and of the same slope as the curve given by Potter and Grant,[6] who made temperature measurements in this region. However, the present workers found the emf reversal to occur at 500° rather than 1100°C.

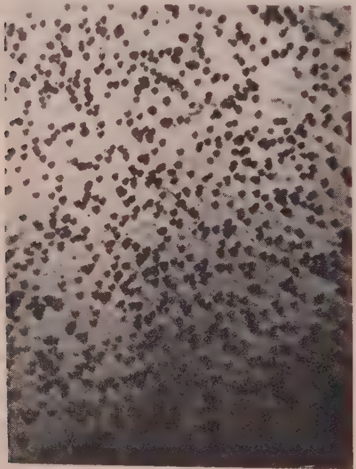

FIG. 3. Dislocation etch pits on an "as received" sample. Pit density is 6×10^6 per cm². Magnification is 480×.

As shown by Marx,[3] the logarithmic decrement of the composite oscillator is given by $\delta_t = KV_d/V_g$, where V_d and V_g are the voltages applied to the driver crystal and developed across the gauge crystal, respectively. The factor K is a constant depending on the geometry of the crystals and parameters of the measuring circuits. Whenever necessary K was determined by direct measurement of free decay on oscilloscope traces.

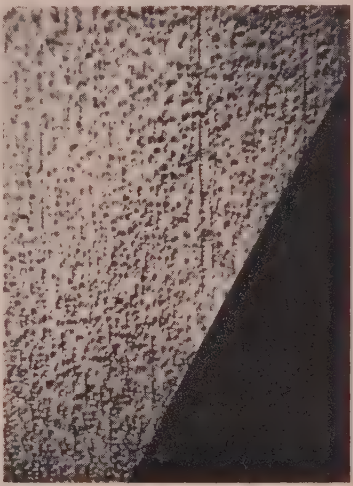

FIG. 4. Dislocation etch pits on a sample slightly deformed near 1300°C. Pit density is 1×10^7 per cm². Magnification is 480×.

The decrement measured in this way reflects energy losses due to all sources including support losses, losses due to glue joints, adherent electrodes, etc. The decrement of the sample portion of the comsite oscillator was calculated by means of the relaon $\delta_s=\{m_t\delta_t-m_q\delta_q\}/m_s$. In this expression δ_t is the tal decrement, δ_q is the decrement due to all sources energy loss except the sample. The quantities m_t, $_q$, and m_s are the masses of the total composite cillator, quartz bars plus thermal buffer rod, and the mple, respectively.

---

[5] The tungsten wire used was 0.020-in. process LG wire obtained from General Electric, Euclid Branch, Cleveland, Ohio. The molybdenum was 0.020-in. wire obtained from General Electric, Dover Wire Plant, Dover, Ohio.

[6] R. D. Potter and N. J. Grant, Iron Age **163**, 65–69 (March 31, 1949).

The absolute accuracy of the experimental measureents was limited by the determination of δ_q. Unedictable changes of as much as $\pm1\times10^{-5}$ were inoduced into the decrement by the mounting, disounting and glue joint changes necessary in determing δ_t and δ_q for the same setup. However, this did not ffect measurements of relative changes of δ_s in a given un.

Two other factors influenced the accuracy of the xperiment. The change in elastic constants upon heatg changes the position of the nodal points, and thus he support losses. However, this effect could be exerimentally determined and largely corrected. In addion, the presence of thermal gradients in the sapphire od causes an unknown error. However, in view of the ery low internal friction in sapphire below 1400°C at 0 kc/sec and the short distance required for the emperature to drop below this value, this error is elieved to be relatively small. Thus it is considered hat relative changes in δ_s of $\pm0.2\times10^{-5}$ could be oberved during a given run. Absolute values of δ_s were nown to about $\pm1.2\times10^{-5}$.

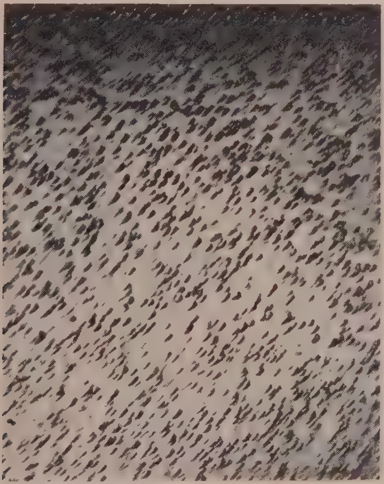

FIG. 5. Dislocation etch pits on a sample slightly deformed ear 1300°C and annealed at 1900°C. Pit density is 8×10^6 per m². Magnification 480×.

The strain amplitude was determined by use of the xpression $\epsilon_g=(cf^{-2})V_g$ developed by Marx.[3] Here ϵ_g the maximum strain amplitude in the gauge crystal, is a constant, and f is the frequency of vibration. In his experiment maximum strain in the sapphire crystal as 10^{-5} or less.

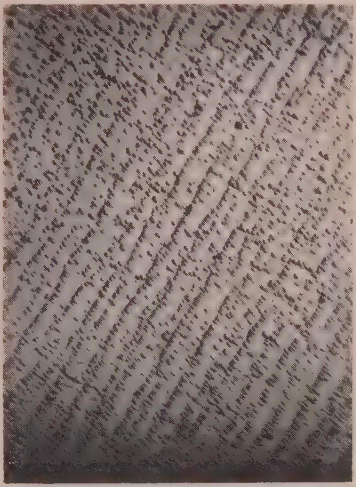

FIG. 6. Dislocation etch pits on a polygonized portion of the crystal shown in Fig. 5. Magnification 480×.

Specimens were deformed in tension at 1300° and at about 1900°C by applying an axial stress. At the lower temperature, stresses between 5.9×10^8 and 7.9×10^8 d/cm² gave elongations up to 20% in 24 hr. At the higher temperature, a stress of approximately 2.2×10^8 d/cm² was sufficient to cause 20% elongation in about 5 min.

III. EXPERIMENTAL RESULTS

A. Surface Etching Studies

Using the technique developed by Scheuplein and Gibbs[7] for etching dislocations on the surface of corundum crystals, studies of the dislocation density and distribution were made on the samples used in the damping measurements.

The corundum crystals used could be divided into four groups. They were the "as received," i.e., undeformed, samples; samples slightly deformed at 1300°C (1 to 2% elongation); samples heavily deformed near

FIG. 7. Dislocation etch pits on a sample heavily deformed in an oxygen flame near 1900°C. Pit density is 2×10^7 per cm². Magnification 480×.

---

[7] R. J. Scheuplein and P. Gibbs, J. Am. Ceram. Soc. 42, 458–472 (1960).

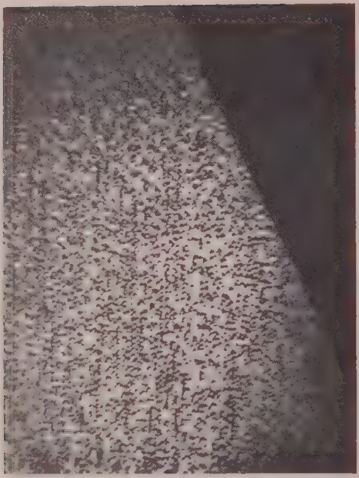

FIG. 8. Dislocation etch pits on a sample heavily deformed near 1300°C. Pit density is 4×10^7 per cm^2. Magnification 480×.

1300°C (about 20% elongation); and samples heavily deformed above 1900°C in an oxygen-gas flame.

The density of the dislocation etch pits was largely determined by the amount of deformation of the sample while the etch pit distribution was determined by the temperature at which the crystal was deformed and the temperatures to which it was exposed following deformation.

Figure 3 is a photomicrograph of the etched surface of an "as received" corundum sample. The density of the randomly spaced etch pits is about 6.7×10^6 pits/cm^2. This specimen was exposed to a maximum temperature of 1800°C. The density and distribution of etch pits shown here is characteristic for undeformed Linde rods.

Figure 4 shows the etch pits on the surface of a sample slightly deformed near 1300°C and not exposed to temperatures above that at any time. The edge of the sample (which is parallel to the rod axis) is shown in the photograph. The dislocations are partially arranged in slip planes.

A second slightly deformed sample is shown in Fig. 5. As part of the experimentation it was exposed to temperatures in excess of 1900°C. The result was a rearrangement of the dislocations to an apparently random distribution with the exception of polygonization taking place in a small part of the rod. The portion which polygonized was a diagonal section about 1 mm wide. Figure 6 is a photomicrograph of the polygonized portion of this rod. The rod axis is parallel to the short side of the photo in both instances. In Fig. 6 the slip planes are about 30° to the rod axis, i.e., at a right angle to the rows of dislocations. Density of the etch pits is about 8×10^6 pits/cm^2.

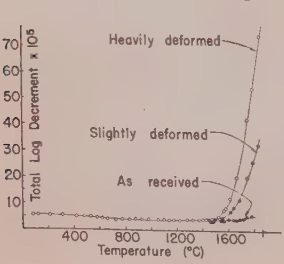

FIG. 9. Log decrement vs temperature for three samples with different amounts of deformation.

Figure 7 shows the dislocation etch pits on a sample which was heavily deformed near 1900°C in an oxygen-gas flame. The dislocations are randomly spaced due to the exposure to the extreme temperature. Etch pit density is about 1.7×10^7 pits/cm^2.

The result of heavy deformation (20% elongation) near 1300°C is shown in Fig. 8. The etch pits are arranged in slip planes with an average density of about 4×10^7 pits/cm^2. Maximum temperature reached with this sample was 1760°C. This apparently caused no dislocation rearrangement.

B. Internal Friction

The internal friction exhibited by an aluminum oxide single crystal is dependent upon the history of the particular sample. The internal friction of the "as received" samples was less than the background damping of the apparatus at all temperatures to 1800°C. Figure 9 shows the total logarithmic decrement (including support losses) for three different samples, each of which was deformed a different amount. The "as received" sample shows no significant increase in damping, while the two deformed rods exhibit a marked increase in damping beginning about 1450°C. When plotted as a function of $(1/T)°\mathrm{K}^{-1}$, the log of the damping increase forms a straight line. Thus it is apparently thermally activated.

Figures 10 and 11 show the results of internal friction measurements for two samples which were deformed at 1300°C. In both cases two successive runs are shown. These figures show the generally observed pattern in which the first run shows greater damping than the second. During a normal damping run the sample is above 1700°C for approximately 15 min. The dislocation density in both these specimens is greater than 10^7 cm^{-2}. The dislocations are predominantly in slip lines. Etched surfaces of the two specimens were similar in appearance to that shown in Fig. 8.

Figure 12 shows data for a slightly deformed sample (1 to 2% elongation). Again the first run gives greater damping than the second. However, the data of the first run shows less damping at a given temperature than any run on a heavily deformed sample. Between the times of making the two runs, this sample was annealed at a temperature in excess of 1900°C for 5 min. Considerable rearrangement of the dislocations and partial polygonization of the crystal resulted from this treatment. Photomicrographs of the etched surface of this sample are shown in Figs. 5 and 6. The dislocation distribution was random throughout practically l but the polygonized section, which formed a section bout 1 mm wide near the center of the rod. Following his heat treatment, the second run of Fig. 12 was made. he damping was reduced by a factor of 5.

Figure 13 shows the damping observed for a sample eavily deformed near 1900°C in the oxygen-gas flame. he damping is between that of the samples heavily nd lightly deformed at 1300°C. The dislocation denity and distribution are shown in Fig. 7. The very igh deformation temperature resulted in a random istribution of dislocations.

IV. DISCUSSION AND CONCLUSIONS

It has been shown that the high temperature internal riction of aluminum oxide single crystals is greatly nhanced by plastic deformation. The "as grown" apphire crystals showed a log decrement of less than $\times10^{-5}$ throughout the entire range of 1800°C covered t strain amplitudes of 10^{-5} or less. Cold-worked, i.e., deormed near 1300°C, samples exhibited measurable inernal friction. Log decrements of 4×10^{-3} were measured t the highest temperatures achieved. It is believed that his increase is due to dislocations in that the most bvious structure change is the greatly increased disocation density previously described.

Some difficulties present themselves when interpreting he results in terms of a specific model. The question whether or not the basal dislocations in aluminum oxide separate into four quarter partials as proposed by Kronberg[8] is presently unresolved. In addition, the possible dislocation pinning mechanisms, including strong electrostatic effects, are more numerous and complicated than for simpler crystals. It would also be desirable to make internal friction measurements as a function of controlled impurity content. Linde Company estimates place the impurity content of the crystals used at 10 to 100 parts per million of Fe and 1 to 10 ppm Mg and Si plus small amounts of Ca, Ga, Pb, Ni, etc.

On the assumption that the observed increase in internal friction of the deformed rods was due to stress induced motion of dislocations, a lower limit for the average distance moved by the dislocations was estimated. By assuming that the dislocation motion took place at a constant stress equal to the maximum stress one gets the maximum energy per unit distance moved that a dislocation could have taken from the stress field. Hence, considering one-half cycle, it follows that

$$N\sigma_R bx=\delta\sigma^2/2\mu. \qquad (1)$$

Here N is the total length of dislocation line per unit volume, and σ_R is the resolved shear stress. From etch pit counts the largest value of N was about 4×10^7 cm^{-2}. The largest log decrement observed was 4×10^{-3} and the maximum strain amplitude, σ/μ, in this experiment was 10^{-5}. The radio σ/σ_R was 2.3. In corundum, b $=4.75\times10^{-8}$ cm. Thus

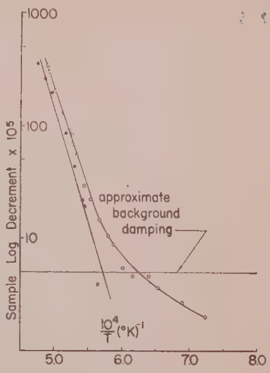

FIG. 10. Arrhenius plot of internal friction data for sample heavily deformed near 1300°C.

$$x=2.6\times10^{-8}\text{ cm}. \qquad (2)$$

Since the assumptions made above would tend to underestimate x, we see that the average dislocation moved at least a lattice constant, and probably not much more in the present experiment.

A plot of the logarithm of the damping vs (T^{-1})°K is approximately a straight line and the damping is observed to be strain amplitude independent $(\epsilon<10^{-5})$. If the damping is as appears, thermally activated motion of dislocations, the following inequality holds

$$\sigma_R bly/kT<1, \qquad (3)$$

where l is the length of dislocation line moved as a unit through an average distance y. The smallest reasonable value of y is about b. The maximum temperature of this experiment was 2120°K and the largest value of σ_R was 10^7 d/cm². Substitution of these values gives

$$l<13\times10^{-6}\text{ cm}=270a. \qquad (4)$$

As shown by the above considerations, enough dislocation motion must be present so that all the dislocation line moves an average of at least one lattice distance a. Yet the dislocation must move in relatively short sections at a time. There is no amplitude dependence, therefore, no stress induced breakaway or dis-

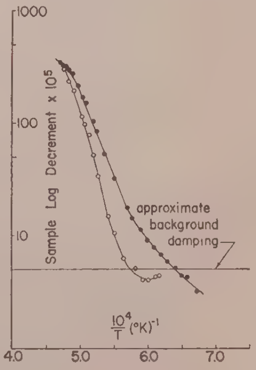

FIG. 11. Arrhenius plot of internal friction data for sample heavily deformed near 1300°C.

---

[8] M. L. Kronberg, Acta Met. 5, 507–524 (1957).

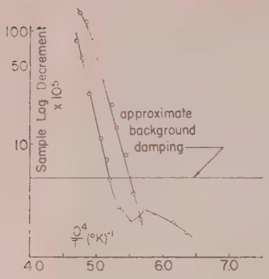

FIG. 12. Arrhenius plot of internal friction data for sample slightly deformed near 1300°C.

location multiplication. The model of the motion is one in which short segments of dislocation line move at most a few lattice distances each in independent thermally activated events.

Four general mechanisms for this motion have been considered. They are dislocation climb from stress induced net diffusion of vacancies to or from the dislocations, stress induced motion of dislocations over Peierls barriers, the dragging mechanism in which lattice imperfections such as impurities are carried along with the moving dislocations, and the increased separation of partial dislocations under the action of the applied stress.

The climb mechanism does not appear able to explain the damping of the present experiment. To account for the observed damping at the highest temperatures, about one vacancy per atomic length of dislocation must diffuse to the dislocation line during one-half cycle of the applied stress, i.e., 10^{-5} sec. On assuming a vibrational frequency of 10^{13} sec^{-1} for a vacancy and the lowest activation energy, 70 kcal/mole for vacancy motion consistent with published work on Al_2O_3,[9] one gets an average jump frequency for vacancies of about 7×10^5 sec^{-1}. During one-half cycle of applied stress, the vacancies can move on the average only about 3 lattice distances. For this to account for the observed damping there would have to be about one vacancy per every 10 atoms near the dislocation. This is an unreasonably high value.

As mentioned, the dislocations might exist in sapphire as extended dislocations composed of four quarter partial dislocations separated by stacking faults. Although this has not been experimentally observed in Al_2O_3, it has been observed in structurally similar talc.[10] It is possible to increase the width of the stacking fault between the partial dislocations by applying an external stress in the proper direction. If there were some impediment to the motion of the partials so as to get phase differences between the applied stress and the motions, internal friction would result.

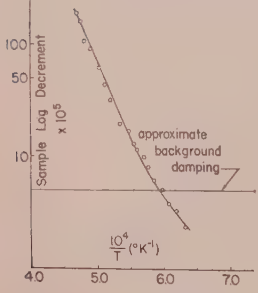

FIG. 13. Arrhenius plot of internal friction data for sample deformed near 1900°C in an oxygen-gas flame.

An upper limit for the damping to be expected from the model of half dislocations described by Cottrell[11] may be calculated by the following procedure.

The force between two partial dislocations is

$$F=(k_1/r)-\epsilon, \tag{5}$$

where ϵ is the stacking fault energy per unit area, r is the separation of the partials, and k is a constant. When no externally applied stress is present, the separation is given by

$$(k_1/r_1)-\epsilon=0. \tag{6}$$

If a stress σ is applied, the separation increases to r_2, where

$$(k_1/r_2)-(\epsilon+k_2\sigma)=0. \tag{7}$$

The constant k_2 is determined by geometry and the Burgers vector of the partial dislocations. The increase in separation of the partials is

$$\Delta r=k_1/\epsilon-k_1/\epsilon(1+k_2/\epsilon\sigma), \tag{8}$$

and if $k_2\sigma\ll\epsilon$, which it must be for this discussion to be valid,

$$\Delta r=k_1k_2\sigma/\epsilon^2. \tag{9}$$

By assuming that all of this motion takes place at a stress equal to the maximum, it follows that the largest log decrement possible is

$$\delta_m=2\mu Nk_1k_2^2/\epsilon^2. \tag{10}$$

As given by Cottrell $k_1=\mu a^2/24\pi$ and $k_2=a/2\sqrt{6}$. On assuming $\epsilon=20$ ergs/cm² and using values of the other constants appropriate to corundum, it follows that

$$\delta_m\cong10^{-3}. \tag{11}$$

If all conditions were proper, this model might possibly account for measurable damping.

However, in order for the work done in increasing the separation to be unrecoverable, there must be a dragging mechanism. The result is a relaxation mechanism with a characteristic relaxation time.

The observed high temperature damping increases in corundum appears to be thermally activated. Therefore, $\tau^{-1}=\nu=\nu_0\exp(-Q/k\tau)$. To estimate the temperature of the relaxation peak at 50 kc/sec, take $Q=8$

---

[9] G. C. Kuczynski, *Kinetics of High Temperature Processes* (John Wiley & Sons, Inc., New York, and The Technology Press of MIT, Cambridge, Massachusetts, 1959), Discussion, Chap. 20–24, p. 197.

[10] S. Amelinckx, Phil. Mag. 5, 533–535 (1960).

[11] A. H. Cottrell, *Dislocations and Plastic Flow in Crystal* (Clarendon Press, Oxford, 1953), p. 53.

al/mole and set $\nu=10^5$ sec^{-1} in this equation. A asonable upper limit for ν_0 is 10^{13} sec^{-1}. This gives the mperature of the peak to be $T=2180$°K.

This assumed value of $\nu_0=10^{13}$ sec^{-1} predicts the istence of a damping peak near the highest tempera- re in this experiment. This is not observed. Assuming e lower and more reasonable value, $\nu_0=10^{11}$ sec^{-1}, ves $T=2900$°K. This temperature is too high for the served increase in damping to be the beginning of a eak centered on it. The damping at 2100°K is already e maximum expected from this model.

The foregoing considerations make it appear very nlikely that the observed damping is caused by a ress induced increase in the separation of partial islocations. It is possible, though, that in some crystals which dislocations exist as partials a relaxation peak used by this mechanism might exist.

If the observed damping is the beginning of a Bordoni eak as expected from thermally activated motion over eierls barriers, essentially all of the dislocation line the crystal must be along close packed directions nd be strongly pinned in a relatively few places. This llows from the fact that essentially all of the disloca- ion line must move an average of at least one lattice istance to account for the damping. It seems quite nprobable that the dislocations produced by plastic eformation in these impure crystals are arranged in uch an orderly manner.

Roger Chang[2] has reported the possible existence of Bordoni peak at high temperatures in the internal riction data for Al_2O_3. He observed a peak of relaxation trength about 5×10^{-4}, having an activation energy f 60 kcal/mole in low frequency experiments. The peak s centered on 1450°C at 11 cps on 1570°C at 44 cps.

On the assumption that τ_g the relaxation time as- ociated with Chang's data follows an Arrhenius equa- ion, the peak reported by him would be near 3000°C t 50 kc/sec. Therefore, one would not expect to see his peak in the experiment reported here. The ac- uracy was such that a damping peak of 5×10^{-4} could e resolved below 1750°C. Such a peak was not bserved.

It seems clear that if dislocations are involved in the amping reported here, they must move at least one attice constant in one cycle at temperatures near 800°C. From this, it may be concluded that the ordoni peak occurs below 1800°C at 50 kc/sec, if it xists in the structures studied here. Such a peak might e absent in the present study for one or more of the llowing reasons:

(a) Damping in the thermal gradient in the sapphire uffer rod might be sufficient to wash it out.

(b) The large observed damping in deformed samples might arise from dislocations which are not aligned in Peierls troughs, while the sensitivity of our machine does not allow the observation of those which do have appropriate crystallographic orientation.

The remaining mechanism and the most probable is the dragging mechanism. This model pictures the dislocation motion as being hindered by pinning points being dragged along by diffusion, by an atmosphere of pinning points throughout the crystal, or by the necessity of continued breaking of interatomic bonds caused by the core structure of the dislocation.[12]

The activation energy Q' for motion by this mechanism is stress dependent.

$$Q'=Q\pm lb^2\sigma, \tag{12}$$

where l is the mean distance between dragging points. Accordingly the variation of internal friction with temperature and stress will be given by the following.

The form of the stress dependent activation energy effectively puts a bias on the vibrating dislocation favoring jumps in one direction. The net strain rate ϵ due to this is

$$\dot{\epsilon}=K\nu[\exp(-Q/kT)][\exp(\sigma b^2l/kT)-\exp(-\sigma b^2l/kT)]. \tag{13}$$

The internal friction is approximately

$$\delta=\sigma\dot{\epsilon}/(\sigma\epsilon f/2)=2\dot{\epsilon}/f\epsilon, \tag{14}$$

where f is the frequency of vibration. If $\sigma b^2l/kT<1$, a condition which has been assumed to hold throughout this discussion, we get

$$\delta=[2K\nu/f][\exp(-QkT)][\mu b^2l/kT]. \tag{15}$$

In Eqs. (13) and (15) K is a constant determined by the properties of the crystal under consideration, the pinning mechanism, dislocation density, etc. This equation predicts strain amplitude independent internal friction.

A detailed analysis of the internal friction would depend upon more knowledge of the interactions between dislocations and other imperfections. Further studies of the effects of controlled amounts of impurities, the effect of much higher strain amplitudes, the frequency dependence of the damping, studies of the core structure of the dislocations, and the extent of dissociation into partial dislocations are needed.

---

[12] H. G. Van Bueren, Physica **24**, 831–837 (1958).

JOURNAL OF APPLIED PHYSICS VOLUME 32, NUMBER 12 DECEMBER, 19

Momentum and Energy of Waves

J. R. Pierce
Bell Telephone Laboratories, Murray Hill, New Jersey

(Received February 27, 1961)

Elementary arguments of conservation of energy and momentum are used to derive expressions for what Sturrock terms the "formal" momentum, angular momentum, and energy of a plane wave in a moving medium. If E is the energy per unit length, p the momentum per unit length, q the angular momentum per unit length, v_f the phase velocity, and if the angular variation of a circulatory polarized wave is as $\exp(-jn\theta)$,

$$p=E/v_f,$$
$$q=nE/\omega.$$

If E_0 is the energy per unit length observed moving with the medium, and then if the medium moves past the observer with a velocity u and the observer measures a phase velocity v_f, he observes an energy per unit length E,

$$E=E_0/(1-u/v_f).$$

When p, q, and E are not the physical momenta and energy, they lead to the correct power and force for sinusoidal sources moving with respect to the medium.

1. INTRODUCTION

The linear and angular momenta of waves have obvious usefulness in quantum mechanics in which phonons and quasi-particles exhibit the momenta we are accustomed to in photons and material particles.

Momentum can be useful also in connection with classical electromagnetic and acoustic waves although many books on physical acoustics make little or no mention of momentum. Thus, the behavior of the traveling-wave parametric amplifier can be understood in terms of the conservation of momentum and energy.[1]

One advantage of dealing with energy and momentum is that results apply to both electrical and mechanical systems—to any systems, in fact, in which a wave can be assigned energy and momentum. Thus, it is desirable to obtain simple relations concerning energy, power, and momentum, and their conservation.

Such relations are primarily useful in dealing with the external properties of nonlinear systems when they are acted upon by small signals and behave in an approximately linear manner. Such systems include electron beams, plasmas, and systems supporting mechanical waves. A typical problem is that of the coupling of waves in an electron beam to electromagnetic waves in a traveling-wave tube.

One approach is to work with small-signal solutions of the actual nonlinear differential equations of the system. L. R. Walker has done this in connection with waves on electron streams.[2] Such a treatment yields useful externally observable quantities such as field, force, current, and power. It also yields expressions valid to a particular power in a series expansion for physical quantities such as particle displacement and momentum. These internal quantities can be properly related to external quantities.

An entirely different approach is possible if the system does indeed behave like a linear system at low sign levels. One can deal entirely with a *hypothetical* syste in which an appropriate number of the variables (suc as electric field, magnetic field or current, convectio current, and ac velocity) are related by exactly line equations which are obtained by linearizing the no linear equations which relate these selected variables i the actual physical system.[3] This saves considerabl mathematical pain. One simply asserts that, if at lo signal levels the actual nonlinear system behaves e ternally as if it were linear, then in its interactions wit other systems it can be replaced by a truly linear syste which obeys linear equations exactly. We must r member, however, that when we have done this w cannot use the solutions of the linear equations relatin the selected variables to obtain correct second-ord values for all quantities describing the original nonlinea system (including, for instance, particle positions an momenta).

We can go further and seek any quantities which, i connection with the external properties of the trul linear system, exhibit behavior like that of such servic able quantities as momentum and energy per uni length, without demanding at all that such quantiti can be identified with the momenta or energies of pa ticular parts of the original nonlinear system. It is suc quantities that Sturrock has found by means of th Lagrangian function.[4] The energy and momentum h arrives at are consistent with external behavior, bu they do not always correspond to the actual physic energy and momentum. Hence, Sturrock calls them th *formal* energy and momentum.

It is, of course, important to know under what ci cumstances such quantities are valid and useful. In pr ceeding from the Lagrangian function one could for the actual nonlinear stress tensor and select the quad ic parts; this should lead to actual physical mo- enta. Or one could retain only the quadratic parts of e Lagrangian and form the stress tensor from them; is should lead to "formal" quantities. Sturrock dis- sses this matter,[5] which is beyond my ken.

---

[1] J. R. Pierce, J. Appl. Phys. **30**, 1341–1346 (1959).

[2] L. R. Walker, J. Appl. Phys. **25**, 615–618 (1954); **26**, 1031–1033 (1955).

[3] J. R. Pierce and W. H. Louisell, Proc. Inst. Radio Engrs. 4 425–427 (1955).

[4] P. A. Sturrock, J. Appl. Phys. **31**, 2052–2056 (1960).

Sturrock says that the formal energy and momentum e valid and useful for systems which are describable terms of a quadratic Lagrangian function.[4] In this per the writer derives expressions for formal energy d momentum from elementary considerations of con- rvation of energy and momentum. The results agree th those of Sturrock. They are found necessarily to ply to systems excited by a sinusoidal source moving th respect to the medium. In particular cases not eeting these criteria, the formal momentum does not ve the correct force on the source (or sink) of the wave. he author leaves the interpretation of Sturrock's cri- rion in particular cases such as these to wiser men an he.

2. MOMENTUM OF A PLANE WAVE IN A LINEAR MEDIUM

A plane wave is taken as one in which the variation all quantities in some direction z, called the direction propagation, is $\exp(-j\beta z)$. The variations along her axes may be any functions of x and y which are dependent of z.

If we consider a wave packet made up of a narrow nge of β, if E is the energy per unit length (or per unit lume), the power P must be [6]

$$P=Ev_g, \tag{2.1}$$

$$v_g=(\partial\beta/\partial\omega)^{-1}, \tag{2.2}$$

may be power or power per unit area; v_g is the group locity.

Similarly, if p is the momentum per unit length (or r unit volume), the momentum flow b must be

$$b=pv_g. \tag{2.3}$$

Let us now consider a linear medium capable of sup- rting a wave, indicated by the horizontal band in g. 1. Suppose that a wave of constant amplitude is ing set up by a discontinuity moving to the left with velocity u. Suppose that to the left of this discon- uity there is no wave; to the right a wave of constant plitude travels with a phase velocity v_f and a group locity v_g.[7] Wave velocities and other directed wave antities will be considered positive if the direction is the right.

There are two sources of energy, the force F which ives the discontinuity to the left and the power P_1 supplied by a generator moving with the discontinuity. We will imagine that the medium is dispersive and has a monotonic variation of β with frequency; this makes it easy to see that we can set up just one wave of one frequency, for in this case the wave velocity and frequency will match the power source P_1 at one frequency only.

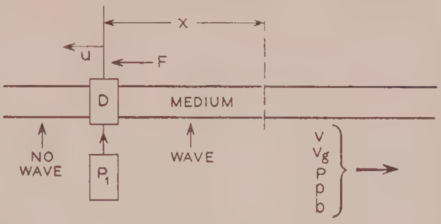

FIG. 1. A wave set up in a medium by a source of power P_1 moving to the left with a velocity u.

Let us now apply the conservation of energy. The stored energy between the moving generator and some fixed reference point a distance x away from the moving generator is

$$Ex=xP/v_g. \tag{2.4}$$

The rate of change of this stored energy is

$$(P/v_g)dx/dt=Pu/v_g. \tag{2.5}$$

We see that this must equal the power supplied less the power flowing to the right past x.

$$\begin{aligned} Pu/v_g&=P_1+Fu-P,\\ P[(u/v_g)+1]&=Fu+P_1. \end{aligned} \tag{2.6}$$

If we apply the conservation of momentum in a similar manner we obtain

$$b[(u/v_g)+1]=-F. \tag{2.7}$$

For particles and for plane electromagnetic waves momentum flow is proportional to power. One of the assumptions that we shall make is that for a particular frequency (and hence, for a particular group and phase velocity), momentum flow b is proportional to power P by a factor a. The factor a is intrinsic to a particular frequency and hence cannot depend on the velocity of the source. Thus, we write

$$b=aP. \tag{2.8}$$

From (2.6)–(2.8),

$$P[(u/v_g)+1](1+au)=P_1. \tag{2.9}$$

If the discontinuity moves with the phase velocity of the wave, the frequency of the moving source is zero. The discontinuity can set up the wave with no power P_1 from the source. In simple cases, a moving charge or magnet can set up an electromagnetic wave in a circuit, and a moving transverse pressure can set up a wave in a stretched string in this fashion. Thus, we let

$$v_f=-u \tag{2.10}$$

$$P_1=0, \tag{2.11}$$

---

[5] P. A. Sturrock, Phys. Rev. **121**, 18–19 (1961).

[6] J. W. S. Rayleigh, *The Theory of Sound* (MacMillan and mpany, Ltd., London, 1894), Vol. 1, Appendix.

[7] In the case of a transmission line, a unidirectional excitation be attained by using two separated sources which are properly ased, or by properly relating the series voltage and shunt rent of the source. Similar means appear to be effective in er cases.

We see that (2.9) can be satisfied only if

$$v_f = v_g \qquad (2.12)$$

or

$$a = 1/v_f. \qquad (2.13)$$

Condition (2.12) will be met in special circumstances only; we conclude that (2.13) must hold, so that the momentum flow b and the momentum per unit length p are

$$b = P/v_f \qquad (2.14)$$

$$p = P/v_f v_g = E/v_f. \qquad (2.15)$$

Relation (2.15) corresponds exactly to that which one obtains from equations (10) of a paper by Sturrock that was cited earlier.[4] Both apply to propagation in any direction in which a wave is a plane wave. Sturrock designates the phase constant for the r direction by k_r, and in our notation his relation would be

$$p_r = Ek_r/\omega. \qquad (2.16)$$

In the derivation of (2.14) and (2.15) any variation of the plane wave in directions normal to the direction considered could be ignored.

We should note that the derivation of (2.14) and (2.15) depends on motion of the source (or sink) of the wave. If we let $u=0$, then (2.6) tells us merely that the power in the wave is the power in the wave, and (2.7) tells us merely that the momentum flow is equal to the force.

There is a simple physical example in which the formal momentum is not equal to the momentum of the moving particles of the medium, and in which the formal momentum does not give the correct force on a source which is stationary with respect to the medium. Imagine that the medium consists of a number of physical oscillating bodies constrained to move normal to the direction of propagation; the little circles of Fig. 2 represent these oscillators. A moving discontinuity in the form of a frictionless sloping spring guide can be used to set up a wave in this system, as illustrated. The discontinuity experiences a longitudinal force in setting up the wave; it would experience an equal and opposite force if it were moved backward in such a way as just to destroy the wave.

If the medium moves past a fixed discontinuity, the same force is observed, a force which corresponds to the formal momentum of the wave. Yet the oscillating oscillators of themselves have no longitudinal momentum. In exciting the oscillators the source exerts a longitudinal force on whatever medium constrains the oscillators to motion normal to the direction o propagation.

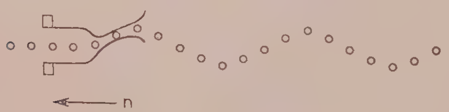

FIG. 2. A moving discontinuity setting up a wave.

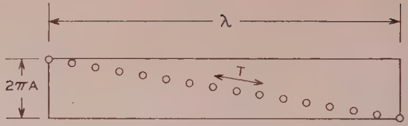

FIG. 3. Development of a wave consisting of a helical displacement of amplitude A.

A wave in such a medium cannot be excited by single source which does not move along the medium However, if we connect the oscillators with a string o tension T, the wave then has nonzero group velocit and power and can be excited by a fixed source.

Such a medium will support a right-handed or left handed circularly polarized wave in which the oscillator all lie on a helix. Let us develop the cylinder containin the helix along which the oscillators lie, as shown i Fig. 3. Let A be the displacement of the oscillators from the axis. For linear behavior we must have

$$2\pi A \ll \lambda. \qquad (2.17$$

The power P will be the circumferential driving forc times the angular velocity; when (2.17) holds,

$$P = \beta\omega T A^2. \qquad (2.18$$

The component of the tension in the z direction T will be, when (2.17) holds,

$$T_z = T - (1/2)(P/v_f). \qquad (2.19$$

The only force due to the excitation of the wave whic is exerted on the fixed source is the force $P/2v_f$ due t the reduction of tension. If the formal momentum flow gave the correct force on a fixed source, the force woul have to be P/v_f. The formal momentum is a usefu quantity only in connection with sources which mov with respect to the medium.

In plane electromagnetic waves and longitudinal sound and plasma waves, however, the "physical" mo mentum which gives the force on a fixed reflector o absorber is also the momentum as given by (2.14 or (2.15).

It is of interest to consider another example i which the blind use of formal momentum would lea to an incorrect result. If we move along and give each oscillator of Fig. 2 an appropriate sharp transverse ta by means of a smooth plane surface parallel to th direction of motion, we can create or destroy a wav without exerting any longitudinal force.

In this excitation by sharp blows, many frequencies are present in the source, while we assumed earlier a continuous process involving only the frequency ω o the wave and its frequency ω_1 as observed at the moving source, which is related to ω by

$$\omega/\omega_1 = v_f/(u+v_f) = (1+u/v_f)^{-1}. \qquad (2.20$$

note [from (2.6)] that the total rate of production power at frequency ω, which we will call P_ω, is

$$P_\omega = P[1+(u/v_g)]. \tag{2.21}$$

om (2.9), (2.13), and (2.20) we see that

$$P_\omega/\omega = P_1/\omega_1. \tag{2.22}$$

is is the Manley-Rowe relationship which should ply in the case of a lossless frequency conversion ocess.

We see that in deriving relations (2.14) and (2.15) ich give a formal momentum useful in many prob- ns we have made a number of assumptions:

(a) We have assumed a moving source.

(b) We have assumed a conservative linear system which the only time variation allowed is sinusoidal. e frequency depends on whether the oscillation is served at a fixed point or at the moving discontinuity.

(c) We have assumed that for a given wave at a ven frequency the momentum is proportional to the wer.

3. POWER AND ENERGY OF WAVES IN MOVING MEDIA

Let us add subscripts o to all the wave velocities in pressions (2.9), (2.13), and (2.1). We obtain for the ergy per unit length E_o

$$E_0 = \frac{P_1}{v_{g0}(u/v_{g0}+1)(u/v_{f0}+1)}. \tag{3.1}$$

et us now make a Galilean transformation into a co- rdinate system attached to the source of power P_1; this system the group and phase velocities will be lled v_f and v_g. The energy per unit length E, which given by P_1/v_g, will be, as Sturrock points out,

$$E = \frac{E_0}{1-u/v_f}. \tag{3.2}$$

The energy E_o per unit length for a wave, as evalu- ted by an observer who sees the medium as fixed with spect to himself, is always positive. Thus, from (3.2), the phase velocity of a wave in a moving medium is ss than the velocity of the medium, the energy per nit length must be negative. Further, if we wish to now explicitly the formal energy of a wave in a moving edium, we need merely to compute the energy as bserved moving with the medium and use (3.2).

It is a simple matter to show that in the case of ngitudinal space-charge waves this leads to the result iven by Chu in 1951.[3]

4. ANGULAR MOMENTUM

Let us consider the excitation of a circularly polarized ave by a moving couple C. Relations (2.9) and (2.13) are general relations which apply to this as to other cases. If the circularly polarized wave varies as $\exp(-jn\theta)$, where θ is the angle about the axis, the angular velocity $\dot{\theta}_1$ as seen by the moving couple is

$$\dot{\theta}_1 = (\omega/n)[1+(u/v_f)]. \tag{4.1}$$

The power P_1 supplied by the couple is

$$P_1 = C\dot{\theta}_1 = C(\omega/n)[1+(u/v_f)]. \tag{4.2}$$

From (2.9). (2.13), and (4.2) we obtain

$$C = P(n/\omega)[1+(u/v_g)]. \tag{4.3}$$

If g is the angular momentum of the wave per unit length, we see that the moving couple must produce angular momentum at a rate $q(u+v_g)$. Thus from (4.3) we see that the angular momentum per unit length must be

$$q = nP/\omega v_g. \tag{4.4}$$

S. P. Morgan kindly computed for the writer the angular momenta of waves of various orders in a circular cyclindrical waveguide and obtained just this result.

We can see that (4.4) also agrees with the case of the system of oscillators coupled by a string of tension T which was discussed in Sec. 2. The power P fed into such a system is the couple driving it times the angular velocity ω; the rate of transfer of angular momentum to it is the couple; hence, the angular momentum per unit length q must be given by $P/\omega v_g$.

We should note that, like the linear momentum and the energy, the formal angular momentum may not correspond to a physical momentum. For instance, assume a circular cylindrical array of confined rods which can transmit longitudinal waves only. If the array is excited by a cam which produces a circularly polarized longitudinal motion, a torque will be exerted on the rotating cam, and the magnitude of this torque will be given by the formal angular momentum q of (4.4).

5. DISCUSSION

A simple explanation of the negative energy of the slow longitudinal space-charge wave in an electron beam is that the charge density is highest in regions of less than average velocity. Transverse waves act as if they had negative energy,[8,9] and yet a transverse velocity component due to a wave cannot decrease the net longitudinal particle velocity. Concerning this, Sturrock remarks[4]:

"It is commonly believed that the negative-energy attribute of slow waves is peculiar to systems in which the vibratory motion is parallel to the dc velocity. The instability of [a transverse wave] system lends

---

[8] H. H. Haus and D. L. Bobroff, J. Appl. Phys. 28, 694–704 (1957).

[9] J. W. Kluver, J. Appl. Phys. 29, 618–622 (1958).

weight to the belief that slow waves in a moving medium capable of transverse vibrations again has negative energy in some sense, although one can see that the physical energy of such a system must be positive. . . . Pierce has stated that 'an analysis shows that when a torsional wave is coupled purely by couples about the axis to the slow torsional wave on a parallel rod moving axially with respect to the first, no gaining wave results.' . . . If . . . one looks for the resolution of this paradox within the framework of the small-amplitude energy theorem, one is led to conjecture that the mathematical model considered by Pierce was not a valid model of a dynamical system in that the equations were were not derivable from a Lagrangian function."

The writer surmised earlier[10] that, in the case of torsional waves, growing waves might be explained by "longitudinal forces associated with the coupling (to the exciting source—in this case another wave)." It appears that in the excitation of sinusoidal waves in any physical system by any source which moves with respect to the medium and which exerts sinusoidal and steady forces only (and not a sequence of blows, as discussed in Sec. 2) certain longitudinal forces are always present. These are just the forces prescribed by the formal momentum. These forces are necessary if we are to have waves which exhibit the phenomenon of negative energy and which lead to growing waves.

---

[10] J. R. Pierce, J. Appl. Phys. 25, 179–183 (1954).

JOURNAL OF APPLIED PHYSICS VOLUME 32, NUMBER 12 DECEMBER, 196

Magnetic Domain Patterns in Cr-Modified Mn_2Sb

J. D. Wolf and J. E. Hanlon
Engineering Research Laboratory, Engineering Department, E. I. du Pont de Nemours & Company, Wilmington, Delaware

(Received November 11, 1960; in final form August 11, 1961)

The relationship between microstructure and the magnetic properties of Cr-modified Mn_2Sb has been studied using the Bitter pattern technique. The solid solution formed when Cr is substituted for Mn in Mn_2Sb exhibits a ferrimagnetic to antiferromagnetic first order phase transformation which occurs at about room temperature for 5 at.% Cr. In the transformation temperature range, we have followed the initiation and growth of the ferrimagnetic phase by observing the associated domain patterns. In addition, the Bitter pattern technique has been used to examine precipitates with magnetic properties differing from the matrix.

INTRODUCTION

In this article, we discuss the use of the Bitter pattern technique[1] to study the magnetic transition and microstructure of chromium-modified Mn_2Sb. Mn_2Sb has the Cu_2Sb tetragonal crystal structure, is ferrimagnetic with a Curie temperature of 277°C, and has a saturation magnetization corresponding to one Bohr magneton per Mn atom.[2] Chromium-modified Mn_2Sb exhibits a ferrimagnetic to antiferromagnetic first-order phase transformation, without change in crystal symmetry.[3] The transformation temperature varies directly with Cr concentration.

As the temperature is raised into the transition range, the solid solution transforms from antiferromagnetic to ferrimagnetic, and magnetic domains appear which can be observed by Bitter patterns. We thus can follow the initiation and growth of the magnetic phase. In addition, the phases in the microstructure with magnetic properties differing from the matrix are distinguishable.

EXPERIMENTAL PROCEDURE

The samples used in the present investigation wer prepared by melting a mixture of the elemental powder in a recrystallized alumina crucible under an argo atmosphere. The single crystals studied were grow from the melt by the Czochralski method. The polycrystalline slugs or single crystal boules were rough-cut, mounted in Bakelite, and polished. The final surfac finish was obtained by alternately etching with a 5% bromine-ethanol solution and polishing on a Linde I wheel, until no disturbed metal was observed unde metallographic examination at 250 ×.[4] The colloida suspension of magnetite was prepared according to th recipe of W. O. Baker and F. H. Winslow.[5]

In an experimental run, a few drops of colloid wer placed on the polished sample surface which then wa covered with a microscope cover glass. The sampl temperature could be varied continuously betwee 0° and 40°C by either chilling with ice or heating with all Constantan coil mounted on the sample assembly. e sample temperature was measured by a copper-nstantan thermocouple imbedded in the Bakelite se to the exposed surface. A Reichert metallograph s used to observe the Bitter patterns, which arise m the segregation of colloid to domain walls and gnetic interphase boundaries. A magnetic field was plied to the specimen while under observation in ler to observe which parts of the structure were bile.

---

[1] F. Bitter, Phys. Rev. 38, 1903 (1931).

[2] Charles Guillard, thesis, University of Strasbourg, 1943, Chap. III.

[3] T. J. Swoboda, W. H. Cloud, T. A. Bither, M. S. Sadler, and H. S. Jarrett, Phys. Rev. Letters 4, 509 (1960).

[4] G. L. Kehl, *The Principles of Metallographic Laborator Practice* (McGraw-Hill Book Company, Inc., New York, 1943 2nd ed., p. 46ff.

[5] C. Kittel and J. K. Galt, *Solid State Physics*, edited by F Seitz and D. Turnbull (Academic Press Inc., New York, 1956 Vol. 3, p. 493.

RESULTS AND DISCUSSION

When the Mn concentration exceeds the solubility nit in Mn_2Sb, the Mn–Sb phase diagram[6] indicates at an eutectic distribution will appear in the micro-ructure. Mn-poor samples will contain ferromagnetic nSb as a second phase. If the Mn_2Sb sample is pre-red by nonequilibrium techniques, both the MnSb ase and the eutectic may be present.

In Fig. 1, a photomicrograph of a Bitter pattern of n_2Sb is shown. The sample is a Czochralski-grown ystal with the eutectic constituent lying on (001) anes. The habit plane of the eutectic was established optical examination of samples with various orien-tions. In this figure the eutectic appears as horizontal ingers. The easy direction of magnetization, the *c* is, is in the plane of the photograph. The columnar pattern in Fig. 1 was identified as a magnetic domain structure since it changed shape in an applied magnetic field. The domain walls could be moved easily by the 100-gauss field of a small permanent magnet. The magnetic energy at the eutectic is reduced by fingers of reversal domains. Consistent with the large anisotropy energy of Mn_2Sb,[3] we have never observed closure domains with magnetization along an a axis.

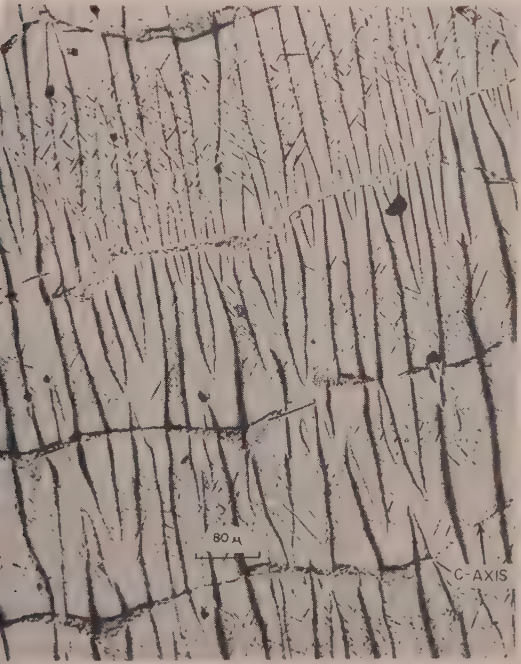

FIG. 1. Magnetic domains in Mn_2Sb oriented with the *c* axis parallel to the sample surface.

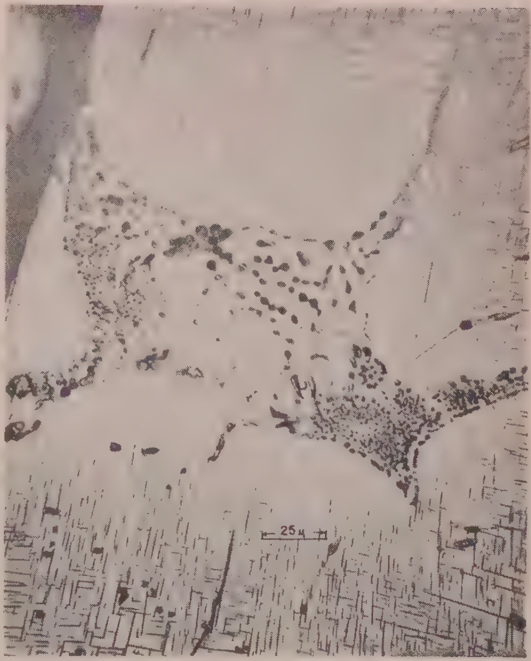

FIG. 2. Microstructure of Mn_2Sb, etched.

The cross-hatched fine structure in the background was stationary in the presence of an applied magnetic field of about 1000 gauss, and was tentatively attributed to a magnetic second phase. To test this hypothesis, another specimen from the same boule was polished exposing an (001) plane and chemically etched to reveal optically the presence of the suspected second phase. Figure 2 is a photomicrograph of the etched specimen. At high magnification, the eutectic is seen to consist of Mn dispersed in a continuous Mn_2Sb matrix. A cross-hatched precipitate is apparent with many of the features of the magnetic second phase exhibited in Fig. 1. The precipitate stops short of the eutectic and is therefore probably incompatible with it. An x-ray investigation established that the habit planes of this precipitate are (101) and equivalent planes.[7] Since the only other magnetic phase known in the Mn-Sb system is the compound MnSb, which should not be present near the eutectic, we associate the cross-hatched structure in this specimen with a solid-state precipitate of

---

M. Hansen, *Constitution of Binary Alloys* (McGraw-Hill Book mpany, Inc., New York, 1958), p. 951.

[7] J. J. Cox (private communication).

MnSb. The thin needles emanating from the eutectic region are thought to be mechanical twins.

In several specimens which were low in manganese content, large globular particles were continuous with the cross-hatched precipitate, and so were the same phase. These massive particles exhibited a domain structure below the matrix transformation temperature, thereby providing additional evidence that they and the cross-hatched precipitate are MnSb.

Figure 3 is a sequence of Bitter patterns which shows the appearance and growth of the magnetic phase in $Mn_{1.9}Cr_{0.1}Sb$. The magnetization versus temperature plot for this sample is given in Fig. 4, showing the temperature at which the photomicrographs of Fig. 3 were taken. It will be noted that the cross-hatched MnSb phase is more easily resolved at the beginning of the transformation when the matrix is nonmagnetic.

The photomicrograph, Fig. 3(a), is a view of an eutectic region below the transition range. The only part of the matrix which is ferrimagnetic at 2°C is in the vicinity of eutectic patches. In all specimens studied, the transformation was observed to initiate at the eutectic. The amount of MnSb present accounts for the residual magnetization below the transition range. In Fig. 3(b), the sample is about $\frac{1}{3}$ of the way through the magnetic transition. The domains have grown out from the eutectic. In Fig. 3(c), we see the same region $\frac{2}{3}$ of the way through the transition. The matrix at large distance from the eutectic is still nonmagnetic. The fully transformed specimen is shown in Fig. 3(d). The magnetic transformation has also been studied using time-lapse photography. The time-lapse motion pictures show that the magnetic transformation proceeds continuously from the eutectic areas into the surroundin matrix. One possible explanation for this behavior that the manganese particles in the eutectic scaveng chromium, leaving the adjacent matrix Cr-poor. Th transition temperature in these areas would thus b lowered.

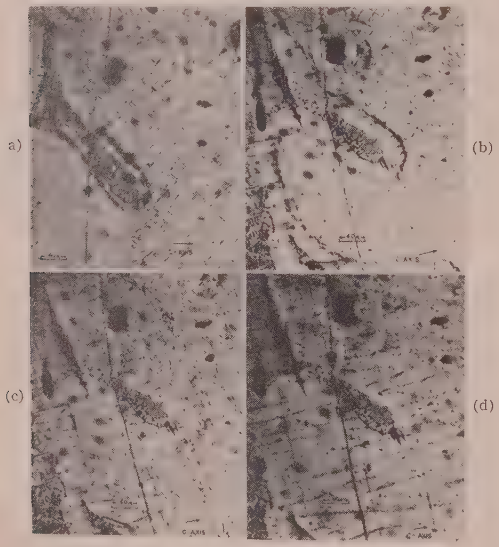

FIG. 3. Sequence of Bitter patterns showing the ferrimagnetic-antiferromagnetic transformation.

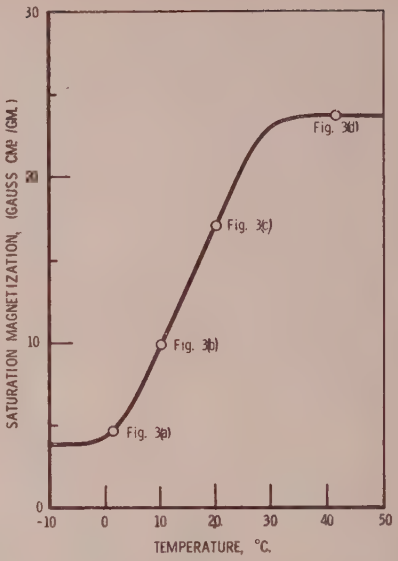

FIG. 4. Saturation magnetization versus temperature for the sample of Fig. 3.

Subsequent electron probe measurements[7] hav shown that the cross-hatched phase has the compositio MnSb and also that there is a deficiency of chromiu in the neighborhood of the eutectic. This evidence is i agreement with out interpretation of the Bitter patter and the microstructure.

CONCLUSIONS

The Bitter pattern technique has been used to investigate the effect of minor phases on the ferrimagnetic antiferromagnetic transformation in Cr-modifie Mn_2Sb. It was concluded that the transformatio initiates at eutectic areas, because of Cr segregatio and proceeds into the surrounding matrix. The Bitte pattern technique supplied supporting evidence for th identification of a precepitated phase of MnSb.

ACKNOWLEDGMENTS

The authors are indebted to Dr. J. J. Cox for preparing the samples used in the present investigation an for informing them of the electron probe results. W also wish to acknowledge T. J. Hartz for his valuabl technical assistance and F. J. Darnell for helpfu discussions.

JOURNAL OF APPLIED PHYSICS VOLUME 32, NUMBER 12 DECEMBER, 1961

Growth from the Melt. III. Dendritic Growth

G. F. Bolling and W. A. Tiller
Westinghouse Research Laboratories, Pittsburgh, Pennsylvania

(Received March 20, 1961)

A mathematical treatment of steady-state dendritic growth from pure and alloy liquids has been developed for isothermal and nonisothermal dendrites. The velocity of dendritic growth, dendrite size, dendrite direction, and the alloy content of the dendrite have been calculated as a function of the bath supercooling, the alloy content of the bulk liquid, and the atomic kinetics of the material. To specify the problem completely it was necessary to choose some "optimization" condition. We have chosen the condition of "maximum velocity." Comparison of the theoretical predictions with experimental data for pure nickel, tin, and ice, and for KCl and acetic acid solutions have been made. Satisfactory agreement with experiment was found using the atomic mechanism of "uniform interface advance."

THE name "dendrite" has been given to the particular crystal morphology resembling a tree that one observes so often in nature. Dendrites have been observed during growth from the melt, from liquid or solid solutions, from the vapor, and during electrocrystallization. Descriptions of dendritic growth in these instances have been given by Weinberg and Chalmers,[1–3] Schlipf,[4] and Graf[5] for growth from the melt; by Papapetrou[6] for growth from liquid solutions; and by Wranglen[7] for growth during electrocrystallization. These investigations have enabled us to understand, in a qualitative sense, the basic phenomena associated with dendritic growth. We believe that it is now advantageous to examine this understanding from a quantitative view point and will attempt to do so here.[8]

Our aim is threefold; and, while we limit ourselves to growth from the melt, the general approach used can be extended to other growth media. First, we will establish why a dendrite forms. Second, we will examine the characteristics of a dendrite, such as shape, size, growth rate, and crystallographic orientation. Finally, we will study the consequences of dendritic growth, such as redistribution of the solute present in the melt, as the treatment proceeds.

I. FORMATION OF DENDRITES

There is a tendency for dendritic growth whenever the difference in Gibbs' free energy between the nutrient phase and the solid, $\Delta G = G_n - G_s$, is positive and increases with distance ahead of the solid-liquid interface. In a pure melt the dendritic morphology can develop into the major growth morphology only if the gradient of temperature in the liquid is negative at the interface. For alloy liquids it is possible to develop the dendritic morphology with a positive temperature gradient in the liquid, provided the solute distribution is such that $d\Delta G/dx > 0$ at the interface, where x represents distance ahead of the interface.[9] The main characteristic of the solid that forms when the temperature gradient in the liquid at the interface is negative is that it possesses a tree-like growth form, having a trunk and branches of different order extending in unique directions relative to the crystallographic form of the material. It is under these conditions that one observes the true dendrite. In the case of the positive temperature gradient, one often observes indistinct branches on the trunk and no unique crystallographic direction for the dendrite axis.

To begin simply, we consider the initial growth development of a sphere of solid in a pure supercooled melt. In order to prevent confusion we will define the temperature differences to be used as follows: $\delta T = T_E - T_i$, interface supercooling; $\Delta T^* = T_i - T_\infty$, bath undercooling; $\Delta T = T_M - T_\infty$, bath supercooling. These various temperatures are shown in Fig. 1. T_M is the melting temperature of the pure bulk material, T_E is the "equilibrium" temperature (which is a function of the curvature of the solid-liquid interface and the solute concentration if solute is present), T_i is the interface temperature, and T_∞ is the bath temperature.

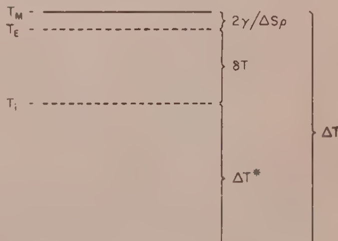

Fig. 1. Important temperatures involved in dendritic growth: T_M = melting temperature of pure bulk material, T_E = equilibrium temperature of the material (pure or alloy), T_i = interface temperature, and T_∞ = bath temperature.

---

[1] F. Weinberg and B. Chalmers, Can. J. Phys. **29**, 382 (1951).

[2] F. Weinberg and B. Chalmers, Can. J. Phys. **30**, 488 (1952).

[3] B. Chalmers, Trans. Am. Inst. Mining, Met., Petrol., Engrs. **200**, 519 (1954).

[4] J. Schlipf, Z. Krist. **107**, 35 (1956).

[5] L. Graf, Z. Metallk. **42**, 336 (1951).

[6] A. Papapetrou, Z. Krist. **92**, 89 (1935).

[7] G. Wranglen, Acta. Chem. Scand. **9**, 661 (1955).

[8] It was drawn to our attention after completing this paper that an elegant mathematical analysis has been recently given for needle-shaped crystal growth by Temkin.[29] Since some of this treatment is parallel in reasoning and similar in general to the method used in description of the non-isothermal dendrite, similar conclusions in this area may be inferred from Temkin's treatment. Appendix III has been added for comparison of methods and results, and otherwise no reference has been given to this work in the completed text.

[9] W. A. Tiller and J. W. Rutter, Can. J. Phys. **34**, 96 (1956).

The temperature difference, δT, controls the rate of atomic deposition onto the solid, dependening upon the particular mechanism of deposition that is operative. For now, we may simply characterize a growth law as

$$V=f[\Delta G(0),\phi], \tag{1}$$

where $\Delta G(0)$ is the value of ΔG at the interface between solid and liquid; ϕ is a variable related to the orientation of the solid-liquid interface, and V is the velocity of growth at the interface normal to this orientation. For a pure material $\Delta G(0)=\delta T$; even for an alloy this is a good and useful approximation. The different functions, f, associated with the different atomic mechanisms will be discussed later.

The bath undercooling, ΔT^*, controls the rate of heat flow away from the sphere and, therefore, the rate of dissipation of latent heat into the bulk liquid. It subsequently controls the macroscopic freezing rate, V. We can see, therefore, that the interface temperature, T_i, must be at some value such that the atomic deposition rate given by Eq. (1) with the appropriate mechanism is equal to the macroscopic freezing rate determined by the heat transfer from the sphere.

Let us suppose that, apart from continued growth as a sphere, at some point in the growth process an asymmetry of shape appears which continues to grow until the sphere is just the core of a body with arms extending in specific crystallographic directions. The sphere could only have ceased maintaining its shape, in the absence of thermal fluctuations, for the following reason. A shape anisotropy would have developed with constant T_i if there were an anisotropic atomic deposition mechanism and/or an anisotropic surface free energy γ at the solid-liquid interface. Under the action of these influences, the spherical body would have elongated in certain directions, depending upon the specific anisotropy, in an ellipsoidal fashion. The ends of the elongated regions of the body would now be better shaped for the evolution of heat than the central regions so that the elongation would continue, and we have what may be called the core of a dendrite. This dendrite core might have also developed as a fluctuation phenomenon on the sphere. If a thermal fluctuation had occurred on the surface of the sphere to produce a protuberance, this point would have been better shaped for the evolution of heat than other regions on the sphere and would have continued to elongate. Once again rod-forms would have protruded from the sphere and propagated.

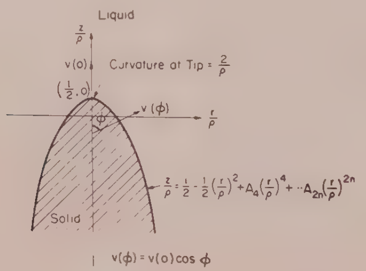
Liquid
$\frac{z}{\rho}$
$v(o)$
Curvature at Tip = $\frac{2}{\rho}$
$(\frac{1}{2},0)$
$v(\phi)$
ϕ
$\frac{r}{\rho}$
$\frac{z}{\rho}=\frac{1}{2}-\frac{1}{2}(\frac{r}{\rho})^2+A_4(\frac{r}{\rho})^4+\cdots A_{2n}(\frac{r}{\rho})^{2n}$
Solid
$v(\phi)=v(o)\cos\phi$

FIG. 2. Schematic illustration of a rotationally symmetric dendrite growing at velocity V in the Z direction.

A simple phenomenological explanation may thus be given for the formation of a dendrite core. The problem of dendrite direction will be examined after the characteristics of dendritic growth are investigated. However, since it is obvious from experiment that dendrites form in particular crystallographic directions, we may conclude that shape fluctuations will give rise to dendrites only if they are consistent with an anisotropy in the system. Similarly, we conclude that dendritic growth is evidence of an anisotropy of either γ or atomic kinetics.

II. DENDRITIC GROWTH CHARACTERISTICS

We will examine the axial freezing velocity, the thickness, and the crystallographic orientation of the dendrite core as a function of the bath supercooling, ΔT, for both pure and alloy melts; this latter has generally been the only experimental variable in the dendritic growth process apart from the purity of the material. A new variable is introduced into the process if one extracts the dendrite from the melt at some constant rate.[10,11] The present treatment will deal primarily with the case where the dendrite is not extracted from the melt although some of the differences that arise due to the introduction of this new variable will be considered in the discussion.

A quantitative description of these characteristics may only be developed if several simplifications are made. In addition, several assumptions are necessary in order to treat the problem at all. These simplifications and assumptions can be justifiably relaxed when the treatment is applied to real dendrites. However, in this section we will proceed in a stepwise fashion, introducing the concepts necessary for the description without at all times detailing them or referring to the limitations of the treatment. For example, we limit ourselves initially to the description of dendrites that have rotational symmetry; this will not be the case in general and would certainly not be the case for the dendritic growth of an anisotropic element such as bismuth. A critical discussion of such broad limitations and of the more particular items will be attempted later.

A. General Description of Ideal Dendrite

Consider a dendrite core with rotational symmetry growing in the axial direction at constant velocity V in an infinite bath as illustrated in Fig. 2. Let the density of the liquid and the solid be the same so that no fluid flow occurs as the dendrite propagates. Let the bath temperature and the bath concentration be

---

[10] E. Billing, Proc. Roy. Soc. (London) **A229**, 346 (1955).
[11] A. I. Bennett and R. L. Longini, Phys. Rev. **116**, 53 (1959).

T_∞ and C_∞, respectively. Let the dendrite core have the general shape

$$Z/\rho=\tfrac{1}{2}-\tfrac{1}{2}(r/\rho)^2+A_4(r/\rho)^4+A_6(r/\rho)^6 + \cdots A_{2n}(r/\rho)^{2n}, \quad (2)$$

where ρ is the radius of curvature at the dendrite tip $(r/\rho=0, Z/\rho=\tfrac{1}{2})$.

The differential equations for heat and solute transport to be solved for steady-state growth in the moving co-ordinate system fixed to the dendrite cap are

$$[\nabla^2+(V/\alpha_{ij})\partial/\partial Z]\theta_{ij}=0, \quad (3)$$

where $i=s$ or l (solid or liquid), $j=s$ or T (solute or temperature), and α_{ij} is the diffusivity, e.g., θ_{ss} refers to the solute distribution in the solid phase. We will, for the moment, consider the cases where α_{ss} and α_{sT} are negligible and will thus be concerned only with transport in the liquid phase. The flux conditions that must be satisfied at the solid-liquid interface, $F(Z/\rho,r/\rho)=0$, are

$$(V_n/\alpha_{ls})(1-k_0)\theta_{ls}=-\partial\theta_{ls}/\partial n, \quad (4a)$$

and

$$V_nL/K_{lT}=-\partial\theta_{lT}/\partial n, \quad (4b)$$

where V_n is the surface-normal component of the freezing velocity, K_{lT} is the thermal conductivity, L is the latent heat of fusion/cc, k_0 is the equilibrium solute partition coefficient between the two phases, and n refers to the direction of the surface normal. Since the entropy of fusion per unit volume, ΔS, is L/T_M, $\alpha_{lT}=K_{lT}/C_{lT}$, where C_{lT} is the specific heat/cc, and T_i/T_m is usually close to unity, Eq. (4b) may be put in the form of (4a), giving

$$(V_n/\alpha_{lT})(\Delta S/C_{lT})\theta_{lT}=-\partial\theta_{lT}/\partial n. \quad (4c)$$

In this way a general flux condition can be established for comparative purposes as

$$\epsilon_{ij}=-(\partial \ln\theta_{ij}/\partial n), \quad (5)$$

where $\epsilon_{ls}=(V_n/\alpha_{ls})(1-k_0)$ and $\epsilon_{lT}=(V_n/\alpha_{lT})(\Delta S/C_{lT})$. Since $\alpha_{lT}/\alpha_{ls}\approx10^4$ for metals and $C_{lT}/\Delta S\approx5$, we obtain $\epsilon_{ls}/\epsilon_{lT}\sim10^4$. Thus, although the isotherms and isoconcentrates will have the same shape, for metals the parametric distortion of the isoconcentrates will be 10^4 times as great as that for the isotherms.

The general solution to Eq. (3) is

$$\theta_{lj}-\theta_{lj}^{\infty}=\int_0^{\infty} A(b)e^{\lambda_j(Z-Z_0)}J_0(br)db, \quad (6)$$

where $\lambda_j=-(V/2\alpha_{lj}\{1+[1+4b^2(\alpha_{lj}/V)^2]^{\frac{1}{2}}\}$; θ_{lj}^{∞} is the solute concentration or temperature in the liquid at infinity, b^2 is the separation constant used in solving Eq. (3), and J_0 is a Bessel function. The particular solution of Eq. (6) subject to the restrictions of Eq. (5) on the general surface given by Eq. (2) is too difficult to be obtained here; therefore, we will consider instead several approximate but useful solutions.

B. The Isothermal Dendrite

An exact solution to Eq. (3) subject to the satisfaction of Eq. (5) on $F(z,r)=0$ given by Eq. (2) with $A_4=A_6=\cdots A_{2n}=0$ has been found by Ivantsov[12] and is given by

$$(\theta_{lj}-\theta_{lj}^{\infty}/\theta_{lj}^{i}-\theta_{lj}^{\infty}) =E_i(-V\rho g/2\alpha_{lj})/E_i(-V\rho/2\alpha_{lj}) \quad (7)$$

and

$$(V/\alpha_{lj}\epsilon_{lj})(\theta_{lj}^{i}-\theta_{lj}^{\infty})/\theta_{lj}^{i} =-(V\rho/2\alpha_{lj})e^{(V\rho/2\alpha_{lj})}E_i(-V\rho/2\alpha_{lj}), \quad (8)$$

where θ_{ij}^{i} is a constant value of θ_{lj} at the interface. E_i is the tabulated integral exponential function and the normalized co-ordinate $g=(Z/\rho)+[(r/\rho)^2+(Z/\rho)^2]^{\frac{1}{2}}$ is used. Thus, since the θ_{lj}^{i} are constants, the surface of a growing paraboloid of revolution is both an isotherm and an isoconcentrate. Equation (8) which is derived from Eqs. (7) and (5) yields a relationship for ρ in terms of V if $\theta_{ls}=0$. In fact, considering this case only, the product $V\rho$ must be almost a constant to satisfy Eq. (8), i.e., blunt paraboloidal needles would grow at low rates and sharp paraboloidal ones at high rates in a medium of given physical properties.

When both solute and heat flow are considered, Eq. (8) must be satisfied simultaneously for both the heat and solute flows given by Eq. (7). The interface concentration θ_{ls}^{i} is given by the following equation:

$$\theta_{lT}^{i}=T_M-(2\gamma/\Delta S\rho)-\delta T+m_L\theta_{ls}^{i}, \quad (9)$$

where T_M is the melting point of pure solvent, and m_L is the liquidus slope for the solute in this solvent. Thus, by applying Eq. (8) for both solute and heat flow plus Eq. (9), one finds the value of θ_{ls}^{i} and the relationship between V and ρ. We will return to these calculations later.

C. Inconsistency of the Isothermal Dendrite

For the steady-state propagation of a dendrite cap (we reserve the term dendrite tip to mean only that point of the surface on the axis of revolution; the cap is the region in its general vicinity) without change of shape, a fixed geometrical relationship must exist between the axial velocity $V(0)$ and the normal velocity $V(\phi)$ at points of the surface whose normal vectors make an angle ϕ with the dendrite axis such that

$$V(\phi)=V(0)\cos\phi. \quad (10)$$

The shape of the thermal field and the relative atomic kinetics of growth in these directions must be mutually consistent in order to satisfy this relationship. For the

---

[12] G. P. Ivantsov, Doklady Akad. Nauk. SSSR **58**, 567 (1947), translation, *Growth of Crystals* (Consultants Bureau Inc., New York, 1958), Vol. I, p. 76.

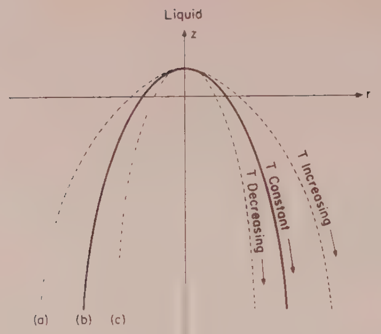

FIG. 3. Relative dendrite cap temperature for dendrites of the same radius of curvature which fall either outside or inside a paraboloid of revolution (curve b).

cap shape of a paraboloid of revolution the surface is isothermal, and, since the curvature, Ω, decreases as ϕ increases, the departure from thermodynamic equilibrium, δT, increases as ϕ increases. If we assume, for the sake of example, that the surfaces are all atomically rough so that in Eq. (1) $f(\Delta G(0),\phi)=\mu\delta T$, where μ is a constant independent of ϕ, then Eq. (10) cannot be satisfied since $V(\phi)$ will be too large. The surfaces growing in the ϕ direction will grow outside of the cap shape determined at the tip until the interface temperature for that value of ϕ has increased enough that Eq. (10) can be satisfied for the atomic kinetics as well as for heat flow. With this manner of reasoning, we can see that, if dendrite cap shapes exist with the same curvature at the tip such as illustrated in Fig. 3, in which curve (b) represents a paraboloid of revolution, then the surface temperature increases as ϕ increases for curve (a) and decreases as ϕ increases for curve (c). This allows the departure from thermodynamic equilibrium at any ϕ to decrease or increase for curves (a) and (c), respectively, relative to curve (b). This shows that the rate of growth in any direction is dependent upon the total cap shape, and that this conclusion is not likely to depend upon either the type or the isotropy of the atomic mechanism which is operative.

D. Nonisothermal Dendrite; Transport in Solid; $\theta_{ls}=0$

Consider the dendrite trunk illustrated in Fig. 2, and let us calculate the magnitude of the heat flux: (a) into the interface at the tip due to transport in the solid, and (b) the additional heat flux into the liquid from the tip due to the nonisothermal nature of the cap. We will hereafter choose α and D to refer to thermal and solute diffusivity, respectively.

(a) Using the simple diffusive transport relationship, $r^2=\alpha_s t$, where $t=\text{time}=-\Delta Z/V$, we may expect that for any isotherm in the solid, ΔZ is given approximately by the following relationship:

$$\Delta Z=-(V/\alpha_s)r^2. \tag{11}$$

The isotherm shape relative to the dendrite cap shape is illustrated in Fig. 4 for the values of ρ of interest to us here. Thus, if $\Delta\theta(\beta)$ is the temperature difference between the tip and the location on the surface $r/\rho=\beta$, the temperature gradient along the axis of the dendrite at the tip is given by

$$\left.\text{grad}T_s\right]_{\substack{r=0\\ Z-Z_0=0}}=-\lim_{\beta\to0}\frac{\Delta\theta(\beta)}{[Z_0-Z(\beta)-\Delta Z(\beta)]}$$

$$=-\lim_{\beta\to0}\frac{\Delta\theta(\beta)}{[(\beta^2\rho/2)+(V/\alpha_s)\beta^2\rho^2]}, \tag{12}$$

where the dendrite shape is given by Eq. (2) and

$$\Delta\theta(\beta)=(\gamma/\Delta S)[(2/\rho)-(1/\bar{R})]+[\delta T(0)-\delta T(\beta)], \tag{13}$$

with $\bar{R}$ equal to the total radius of curvature at $r/\rho=\beta$. It can be readily shown that, for $\beta\ll1$, $1/\bar{R}=2(1-\beta^2)/\rho$ so that

$$(\gamma/\Delta S)[(2/\rho-1/\bar{R})]=(2\gamma/\Delta S)(\beta^2/\rho). \tag{14}$$

If we assume that the atomic mechanism of growth is that of uniform interface advance (see Sec. G), then

$$V(\beta)=\mu(\beta)\delta T(\beta). \tag{15}$$

There μ is a function only of β. Since $\mu(\beta)$ can be expanded as an even power series in β about $\beta=0$, we have

$$\mu(\beta)=\mu(0)[1+a'\beta^2+a''\beta^4+\cdots]. \tag{16}$$

Using Eqs. (10), (15), and (16), and expanding $\cos\phi$ in terms of β for $\beta\ll1$, one finds

$$[\delta T(0)-\delta T(\phi)]=\beta^2[a'+\tfrac{1}{2}]\delta T(0). \tag{17}$$

Therefore, from Eqs. (12)–(14) and (17), we have

$$\left.-\text{grad}T_s\right]_{\substack{r=0\\ Z-Z_0=0}}=\frac{(2\gamma/\Delta S\rho)+(a'+\frac{1}{2})\delta T(0)}{[(\rho/2)+V\rho^2/\alpha_s]}. \tag{18}$$

In general, for the magnitude of ρ that we are concerned with here, we find $(V\rho^2/\alpha_s)\ll(\rho/2)$. The flux of heat into the tip from the solid can be gained by multiplying Eq. (18) by K_s, the thermal conductivity of the solid.

(b) Since Eq. (6) represents a general solution to the

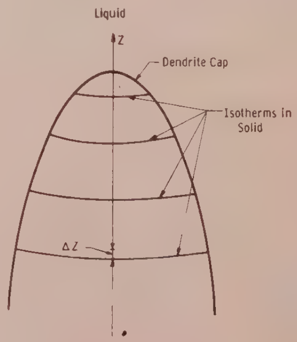

FIG. 4. Schematic illustration of the paraboloidal isotherm shape relative to a dendrite cap for small radii of curvature of the dendrite cap.

iffusion equation, we can use it as a correction factor o the isothermal solution given by Eq. (7) when the endrite surface is not a paraboloid of revolution and s not isothermal. Thus, the correct temperature disribution in the liquid T_L^* is related to θ_{lT} given by Eq. (7) in the following manner:

$$T_L^*-\theta_{lT}=\int_0^\infty A(b)e^{-\lambda[(Z-Z_0)/\rho]}J_0\left(b\frac{r}{\rho}\right)db, \qquad (19)$$

vhere $\lambda=(V\rho/2\alpha_L)\{1+[1+b^2/(V\rho/2\alpha_L)^2]^{\frac{1}{2}}\}$. Since we re interested only in heat flow at the tip of the dendrite nterface, we can expand Eq. (19) and need consider nly

$$T_L^*-\theta_{lT}=\int_0^\infty A(b)db-\frac{(Z-Z_0)}{\rho}\int_0^\infty \lambda A(b)db$$
$$-\frac{1}{4}\left(\frac{r}{\rho}\right)^2\int_0^\infty b^2A(b)db. \qquad (20)$$

Taking θ_{lT} to be the correct solution at the tip $[(Z-Z_0)/\rho=0,\ r/\rho=0]$, the first integral is zero, nd the temperature difference between the tip and neighboring points (β) on the cap is given by

$$\Delta\theta(\beta)=\frac{\beta^2}{2}\int_0^\infty\left(\lambda-\frac{b^2}{2}\right)A(b)db. \qquad (21)$$

It is shown later that our region of interest is $10^{-3}<(V\rho/2\alpha_L)<10^{-1}$; therefore, at $Z=Z_0$, from Eq. (7) we can see that $\theta_{lT}-\theta_{lT}^\infty\approx0.1(\theta_{lT}^i-\theta_{lT}^\infty)$ when $g\sim10\rho-10^3\rho$. Since the temperature is approximately the ambient temperature at this value of g, we see that in Eq. (19) $A(b)\rightarrow0$ for $b>10\rho$ to $10^3\rho$ depending upon the magnitude of $V\rho/2\alpha_L$, and in fact $b\sim(V\rho/2\alpha_L)\ll1$. Again as b varies from 0 to $b_{\max}$, λ varies from $V\rho/2\alpha_L$ to approximately $b_{\max}$ when $b_{\max}>(V\rho/2\alpha_L)$, and since $b_{\max}<1$, λ is large with respect to $b^2/2$, and the $b^2/2$ term in Eq. (21) can be neglected with respect to λ. Thus, from Eqs. (13), (14), (17), and (21) we have

$$\int_0^\infty \lambda A(b)db\approx2\left\{\frac{2\gamma}{\Delta s\rho}+[a'+\tfrac{1}{2}]\delta T(0)\right\}. \qquad (22)$$

The increase in the temperature gradient in the liquid at the tip may now be obtained by differentiating Eq. (19) with respect to $(Z-Z_0)$ so that by using Eq. (22)

$$\operatorname{grad}(T_L^*-\theta_{lT})\Big]_{Z-Z_0=0}^{r=0}$$
$$=-\frac{2}{\rho}\left\{\frac{2\gamma}{\Delta s\rho}+[a'+\tfrac{1}{2}]\delta T(0)\right\}. \qquad (23)$$

Thus, for the region of interest, i.e., where $V\rho/2\alpha_s\ll\frac{1}{4}$, Eqs. (18) and 23 may be equated.

Since the thermal conductivities K_s and K_L are generally different, the heat flux to the dendrite tip from the solid will not be equal to the additional heat flux away from the dendrite tip in the liquid. Thus, Eq. (8) may not be used as the constraining boundary condition in the general case, but may be used only in those special cases where $K_L=K_s$. The proper "conservation of heat equation" which applies at the tip is the following:

$$-\frac{V\rho}{2\alpha_L}\left\{1+\frac{\psi}{LV}\left[\frac{K_s}{1+(2V\rho/\alpha_s)}-K_L\right]\right\}$$
$$\times e^{(V\rho/2\alpha_L)}E_i\left(-\frac{V\rho}{2\alpha_L}\right)=\frac{C}{L}\left[\Delta T-\delta T(0)-\frac{2\gamma}{\Delta s\rho}\right],$$

with

$$\psi=(2/\rho)[(2\gamma/\Delta S\rho)+(a'+\tfrac{1}{2})\delta T(0)]. \qquad (24)$$

In Eq. (24) it is assumed that $T_i/T_m\approx1$. Equation (24) reduces to Eq. (8) when either $\psi=0$ or $K_L=K_s/(1+2V\rho/\alpha_s)$. An equivalent but more complex equation than (24) is obtained when the restriction that $T_i/T_m\approx1$ is relaxed.

E. Nonisothermal Dendrite; Transport in Solid; $\theta_{ls}\neq0$

Provided that the dendrite cap for $0\overline{<}r/\rho\overline{<}\beta$ is an isoconcentrate, Eq. (24) becomes

$$-\frac{V\rho}{2\alpha_L}\left\{1+\frac{\psi}{LV}\left[\frac{K_s}{1+(2V\rho/\alpha_s)}-K_L\right]\right\}e^{(V\rho/2\alpha_L)}E_i\left(-\frac{V\rho}{2\alpha_L}\right)$$
$$=\frac{C}{L}\left[\Delta T+m_LC_i-\delta T(0)-\frac{2\gamma}{\Delta s\rho}\right], \qquad (25)$$

where C_i is the solute concentration on the dendrite cap, and ΔT is the supercooling of the melt relative to the melting temperature of the pure material. When the dendrite cap is not an isoconcentrate, the concentration on the cap can be expanded as an even power series in β, i.e.,

$$C_i(\beta)=d_0+d_1\beta^2+d_2\beta^4+\cdots. \qquad (26)$$

In this case Eq. (25) holds but with $C_i=d_0$ and

$$\psi=(2/\rho)[m_Ld_1+(2\gamma/\Delta S\rho)+(\alpha'+\tfrac{1}{2})\delta T(0)]. \qquad (27)$$

We can no longer use Eq. (8) to determine d_0 since the solute flux boundary condition must also include any effects due to diffusion in the solid and the additional diffusion in the liquid due to the nonisoconcentrate nature of the dendrite surface. Taking, as in Sec. D,

$$C_L^*-\theta_{ls}=\int_0^\infty A'(b)e^{-\lambda'(Z-Z_0/\rho)}J_0\left(b\frac{r}{\rho}\right)db, \qquad (28)$$

where

$$\lambda'=(V\rho/2D_L)\{1+[1+b^2/(V\rho/2D_L)^2]^{\frac{1}{2}}\},$$

with D_L= diffusion coefficient in the liquid, we can readily calculate

$$\mathrm{grad}C_s\Big]_{\substack{r=0\\Z-Z_0=0}}=-\frac{2d_1}{\rho[1+2V\rho/D_s]}$$

and

$$\mathrm{grad}(C_L^*-\theta_{ls})\Big]_{\substack{r=0\\Z-Z_0=0}}=-\int_0^\infty \lambda' A'(b)db. \qquad (29)$$

Unfortunately we cannot evaluate the integral in Eq. (29) since $b^2/2$ cannot be neglected with respect to λ. This is because $V\rho/2D_L>1$ generally. The general solute flux equation at the tip becomes

$$-\frac{V\rho}{2D_L}\left[1-\frac{D_L}{d_0V(1-k_0)}\left(D_s\,\mathrm{grad}C_s\Big|_{\substack{r=0\\Z-Z_0=0}}-D_L\,\mathrm{grad}(C_L^*-\theta_{ls})\Big|_{\substack{r=0\\Z-Z_0=0}}\right)\right]\times e^{V\rho/2D_L}E_i\left(-\frac{V\rho}{2D_L}\right)=\frac{d_0-C_\infty}{d_0(1-k_0)}. \qquad (30)$$

For the purposes of calculation we would choose $d_1=d_2=\cdots d_n=0$.

F. Optimization Conditions

Our problem is not yet completely specified. Consider the case where $\theta_{ls}=0$. Choosing the cap shape given by Eq. (2), we begin with a problem in n unknowns $[\rho,A_4\cdots A_{2n}]$. The solution to the heat flow problem of Eq. (6) adds $n+1$ more unknowns $[A(b),V]$ of which n can be satisfied by applying Eq. (5), or the general equation from which Eq. (24) was derived, on the surface given by Eq. (2). At the end of this step we have $(n+1)$ unknowns $[\rho,\ A_4\cdots A_{2n},\ V]$. Assuming that the atomic mechanism of growth is known, since $\theta_{lT}{}^i$ and $\bar{R}$ are known as functions of position, $\delta T(\phi)$ and thus $V(\phi)$ are known as functions of position. Then, by applying Eq. (10) at n points on the surface, we are left with just one unknown (we choose V). The problem is not completely specified, and we must choose some other condition to make it completely specified before proceeding further.

If this were an equilibrium situation, one would use the condition of minimum free energy; however, in a steady-state nonequilibrium situation we must choose a different condition. One would expect that the area of irreversible thermodynamics should yield the desired condition, and that it might be "minimum rate of entropy production." However, no one has been able to prove unequivocably that this condition is valid for growth processes although it has been attempted.[13] Another condition that has been tried, again without adequate justification, is "maximum linear velocity of phase transformation."[14]

We will use this latter condition of maximum velocity, first, because it is the only tractable method available and, second, *a posteriori*, because the calculations can be set in reasonable agreement with experimental observations. Optimizations other than the two mentioned were investigated, for example, "maximum volume of phase transformation per unit time." These are not presented, primarily because they did not give results which successfully explained the dendrite characteristics. The condition of "minimum rate of entropy production," on the other hand, gave interesting results in the simple case where we could apply it. This case is developed in Appendix I.

G. Atomic Kinetics

Two major mechanisms must be considered when dealing with the atomic kinetics of the freezing process.[18] First, a surface may advance by the lateral motion of steps originating at either a screw dislocation source or at a site of two-dimensional nucleation. A region of surface undergoes no change and does not advance normal to itself except during the passage of a step. Second, the surface advances normal to itself without needing steps, i.e., in the presence of a driving force every increment of surface is capable of continual change leading to advance of the surface. When discussing uniform interface motion, Turnbull,[15] using absolute rate theory, Hillig and Turnbull,[16] using simple rate theory, and Jackson and Chalmers,[17] using a "sticking probability" factor with absolute reaction rate theory all show that the rate of interface advance at small undercoolings is linearly related to the undercooling at the interface

$$V=\mu_1\delta T. \qquad (31)$$

The rate constant μ_1 may differ in these treatments in the range 1∼100 cm/sec/°C depending on the choice of constants. A somewhat similar factor was used by Hillig and Turnbull[16] who suggested that not all surface sites were active at the interface and that, in Eq. (31), μ_1 is some function of δT.

More recently, Cahn[18] has proposed that an interface may be diffuse, and that interface motion will not be limited to the occupation of discrete atomic sites on the interface. A few of the cogent numerics of his treatment are developed in Appendix II; here we will merely state some pertinent conclusions for this model.

Cahn[18] concludes that the mechanism for interface motion is intrinsically connected to the magnitude of he driving force for the transformation, and that three istinct regions of driving force must be considered. irst, at low driving forces, the initial perturbation re- uired to propagate a particular crystal face in its ormal direction is greater than the driving force, and hus lateral growth initiated at a screw dislocation or y two-dimensional nucleation would be required. econd, at high driving forces, the interface may ad- ance by uniform motion in its normal direction. Finally, range of indistinctness will exist between these two xtremes. In terms of an accommodation factor for uni- orm motion of the face considered, it would be zero at ow driving forces, being inhibited by the lateral motion f steps, and grow as the driving forces increased.

---

[13] J. S. Kirkaldy, Can. J. Phys. **37**, 739 (1959).

[14] C. Zener, Trans. Am. Inst. Mining, Met., Petrol. Engrs. **167**, 550 (1946).

[15] D. Turnbull, *Thermodynamics in Physical Metallurgy* (American Society for Metals, Cleveland, Ohio, 1950), p. 282.

[16] W. Hillig and D. Turnbull, J. Chem. Phys. **24**, 219 (1956).

[17] K. A. Jackson and B. Chalmers, Can. J. Phys. **34**, 473 (1956).

[18] J. Cahn, Acta Met. **8**, 554 (1960).

Hillig and Turnbull[16] show that $\mu_1=\zeta\delta T$, where $\gtrsim 10^{-3}$ for the screw dislocation mechanism. However, f one considers the steps to be diffuse, ζ can be as large s unity (Appendix II). As discussed in Appendix II, ve may write a growth law for all supercoolings using n accommodation factor η such that

$$V=\eta\mu\delta T, \tag{32}$$

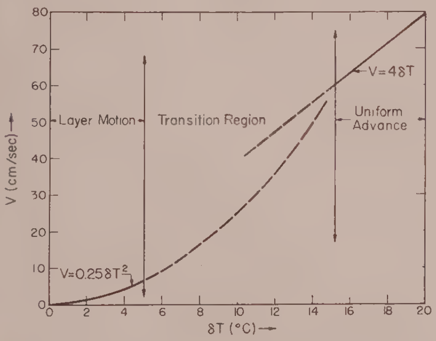

FIG. 5. Atomic kinetics for a diffuse interface (tin).

where μ is a constant at least for a particular crystal face. At small supercoolings $\eta=\zeta\delta T$ and changes continuously to $\eta=1$ at large supercoolings. An example of this type of variation for tin is given in Fig. 5, where it is assumed, for example, that the low driving force range extends to $\Delta T=10^{-2}\,T_m$, and thus the linear range does not begin until $\Delta T\approx 3.14\times 10^{-2}T_m$.

III. MAXIMUM VELOCITY DENDRITE

All the constraints to be placed upon the growing dendrite have now been discussed. There only remains the application of these considerations to determine the dendrite growth characteristics. The critical assumption to be made in this application is that the dendrite will develop those particular body dimensions that allow it to satisfy all the constraints, and which, simultaneously, allow it to propagate with the maximum possible velocity for a particular value of ΔT. Four separate cases will be considered, isothermal and nonisothermal dendrites both with and without $\theta_{ls}=0$.

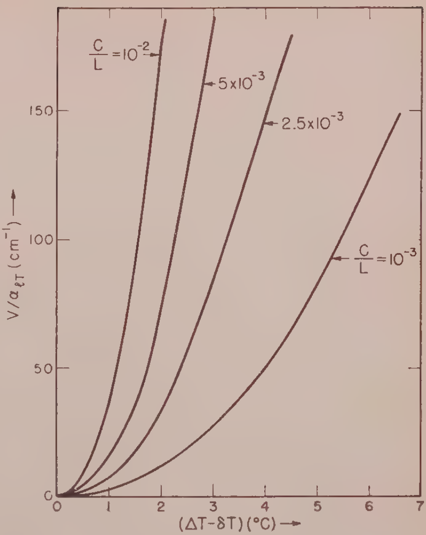

FIG. 6. Ratio of isothermal dendrite freezing velocity V to thermal diffusivity of the liquid α_{lT} as a function of $(\Delta T-\delta T)$ for several values of the thermal parameter C/L.

The calculations will be compared with the experimental data for dendritic growth in nickel, tin, and ice.

A. Isothermal Dendrite, $\theta_{ls}=0$

In this section a dendrite having a thermal field described by Eqs. (7) and (8) will have its velocity V maximized by variation of ρ. These calculations are applied to dendrites of tin, nickel, and ice. In Sec. C calculations are made for these materials for nonisothermal dendrites to illustrate the magnitude of effect that this assumption may have in certain cases.

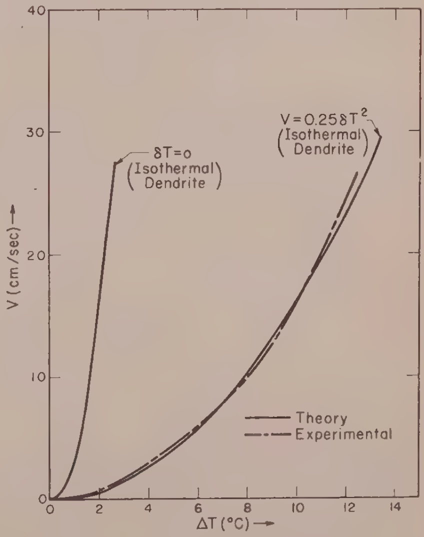

FIG. 7. Plot of dendrite freezing velocity V as a function of bath supercooling ΔT for tin.

Using Eq. (8), Fig. 1, and the assumption that $T_i/T_m \approx 1$, we have the relationship (an equivalent but slightly more complex equation would be obtained without this restriction)

$$(-V\rho/2\alpha_L)e^{(V\rho/2\alpha_L)}E_i(-V\rho/2\alpha_L) = (C/L)[\Delta T-\delta T-(2\gamma/\Delta S\rho)]. \quad (33)$$

In Eq. (33), $e^{(V\rho/2\alpha_L)}\approx 1$ and

$$E_i(-V\rho/2\alpha_L)\approx -\ln(\gamma^* V\rho/2\alpha_L)$$

for the magnitude of $V\rho/2\alpha_L$ in the region of interest (γ^*=Euler's constant, 1.78). Maximizing V by differentiation of Eq. (33) with respect to ρ and setting $dV/d\rho=0$ yields the following expression:

$$\rho^2-[(\Delta T-\delta T)(C/L)\cdot(2\alpha_L/V)]\rho + (8\gamma\alpha_L C/\Delta SVL)=0. \quad (34)$$

From Eq. (34) we find $\rho_{\min}$ to be given by

$$\rho_{\min}=4\gamma\ \ \Delta S(\Delta T-\delta T). \quad (35)$$

Thus

$$T_M-T_E=(\Delta T-\delta T)/2, \quad (36)$$

and

$$-(V^*\rho_m/2\alpha_L)\ \ln\gamma^*(V^*\rho_m/2\alpha_L) = (C/L)(\Delta T-\delta T)/2, \quad (37)$$

where V^* is the maximum freezing velocity for the chosen growth conditions. A graphical solution of Eq. (33) was made to determine the error arising from the approximations leading to Eq. (34), and it was found that $\rho_{\min}$ given by Eq. (35) is in error by less than 10%.

For most materials of interest $\gamma/\Delta S\approx 10^{-5}$, so that the magnitude of V^* is controlled primarily by the magnitudes of $(\Delta T-\delta T)$, C/L, and α. In Fig. 6, V^*/α_L is plotted against $\Delta T-\delta T$ for several values of C/L. For tin, nickel, and ice, respectively, the values of $C/L=4\times10^{-3}$, 2×10^{-3}, and 10^{-2}; whereas, $\alpha=0.2$, 0.1, and 0.00144. In Figs. 7–9, plots of V versus ΔT for $\delta T=0$ are given for tin, nickel, and ice, respectively, and compared with the experimental data for these systems.[19–21] We can see that the dendrite growth problem is not completely thermally determined, and that we must add some value of δT at each value of V^* to bring the theoretical predictions into registry with the experimental data. In this manner we may determine the atomic kinetics of the freezing process, $V=f(\delta T)$, for each of these materials if they exhibit this type of dendrite cap shape.

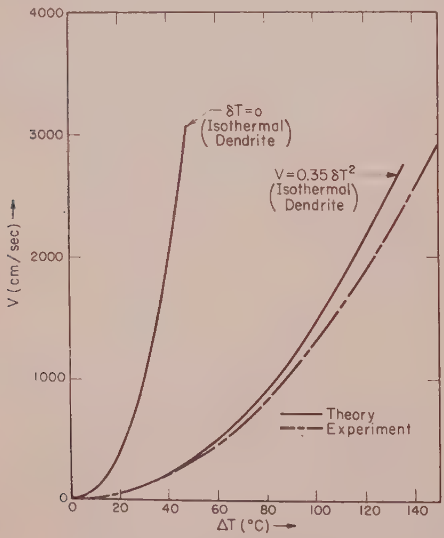

FIG. 8. Plot of dendrite freezing velocity V as a function of bath supercooling ΔT for nickel.

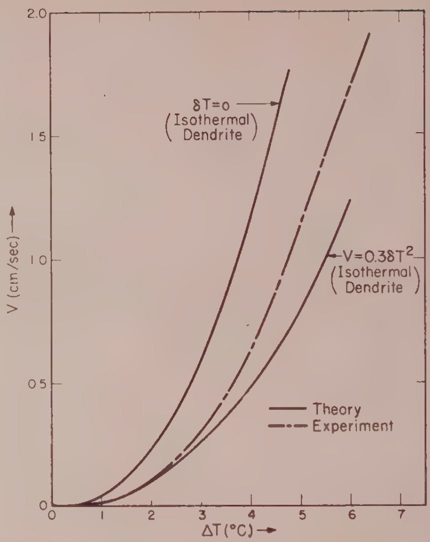

FIG. 9. Plot of dendrite freezing velocity V as a function of bath supercooling ΔT for ice.

It can be seen from these figures that $\eta\mu/\delta T=0.25$, 0.35, and 0.3, respectively, provide registry between the theoretical predictions for the isothermal dendrite and experiment at small supercoolings.

The dendrite size, R, one centimeter behind the tip, may be obtained from Eq. (35) and the paraboloidal shape equation which gives $R/\rho\approx(-z/\rho)^{\frac{1}{2}}$. Thus for $\Delta T-\delta T=1°$ and 10°C, respectively, $\rho=4\times10^{-5}$ cm and 4×10^{-6} cm; and $R=6.3\times10^{-3}$ cm and 2×10^{-3} cm.

B. $\theta_{ls}\neq 0$

Returning to Eqs. (8) and (33), when there is solute present in the melt, there are now two conditions to be satisfied simultaneously by Eq. (8). These are

$$-(V\rho/2\alpha_L)E_i(-V\rho/2\alpha_L)e^{(V\rho/2\alpha_L)} = (C/L)(\Delta T-\delta T-(2\gamma/\Delta S\rho)+m_L C_i) \quad (38)$$

---

[19] A. Rosenberg and W. C. Winegard, Acta Met. 2, 242 (1954).
[20] J. Walker (private communication).
[21] K. A. Jackson, discussion to reference 24.

and

$$-\frac{V\rho}{2D_L}e^{(V\rho/2D_L)}E_i\left(-\frac{V\rho}{2D_L}\right)=\frac{1}{1-k_0}\frac{(C_i-C_\infty)}{C_i}. \quad (39)$$

Here D_L is the diffusion coefficient in the liquid, and k_0 is the solute partition coefficient at the interface. Using the usual definition of an effective partition coefficient, i.e., $k_e=C_s/C_\infty=k_0C_i/C_\infty$, we can rearrange Eq. (39) to yield

$$k_e=\frac{k_0}{1+(1-k_0)(V\rho/2D_L)e^{(V\rho/2D_L)}E_i(-V\rho/2D_L)}. \quad (40)$$

If we consider the more common case of $k_0<1$, we can see that the value of k_e at the dendrite tip can only approach unity (no depletion) when the quantity $-(V\rho/2D_L)e^{(V\rho/2D_L)}E_i(-V\rho/2D_L)$ approaches unity. In Fig. 10, k_e/k_0 is plotted against the parameter $V\rho/2D_L$ for several values of k_0, and it can be seen that $k_e\rightarrow k_0$ for small values of $V\rho/2D_L$, and that $k_e\rightarrow 1$ for large values of $V\rho/2D_L$. This may produce a significant depletion of solute in the solid for $k_0<1$ and an excess of solute for $k_0>1$.

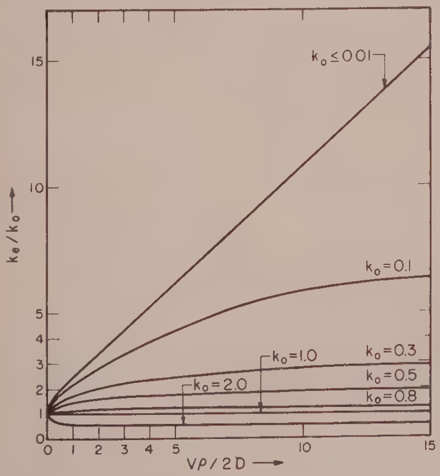

FIG. 10. The ratio of interface concentration C_i to bath concentration C_∞ ($C_i/C_\infty=k_e/k_0$) as a function of the dimensionless parameter $V\rho/2D_L$ for several values of partition coefficient k_0.

Since $C_i=k_eC_\infty/k_0$, we may now differentiate Eq. (38) with respect to ρ to obtain the value of ρ producing the maximum velocity just as we did earlier with Eq. (33) for $\theta_{ls}=0$. In order to obtain a manageable solution, it is necessary to approximate the variation between k_e/k_0 and $V\rho/2D_L$ as linear, i.e., $k_e/k_0=A+BV\rho/2D_L$. With this approximation Eq. (34) becomes

$$\rho^2-(\Delta T-\delta T+m_LAC_\infty)\frac{2\alpha_LC}{VL}\rho+\frac{8\gamma\alpha_LC}{\Delta sVL}=0. \quad (41)$$

Thus, $\rho_{\min}$ is given by

$$\rho_{\min}=4\gamma/\Delta S(\Delta T-\delta T+Am_LC_\infty), \quad (42)$$

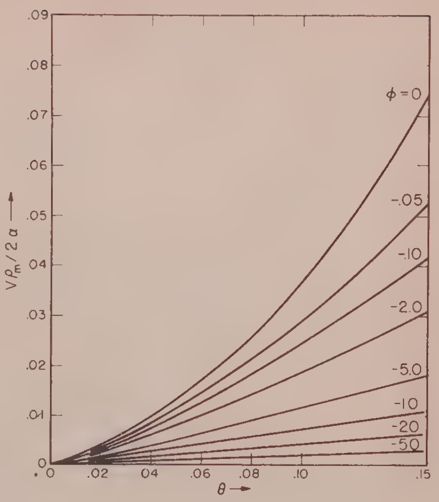

FIG. 11. Plot of the dimensionless variable $V\rho/2\alpha_L$ versus the dimensionless variable $\theta=(c/L)(\Delta T-\delta T+m_LC_\infty A)$ for several values of the dimensionless parameter $\phi=C\alpha_Lm_LC_\infty B/LD_L$.

and V^* is given by

$$-\frac{V^*\rho_m}{2\alpha_L}\left(\ln\gamma^*\frac{V^*\rho_m}{2\alpha_L}+\frac{C\alpha_L}{LD_L}m_LBC_\infty\right)=\frac{C}{L}\left(\frac{\Delta T-\delta T+Am_LC_\infty}{2}\right). \quad (43)$$

Since A is positive with a value between 1 and 2 for $k_0<1$, as C_∞ increases, ρ must also increase (m_L is negative). We can also see from Eq. (42) that no real dendrites are possible unless $\Delta T-\delta T>|m_LC_\infty|$ [since $A\rightarrow 1$ as $(V\rho/2D_L)\rightarrow 0$].

In Fig. 11 we have plotted $V^*\rho_m/2\alpha_L$ against

$$\theta=(C/L)(\Delta T-\delta T+m_LC_\infty A)$$

for several values of $\phi=(C\alpha_L/LD_L)m_LC_\infty B$. To determine the theoretical value of V^* with a certain solute of concentration C_∞, the following procedure should be adopted. Choose a reasonable value for $V\rho/2\alpha_L$

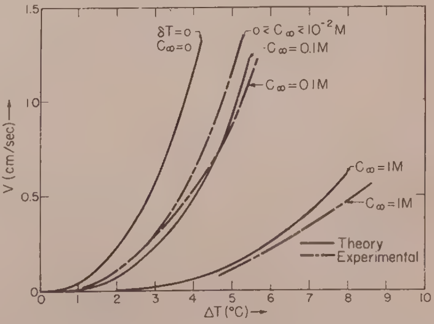

FIG. 12. Isothermal dendritic growth of ice from KCl solution.

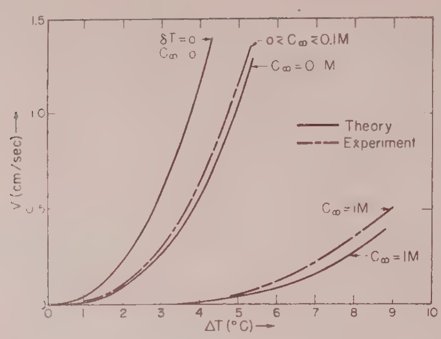

FIG. 13. Isothermal dendritic growth of ice from acetic acid solutions.

(3×10^{-3}, for example), calculate $V\rho/2D_L$, and select the appropriate values of A and B by taking tangents at the value of $V\rho/2D_L$ in Fig. 10. Using Eq. (43), $\Delta T-\delta T+m_LC_\infty A$ can now be calculated. From this ρ_m can be calculated using Eq. (42), and thus V^* can be determined. Using Fig. 9, the value of δT required to drive the dendrite at this value of V^* for pure water can be found; thus ΔT for this value of V^* can also be found. In this manner the freezing rates for isothermal ice dendrites grown from aqueous solutions of KCl and acetic acid as a function of ΔT have been determined and plotted in Figs. 12 and 13 along with the experimental data for these systems[21] ($\Delta T=0$ occurs at 0°C). In these calculations we chose $D_L=1.0\times10^{-5}$ cm²/sec and the values of m_LC_∞ given by the $V=0$ intercepts on these figures.

For values of $V\rho/2D_L \lesssim 0.1$, we found it preferable to choose $A=1$ and $B=-E_i(-V\rho/2D_L)e^{(V\rho/2D_L)}+(V\rho/4D_L)e^{(V\rho/D_L)}E_i^2(-V\rho/2D_L)$ gained from the expansion of Eq. (40) rather than use the tangent method. Again, a graphical solution of Eq. (38) was made to determine the error arising from the approximations leading to Eq. (41), and it was found that $\rho_{\min}$ given by Eq. (42) was in error by less than 10%.

C. Nonisothermal Dendrite, $\theta_{ls}=0$

The previous analyses in Secs. A and B are applicable if $\psi=0$ or $K_L=K_s/(1+2V\rho/\alpha_{sT})$ as discussed earlier since, for either of these conditions, Eq. (24) reduces to Eq. (8). However, in the general case, we must use Eq. (24). In order to determine the value of ρ giving maximum velocity, in this case, we could differentiate Eq. (24) with respect to ρ. However, this leads to a quartic equation in ρ which appears totally unmanageable with respect to a simple algebraic solution. Instead, it is better to assume that $2V\rho/\alpha_s \ll 1$ (to be justified later) and to rearrange Eq. (24), using Eqs. (15) and (16), assuming uniform interface advance (i.e., $\eta=1$) in the following way:

$$\rho=\frac{\dfrac{\Delta K}{\alpha_LL}[-E_i(-x)e^x]\left(\dfrac{2\gamma}{\Delta S}+\dfrac{2\alpha_L}{\mu}[a'+\tfrac{1}{2}]x\right)+\left(\dfrac{2\gamma}{\Delta S}\dfrac{C}{L}+\dfrac{2\alpha_LC}{\mu L}x\right)}{(C\Delta T/L)-[-xe^xE_i(-x)]},\qquad(44)$$

where $\Delta K=K_s-K_L$ and $x=V\rho/2\alpha_L$.

To obtain the desired data from Eq. (44), one must choose several values of μ for each value of ΔT, and from a plot of ρ versus x for each of these cases V^* can be found. From a plot of V^* versus μ for that value of ΔT, the value of μ satisfying the experimental data may be found. For these calculations we will assume that

TABLE I.

Dendrite	a'	C_L/L °C^{-1}	α_L cm²/sec	$\Delta K/K_L$	$\gamma/\Delta S$ cm-°C	ΔT_{exp} °C	V_{exp} cm/sec	ρ_{calc} cm	μ_{calc} cm/sec/°C	δT_{calc} °C
Nickel	0	2×10^{-3}	0.1	+1	10^{-5}	123	2×10^3	6×10^{-6}	175	11.4
						87	1×10^3	8×10^{-6}	175	5.7
						45	0.25×10^3	1×10^{-5}	200	1.25
					1.7×10^{-5}	87	1×10^3	8×10^{-6}	450	2.22
Tin	0	4×10^{-3}	0.2	+1	6.5×10^{-6}	13.3	30	5.4×10^{-5}	25	1.2
						7.8	10	7.6×10^{-5}	20	0.5
						3.7	2.5	2.7×10^{-4}	14	0.179
					10^{-5}	13.3	30	5.4×10^{-5}	32	0.94
					6.5×10^{-6}	13.3	10	1.7×10^{-4}	7.5	1.33
						7.8	3.33	2×10^{-4}	4	0.833
						3.7	0.83	4.6×10^{-4}	3	0.276
Ice	0	1.25×10^{-2}	1.44×10^{-3}	+2	1.5×10^{-6}	4.77	1.0	2.2×10^{-5}	7.5	0.133
						3.67	0.5	2.6×10^{-5}	4	0.125
						1.57	0.056	10^{-4}	1.25	0.045
					2.4×10^{-6}	4.77	1.0	2.2×10^{-5}	100	0.01
						3.67	0.5	N. S.[a]	N. S.	
						1.57	0.056	N. S.	N. S.	

[a] N. S. = No solution.

$a' \ll \frac{1}{2}$. Further, as an aid, we know that ρ must be positive and therefore that

$$-xE_i(-x)e^x < C\Delta T/L. \tag{45}$$

Thus, if $(C/L)\Delta T = 5\times10^{-3}$, 5×10^{-2}, and 5×10^{-1}, x must be less than about 7×10^{-4}, 10^{-2}, and 4.5×10^{-1}, respectively. We are therefore justified in neglecting $2V\rho/\alpha_s$ compared to unity.

In Table I, μ, ρ, and δT have been calculated by the above procedure for different values of ΔT for dendrites of nickel, tin, and ice. For nickel with $\gamma/\Delta S = 10^{-5}$, μ is almost a constant and quite large, $\mu \approx 175$; however, if γ is taken from Turnbull's nucleation data,[15] μ becomes extremely large, i.e., $\mu = 450$. For tin, using the data of Rosenberg and Winegard[19] and Turnbull's[15] value for γ, μ is not a constant but has $a \pm 25\%$ variation about $\mu = 20$. If one corrects this data after Jackson,[22] μ has an even larger variation about $\mu = 4$. For ice, if one uses the data of Lindemeyer as contributed by Jackson[21] and $\gamma = 20$ ergs/cm^2 as used by Fletcher,[23] again μ is not a constant but has a large symmetrical variation about $\mu = 4$. If one uses Turnbull's[15] value for γ ice, fit with experiment can only be had at large values of V ($V = 1$ cm/sec) and here with $\mu \approx 100$. At smaller values of V_{exp}, no value of μ allows V^* (calculated) to be as large as V_{exp} for a particular ΔT. We can thus see that, for these materials at least, the proper choice of γ is essential for determining the proper value of μ. It may also be necessary to consider that the value of γ that we must use may vary with the actual freezing velocity.

It is of considerable interest to note that the treatment of the isothermal dendrite, case (i), predicts that δT is large, and that the kinetics of a screw dislocation mechanism appear to be applicable. Whereas, the above treatment for a nonisothermal dendrite predicts that δT will be much smaller, and that no general mechanism appears to be applicable.

D. Nonisothermal Dendrite, $\theta_{ls} \neq 0$

We are capable of treating only the case where the dendrite cap is an isoconcentrate. In this case we find that

$$\rho = \frac{\dfrac{\Delta K}{\alpha_L L}\left[-E_i(-x)e^x\right]\left[\dfrac{2\gamma}{\Delta S} + \dfrac{2\alpha_L}{\mu}(a' + \tfrac{1}{2})x\right] + \left[\dfrac{2\gamma}{\Delta S}\left(\dfrac{C}{L}\right) + \dfrac{2\alpha_L C}{\mu L}x\right]}{(C/L)(\Delta T + m_L C_i) - (-xe^x E_i(-x))},$$

where

$$C_i = C_\infty \Big/ \left\{1 - (1 - k_0)\left[-\frac{\alpha_L}{D_L}xE_i\left(-\frac{\alpha_L}{D_L}x\right)e^{(\alpha_L/D_L)x}\right]\right\}. \tag{46}$$

By using the same procedure with Eq. (46) as described earlier for the treatment of Eq. (44), a calculated value of V^* may be obtained for any m_L, k_0, and C_∞ at a particular ΔT and compared with V_{exp}. To perform this comparison it must be assumed that μ is unchanged from that of the pure material, and that μ may be found by interpolating or extrapolating the data given in Table I. Using this procedure, with $D_L = 10^{-5}$ cm^2/sec and $\gamma/\Delta S = 1.5\times^{-6}$ cm°C, the maximum velocity of ice dendrites grown from KCl and acetic acid solutions is shown as a function of ΔT in Fig. 14. Here again, ΔT is measured relative to 0°C. Comparing Fig. 14 with Figs. 12 and 13, we can see that the fit is better with the acetic acid solution data but worse with the KCl data than the isothermal dendrite treatment. It is of interest to note that, as C_∞ increases, the value of ρ that yields $V_{\max}$ decreases from the value for $C_\infty = 0$ at that value of V. For example, at $V_{\text{exp}} = 0.15$, $\rho_{\text{calc}} \approx 4\times10^{-5}$ for pure ice, but from a $1M$ KCl solution $V_{\text{calc}} = 0.15$ occurs with $\rho_{\text{calc}} = 2\times10^{-5}$. This effect is in the opposite direction to that predicted by Eq. (42).

E. Dendrite Growth Direction

1. *Rod Forms*

As discussed in Sec. I, both thermal fluctuations and anisotropic characteristics of the solid will cause a spherical particle in a supercooled liquid to develop protuberances which eventually become dendrites. If the solid exhibits no anisotropic characteristics (i.e., thermal properties, atomic kinetics of phase transition, V, and solid-liquid interfacial energy, γ, are all isotropic), a dendrite can grow equally fast for constant shape in any crystallographic direction. Thus, the existence of a preferred crystallographic direction of dendrite growth indicates the presence of anisotropic characteristics of the solid.

In general, the thermal properties of the solid have little influence on dendritic growth since most of the evolved heat flows into the liquid, and, of course, cubic materials exhibit isotropic thermal properties. For metals, if only a slight anisotropy in γ is expected, it seems very probable that the ϕ dependence of Eq. (1) is the important anisotropic characteristic of the solid accounting for a specific dendrite orientation for a certain material. We will illustrate this effect where,

---

[22] K. A. Jackson, *Growth and Perfection of Crystals* (John Wiley & Sons, Inc., New York, 1958), p. 308.

[23] N. H. Fletcher, J. Chem. Phys. **29**, 572 (1958).

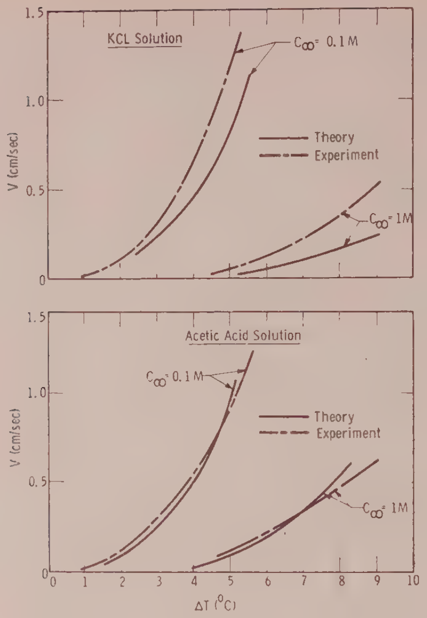

FIG. 14. Dendrite growth of ice, nonisothermal.

in Eq. (32), we choose $\eta\mu$ as a constant independent of δT but as a function of orientation.

Our choice of optimization condition leads to the conclusion that the dendrite will grow in that direction which yields the greatest axial velocity of growth. As discussed earlier, the product $V\rho^*$ should be almost a constant depending only upon T_i-T_∞ for a particular system (ρ^* is the effective radius of curvature of a real dendrite determined by approximating it with an isothermal dendrite having a radius of curvature ρ^* at its tip). From Eq. (37) we can see that the dendrite velocity, V, is maximized by growth in that direction which is the best compromise between small δT and small ρ^*. From Fig. 3 we can deduce that ρ^* will decrease the slower growing are the faces in the ϕ direction since an increased departure from thermodynamic equilibrium is required to satisfy Eq. (10).

Consider the growth of an isothermal dendrite for which μ is a function of ϕ and $\eta=1$. There are generally only two types of crystal faces that need be considered: (1) the face growing in the 0 direction which is the axial direction, and (2) the slowest growing crystal faces in the system which are usually the most close-packed faces in the system. Since symmetry is required, let them make an angle ϕ with the specimen axis. For stability of the isothermal dendrite, Eq. (10) requires that $\mu(\phi)\lesseqgtr\mu(0)\cos\phi$. When this condition is fulfilled, we may calculate the difference in curvature between the 0 direction and the ϕ direction on the dendrite as a function of ρ and can determine ρ by requiring that

$$\mu(\phi)\delta T(\phi)=\mu(0)\delta T(0)\cos\phi. \tag{47}$$

Recalling that the curvature, $1/\bar{R}$, of a surface, $Z=f(r,\rho)$, is given as

$$\frac{1}{\bar{R}}=-\frac{1}{(1+Z'^2)^{\frac{1}{2}}}\left(\frac{Z'}{r}+\frac{Z''}{1+Z'^2}\right), \tag{48}$$

which, for a paraboloid of revolution, is

$$1/\bar{R}=\cos\phi(1+\cos^2\phi)/\rho, \tag{49}$$

since $Z'=-\tan\phi$. Thus, $\delta T(\phi)$ is given by

$$\delta T(\phi)=\delta T(0)+\frac{\gamma(0)}{\Delta s}\left(\frac{2}{\rho}-\frac{\gamma(\phi)/\gamma(0)}{\bar{R}}\right)$$

$$=\frac{\mu(0)}{\mu(\phi)}\delta T(0)\cos\phi \tag{50}$$

and

$$\rho=\frac{2\gamma(0)}{\Delta s\delta T(0)}\left\{\frac{1-[\gamma(\phi)/2\gamma(0)]\cos\phi(1+\cos^2\phi)}{[\mu(0)/\mu(\phi)]\cdot\cos\phi-1}\right\}. \tag{51}$$

For constant $\delta T(0)$ and ΔT, Eq. (37) gives $V\rho=$constant so that V will be maximized by minimizing ρ. The growth direction that minimizes ρ in Eq. (51) for constant $\delta T(0)$ is a direction of interest. This direction is one which: (i) maximizes $\mu(0)/\mu(\phi)$, (ii) minimizes ϕ, and (iii) maximizes $\gamma(\phi)/\gamma(0)$. Since μ may be expected to decrease as the reticular density of the face increases, one would expect that ρ is minimized by growth in that direction which is symmetrically bounded by the faces of greatest packing that make the smallest angle ϕ with the 0 face. This is consistent with experiments and deductions of Weinberg and Chalmers for most metals.[2] In fact, we can see these close-packed planes on a ⟨100⟩ dendrite of Pb, exposed by decanting, in Fig. 15. We are, of course, not justified in maintaining $\delta T(0)$ constant, and we may find in some cases that growth in a different direction may occur with a larger ϕ, but with a sufficiently smaller $\delta T(0)$ that this direction may give a larger V. In such cases it is likely that dendrites of both orientations will exist.

There are two other cases of interest: (i) screw dislocation mechanism in 0 and ϕ directions, here $\mu=\mu'\delta T$, and (ii) uniform interface advance in the 0 direction and screw dislocation mechanism in the ϕ direction, here $\mu(0)=$constant, and $\mu(\phi)=\mu'(\phi)\delta T$. For these two cases, ρ is given by

$$\rho=\frac{2\gamma(0)}{\Delta s\delta T(0)}\left\{\frac{1-[\gamma(\phi)/2\gamma(0)]\cos\phi(1+\cos^2\phi)}{[\mu'(0)/\mu'(\phi)]^{\frac{1}{2}}\cos\phi^{\frac{1}{2}}-1}\right\} \tag{52}$$

and

$$\rho=\frac{2\gamma(0)}{\Delta s\delta T(0)}\left\{\frac{1-[\gamma(\phi)/2\gamma(0)]\cos\phi(1+\cos^2\phi)}{[\mu(0)\cos\phi/\mu'(\phi)\delta T(0)]^{\frac{1}{2}}-1}\right\}. \tag{53}$$

It should be noted that the minimization of ρ in Eqs. (52) and (53) leads to the same conclusions as drawn from Eq. (51). Thus, even though we may not know which growth law is valid for a material, we may have a reasonable degree of confidence in these conclusions.

2. *Lath Forms*

When the atomic mechanism of growth on the slowest growing crystal faces is slow compared to a mechanism induced by the presence of a self-perpetuating step on these faces, a ribbon or lath-like dendrite may result. For example, if a dendrite of diamond-cubic material contains at least 2−{111} closely spaced twins, as shown in Fig. 16(b), it will readily propagate in the $\langle 211\rangle$ directions as a flat strip with the {111} plane surfaces as the ribbon plane rather than in the $\langle 100\rangle$ directions as a rod-form. This is because the re-entrant corners formed on the cap at the twin planes allow growth to proceed at an appreciable rate with a much smaller δT than that needed for the slow growing faces of the $\langle 100\rangle$ rod form. The lath form grows in the $\langle 211\rangle$ direction because this is the direction of best balance between ρ^* and δT; in some cases the lath form grows in the $[2\bar{1}\bar{1}]$ rather than the $[\bar{2}11]$ direction when the number of twins and their spacing allows the $(2\bar{1}\bar{1})$ face to proceed at a smaller δT than the $(\bar{2}11)$ face for the same δT. In fact, if sufficient solute is present in the melt, it will tend to segregate at the re-entrant corners, and they will not be so efficient as sites for layer initiation, and another growth direction may form. Here the dendrite orientation becomes the $\langle 110\rangle$ and must provide faster growth than the $\langle 211\rangle$ dendrite by virtue of a better balance between δT and ρ^*.[24]

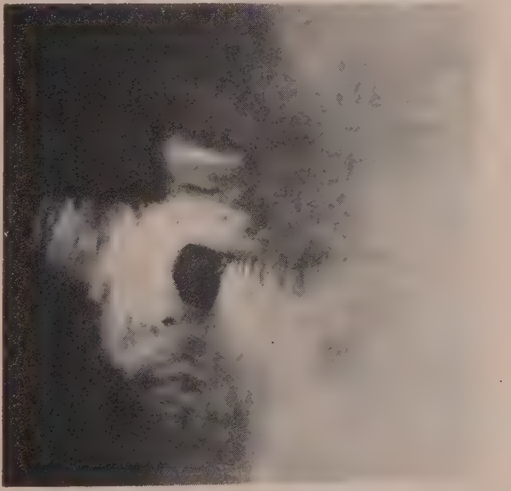

Fig. 15. Cap of a lead dendrite grown at low bath supercooling. The tip region is paraboloidal in shape; however, the cap exhibits traces of the four symmetrically displayed {111} planes about the $\langle 100\rangle$ direction. This is evidence of some growth anisotropy. 900×.

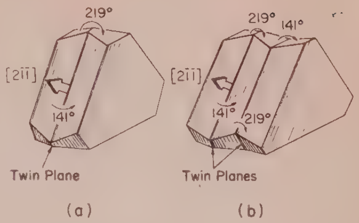

Fig. 16. (a) Dendrite seed of diamond-cubic material containing one twin plane. (b) Dendrite seed of diamond-cubic material containing two twin planes.

3. *Branching*

Some distance back from the tip of the dendrite the body should start to approach the shape of a cylinder, and conditions leading to the development of stable shape perturbations will form. These conditions will develop for the same reasons that led to the development of the original dendrite trunk. Although it might be of value to be able to predict the conditions sufficient to produce a stable or growing shape perturbation, the mathematics are too complicated to enable us to do so with any certainty. In any event, the branches will develop in those directions that give a maximum axial velocity, these being the same as the trunk orientation or some equally perferred direction.

IV. DISCUSSION

This section is divided into three parts. The first is a review of the important assumptions that were used; the second deals with some further possible applications of the theoretical description; and in the final portion we attempt to assess the conclusions that may be drawn.

A. Assumptions

The first, and perhaps most important, assumption was that dendritic growth is a true steady-state growth process. We have restricted our quantitative treatment to dendrites of rotational symmetry and assumed that the material properties were constant regardless of the freezing velocity, that fluid flow could be neglected, and that an infinite liquid environment existed. Finally, we made the very important assumption that the dendrite propogates through the supercooled liquid at the maximum possible velocity consistent with the satisfaction of all constraints.

Steady-state growth is possible only when the cap of the dendrite displays a smooth surface, and it seems likely that this can result only if the atomic kinetic mechanism is that of a diffuse interface motion. If the atomic attachment were by two-dimensional nucleation on particular faces near the cap, flats would develop at certain poles of the cap, and layers would flow from these sources to feed the remainder of the cap contour. If the layer sources occurred at any other pole than the axis, flats would develop, enlarge, and then disappear as the tip advanced, and eventually a new flat would form at that pole but much closer to the tip. Growth in this manner cannot be considered as steady-state but only as periodic. This produces a real qualitative difference from steady-state; however, if the oscillation of the cap morphology due to the formation of flats, which might eventually develop into side branches, produced only a small change in the cap contour, within $-(Z-Z_0)\lesssim 2\rho$, we might expect that the numerical results of the steady-state treatment would be closely applicable.

---

[24] G. F. Bolling and W. A. Tiller, *Metallurgy of Elemental and Compound Semiconductors* (Interscience Publishers, Inc., New York, 1961), Metallurgical Society Conferences, Vol. 12 (Boston, 1960), p. 97.

Atomic attachment facilitated by screw dislocations could yield a smooth surface if these sources were active only in the vicinity of the tip. It is not inconceivable that this is possible for the metals normally examined for dendritic growth; however, the exact dislocation geometry is not known. Conversely, if screw dislocations acted only as sources on the most densely packed planes, the preceding arguments about two-dimensional nucleation would apply.

The limitation imposed by the choice of rotational symmetry is primarily a numerical one. However, it would be possible to treat the case of steady-state growth of an ellipsoidal dendrite by calculating the important elements of the temperature distribution in a manner similar to that used for Eq. (19) *et seq.* In this case, the Bessel function in r must be replaced by a cosine function in x and y with the appropriate change in the variable b, i.e., for a nonrotationally symmetric dendrite, Eq. (6) must be replaced by

$$\theta_{lj}-\theta_{lj}^{\infty}=\int_0^{\infty}\int_0^{\infty} A(p_1,p_2)e^{\lambda_j(Z-Z_0)} \times\cos(p_1x+p_2y)dp_1dp_2, \quad (54)$$

with

$$\lambda_j=-(V/2\alpha_{lj})\{1+[1+4(p_1^2+p_2^2)\alpha_{lj}^2/V^2]^{\frac{1}{2}}\}.$$

This same procedure can, in principle, be applied to a dendrite of any symmetry type. However, the difficulty that arises for any dendrite of highly anisotropic material is not that of shape, but that it is most unlikely to exhibit a steady-state cap shape as compared to dendrites of rotational symmetry which arise primarily from the cubic family of crystal structures. A dendrite in a material with very anisotropic growth characteristics will exhibit a cap shape that is related to the equilibrium form of the crystal or, alternatively, to an end form of some sort which is displayed periodically along the length of the dendrite. In growth from solution, many such end-form dendrites are seen.[6] We expect that nickel and tin would approximate steady-state dendrites with rotational symmetry. However, ice is a questionable candidate.

Natural convection was neglected in the determinations of the temperature distribution and the solute distribution about the growing dendrite. Natural convection is present in the liquid because of the different densities of liquid and solid, ρ_L and ρ_s, respectively, and the principle of conservation of mass yields a condition for the convective velocity, U, at the interface. The interface moves normal to itself with a velocity V_n; hence, the mass solidified per unit surface area per unit time is ρ_sV_n. In the fluid there exists a convective motion which at the interface has the normal velocity U_n. Thus, the net velocity is (V_n-U_n), and this causes a mass flow per unit surface area per unit time of amount $\rho_L(V_n-U_n)$. Equating mass flows we have

$$U_n=-\epsilon V_n, \quad (55)$$

where $\epsilon=(\rho_s-\rho_L)/\rho_L$. Chambré[25] has shown for plane, cylindrical, or spherical solidification in which the interface advances at a rate proportional to $(\text{time})^{-\frac{1}{2}}$, that unless ϵ is appreciable, with respect to unity, the temperature distribution in the liquid and solid is essentially unaltered from the $\epsilon=0$ case. Since $\epsilon<0.1$ for any material we may wish to consider, the effect of natural convection upon the temperature distribution during dendritic growth can be justifiably neglected. Further, since it is primarily the ratio of U_n/V_n that is important for determining the effects of natural convection on diffusive transport processes, the same conclusions should apply to the solute distribution.[24]

In the numerical treatment it was explicitly assumed that the following material parameters, K_s, α_s, C_s, L, γ, and k_0, remained constant no matter how large the freezing velocity, V, became. Alternatively, one could suppose that, as V increases, an excess of vacancies are formed in the solid, making it of higher free energy than bulk solid in equilibrium at T_i. In this case, since L changes, γ will probably change, and if the vacancy concentration is higher than it should be, K_s, α_s, C_s, and k_0 will change. One would expect L and γ to decrease and K_s, α_s, and C_s to change in the direction of K_L, α_L, and C_L.

The assumption of an infinite liquid was also made. However, in practice, a melt may be considered infinite with respect to the dendrite when its boundaries are $\sim 10\alpha_L/V$ away from the body of the growing dendrite, and it is sufficiently long for steady state to be reached. It is also possible that a different steady state, not corresponding to the case we have considered, may be reached. For example, the results of Rosenberg and Winegard[19] have been criticized[22] on the basis that their dendrites grew along the surface of the tin melt at the liquid-air interface. In such a case our treatment would not apply without modification. Nevertheless, other results for tin[22] indicate that the difference achieved with a melt that completely encloses the growing dendrites contributes to a decrease in the growth rate for a particular ΔT, i.e., a change in degree and not in nature.

The optimization condition of maximum velocity was imposed upon our solutions to determine completely the dendrite characteristics. No rigorous justification can be given for this assumption although the reasons for choosing maximum velocity are self evident. On the other hand, we could have assumed situations where the problem was specified. For example, if the dendrite growth were periodic rather than steady-state, there might be some cases where the kinetics of nucleation at specific layer sources were such as to determine completely our solutions without invoking an optimization condition. This alternative, however, seems to be too arbitrary.

---

[25] P. L. Chambré, Quart. J. Mech. and Appl. Math. IX-2, 224 (1956).

B. Further Applications

1. Aggregates of Dendrites

If we consider a close-packed array of dendrites originating at some instant of time at some plane in the liquid and growing in the same direction, we might ask what minimum center-to-center spacing, $a_{\min}$, these dendrites could have without perturbing the tip propagation of each other. We know that no matter what value of $a_{\min}$ is chosen, thermal field interaction will occur at the plane of origin after the dendrites have developed to a certain length. We must therefore arbitrarily choose to find the minimum value of a for which dendrites of length $N\rho$ overlap their thermal fields beyond the $[T_\infty+M(T_i-T_\infty)]$ isotherm at the plane of origin. For isothermal dendrites, $a_{\min}$ is given by

$$\frac{E_i[-(V\rho/2\alpha_L)g_c]}{E_i(-V\rho/2\alpha_L)}=M, \tag{56}$$

where $g_c=N+[N^2+(a_{\min}/2\rho)^2]^{\frac{1}{2}}$. Choosing $M=0.1$ for simplicity and $N=-1$, -10, and -100, respectively, we obtain $a_{\min}/2\rho=440$, 450, and 530 for $V\rho/2\alpha_L=10^{-3}$; $a_{\min}/2\rho=67$, 75.3, and 132 for $V\rho/2\alpha_L=10^{-2}$; and $a_{\min}/2\rho=12$, 18.5, and 48.1 for $V\rho/2\alpha_L=10^{-1}$. Using the data in Table I and interpolating the above, we find that, for $N=-10$, $a_{\min}/(\alpha_L/V)\approx 5$, 0.5, and 2.5 for nickel, tin, and ice, respectively. Thus, we see that $a_{\min}\sim\alpha_L/V$, as might be guessed for a transport controlled process. The problem of dendrite branching could be approached in a fashion analogous to the foregoing; however, the procedure would be much more complex because of the time dependent nucleation of branches, one after another as the dendrite core propagates.

2. Dendrites Pulled at a Constant Rate

The same general procedure can be applied to the case where the dendrite is pulled from the melt as a filament or ribbon. Since the pulling velocity is constant, a different optimization condition must be used. In this case we prefer to choose the "maximum interface temperature" condition.[26] The application of this condition to the determination of ρ requires an intimate knowledge of the temperature distribution in the crucible with $V=0$. Since this is not generally known except for particular experimental designs, we shall not attempt to analyze this process here.

3. Growth from Solution

The case of dendritic growth from solution can be treated by our procedure. For an isoconcentrate dendrite, Eq. (39) should be used rather than Eq. (33) for determining the maximum velocity. However, it is somewhat more tedious if one cannot use the approximation $E_i(-V\rho/2D_L)\approx\ln(\gamma^*V\rho/2D_L)$. For a nonisoconcentrate dendrite one can perform calculations analogous to Eq. (19) *et seq.* to develop the correct solute distribution in the vicinity of the tip. The correct solute flux equation at the tip can be developed; it will be analogous to Eq. (24) and can then be differentiated to yield the maximum velocity. However, this procedure will be difficult to follow if $V\rho/2D_L>1$. Dendrite caps of anisotropic shape can also be treated but with considerably more difficulty.

C. Conclusions

We concluded quite early in our treatment that the problem of determining dendrite characteristics is generally not completely determined, and that some optimization condition must be chosen to facilitate the solution. To do this we chose the condition of "maximum linear velocity" and were able to calculate (i) the dendrite velocity, V, and the dendrite size, R, as a function of both supercooling, ΔT, and the bath solute concentration, C_∞; (ii) the dendrite direction; and (iii) the solute concentration in the dendrite as a function of its freezing velocity. It was found that, for $k_0<1$, the dendrite is depleted in solute and, for $k_0>1$, the dendrite is enriched in solute. It was deduced that the existence of a specific dendrite direction in a given system is evidence for anisotropy of solid-liquid interfacial energy, γ, or anisotropy of atomic kinetics. Finally, it was found that temperature variation on the surface of a dendrite and heat transfer in the solid must be taken into account when attempting to fit theory and experiment.

The atomic kinetic data determined by matching experiment with theory for a nonisothermal dendrite is very different than that for an isothermal dendrite. Matching with a nonisothermal dendrite leads to the diffuse interface as the most reasonable mechanism; but since some temperature dependence of μ is observed, this leads us to anticipate that the material parameters may not be constant with change of V. The necessity or validity of this conclusion has not been tested experimentally. It is therefore of questionable value to attempt either the analysis of more complex situations in the same manner or to incorporate more complex assumptions in the present treatment. Thus, although we have not exhausted the possible instances of dendritic growth by any means, we have treated the most likely case of growth from the melt for metals of high symmetry.

---

[26] G. F. Bolling and W. A. Tiller, J. Appl. Phys. **31**, 2040 (1960).

ACKNOWLEDGMENT

We are indebted to Dr. D. R. Hamilton for directing our attention to the analysis of Temkin.

APPENDIX I. THE SIMPLE DENDRITE AND ENTROPY PRODUCTION

(i) Here we shall treat a simple dendrite model consisting of a rod of radius R with a hemispherical cap. The first treatment for the growth velocity which follows is originally due to Fisher.[27] For this particular shape it is assumed that the steady-state temperature distribution around a stationary source is a good approximation since $V/\alpha_L \ll 1$. Thus the temperature distribution is

$$T = T_\infty + (T_i - T_\infty)(R/r). \qquad \text{(I1)}$$

The axial freezing velocity is obtained through the thermal flux condition at the cap by considering the "rate of increase of volume" of the hemisphere. Thus,

$$V = dR/dt = 2K_L(T_i - T_\infty)/LR. \qquad \text{(I2)}$$

Using the relationship $T_m - T_i = (2\gamma/\Delta SR)$, as in Fig. 1, but neglecting δT, and substituting in (I2) we obtain

$$V = K_L(T_i - T_\infty)(T_M - T_i)/\gamma T_M. \qquad \text{(I3)}$$

$V_{\max}$ is obtained by setting $dV/dT_i = 0$; thus,

$$T_i = \tfrac{1}{2}(T_M + T_\infty), \qquad \text{(I4)}$$

and

$$V_{\max} = K_L \Delta T^2 / 4\gamma T_M,$$

as obtained by Fisher.[27]

If δT is included in the foregoing treatment, the following result is obtained in the same manner:

$$T_i = \tfrac{1}{2}(T_M + T_\infty - \delta T),$$

and

$$V_{\max} = (K_L/4\gamma T_M)(\Delta T^2 - \delta T^2). \qquad \text{(I5)}$$

(ii) We are now interested in calculating the entropy production for this simple dendrite. Three entropy producing contributions need to be considered: the surface energy of the rod body, the irreversible loss due to the temperature gradients set up in the system by the advancing tip, and the departure from kinetic equilibrium over the cap of the dendrite. The rate of entropy production for these three are arranged respectively in the total entropy production

$$\left(\frac{dS}{dt}\right)_{\text{total}} = -\frac{1}{T}(2\pi R\gamma V) + K_L \int_{V_0} \left(\frac{\text{grad}T}{T}\right)^2 dV_0 + \frac{1}{T}(\pi R^2 \Delta s \delta T V), \qquad \text{(I6)}$$

where V_0 is the volume of integration. The last term is neglected in order to compare with Fisher's[27] solution for this dendrite model, and we use

$$\text{grad}T = -(T_i - T_\infty)(R/r^2)$$

and

$$\int_{V_0} dV_0 = \int_{-\pi}^{\pi}\int_{-\pi}^{\pi}\int_{R}^{\infty} r^2 \sin\theta\, dr\, d\theta\, d\phi$$

to obtain

$$\left(\frac{dS}{dt}\right)_{\text{total}} = \frac{2\pi K_L(T_i - T_\infty)}{T_M^2} \times \left\{-\frac{2\gamma T_M}{L} + R(T_i - T_\infty)\right\}. \qquad \text{(I7)}$$

Finally, substituting for R from $T_m - T_i = (2\gamma/\Delta SR)$, we obtain

$$\left(\frac{dS}{dt}\right)_{\text{total}} = \frac{4\pi\gamma K_L}{LT_M}(T_i - T_\infty)\left\{\frac{T_i - T_\infty}{T_M - T_i} - 1\right\}. \qquad \text{(I8)}$$

If it is supposed that a principle of minimum entropy production applies and determines the condition for optimization of dendritic growth, we might set $(d/dT_i)(dS/dt)_{\text{total}} = 0$ and determine T_i. However, such a procedure leads to a minimum that yields a *negative* rate of entropy production in Eq. (I8). We can only require instead that $(dS/dt)_{\text{total}} \geqslant 0$. Apart from the trivial solution, $T_i = T_\infty$, this yields the condition

$$T_i \geqslant (T_M + T_\infty)/2. \qquad \text{(I9)}$$

This is identical with the condition for maximum velocity in Eq. (I4) at the lower limit.

When a growth law is required, i.e., $V = f(\delta T)$ and δT is not zero, Eq. (I6) yields in a similar manner as in obtaining (I8) the form

$$\left(\frac{dS}{dt}\right)_{\text{total}} = \frac{4\pi\gamma K_L}{LT_M}(T_i - T_\infty)\left\{\frac{T_i + \delta T - T_\infty}{T_M - T_i - \delta T} - 1\right\}. \qquad \text{(I10)}$$

Now, however, maximum velocity is not required, but rather the condition $(d/dT_i)(dS/dt)_{\text{total}} = 0$ is sought for a minimum in the entropy production. Therefore, we may not set $(d\delta T/dT_i) = 0$, as in deriving Eq. (I5). It is found, even in this simple case that the minimum may yield a negative value of $(dS/dt)_{\text{total}}$, depending upon the value of $d\delta T/dT_i$.

Alternatively, investigation of the condition for positive entropy production yields

$$T_i \geqslant \tfrac{1}{2}(T_M + T_\infty) - \delta T. \qquad \text{(I11)}$$

Thus, by comparison with Eq. (I5) we may conclude that the condition for maximum velocity occurs at a value of positive entropy production which is not a minium.

Therefore, the only thermodynamically tenable state of minimum entropy production in this case is "zero entropy production." This result is inconsistent with he reasoning that in any nonequilibrium process the ntropy of the universe must increase. We must there- onclude that either minimum entropy production is ot the proper optimization condition, or that we have eglected an important but not obvious contribution o the entropy production during the dendritic growth rocess.

---

[27] J. C. Fisher, as communicated to B. Chalmers and associates, 1953; quoted in reference 19.

APPENDIX II. GROWTH MECHANISMS

For atomically rough solid-liquid interfaces, or where the exact nature of the interface is ignored, two simple rate equations are available for the atomic kinetics. Turnbull[15] applied the approach of absolute rate theory to obtain

$$V=\lambda(kT/h)\cdot(\Delta S/RT)\cdot e^{-(\Delta F_A/RT)}\cdot\delta T\approx\mu_1'\delta T, \qquad \text{(II1)}$$

where λ is the interatomic spacing normal to the interface, ΔF_A is the free energy of activation for the freezing process, and the other constants have their usual meanings. ΔF_A is expected to be small, and it is not unreasonable to suppose that the entropy of activation for freezing is zero, and that the activation energy is about equal to or less than that for liquid diffusion. With this reasoning μ_1' would be obtained in the range 10–100 cm/sec/°C for most metals.

Later, Hillig and Turnbull[16] pointed out that simple rate theory yields

$$V=D\Delta S\delta T/lRT\approx\mu_1''\delta T, \qquad \text{(II2)}$$

where D is the diffusion coefficient for transport across the interface, and l is the jump distance. If D is chosen as the coefficient for liquid diffusion and $l\approx\lambda$, then μ_1'' is of the order 1 cm/sec/°C.

Jackson and Chalmers[17] added an accommodation factor to the absolute rate equation. Using their assumption, the rate of freezing may be written as

$$V=N_LV_0A_FG_F\cdot(kT/h)(\Delta S/RT)e^{-(Q_F/RT)}\cdot\delta T$$
$$=\mu_1'''\delta T, \qquad \text{(II3)}$$

where N_L is the number of atoms per cm^2 at the interface, V_0 is the atomic volume in the solid, and A_FG_F embodies the accommodation factor. This latter may be related to the fraction of active sites, or to the sticking probability at the interface. Choosing Q_F to be the activation energy for liquid diffusion and with the choice $A_FG_F\approx(1/100)^{17}$ we obtain μ_1''' of the order 1 cm/sec/°C. There is a certain amount of flexibility in choosing the numbers, but it may be seen that

$$\mu_1'''\approx A_FG_F\mu_1'.$$

Cahn[18] proposed that interface motion might not be limited to the occupation of discrete atomic sites. Without reviewing his theory in detail, we note that the interface may be *diffuse*, "the change from one phase to the other is gradual occurring over several atom planes, in contrast to a sharp surface . . . confined to one interplanar distance."[18] With the concept of diffuseness, the resistance to motion would be greatest for close-packed planes (which would have the greatest tendency to be singular) and tend to zero for irrational index planes.

Cahn[18] showed that the surface tension γ of an interface may be described as

$$\gamma=[1+g(\alpha)]\gamma_0, \qquad \text{(II4)}$$

where $g(\alpha)\geq 0$ is a dimensionless periodic function of the coordinate α where α represents the advance of the in-interface from an equilibrium position at which $g(\alpha)=0$. The period of this function is obviously the interplanar distance in the direction defining γ_0 at equilibrium, which is a low-index direction in the system. For an interface slightly departed from a low-index plane, it was then shown that the interface might be considered stepped, such that the steps had a width

$$W=\lambda/g(\alpha)_{\max}{}^{\frac{1}{2}}, \qquad \text{(II5)}$$

and that the excess energy ϵ per unit length of step was

$$\epsilon=\lambda\gamma_0 g(\alpha)_{\max}{}^{\frac{1}{2}}. \qquad \text{(II6)}$$

Thus the surface tension of this interface may be written

$$\gamma'=\gamma_0[1+g(\alpha)_{\max}{}^{\frac{1}{2}}\theta], \quad \text{for} \quad \theta \text{ small}, \qquad \text{(II7)}$$

where θ is the departure in angle from the low-index plane.

The conditions upon driving force for the characteristics of interface motion are that

$$-\Delta F_M>[(\pi\gamma_0 g(\alpha)_{\max}V_M/\lambda]$$

produces uniform motion and that

$$-\Delta F_M<[\gamma_0 g(\alpha)_{\max}V_M/\lambda]$$

necessitates stepwise growth with a step energy ϵ independent of $-\Delta F_M$, where $-\Delta F_M$, is the driving force per mole and V_M is the molar volume. In the region of $-\Delta F_M$ between these extremes some nucleation process might occur giving rise to nearly indistinct steps of an energy that would depend upon the exact magnitude of $-\Delta F_M$.

In the treatment of Hillig and Turnbull[16] it was proposed that only a fraction η of the sites at a surface were active for growth. Then by using the concept of growth aided by screw dislocations,[28] they proposed that the active sites existed only at step edges in the spiral ramp produced by the screw dislocation. If this reasoning is used in conjunction with the theory of Cahn,[18] it may be concluded that growth can be aided by screw dislocations until a critical driving force is exceeded. Further, we propose that the number of active sites for growth per unit atomic length of step may not be unity but rather a number W/λ.

Thus a definite meaning may be ascribed to the process of accommodation at a diffuse interface. On the faces considered, for $-\Delta F_M$ small, accommodation is zero except at steps where the accommodation is unity; for $-\Delta F_M > \pi\gamma_0 g(\alpha)_{\max} V_M/\lambda$ the accommodation approaches unity everywhere. The activated process should be similar to that for liquid diffusion. Therefore we may write a growth law for all supercoolings using an accommodation factor η;

---

[28] F. C. Frank, Discussions Faraday Soc. 5, 48 (1949).

$$V = \eta\mu\delta T, \tag{II8}$$

where $-\Delta F_M > \pi\gamma_0 g(\alpha)_{\max} V_M/\lambda$, $\eta \approx 1$. Otherwise, foling Cahn[18] (or Hillig and Turnbull[16]), we obtain first that $\eta = (\lambda/4\pi\rho_c)\cdot(W/\lambda)$, where ρ_c is the critical nucleus size. Cahn[18] shows that

$$\rho_c = -\epsilon\ \lambda\Delta F_V = \gamma\cdot g(\alpha)_{\max}{}^{\frac{1}{2}} V_M/\Delta S\delta T,$$

and

$$W/\lambda = 1/g(\alpha)_{\max}{}^{\frac{1}{2}}.$$

Then

$$\eta = \xi\lambda\Delta S\delta T/4\pi\gamma_0 g(\alpha)_{\max} V_M, \tag{II9}$$

where for every "site" at this step there will be ξ atoms available in the liquid. In order to estimate ξ without relegating it to the state of another adjustable parameter, we note that for uniform motion $\eta \approx 1$ and $-\Delta F_M > \pi\gamma_0 g(\alpha)_{\max} V_M/\lambda$. Thus, in Eq. (II9) we may obtain $\xi \approx 4$ when $-\Delta F_M$ is set as $\Delta S\delta T$. Hillig and Turnbull chose a number $\xi \approx 3$.

Finaly, to obtain the proposed growth law, Eq. (II8), we must choose both μ and $g(\alpha)$. These will both be orientation dependent. As the direction considered departs from low index planes, with any anisotropy in the system, γ_0 should increase; $g(\alpha) \rightarrow 0$; and the quantity $\eta\mu$ should approach the values μ_1 for rough interfaces. We expect $100 > \mu_1 > 1$ cm/sec°C; however, in the treatment used, we may identify μ as a constant ($\mu = \mu_1$ for an interatomic spacing λ identical with that in the diffuse layer).

In order to make a better estimate we note that linear growth laws do not seem to apply at low supercoolings and arbitrarily choose, for example, that the critical driving force, in Cahn's model, is not exceeded for $0.01T_M$. Thus,

$$g(\alpha)_{\max} > \Delta S\delta T_c\lambda/\gamma_0 V_M = L\delta T_c\lambda/T_M\gamma_0 V_M, \tag{II10}$$

and using $\delta T_c \approx 0.01T_m$ and according to Turnbull's work on nucleation,[15] $(\gamma_0 V_M/\lambda L) \approx 0.45$ for metals, we obtain $g(\alpha)_{\max} \gtrsim 0.02$.

We can only ask, in the absence of other knowledge of diffuseness, whether or not this is reasonable. Using Cahn's[18] theory, this predicts that the interfaces cannot be more diffuse than about two interatomic distances on a simple binding model. Substituting (II9) and (II10) in (II8), we obtain

$$\delta T \lessgtr 0.01T_M, \qquad V \lesssim \frac{45\lambda\Delta s}{\pi\gamma_0 V_M}\mu\delta T^2, \tag{II11}$$

$$\delta T > (\pi\gamma_0 V_M/45\lambda\Delta s), \quad V \approx \mu\delta T.$$

The rates could be increased in the region $\delta T \leq 0.01T_M$ by a factor, m, if there were m suitable located screw dislocations to give a growth source of strength m.

In Fig. 5 of the text, we have plotted (II11) for tin using $\mu = 4$ cm/sec°C, in reasonable agreement with the values μ_1', μ_1'', and μ_1'''.

APPENDIX III

Temkin[29] has considered the crystal growth of a needle-shaped body into a supercooled melt. The complication due to solutes present in the melt were neglected, but both curvature and the necessity for a growth law were taken into account as they vary along the surface of a real dendrite. Because a rigorous solution to the steady-state problem of dendritic growth is exceedingly difficult he assumed that the paraboloid of revolution of Ivantsov[12] was a good first approximation to the body shape. Second, he assumed a growth law for uniform interface advance. An elegant solution to the heat flow problem was then constructed which matched the boundary conditions in the vicinity of the dendrite tip for a body that exhibited the temperature variation along its surface to satisfy both curvature and growth law requirements in the steady state. This solution has the form[29]

$$-\frac{V\rho}{2\alpha_L}e^{V\rho/2\alpha_L}E_i\left(-\frac{V\rho}{2\alpha_L}\right) = \frac{C}{L}\frac{\Delta T}{[1+(L_1/\mu\rho)+(L_2\gamma/V\rho^2)]}, \tag{IIIT17}$$

where

$$L_1 = \frac{K_L}{L}\left[N_1 + \frac{K_S}{K_L}M_1\right], \quad L_2 = \frac{K_L}{L\Delta S}\left[N_2 + \frac{K_S}{K_L}M_2\right],$$

and where the constants M_1, M_2, N_1, and N_2 are integrals involving Bessel functions of several kinds which may be evaluated numerically; the material parameters have been rephrased in our notation in (IIIT17).

At this stage the solution was still unspecified, yielding only the variation of the quantity $V\rho$. For comparison, our Eq. (24) may be rearranged in the form

$$-\frac{V\rho}{2\alpha_L}e^{(V\rho/2\alpha_L)}E_i\left(-\frac{V\rho}{2\alpha_L}\right) = \frac{C_L}{L}(\Delta T)\frac{\{1-[\delta T(0)/\Delta T]-2\gamma/\Delta S\rho\Delta T\}}{[1+(4\gamma\Delta K/L\Delta SV\rho^2)+(\Delta K/L\mu\rho)]}. \tag{III1}$$

These two equations yield the same type of variation since the bracket in the numerator is approximately unity as seen from the data of Table I. However, let us proceed further. Equation (III1) may be phrased as

---

[29] D. E. Temkin, Soviet Phys.—Doklady 5, 609 (1960).

$$-xe^{x}E_i(-x)=C_L y/\Delta S, \qquad \text{(III2)}$$

where $y=F(V,\rho)$, $(V\rho/2\alpha_L)=x$, etc. This form is plotted in Fig. 17, where it can be seen that, as x diminishes, a power relation may be derived in the form

$$x=Ay^{B}. \qquad \text{(III3)}$$

The value of the intercept A is directly related to the specific choice of the quantity $(C_L/\Delta S)$; the exponent $B=B(V,\rho)$, however, is a function of the range considered for x. In Fig. 17 the value of B appears to be 1.1, for $10^{-7}\gtrsim x\gtrsim 3\times 10^{-4}$; whereas, for variation of x we have

$$\begin{aligned} B&=d\ln x/d\ln[-xe^{x}E_i(-x)]\\ &\approx \ln\gamma^{*}x/(1+\ln\gamma^{*}x), \quad \text{as} \quad x\rightarrow 0. \qquad \text{(III4)}\end{aligned}$$

The region of interest for x found in Table I of the text for several materials is $10^{-3}\gtrsim x\gtrsim 10^{-1}$; here we find $1.19\gtrsim B\gtrsim 1.75$.

Temkin placed Eq. (IIIT17) in the form of Eq. (III3) and obtained the following:

$$\frac{V\rho}{2\alpha_L}=A\left\{\frac{C_L}{L}\frac{\Delta T}{[1+(L_1/\mu\rho)+L_2\gamma/V\rho^2]}\right\}^{B}. \qquad \text{(IIIT18)}$$

Since the problem was still unspecified at this stage, Temkin also chose to use the "maximum velocity" condition with the specific choice that $B=\text{constant}$.

We previously used the procedure represented by Eq. (III3) for treating the isothermal dendrite,[24] and although we found it to be very useful there, we do not consider this approximation to be perfectly valid in the complete treatment of the nonisothermal dendrite; for the important range of x exhibited by real dendrites, B is not independent of x. This follows from an examination of the differentiation of any equation of the form (III3), where the exponent B is a function of the important variables. Rephrasing Eq. (IIIT18) to read $V\rho/2\alpha_L=A[F(V,\rho]^{B(V,\rho)}$, the differentiation with respect to ρ setting $(dV/d\rho)=0$ yields

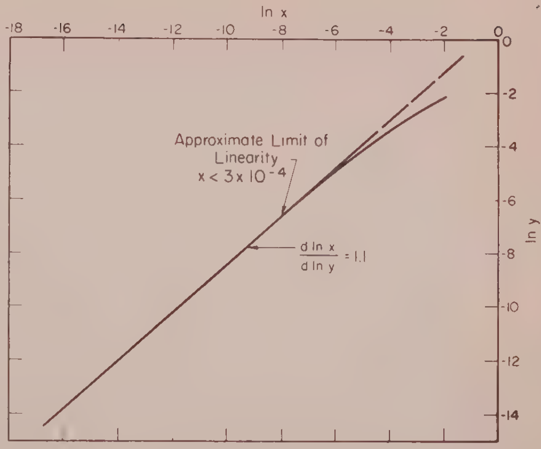

FIG. 17. Equation III-1 for tin plotted on a $\log_e$-$\log_e$ scale with $x=V\rho/2\alpha_L$ and

$$y=(\Delta S/C_L)[(-V\rho/2\alpha_L)E_i(-V\rho/2\alpha_L)e^{(V\rho/2\alpha_L)}].$$

$$\frac{V^{*}}{2\alpha_L.1}=F(V,\rho)^{B(V,\rho)}\left[\left(\frac{dB(V,\rho)}{d\rho}\right)\ln F(V,\rho)+\frac{B(V,\rho)}{F(V,\rho)}\frac{dF(V,\rho)}{d\rho}\right]. \qquad \text{(III5)}$$

In considering B as a constant, the first term in Eq. (III5) is neglected. $[dB(V,\rho)/d\rho]$ may be evaluated from Eq. (III4), and then from the data in Table I it can be seen that, for Sn, this term increases from about 10% to about 60% of the second term as ΔT increases from 3.7° to 13.3°C. For Ni and ice, the first term is 200% and 175% of the second for $\Delta T=123°$ and 4.77°C, respectively. Therefore, since we are interested in calculating values of μ from the fit with experimental data, the assumption of a constant B will introduce an error in magnitude for μ and, more important, will disguise any variation of μ with V. The power relation approach of Temkin[29] is therefore somewhat prohibitive to an accurate analysis of the maximum velocity dendrite. However, this is the only drawback in his very elegant treatment of the needle-shaped crystal.

JOURNAL OF APPLIED PHYSICS VOLUME 32, NUMBER 12 DECEMBER, 1961

High-Field Conductivity in Germanium and Silicon at Microwave Frequencies*

J. Zucker,† V. J. Fowler, and E. M. Conwell
General Telephone and Electronics Laboratories, Bayside, New York

(Received February 17, 1961)

The effect on the conductivity of germanium and silicon samples of 2.85-kMc electric fields up to peak values of 10 000 v/cm was measured. These measurements differ from earlier ones in that: (1) the microwave field was in the form of progressive rather than standing waves, which made possible more accurate determination of the field strength in the sample, and (2) to determine whether any frequency effects occur at 2.85-kMc conductivity was measured at high dc fields on the same samples. From the average conductivity under microwave excitation the instantaneous conductivity was calculated and found to agree, within experimental error, with the dc conductivity, indicating that the conductivity can still follow the 2.85-kMc field at least up to peak fields of 10 000 v/cm.

1. INTRODUCTION

The high-field dc conductivity of germanium and silicon has been measured by many workers.[1] The conductivity of germanium excited by high 35-kMc fields has been investigated by Seeger[2] using the technique of Morgan.[3] From a comparison of his 35-kMc data with dc pulse data taken by other workers, Seeger concluded that the mobility in germanium was frequency-independent at strong 35-kMc fields down to liquid nitrogen temperature and for weak 35-kMc fields down to 200°K. These conclusions seem reasonable according to the simple Drude-Zener[4] theory of high-frequency conductivity. This theory predicts that low-field conductivity at frequency ω should equal the dc conductivity provided the square of $\omega\tau$, where τ is the momentum relaxation time, is much less than unity. Since the relaxation time for germanium at room temperature is of the order of 3×10^{-13} sec or less, no departure from the dc conductivity should be detectable at room temperature for frequencies much less than 100 kMc. At liquid nitrogen temperature, the relaxation time in Ge is about ten times its room temperature value so that no change in conductivity should be detectable below about 10 kMc, according to the simple theory. If the criterion $\omega\tau \ll 1$ is applied also at high fields, it leads to a prediction of smaller frequency effects for a given ω than at weak fields, since the relaxation time is reduced due to the increased average speed of the carriers. However, the magnitude of the relaxation time is not the only determinant of the absence or presence of frequency effects. Another factor which must be considered is the time required for the distribution to reach its steady state at any given value of electric field. If this time is longer than the weak-field relaxation time, which is not unlikely, strong-field frequency effects may occur at lower frequencies than indicated by the value of $\omega\tau$.

Seeger's work is not felt to be conclusive for two reasons. First, it was based on comparison between his microwave data and dc pulse data taken on different samples by other workers. It is well known that orientation and the degree of uniformity of a sample affect considerably the behavior of the strong-field conductivity of germanium and silicon. The only way to eliminate these variables in a study of frequency effects is to make measurements at the various frequencies on the same sample. Second, his method for determining the microwave field in the samples has poor accuracy for high resistivity samples, because it is based on a measurement of the power absorbed by the sample. Seeger found considerably smaller changes in conductivity with field for samples with high resistivity of the order of 20 ohm cm than for samples of about 3 ohm cm. Dc pulse data for the same range of resistivities and field intensities, however, showed about the same changes for high and low resistivities.[5] Since the discrepancy between Seeger's microwave data and the dc pulse data was not greater at liquid nitrogen temperature than at room temperature, its source does not seem to be a frequency effect. Thus it is most likely that the differences were due to the poor accuracy in the microwave field determination. It therefore seems advisable to adopt a different technique for applying the microwave field to the samples under test, one which leads to better accuracy in electric field determination. One such technique is to apply the field in the form of a traveling wave and to calculate the field at the sample from the transmitted power. If the sample is made small enough, no correction need be made for the small amount of power absorbed by the sample. The transmitted power will be large and easily measured with standard methods.

The present work contains a report on measurements of high-field conductivity under excitation with 2.85-kMc pulses, and with dc pulses. The materials used were germanium and silicon at room temperature, and germanium at liquid nitrogen temperature. Field intensities up to 10 kv/cm were used. For the 2.85-kMc case

---

* Work supported by Air Force Cambridge Research Center.

† A portion of this work constitutes part of a thesis submitted in partial fulfillment of the requirements for the Ph.D. degree, Department of Physics, New York University, New York.

[1] See, for example, J. B. Gunn, *Progress in Semiconductors* (John Wiley & Sons, Inc., New York, 1957), Vol. 2, p. 246. This paper contains references to earlier work.

[2] K. H. Seeger, Phys. Rev. **114**, 476 (1959).

[3] T. N. Morgan, J. Phys. Chem. Solids **8**, 245 (1959).

[4] See, for example, F. Seitz, *Modern Theory of Solids* (McGraw-Hill Book Company, Inc., New York, 1940).

[5] J. Zucker, J. Phys. Chem. Solids **12**, 350 (1960).

he quantity actually measured was the average current hrough the sample while it was subjected to the high-nicrowave field. To determine from this the instananeous conductivity as a function of microwave field it vas necessary to solve an integral equation. This was lone in an approximate fashion, although to good ccuracy, by making use of the observation that the ariation of the average current with peak microwave ield is very well represented by a simple empirical unction with two parameters. The resulting instananeous conductivity vs field was then compared with he dc conductivity vs field.

2. EXPERIMENTAL TECHNIQUES

2.1 Sample Fabrication

A sample geometry found suitable for both dc pulse nd microwave measurements is shown in Fig. 1. It onsisted of a narrow filament ground onto a cylinder of ingle crystal germanium or silicon. The one massive nd served to eliminate injection into the filament luring the pulse.[5] The length of the filament was about .5 mm while its diameter was about 0.2 mm. The amples were made by grinding with an air-driven liamond wheel. For this process they were mounted on lathe having an extremely slow automatic feed (0.25 n. per hr). The wheel was presented at an angle of bout 45° to the end of the sample blank and the sample vas rotated. The work was water cooled to prevent verheating and fracture.

To minimize surface effects, germanium samples were tched in a CP4 bromine solution, while silicon samples vere etched in sodium hydroxide. Contacts to the ermanium samples were made by first gold plating vith a solution of gold cyanide containing small quanities of indium for *p*-type and antimony for *n*-type amples, and then soldering with a low-melting point older such as cerroseal. Contacts to the silicon samples were made by first plating in the same way as the germanium samples and then alloying in an atmosphere of pure dry hydrogen at 900°C for five minutes. All the samples reported on were oriented in the 110 direction, using the light figure technique[6] for this purpose.

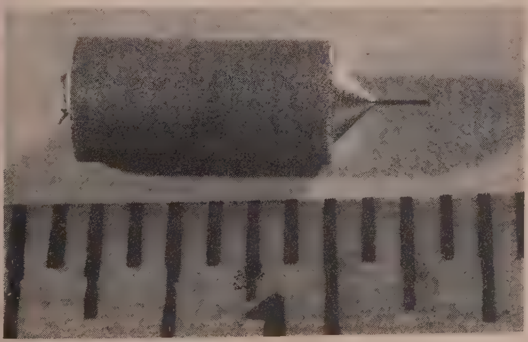

Fig. 1. Photograph of sample used for measurement of strong-field dc and *S*-band microwave conductivity of Ge and Si.

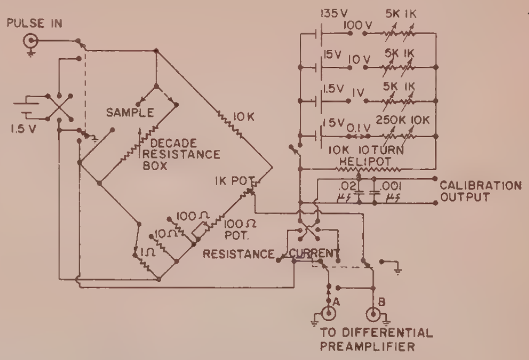

Fig. 2. Schematic of substitution bridge and dc shift source for the measurement of strong-field conductivity using 3-μsec pulses.

2.2 dc Pulse Measurements

The dc pulse measurements were made in either of two ways, depending on the sample. For germanium samples having a room-temperature resistivity more than 5 ohm cm a substitution bridge technique was employed similar to that used by Bray.[7] A dc shift source for more precise pulse height measurements was added to the basic bridge circuit. A schematic of the circuitry appears in Fig. 2. The bridge was supplied with 3-μsec pulses from a conventional high-voltage pulse generator. The null indicator for the bridge was a Tektronix 535 oscilloscope with a 53/54D preamplifier. The current through the sample was equal to the pulse voltage V_I across the resistance in series with the sample divided by this resistance R_I. A variable dc source calibrated with a K–2 potentiometer was used as a shift generator in measuring pulse heights. This method is insensitive to variations in the gain of the oscilloscope amplifier and is substantially more accurate than would be measuring the pulse heights from the oscilloscope face. Pulse heights were measured by shifting the pulse tops into coincidence with a zero level established by feeding the same signal into each channel of the preamplifier. The voltages necessary to achieve these coincidences were read from the dial of a ten-turn Helipot having a rated linearity of $\frac{1}{2}\%$. This, together with the $\frac{1}{2}\%$ precision with which a coincidence may be established, led to errors in pulse height determination and therefore current of 1%. Errors in total sample resistance were only $\frac{1}{2}\%$.

The resistance R_s determined in this way was the sum of the filament resistance R_f and the end resistance. With the latter denoted by ϵR_f, $R_s = R_f(1+\epsilon)$. The value of ϵ at low fields, $\epsilon(0)$, was obtained by passing a small current through the sample and measuring the

---

[6] G. H. Schwuttke, J. Electrochem. Soc. **106**, 315 (1959).

[7] R. Bray, Phys. Rev. **100**, 1047 (1955).

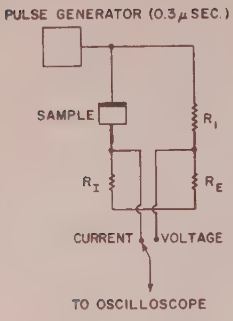

FIG. 3. Resistance network for the measurement of strong-field conductivity with 0.3-μsec pulses.

ratio V_c/V_t, where V_c was the voltage drop between the massive end contact and the base of the narrow filament and V_t was the voltage across the whole sample. Then,

$$\epsilon(0)=V_c/V_t/1-V_c/V_t. \tag{1}$$

The measured values of $\epsilon(0)$ for the samples of the present study ranged from 0.03 to 0.09. As the electric field increases, ϵ decreases, the ratio of $\epsilon(E)$ to $\epsilon(0)$ being approximately $R_s(0)/R_s(E)$. The ratio of the conductivity at the field E to the low-field conductivity is then

$$\sigma(E)/\sigma(0)=\frac{R_s(0)}{R_s(E)}\,\frac{1+\epsilon(0)R_s(0)/R_s(E)}{1+\epsilon(0)}. \tag{2}$$

From similar considerations the electric field intensity in the filament is

$$E=\frac{V_IR_s(E)}{R_I[1+\epsilon(0)R_s(E)/R_s(0)]L_f}, \tag{3}$$

where L_f is the filament length. Even if the error in $\epsilon(E)$ determined as described were as much as 25% of $\epsilon(0)$, the maximum error in $\sigma(E)/\sigma(0)$ would be less than 4% for all the samples measured. The maximum error in E was about 6%, with the error being much less than this in most cases.

This technique could not be used for lower resistivity germanium samples and for any of the silicon samples because it was found that the 3-μsec pulses caused lattice heating. The evidence for heating was a decrease in current during the pulse. To avoid this, shorter pulses were necessary. Since the bandwidth of the bridge and the 53/54 D preamplifier was not adequate for the 0.3-μsec pulses used to avoid heating, the network of accurately measured carbon resistors shown in Fig. 3 was used. With this arrangement, the sample resistance R_s is given by

$$R_s=(V_E/V_I)(R_I/R_E)(R_1+R_E)-R_I, \tag{4}$$

and the voltage across the sample by

$$V_s=V_E(1+R_1/R_E)-V_I. \tag{5}$$

The ratio of conductivities is again given by expression (2), and the electric field is

$$E=V_s/L_f[1+\epsilon(E)]. \tag{6}$$

A calibrated Tektronix 53/54L preamplifier was use in place of the 53/54D unit. The accuracy of a singl measurement of voltage was 3%. This, together wit the errors due to the massive end, caused a maximu possible error in the ratio of conductivities of 15%, wit the error generally about 10%. The error in electri field intensity was between 5 and 9.5%, depending o the size of the end correction.

The measurements at room temperature were mad with the samples immersed in oil (Dow Corning silicon oil No. 703) which acted as a thermostatic bath. Th samples were immersed directly in a liquid nitroge bath for the low-temperature measurements. [The resulting data points for $\sigma(E)/\sigma(0)$ vs field of the sample studied are shown in Figs. 7–10.]

2.3 2.85-kMc Measurements

The apparatus used for the 2.85-kMc measurement is shown in Figs. 4 and 5. It consisted of a short sectio of 2.840-in. by 0.074-in. brass waveguide, which serve as the sample holder, with stainless steel E-plane taper on both ends leading to standard RG-48/U waveguide The waveguide was terminated with a matched loa and reflected waves were eliminated by means of a E–H tuner at the large end of the tapered section. I this manner it was possible to transmit the full 100 kw of power generated by a 2J31 magnetron as a traveling wave through the sample holder and into the powe termination without producing breakdown in th sample holder. Cooling of samples to liquid nitroge temperature was accomplished by first pressurizing th waveguide with dry nitrogen to eliminate frosting an then pouring liquid nitrogen into a brass well fixed to th top of the sample holder. The well and sample holde were thermally insulated with a Styrofoam-lined box The stainless steel tapered section afforded some therma insulation between the sample holder and the rest of th system. Despite the large mass of the sample holder

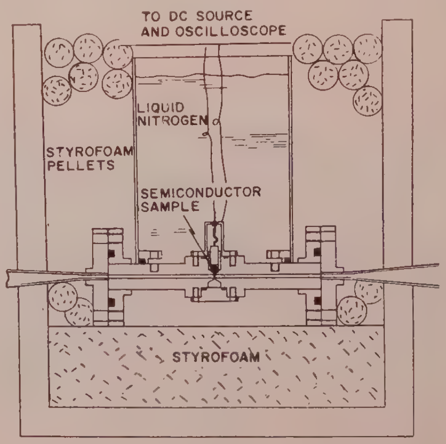

FIG. 4. Waveguide sample holder for 2.85-kMc measurements.

quid nitrogen temperature was reached and held for a me sufficient for a measurement series with acceptable xpenditure of coolant. The sample was installed in a ell in the top wall of the waveguide with the filament ridged across the narrow dimension of the guide, as hown in Fig. 4. The massive portion of the sample was nsulated from the well by means of a synthane bushing nd thin Teflon tape. The rf current was transmitted to he filament through the massive portion of the sample hich was capacitively coupled to the bottom of the ample well through the Teflon tape and through a wire hich was soldered to the tip of the filament and conected to the bottom wall of the waveguide.

Conditions were established to ensure that the rf eld within the sample would be uniform and unaffected y currents in the sample. The sample was located in he center of the waveguide with the sample axis perendicular to the waveguide axis so that the fields ncident upon the sample were uniform and equiphase. n addition, the sample radius was made much smaller han a quarter of a guide wavelength to prevent varitions resulting from internal reflections in the sample. he sample radius was 0.01 cm, whereas a quarter avelength in the waveguide at the signal frequency as 3.85 cm. Since the sample was located in an equihase plane, low-frequency circuit concepts could be pplied to determine the effect of the sample current pon the field in the sample. The sample was regarded s a two-terminal device of impedance Z_{sample} connected o a generator having an internal impedance Z_g. For the aveguide configuration used in these experiments, Z_g which is the driving-point impedance seen looking from he sample terminals into the waveguide) is given by

$$Z_g = \frac{b\eta}{a}[1-(\lambda/2a)^2]^{-\frac{1}{2}}, \qquad (7)$$

here a and b are the width and height of the waveguide, η is the intrinsic impedance of free space (377 ohms), nd λ is the free-space wavelength (10.52). The sample mpedance is

$$Z_{\text{sample}} = b/\pi r_0^2(\sigma + i\omega\epsilon), \qquad (8)$$

where r_0 is the sample radius, σ its conductivity, and ϵ its dielectric constant. The sample current has negligible effect upon the field in the sample as long as the sample impedance is much larger than Z_g. In the present experiments Z_g was 14.3 ohms, and the minimum sample impedance was 190 ohms. Therefore, the maximum variation in sample fields produced by current in the sample was 7%.

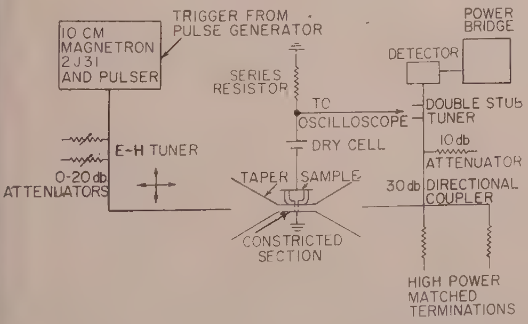

FIG. 5. Block diagram of 2.85-kMc apparatus.

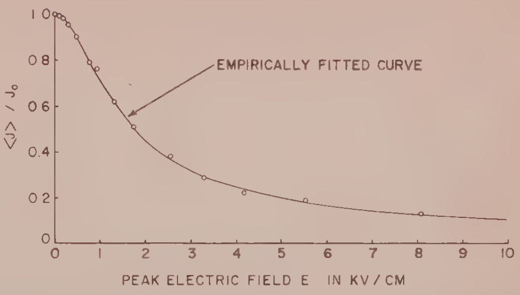

FIG. 6. Ratio of average currents with and without 2.85-kMc excitation vs peak 2.85-kMc field for a 5-ohm cm n-Ge sample. The solid line represents the empirically fitted curve

$$\langle J\rangle/J_0 = (1-\sigma_\infty/\sigma_0)[1+(E_1/E_c)^2]^{-\frac{1}{2}} + \sigma_\infty/\sigma_0$$

with $E_c = 1.0$ kv/cm, $\sigma_\infty = 0$.

As a result of these considerations, the microwave field in the filament can be calculated from the power density of the traveling wave at the sample, which was to a good approximation just the power transmitted down the waveguide to the matched load plus the insertion loss due to the section of waveguide between the sample and the power detector. This insertion loss was 0.42 db. The average transmitted power was measured with a PRD type 650 power bridge in conjunction with a Narda 561 coaxial detector. The peak field in the sample E_1 is related to the average power P_s, by

$$E_1 = (b/L_f)(4\eta\lambda_g P_s/A\lambda f\Delta t)^{\frac{1}{2}}, \qquad (9)$$

where A is the cross-sectional area of the constricted section of the guide, (7.2 cm by 0.188 cm), λ_g is the wavelength in the guide (15.5 cm), f is the pulse repetition frequency, and Δt is the pulse duration. The factor b/L_f is the ratio of the narrow dimension of the constricted section of the guide to the fiber length. This factor arises because the voltage appearing across the gap b is impressed across the filament of length L_f. From the known accuracies of factors entering into the expression for E_1, the error in E_1 was determined to be of the order of 10%.

Measurements were made of the average current in the sample produced by a small dry cell with and without microwaves incident on the sample. As in the dc-pulse measurements, two different methods were used in these measurements. One involved the use of 3-μsec pulses and a substitution bridge similar to that described previously energized by a 3-v dry cell; the other used 0.25-μsec pulses together with a circuit consisting of a carbon resistor and 3-v dry cell in series with the sample. As in the dc pulse measurements, a 53/54D

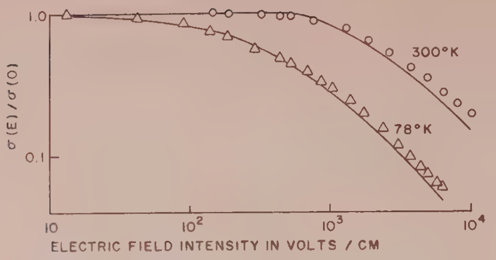

FIG. 7. $\sigma(E)/\sigma(0)$ of 5-ohm cm n-type Ge vs instantaneous 2.85-kMc field (solid lines) and vs dc-pulsed field (data points) at 300° and at 78°K.

preamplifier was used for the first method, a 53/54L preamplifier for the second method. In both cases the resistance in series with the sample was chosen small compared to the sample resistance so that the ratio of average current during the microwave pulse to the current in the absence of microwaves could be easily obtained from the measured quantities. This ratio was equal to the ratio of the resistance required to balance the substitution bridge in the absence of microwaves to that required to balance the bridge with microwaves on the sample, or, for the second method, to the ratio of the voltage across the series resistor with microwaves on to the voltage without microwaves on. The ratio of average current during the pulse, $\langle J\rangle$, to the current without microwaves, J_0, obtained for a 5-ohm cm sample of n-Ge at room temperature is plotted in Fig. 6. Shown also in this figure as a solid line is a calculated curve from the empirical formula

$$\frac{\langle J\rangle}{J_0}=\left(1-\frac{\sigma_\infty}{\sigma_0}\right)[1+(E_1/E_c)^2]^{-\frac{1}{2}}+\frac{\sigma_\infty}{\sigma_0}, \qquad (10)$$

where $E_c=1.0\times10^3$ volts/cm, and $\sigma_\infty=0$. This formula is seen to fit these data quite well, and the same formula with different values of the parameters E_c and σ_∞ gave as good fit to the microwave data taken on the other samples of this study.

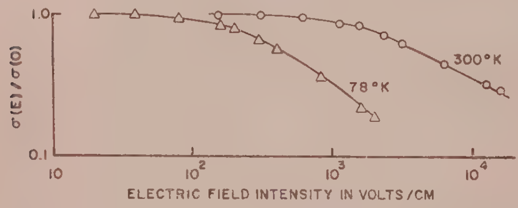

FIG. 8. $\sigma(E)/\sigma(0)$ of 5-ohm cm p-type Ge vs instantaneous 2.85-kMc field (solid lines) and vs dc-pulsed field (data points) at 300° and at 78°K.

3. COMPARISON OF MICROWAVE AND DC PULSE MEASUREMENTS

In order to compare the microwave measurements with the dc measurements, the instantaneous conductivity at a field E must be deduced from the measured $\langle J\rangle$, which may be written

$$\langle J\rangle=\frac{1}{2\pi}\int_{\omega t=0}^{2\pi}J(E)d\omega t, \qquad (11)$$

where $E=E_0+E_1\cos\omega t$, E_0 being the dc field strength. Since $E_0\ll E_1$, a Taylor series expansion of $J(E)$ in powers of E_0 can be made, and to a good approximation,

$$J(E)=J(E_1\cos\omega t)+E_0\left(\frac{dJ}{dE}\right)_{E_1\cos\omega t}. \qquad (12)$$

Since the first term of (12) will not contribute to the time average, use of (12) in (11) leads to

$$\langle J\rangle=\frac{E_0}{2\pi}\int_{\omega t=0}^{2\pi}\left(\frac{dJ}{dE}\right)_{E_1\cos\omega t}d\omega t. \qquad (13)$$

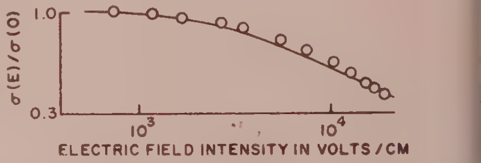

FIG. 9. $\sigma(E)/\sigma(0)$ of 5-ohm cm n-type Si vs instantaneous 2.85-kMc field (solid line) and vs dc-pulsed field (data points) at 300°K.

This equation must be solved for dJ/dE using the experimentally obtained $\langle J(E_1)\rangle$. In practice, a very good approximate solution of this integral equation was obtained with relatively little effort by making use of the observation that the data were well fitted by the empirical function (10). With this function for $\langle J(E_1)\rangle$ a solution of (13) is

$$\frac{dJ}{dE}=\sigma_\infty+\frac{\sigma_0-\sigma_\infty}{1+E^2/E_c^2}. \qquad (14)$$

Upon integration this gives, for the instantaneous J vs E,

$$J=(\sigma_0-\sigma_\infty)E_c\tan^{-1}(E/E_c)+\sigma_\infty E. \qquad (15)$$

The plots of instantaneous $\sigma(E)/\sigma(0)$ vs E calculated from (15) using the values of σ_∞ and E_c obtained by

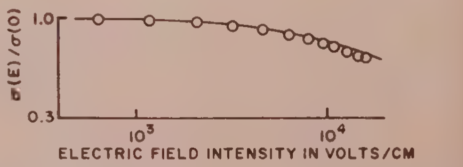

FIG. 10. $\sigma(E)/\sigma(0)$ of 25-ohm cm p-type Si vs instantaneous 2.85-kMc field (solid line) and vs dc-pulsed field (data points) at 300°K.

natching the empirical formula (10) to the experimental $J\rangle/J_0$ vs E_1 are shown as solid lines in Figs. 7 through 0 for the different samples studied. Also shown in these igures are the experimental $\sigma(E)/\sigma(0)$ vs E data obained for the same samples with dc pulses. It is seen hat in all cases the two sets of data are in agreement to vithin experimental error. It is concluded that at 2.85 kMc the conductivity of Ge can still, at least within the range of fields employed here (up to about 10 kv/cm), quite closely follow the field at liquid nitrogen temperature as well as at room temperature. The same conclusion can be drawn concerning the conductivity of Si at room temperature.

ACKNOWLEDGMENTS

It is a great pleasure to thank Professor A. Many of the Hebrew University, Jerusalem, for initiating this work while on sabbatical leave at these laboratories. We wish also to thank Mr. A. Willis for excellent technical assistance, Mr. V. Petruzelli for fabricating the samples, and Dr. K. Arnold and Miss M. Tilton for furnishing the single crystals of Ge and Si.

JOURNAL OF APPLIED PHYSICS VOLUME 32, NUMBER 12 DECEMBER, 1961

Space-Charge Instabilities in Electron Diodes and Plasma Converters*

Charles K. Birdsall and William B. Bridges†
Department of Electrical Engineering, University of California, Berkeley, California

(Received February 27, 1961)

Space-charge instabilities in diodes have been found to produce variations in potential and current that are larger than predicted from classical static analyses and, moreover, which produce sustained electrokinetic oscillations. This report reviews the classical static solution and presents the new transient solution briefly. As applications, tentative explanations are offered for recent observations of extra shot-noise smoothing and of oscillations in thermionic converters.

I. PHYSICAL MODEL

The diode model taken for static and transient solutions is that of two infinite charge-permeable parallel-plane electrodes with the stream velocity normal to the planes. The stream is injected into the region through one plane and can leave through the other or be returned to the injection plane. Upon reaching either plane, the stream is assumed to be annihilated. The stream is injected with a velocity v_0 with no distribution (zero temperature). While this last assumption is quite different from the conditions occurring near emitting cathodes, it appears that a number of the important characteristics of the oscillations of a potential minimum can be predicted by this model. For simplicity, both electrodes have been taken to be at the same potential, although this choice is not necessary to the argument; the diode is thus short circuited. The zero potential is chosen as that required to bring the injected stream to rest, i.e., potential of the cathode. No neutralization is assumed.

II. CLASSICAL STATIC SOLUTION

Some possible static solutions for potential between the electrodes are shown in Figs. 1 and 2; these curves are the classical solutions as given two decades ago, e.g., by Salzberg and Haeff[1] or Fay, Samuel, and Shockley.[2] (The potential curves shown are appropriate to electrons; the diagram should be inverted for ions.) The fraction of injected current reaching the second plane and the returned current as a function of the injected current are shown in Fig. 3. With no injected current, the potential is constant as in curve (A'). With some current injected, the potential has been depressed to curve (B'). The transmitted current reaches a maximum value at (C), called *limiting current*, and the corre-

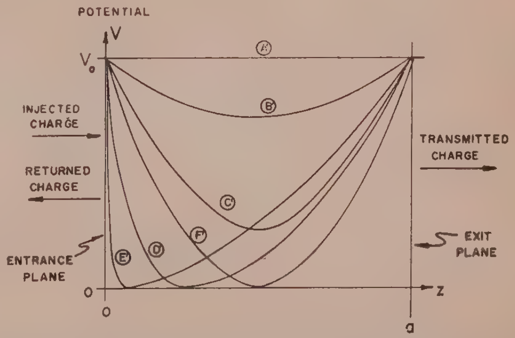

FIG. 1. Static solutions for potential $V(z)$ within a diode with both electrodes held at potential V_0. Curves A', C', and F' are for no returned charge; curves D' and E' include effect of returned charges.

---

* This research was supported by the U. S. Air Force through the Air Force Office of Scientific Research of the Air Research and Development Command.

† Present address: Hughes Research Laboratory, Malibu, California.

[1] B. Salzberg and A. V. Haeff, RCA Rev. 2, 336 (1938).

[2] C. E. Fay, A. L. Samuel, and W. Shockley, Bell System Tech. J. 17, 49 (1938).

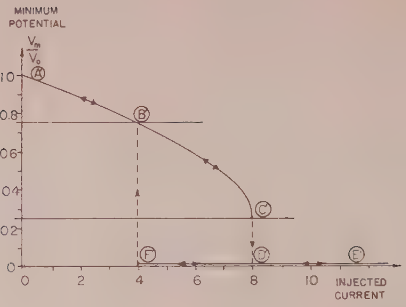

FIG. 2. Plot of the potential at the minimum V_m as a function of the injected current. Current is given in units of space-charge-limited diode current, i.e., for electrons, one unit is $(4\epsilon_0/9)(-2e/m)^{\frac{1}{2}}(V_0^{\frac{3}{2}}/a^2)=-(2.33/10^6)\times(V_0^{\frac{3}{2}}/a^2)$.

sponding potential variation is curve (C'), with a minimum of $\frac{1}{4}$ of the potential at the injection plane. [At this current, the transit time across the diode is roughly a half-cycle of the plasma frequency corresponding to the density at the potential minimum ω_{pm}, hinting (perhaps) at the time scale of the transient case.] Any further increase of injected current, however small, causes the potential minimum to drop to zero (in the static analysis) and charges are returned to the injection plane, reducing the transmitted current to point (D) and the potential curve (D'). Further increase in injected current causes the potential minimum to move toward the injection plane and the transmitted current to decrease. In the limit of infinite injected current (e.g., from a copiously emitting cathode surface), the position of the potential minimum coincides with the injection plane, and the potential follows the usual $z^{\frac{4}{3}}$ (Child's) law. If, after the drop to (D) and (D'), the injected current is decreased, the recovery of the potential minimum follows a different sequence. In the static analysis, the potential minimum remains at zero, and its position moves out toward the center of the space, and the transmitted current increases. A second discontinuity (this time, only in potential and velocity), is reached at (F) when the potential minimum is at the center of the diode, curve (F'), and the transmitted current just equals the injected current previously obtained at (B) and (B'). Any further decrease of injected current, however slight, in the static analysis, causes the potential minimum to jump to (B').

This description of events is based on the solutions of the static equations.

The classical approach, in essence, was to obtain all of the possible *static* solutions for potential, first with no returning current and next, allowing returning current; it was found that solutions could be obtained for *all* values of injected current, with two "states" possible between 4 and 8 units of injected current. Because there is no gap in the solutions, one is tempted to say that the story is complete. Yet, it is not clear that the second state is stable and the transitions from C to D and F to B are left mysterious. These steps cannot occur in zero time as, for example, there is much more charge in the diode in D than in C and in F than in B; the excess charge can only be accumulated (C to D, from the injected current), or removed (F to B, by the returned current) in finite time. Hence, there are "least times" associated with the changes of state, and these times are found to be comparable with the time taken by a charge to cross the diode. Now, the temptation is to consider the transition as a transient of limited duration in time, with any initial overshoot in potential or charge or current (C to D or F to B) disappearing in a short time, perhaps in a few "least times." However, this conjecture implies some mechanism for dissipation of the transient into some random form of energy approximating a static state. No such mechanism exists in the model used which has a zero-temperature stream with no collisions and with no external damping mechanism such as a resistor connected between the electrodes. *Thus, we state that after initiation of instability, the oscillations cannot die out and that the subsequent solutions for potential or current or charge cannot be wholly static.* Moreover, if one were to take the static state II solutions D-E-F as roughly the mean of the oscillations, the size of the oscillations in current and potential would be expected to be large, roughly that of the static values at C'. Conversely, the wholly-static solutions D-E-F cannot be obtained unless the diode or environs contain some form of heat (i.e., untuned) sink. Even with a sink of some sort, the oscillations need not decay, but they may reach a steady-state oscillation of limited amplitude, as is evidenced by observation of this type of oscillation in actual tubes.

Another point of departure from the classical solution is the possibly embarrassing question of what physical process divides a zero-velocity-spread (zero-tempera-

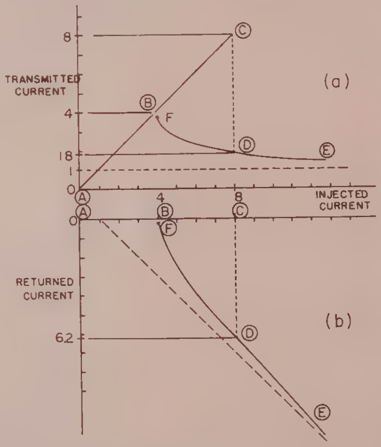

FIG. 3. (a) Static solutions for the transmitted current as a function of the injected current. (b) Static solutions for the returned current as a function of the injected current. The letters correspond to the potential curves of Fig. 1. The jump at C may be traversed only C to D; the gap at BF may be crossed only from F to B.

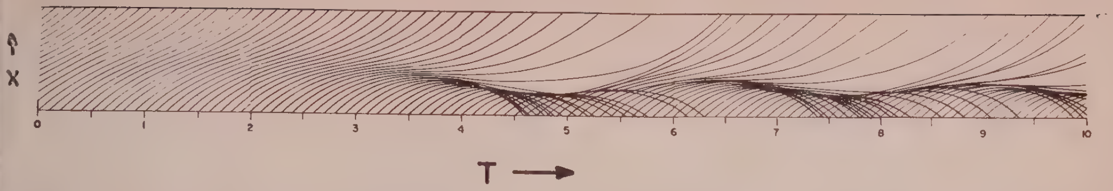

FIG. 4. Charge trajectories for diodes in transition from C, C' to D, D' in Figs. 1-3. The injected current before $T=0$ was at 7 units and the flow was stable; at $T=0$ the existing and injected charges were all weighted to correspond to an injected current of 8.2 units, thus initiating the instability. The unit of time $T=1$ is the transit time of one sheet in vacuum; roughly 3 units equal $\tau_{pm}=2\pi/\omega_{pm}$, where ω_{pm} is the plasma frequency at the potential minimum at limiting current (8 units). The returned and transmitted charges are annihilated on reaching either electrode. The continued periodic behavior is in striking contrast with the classical static solutions; the time-averaged transmitted and returned currents (calculated starting from $T=4$, roughly where initial effects have largely disappeared) are in the vicinity of, but not equal to, those of the static solution.

ture) stream into a transmitted fraction and a returned fraction, and yet this process must be wholly static! It is tempting to answer that one needs but a *small* velocity spread (the transmitted fraction is drawn from the faster part of the stream) as did Strutt and Van der Ziel[3] or that the potential minimum fluctuates a *small* amount in time and space, acting as a periodic gate, with the desired current division when time-averaged. Such answers sometimes make a nonphysical result into the proper one; in this problem, however, after the transient is initiated, we find that the potential minimum executes *very large* fluctuations, and these do not damp out but are sustained. The question of stream division is thus purely academic.

III. NEW TRANSIENT SOLUTION

The calculation of the behavior in time of this current-limiting process has been accomplished by Bridges and Birdsall[4] by abandoning the continuous fluid (fluid-dynamic or hydrodynamic) model used in the static solution and going over to a model using discrete charges. This change of method is necessitated by the expectation of a multivalued velocity (multiple streaming). The calculation is now for the trajectories of the charges as they move under the influence of their own space-charge fields and the electrode fields. The charges are approximated as sheets of zero thickness. The electrode potentials are held fixed, i.e., the diode is short-circuited. The resulting equation of motion for the jth sheet is

$$\frac{d^2x_j}{dT^2}=\frac{2\alpha}{9n}\{\sum_i x_i-N_j-\tfrac{1}{2}\}$$

$$+\text{acceleration due to the fields of the electrodes,} \quad (1)$$

where x_j is the position of the jth charge (normalized to the diode spacing, a), T is the time (normalized to the space charge free-transit time a/v_0), $2\alpha/9n$ is a weighting factor dependent on the number of charges chosen to represent unit current, and N_j is the number of charges between the jth and the exit plane. The sum is taken over all charges in the space.

A typical (machine-calculated) set of trajectories is shown in Fig. 4. (The field due to electrodes is taken as zero here; trajectories with these fields have been calculated by Lomax[5] which show similar behavior.) The case shown is where the charge distribution at time $t=0$ corresponded to state (C,C') on Figs. 1–3, and the current was chosen to be slightly greater than the limiting value ($\alpha=8.2$ as against $\alpha=8.0$). The subsequent trajectories then exhibit a collapse in potential and the returning of charges, with a corresponding decrease in transmitted current. Note that no stable zero potential minimum is reached but that the potential minimum rebounds and continues to oscillate, thus strongly modulating the transmitted and the rejected current. Some potential profiles are shown in Fig. 5 for specific times in the trajectory plot; similar plots are found in Twombly and Lauer.[6] Figure 6 shows the

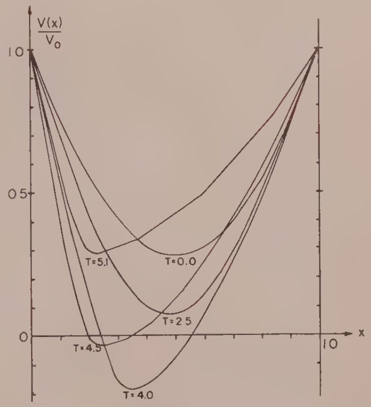

FIG. 5. Potentials $V(x)$ at different times during instability. The minimum goes considerably negative then, as charge is returned, rises well above zero again in contrast with the virtual cathode ($V_m=0$) solution from statics. The time-averaged potential is in the vicinity of, but not equal to, that of the static solution.

---

[3] M. J. O. Strutt and A. Van der Ziel, Physica 6, 977 (1939).

[4] W. B. Bridges and C. K. Birdsall, University of California, Berkeley, Electronics Research Laboratory Report, Series No. 60, Issue No. 303, August 2, 1960. (Also presented at the Conference on Electron Tube Research, Seattle, June 30, 1960.)

[5] R. J. Lomax, J. Electronics and Control 9, 127 (1960).

[6] J. C. Twombly and J. E. Lauer, University of Colorado Engineering Experiment Station, Boulder, Colorado, Technical Report No. 2, December 1, 1960.

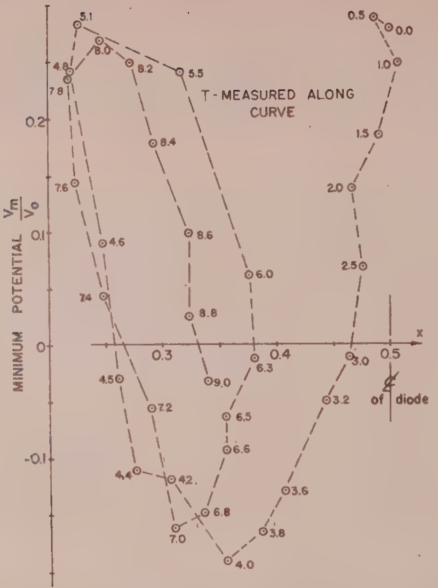

FIG. 6. Path of the potential minimum $V_m(x,t)$ starting at $T=0$. The total swing is roughly half the applied potential, considerably beyond any small-signal type of behavior. The initial "hook" near $T=0$ is a peculiarity of our method of starting instability, the re-weighting of charges already in the diode at $T=0$ rather than just the subsequent injected charge; thus the initial part of the curve would not generally occur. The time to the first minimum and the subsequent times to successive minima are all about $\Delta T=3$ units or each is about τ_{pm}. The oscillatory behavior does *not* tend to decay; the time-averaged value of the minimum is not zero as it is in the static solution.

path of the potential minimum for the first few oscillations; the calculation has been carried much longer in time with no evidence of change of the oscillations. The potential dips about 20% below zero and rises about 20% above zero. The excursion is thus about twice as large as the dc potential at the minimum (C,C') and can hardly be called small signal! Figure 7 shows the charge velocities in the diode at times $T=0$, $T=4.0$, $T=4.5$; note the multiple streaming which occurs.

IV. PERIOD AND MODE OF OSCILLATION, TIME-AVERAGED VALUES AND WAVES

The period of these oscillations is numerically close to that of the electron-plasma frequency corresponding to the density at the potential minimum of state (C,C'). However, one should *not* infer from this information that the mode of oscillation is such that an electron or some portion of the stream is in sinusoidal or simple harmonic motion (with particle motion governed by $\ddot{x}=-\omega_{\text{pm}}{}^2x$, with this x measured from the center of the diode) as, for example, in small-signal space-charge waves, or in a Barkhausen oscillator. At limiting current, an excess current first causes a depression in potential which then retards the current, again increasing the charge and further depressing the potential. This avalanche process results in accumulation of most of the charge at one place as seen at $T=4.0$ to 4.5 in Fig. 4. If this set of charges is now approximate as one sheet of large charge, then the motion of the set is "antiharmonic" (with particle motion governed by $x=+\omega^2\ddot{x}$ with x measured from the center of the diode) with rapid acceleration toward the input plane and subsequent annihilation of the set at that plane. As the diode is now rid of much of its charge, the potential rises, then the new injected charge restarts the limiting process. The injected charge sustains the avalanche-type oscillation.

TABLE I.

	Classical values at D', D	Time-averaged values of transient solutions
Potential at the minimum	0	Approx 0
Position of the minimum	$0.25a$	Approx $0.31a$
$\left(\frac{\text{Transmitted current}}{\text{Injected current}}\right)$	$\frac{1.8}{8}=0.22$	0.38

The time-averaged and static values of several quantities are compared in Table I. The averages were made over about six cycles of the oscillation.

Note that the average minimum is nearer the center of the diode and that the average transmitted current is nearly twice that of the classical solution.

In addition, one might ask the significance of the result from statics, that $\omega_{\text{pm}}\tau\approx\pi$ transit angle at limit-

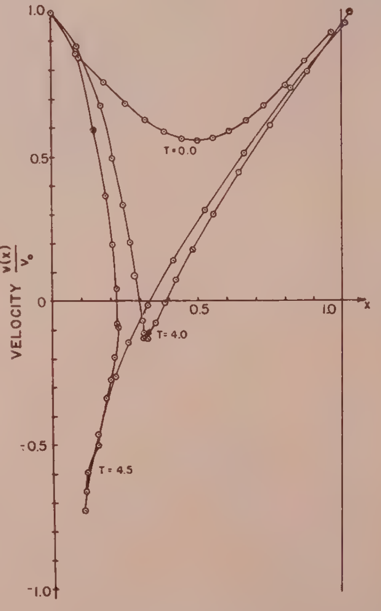

FIG. 7. Particle velocities in the diode at times $T=0$, $T=4.0$, and $T=4.5$. This phase space shows clearly the multivalued velocity or multiple-streaming nature of the instability. The lines joining the velocities of the finite number of sheets are assumed to be the location of velocities for a continuous-stream model.

ng current mentioned earlier. Pierce[7] used a model with an electron stream injected into a short-circuited diode with a stationary neutralizing background, and assumed that small signals would produce a fluctuating potential which was exponential with distance [like $\exp(j\beta x)$] and with time dependence as $\exp(j\omega t)$. There are two waves in this anisotropic medium. One wave behaves as $\exp j(\omega t-\beta x)$, the faster space-charge wave (although at frequencies $\omega<\omega_p$, this wave has a negative phase velocity and possibly could provide feedback). The two β's will have the same magnitude (so that the potential may vary as $\sin\beta x$) if one has $\omega_{\text{real}}=0$; at this combination, $\beta=\pm\omega_p/v_0$. If now the charge is large enough to make $\beta a=\pi$ (or $\omega_p a/v_0=\pi$) meaning $\omega_p T=\pi$, then ω becomes imaginary and instability occurs. (Pierce[8] stated that allowing the background to fluctuate did not change the onset of instablity.) Pierce's result more or less inspired this project which started out as an attempt to see if there was a tie between limiting current and the response of a cathode potential minimum to shot-noise excitation and the dependence of the response on ω_p, as is discussed later; we gratefully acknowledge this debt.

We have extended Pierce's analysis to include wave propagation normal to x. We find that space-charge wave propagation *transverse* to the stream velocity starts at $\omega_p T=\pi$ and at $\omega_{\text{real}}=0$. That is, fluctuations in kinetic and potential energy in the stream, which usually flow along the stream, can now flow normal to the stream. If such energies are absorbed (say, at the edge of a stream of finite diameter), then at limiting current the stream energy will decrease, and an ordered transition to a new state may occur. However, if such propagation has no place to go (as in the infinite diode) or is reflected (most certainly in a short-circuited diode), then after initiation of these waves, some fluctuations may be trapped in the diode. Hence, there can be an increase in fluctuations with time, e.g., in field energy ($\epsilon_0 E^2/2$), at the expense of stream kinetic energy. Once this process starts, the energy exchange continues to grow in time in the diode (a non-convected instability) through small signals and into a large-signal oscillation state.

Our wave analysis is incomplete and no serious attempt has been made on a wave-like analysis without the neutralizing background. This background, of course, removes the dc potential minimum, and raises the value of limiting current; however, we speculate that where onset of instablity can be tied to a general description (some form of invariant) like plasma transit angle, then comparison among different models can have meaning.

V. EARLY EXPERIMENTS

Experimentally, the existence of a limiting current for electron streams has been widely observed as it occurs in common radio receiving tubes, such as beam-power tetrodes, like the 6L6, and also in high-power transmitting tubes, as for example, given recently by Sutherland.[9] These observations usually have been of direct- or average-current changes. In addition, near limiting, large "spurious" oscillations sometimes are obtained, with frequencies which tend to be unrelated to external circuitry, but are current and/or voltage tunable (i.e., related to density and transit time). The authors know of no experimental studies relating these oscillations (their onset, frequency, tunablity, etc.) to the transient accompanying limiting as given earlier. One reason may be that the oscillations were at such high frequency that the tube leads were essentially useless for measurement. However, a more pertinent reason may be that the oscillation, requiring the diode to be short-circuited, or nearly so, produces little voltage fluctuation at the electrodes; thus, to observe these oscillations more intimately, one should use a probe electrode between the diode electrodes and measure the voltage fluctuating between the probe and, say, the input electrode. A possible probe configuration is shown in Fig. 8. Of course, one may use this mode and configuration for a useful oscillator or stream modulator.

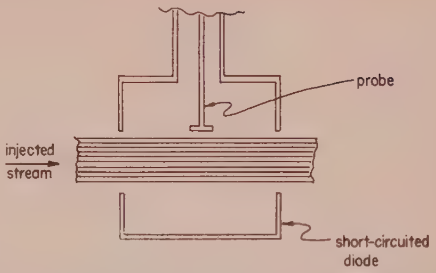

FIG. 8. Suggested probe location for observing diode instabilities of short-circuit type. The probe may be a wire or ring or cylinder, essentially coupled to the voltage fluctuations of the instability.

VI. RELATION TO SHOT-NOISE REDUCTION IN ELECTRON STREAMS

The limiting mechanism, while a nuisance when producing oscillations, may also play a role in reducing (or enhancing) the current fluctuations of the injected stream, i.e., shot-noise smoothing at frequencies comparable with ω_{pm}. Several workers using electron guns of the Currie type[10] in microwave traveling-wave tubes have obtained lowest noise figures while operating in the vicinity of the limiting current of the first-anode region; this has been presented very clearly by Berghammer[11] and also by Mueller.[12] It appears that less than full shot noise emerges from these regions. We postulate that an injected low-frequency increase in current will cause limiting, then return of electrons to the cathode, causing a reduction in the injected current and, hence, recovery of the initial state; i.e., the loop *CDFBC* in Fig. 3 is traversed and in a time comparable with $2\pi/\omega_{\mathrm{pm}}$ but with continued ringing. A decrease in current ("hole") is compensated differently, first by an increase in the potential minimum and, hence, acceleration of charge which tends to fill the hole, and then by an increase in emission and further tendency toward filling the hole; again the reaction rate is a time comparable with $2\pi/\omega_{\mathrm{pm}}$, and again there would be ringing. We boldly assume that onset of limiting, even in complex guns such as these, is still characterized by $\omega_{\mathrm{pm}}\tau=\pi$, where τ is the transit time between two effective electrodes; in addition, we expect the "ringing" of the transmitted current at frequency ω_{pm}, even with streams with finite velocity spread. Of course, some changes are expected, such as damping of the ringing. These effects are implied to be relatively large signal from our analysis; however, note that similar results as far as period of oscillation is concerned were obtained in a small-signal analysis by Whinnery[13,14] in which one sheet of relatively small charge was injected into the minimum as calculated from statics (with a velocity spread). As the frequency of the fluctuation increases, the ability of the minimum to respond rapidly decreases. Near ω_{pm} one might expect the possibility of almost perfect compensation or, just the opposite, constructive interference and large enhancement.

---

[7] J. R. Pierce, J. Appl. Phys. **15**, 721 (1944).

[8] J. R. Pierce, J. Appl. Phys. **21**, 1063 (1950).

[9] A. D. Sutherland, IRE Trans. on Electron Devices **ED-7**, 268 (1960).

[10] M. R. Currie, Proc. Inst. Radio Engrs. **46**, 911 (1958).

[11] J. Berghammer, RCA Rev. **21**, 369 (1960).

[12] W. M. Mueller, Proc. Inst. Radio Engrs. **49**, 642 (1961).

In the more conventional diode gun, operation is generally with transmitted currents well below saturation, effectively with injected current well beyond that at point *E* in Fig. 3. If one believes in this curve, it is obvious that a slow- or low-frequency fluctuation in injected current results in a much smaller fluctuation in the transmitted current. It is difficult to say what "load line" should be used at higher frequencies. Unfortunately, the existence of this part of the curve is put in doubt by our results. We do postulate that the ordinary cathode potential minimum has much the same character as the diode minimum found at limiting current; that is, there are relatively large potential fluctuations at high frequency. It is expected that addition of a finite velocity spread (nonzero temperature) will not alter the character of this behavior, possibly only the amplitude; preliminary results with a stream of two velocity classes bear this out. We do not yet have results for limiting initiated by ac fluctuations in injected current or velocity or for smoothing once limiting is achieved. It is fully expected that such excitation, at relatively small amplitude but at the proper frequency, may readily trigger limiting, and that, with limiting, fluctuations can either be damped or enhanced, much as found by Tien and Moshman.[15]

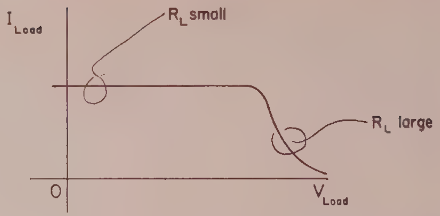

FIG. 9. Typical measured diode volt-ampere characteristics of a plasma-diode converter obtained by varying the load resistance, $R_L=V_L/I_L$; these are time-averaged values. The current is essentially all electron current.

VII. RELATION TO PLASMA DIODE OSCILLATIONS

Static calculations for plasma diodes have shown that there can be more than one potential shape for a given boundary condition, as by Auer[16] and Eichenbaum and Hernqvist[17] for finite temperature ions and electrons; these results show that instabilities can occur and, in the sense given earlier, that there may be no wholly dc state. Indeed, oscillations in the several hundred kilocycle range have been observed in plasma diodes (plasma converters or plasma thermocouples) by Eichenbaum and Hernqvist, and in the kilocycle to few megacycle range by Garvin *et al.*[18] Of course, such diodes can be operated in different regimes (e.g., essentially collisionless, or collision dominated) or with different electrode shapes, and within each regime there may be oscillations due to different causes at different operating points. We speculate that the space-charge instability given earlier may occur in some of these regimes under certain operating conditions. Our objective is to apply a relatively simple theory in order to obtain the approximate *physical* behavior without going through the complex calculations necessary to obtain the complete answer.

We will assume that there may be cases where space-charge effects predominate as contrasted with, for example, velocity spread or temperature effects. We have already found, as mentioned above, that an elementary initial velocity spread alters very little the oscillations in an electron diode that occur with no initial velocity spread. Thus, in the following it will be assumed that all of the electrons are injected with the average thermal velocity called v_T; the electrons are treated as if they have been accelerated from rest by potential V_T corresponding to $v_T[v_T^2=(2e/m)V_T]$; V_T is on the order of 0.2 v. The zero in potential is chosen to be that at which electrons come to rest. Also, we have found that addition of a small resistance between cathode and anode alters very little the oscillations found with a short circuit.

It is convenient to divide the operation of a diode into three regions: large load resistance, optimum load re-

---

[13] J. R. Whinnery, IRE Trans. on Electron Devices **ED-1**, 221 (1954).

[14] J. R. Whinnery, IRE Trans. on Electron Devices **ED-7**, 218 (1960).

[15] P. K. Tien and J. Moshman, J. Appl. Phys. **27**, 1067 (1956).

[16] P. L. Auer, J. Appl. Phys. **31**, 2096 (1960).

[17] A. L. Eichenbaum and K. G. Hernqvist, J. Appl. Phys. **32**, 16 (1961).

[18] H. L. Garvin, W. B. Teutsh, and R. W. Pidd, J. Appl. Phys. **31**, 1508 (1960).

sistance, and small load resistance. Figure 9 shows a typical V-I characteristic of a planar, collisionless thermionic converter diode; the product V-I is a maximum, R_L is optimum, at the knee of this curve. The ions, typically Cs^+, may come from the cathode where they are produced by surface ionization, or may be injected from a separate source.

A. Small Load Resistance

In this region of operation, the potential within the diode will follow the sequence shown in Fig. 10 as the load resistance is made smaller. In (a), operation is at the knee of the V-I curve of Fig. 9, where $V_L+\phi_a=\phi_c$; the electric field is zero across the diode except as noted in case C. In (b), V_L has been reduced slightly so that there is a negative electric field, hence a tendency for ions to drift toward the cathode. Let us assume that the ion population is just sufficient to maintain space-charge neutralization at the knee. Thus, at (b), with some ions drained out of the central portion of the diode, the net space charge in this region becomes more and more negative, and at some time the electron current may limit in a manner similar to that presented earlier for the short-circuited diode. When this occurs, the potential minimum rings with a period on the order of the electron transit time. In this oscillatory state, the time-average electric field is such that ions now move toward the potential minimum. The ions cause the potential at the minimum to increase and quench the oscillation, again allowing saturated current to flow. The load impedance at the high frequency of electronic oscillation may be quite different from the dc or low frequency impedance; the high frequency impedance has been assumed to be zero for simplicity although the electronic oscillation is not seriously affected by finite impedance. If the load voltage is provided by a battery (effectively a dc short), then V_L does not decrease with the reduction in average electron current during oscillation; if the load is a resistor at low frequencies, then V_L decreases during ringing and alters the rate at which ions tend to fill the minimum. The whole sequence given here is repetitive.

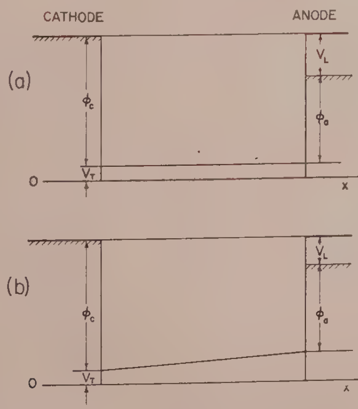

Fig. 10. Potential due to the electrodes in a diode. At zero potential, the average electron is at rest; eV_T is average energy of the emitted electrons. ϕ_c and ϕ_a are cathode and anode work functions. In (a), operation is at the knee of V-I curve. In (b), V_L has been reduced creating a field which causes ions to drift toward the cathode and destroy the neutralization.

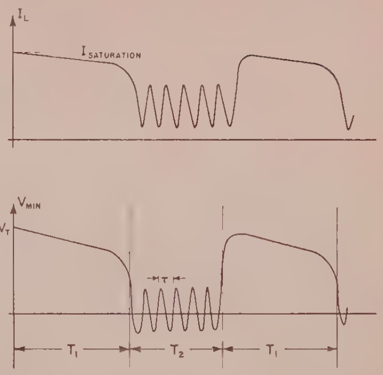

Fig. 11. Diode current I_L and potential at the minimum, $V_{\min}$ as a function of time t.

The behavior of the electron current and the potential at the potential minimum with time is sketched in Fig. 11. At the start, $V_{\min}$ is at the cathode; ions drain toward the cathode at a speed governed in part by the electric field; $V_{\min}$ decreases below V_T and the position of the minimum moves toward the anode. The current remains at the saturated value. After the time interval T_1, the negative space charge causes electron current limiting to take place, and then $V_{\min}$ and I_L oscillate at some high frequency of period τ. Ions now move toward the minimum, causing $V_{\min}$ to rise until the limiting-current oscillation is quenched after an interval T_2, and the initial state is recovered; the ion speed and the length of the period of oscillation T_2 are again governed in part by the electric field which now acts to attract ions toward the potential minimum. As R_L is reduced, the field for ion draining increases, so that the onset of oscillation occurs in a shorter interval, that is, T_1 decreases; the effect agrees qualitatively with the data of Garvin *et al.*[18] The factors governing the time T_2 as R_L decreases are several (the electric field, the distance to the minimum, and the depth of the minimum) and do not appear to be simply related. The period τ is on the order of half the electron transit time across the diode and hence should decrease as R_L is decreased. The frequency $f=1/\tau$ will be much larger than $1/T$ and is likely to be in the very-high frequency microwave range, 100 Mc and up. We are unaware of observations made in this frequency range.

B. Large Load Resistance

In this region of operation, as the load resistance is increased, the anode potential decreases, and the field at the cathode becomes a retarding field for electrons. Again we assume that there is just sufficient ion population to maintain neutralization at the knee.

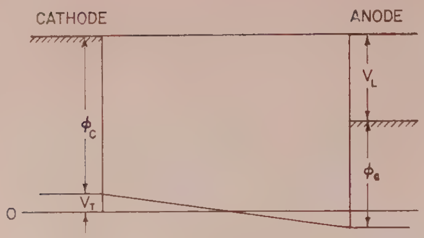

FIG. 12. Same as Fig. 10 but with V_L increased, creating a field which causes ions to drift toward the anode and destroy the neutralization.

If R_L has been increased such that $V_L+\phi_a>\phi_c+V_T$, then a retarding field (for electrons) exists over the whole diode, and ions tend to be drained away from the cathode as shown in Fig. 12. Electron current limiting and attendant high-frequency oscillations may again occur with the majority of electrons reflected near the cathode. Lomax[15] has shown that the oscillatory behavior still occurs in a retarding field electron diode. Because the potential minimum now occurs at or near the anode, the ions, moving toward the anode, do not neutralize the electron space charge near the cathode. Hence, the oscillations are not quenched and there is no low frequency repetitive behavior as with small load resistance. The small electron current reaching the anode represents the high velocity electrons of the cathode velocity distribution which were ignored in exploring the mechanism of oscillation. This current will be modulated by the fields of the high-frequency oscillations of the electronic space charge near the cathode.

C. Maximum Power Point (Knee)

At the knee of the *V-I* curve, the power to the load is maximum. At this point there is no electric field in the diode and no net space charge. Thus, the tendency to electron-current limit is small. However, Jepsen[19] has shown that this model, with electrodes shorted and with an ac field reversal in the middle of the diode, can exhibit oscillations of a *small* signal nature.

The question of the effect of positive sheaths at the electrodes may be raised. These sheaths have been ignored in *A*, *B*, and *C* above. If sheaths occur, changes of V_L may still cause ion drainage from the central region toward one or the other electrode, and allow net negative space charge to occur in this region. Then, electron current limiting may again occur. However, with sheaths, the details of start oscillation and recovery are not clear.

VIII. FURTHER COMMENTS

In passing, we note that a stream in a drift tube, where there is a similar critical current (see, for example, Haeff[20]), should also exhibit similar oscillatory behavior but with changes in the detailed description. Here the onset occurs at a critical width of the stream in space charge wavelengths (rather than length in terms of plasma transit angle as in the diode case) but is again associated, we think, with the point at which transverse propagation may take place.

Also, two streams injected into a diode (or drift tube) from opposite sides again give a model with a limiting current. Beyond limiting, there should be a large-oscillation potential very similar to the single-stream case, and corresponding oscillatory transmitted and returned current for both streams. The well-known double streaming time- or distance-growing waves are *not* the culprit here.

IX. CONCLUSIONS

Space charge instabilities have been shown to produce oscillations of large amplitude in voltage, current, and velocity that are sustained in time. Some of the time-averaged values were found to differ substantially from the classical static solutions. The charge motion with one species is shown to be "anti-harmonic," or avalanching, and is periodically restarted by the continual injection of charge. This behavior is alleged to enhance the smoothing of cathode-current fluctuations, as is observed in low-noise tubes at frequencies below the frequency of the oscillation. This phenomenon is proposed as a mechanism responsible for some types of plasma-diode oscillations.

ACKNOWLEDGMENTS

We are grateful to Neil Lincoln for much of the computer programming, to the U. S. Air Force through the Air Force Office of Scientific Research of the Air Research and Development Command for research support, and to the Regents of the University of California for computer time. We are also grateful to Dr. H. Hurwitz and the journal referee for their comments on the plasma diodes.

---

[19] R. L. Jepsen, Proc. Inst. Radio Engrs. **45**, 1069 (1957).

[20] A. V. Haeff, Proc. Inst. Radio Engrs. **27**, 586 (1939).

OURNAL OF APPLIED PHYSICS VOLUME 32, NUMBER 12 DECEMBER, 1961

Magnetically Confined Cold-Cathode Gas Discharges at Low Pressures

R. L. Jepsen
Varian Associates, Palo Alto, California

(Received March 27, 1961; in final form, August 16, 1961)

Most previous treatments have been restricted to calculations of striking characteristics of planar and cylindrical magnetrons. In the present paper, a theory is developed which considers some effects of space charge in inverted and normal magnetrons and in Penning structures. Estimates are made of current flow and its dependence on voltage, magnetic field, electrode geometry, and pressure. It is shown that discharges of much greater intensity may be expected in normal magnetrons with filamentary cathodes than in inverted magnetrons with filamentary anodes. It is also shown that comparable maximum discharge intensities should be obtainable in Penning structures and in normal magnetrons. A scaling relation involving magnetic field and radial dimensions of the electrodes is obtained.

I. INTRODUCTION

ALTHOUGH the utility of magnetic fields in extending the operation of cold-cathode gas discharges to low pressures has long been recognized,[1] theoretical treatments of such discharges are far from complete or adequate. In recent years discharges of this type have become increasingly important through applications as ion and electron sources,[2] pressure gauges,[3–9] and vacuum pumps.[10–12] With improved understanding of their characteristics, other important applications may emerge, such as to mass spectrometry, to optical spectroscopy, and to the generation and detection of microwaves and millimeter waves. In addition, a clearer picture of these discharges may contribute to a better comprehension of the much more complex plasmas of interest in thermonuclear research.

For typical values of the relevant parameters, it is observed experimentally that cold-cathode gas discharges employing magnetic fields behave as follows as the pressure is varied: At low pressures the discharge impedance is relatively high, with current being approximately proportional to pressure. At high pressures, however, the discharge is "unconfined," its impedance is comparatively low, and it is affected only slightly by the magnetic field. Voltage across the discharge is then a few hundred volts and the current is power-supply limited. Transitions between the high and low impedance types of operation usually occur in the pressure range 10^{-4} to 10^{-2} mm Hg. Behavior of the discharge in the transition region is exceedingly complex. For reasons of simplicity, the considerations of the present paper are restricted to low pressure, high impedance discharges.

It is well known that magnetically confined gas discharges are maintained through appropriate combinations of magnetic field, electrode geometry, and voltage. Perhaps the simplest structure is one described by Penning[3] and shown in Fig. 1. Other simple geometries of interest include magnetrons, both "normal" and "inverted," as shown in Fig. 2. Although self-sustained gas discharges can be established with many other electrode geometries, the present paper is limited to treatments of Penning and magnetron structures.

II. DISCUSSION OF EXISTING THEORIES

A complete theory for cold-cathode gas discharges should include prediction of current flow (I) through the discharge and descriptions of electron and ion densities and velocity distributions within the discharge space. These quantities should be given as functions of electrode geometry, species of gas, pressure (P), voltage applied to the anode (V_a), magnetic field (B), and electrode materials. If oscillations or other nonconservative interactions occur (in addition to collisions), these should be predicted and described also.

Most of the published theoretical work on this topic is by Haefer,[13–15] Somerville,[16] and Redhead,[9,17] and has been devoted to predictions of striking characteristics

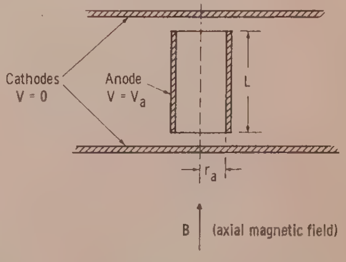

FIG. 1. Long-anode Penning structure (cross-sectional side view).

---

[1] F. M. Penning, Physica **3**, 873 (1936).

[2] A. Guthrie and R. K. Wakerling, *The Characteristics of Electrical Discharges in Magnetic Fields* (McGraw-Hill Book Company, Inc., New York, 1949).

[3] F. M. Penning, Physica **4**, 71 (1937).

[4] F. M. Penning, Philips Tech. Rev. **2**, 201 (1937).

[5] F. M. Penning and K. Nienhuis, Philips Tech. Rev. **11**, 116 (1949).

[6] A. H. Beck and A. D. Brisbane, Vacuum **2**, 137 (1952).

[7] J. H. Leck, *Pressure Measurement in Vacuum Systems* (The Institute of Physics, London, 1957), pp. 88–93.

[8] J. P. Hobson and P. A. Redhead, Can. J. Phys. **36**, 271 (1958).

[9] P. A. Redhead, Can. J. Phys. **37**, 1260 (1959).

[10] L. D. Hall, Rev. Sci. Instr. **29**, 367 (1958).

[11] R. L. Jepsen, LeVide **80**, 80 (1959).

[12] R. Zaphiropoulos and W. A. Lloyd, *1959 Vacuum Symposium Transactions* (Pergamon Press, New York, 1960), p. 307.

[13] R. Haefer, Acta Physica Austriaca **7**, 52 (1953).

[14] R. Haefer, Acta Physica Austriaca **7**, 251 (1953).

[15] R. Haefer, Acta Physica Austriaca **8**, 213 (1954).

[16] J. M. Somerville, Proc. Phys. Soc. (London) **B65**, 620 (1952).

[17] P. A. Redhead, Can. J. Phys. **36**, 255 (1958).

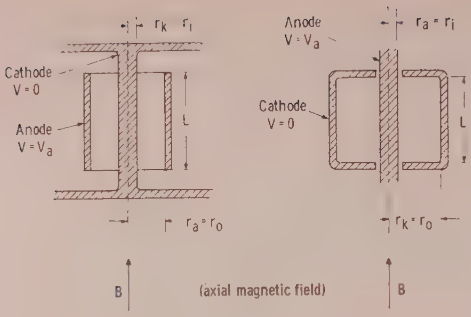

(a) Normal Magnetron (b) Inverted Magnetron

FIG. 2. Normal and inverted magnetrons (cross-sectional side view).

for magnetron structures. As normally displayed, striking characteristics are the loci of points in the V_a-B plane for which the Townsend avalanche equation is satisfied in the absence of space charge. Because the modifications of potential by space charge are not taken into account in these theories, quantitative predictions of current flow have not been obtained.[18] Even though the Penning structure is geometrically and mechanically simpler than the magnetron, the need for considering axial as well as radial electron motion leads to a substantial increase in the complexity of the calculations. To the best of this writer's knowledge, computations of striking characteristics for Penning structures which are analogous to those performed by Haefer, Somerville, and Redhead for magnetrons have not been carried out. It is believed, however, that the same physical processes are relevant, so it is unnecessary to introduce additional concepts in order to obtain equivalent levels of understanding of the magnetron and Penning types of cold-cathode gas discharges.

The physical basis for the theories employed by Haefer, Somerville, and Redhead for magnetron structures is as follows: An initial electron (released by field emission, for example) starts out from the cathode. Under the influence of the crossed electric and magnetic fields, it follows a modified cycloidal path, as indicated in Fig. 3. If it makes a collision with a gas molecule, the electron's momentum may be altered in such a way that recapture by the cathode is precluded. The electron thus freed is able to initiate an avalanche. Because of the constraint imposed on its motion by the magnetic field, the electron can advance radially toward the anode only by making a collision[19] of some sort with gas molecules (provided other nonconservative interactions, such as electron-electron collisions and interaction with time-varying electric fields, can be neglected).

When the energy of an electron's motion exceeds the ionization potential of the gas molecules, some fraction of the collisions will be ionizing. Upon the occurrence of an ionizing collision, the positive ion goes directly to the cathode, and the newly-released electron is added to the avalanche. Thus as the avalanche progresses a distance dr toward the anode, dn electrons will be added. Quantitatively,

$$dn = n\alpha dr,$$

where n is the number of electrons in the avalanche at radius r, and αdr is the number of electron-ion pairs produced by an electron in traveling a distance dr toward the anode. Starting with a single electron freed at the cathode, the number of electrons n_a arriving at the anode in the avalanche is

$$n_a = \exp \int_{r_k}^{r_a} \alpha dr. \tag{1}$$

The number of positive ions produced by this avalanche is just $n_a - 1$. Let Γ be the number of avalanche-initiating electrons freed at or near the cathode for each electron-ion pair produced in the avalanche. The condition that a cold-cathode gas discharge be self-sustaining is that each avalanche gives birth to one new avalanche. Thus the Townsend avalanche equation is

$$\Gamma\left(\exp \int_{r_k}^{r_a} \alpha dr - 1\right) = 1$$

or

$$\int_{r_k}^{r_a} \alpha dr = \ln\left(1 + \frac{1}{\Gamma}\right). \tag{2}$$

The quantity α depends on electric field (E), magnetic field (B), and the species of gas [through ionization potential (V_i) etc.]. The Γ coefficient depends on E_k (the electric field at the cathode), B, P, cathode material, details of cathode geometry, species of gas, and ion energy. The various theoretical treatments by Haefer, Somerville, and Redhead differ in the ways in which both α and Γ are dealt with.

III. EFFECTS OF SPACE CHARGE

A. Preliminary

As stated earlier, approximate solutions to Eq. (2) have been obtained for magnetron structures by Haefer,[13–15] Somerville,[16] and Redhead.[9,17] Since space charge effects were neglected, the results are limited to predictions of striking characteristics. We remark in passing that in some cases this neglect of space charge may not be permissible, even for calculations of striking haracteristics.[20] This point will not be elaborated urther in the present paper.

---

[18] Haefer[15] includes space charge in an approximate way which permits qualitative, but not quantitative, prediction of current-voltage characteristics.

[19] There are several different kinds of collisions which electrons can make with gas molecules. One type is elastic, in which the momentum of the electron is altered while its energy is conserved. A second type is inelastic in which the molecule is excited to a higher energy state. A third type is inelastic in which ionization of the molecule occurs.

Equation (2) should also hold in the steady state when finite currents flow. In this case, however, the electric field is modified by the presence of space charge, hus changing both α and Γ. Upon taking space charge properly into account, $I-V_a$, $I-B$, and $I-P$ characteristics, for example, should be obtainable from solutions of this equation. Calculations which include space charge in a realistic fashion are clearly difficult and complex. This problem is formulated further by Helmer and Jepsen.[21]

In cold-cathode gas discharges at high pressure, a plasma which is essentially electrically neutral (equal numbers of positive ions and electrons) exists throughout a large portion of the region occupied by the discharge. At low pressures the situation is quite different. Rates of production of ions and electrons are nearly equal, but the transit times for positive ions from point of production to the cathode are *much less* than the transit times of the electrons to the anode. Thus the space charge between cathode and anode arises primarily from the *electrons*, and is, therefore, of negative sign.[15,17]

It is likely that for discharges of sufficiently low intensity an avalanche theory which includes space charge will suffice to predict the main features. For the more intense discharges, however, it appears that space charge density builds up to the point that oscillations or instabilities occur within the space charge. In this event an avalanche theory alone is no longer adequate to describe the discharge behavior.

From the nature of the avalanche process, charge density will increase roughly exponentially with distance from the cathode; this, of course, is modified by geometrical factors and by variations of α with position. One consequence of the existence of oscillations or instabilities within the discharge is that electrons are provided with alternative means of reaching the anode. This in turn means that the distribution of space charge can be strongly modified from that arising through avalanche processes alone. For example, it is quite conceivable for Penning structures (Fig. 1) and normal magnetrons [Fig. 2(a)] that charge density will at first increase rapidly with radial position (avalanche processes dominant), and then increase much more slowly or even decrease with radial position as oscillations or instabilities dominate the electron transport process. Sputtering patterns on the cathodes of Penning structures and the distribution of light emitted from the discharge do, in fact, suggest such a behavior.

From the above discussion it is clear that the effects of space charge are both important and complex. At this point we cannot really say in detail what the space-charge distribution will actually be. We can, however, obtain useful and relevant information by considering the case of *uniformly distributed* space charge. In particular we can compute the maximum amount of charge that can be "contained" within simple geometries, and we can see how this maximum charge depends on various parameters. Rate of ion production and discharge intensity are, of course, intimately tied to the number of electrons present in the discharge space.

In the case of nonuniform space charge (which is the one that generally exists), the maximum amount of charge that can be contained will be different. Despite this, the dependences of the maximum charge on the various parameters should be quite similar to those for the uniform space charge case. Results and predictions obtained from uniform space charge calculations should therefore provide useful insight into the behavior and characteristics of the discharges, and should serve as a guide for further experimental work and for refinement of the theory.

B. Uniformly Distributed Charge between Long Coaxial Cylinders

Consider first the modifications of electric field and potential produced by uniformly distributed space charge located between a pair of coaxial cylinders which are long compared with the spacing between them. For this computation we employ the divergence equation in mks units:

$$\nabla\cdot\mathbf{E}=\rho/\epsilon_0.$$

With the cathode and anode potentials zero and V_a, respectively, and for no azimuthal or longitudinal variations in the potential, the divergence equation yields

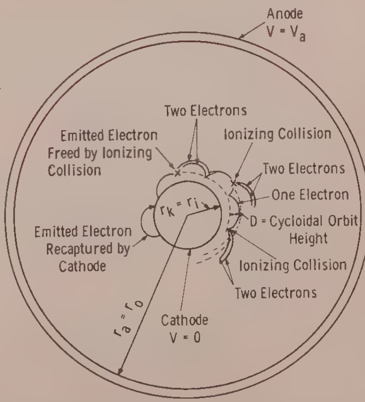

FIG. 3. Idealized representation of avalanche initiation in a normal magnetron. Magnetic field B is parallel to the axis of the concentric cylinders.

---

[20] S. C. Brown, *Basic Data of Plasma Physics* (Technology Press, Cambridge, Massachusetts, and John Wiley & Sons, Inc., New York, 1959), pp. 247–248.

[21] J. C. Helmer and R. L. Jepsen, Proc. I.R.E. (to be published).

for the electric field

$$rE_r = -\frac{V_a}{\ln(r_a/r_k)} - \frac{\rho}{4\epsilon_0 \ln(r_a/r_k)} \times[(r_a^2-r_k^2)-2r^2\ln(r_a/r_k)]. \quad (3)$$

Defining E_k as the electric field at the cathode, the total charge contained between the anode and cathode of length L may be written, using Eq. (3), as

$$q = -4\pi\epsilon_0 L \frac{[V_a + r_k E_k \ln(r_a/r_k)]|r_a^2-r_k^2|}{[(r_a^2-r_k^2)-2r_k^2\ln(r_a/r_k)]}. \quad (4)$$

Maintenance of the discharge is dependent on the availability of secondary electrons from the cathode. The freeing of these electrons depends strongly on E_k. As in the problem of space-charged limited emission in the thermionic diode, it is plausible to assume the $|q|$ has a maximum value when $E_k=0$. Thus

$$q_m = -\frac{4\pi\epsilon_0 V_a L |r_a^2-r_k^2|}{[(r_a^2-r_k^2)-2r_k^2\ln(r_a/r_k)]}. \quad (5)$$

Equations (4) and (5) may be combined to give

$$q/q_m = 1 + (r_k E_k/V_a)\ln(r_a/r_k). \quad (6)$$

For later use it is convenient to rewrite Eq. (3) in terms of (q/q_m).

$$rE_r = -\frac{V_a}{\ln(r_a/r_k)}\left[1-\left(\frac{q}{q_m}\right)\frac{(r_a^2-r_k^2)-2r^2\ln(r_a/r_k)}{(r_a^2-r_k^2)-2r_k^2\ln(r_a/r_k)}\right]. \quad (7)$$

Thus far the above treatment applies equally to normal and to inverted magnetrons. It is now of interest to compare q_m for these two cases. To facilitate this comparison, let r_0 and r_i be the radii of the outer and inner cylinders, respectively. For the normal magnetron, $r_a=r_0$ and $r_k=r_i$. Then

$$q_{mn} = -\frac{4\pi\epsilon_0 V_a L}{1-[2r_i^2/(r_0^2-r_i^2)]\ln(r_0/r_i)}. \quad (8)$$

In the filamentary cathode limit this becomes

$$q_{mn}|_{r_i \ll r_0} \simeq -4\pi\epsilon_0 V_a L. \quad (9)$$

For the inverted magnetron, $r_a=r_i$ and $r_k=r_0$. Thus

$$q_{mi} = -\frac{4\pi\epsilon_0 V_a L}{-1+[2r_0^2/(r_0^2-r_i^2)]\ln(r_0/r_i)} \quad (10)$$

and

$$q_{mi}|_{r_i \ll r_0} \simeq -\frac{4\pi\epsilon_0 V_a L}{2\ln(r_0/r_i)}. \quad (11)$$

Taking the ratio between Eqs. (9) and (11),

$$\left.\frac{q_{mn}}{q_{mi}}\right|_{r_i \ll r_0} \simeq 2\ln(r_0/r_i). \quad (12)$$

This equation shows that for $r_i \ll r_0$, *much more uniformly distributed negative space charge can be contained in a normal magnetron than in an inverted magnetron* before the electric field at the cathode is reduced to zero. Physically, this result is closely related to the fact that in the absence of space charge, the electric field at the cathode is greater (in magnitude) than at the anode in a normal magnetron, while the converse holds for the inverted magnetron.

C. Uniformly Distributed Charge in a Long-Anode Penning Structure

Since we believe that the same physical processes are relevant in both magnetron and Penning types of cold-cathode gas discharges, it is reasonable to treat space charge similarly in the two cases. In the present computation we shall assume that the Penning structure is sufficiently long in comparison with its diameter that end effects are negligible. One exception to this assumption is that the cathodes, which are located at the ends, are effective in establishing the zero of potential for the structure.

Solution of the divergence equation for this case yields

$$E_r = \frac{\rho}{2\epsilon_0} r. \quad (13)$$

Defining V_0 as the potential on the axis near the central region, the total charge contained within the anode may be written as

$$q = -4\pi\epsilon_0 (V_a - V_0) L. \quad (14)$$

A reasonable assumption is that the potential inside the anode will not be depressed by space charge to a value which is appreciably negative with respect to the cathodes, which are located in the end regions. Thus, in analogy with the magnetron case, we shall assume that q has a maximum value when $V_0=0$:

$$q_{mp} = -4\pi\epsilon_0 V_a L. \quad (15)$$

In terms of the ratio of the amount of charge actually present in the cell to the maximum, E_r and V_0 are conveniently written as

$$E_r = -\frac{2V_a}{r_a}\frac{r}{r_a}\frac{q}{q_{mp}} \quad (16)$$

$$V_0 = V_a\left(1-\frac{q}{q_{mp}}\right). \quad (17)$$

That space-charge depression of potential is in fact significant has been shown by an experiment in which the energy spectrum of positive ions striking the cathodes of a Penning structure was examined. The measurements indicated that V_0 had been depressed by space charge by a large rather than by a trivial amount. For example, with $V_a=3$ kv, values of V_0 near 1 kv were obtained under typical conditions.[22]

D. Comparison between Corresponding Magnetron and Penning Structures

From Eqs. (9), (11), and (15) we see that the maximum charge that can be contained in the Penning cell is the *same* as in the normal magnetron with a filamentary cathode, and is much larger than that for the inverted magnetron. It can also be shown that the electric field and potential distributions are the same in the two structures (normal magnetron and Penning cell) when $q=q_m$.

One consequence of having a large amount of space charge present in a Penning structure is that it is thereby converted from a "parallel-field" device to a "crossed-field" device of the normal magnetron type. It is therefore not surprising that the same maximum charge can be contained in the two structures. There are, however, substantial differences between them. In a normal magnetron, space charge perturbs the electric field and potential distribution between anode and cathode, but does not change the potential along the axis. In a Penning structure, on the other hand, the same amount of trapped charge affects the electric field inside the anode much more strongly. Correspondingly, the potential along the axis is depressed from V_a to V_0. This difference is compared in Fig. 4.

With the potential inside the anode depressed significantly by space charge, the Penning structure becomes, in essence, a normal magnetron with a virtual cathode located on the axis. The "effective" anode voltage is now (V_a-V_0) rather than V_a. The virtual cathode differs from a real cathode in that it is "electrically soft"; that is, V_0 is not determined by the externally applied voltage alone, but depends on the amount of charge q that is trapped; q, in turn, depends on many factors, including V_0 itself.

It is worth noting here that for both the Penning structure and the normal magnetron with a filamentary cathode, q_m varies linearly with anode voltage, is proportional to anode length, and is *independent of anode diameter*.[23] This last point is of evident importance to the problem of increasing the amount of discharge current in a given volume.

IV. THE QUANTITY (I/P)

A. (I/P) for Penning Structures

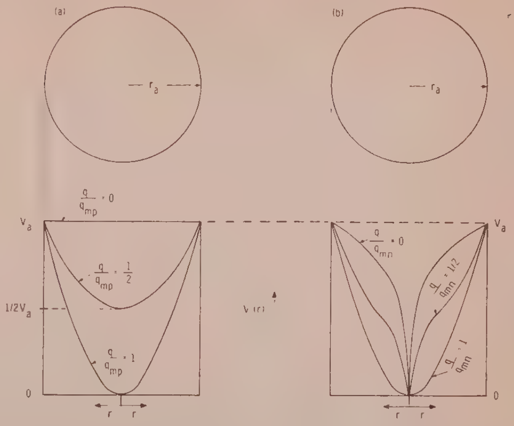

FIG. 4. Comparison of the modifications of potential produced by uniformly distributed space charge in (a) Penning structures and (b) in normal magnetrons.

Suppose we have a charge q distributed uniformly inside a long-anode Penning cell. Let us assume that the electrons migrate toward the anode via a series of collisions with gas molecules, and assume further that upon making inelastic collisions the electrons lose all of their energy, so they start out from the point of collision with zero initial velocity. In addition, let us neglect the axial motion of the electrons, and neglect also the ionization produced as a result of their axial motion. We may remark at this point that for small values of (q/q_{mp}) the radial electric field will be small; in this case the neglect of axial motion and the consequent ionization is not justified.

Under the influence of the radial electric and axial magnetic fields, the electrons will move in orbits which are approximately cycloidal provided the electric field is substantially uniform over the orbit; an alternative statement of this condition is that the orbit height should be small compared with the anode radius. It is readily shown that the cycloid height D (see Fig. 3) is related in MKS units to E_r and B through

$$D=(2m/e)|E_r|/B^2. \tag{18}$$

Within the orbit the electron velocity varies between zero and $2|E_r|/B$, and the average azimuthal velocity is

$$\bar{v}=|E_r|/B. \tag{19}$$

The mean time between ionizing collisions τ_c depends on electron velocity v in the manner indicated in Fig. 5. One simple procedure is to approximate τ_c by the step-function

$$\left.\begin{array}{ll}\tau_c\to\infty & \text{for}\quad 0\leq v\leq v' \\ \tau_c=C/P & \text{for}\quad v>v'\end{array}\right\}, \tag{20}$$

where C is a constant which depends on the species of gas but which is independent of pressure and electron velocity. We can then say that on the average a fraction f of the electrons have energies sufficient to produce ionization with the mean collision time $\tau_c=C/P$, and that the remaining fraction $(1-f)$ of the electrons have

---

[22] It is of interest to note in passing that a capacitance of the anode defined as $C_a\equiv-q/(V_a-V_0)$ is just $C_a=4\pi\epsilon_0 L$. For L in centimeters: $C_a/L\simeq1.11$ $\mu\mu$f/cm.

[23] That q_m is independent of anode diameter is closely related to the fact that the perveance of an electron beam which fills a fixed fraction of a drift tube is independent of drift tube diameter. See, for example, J. R. Pierce, *Theory and Design of Electron Beams* (D. Van Nostrand Company, Inc., Princeton, New Jersey, 1949), pp. 161–164.

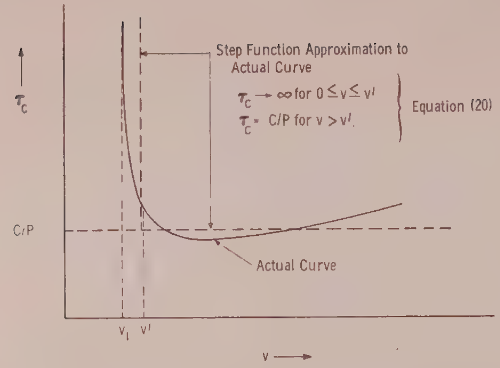

Fig. 5. Qualitative plot of mean time between ionizing collisions τ_c as a function of electron velocity v. A step function approximation to the actual curve is also plotted. v_i is the electron velocity corresponding to the ionization potential of the gas.

energies which are too low to cause appreciable ionization. The fraction f can be computed with varying degrees of sophistication and refinement. In view, however, of the other approximations involved, we shall proceed by considering only the average azimuthal velocity of the electrons, thus neglecting the effect of variations in velocity which occur within the arches of the individual cycloids.

Corresponding to the velocity v' is an electric field E_r' and a radius r'. Only those electrons located between r' and r_a have $v > v'$. The fraction f is thus

$$f = 1 - (r'^2/r_a^2). \tag{21}$$

Using Eqs. (16) and (19) the expression for f becomes

$$f = 1 - \left(\frac{Br_a v'}{2V_a} \frac{q}{q_{mp}}\right)^2. \tag{22}$$

Assuming that all of the discharge current I arises from ionizing collisions, an expression for (I/P) is just

$$I/P = -(fq/C). \tag{23}$$

Combining with Eqs. (15) and (22),

$$\frac{I}{P} = \frac{4\pi\epsilon_0 V_a L}{C} \frac{q}{q_{mp}} \left[1 - \left(\frac{B r_a v'}{2V_a} \frac{q_{mp}}{q}\right)^2\right] \frac{\text{amp}}{\text{mm Hg}}. \tag{24}$$

In Fig. 6 (I/P) is plotted against (q/q_{mp}) from Eq. (24) for a set of parameters that typically yields an (I/P) of about 10 amp/mm Hg. It is seen that $(q/q_{mp}) \simeq 0.6$ is required for the generation of the experimentally observed (I/P). Such a large value of (q/q_{mp}) means, of course, that modifications of potential and electric field by space charge must be major in extent rather than insignificant. This is consistent with the earlier observation (Sec. IIIC) regarding potential depression as inferred from the energy spectrum of positive ions arriving at the cathodes.

It should be recalled that the effects due to axial motion of the electrons were neglected in deriving Eq. (24). Such effects will become dominant in importance when (q/q_{mp}) is small. Thus, even in the uniform space charge case, the behavior of (I/P) when (q/q_{mp}) is small may be expected to deviate substantially from that predicted by Eq. (24).

B. (I/P) for Magnetrons

Expressions corresponding to Eq. (24) are much more difficult to obtain for magnetrons. This arises from the more complex relationship between radius and electric field [compare Eq. (7) with (16)]. We therefore present for comparison expressions only for the special case where $r_i \ll r_0$ and $q = q_m$. The results are

$$\left(\frac{I}{P}\right)_n \simeq \frac{4\pi\epsilon_0 V_a L}{C}\left[1 - \left(\frac{B r_0 v'}{2V_a}\right)^2\right] \tag{25}$$

for normal magnetrons, and

$$\left(\frac{I}{P}\right)_i \simeq \frac{4\pi\epsilon_0 V_a L}{C}\left(\frac{2V_a}{B r_0 v'}\right)^2 \frac{1}{[2\ln(r_0/r_i)]^3} \tag{26}$$

for inverted magnetrons.

C. Comparisons

Upon comparing Eq. (25) with Eq. (24) evaluated at $q = q_{mp}$ and for $r_a = r_0$, it is seen that (I/P) is the *same* for the normal magnetron as for the Penning structure. This is so because both the total charge contained and the electric field distribution are the same for the two structures under these conditions, as noted above in Sec. IIID. For small values of (q/q_m) the behaviors of Penning and normal magnetron structures should be quite different. In the Penning structure the fraction f approaches zero because the radial electric fields are small in the absence of space charge. (In this case, however, axial motion of the electrons becomes dominant in importance, as remarked in Sec. IVA.) In the normal magnetron the radial electric fields are large even without space charge, whence f may be large.

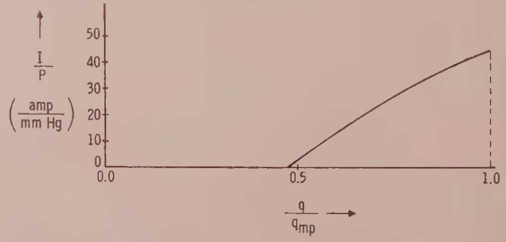

Fig. 6. (I/P) as a function of (q/q_{mp}) from Eq. (24). The parameters chosen are $V_a = 4\times10^3$ volts, $(Br_a) = 9\times10^{-4}$ webers/meter, $L = 2\times10^{-2}$ meters, $C = 1.5\times10^{-10}$ mm Hg/sec. [This value for C is consistent with data for argon and nitrogen compiled by Dushman. See, for example, S. Dushman, *Scientific Foundations of Vacuum Technique* (John Wiley & Sons, Inc., New York, 1949), p. 351.] and $v' = 4.2\times10^6$ meters/sec. (This velocity corresponds to a kinetic energy of 50 ev).

A detailed comparison between normal and inverted magnetrons over all ranges of the parameters, including (q/q_m), is not simple. In certain parameter ranges, inverted magnetrons will, on the uniform space charge theory, draw current when normal magnetrons will not operate at all. For other ranges of the parameters, however, especially those appropriate to relatively intense discharges, normal magnetrons appear to win out. One reason for this is that the maximum charge that can be contained inside the inverted magnetron is reduced from that for the normal magnetron by the factor $2\ln(r_0/r_i)$, as shown by Eq. (12).

D. The Γ Coefficient

Recall from Sec. II that Γ is the number of avalanche-initiating electrons freed at or near the cathode for each electron-ion pair produced in the avalanche. If Γ is too small, one avalanche does not give birth to a new avalanche, and the discharge is not self-sustaining. If Γ exceeds some minimum value, the number of avalanches in process will increase with time until space charge effects modify both α and Γ in such a way that the Townsend avalanche equation is satisfied. In general we expect (q/q_m), and with it (I/P), to increase with increasing Γ. Γ is itself affected by (q/q_m) through reduction of the electric field at the cathode by space charge.

Electrons which are released from a cathode have a high probability of recapture unless collisions (or other nonconservative interactions) occur before they have returned to the cathode surface. For such electrons, Γ will be related to the distance d traveled between leaving and returning to the cathode by the relation

$$\Gamma \propto \left[1-\exp\left(-\frac{d}{\lambda}\right)\right], \tag{27}$$

where λ is an appropriately averaged mean free path for collisions between the electrons and gas molecules.

In a Penning structure the secondary electrons travel axially from one cathode to the other, while in a magnetron they move in modified cycloidal paths from point to point on the cathode surface. The distance d is therefore much greater in a long-anode Penning cell than in a magnetron. In addition, d varies inversely as B^2 in magnetrons but is independent of B in a Penning cell. Thus Γ should be appreciably different for the two structures, and should in general be greater for the Penning cell.

E. Voltage

At low voltages several factors combine to discourage the establishment of a self-sustained discharge. One is that the number of ionizing collisions that an avalanche-initiating electron can make is energetically limited; another is that other collision processes become dominant in importance; and a third factor is that the Γ coefficient is small.

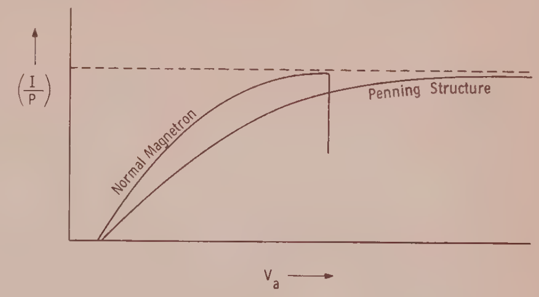

FIG. 7. Qualitative comparison of the voltage dependences of (I/P) for a normal magnetron and an "equivalent" long-anode Penning structure.

The voltage at which a discharge will strike depends on many factors, some of which have been considered in the theoretical treatments of Haefer,[13-15] Somerville,[16] and Redhead.[9,17] The current may or may not be zero at the striking voltage, and hysteresis may occur in the neighborhood of the striking voltage, especially with a Penning structure.

At intermediate voltages (I/P) increases rapidly with voltage for several reasons. One is that q_m is linearly proportional to V_a; a second is that (q/q_m) increases through the dependence of Γ on ion energy.

Although the behaviors of Penning and magnetron structures may be similar at intermediate voltages, the situation is quite different at high voltages. In the case of the magnetron, q rises with increasing voltage, goes through a maximum, and then falls off as voltage is increased further. This decline in q at high voltages occurs when the orbit height D becomes appreciable in comparison with the cathode-anode spacing, leading to a reduction in avalanche size (and hence to a reduction in q) by reducing the number of ionizing collisions made by an avalanche-initiating electron. For V_a large enough, the discharge will go out altogether. At low pressures the upper extinction voltage should lie substantially below the ordinary magnetron cutoff voltage.

In the case of the long-anode Penning structure, the virtual cathode is electrically "soft." Electric field, potential along the axis (V_0), and orbit heights are determined by q. Thus, for example, it is possible for q to remain constant as V_a is increased. In this case (V_a-V_0) will remain constant, as shown by Eq. (14). Voltage dependences of (I/P) for the normal magnetron with a filamentary cathode and the equivalent long-anode Penning structure are compared qualitatively in Fig. 7.

F. Magnetic Field

In Eq. (24) an explicit dependence of (I/P) on (Br_a) is exhibited for the Penning cell. Of greater importance is the further dependence of (I/P) on B and r_a through (q/q_m). If B is too small, the electron orbit heights will be too large for the discharge to exist. Above some critical value of B, existence of the discharge becomes

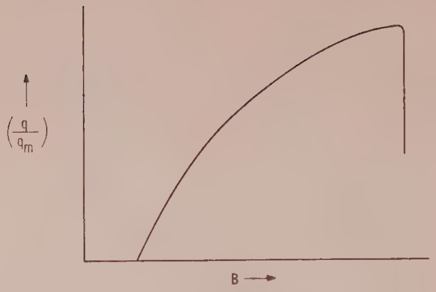

FIG. 8. Expected dependence (qualitative) of (q/q_m) on magnetic field B.

possible, as indicated by the theories for striking characteristics.[9,13–17] As B is increased further, the number of ionizing collisions made by an avalanche-initiating electron, and correspondingly the avalanche size and (q/q_m), will increase. However, when B becomes so large that the maximum energy attained by an electron in its cycloidal orbit falls below that necessary to produce ionization, electron attrition by other collision processes can cause (q/q_m) to fall to zero. This behavior is indicated qualitatively in Fig. 8.

As noted above, (I/P) depends explicitly on the product (Br_a). We now argue that the condition

$$Br_a = \text{constant} \tag{28}$$

leads to a constant value of (q/q_m) and hence to a constant value of (I/P). To maintain (q/q_m) constant for fixed anode voltage, a plausible requirement is that the number of ionizing collisions made by an avalanche-initiating electron in its trip from cathode to anode be preserved. This implies that D/r should be preserved at corresponding points in scaled structures. From Eqs. (16) and (18) we see that

$$\frac{D}{r_a} \propto \frac{E_r}{B^2 r_a} \propto \frac{V_a}{(Br_a)^2}. \tag{29}$$

Thus for fixed voltage (q/q_m) *and* (I/P) *are constant in scaled Penning cells, provided that the product of magnetic field and anode diameter is held constant.* Equation (28) thus provides us with a scaling relation of evident utility. Except for the dependence of the Γ coefficient on magnetic field, the same remarks apply to magnetrons.

G. Pressure

According to Eq. (24), (I/P) exhibits no explicit dependence on pressure. In general, however, (q/q_m) depends on pressure through the Γ coefficient [see Eq. (27)]. Thus (I/P) is expected to fall off at low pressures. In the absence of hysteresis, the pressure at which the discharge extinguishes may be determined from the striking characteristics.[9,13–17]

V. CONCLUSION

In contrast with much of the work with high pressure plasmas, the present treatment is restricted to pressures sufficiently low that the transit times for positive ions are much shorter than for electrons, whence the resulting space charge is negative. The above calculations are performed for the artificial case of uniformly distributed charge, the relevance and limitations of which are discussed briefly in Sec. IIIA. In particular, dependences of (I/P) on several of the significant parameters are obtained. Although non-uniform space charge distributions characterize actual discharges, the general *forms* of the (I/P) dependences should be similar. Qualitative agreement with experimental observations may therefore be expected.

A limited amount of experimental information on $I-V_a$, $I-B$, and $I-P$ characteristics for inverted and normal magnetrons and for Penning structures is given in references 4–11 and 15. By and large these results are in excellent qualitative agreement with the theory presented above. In reference 21 certain recent experimental observations on discharges in Penning cells are reported and interpreted in the light of this theory.

ACKNOWLEDGMENTS

The author wishes to acknowledge contributions by many of his colleagues to various aspects of the problems associated with magnetically confined cold-cathode gas discharges. The fine experimental work by S. L. Rutherford, S. L. Mercer, and B. E. Kietzmann has provided important qualitative and semiquantitative tests of the theory; these experiments have been greatly facilitated by the expert technical assistance of J. Davis. Dr. J. C. Helmer has contributed in numerous ways to the problems involved—through experiments, through theoretical work, and through illuminating and stimulating discussions.

OURNAL OF APPLIED PHYSICS VOLUME 32, NUMBER 12 DECEMBER, 1961

Harmonic Generation and Frequency Mixing in Ferromagnetic Insulators

R. L. Jepsen*
Varian Associates, Palo Alto, California

(Received July 17, 1961)

When a transverse rf magnetic field is applied to a ferromagnetic insulator, a second harmonic frequency term arises in m_z (the axial or longitudinal component of the rf magnetization). If in addition an axial component of the rf field is applied, then a second harmonic frequency term appears in m_t (the transverse component of the rf magnetization) as well. It happens further that m_t exhibits *two* dc magnetic field resonances. One resonance occurs when the material is biased to the fundamental, and the other arises when the material is biased to the second harmonic.

In a similar way, application of two frequencies having both axial and transverse components results in sum and difference frequency terms appearing in m_t, in addition to the usual m_z. The mixed frequency terms in m_z are resonant for the two values of dc magnetic field corresponding to the two applied frequencies. The mixed frequency terms in m_t exhibit additional resonances for dc magnetic fields corresponding to the sum and difference frequencies.

The present paper describes calculations of second harmonic generation and second-order frequency mixing under the assumption of uniform precession of the magnetization, for small and ellipsoidally shaped samples of material and with loss included in the Landau-Lifshitz form. A simple case of third harmonic generation is also discussed. Results of the calculations are applied to a simple example of second harmonic generation. The detailed calculations and results are contained elsewhere in a rather lengthy report.

I. INTRODUCTION

FUNDAMENTAL understanding of the large signal properties of ferrites (and other ferromagnetic insulators) is important to the interpretation of certain experimental observations and to the design of such devices as harmonic generators, frequency mixers, and ferromagnetic microwave amplifiers. With ferrites, two types of large signal effects arise. One is the normal appearance of nonlinearities under the condition of uniform precession of the magnetization; the other is the growth of spin waves, which results in a breakdown of the uniform precession and gives rise to the early onset of saturation. This latter effect has been treated extensively by Suhl.[1,2] A related effect, which has been treated by Schlömann *et al.*,[3,4] is the growth of spin waves from the application of sufficiently large longitudinal rf magnetic fields. The present paper is restricted to considerations of nonlinearities which arise under uniform precession.

A set of detailed second-order calculations of harmonic generation and frequency mixing has been carried out under the following conditions and assumptions:

(1) Samples are small enough that the applied dc and rf magnetic fields are uniform throughout the material.

(2) Retardation effects are unimportant.

(3) Samples are ellipsoidal in shape, whence boundary effects are taken into account through demagnetizing factors N_x, N_y, and N_z.

(4) Two different frequencies of rf magnetic field are applied at the same time; both have longitudinal in addition to the usual transverse components.

(5) Loss is included in the Landau-Lifshitz form via the damping parameter α.

(6) Only the uniform precessional mode is excited.

Approximate expressions (for small values of the damping parameter α and the applied rf magnetic fields) for the fundamental, second harmonic, mixed frequency, and zero frequency parts of the magnetization are obtained and recorded in detail in a report by the present author.[5] Because of its length and complexity, publication of the report as a paper in the standard technical journals is hardly appropriate. In this paper we outline the method of calculation, apply the results to a simple case of second harmonic generation, and discuss second-order frequency mixing.

Also contained in reference 5 is a calculation of third harmonic generation with loss neglected and for a spherical sample shape. A brief discussion of the results is included in the present paper.

Subsequent to preparation of reference 5, related theoretical work has been described by Morgenthaler.[6,7]

II. DESCRIPTION OF THE SECOND-ORDER CALCULATIONS

The second-order calculation begins with the equation of motion of magnetization in the Landau-Lifshitz form[8]

$$d\mathbf{M}/dt=\gamma(\mathbf{M}\times\mathbf{H})+(\gamma\alpha/M_0)(\mathbf{M}\times\mathbf{M}\times\mathbf{H}) \qquad (1)$$

---

[*] Work performed at Harvard University while on sabbatical leave from Varian Associates.

[1] H. Suhl, Proc. IRE **44**, 1270 (1956).

[2] H. Suhl, J. Phys. Chem. Solids **1**, 209 (1957).

[3] E. Schlömann, J. J. Green, and U. Milano, J. Appl. Phys. **31**, 386S (1960).

[4] E. Schlömann and R. I. Joseph, J. Appl. Phys. **32**, 165S (1961).

[5] R. L. Jepsen, "Harmonic generation and frequency mixing in ferromagnetic insulators," Scientific Report No. 15, AFCRC-TN-58-150, Gordon McKay Laboratory of Applied Science, Harvard University, Cambridge, Massachusetts (May 25, 1958). ASTIA Document No. AD 152381.

[6] F. R. Morgenthaler, J. Appl. Phys. **30**, 157S (1959).

[7] F. R. Morgenthaler, J. Appl. Phys. **31**, 95S (1960).

[8] L. Landau and E. Lifshitz, Physik Z. Sowjetunion **8**, 153 (1935).

(where $\gamma<0$ for electrons). **H**, the magnetic field inside the material, is written as

$$\mathbf{H}=(h_x-N_xm_x)\hat{x}+(h_y-N_ym_y)\hat{y}+[(H_0^e+h_z)-N_z(M_0+m_z)]\hat{z}, \quad (2)$$

and **M** is written as

$$\mathbf{M}=m_x\hat{x}+m_y\hat{y}+(M_0+m_z)\hat{z}. \quad (3)$$

H_0^e is the steady magnetic field applied externally to the material. Lower case "m" and "h" are used to denote rf magnetizations and externally applied rf magnetic fields. For example, h_x is written as

$$h_x=h_{1x}\cos u_1+h_{2x}\cos u_2+h_{3x}\sin u_1+h_{4x}\sin u_2, \quad (4)$$

where $u_1\equiv\omega_1t$ and $u_2\equiv\omega_2t$, and m_x is assumed to be of the form

$$\begin{aligned}m_x=a_0&+a_1\cos u_1+a_2\cos u_2+a_3\sin u_1+a_4\sin u_2\\&+a_5\cos 2u_1+a_6\cos 2u_2+a_7\sin 2u_1+a_8\sin 2u_2\\&+a_9\cos(u_1+u_2)+a_{10}\cos(u_1-u_2)\\&+a_{11}\sin(u_1+u_2)+a_{12}\sin(u_1-u_2). \quad (5)\end{aligned}$$

In all, there are 39 unknown coefficients a_0, $a_1\cdots a_{12}$, b_0, $b_1\cdots b_{12}$, c_0, $c_1\cdots c_{12}$. To solve for these, **H** and **M** as given in Eqs. (2)–(5) are substituted into the equation of motion of magnetization. From these substitutions three scalar equations are obtained, each containing a constant term plus terms in sines and cosines of u_1, u_2, $2u_1$, $2u_2$, $u_1\pm u_2$, and higher order terms which can be neglected. As usual the multiplier of each of these terms is equated to zero separately, and the resulting set of simultaneous equations is solved for a_0, $a_1\cdots a_{12}\cdots$.

Solutions of the equations which are essentially exact to order h^2 and for α small are obtained and recorded in reference 5. Because of their complexity most of the results are not reproduced here.

III. SECOND HARMONIC GENERATION

For purposes of illustration, an application of the results to a simple case of second harmonic generation is presented below. In this example the applied rf magnetic field (one frequency) has linearly polarized components along the x and z axes which vary as $\cos u$. Thus

$$\begin{aligned}\mathbf{H}^e&=h_x\cos u\hat{x}+(H_0^e+h_z\cos u)\hat{z},\\u&\equiv\omega t+\phi. \quad (6)\end{aligned}$$

The second harmonic components for the magnetization are (from reference 5):

$$\begin{aligned}m_{x\,\text{2nd harm}}=&-\left(\frac{\gamma^2M_0}{2D(\omega)D(2\omega)}\right)(2\omega^2+\omega_y^2)(\omega^2-\omega_x\omega_y)[(2\omega)^2-\omega_x\omega_y]h_xh_z\cos 2u+\frac{\gamma^2M_0\alpha\omega}{2D(\omega)D(2\omega)}\\&\times\{[2\omega^2(\omega_x+\omega_y)+\omega_y(\omega^2+\omega_y^2)][(2\omega)^2-\omega_x\omega_y]+(\omega_x+3\omega_y)(\omega^2-\omega_x\omega_y)[(2\omega)^2-\omega_x\omega_y]\\&+\omega_y(\omega_x+\omega_y)(\omega_x+2\omega_y)(\omega^2-\omega_x\omega_y)\}h_xh_z\sin 2u \quad (7)\end{aligned}$$

$$\begin{aligned}m_{y\,\text{2nd harm}}=&-\left(\frac{\gamma^2M_0}{2D(\omega)D(2\omega)}\right)\omega(\omega_x+2\omega_y)(\omega^2-\omega_x\omega_y)[(2\omega)^2-\omega_x\omega_y]h_xh_z\sin 2u-\left(\frac{\gamma^2M_0\alpha}{2D(\omega)D(2\omega)}\right)\\&\times\{\omega^2[\omega_x(\omega_x+\omega_y)+2(\omega^2+\omega_y^2)][(2\omega)^2-\omega_x\omega_y]+[2\omega^2+\omega_y(\omega_x+\omega_y)](\omega^2-\omega_x\omega_y)[(2\omega)^2-\omega_x\omega_y]\\&+\omega_x(\omega_x+\omega_y)(2\omega^2+\omega_y^2)(\omega^2-\omega_x\omega_y)\}h_xh_z\cos 2u \quad (8)\end{aligned}$$

$$\begin{aligned}m_{z\,\text{2nd harm}}=&\frac{\gamma^2M_0}{4D^2(\omega)}\{(\omega^2-\omega_x\omega_y)^3+\alpha^2[\omega^2(\omega_x^2+\omega_y^2)+2\omega_x^2\omega_y^2](\omega^2-\omega_x\omega_y)+(\omega_x-\omega_y)[\omega_y(\omega^2-\omega_x\omega_y)^2\\&-\alpha^2\omega^2(\omega_x+\omega_y)(\omega^2+\omega_y^2)]\}h_x^2\cos 2u-\frac{\gamma^2M_0}{4D^2(\omega)}\{\alpha\omega(\omega_x+\omega_y)(\omega^2-\omega_x\omega_y)^2+\alpha^3\frac{\omega_x}{\omega}(\omega^2+\omega_y^2)\\&\times[\omega^2(\omega_x^2+\omega_y^2)+2\omega_x^2\omega_y^2]+\alpha\omega(\omega_x-\omega_y)(\omega^2+\omega_x\omega_y+2\omega_y^2)(\omega^2-\omega_x\omega_y)\}h_x^2\sin 2u \quad (9)\end{aligned}$$

$D(\omega)$ and $D(2\omega)$ are resonance denominators which, for α small, are given by

$$\begin{aligned}D(\omega)&\equiv(\omega^2-\omega_x\omega_y)^2+\alpha^2[\omega^2(\omega_x^2+\omega_y^2)+2\omega_x^2\omega_y^2]\\D(2\omega)&\equiv[(2\omega)^2-\omega_x\omega_y]^2\\&\quad+\alpha^2[(2\omega)^2(\omega_x^2+\omega_y^2)+2\omega_x^2\omega_y^2] \quad (10)\end{aligned}$$

ω_x, ω_y and H_{eff} are defined as

$$\begin{aligned}\omega_x&\equiv-\gamma[H_0^e+(N_x-N_z)M_0]\\\omega_y&\equiv-\gamma[H_0^e+(N_y-N_z)M_0] \quad (11)\\-\gamma H_{\text{eff}}&\equiv(\omega_x\omega_y)^{\frac{1}{2}}.\end{aligned}$$

We note that

$$\omega_x-\omega_y=-\gamma(N_x-N_y)M_0.$$

The following important features are observed from examinations of Eqs. (7)–(11):

(1) m_z depends only on transverse rf magnetic fields; it is independent (to order h^2) of the presence or absence of longitudinal rf magnetic fields.

(2) Transverse magnetization m_t(m_x or m_y) arises from the *simultaneous* presence of transverse and longitudinal rf magnetic fields.

(3) As usual, m_z exhibits a resonance near $-\gamma H_{\text{eff}}=\omega$.

(4) The transverse magnetization exhibits *two* resonances; one is near $-\gamma H_{\text{eff}}=\omega$, and the other is near $-\gamma H_{\text{eff}}=2\omega$.

(5) Because loss is included (through the damping parameter α), quantitative calculations can be made at resonance.

We thus see that there are three conditions under which relatively effective harmonic generation should be obtainable: (1) via longitudinal magnetization with the material biased to the fundamental, (2) via transverse magnetization with the material biased to the fundamental, and (3) via transverse magnetization with the material biased to the second harmonic.

It is of interest to make quantitative comparisons among these three modes of operation. To do this, consider the simple case for which $\omega_x=\omega_y$ (i.e., the sample is cylindrically symmetric about the z axis; $N_x=N_y$). Evaluated at $-\gamma H_{\text{eff}}=\omega$, and using Eqs. (10)–(11), Eqs. (7–9) may be written

$$m_{x\,\text{2nd harm}}\big|_{\omega}=\frac{M_0h_xh_z}{4\alpha(\omega)H^2(\omega)_{\text{eff}}}\sin 2u \tag{12}$$

$$m_{y\,\text{2nd harm}}\big|_{\omega}=-\frac{M_0h_xh_z}{4\alpha(\omega)H^2(\omega)_{\text{eff}}}\cos 2u \tag{13}$$

$$m_{z\,\text{2nd harm}}\big|_{\omega}=-\frac{M_0h_x^2}{8\alpha(\omega)H^2(\omega)_{\text{eff}}}\sin 2u. \tag{14}$$

Thus the ratio of transverse to longitudinal second harmonic magnetization is

$$\left|\frac{m_{x\,\text{2nd harm}}}{m_{z\,\text{2nd harm}}}\right|_{\omega}=2\frac{h_z}{h_x}. \tag{15}$$

For equal magnitudes of transverse and longitudinal applied rf magnetic fields, the second harmonic transverse magnetization is twice as great as the longitudinal in the present example.

It must be remarked, however, that sample shapes for which the transverse demagnetizing factors are unequal ($\omega_x\neq\omega_y$) lead to enhancement of m_z, as pointed out by Pippin.[9,10] Inclusion of loss and demagnetizing factors permits quantitative calculations to be made of this enhancement. A corresponding increase in m_x and m_y does not occur. These points are elaborated in reference 5.

When the dc magnetic field is biased to the second harmonic (i.e., $-\gamma H_{\text{eff}}=2\omega$), Eq. (7) becomes

$$m_{x\,\text{2nd harm}}\big|_{2\omega}=-\frac{M_0h_xh_z}{2\alpha(2\omega)H^2(2\omega)_{\text{eff}}}\sin 2u. \tag{16}$$

Since

$$H(2\omega)_{\text{eff}}=2H(\omega)_{\text{eff}}, \tag{17}$$

and if the material has a constant absolute line width,

$$\alpha(2\omega)=\alpha(\omega)/2, \tag{18}$$

then the ratio of second harmonic (transverse) magnetizations for the two bias fields is

$$\frac{|m_{x\,\text{2nd harm}}|_{2\omega}}{|m_{x\,\text{2nd harm}}|_{\omega}}=1. \tag{19}$$

Thus, in the present example, biasing the material to the second harmonic field is as effective as biasing to the fundamental.

From the preceding comparisons it would seem that little advantage accrues from obtaining harmonic generation via m_t rather than m_z, particularly in view of the enhancement of m_z obtainable with sample shapes having unequal transverse demagnetizing factors.[9,10] There are, however, certain features which may render harmonic generation via m_t attractive and important.

When biased to the fundamental, rf heating and breakdown of the uniform precession limit the transverse rf magnetic fields that can be utilized.[1,2] It would appear that much larger *longitudinal* rf magnetic fields can be applied before running into either of these limitations.[3,4] From Eq. (15) harmonic generation via m_t would become correspondingly more effective than that via m_z.

Biasing to the second harmonic should greatly increase the rf magnetic field that can be applied for two reasons. One is that rf heating is strongly reduced, and the other is that much larger driving fields can be applied before breakdown of the uniform precession occurs.[11] In addition, the reduced absorption (by virtue of being biased an octave above resonance) increases efficiency of utilization of fundamental power. On the other hand, additional power will be absorbed from the second harmonic output since the material is now resonant there.

Summarizing briefly, three methods for obtaining enhanced second harmonic generation have emerged. In the first, the rf magnetic field is applied transversely, and harmonic generation is obtained via m_z; enhancement is achieved through sample shape factors. For the second method, the applied rf magnetic field has both longitudinal and transverse components, and harmonic generation is obtained via m_t; enhancement results from increasing the longitudinal component of the rf magnetic field. In the third method, the dc magnetic field is adjusted for resonance at the second harmonic frequency, the rf magnetic field has both longitudinal and rf components, and harmonic generation is obtained via m_t; enhancement arises from the now permissible application of larger rf magnetic fields, both

---

[9] J. E. Pippin, "Frequency doubling and mixing in ferrites," Scientific Report No. 2, AFCRC-TN-56-369, Gordon McKay Laboratory, Harvard University, Cambridge, Massachusetts (May 5, 1956).

[10] J. E. Pippin, Proc. Inst. Radio Engrs. 44, 1054 (1956).

[11] This point is discussed in some detail in the Appendix in reference 5.

transverse and longitudinal. Which of these three methods of producing harmonic generation will turn out in practice to be the most effective remains to be determined.

IV. THIRD HARMONIC GENERATION

Also contained in reference 5 is a brief treatment of third harmonic generation with applied rf magnetic fields having both longitudinal and transverse components, but with loss neglected and for a spherically shaped sample. One result is that *three* dc magnetic field resonances now occur: fundamental, second harmonic, and third harmonic. Another result is that if the rf magnetic field has only transverse components, then third harmonic generation is obtained only via m_t (in direct contrast with the situation for second harmonic generation).

V. FREQUENCY MIXING

Calculations similar to those for second harmonic generation were carried out for frequency mixing in reference 5. One result is that in the absence of longitudinal components of applied rf magnetic fields, mixing occurs only via m_z (as in second harmonic generation). And if, for example, one rf magnetic field is applied longitudinally and the other transversely, then mixing occurs only via m_t.

For frequency mixing via m_z, resonance occurs for two values of the magnetic field, namely for $-\gamma H_{\text{eff}}$ near ω_1 and near ω_2. For frequency mixing via m_t, there may be *four* resonances; these occur near the two applied frequencies and near the sum and difference frequencies.

As in the case of harmonic generation, frequency mixing may be accomplished under a variety of conditions. Factors which are affected by the choice of operating parameters include rf heating, breakdown of the uniform precession, power absorption at the fundamental and mixed frequencies, and conversion efficiency. The theory developed in reference 5 permits a partial evaluation to be made of mixer behavior under several conditions of operation.

In most applications it has been customary to operate with the material resonant at the local oscillator frequency. As the present work shows, other resonant conditions can be employed. It may develop that significant advantages will accompany operation under one of these other conditions.

Although experimental tests of the theory appear to be straightforward, none have been described in the literature. In most of the experimental work reported in recent years, interesting and useful results from a device standpoint have been obtained under experimental conditions (sample sizes, sample shapes, and power levels) to which the present theory is completely inapplicable.[12–16] Whether the practical devices that can be designed on the basis of the present theory will turn out to be superior or inferior to those designed otherwise remains to be determined.

VI. CONCLUSIONS

The application of longitudinal components of rf magnetic fields in addition to the usual transverse components gives rise to two new features. One is that harmonic generation and frequency mixing occur via m_t, instead of or in addition to the usual m_z. The other is that additional bias field resonances emerge for harmonic generation and frequency mixing. Considerations of rf heating, breakdown of the uniform precession, power absorption at the various frequencies, and conversion efficiency suggest that certain of these new operating conditions may be attractive and important.

Inclusion of loss and demagnetizing factors permits quantitative calculations to be made in certain cases of interest. For example, the enhancement of harmonic generation through sample shape factors[9,10] can be estimated.

In testing the theory described above, care must, of course, be taken to ensure that adequate correspondence exists between the experimental conditions and those assumed for the theory. The sample should be small enough that the applied magnetic fields (both dc and rf) are uniform over the sample, and that retardation effects are negligible. Ellipsoidal sample shapes should be employed so that the concept of demagnetizing factors is valid. Values of applied rf magnetic fields must be low enough that only the uniform precessional mode is excited.

ACKNOWLEDGMENTS

The author wishes to thank Dr. C. L. Hogan for providing much of the motivation for these calculations and for many valuable suggestions. He wishes to thank also Professor N. Bloembergen, Professor R. V. Jones, and Dr. J. E. Pippin for interesting and useful discussions, and Dr. M. W. Muller for critical review.

---

[12] W. P. Ayres, P. H. Vartanian, and J. L. Melchor, J. Appl. Phys. **27**, 188 (1956).

[13] J. L. Melchor, W. P. Ayres, and P. H. Vartanian, Proc. Inst. Radio Engrs. **45**, 643 (1957).

[14] M. T. Weiss, J. Appl. Phys. **29**, 421 (1958).

[15] E. N. Skomal and M. A. Medina, J. Appl. Phys. **29**, 423 (1958).

[16] W. P. Ayres, IRE Transactions **MTT-7**, 62 (1959).

OURNAL OF APPLIED PHYSICS VOLUME 32, NUMBER 12 DECEMBER, 1961

A Method for Measuring the Conductivity in a High Electron Density Plasma

K. B. Persson
General Electric Research Laboratory, Schenectady, New York

(Received April 3, 1961)

The interaction between the solenoidal electric field and a ircular cylindrical plasma column is used as the basis for the esign of a pulse-operated bridge suitable for transient measureients of the electrical conductivity in the high-electron density lasma. The solenoidal electric field is generated in a single layer olenoid with a special shield preventing the axial electric field rom interacting with the plasma, thereby avoiding the electric olarization and associated effects. The time varying magnetic eld generated by the solenoid and the induced electric field are hen the only fields interacting with the plasma, and these fields enetrate essentially unperturbed into the plasma as long as the kin depth of the plasma is large in comparison with its radius. he upper limit for the measurable conductivity is determined by he skin depth of the plasma, while the lower limit is determined y the noise level in and the maximum allowed signal on the ridge. The maximum allowed signal on the bridge is either determined by the fact that the solenoidal electric field must be sufficiently small so it does not disturb the thermal state of the plasma to a measurable degree, or else that the amplitude of the electron cyclotron frequency corresponding to the amplitude of the time varying, but essentially uniform, magnetic field must be negligible in comparison with the electron collision frequency ν_m so that nonlinear magnetic field effects are avoided. This makes the bridge most useful in the high pressure range ($\nu_m > \omega$) where the ratio between the upper and lower limits for the measurable conductivity in a typical afterglow plasma can be approximated as $10^{13}p/\omega$, while the upper limit as determined by the skin depth is $10^{10}/\omega$ ohm^{-1} cm^{-1} for a plasma with 1 cm radius. A Gaussian-like pulse with a width of approximately 1 μsec is applied to the solenoids which are close to critically damped in the corresponding frequency range, resulting in a time resolution of less than $\frac{1}{3}$ of a μsec for the conductivity measurement.

INTRODUCTION

THE general aspects of the linear interaction between the solenoidal electric field and the plasma vith rotational symmetry and finite dimensions, smaller han the vacuum wavelength of the applied field, have een discussed in a previous report.[1] The general conlusion from the investigation of this interaction nechanism was that it can be used for measurements ver the whole range of the plasma parameters, but that ome ranges are more convenient than others. One can listinguish between two distinctly different ranges: the ow-pressure and high-frequency range where the ion ind electron collision frequencies are smaller than or at he most comparable with the frequency of the applied ield, and the high-pressure and low-frequency range vhere the same collision frequencies are large in comarison with the frequency of the applied field. The nteraction between the solenoidal electric field and the lasma with finite dimensions is exceedingly complex n the low-pressure and high-frequency range due to he excitation of resonant modes of various kinds. The ariety of resonant modes is particularly large in the resence of a static magnetic field. The situation is onsiderably simpler in the high-pressure and lowrequency range. The amplitudes of the various modes vhich can be excited in this range are negligible as long s the smallest characteristic length of the dominant vave mechanism, the wavelength or the damping ength, is large in comparison with the critical dimension f the plasma. This range is therefore particularly uitable for measurements on the plasma over a large ange of the electron density and the pressure. It is the urpose of this report to describe a method for measurng the conductivity of a steady state or transient lasma and which is applicable over a large range of the electron density, the pressure of the gas, and the transient time constant of the plasma.

The kind of measurements which can be done on a plasma through the interaction between an electromagnetic field and the plasma are easily classified. In the low-pressure and the high-frequency range where the damping length of the pertinent wave mechanism is large in comparison with the wavelength, one can study the plasma either by observing the wave velocity, which generally is a function of the electron density, or the damping of the wave, which is a function of the collision frequencies. These observations therefore give information about the electron density and the collision frequencies in the plasma. When these quantities are measured through observations on the wave propagation it is necessary that the length of the plasma along the direction of propagation be long in comparison with the wavelength. When the same quantities are measured through observations on a resonant mode it is generally required that the dimensions of the plasma are in the range one-half to one wavelength. The only measurement which can be done when the plasma dimensions are much smaller than the wavelength of the pertinent wave mechanism inside the plasma takes the form of a measurement of an impedance or elements of an impedance tensor. The latter is the only kind of measurement which can be done through the interaction between the electromagnetic field and the plasma in the high-pressure and low-frequency range. The method which is described in this report is operating in this range and utilizes a solenoidal electric field generated by an essentially uniform time-varying magnetic field for the interaction with a plasma of rotational symmetry where the axis of rotation is parallel with the time-varying magnetic field.

The solenoidal electric field can be generated in a microwave cavity as well as in ordinary solenoid. A

---

[1] K. B. Persson, General Electric Research Laboratory Rept. No. 60-RL-2545G (November, 1960).

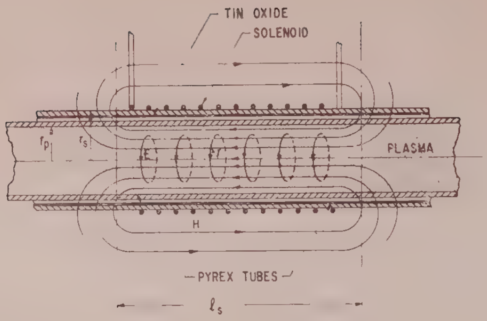

FIG. 1. The solenoid.

description of a microwave cavity which is particularly well suited for measurements on the plasma in the 3000 Mc frequency range can be found in a paper by Brown and Buchsbaum.[2] The real advantages of the solenoidal electric field configuration do, however, show up most prominently in the low-frequency range (100 kc to 10 Mc), where it generally is necessary to use a solenoid for the generation of the desired field configuration. The discussion in this report will apply in particular in this frequency range although the conclusions in general can be carried over into the microwave range with only slight modifications.

THEORY

Figure 1 shows the principal field and plasma configuration that will be discussed. A cylindrical plasma with rotational symmetry, long in comparison with its radius r_p, is confined within a tube made of nonconducting material. It is located concentrically within a second circular cylindrical tube which also is made of nonconducting material. The second tube carries a solenoid which is long relative to its own radius but short in comparison with the total length of the plasma. The solenoid is made with uniform pitch and such that the resonance frequency of the solenoid itself is large in comparison with the frequency of the current carried by the solenoid. The effective length of the solenoid is l_s. The dimensions of the solenoid are much smaller than the vacuum wavelength of the applied frequency. On the inside of the second tubing is applied a tin oxide coating with a thickness that is much smaller than the skin depth of the tin oxide at the applied frequency, but which is sufficiently thick so that the conductance between the two ends of the tin oxide cylinder with the length L is sufficiently large to prevent the axial electric field, which is associated with a plain solenoid, from penetrating into the plasma. The tin oxide coating is applied in order to ensure that only the time-varying magnetic field, generated by the solenoid, is allowed to penetrate into the plasma. If the axial electric field were allowed to interact with the plasma, it would give rise to capacitive effects which would obscure greatly the interpretation of the measurements based on the simple interaction with the solenoidal electric field.

As the length l_s of the solenoid is large in comparison with its radius it is reasonable to assume that the time-varying magnetic field generated by the current carrying solenoid is uniform within the major part of the interaction volume. The solenoidal electric field E within this volume can then be written as

$$\mathbf{E}=(\mathbf{r}/2)\times\partial\mathbf{B}/\partial t, \qquad (1)$$

where $\mathbf{B}$ is the time-varying magnetic field and $\mathbf{r}$ the radius vector from the axis of rotational symmetry. This electric field is the only electric field of consequence within the plasma, as long as the radius r_p of the plasma is small in comparison with the skin depth δ of the plasma at the frequency of the applied field. Assuming that the collision frequency ν_m of the electrons is larger than the frequency of the applied field, the criterion for when the plasma fields can be neglected in comparison with the applied fields can be written as

$$r_p^2 \ll \delta^2 = 2\nu_m c^2/\omega\omega_p^2, \qquad (2)$$

where c is the velocity of light, and ω_p is the plasma frequency ($\omega_p^2 < e^2 n/m\epsilon_0$). The same criterion written in terms of the electron density n is

$$n < \frac{2m\epsilon_0}{e^2}\frac{\nu_m}{\omega}\left(\frac{c}{r_p}\right)^2. \qquad (3)$$

The momentum transfer collision frequency ν_m of the electrons in their interaction with the neutral particles is in the range 10^8 to 10^{10} times the pressure p in mm Hg. Using 10^9 p sec^{-1} as a representative value, assuming that the radian frequency of the applied field is 10^7 rad/sec and that the radius of the plasma is 1 cm, one finds that the conductivity of the plasma is resistive when the pressure is larger than 10^{-2} mm Hg. The approximation above, the neglect of the plasma fields, is then valid when the electron density is less than 10^{13} p cm^{-3}. The conductivity of the plasma can under these circumstances be written as

$$\sigma = e^2 m/m\nu_m = \omega_p^2\epsilon_0/\nu_m. \qquad (4)$$

The fields associated with the plasma currents are of necessity much smaller than the applied fields in this approximation. Only methods able to recognize these small plasma fields are therefore suitable for measurements on the plasma under these circumstances. The magnetic flux generated by the circulating plasma currents is easily evaluated when the length l_s of the interaction zone is large in comparison with the diameter of the plasma. This plasma magnetic field induces a voltage ΔV in the solenoid and can be treated as a perturbation quantity. Quite generally, if the solenoid and the plasma are considered as a transformer with the solenoid as the primary winding and the plasma as a one-turn secondary winding with the resistances R_s

---

[2] S. J. Buchsbaum and S. C. Brown, Phys. Rev. **106**, 196 (1957).

d R_p and inductances L_s and L_p, respectively, and ith the mutual inductance M_{sp}, the perturbation ltage ΔV satisfies the following differential equation

$$\left(R_s+L_s\frac{\partial}{\partial t}\right)\left(R_p+L_p\frac{\partial}{\partial t}\right)\Delta V=-M_{sp}^2\frac{\partial^2 V}{\partial t^2}, \tag{5}$$

here V is the voltage impressed on the primary windg of the solenoid. The effect of the inductance L_p of e plasma secondary can be completely neglected when e skin depth of the plasma is large in comparison with s diameter, and the final differential equation which termines the perturbation voltage which can be easured in the solenoid is

$$\frac{\partial\Delta V}{\partial t}+\frac{R_s}{L_s}\Delta V=-\frac{M_{sp}^2}{R_pL_s}\frac{\partial^2 V}{\partial t^2}. \tag{6}$$

he coefficient on the right-hand side of this equation n be written as

$$M_{sp}^2/R_pL_s=r_p^4\langle\omega_p^2\rangle/8r_s^2c^2\nu_m \tag{7}$$

ith the average $\langle\omega_p^2\rangle$ defined as

$$\langle\omega_p^2\rangle=\frac{8}{r_p^4}\int_0^{r_p} rdr\int_r^{r_p}\omega_p^2 rdr, \tag{8}$$

rovided the solenoid is long relative to its diameter.

Two different time dependencies of the voltage V will e discussed. In the first case V is simply a sinusoidally me-varying voltage with the amplitude V_0 and the dian frequency ω, while in the second case it is a aussian-like pulse. The relative virtues of the two me dependencies will appear in the following discuson. The steady state solution for the differential quation (6) when the voltage V is a sinusoidally time arying signal is

$$\begin{aligned}\frac{V}{V}&=\frac{r_p^4\omega^2}{8r_s^2c^2\nu_m[j\omega+(R_s/L_s)]}\langle\omega_p^2\rangle\\&=\frac{\mu_0 r_p^4\omega^2}{[8r_s^2j\omega+(R_s/L_s)]}\langle\sigma\rangle=\mathcal{C}\frac{\langle n\rangle}{\nu_m},\end{aligned} \tag{9}$$

here the averages $\langle\sigma\rangle$ and $\langle n\rangle$ are defined as the verage $\langle\omega_p^2\rangle$ in formula (8). A measurement of the tio $\Delta V/V$ gives information about the ratio between e average electron density $\langle n\rangle$ and the collision requency ν_m. The proportionality constant $\mathcal{C}$, which is efined by the formulas above, is not easily evaluated xactly due to the presence of end effects. It is however asily determined experimentally by replacing the lasma with a medium of known conductivity (ionic olutions of various kinds), provided the conductivity f this medium is ohmic within the frequency range of terest. It is interesting to notice that if the resistance $_s$ is much smaller than the impedance ωL_s, the proportionality constant $\mathcal{C}$ becomes independent of the number of turns N which are used in the solenoid.

The ratio between the perturbation voltage ΔV and the applied voltage V is measured simplest in a bridge circuit which preferably contains two identical solenoids, one of which is interacting with the plasma. The bridge is balanced in the absence of the plasma, and the unbalanced signal which is observed in the presence of the plasma is then a measure of the ratio $\langle n\rangle/\nu_m$. It is desirable that the bridge be operated only in the range where the unbalanced signal is directly proportional to the ratio $\langle n\rangle/\nu_m$. This is ensured by requiring that the unbalanced signal not be larger than $V/10$. The unbalanced signal on any linear bridge which is less than this value is for all practical purposes proportional to the linear disturbance of the bridge. It is important, however, that the solenoidal electric field applied to the plasma is sufficiently small, so that no significant heating of the plasma occurs during the measurement. This puts an upper limit $V_{\max}$ on the voltage V. The electron temperature T_m is, in the constant collision frequency approximation, related to the gas temperature T_g and the applied electric field E as follows:

$$T_m=T_g+(M/3k)(eE/m\nu_m)^2, \tag{10}$$

where M and m are the masses of the neutral gas particle and the electron, respectively, while k is the Boltzmann constant. Assuming that the measurement is done on a plasma in thermal equilibrium, that is, that there is no other applied field but the measuring field present, one finds that the maximum unbalanced signal can be written as

$$\Delta V_{\max}=\frac{1}{10}V_{\max}\cong\frac{\pi}{50}\frac{r_s^2N}{r_p}\frac{m\nu_m}{e}\left(\frac{3kT_g}{M}\right)^{\frac{1}{2}} \tag{11}$$

if N is the number of turns in the solenoid and provided the temperature rise in the electron gas due to the measuring field is equal to 1% of the gas temperature T_g. Formula (11) is derived in a very conservative manner and should be used only as a guide for the construction of the solenoid and the bridge. The nonlinearities associated with the rise in the electron temperature due to the measuring field can in most cases be observed experimentally and are therefore easily avoided. The situation is principally different when the measurements are done on a "live" plasma where other large applied fields are present. The uncertainty in the theory is however such that sufficiently good values for $\Delta V_{\max}$ and $V_{\max}$ are obtained when the electron temperature T_m is substituted for the gas temperature T_g in formula (11).

The smallest observable value of the unbalanced signal $\Delta V_{\min}$ is determined by the average noise voltage V_n which is developed in the solenoid. It can be written[3] as

$$V_n^2=\frac{2kT}{\pi}\int_{\omega 1}^{\omega 2}Rd\omega\cong kT\omega^2L_s/\pi Q, \tag{12}$$

---

[3] F. E. Terman, *Radio Engineers Handbook* (McGraw-Hill Book Company, Inc., New York, 1946), p. 476.

with Q determined by the losses in the solenoid. Assuming that the length l_s of the solenoid is sufficiently large in comparison with its radius r_s so that its inductance can be written as $L_s = \mu_0 \pi r_s^2 N^2 / l_s$, one finds the useful range for the measurements on the plasma in terms of the ratio

$$\frac{\Delta V_{\max}}{\Delta V_{\min}} = \frac{1}{100}\frac{V_{\max}}{V_n} \cong \frac{\pi}{500}\frac{r_s}{r_p}\left(\frac{3Ql_sT_m}{\mu_0 M T_g}\right)^{\frac{1}{2}}\frac{m}{e}\frac{\nu_m}{\omega}, \qquad (13)$$

provided the $\Delta V_{\min}$ is ten times the average noise voltage V_n. With the following numbers $r_p/r_s = 1/2$, $Q = 100$, $l_s = 20$ cm, $\nu_m = 10^9\ p$ sec^{-1} (p in mm Hg), $\omega = 10^7$ rad/sec, and $T_m = T_g$ (the afterglow plasma), and with the plasma generated in molecular hydrogen the ratio above is approximately $2 \times 10^6\ p$, showing that it is theoretically possible to make measurements of the conductivity of the plasma over six decades at a pressure of 1 mm Hg.

When the measurements are done on a transient or decaying plasma, it becomes necessary to consider the time constants for the circuits involved in the measurements. The time constant for the transients in the solenoid, which was chosen as an example above, is $Q/\omega = 10^{-5}$ sec. This time constant should be at least ten times smaller than the time constant for the decaying plasma, implying that this solenoid cannot be used for measurements on a plasma which decays with a time constant smaller than 10^{-4} sec. In order to make measurements on a plasma which decays or changes faster than this, it is necessary to either increase the frequency of the applied field or decrease the Q of the circuit. An increase of the frequency decreases the maximum measurable electron density and is not desirable. The other alternative, a decrease of the Q of the circuit, decreases the available range for measurements, provided a sinusoidal signal is used. This decrease of the available range can however be compensated for by replacing the sinusoidal signal V in the differential equation (6) with a suitable pulse function.

A pulse function and all its higher derivatives constitute an infinite series of linear independent functions. The unbalanced signal which is obtained when a pulse is applied to the bridge is therefore most conveniently expanded in terms of the pulse function and its derivatives. The solution to the differential equation (6) can then be written as

$$\Delta V = -\frac{R_s}{R_p}\left(\frac{M_{sp}}{L_s}\right)^2 \sum_{i=2}^{\infty}\left(-\frac{L_s}{R_s}\right)^i \frac{\partial^i V}{\partial t^i}. \qquad (14)$$

The most convenient pulse function to use is the Gaussian function of the form $V_0 \exp[-(t/\tau)^2/2]$, where V_0 is the amplitude and τ a measure of the width of the pulse. The unbalanced signal can then be written as

$$\Delta V = -V_0 \frac{R_s}{R_p}\left(\frac{M_{sp}}{L_s}\right)^2 \sum_{i=2}^{\infty}\left(\frac{L_s}{\tau R_s}\right)^i \exp\left[-\frac{1}{2}\left(\frac{t}{\tau}\right)^2\right] H_i\left(\frac{t}{\tau}\right), \qquad (15)$$

where $H_i\ (t/\tau)$ is the Hermite polynomial of the ith degree. If the frequency spectrum of the Gaussian pulse and the losses in the solenoid at these frequencies are considered, one finds that $L_s/(\tau R_s)$ is approximately equal to $Q/2\pi$, where Q is an average value within the frequency range of the Gaussian pulse. The series (15) shown above converges rather rapidly when the average Q is much less than 2π. One can, then, in the first order approximation neglect all terms but the first in the description of the unbalanced signal. That is,

$$\frac{\Delta V}{V_0} = -\frac{M_{sp}^2}{R_p R_s}\frac{1}{\tau^2}\exp\left[-\frac{1}{2}\left(\frac{t}{\tau}\right)^2\right]\left\{\left(\frac{t}{\tau}\right)^2 - 1\right\}. \qquad (16)$$

The maximum of the unbalanced pulse is, as will be seen later, most convenient for the measurements on the plasma. It is obtained when $(t/\tau)^2 = 3$ and hence

$$\left(\frac{\Delta V}{V_0}\right)_{\max} \cong -\frac{9}{\tau}\frac{M_{sp}^2}{R_p R_s} \cong -\frac{9\pi}{8}\frac{N^2 r_p^4}{R_s l_s \tau^2}\langle\sigma\rangle. \qquad (17)$$

The use of low Q circuits or pulse operated circuits will raise the relative noise level of the device. However, this can be more than compensated for because it is possible to apply larger amplitude of a pulse than of a steady-state signal before the plasma is significantly disturbed. This is particularly important in measurements on decaying plasmas when the cumulative effect of a continuously applied signal may be quite severe. The pulse will not influence the plasma except during the very short time it is applied.

The influence of the pulsed signal on the plasma can be estimated by comparing the length in time τ of the pulse with the most important time constants of the plasma. The e-folding time for the establishing of the asymptotic value for the electron drift velocity is ν_m^{-1} sec and will be assumed to be much smaller than the time τ, so that the transient effects of the electron drift velocity can be neglected. The influence of the pulse on the electron temperature of the plasma is then determined by the following differential equation:

$$\frac{\partial}{\partial t}\left(\frac{3}{2}p_m\right) - \nabla^2\left(\frac{5}{2}\frac{kT_m}{m\nu_m}p_m\right) + \left(\frac{3m}{M}\right)\nu_m p_m\left(1 - \frac{T_g}{T_m}\right) = (\mathbf{J}\cdot\mathbf{E}), \qquad (18)$$

where p_m is the partial pressure of the electron gas. This is the energy balance equation for the low-temperature electron gas when only elastic collisions are included, where the collision frequency ν_m is independent of the electron energy, and where the influence of the space charge fields is neglected. The first term is due to the energy storage in the electron gas in terms of the specific heat; the second term accounts for the energy losses due to the heat conduction in the electron gas;

he third term brings in the energy losses due to the lastic collisions, while the fourth term is the power fed nto the electron gas by the applied measuring pulse. The equation is very complex and it will, for the sake f simplicity, first be integrated over the whole volume f the plasma. For the cylindrical plasma column it then akes the following appearance:

$$\left(\frac{3}{2}\right)\frac{\partial}{\partial t}\langle p_m\rangle+\left(\frac{3m}{M}\right)\nu_m\{\langle p_m\rangle-k\langle n\rangle T_g\}+\int_A \mathbf{Q}\cdot\mathbf{dA}=\frac{e^2}{m\nu_m}\langle nE^2\rangle, \quad (19)$$

where Q is the energy flow vector, and A is the surface at the boundary of the plasma, while the average $\langle\rangle$ now is defined as

$$\langle p_m\rangle=\frac{2}{R^2}\int_0^R rp_m dr. \quad (20)$$

We will assume that the electron density essentially is independent of the spatial coordinates, but that it is practically equal to zero at the boundary of the plasma. There will then be a "heat barrier" at the boundary of the plasma, and the energy loss due to the heat conduction at the boundary can then be neglected. It will furthermore be assumed that the time variations in the electron density are very slow in comparison with the pulse time τ. The solution to the differential equation (19) can then be written as

$$\langle T_m\rangle-T_g=\frac{M}{3}\left(\frac{e}{m\nu_m}\right)^2\langle E^2\rangle\left[1-\exp\left(-\frac{2m\nu_m}{M}t\right)\right]. \quad (21)$$

The electron temperature reaches the asymptotic value

$$\langle T_m\rangle-T_g=\frac{M}{6}\frac{eE_R^2}{m\nu_m}, \quad (22)$$

with E_R equal to the solenoidal electric field close to the boundary of the plasma when the pulse length τ is much longer than the time constant $\tau_h=M/(2m\nu_m)$. However, when the pulse length is much smaller than this time constant one finds that

$$\langle T_m\rangle-T_g=\frac{\tau}{3}\frac{e^2E_R^2}{m\nu_m}. \quad (23)$$

It is easily seen from Eq. (18) that the heat conduction mechanism can be neglected entirely in the high-pressure limit. The electron gas is heated locally and one finds, with the assumptions made above, that the time dependence and spatial dependence of the electron temperature then also are determined by Eq. (21), provided the average signs $\langle\rangle$ are removed. The temperature differences (T_m-T_g) as shown by formulas (22) and (23) are then twice as large. The heat conduction process can be neglected when

$$\frac{40}{3}\frac{kM}{m^2\nu_m^2}\frac{T_{mR}}{R^2}\ll 1, \quad (24)$$

where T_{mR} is equal to the maximum electron temperature close to the boundary of the plasma. The plasma is then heated nonuniformly, and most of the energy is fed into the electron gas close to the boundary of the plasma. There is a time constant associated with the propagation of energy from the boundary to the interior of the plasma. This time constant is most easily obtained by assuming that the electron temperature is only slightly larger than the gas temperature and by linearizing the first two terms of Eq. (18). The most important time constant for the heat conduction process is the time constant τ_{hc} for the fundamental "heat diffusion" mode, and it can be written as

$$\tau_{hc}\cong R^2m\nu_m/10kT_m. \quad (25)$$

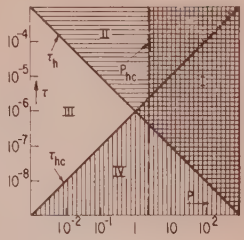

FIG. 2. The interaction ranges.

The influence of the measuring pulse on the electron temperature of the plasma can now easily be illustrated. It will be done for a hydrogen plasma of 1 cm radius, assuming $\nu_m=p\ 10^9\ \text{sec}^{-1}$ (p in mm Hg) and with $kT_m/e=1/20$ v. The two fundamental time constants are then $\tau_h=p^{-1}\ 10^{-6}$ and $\tau_{hc}=p\ 10^{-6}$ sec. These two time constants and the heat conduction limit (23) are plotted logarithmically as functions of the pressure in Fig. 2. The resulting diagram can be divided into four fundamentally different areas. The length of the pulse is larger than τ_h, and the pressure is sufficiently high in range I, so that the heat conduction mechanism can be neglected. If therefore the pulse length τ and the pressure of the plasma fall in this range, one can conclude that the asymptotic local temperature is reached. The pressure in range II is sufficiently small so that the heat conduction mechanism is fully developed, while the pulse length still is longer than τ_h. The temperature of the plasma in this range is therefore equal to the asymptotic average temperature and is essentially constant throughout the plasma. The pulse length in range III, on the other hand, is less than τ_h, while the pressure is sufficiently low so that the heat conduction mechanism is effective. The electron temperature reached, in this case, is therefore an average temperature which essentially is constant throughout the plasma, but which is less than the asymptotic value and in the first approximation proportional to the pulse length. In range IV, finally, the pulse length is less than both τ_h and τ_{hc}, meaning that the pulse length is so small that neither the asymptotic value nor the average temperature can be reached throughout the plasma, although the pressure may be so low that the heat conduction mechanism is a dominant mechanism. That is, the electron temperature in this range is always a function of the spatial coordinates when the applied field is nonuniform besides being a function of the pulse length.

When measurements are pursued in ranges I and IV, it is necessary that the amplitude of the pulse be sufficiently small so that the thermal condition of the electron gas is not disturbed to a measurable degree. The applied solenoidal electric field gives rise to an undesirable nonuniform heating of the electron gas in these ranges. The amplitude restriction of the pulse is the same in these ranges as for the steady state sinusoidal signal which was discussed previously [formula (11)]. The restriction on the amplitude of the pulse is not as important in ranges II and III since the plasma in these ranges is heated uniformly, in spite of the fact that the applied field is nonuniform. A matter of interest is the fact that in these ranges the pulse amplitude can be raised considerably in comparison with the allowed amplitude, provided one is interested only in relative measurements. The temperature of the electron gas can, if it is raised uniformly, be raised so high that considerable ionization or quenching of recombination or attachment occur during the pulse. The ionization is, with few exceptions, proportional to the electron density. The increased electron density which is obtained during the pulse is obtained from the electron density that existed before the application of the pulse by multiplying it with a factor independent of the electron density and the spatial coordinates, but which is a function of the pulse length τ and the pulse amplitude. A nonuniform heating of the plasma would, however, make this multiplying factor a function of the spatial coordinates as well, and this is the reason why the amplitude criterion must be adhered to strictly in ranges I and IV.

The discussion above of the influence of the pulse on the electron temperature applies, as presented, only to the afterglow plasma. Similar considerations must be applied when the measurements are done on steady-state plasmas. The pulse amplitude used in these cases can, of course, be considerably larger than when the measurements are done on the afterglow plasma. As soon as it can be expected that the measuring pulse will cause a nonuniform heating of the plasma, it is necessary to restrict the amplitude of the measuring pulse such that the power delivered to the electron gas by the measuring pulse is small in comparison with the power delivered to the electron gas by the maintaining fields. This restriction is not so critical when the measuring pulse gives rise to a uniform heating of the electron gas.

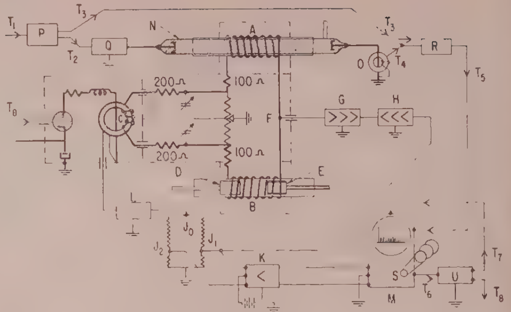

Fig. 3. The bridge.

The momentum transfer collision frequency ν_m is a function of the electron temperature in the general case. A nonuniform heating by the measuring pulse cannot be tolerated when ν_m is a strong function of the electron temperature. The amplitude of the signal used for measurements then must always be sufficiently small, so that the thermal condition of the plasma is not disturbed to a measurable degree. Whether this is the case or not is easily verified experimentally by varying the amplitude of the measuring signal.

THE BRIDGE

The pulse-operated bridge with its auxiliary circuits which the author has found most convenient for measurements on transient plasmas is shown schematically in Fig. 3. The two single-layer solenoids, *A* and *B*, are of the design shown in Fig. 1 and are made as identical as possible. They are located symmetrically in separate compartments of a shielding box of brass. The glass tubes on which the solenoids are wound stick out through the walls of the brass box so that the interior of the solenoids can be reached from the outside. The solenoids are coupled together forming a bridge which is symmetric with respect to ground or the shielding box. The pulse applied to the bridge is supplied through a transformer *C* which is designed to deliver as symmetric a pulse as possible with respect to the shield. This transformer consists of a toroid of ferrite located concentrically in a brass tube with a coaxial center conductor. The coaxial conductor serves as the primary, and a relatively few turns wound on the ferrite toroid serve as the secondary winding of the transformer. The current pulse through the primary of the transformer is generated by discharging a suitable capacitance controlled by a high-current hydrogen thyratron. The circuit elements in the primary circuit are chosen such that the pulse delivered by the secondary resembles a Gaussian pulse with a width of approximately 1 μsec.

The symmetric transformer and the two solenoids constitute the main elements of the bridge. In order to avoid undesirable transients in the solenoids, resistive elements are introduced between the solenoids and the secondary of the transformer. These resistive elements are chosen so that the solenoids essentially are critically damped within the frequency range given by the pulse enerated in the transformer. It is of course impossible o design the solenoids so that they are truly identical s well as making a transformer perfectly symmetrical. mall trimming elements are therefore introduced to ompensate for differences between the fundamental ridge elements. The plasma to be investigated is inerted in the solenoid A, as indicated in Fig. 3. Elements nserted in the solenoid B are used for partial eliminaion of the differences between the two solenoids. The ifference in inductance is mostly compensated for by nserting the metal slug D in the solenoid B, while the ifference in losses or resistance to a high degree is liminated by inserting concentrically a thin-walled etal cylinder E in the other end of the solenoid B. his metal cylinder will in the first approximation only nfluence the losses or the resistance of this solenoid, rovided the wall thickness of the metal cylinder is uch less than the skin depth of the metal within the requency range of the pulse applied to the bridge. Both he metal slug and the metal cylinder are mounted on icrometer screws for smooth action. The remaining lectrical asymmetries are eliminated with the help of mall capacitive and resistive trimming elements. The unbalanced signal which appears at the point F of the ridge can in this manner be made less than 1 part in 10^4 of the signal appearing across one of the solenoids. better sensitivity than this can be achieved with the help of the auxiliary electronic circuits. Their functioning is best illustrated in the following description of the operation of the bridge.

The discharge tube is inserted in the solenoid A. The bridge is balanced as well as possible in the manner indicated above. The resulting unbalanced signal at the point F is uniquely related to the shape of the input pulse and the circuit elements in the bridge, but it bears no resemblance to the input pulse, provided the bridge is well balanced. The metal cylinder E is now partially moved out from the interior of the solenoid B so that the unbalanced signal at the point F gets the shape which corresponds to a resistive unbalance of the bridge. The leading term of the series expansion of the "unbalanced" pulse as shown in formula (14) is the second-time derivative of the pulse applied to the bridge. This is essentially the only term in the unbalanced signal when the bridge is more than critically damped. The relation between the input pulse and the unbalanced pulse when the bridge is unbalanced resistively is shown schematically in Fig. 4. The left curve of this figure shows the shape of the pulse across one of the solenoids, while the right curve shows the form of the unbalanced pulse appearing at the point F due to the resistive unbalance of the bridge. The unbalanced signal in Fig. 4 is symmetric. The heights of the three peaks are, in practice, different, but any one of them can, in principle, be used for measurements of the plasma conductivity although it is most convenient to use the first peak.

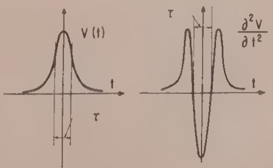

FIG. 4. The bridge pulses.

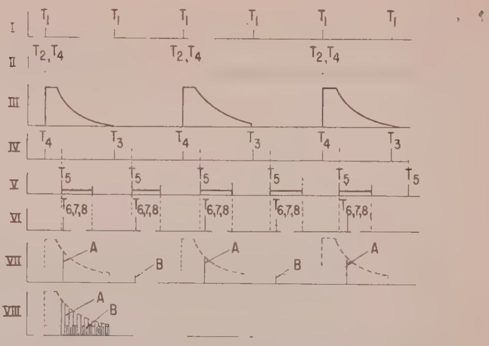

FIG. 5. The trigger and pulse schedule.

The unbalanced signal is now fed into an attenuator and amplifier combination G and H, which has sufficiently large input impedance so that the point F is unloaded. From this amplifier the pulse if fed into one side J_1 of a symmetric resistive mixer J, which is attached to the heavily biased differential amplifier K. The bias of this amplifier is sufficiently larger than amplitude of the signal coming from the amplifier H so that this signal is blocked unless a large second signal is applied to the point J_0 of the mixer. This second signal is in the form of a pulse which is derived from the original pulse applied to the bridge through the transformer C. It is shaped, amplified, and delayed in the unit L so that the pulse appearing at the point J_0 coincides with the first peak of the unbalanced signal as it appears at the point J_1. The elements of the mixer are chosen so that a negligible fraction of the unbalanced signal appears at the point J_2, while the second signal coming from the unit L will give identical signals at the points J_1 and J_2. The second signal therefore does not appear at the output terminals of the differential amplifier K since the signal there is proportional to the difference between the two signals at J_1 and J_2. The output signal from K is therefore that part of the unbalanced signal which coincides with the pulse coming from the unit L. The amplitude of the pulse coming from the unit L, as well as the bias and the amplification in the differential amplifier K, can be adjusted so that very small variations in the first peak of unbalanced signal can be observed. The sensitivity of the bridge is enhanced considerably in this manner. The signal from the differential amplifier K finally is displayed on the screen of the oscilloscope M.

A measurement of the time varying conductivity in a decaying plasma will now be explained with the help of Figs. 3 and 5. Figure 5 shows schematically the relation in time between the various necessary trigger pulses,

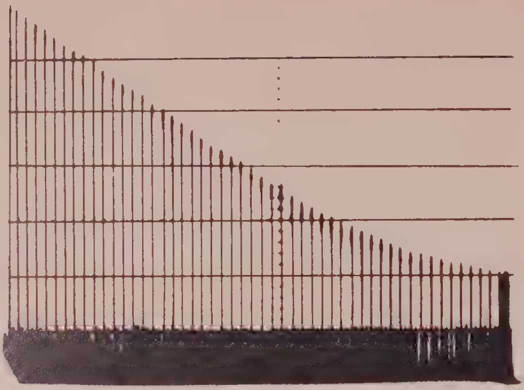

FIG. 6. A segment of a decay curve.

the discharge pulse, the decaying plasma, and the measurement of the conductivity in the plasma. A set of trigger pulses T_1, uniformly spaced in time and with the rate of 1 to 2 per sec, are fed into the unit *P* which generates the trigger pulses T_2 and T_3. These triggers are alternate; that is, every second trigger T_1 generates a trigger T_2, while all the remaining triggers T_1 generate the triggers T_3. The triggers T_2 are fed into the pulse generator *Q* which delivers a pulse with sufficiently large voltage to break down the gas in the discharge tube *N* and has low enough impedance and sufficiently high power to generate a high electron density plasma. The current pulse through the discharge tube is also fed through the transformer *O* that delivers the trigger pulses T_4 to the trigger delay unit *R*. The triggers T_3 are bypassing the pulse unit *Q* and the discharge tube and are fed directly to the trigger delay unit *R*. Each trigger T_3 and T_4 generates in the unit *R* the trigger T_5, which can be delayed an arbitrary time within the time interval between two consecutive pulses T_1. The triggers T_5 start the horizontal sweep of the oscilloscope *M*, which in turn generates the triggers T_6 that with the help of the potentiometer *S* can be delayed to appear at any time during the horizontal sweep. The triggers T_6 are fed into the pulse generator *U* which generates the pulses T_7 and T_8. The pulses T_7 are used to intensify the electron beam of the oscilloscope at the time when the unbalanced pulse from the bridge is displayed on the screen, while the pulses T_8 ignite the thyratron that controls the pulses applied to the bridge. The average conductivity of the decaying plasma is therefore measured immediately after the trigger T_8 has arrived at the thyratron. The time interval between the triggers T_1 is sufficiently long so that the plasma decays completely in this time interval. As the plasma is generated only for every second trigger T_1 and since the triggers T_3 bypass the discharge tube, it follows that every second measurement on the bridge is a "zero" measurement, that is, a measurement in the absence of the plasma. The pulses *A* in the diagram VII of Fig. 5 are the "unbalanced" pulses from the bridge in the presence of the decaying plasma, while the pulses *B* are the "zero" pulses measured in the absence of the plasma. The time difference between the consecutive triggers T_5 and T_6 or T_8 are controlled by the potentiometer *S*. This potentiometer is coupled mechanically to the motor, which increases the delay time between T_5 and T_6 slowly so that each measurement of the conductivity in the decaying plasma or of the "zero" pulse occurs at a somewhat later time after each discharge pulse. A camera, photographing the pulses on the screen of the oscilloscope during the time when the trigger T_6 moves from the beginning to the end of the horizontal sweep (indicated by the horizontal heavy lines in diagram V of Fig. 5), therefore gives a picture such as that shown in diagram VIII of Fig. 5.

An actual photographic recording of the corresponding measurement on a decaying plasma is shown in Fig. 6. The difference between the high pulses recorded in the presence of the decaying plasma and the "zero" pulses is proportional to the average conductivity of the plasma. Since the bridge is linear, and since the average conductivity of the plasma can be measured over many orders of magnitudes, it is obvious that what can be recorded on one photograph is only a segment of the decay curve. The time when the horizontal sweep is started relative to the discharge pulse can be varied with the help of the delay unit *R* so that the horizontal sweep occurs during any predetermined time in the afterglow. A proper adjustment of the speed of the horizontal sweep, of the time it starts, of the attenuator *G*, and of the amplification in the differential amplifier in the scope allows an efficient use of each photograph of a segment of the decay curve. The whole decay curve is obtained by photographing overlapping segments of

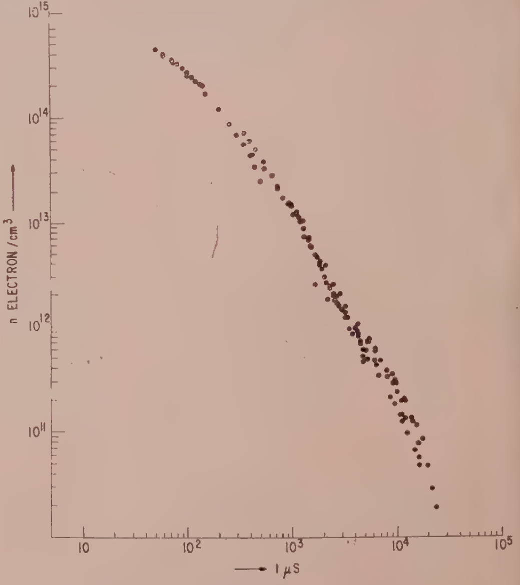

FIG. 7. Conductivity decay in neon.

the decay curve so that the scale changes (caused by changes in the amplification or attenuation) between photographs of neighboring and overlapping segments of the decay curve are evaluated easily from the photographs. An example of the decay of the average electron density in the afterglow of a plasma generated in neon of a pressure of 2 mm Hg measured with the bridge and the technique described in this report are shown in Fig. 7. The purpose of this report is to describe the device and the technique for measurements on high electron density plasmas with the help of the interaction between the solenoidal electric field and the plasma with rotational symmetry. No attempt is therefore made to interpret or explain the decay curve shown in Fig. 7, in particular because there are good reasons to believe that the neon used was not especially clean. The problem of generating well-defined high electron density plasmas in clean gases is a problem in itself and deserves special attention. The composite decay curve shown in Fig. 7 therefore serves only as an illustration of the range and applicability of the solenoidal electric field and bridge method for measuring the average electron density.

SUMMARY

The use of the solenoidal electric field for measurements on the plasma with rotational symmetry makes it possible to investigate plasmas over a larger range, in terms of the plasma parameters, than has been possible in the past. The method can of course only be used in its linear range of interaction which, however, is quite large. The upper limit for the measurable electron density or the conductivity is determined by the skin depth of the plasma at the frequency of the applied field. This limit is independent of the amplitude of the probing signal and of the plasma resonance mechanism. The lower limit is determined by the noise level of the particular device that is used for the measurements and by the maximum allowed amplitude of the probing field. The maximum allowed probing field is determined by the fact that this field must be sufficiently small so that the dynamic thermal equilibrium is not disturbed to a measurable degree.

The fact that the characteristic length, wavelength, or skin depth of the electromagnetic wave mechanism within the plasma must be larger than the critical dimension of the plasma for the interaction to be linear implies that the plasma fields are small in comparison with the applied fields. The presence of the plasma can therefore be observed only as a perturbation in whatever device is used for the measurements. The conventional microwave cavity method for measuring the average electron density is such a method, and the bridge method described in this report is another of the same kind. The solenoidal electric field configuration is particularly well-suited in the low-frequency range as is demonstrated in this report, although it can be used in the microwave range.[2] The simplest form of the solenoidal electric field is generated in the plain solenoid carrying an alternating current. The axial electric field associated with this kind of solenoid must, however, be removed with shields of special design. The measuring device may consist of a very crude form of bridge containing one or more solenoids. The bridge is balanced, and the unbalanced signal which is obtained when the plasma is introduced in one of the solenoids is proportional to the electron density in the plasma, provided the bridge and the various electronic circuits which are used for observing and recording the unbalanced signal are operated within their linear ranges. The voltage applied to the bridge may be sinusoidally time-varying signal or a pulse. It is the author's experience that it is easier to obtain high sensitivity with a pulse-operated bridge when high time resolution is required. For example, the bridge described in this paper has a time resolution of less than $\frac{1}{3}$ μsec and is capable of measuring the conductivity or the corresponding electron density over 4–6 decades. The bridge can be made more sensitive and measure the conductivity over many more decades by sacrificing some of the time resolution and by using a steady state sinusoidal signal.[4] The bridge, with close to critically damped solenoids, is most suitable for pulse operation and when high time resolution is required. The same time resolution is of course also obtained when a sinusoidal signal is applied to this bridge. However, the range for the measurements is generally smaller, and the danger for cumulative effects larger than for the pulse-operated bridge. The application of the steady state sinusoidal signal to the almost critically damped bridge is, however, very useful when single-shot measurements of decaying plasmas must be made.

It is very important in a pulse-operated bridge used for measurements on the plasma that the interaction between the plasma and measuring field is linear, and that the bridge and the various electronic devices, which are used for the observation and recording of the unbalanced signal, are operated in their linear ranges. The linearity of the electronic circuits is easily checked with the use of calibrated attenuators and pulses simulating the unbalanced signal from the bridge. The linearity of the bridge itself can be checked by replacing the discharge tube with containers of the same shape as the discharge tube but containing ionic solutions with known conductivities. A further check on the linearity is obtained in the process of measuring overlapping segments of the decay curves.

The nonlinearities which appear in the interaction between the electromagnetic field and the plasma are of many different kinds, some of which have been pointed out and discussed in previous papers.[1,5] Some of the nonlinear terms such as, for example, the heating of the electron gas are common to all field and plasma configurations, while others are characteristic of different field and plasma configurations or frequency ranges. The term $\mathbf{w}_m \times \mathbf{B}_1$ in the momentum balance equation

---

[4] Quarterly Progress Rept., Research Lab. of Electronics, Massachusetts Institute of Technology, Cambridge (April, 1958).

[5] K. B. Persson, General Electric Research Laboratory Rept. No. 60-RL-2490G (September, 1960).

$$(d\mathbf{w}_m/dt)+\nu_m\mathbf{w}_m=-(e/m)(\mathbf{E}+\mathbf{w}_m\times\mathbf{B}_1) \qquad (25)$$

for the electrons is one of the more important nonlinear terms in the interaction between the solenoidal electric field and the plasma in the low-frequency range. The electric field is, in this case, generated by a sinusoidally time-varying, but essentially uniform, magnetic field with the amplitude B_1. The interaction between the solenoidal electric field and the plasma can therefore be considered linear only when $|\mathbf{w}_m\times\mathbf{B}_1|$ is much less than $|E|$. This leads to the following criterion for linearity:

$$1\gg eB_1/m(\omega^2+\nu_m{}^2). \qquad (26)$$

In the high-pressure and low-frequency range, where ω is less than the collision frequency ν_m, this expression can be written as

$$1\gg eB_1/m\nu_m. \qquad (27)$$

This expression, which according to the derivation above only applies in the high-pressure and low-frequency range, should actually also be used in the high-frequency and low-pressure range (ω larger ν_m) if resonances are expected in this range. The reason is that the conductivity of the plasma at any one of the resonant frequencies which can be expected in the high-frequency and low-pressure range is very close to the dc conductivity of the plasma. This is generally true whether there is a static magnetic field present or not. Using $10^9\ p$ as a representative value for the collision frequency ν_m, one finds then that the amplitude B_1 of the sinusoidally time-varying, but essentially uniform, magnetic field must be less than $50\times p$ gauss.

The discussion above of the amplitude limit indicates that the bridge which inherently is a high-amplitude device is not too suitable for measurements in the low-pressure range where ω is larger than ν_m. A device better suited for measurements in this range can be made as follows. A solenoid of the design used in the bridge is coupled in parallel with a capacitor forming a parallel resonant circuit with a suitable resonant frequency. This resonant circuit is made tank circuit in a positive feedback oscillator with sufficiently variable elements so that the feedback can be controlled smoothly around the point of oscillation. This circuit is extremely sensitive to any lossy substance which is introduced into the tank circuit when the feedback of the circuit is such that the circuit barely oscillates. The time-varying magnetic field in the tank circuit of this oscillator need only be slightly higher than the noise level of the oscillator and is therefore extremely small. An oscillator based on this principle, oscillating in the range of 1 to 10 Mc and with a time-varying magnetic field of the order of 10^{-4} gauss, was found to be sensitive to lossy substances with a resistivity larger than 10^5 ohm cm.

The main disadvantage of the solenoidal electric field method is that the applied solenoidal electric field is directly proportional to the radius from the center of the plasma, and that therefore the measured quantity is the average shown in formula (9). Another disadvantage is the fact that in the high-pressure and low frequency range, where the bridge is most useful, one can only measure the ratio $\langle n\rangle/\nu_m$. These two disadvantages can, under some circumstances, be quite useful. The bridge described in this report measures the electron density in the high electron density afterglows, where it can be expected that a recombination process is the dominant process in the early afterglow, while a diffusion process is dominant in the late afterglow. This means that in the transition range between these two processes the distribution of the electron density will change from a distribution in the early afterglow, which is essentially independent of the radius, to a distribution in the form of a Bessel function in the late afterglow. The average $\langle n\rangle$ is rather sensitive to this change in the spatial electron distribution, and the transition range will show up as a relatively abrupt decrease with time of the measured quantity $\langle n\rangle/\nu_m$. It can furthermore be expected that in some cases when the measurements are done in high electron density afterglows, the electron-ion interaction is the dominant interaction mechanism for the electrons. The collision frequency ν_m is then reasonably independent of the gas pressure and in the first order approximation proportional to the electron density. The measured quantity $\langle n/\nu_m\rangle$, with the average sign $\langle\rangle$ defined in formula (8), is then independent of the electron density. The measured quantity $\langle n/\nu_m\rangle$ will, in the ranges of the afterglow where this occurs, be independent of the time.

It is, in view of the situation discussed above, highly desirable to develop methods which can complement the bridge method described in this report so that it is possible to make simultaneous measurements in the high electron density plasma of the ratio $\langle n\rangle/\nu_m$ and one of the two quantities $\langle n\rangle$ and ν_m. One such method where it is possible to measure the collision frequency independent of the electron density with the help of a longitudinally applied static magnetic field, is suggested in a previous report.[1] A second method, which is a modification of the conventional microwave cavity method, where the influence of the electric polarization of the plasma is suppressed due to a proper choice of plasma configuration relative to the cavity shape so that the plasma resonance occurs at much higher electron densities than what corresponds to the Langmuir-Tonks plasma resonance, and where $\langle n\rangle$ is measured by virtue of the fact that the frequency of the applied field is higher than the collision frequency ν_m, will be discussed elsewhere.

ACKNOWLEDGMENT

The author is very indebted to Leonard Prescott for his work on the bridge and associated electronic circuits.

JOURNAL OF APPLIED PHYSICS VOLUME 32, NUMBER 12 DECEMBER, 1961

Effect of Residual Gases on the Properties of Indium Films

HOLLIS L. CASWELL
IBM Yorktown Research Laboratory, Yorktown Heights, New York

(Received March 29, 1961)

Indium films have been deposited at pressures less than 10^{-9} mm Hg and at higher pressures of specific residual gases. N_2, H_2, CH_4, A, CO, and CO_2 were found to have no measurable effect on the electrical or superconducting properties of these films when present in partial pressures of 10^{-5} mm Hg. For oxygen, a pronounced effect was observed when K (the ratio of oxygen molecules to indium atoms striking the substrate) exceeded 3%. The room temperature resistivity increased from 9.0 μohm-cm to 14 μohm-cm, the critical temperature decreased from (3.402 ± 0.005)°K to (3.389 ± 0.002)°K, the effective magnetic penetration depth increased from 630 ± 100 A to over 1000 A. For $10^{-3}<K<3\times10^{-2}$, a larger apparent penetration depth was observed for films deposited through a mask due to edge effects. It was shown that indium films could be deposited at 100 A/sec on clean, baked substrates at 10^{-5} mm Hg with characteristics indistinguishable from those of films deposited in ultrahigh vacuum provided the partial pressures of oxygen and water vapor were below 10^{-7} and 10^{-5} mm Hg, respectively.

INTRODUCTION

A STUDY has been made of the influence of residual gases on the properties of indium films similar to that recently reported for tin.[1] One objective was to measure the characteristics of high purity indium films where the maximum impurity concentration due to residual gases was a few parts per million. A second was to determine in what manner the presence of specific residual gases altered these characteristics. A third was to evaluate the relative advantages of indium and tin films as gates in superconducting cryotrons. The reader is referred to the previous paper[1] for a description of the experimental techniques employed.

EXPERIMENTAL RESULTS

I. Film Groups

In discussing the results, it is convenient to divide the various films into the following four groups:

A. Pure films. These films were prepared under conditions where K (the ratio of residual gas molecules striking the substrate to indium atoms adhering to the substrate) was less than 10^{-5}. The total pressure during these evaporations was less than 10^{-9} mm Hg consisting principally of nitrogen, hydrogen, and carbon monoxide.

B. Films lightly doped with oxygen. For these films, reagent grade oxygen was bled into the system and depositions made under conditions such that

$$10^{-3}<K_{O_2}<3\times10^{-2}.$$

There is appreciable gettering of oxygen by indium so that it was difficult to maintain a constant oxygen partial pressure during an evaporation. Typically, the pressure dropped by a factor of four upon heating the source to operating temperature, and by a factor of two during the actual evaporation. The partial pressure at the moment the shutter was opened was used in determining K_{O_2} since it is felt the initial nucleation period is the most critical in determining the ultimate structure of a film. This provides a maximum value for K_{O_2}.

C. Films heavily doped with oxygen. For these films the oxygen partial pressure was increased such that K_{O_2} was greater than 3×10^{-2}.

D. Films doped with other gases. This group includes films which were evaporated in various partial pressures of N_2, H_2, CO, CO_2, CH_4, A, and H_2O as shown in Table I. In some cases, two gases were introduced during a single evaporation when it was anticipated neither would influence the film's characteristics. No detectable gettering of these gases by an indium film was observed.

II. Physical Characteristics

With the exception of films highly doped with oxygen, the indium films had a bright, mirror-like appearance. These films became electrically continuous at approximately 2000 A, indicating that they grew as isolated crystallites which then fused into a continuous film. Very little evidence of the grain boundaries remained as is illustrated in the electron micrograph of Fig. 1. With tin films, on the other hand, the grain boundaries were quite distinct and the surface topology quite rough (see Fig. 13 of reference 1).

For films highly doped with oxygen, the surface structure is pebbly as illustrated in Fig. 2. Because of their surface roughness, they appear milky white. However, the thickness at which they become electrically continuous is approximately the same as for pure films. This indicates that oxygen does not contribute to a smaller-grained film, but rather inhibits the coalescence of the various grains into a smooth film. In addition, the mobility of the indium atoms is reduced by heavy doping with oxygen as evidenced by the completely random orientation of these films. In contrast, other films were highly oriented with the [010] direction perpendicular to the substrate. However, there is no indication of indium oxide in any film, indicating that the oxygen is probably present interstitially.

---

[1] H. L. Caswell, J. Appl. Phys. 32, 105 (1961).

TABLE I.

Film No.	Pressure (mm Hg)	Thickness (A)	Evaporation rate (A/sec)	K	Mask or trim	T_c (°K)	H_{c0} (oe)	λ_0 (A)	ϵ (%)
101	$<10^{-9}$	6900	170	$<6\times10^{-6}$	M	3.403	322		0
					T	3.403	322	600	
103	2.0×10^{-5} N_2	6600	220	9.1% N_2	M	3.409	327		0
	4.0×10^{-5} H_2			68% H_2	T	3.407	327	660	
104	6.1×10^{-5} H_2O	6600	220	34% H_2O	M	3.402	337		4.7
					T	3.402	322	590	
105	2.7×10^{-5} CO_2	6900	90	25% CO_2	M	3.405	327		0
	3.4×10^{-5} CO			41% CO	T	3.405	327	690	
108	2.2×10^{-5} A	4850	110	18% A	M	3.403	338		2.1
	1.5×10^{-5} CH_4			19% CH_4	T	3.404	331	530	
119	$<10^{-9}$	6350	200	$<4\times10^{-6}$	M	3.401	320		0
					T	3.401	320	520	

III. Electrical Characteristics

With the exception of those films heavily doped with oxygen, the resistivity of all the films at 25°C was found to be (8.9±0.3) μohm-cm, in excellent agreement with the value of 8.8 μohm-cm at 22°C obtained by White and Woods[2] for high-purity bulk indium. The resistivity of films heavily doped with oxygen increased to 14 μohm-cm. However, the Gruneisen characteristic temperature,[3] calculated from liquid helium, liquid nitrogen, and room temperature resistance values (and thus an average value for the temperature range from 78–300°K) was found to be 190±3°K for all films, in good agreement with that of high-purity bulk indium.[4] This means that the linear temperature coefficient of resistivity of the films heavily doped with oxygen increased from 3×10^{-3}/°C to 4×10^{-3}/°C. This is one example where the presence of a residual gas drastically alters the temperature coefficient of resistivity of an evaporated film.

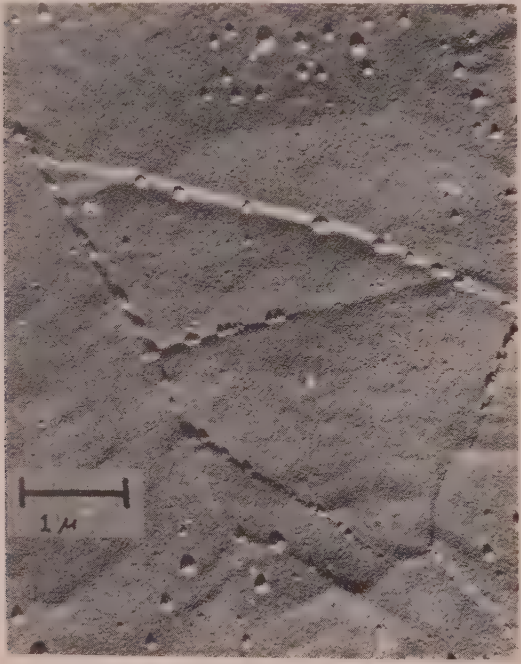

FIG. 1. Electron micrograph of high-purity indium film surface.

The resistivity at liquid-helium temperature of films heavily doped with oxygen was appreciably greater than for other films. For example, the resistivity of a 12 000-A film was 2.56×10^{-7} ohm-cm, while that of an equal thickness pure film was 6.5×10^{-8} ohm-cm (a net increase of 1.9×10^{-7} ohm-cm).

IV. Superconducting Characteristics

The most outstanding characteristic of the indium films, excluding four films heavily doped with oxygen, was their reproducible critical temperature. Of 42 films tested, excluding those indicated above, the average critical temperature was 3.402°K with maximum deviations of +7 millidegrees and −3 millidegrees. The temperature transitions were extremely sharp, generally being less than 5 millidegrees in width and never more than 10. For the four masked films heavily doped with oxygen, the average critical temperature was 3.389°K with maximum deviations of +1 and −2 millidegrees or a decrease of 13 millidegrees from the average critica temperature of other films. If the decrease in T_c, to be expected from the increase in resistivity for these films, is calculated using the initial linear portion of the curves reported for light alloying of bulk superconductors[5] (0.2°K/μohm-cm) then a decrease of 38 millidegrees is obtained. This is the maximum decrease, and in practice one would expect a smaller change. Actually, the validity of this calculation is somewhat questionable since it has been assumed that the surface scattering for the two types of film is the same, whereas the electron micrographs indicate quite different surface structures.

---

[2] G. K. White and S. B. Woods, Rev. Sci. Instr. **28**, 638 (1957).

[3] See, for example, review by D. K. C. MacDonald, *Encyclopedia of Physics*, (Springer-Verlag, Berlin, Germany, 1956), Vol. 14, p. 170.

[4] M. D. Reeber (private communication).

[5] E. A. Lynton, B. Serin, and M. Zucker, J. Phys. Chem. Solids **3**, 165 (1957).

In discussing magnetic field transitions of superconducting thin films, it is necessary to distinguish between films evaporated through masks, and films cut or trimmed from larger film areas. Masked films usually possess edges which are nonuniform in thickness due to mask effects and to surface mobility of the evaporate on the substrate. Trimmed films, on the other hand, have a uniform thickness across their entire width. Because of the importance of these edges, the film pattern shown in Fig. 3 was used to obtain simultaneous measurements on both a trimmed and a masked film. Since masks must be used for most practical applications of superconducting films, it is necessary that "edge effects" be controlled if reproducibility of magnetic field transitions is to be achieved. In evaluating the edge effect, which is quite sensitive to the presence of certain residual gases, it is convenient to define the quantity ϵ as

$$\epsilon = (H_{c0}{}^{M} - H_{c0}{}^{T})/H_{c0}{}^{T},$$

where H_{c0} is the critical field (as defined in Fig. 4) extrapolated to 0°K and the superscripts M and T refer to masked and trimmed films, respectively. ϵ is a measure of the thickness variation in the edge portions of the masked film. Small values ($\epsilon < 5\%$) indicate masked films of fairly uniform electrical cross section due to edge breakup (the thinner edge regions coalesce into electrically discontinuous grains), whereas larger values ($\epsilon > 5\%$) indicate masked films with varying degrees of electrically continuous, sloping edges. Typically, ϵ is less than 3% and is very often zero within experimental error for pure indium films. When oxygen was introduced into the system during evaporations, ϵ increased significantly as illustrated in Fig. 5. A conservative estimate of the maximum allowable oxygen concentration during an evaporation in order that edge breakup not be inhibited is $K_{O_2} < 10^{-3}$. For films doped with other gases, ϵ is less than 3% with the exception of films doped with water vapor (e.g., $\epsilon = 5\%$ for film No. 104 where $K_{H_2O} = 34\%$). Thus it is felt that K_{H_2O} should be maintained below 10% to promote edge breakup.

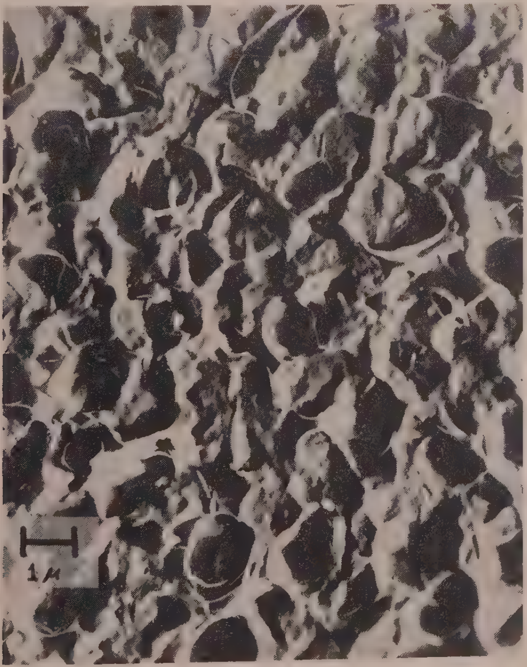

FIG. 2. Electron micrograph of heavily oxygen-doped indium film surface.

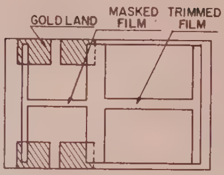

FIG. 3. Mask configuration of evaporated filament.

From $H_{c0}{}^{T}$ and the film thickness, an equivalent magnetic penetration depth λ_0 may be calculated as shown by Ittner.[6] He predicts λ_0 should increase with increasing impurity content; and indeed for the four heavily oxygen doped films λ_0 was found to be greater than 1000 A, whereas for all other films λ_0 was

$$\left(600 \pm {200 \atop 100}\right) \text{A}.$$

To ascertain whether the increased penetration depth was representative of the entire film or only of a filamentary structure in the film, the critical field was determined as a function of measuring current. Pure and heavily oxygen-doped, trimmed films of equal thickness and width were tested. As shown in Fig. 6, there was no significant difference in their current carrying capacity, indicating that the increased pene-

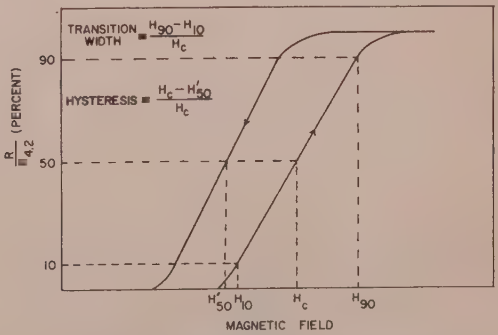

FIG. 4. Diagram of a magnetic field transition illustrating magnetic hysteresis and transition width.

---

[6] W. B. Ittner, III, Phys. Rev. 119, 1591 (1960).

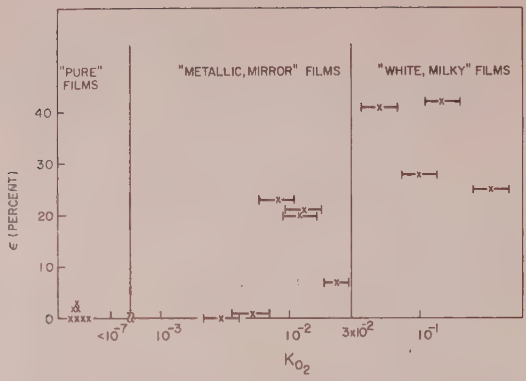

FIG. 5. ϵ as a function of K_{O_2} illustrating the reduction in edge breakup with increasing oxygen concentration.

tration depth is representative of the intrinsic properties of the film material rather than of filamentary behavior.

The transition width of magnetic field switching, as illustrated in Fig. 4, is of particular interest in superconducting devices because it may determine the switching speed of the device. For pure indium films deposited through a mask, the width at all temperatures was less than 8% and often below 2%. The behavior of the films doped with gases other than oxygen was similar. However, the width increased significantly for the oxygen-doped films as is illustrated in Fig. 7. Because it inhibited edge breakup, the oxygen also contributed to nonuniformity in the edge structure and thus to a broad transition.

Magnetic hysteresis, as illustrated in Fig. 4, is important in superconducting devices because it limits the magnetic biasing which may be employed. Hysteresis was generally less than 10% for all masked films with the exception of films doped with oxygen. As shown in Fig. 7, hysteresis for these films was significantly lower, being less than 2%. Hysteresis was less than 9% for trimmed, pure films, and less than 12% for trimmed films lightly doped with oxygen. Only for films heavily doped with oxygen was it significantly higher, averaging 24% at 2.40°K.

V. Vacuum Requirements

From an analysis of the above data, the following criteria were established for obtaining high quality, masked indium films with sharp and reproducible magnetic transitions:

$$K_{O_2} < 0.1\%,$$
$$K_{H_2O} < 10\%,$$
$$K_{\text{other}} < 30\%.$$

At an evaporation rate of 100 A/sec, this would correspond to partial pressures of

$$P_{O_2} < 10^{-7}\text{mm Hg},$$
$$P_{H_2O} < 8\times10^{-6}\text{mm Hg},$$
$$P_{\text{other}} < 2\times10^{-5}\text{mm Hg}.$$

Thus it appears that, as in the case of tin, ultrahigh vacuum is not a necessary condition for obtaining high quality films. To verify this directly, a film was prepared in the following manner. The substrate was baked at 300°C for several hours in a vacuum of 10^{-5}mm Hg (consisting mostly of water vapor, carbon monoxide, and nitrogen) to drive off residual water and then allowed to cool. The following day, to reduce the partial pressure of oxygen in the system prior to depositing the indium test film, indium was evaporated from an auxiliary source over the chamber walls (but not onto the substrate). The partial pressure of water vapor was reduced through the use of a liquid-nitrogen trap. The film deposition was then performed at an evaporation rate of 86 A/sec at a total pressure of 2 to 7×10^{-6}. The characteristics of this film were indistinguishable from those of films deposited in ultrahigh vacuum, showing that it is not the total system pressure which is significant during evaporations but the partial pressures of critical gases. Of course, clean, outgassed substrates must be used.

COMPARISON OF INDIUM AND TIN

Several factors must be considered in determining whether tin or indium is the better cryotron gate material. One of these is the ease with which the metal may be evaporated. Indium has an advantage over tin because it requires lower evaporation temperatures. For example, indium has a vapor pressure of 100μ at 1088°C, whereas 1373°C is required for tin.[7] This makes possible faster evaporation rates with a given power input, contributes to less outgassing from the crucible materials, and reduces radiation from the source. In fact, at any given evaporation rate, the radiation with indium is approximately 40% that with tin which may be quite significant if control of substrate temperature is critical.

Another factor which makes the use of indium more attractive than the use of tin is that indium is less reactive with water vapor. Since conventional systems generally contain large quantities of this gas, indium is a more convenient metal to evaporate.

A comparison of the superconducting properties of

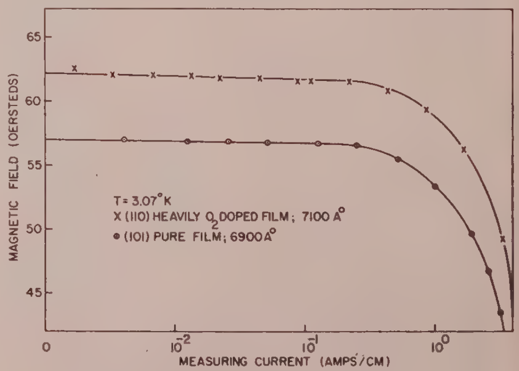

FIG. 6. The critical field of a pure film and a film heavily doped with oxygen as a function of measuring current.

---

[7] See, for example, Saul Dushman, *Vacuum Technique* (John Wiley & Sons, Inc., New York, 1949), p. 748.

tin and indium films is of special importance. In one respect indium has a distinct advantage over tin—namely, the temperature transition of indium films is quite sharp and reproducible, whereas that of comparable tin films is generally broader and occurs over a wide range of temperature (3.70–3.82°K).[1] Also, the magnetic field transitions of masked, indium films are sharper and more reproducible than those of masked, tin films due to more complete edge breakup with indium. Thus, it should be possible to operate a series of indium gates at a higher reduced temperature than a similar series of tin gates with a corresponding reduction in the magnetic field required to switch the gates normal.

The liquid-helium resistivity of the two metals is another area of comparison. Since indium and tin have approximately the same penetration depth, it is desirable to use the metal with the higher resistivity in order to decrease the switching time of devices. In this respect, tin has an advantage over indium. For example, the resistivity of a 3700-A tin film was 0.20μohm-cm, whereas that of an equal thickness indium film was 0.12μohm-cm.

The last factor to be considered in this paper is the stability of tin and indium films at room temperature. This is relatively important because cryogenic devices are often stored at room temperature for extended periods of time. A lack of stability was found in some indium films which is not fully understood at this time. For example, two films (out of approximately 25 evaporated) were removed from the vacuum system, tested in the liquid-helium cryostat, and found to be electrically discontinuous several days later. A third film was kept in ultrahigh vacuum after deposition and cooled several times to approximately 20°K. As illustrated in Fig. 8, its resistance increased progressively with time. The low-temperature quenches appear to have initiated or certainly to have accelerated the breakup of the film into electrically isolated islands. In all three cases where film breakup occurred, the film resistivity immediately after evaporation was unusually high, indicating the existence of voids or large defect concentrations. Fast evaporation rates (of the order of 1000 A/sec) appear to enhance this type of breakup, and breakup appears to be more pronounced in thin films. However, most indium films were found to be quite stable over a period of months as indicated by film No. 124 in Fig. 8. The problem of film breakup was not encountered with tin films deposited and treated in the same manner as these indium films.[8,9]

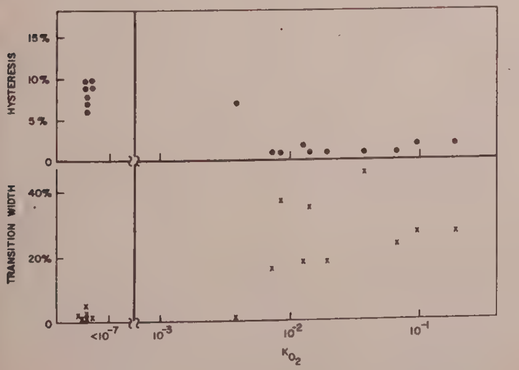

Fig. 7. Magnetic hysteresis and transition width as a function of oxygen concentration.

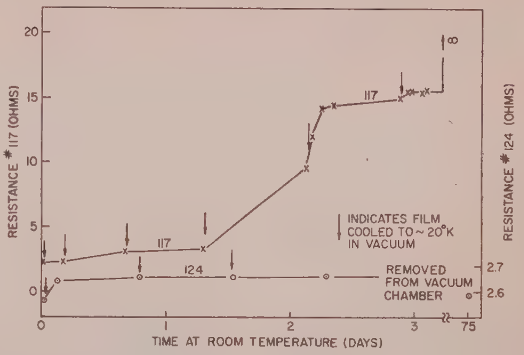

Fig. 8. The resistance as a function of time for two pure, indium films.

In conclusion, the use of tin or indium as a gate material is dictated by the particular application. If the stability problems associated with indium films can be solved, then indium offers several advantages over tin for use in cryogenic circuits.

SUMMARY

The investigation of tin and indium films has shown the importance of reducing the partial pressure of oxygen during the evaporation of these metals. Fortunately, this can be achieved easily by means of chemical gettering. Fresh films of titanium and indium are quite effective. A reduction in the partial pressure of water vapor is also desirable. This may be accomplished by bake out at elevated temperatures or trapping with cold surfaces.

The use of a mask to obtain a desired geometrical pattern may alter a film's characteristics. This is particularly true in the case of magnetic field transitions from the superconducting to the normal state where edge effects play a very important role.

ACKNOWLEDGMENTS

The author is indebted to members of the Cryogenics group at IBM for helpful discussions concerning this work, and in particular to Dr. Irving Ames and Dr. Joseph Priest.

The aid of R. T. Bogardus in preparing and testing the indium films is gratefully acknowledged.

---

[8] Another problem occurs when lead films are evaporated over the ends of an indium gate to make superconducting connections to them. A. E. Brennemann of this laboratory has found that the lead alloys with the indium gate at its ends altering the gate characteristics. The limitations imposed on the use of indium in cryogenic devices by lead diffusion are not fully understood at this time. The problem is not encountered with tin gates, however, possibly because of the low solubility of lead in tin.[9]

[9] Max Hansen, *Constitution of Binary Alloys* (McGraw-Hill Book Company, Inc., New York, 1958), p. 1107.

JOURNAL OF APPLIED PHYSICS VOLUME 32, NUMBER 12 DECEMBER, 1961

Voltage Dependence of Microplasma Density in p-n Junctions in Silicon*

A. Goetzberger and C. Stephens
Shockley Transistor, Unit of Clevite Transistor, Palo Alto, California

(Received February 23, 1961; in final form July 21, 1961)

The voltage distribution of breakdown spots in $p-n$ junctions was measured. A junction in silicon which was uniform in its crystallographic properties, and had an impurity gradient of 10^{22} cm^{-4}, showed two kinds of microplasmas. One type is characterized by bright light emission and low breakdown voltage, and the other has less light emission and higher breakdown voltage. Both have broad distribution of breakdown voltages of the order of several volts. Samples containing a grain boundary show a line of light emitting spots having a minimum spacing of 7000 A versus a 40-A spacing of dislocations along the grain boundary.

I. INTRODUCTION

LIGHT emission phenomena from junctions in avalanche condition have been studied by a number of authors.[1–6] Chynoweth and Pearson[3] showed that there is a correlation between light emitting spots, called microplasmas, and dislocations. This observation was confirmed by Kikuchi and Tachikawa[4] and Goetzberger,[6] but it was also shown that not all of the dislocations participate in the breakdown. W. Shockley[7,8] pointed out that avalanche effect will be nonuniform even in junctions which are perfect except for statistical fluctuations of donor and acceptor concentration. For such cases he derives an exponential dependence of the number of breakdown spots on voltage. This statistical effect, however, can not be identified with the microplasma phenomenon.[9] Microplasmas are more probably caused by structural imperfections in the crystals.

This paper describes measurements of the voltage dependence of the microplasma density in a number of diodes. Two groups of junctions were investigated: (1) Junctions with randomly distributed microplasmas, obtained by diffusion into silicon which was dislocation-free prior to diffusion, as determined by Dash-etch[10]; (2) junctions which contained a grain boundary of known angle of misfit, so that the spacing of the dislocations could be estimated. All the junctions investigated were phosphorus diffused n^+p diodes. No quantitative work has been done on diffusants other than phosphorus, but some boron-diffused junctions showed qualitatively the same behavior.

II. PREPARATION OF SAMPLES AND EXPERIMENTAL TECHNIQUES

All of the junctions were obtained by open-tube diffusion of phosphorus into crucible-grown p-type silicon of 0.4-ohm cm resistivity. In order to obtain uniform deposit of a high phosphorus concentration, the multiple predeposit technique,[11] consisting of several predeposits interrupted by washing of the sample in hydrofluoric acid, was used. Prior to diffusion the silicon slices had been cut parallel to a (100) direction, lapped, polished, and etched to remove approximately 10 μ. The sheet resistance after diffusion was 100 ohms/square, junction depth was 0.5–0.6 μ, and the diodes consisted of mesas of 0.5–1 mm diameter. Some of the samples were enclosed in a guard ring with higher breakdown previously used by one of the authors[12] which made it possible to observe very high densities of microplasmas without interference by surface breakdown.

Light emission was observed and photographed on Polaroid 3000 film through a microscope. Exposure time was a function of junction depth and magnification, and varied from 1 to 5 minutes. For each junction the voltage was increased by steps, and a photomicrograph taken at each voltage, and the number of microplasmas counted.

Contact to the mesa diodes can easily be made to the p-type base or to the thick n-type guard ring by gold thermocompression bonding. When contacts were required for nonguard ring devices, however, special problems were encountered because of the proximity of the junction to the surface. It was found that thermocompression bonding had a tendency to destroy junctions less than 1 μ from the surface. An electroless nickel plate was tried but found not feasible, because during the annealing step, necessary to achieve a good bond, the junction characteristic usually became soft.

Good ohmic contacts on these layers were obtained by the following method. A 50-A thick layer of aluminum was evaporated through a metal mask which confined the contact point. This layer was alloyed in a vacuum at 600°C and then a thicker layer of aluminum was evaporated onto the same spot. The second layer was not alloyed.

---

* Research supported by Air Force Cambridge Research Laboratories under contract.

[1] A. G. Chynoweth and K. G. McKay, Phys. Rev. **102**, 369 (1956).

[2] A. G. Chynoweth and K. G. McKay, Phys. Rev. **106**, 418 (1957).

[3] A. G. Chynoweth and G. L. Pearson, J. Appl. Phys. **29**, 1103 (1958).

[4] M. Kikuchi and K. Tachikawa, J. Phys. Soc. Japan **15**, 835 (1960).

[5] M. Kikuchi, J. Phys. Soc. Japan **15**, 1822 (1960).

[6] A. Goetzberger, *Proceedings of the International Conference in Semiconductor Physics* (Publishing House of the Czechoslovak Academy of Sciences, Prague, 1961), p. 808.

[7] W. Shockley, Solid State Electronics **2**, 35 (1961).

[8] W. Shockley, Bull. Am. Phys. Soc. **5**, 161 (1960).

[9] R. L. Batdorf, A. G. Chynoweth, C. C. Dacey, and P. W. Foy, J. Appl. Phys. **31**, 1153 (1960).

[10] W. C. Dash, J. Appl. Phys. **27**, 1193 (1956).

[11] B. McDonald, A. Goetzberger, and C. Stephens, Bull. Am. Phys. Soc. **4**, 455 (1959).

[12] A. Goetzberger, J. Appl. Phys. **31**, 2260 (1960).

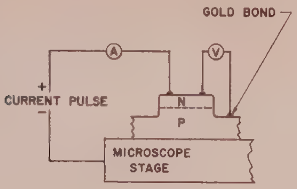

Fig. 1. Method of measuring current input and voltage.

Several precautions were taken electrically to avoid contact resistance and excessive heating of the device. Separate probes were used to measure current input and voltage (Fig. 1). At high current levels a considerable amount of power was dissipated in the junction, which caused the sample to overheat. This effect was reduced by using a pulsed input current, the duration and repetition rate of which was low enough for all pulses to give the same voltage.

III. RESULTS

A. Junction with Randomly Located Microplasmas

The first studies were of a number of junctions without macroscopic structural imperfections. Figure 2 shows the number of microplasmas/mm² versus voltage for a guard ring junction with a distribution of microplasmas that appeared to be spatially random. The middle part of the curve appears to be exponential, with a slope of 3.6 v/decade. Figures 3(a) and (b) are photographs of the light emission, 3(a) for low voltage and 3(b) for high voltage. It also can be seen that there are two kinds of light spots—large bright ones and small ones. The difference between the two kinds can be seen more clearly by direct observation. The large microplasmas appearing in clusters were counted individually. In Fig. 4 these two kinds are plotted separately.

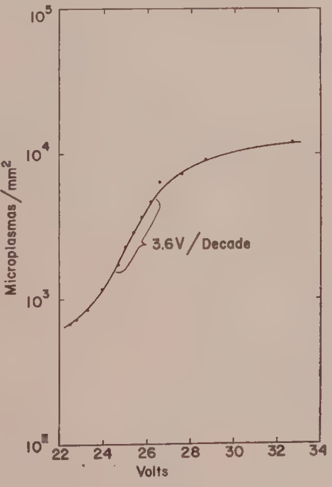

Fig. 2. Microplasma density vs voltage for a guard ring junction with uniform distribution microplasmas. (Area photographed was 0.022 mm².)

B. Junction with a Low-Angle Grain Boundary

A linear array of dislocations such as represented in a grain boundary has a marked influence on the microplasma pattern. Light emission at high voltage from a junction which was perpendicular to the dislocations in a grain boundary of 7° angle of misfit is shown in Fig. 5. Voltage dependence curves of microplasmas for two junctions from the same slice of silicon and the same diffusion run are given in Fig. 6. Due to the linear arrangement of light spots, microplasma density is given per unit length, rather than unit area as in the previous curves. These curves have an exponential portion with slopes between 0.5 and 1.1 v/decade.

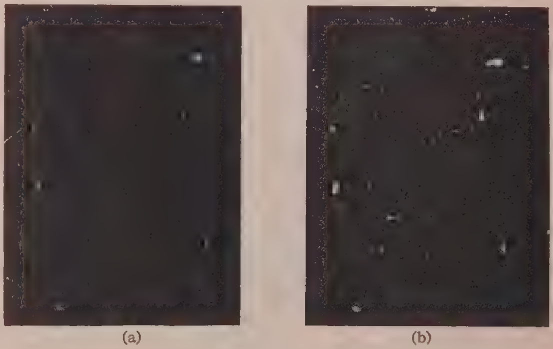
(a) (b)

Fig. 3. (a) Photograph of light emission—at low voltage. (b) Photograph of light emission—at high voltage.

IV. DISCUSSION

A. Junction with Randomly Located Microplasmas

The magnitude and the large spread in slopes from junction to junction, as well as the appearance of the

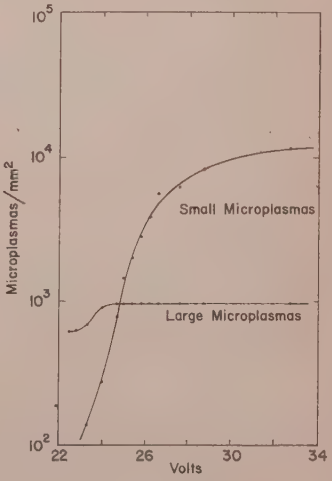

Fig. 4. Density of large and small microplasmas plotted separately vs voltage.

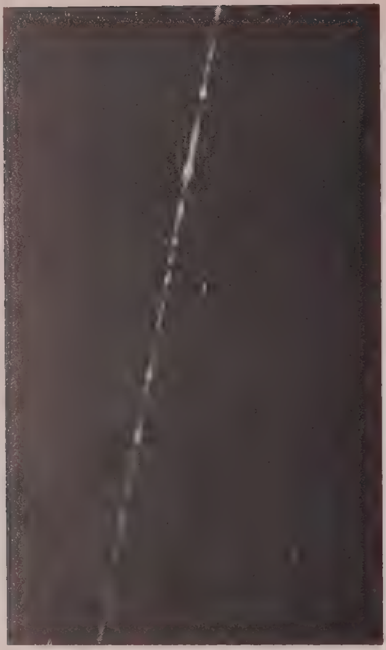

FIG. 5. Photograph of light emission at high voltage from a grain boundary junction.

microplasmas, leads us to the conclusion that the observed light emission is not the statistical distribution of breakdown of an undisturbed junction as described by Shockley,[7,8] but is caused by imperfections. If the observed light emission were the statistical breakdown, one would expect a much steeper rise in the microplasma density at breakdown voltage. Shockley's theory predicts less than 0.1 v/decade, which is a ten times steeper rise of microplasma density at breakdown voltage.

Some information about the nature of the light emission can be obtained from the shape of the distribution curves. All of the curves which could be measured up to high voltages show a decrease in slope in this range This indicates that microplasmas of the type observed have a preferred voltage near which they tend to cluster. This can be seen more clearly if the distribution, rather than the sum of the microplasmas, is plotted against voltage as in Fig. 7, which was obtained by numerical differentiation of the curves of Fig. 4. The bright microplasmas, which are fewer in number, have a maximum increment at 23.8 v, the small ones at 26 v.

The fact that the appearance and distribution of voltage of microplasmas fall into two clearly separable groups indicates that two different types of imperfections occur in the diodes under investigation. A large spread within these two groups indicates that there is a variation in each type of imperfection. Microscopic inspection showed that most of the microplasmas were associated with very small etch pits that had developed during the short etching treatment prior to diffusion. These etch pits did not appear to be dislocation etch pits.

Kikuchi[5] classified weak spots in the junction into four groups according to noise pulses, light emission and multiplication. The large microplasmas in our junction showed noise effect and probably, according to his classifications, belong in group 3 or 4. The classification of the small light spots could not be determined because they appeared at a current density so high that too many microplasmas were present to allow noise measurements.

No definite conclusion could be drawn as to the nature of the imperfections causing microplasmas. Kikuchi[5] and Shockley[7] suggested oxygen precipitates as possible sites of microplasmas. This hypothesis was checked by estimating the concentration of microplasmas per volume.

A rough estimate of the concentration of microplasmas per volume can be made using the experimental data. From Fig. 2 we obtain a maximum concentration of approximately 10^4 microplasmas per mm^2. The space charge layer at the highest voltage is calculated to be 0.9 μ wide, using the graphs of Lawrence and Warner.[13] Only the middle third of this layer has a field high enough to cause microplasmas, thus giving a density of 3×10^{10} cm^{-3} of light spots.

This figure is in good agreement with the density of oxide precipitates of 5×10^{10} found by Kaiser[14] in silicon heat-treated for 45 hr at 1000°C. The agreement, however, should be considered with caution because of the difference in heat treatments. Our sample was treated for 2 hr at 1300°C during diffusion of the guard ring and then 1.5 hr at 900°C during junction diffusion. The 1300° treatment had the effect of dissolving oxygen precipitates, whereas 900° is in the range of precipitation. Any precipitates present in our sample were probably quite small.

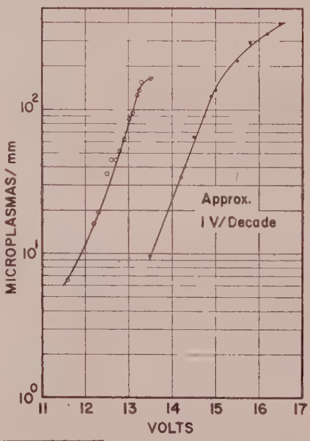

FIG. 6. Microplasma density vs voltage for two grain boundary junctions. (Boundary length photographed was 0.17 mm.)

---

[13] H. Lawrence and R. M. Warner, Jr., Bell System Tech. J. **39**, 389 (1960).

[14] W. Kaiser, Phys. Rev. **105**, 1751 (1957).

B. Microplasmas at the Grain Boundary

Light emission along a grain boundary as reported in this paper is in contradiction to Kikuchi and Tachikawa,[4] who report no light emission in a similar experiment. The reason for their failure to observe the microplasmas was probably preferential diffusion along the grain boundary.[15,16] Their diffusion conditions may have moved the junction at the boundary too far away from the surface to make light observations possible. In order to confirm this explanation, a diffusion was carried out which resulted in a junction depth of 2.5 μ outside of the grain boundary. In this case no light emission could be seen.

The distribution of light spots in cm^{-1} volt^{-1} obtained by differentiating for the two grain boundary junctions corresponding to Fig. 6 is given in Fig. 8. They also show a distribution of breakdown voltages, but only the low-voltage type of microplasmas is observed. Under the experimental conditions this is to be expected since the voltage cannot be raised to the breakdown voltage of the small microplasmas because of the large number of breakdown spots along the grain boundary.

The following points strongly indicate that the microplasmas at the grain boundary are a phenomenon cooperatively produced by dislocations and other imperfections.

(1) Since the single dislocations that make up the grain boundary are not expected to be different from each other, one would expect a rather uniform turn-on along the grain boundary if dislocations alone were responsible for microplasmas.

(2) The number of microplasmas is much smaller than the number of dislocations in the grain boundary. From the angle of misfit for the grain boundary of 7° it follows that the spacing of the dislocations is 40 A. The closest observable spacing of microplasmas on the other hand was 7000 A.

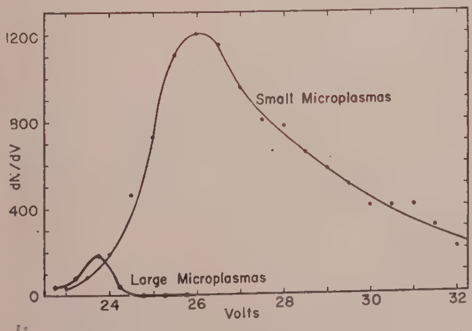

FIG. 7. dN/dV in cm^{-2} volt^{-1} vs voltage, plotted separately for large and small microplasmas (corresponding to Fig. 2).

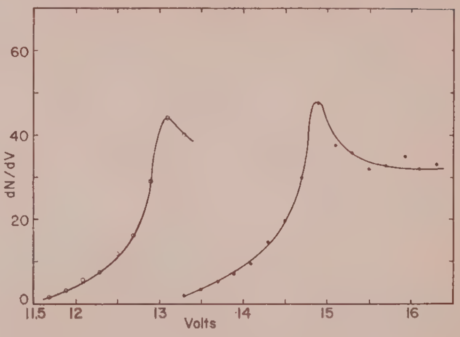

FIG. 8. Increment of microplasma density in cm^{-1} volt^{-1} vs voltage for two grain boundary junctions.

C. Current Carrying Capabilities of Microplasmas

The number of microplasmas increases linearly with current in the exponential part of the voltage dependence curves. Unfortunately this observation does not yield much information about the current voltage relationship for an individual microplasma. In fact, when the number of active microplasmas increases exponentially with voltage, total current and total number of microplasmas are proportional for a wide variety of assumed current voltage relationships. This will be shown for three representative cases.

Case 1. Step Function

$$I=0 \quad \text{for} \quad V<V_B$$
$$I=I_0 \quad \text{for} \quad V\geqq V_B,$$

where V_B = breakdown voltage of microplasma.

Case 2. Current Limited by Resistance R

$$I=0 \quad \text{for} \quad V<V_B$$
$$I=(V-V_B)/R \quad \text{for} \quad V\geqq V_B.$$

Case 3. Step Function plus Resistive Behavior

$$I=0 \quad \text{for} \quad V<V_B$$
$$I=I_0+[(V-V_B)/R] \quad \text{for} \quad V\geqq V_B.$$

The number of microplasmas N is assumed to increase exponentially.

$$N=e^{\alpha(V-V_0)}, \tag{1}$$

where V_0 is the breakdown voltage of the first microplasma to appear.

Case 1. The increment in current is

$$dI=I_0dN=I_0\alpha e^{\alpha(V-V_0)}dV. \tag{2}$$

The total current is obtained by integration

$$I=\int_{-\infty}^{V_{\text{appl}}} I_0\alpha e^{\alpha(V-V_0)}dV=I_0e^{\alpha(V_{\text{appl}}-V_0)}=I_0N(V_{\text{appl}}), \tag{3}$$

where V_{appl} is the applied voltage.

---

[15] H. J. Queisser, K. Hubner, and W. Shockley, Phys. Rev. **123**, 1245 (1961).

[16] S. Amelinckx and W. Dekeyser, *Solid State Physics*, edited by F. Seitz and D. Turnbull (Academic Press, Inc., New York, 1959), Vol. 8, p. 420.

Case 2. The increment in current is

$$dI=\frac{V_{\text{appl}}-V}{R}dN. \tag{4}$$

$$I=\int_{-\infty}^{V_{\text{appl}}}\alpha\frac{V_{\text{appl}}-V}{R}e^{\alpha(V-V_0)}dV=e\frac{\alpha(V_{\text{appl}}-V_0)}{R\alpha}$$

$$=N(V_{\text{appl}})/R\alpha. \tag{5}$$

Case 3. The current in this case is the sum of currents for case 1 and 2, or

$$I=\left(I_0+\frac{1}{R\alpha}\right)N(V_{\text{appl}}). \tag{6}$$

In all three cases, current increases linearly with the number of microplasmas. Evaluation of the experimental data yields in case 1, $I_0=170$ μamp/microplasma; in case 2, $R=1.3\times10^4$ ohms. Under the assumption that all the resistance arises from spreading resistance, we can estimate an upper limit for the diameter of a microplasma from[17]

$$R=\rho/2D,$$

where ρ=resistivity, D=diameter. Assuming case 2 to be valid, we obtain $D=3.1$ μ. Both results are higher than expected. Therefore, case 3 appears to be the best description of the current carrying mechanism of a microplasma. If we assume the threshold current I_0 of a microplasma to be 100 μamp,[18] then the resistance associated with one of the small microplasmas can be calculated to be 2.2×10^4 ohms corresponding to a microplasma diameter of 0.09 μ.

For a grain boundary junction the same consideration results in $R=2.7\times10^3$ ohms, and $D=0.74$ μ.

V. CONCLUSIONS

The experiments on light emission showed that different kinds of microplasmas occur in silicon junctions. These microplasmas have a rather wide distribution of breakdown voltage—an indication that they are caused by some kind of imperfection that itself has a statistical distribution of its properties. A line of light emitting spots could be observed along a grain boundary. The number of these spots, however, was only about 1% of the number of dislocations in the grain boundary. It is therefore concluded that imperfections that are sites of microplasmas are preferentially located along dislocations. The nature of these imperfections is still mysterious. Further investigations of the oxide precipitate hypothesis is necessary, in particular on junctions with different oxygen content and different dislocation density.

ACKNOWLEDGMENTS

The authors wish to thank W. Shockley for valuable advice and stimulating discussions. They are also obliged to N. Zetterquist and R. Julien who prepared the samples for this study.

---

[17] W. Shockley, *Electrons and Holes in Semiconductors* (D. Van Nostrand Company, Inc., Princeton, New Jersey, 1950), p. 99.

[18] A. G. Chynoweth and K. G. McKay, J. Appl. Phys. **30** 1811 (1959).

JOURNAL OF APPLIED PHYSICS VOLUME 32, NUMBER 12 DECEMBER, 1961

Letters to the Editor

Thermionic Properties of HfC

John H. Ingold
General Electric Vallecitos Atomic Laboratory, Pleasanton, California
(Received July 10, 1961)

THE thermionic emission properties of bulk HfC have been measured over the temperature range 1300° to 2100°K.

In addition to the external instrumentation, the experimental apparatus consisted of a plane diode with a copper collector and a hafnium carbide emitter. The emitter was a $\frac{1}{2}$- by $\frac{1}{16}$-in. disk which was vacuum hot-pressed from HfC powders by P. Stephas of this laboratory. The diode was constructed entirely of ceramic and metal parts so that a bakeout temperature of 600°C could be reached. During bakeout the emitter disk was outgassed at 2000°C observed brightness temperature, and then the diode was sealed off at a pressure of 2×10^{-9} mm Hg. The emitter disk had been previously outgassed at 3000°C in an electron beam furnace during the process of bonding it to its support. The emitter was heated by electron bombardment and its temperature was determined by pyrometric observation of the center of the emitter disk. An emissivity of 0.7 was assumed in making temperature corrections.

The saturation emission current was measured as a function of temperature with a constant voltage of 95 v applied to the collector, which was spaced about 1 mm from the emitter. A General Radio type 1230-A electrometer was used to monitor the current. A Richardson plot of the results is shown in Fig. 1. An approximate least-squares fit to the experimental points gives a work function of 4 v and a Richardson constant of 40 amp/cm² deg². On the other hand, the effective work function, as defined by Hensley,[1] ranges from 4.07 to 4.18 v, with an average of 4.13 v.

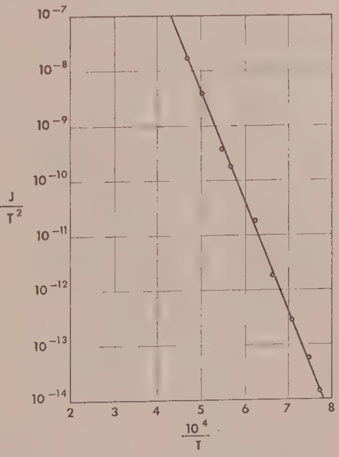

FIG. 1. Richardson plot of experimental data.

---

[1] E. B. Hensley, J. Appl. Phys. 32, 301 (1961). The effective work function is given by the Richardson equation when an "A" value of 120 amp/cm² is assumed.

Erratum: Man-Made Heating and Ionization of the Upper Atmosphere

[J. Appl. Phys. 32, 570 (1961)]

P. A. Clavier
Aeronutronic, A Division of Ford Motor Company, Newport Beach, California

A NUMERICAL error occurred in the computation of Eq. (25) of reference 1. Table III should read:

Table III. F vs T_e.

T_e	F	F_O*	F_O	F_{O2}	F_{N2}
2×10^{2}	6.5×10^{-91}				
5×10^{3}	2.4×10^{-22}	1.8×10^{-5}	5.7×10^{-16}	4.3×10^{-14}	1.58×10^{-11}
1.3×10^{4}	1.4×10^{-3}	2.34×10^{-1}	6.6×10^{-3}	10^{-2}	2.2×10^{-2}

The change in F affects Eqs. (40), (41), and (42). They should read

$$-2.75\times10^{-5}=7.92\ 10^{-2}\frac{n_eF(T_e)}{T_e}-2.60\times10^{-20}\times\frac{n_e^2}{T_e^{\frac{1}{2}}}-6.54\times10^{-10}n_eT_i^{\frac{1}{2}}, \quad (40)$$

$$n_e=\frac{1}{3.36\times10^{-4}-2.88\times10^{3}[F(T_e)/T_e]}, \quad (41)$$

$$n_e=3.25\times10^{7}T_e^{\frac{1}{2}}. \quad (42)$$

The maximum electron density is not changed. The maximum reachable electron temperature, however, is changed from 1.6×10^{3} to 1.3×10^{4}°K. The temperatures of the ions and of the neutral particles are unchanged and remain equal to the ambient temperature.

The maximum power one can absorb by cyclotron interaction in a sphere with a radius of 3 km becomes 722 kw.

It is used in the following manner:

Heating of the electron:	700 kw
Ionization:	1.2 kw
Excitation:	20.8 kw
Bremsstrahlung:	2.17×10^{-9} kw.

I am indebted to Dr. D. Farley for spotting the error.

---

[1] P. A. Clavier, J. Appl. Phys. 32, 570 (1961).

Announcements

Increase in Publication Charge

Starting with the January, 1962, issue, the publication charge for this journal and other AIP-owned journals will be increased to $40 per page. With the great increase in the quantity of material being published and the gradual rise of printing costs, it is necessary to increase publication charges or to raise subscription rates, or both. Our basic justification of the publication charge is that a research investigation is not completed until the results are made generally available through publication. It therefore is proper for the agency which supports the research to include the small amount, estimated at less than 1%, required to support publication. We believe that physicists should have their own copies of many journals and that subscription prices should therefore be kept as low as possible. The "ideal" arrangement toward which we are striving, would have the publication charges cover the costs of editorial work and composition, so that the individual subscriber would have to pay only for the printing and handling of his own copy. Since our ability to finance publication of the journal would not depend on the number of subscribers, there would be no danger that a loss of subscriptions because of the growing use of photocopying would jeopardize continued publication.

Hugh C. Wolfe, *Director of Publications*
American Institute of Physics

Author Index to Volume 32

References with (L) are to Letters to the Editor; (E) to Errata

Abeledo, Carlos R. and P. W. Selwood. Temperature dependence of spontaneous magetization in superparamagnetic nickel—229S
Abbott, A. Neal (see Lavik, Melvin T.)—1795(L)
Abbott, G. L. (see Parker, W. J.)—1679
Abella, I. D. and H. Z. Cummins. Thermal tuning of ruby optical maser—1177(L)
Abernethy, L. L., T. H. Ramsey, Jr., and John W. Ross. Growth of yttrium iron garnet single crystals by the floating zone technique—376S
Abrams, R. H., Jr., and F. E. Jamerson. Thermionic emission of UC-Nb—1783(L)
Adawi, I. Negative resistance and hot electrons—1101
Adler, R., A. Ashkin, and E. I. Gordon. Excitation and amplification of cyclotron waves and thermal orbits in the presence of space charge—672
Aharoni, A. On additivity of imperfections as means for domain nucleation—245S
——, **E. H. Frei, Z. Scheidlinger, and M. Schieber.** Curie temperature of some garnets by the differential thermal analysis technique—1851
Ahearn, A. J. Mass spectrographic analysis of insulators using a vacuum spark positive ion source—1195
Ahearn, A. J. Mass spectrographic detection of impurities in liquids—1197
Albert, P. A. and W. J. Carr, Jr. Temperature dependence of magnetostriction and anisotropy in MnBi—201S
Albers, W., C. Haas, H. J. Vink, and J. D. Wasscher. Investigations on SnS—2220
Akcasu, A. Ziya. Measurement of noise power spectra by Fourier analysis—565
Albini, Frank A. and Robert G. Jahn. Reflection and transmission of electromagnetic waves at electron density gradients—75
Alers, G. A. and D. O. Thompson. Dislocation contributions to the modulus and damping in copper at megacycle frequencies—283
Allgaier, R. S. Valence bands in lead telluride—2185
Altemose, V. O. Helium diffusion through glass—1309
Amelinckx, S. and P. Delavignette. Electron microscope observation of dislocations in talc—341
—— (see Delavignette, P.)—1098
—— (see Ruedl, E.)—2492(L)
——, **G. Strumane, and W. W. Webb.** Dislocations in silicon carbide—1182(E)
—— (see Delavignette, P.)—554(L)
Ames, Dennis B. (see Boucher, Roland A.)—755
Anderson, Elmer E. (see Cunningham, Richard J., Jr.)—388S
Andrews, E. H. Crack propagation in a strain-crystallizing elastomer—452
Appel, J. and S. W. Kurnick. Polaron band model and its application to Ce-S semiconductors—2206
Arai, Thomas T. and John R. Madigan. Response of a thermocouple circuit to nonsteady currents—609
——, **Henry Chessin, and D. S. Miller.** First magnetocrystalline anisotropy constants of some iron-silicon alloys—857
—— **and R. V. Colvin.** Paramagnetism of polycrystalline gadolinium, terbium, and dysprosium metals—336S
—— Electrical resistivities of nickel-niobium solid solutions—97
—— (see Reich, A. D.)—2493(L)
Archard, G. D. Back scattering of electrons—1505
Archard, J. F. Single contacts and multiple encounters—1420
Argyle, B. E. (see Pugh, E. W.)—334S
Armstrong, J. (see Benekek, G. B.)—106S
Arndt, R. A. and R. L. Hines. Radiation enhancement of bulk diffusion in 10% Zn-90% Cu by 30-kev Ne$^+$ ion bombardment—1913
Arnott, R. J. (see Ferretti, A.)—905
Arrott, Anthony and B. R. Coles. Antiferromagnetism of α-Mn and its alloys—51S
——(see Cooper, H. W.)—2506
Arthur, Paul, Jr. (see Swoboda, T. J.)—374S
Asch, G. (see Meyer, A. J. P.)—330S
Ashkin, A. (see Gordon, E. I.)—1137
——. (see Adler, R.)—672
Auberger, Michel and John S. Rinehart. Ultrasonic attenuation of longitudinal waves in plastics—219
Augustyniak, W. M. (see Logan, R. A.)—1201
Auld, B. A. (see Comstock, R. L.)—227S
——, **H. J. Shaw, and D. K. Winslow.** Traveling-wave frequency doubling in ferrites—317S
Austin, A. E. and N. A. Richard. Grain-boundary diffusion—1462
Aven, M., D. T. F. Marple, and B. Segall. Some electrical and optical properties of ZnSe—2261
—— **and D. M. Cook.** Some electrical properties of zinc telluride—cadmium sulfide heterojunctions—960(L)
Averbach, B. L. (see Nagorsen, G.)—688
Ayres, R. U. Acceleration of rigid, conducting, diamagnetic bodies by a magnetic field—1549
Azároff, Leonid V. Role of crystal structure in diffusion. I. Diffusion paths in closest-packed crystals—1658
—— Role of crystal structure in diffusion. II. Activation energies for diffusion in closest-packed structures—1663

Babbitt, R. W. (see Malinofsky, W. W.)—237S
Bady, Isidore and Gilbert McCall. Ferromagnetic resonance due to magnetic fields generated by displacement currents in ferrites—146S
Bailey, Anita I. Friction and adhesion of clean and contaminated mica surfaces—1407
—— Recent work on solid friction at the research laboratory for the physics and chemistry of solids—1413
Baker, G. S. (see Huber, R. J.)—2488(L)
—— (see Huber, R. J.)—2573
Banerjee, B. R., J. M. Capenos, J. J. Hauser, and J. P. Hirth. Dislocation interaction in bcc stainless steel—556(L)
—— (see Capenos, J. M.)—323(L)
Balkanski, Minko and Jean Michel Besson. Double phonon processes in cadmium sulfide—2292
Ball, M., G. Garton, M. J. M. Leask, D. Ryan, and W. P. Wolf. Low-temperature magnetic properties of some rare-earth garnet compounds—267S
Balluffi, R. W. (see Darby, J. B., Jr.)—840
—— (see Heitmann, W. E.)—963(L)
Banks, E., N. H. Riederman, H. W. Schleuning, and L. M. Silber. Preparation and properties of thin ferrite films—44S
Baran, W., W. Breuer, H. Fahlenbrach, and K. Janssen. Some investigations on iron-cobalt permanent magnet alloys of the Vicalloy II type—199S
Barker, R. C. (see Brownell, R. M.)—284S
Barrett, W. A. Demagnetization of twistor bits—35S
Barry, Don and Roy W. Roberts. Useful technique for growing large, single-crystal YIG—1405(L)

Baruch, P. Mobility of radiation-induced defects in germanium—653

Bate, G. Angular variation of the magnetic properties of partially aligned γ-Fe_2O_3 particles—239S

Bate, R. T., J. C. Bell, and A. C. Beer. Influence of magnetoconductivity discontinuities on galvanomagnetic effects in indium antimonide—806

—— **and A. C. Beer.** Influence of conductivity gradients on galvanomagnetic effects in semiconductors—800

Bateman, T., W. P. Mason, and H. J. McSkimin. Third-order elastic moduli of germanium—928

Batterman, Boris W. Imaginary part of x-ray scattering factor for germanium. Comparison of theory and experiment—998

Baugnet, J. M. (see Willis, A. H.)—1622(L)

Beals, Robert J. (see Bernstein, Leonard)—122(L)

Bean, C. P. (see Livingston, J. D.)—1964

Beck, Paul A. (see Sinha, P. O.)—1222

Becker, E. J. (see Becker, J. A.)—411

Becker, J. A., E. J. Becker, and R. G. Brandes. Reactions of oxygen with pure tungsten and tungsten containing carbon—411

Becker, W. M., A. K. Ramdas, and H. Y. Fan. Energy band structure of gallium antimonide—2094

Beer, A. C. (see Bate, R. T.)—800

—— Galvanomagnetic effects in III–V compound semiconductors—2107

—— (see Bate, R. T.)—806

Beinenstock, Arthur. Determination of crystallite size distributions from x-ray line broadening—187

Bekefi, G. and Sanborn C. Brown. Microwave measurements of the radiation temperature of plasmas—25

Bell, J. C. (see Bate, R. T.)—806

—— (see Simon, R.)—46

Bell, James F. Experimental study of the interrelation between the theory of dislocations in polycrystalline media and finite amplitude wave propagation in solids—1982

Bell, W. E. and A. L. Bloom. Discharge photocells for the detection of resonance radiation—906

Belson, Henry S. (see Matcovich, T.)—163S

Benekek, G. B. and J. Armstrong. Pressure and temperature dependence of the Fe^{57} nuclear magnetic resonance frequency in ferromagnetic iron—106S

Bennett, L. C. and J. R. Wiese. Effects of doping additions on the thermoelectric properties of the intrinsic semiconductor $Bi_2Te_{2.1}Se_{0.9}$—562

Bergman, Robert S. (see Hill, Robert M.)—227S

Bergstrom, B. H. (see Gilvarry, J. J.)—400

Bernstein, D. (see Muller, G. M.)—1065

Bernstein, Leonard and Robert J. Beals. Thermal expansion and related bonding problems of some III–V compound semiconductors—122(L)

Besson, Jean Michel. (see Balkanski, Minko)—2292

Bierstedt, P. E. (see Jarrett, H. S.)—57S

Bills, K. W., Jr., and F. S. Salcedo. The swelling of unfilled and highly filled polymers—2364

Biorci, G., A. Ferro and G. Montalenti. Magnetic viscosity due to solute atom pairs—630

Birdsall, C. K. and W. B. Bridges. Space-charge instabilities in electron diodes and plasma converters—2611

Birkenbeil, H. J. and R. W. Cahn. Induced magnetic anisotropy created by magnetic or stress annealing of iron-aluminum alloys—362S

Birks, L. S. Calculation of x-ray intensities from electron probe specimens—387

Birnbaum, G. (see Wagner, W. G.)—1185

Birnbaum, Howard K. and Floyd R. Tuler. Deformation-produced point defects—1403(L)

Birnboim, Meyer H. and John D. Ferry. Method for measuring dynamic mechanical properties of viscoelastic liquids and gels; the gelation of polyvinyl chloride—2305

Bither, T. A. (see Cloud, W. H.)—55S

Blakemore, J. S. and K. C. Nomura. Enantiomorphous character of etch pits in tellurium—745(L)

Blanc, Joseph, Richard H. Bube, and Harold E. MacDonald. Properties of high-resistivity gallium arsenide compensated with diffused copper—1666

Blank, John M. Equilibrium atmosphere schedules for the cooling of ferrites—378S

Bloom, A. L. (see Bell, W. E.)—906

Blume, R. J. (see Budnick, J. I.)—120S

Bobroff, D. L., H. A. Haus, and J. W. Kluver. On E. L. Chu's definition of small-signal rf power of electron beams—749(L)

Bockemuehl, Robert R., James E. Kauppila, and David S. Eddy. Analysis of photojunctions formed by diffusing copper into insulating cadmium sulfide crystals—1324

Boerdijk, A. H. Zero-, first-, and second-order theories of a general thermocouple—1584

Bogert, B. P. (see Kramer, H. P.)—764

Bolef, D. I. Elastic constants of single crystals of the bcc transition elements V, Nb, and Ta—100

Bolling, G. F. and W. A. Tiller. Growth from the Melt. III. Dendritic growth—2587

Bollmann, W. Electron microscope study of radiation damage in graphite—869

Bonfiglioli, G., A. Ferro, and A. Mojoni. Electron microscope investigation on the nature of tracks of fission products in mica—2499

Bonstrom, D. B., A. H. Morrish, and L. A. K. Watt. Magnetic properties of the low-temperature form of magnetite—272S

Born, H. J., S. Legvold, and F. H. Spedding. Low-temperature thermoelectric power of the rare-earth metals—2543

Boucher, Roland A. and Dennis B. Ames. End effect in dc magnetohydrodynamic generators—755

Boudreaux, Lee J. (see Hasty, Turner E.)—1807

Boyd, E. L. (see Budnick, J. I.)—120S

Brandes, R. G. (see Becker, J. A.)—411

Brands, C. W. (see Raymo, C. T.)—1165(L)

Brannen, Eric and H. Froelich. Preliminary operation of a four-sector racetrack microtron—1179(L)

——**, H. Froelich, and T. W. W. Stewart.** Generation of millimeter waves by the electron beam of a microtron—964(E)

Bratina, W. J. (see Martius, U. M.)—280S

Breebe, C. A. A. J. (see van Daal, H. J.)—2225

Breuer, W. (see Baran, W.)—199S

Bridges, W. B. (see Birdsall, C. K.)—2611

Brittain, J. O. (see Mura, T.)—92

Broadhurst, Martin G., Edwin R. Fitzgerald, and Anthony J. Bur. Dielectric properties and side-chain crystallinity of polyvinyl stearate—972

Brodie, I. Emission fluctuations of tungsten-based barium dispenser cathodes—2039

Brody, T. P. Impurity band conduction and the problem of excess current in tunnel diodes—746(L)

Brogeaud, P. (see Straumanis, M. E.)—1382

Brown, N. (see Marcinkowski, M. J.)—375

Brown, Sanborn C. (see Bekefi, G.)—25

—— (see Hall, R. B.)—1835

Brown, William Fuller, Jr. (see Johnson, Clark E.)—243S

—— Domains and extreme-value statistics—278S

Brownell, R. M. and R. C. Barker. Measurements of the domain wall area-mobility product during slow flux reversals—284S

Bruner, L. J. (see Budnick, J. I.)—120S

Bube, Richard H. Cross-section ratios of sensitizing centers in photoconductors—1707
—— (see Blanc, Joseph)—1666
—— Monotonic trap distributions—1621(L)
Budnick, J. I., L. J. Bruner, R. J. Blume, and E. L. Boyd. Nuclear magnetic resonance of Fe^{57} in unenriched Fe—120S
Buehler, E., F. S. L. Hsu, B. T. Matthias, and C. Wahl. Production of magnetic fields exceeding 15 kilogauss by a superconducting solenoid—325(L)
Buffler, C. R. (see Muller, M. W.)—152S
Bundy, F. P. Effect of pressure on emf of thermocouples—483
Buneman, O. Resistance as dissipation into many reactive circuits: Landau damping and Nyquist's noise theorem—1783(L)
Bur, Anthony J. (see Broadhurst, Martin G.)—972
Burnham, D. C. (see Moser, F.)—48
Burns, Gerald. Electron spin resonance in powders—2048(L)
Burrus, C. A. High-frequency silicon varactor diodes—1166 (L)
—— Gallium arsenide Esaki diodes for high-frequency applications—1031
Burstein, E. (see Stiles, P. J.)—2174
Butcher, B. M. and A. L. Ruoff. Effect of hydrostatic pressure on the high-temperature steady-state creep of lead—2136
Butler, C. P. (see Parker, W. J.)—1679

Cable, J. W. (see Wilkinson, M. K.)—48S
——**, E. O. Wollan, W. C. Koehler, and M. K. Wilkinson.** Neutron diffraction study of metallic erbium—49S
Cadoff, I. (see Miller, E.)—2457
Cahn, J. H. (see Simon, R.)—46
Cahn, R. W. (see Birkenbeil, H. J.)—362S
Calawa, A. R. (see Rediker, R. H.)—2189
Callaby, D. R. Determination of the directions of magnetization in polycrystalline ferrites—298S
Callen, Earl R. Anisotropic Curie temperature—221S
Callen, Herbert. Note on the back reaction term in ferromagnetic relaxation equations—738(L)
——(see Haas, C. Warren)—157S
Campbell, Robert B. and Carl A. Julien. Structure of Alnico V—192S
—— **and Carl A. Julien.** Ferromagnetic phase of Mn-Al—346S
Capenos, J. M. (see Banerjee, B. R.)—556(L)
—— **and Bani R. Banerjee.** Transmission electron microscopy of Alnico V—323(L)
Carabateas, E. N., S. D. Pezaris, and G. N. Hatsopoulos. Interpretation of experimental characteristics of cesium thermionic converters—352
Cardona, Manuel. Fundamental reflectivity spectrum of semiconductors with zinc-blende structure—2151
—— Optical studies of the band structure of InP—958(L)
Carlson, Henry A. and H. A. Richard Wegener. Variant in technique for A. R. Lang's x-ray diffraction topography—125(L)
Carmichael, A. J. and H. W. Holdaway. Phenomenological elastomechanical behavior of rubbers over wide ranges of strain—159
—— **and H. W. Holdaway.** Application of the three-parameter stress function to natural rubbers of widely different hardness—1724
Carr, W. J., Jr. (see Albert, P. A.)—201S
Carson, J. E. and R. L. White. Zero-field splitting of the Cr^{3+} ground state in YGa and YAl garnet—1787(L)
Carter, David L. A cw solid state, push-pull maser in the 5- to 6-millimeter wavelength region—2541
Caswell, H. L. Effect of residual gases on the properties of indium films—2641
—— Effect of residual gases on superconducting characteristics of tin films—105
—— (see Priest, J.)—1772
Caughey, T. K. and J. K. Dienes. Analysis of a nonlinear first-order system with a white noise input—2476
Chambers, F. W. (see Cole, H.)—1942
Chang, Roger. Dislocation relaxation phenomena in oxide crystals—1127
Charles, R. J. Polarization and diffusion in a silicate glass—1115
—— (see Hillig, W. B.)—123(L)
Chase, A. B. (see Lefever, R. A.)—962(L)
Chen, C. W. Metallurgy and magnetic properties of an Fe-Co-V alloy—348S
Cherry, L. V. and W. E. Wallace. Magnetic characteristics of some intermetallic compounds between manganese and the lanthanide metals—340S
Chessin, Henry (see Arajs, Sigurds)—857
Chester, P. F. Cross-doping agents for rutile masers—866
—— Electron spin resonance in semiconducting rutile—2233
Chikazumi, Soshin. Epitaxial growth and magnetic properties of single-crystal films of iron, nickel, and permalloy—81S
Chiou, C. (see Priest, J.)—1772
Chou, Y. T. and R. W. Whitmore. Single and double pile-up of dislocations in MgO crystals—1920
Christenson, E. L. (see Domenicali, C. A.)—2450
Christopher, M. E. (see Machlup, S.)—1387
Christy, R. W. and W. E. Daniels, Jr. Electrical conductivity of NaCl during high-temperature creep—1265
Claassen, Richard S. Excess and hump current in Esaki diodes—2372
Clark, A. E. and R. E. Strakna. Elastic constants of single-crystal YIG—1172(L)
Clark, John. Perturbation techniques for miniaturized coaxial *Y*-junction circulators—323S
Clavier, P. A. Man-made heating and ionization of the upper atmosphere—570
—— Propagation in a plasma—578
—— Man-made heating and ionization of the upper atmosphere—2651(E)
Cline, R. S. (see Hu, Hsun)—1392
—— (see Hu, Hsun)—760
Clingman, W. H. and R. G. Moore, Jr. Application of ferroelectricity to energy conversion processes—675
Cloud, W. H., T. A. Bither, and T. J. Swoboda. Exchange inversion in Mn$_{2-x}$Cr$_x$Sb—55S
Cnare, Eugene C. Electrically imploded-exploded aluminum tube—1275
—— Observations on the striation of electrically exploded copper foils—1043
Cobine, J. D. and G. A. Farrall. Experimental study of arc stability—328(E)
Coble, R. L. Sintering crystalline solids. I. Intermediate and final state diffusion models—787
—— Sintering crystalline solids. II. Experimental test of diffusion models in powder compacts—793
Cochran, W., S. J. Fray, F. A. Johnson, J. E. Quarrington, and N. Williams. Lattice absorption in gallium arsenide—2102
Cohen, M. S. Anisotropy in permalloy films evaporated at grazing incidence—87S
——**, D. O. Smith, and G. P. Weiss.** Oblique-incidence anisotropy in evaporated films—1405(E)
Cole, H., F. W. Chambers, and C. G. Wood. X-ray polarizer—1942
Coleman, R. V. (see Laukonis, J. V.)—242
Coles, B. R. (see Arrott, Anthony)—51S
Collins, R. J. (see Nelson, D. F.)—739(L)
Colvin, R. V. (see Arajs, Sigurds)—336S

Comstock, R. L., B. A. Auld, and Glen Wade. Parametric effects in magnetoacoustic resonance—227S
Condas, George A. and Frederick O. Wooten. Properties of thin antimony films deposited in high vacuum—323(L)
Conger, Robert L. Nonlinear damping losses in YIG—1525
Conwell, E. M. (see Zucker, J.)—2606
Cook, C. J. and William J. Fredericks. Interaction of slow electrons with insulating crystals. I. Absorption coefficient for cleaved alkali halides; experimental techniques—860
Cook, D. M. (see Aven, M.)—960(L)
Cook, J. S. Dislocation etching solution for potassium chloride and other alkali halides—2492(L)
—— (see Mason, Donald R.)—475
Cooper, H. W., A. S. Arrott, and H. W. Paxton. Magnetic investigation of pure manganese and of several of its alloys—2506
Cooper, R. W. (see Pearson, R. F.)—265S
Coren, R. L. and H. J. Juretschke. Magnetoresistance and magnetic switching in Permalloy films—292S
Cosgrove, G. J., J. P. McHugh, and W. A. Tiller. Effect of freezing conditions on the thermoelectric properties of BiSbTe$_3$ crystals—621
Cowan, Robert D. Proposed method of measuring thermal diffusivity at high temperatures—1363
Cox, N. L. (see Swoboda, T. J.)—374S
Cristal, E. G. and J. Van Bladel. Fields in cavity-excited accelerators—1715
Croft, William J. (see Lemaire, Henry P.)—46S
Croll, I. M. (see Greiner, J. H.)—188S
Cuff, K. F., M. R. Ellet, and C. D. Kuglin. Oscillatory magnetoresistance in the conduction band of PbTe—2179
Culp, F. L. and H. L. Hooper. Study of impact cratering in sand—2480
Cummins, H. Z. (see Abella, I. D.)—1177(L)
Cunningham, Richard J., Jr., and Elmer E. Anderson. Effect of indium substitution in yttrium iron garnet: high permeability garnets—388S
Curran, D. R. On the possibility of detecting shock-induced second-order phase transitions in solids. The equation of state of Invar—1811
Cutler, M. Thermoelectric measurements at small-area contacts—1075
—— Thermoelectric behavior of *p-n* junctions—222
Czachor, A. and J. Piekoszewski. Effect of reactor fast neutrons on electron-hole recombination in germanium—1837

Dale, Brian and F. P. Smith. Spectral response of solar cells—1377
Damm, Charles C. (see Hunt, Angus L.)—1937
Danforth, W. E. and Albert J. Williams. On the thermionic properties of ZrC, UC, and ZrC·UC mixture—1181(L)
Daniel, T. Bruce. (see Lavik, Melvin T.)—1795(L)
Daniels, W. E., Jr. (see Christy, R. W.)—1265
Darby, J. B., Jr., C. T. Tomizuka, and R. W. Balluffi. Self-diffusion in silver during plastic deformation in torsion—840
Darnell, F. J. Magnetization process in small particles of CrO$_2$—1269
—— Exchange anisotropy in oxidized iron-cobalt particles—186S
—— (see Oppegard, A. L.)—184S
—— (see Jarrett, H. S.)—57S
Daughton, J. M., T. A. Smay, A. V. Pohm, and A. A. Read. Magnetic film devices using passive loading—36S
Davey, John E. Textural properties of germanium films—877
Davidson, Burton (see Littman, Howard)—217
Day, T. B. and J. Sucher. Possibility of a spin wave magnetic-moment detector—1788(L)
De Beukelaer, R. C. (see Willis, A. H.)—1622(L)
De Blois, R. E. Ferromagnetic nucleation sources on iron whiskers—1561
Deetscreek, V. D. (see Schuele, W. J.)—235S
Dekeyser, W. (see Rueda, F.)—1799(L)
Delaney, E. (see Ferretti, A.)—905
Delavignette, P., H. B. Kirkpatrick, and S. Amelinckx. Dislocations and stacking faults in aluminum nitride—1098
—— (see Amelinckx, S.)—341
—— **and S. Amelinckx.** Interaction between vacancies and stacking fault ribbons in graphite—554(L)
—— (see Ruedl, E.)—2492(L)
DeLosh, R. G. (see Phillips, R. L.)—1406(E)
—— (see Phillips, R. L.)—551(L)
deMars, G. A. (see Statz, H.)—218S
Denton, R. T. Theoretical and experimental characteristics of a ferromagnetic amplifier using longitudinal pumping—300S
Derick, L. (see Frosch, C. J.)—2060(L)
Dermit, G. (see Weinreich, O.)—1170(L)
Diamond, Howard. Variation of permittivity with electric field in perovskite-like ferroelectrics—909
Dibelius, N. R. (see Mullaney, G. J.)—668
Dienes, J. K. (see Caughey, T. K.)—2476
Dietz, R. E., J. J. Hopfield, and D. G. Thomas. Excitons and the absorption edge of ZnO—2282
di Francia, G. Toraldo. Spherical lenses for infrared and microwaves—2051(L)
Dillon, J. F., Jr. New characteristic in the temperature dependence of ferrimagnetic resonance linewidth in some rare-earth doped yttrium iron garnets—159S
Dimmock, J. O. and R. G. Wheeler. Exciton structure and Zeeman effects in cadmium selenide—2271
Diorio, A. F. (see L. Mandelkern)—1509
Domenicali, C. A. and E. L. Christenson. Effects of transition metal solutes on the electrical resistivity of copper and gold between 4° and 1200°K—2450
Dousmanis, George C. Fast-risetime excitation to achieve nonequilibrium and amplifying carrier distributions—2005
Douthett, D. D., I. Kaufman, and A. S. Risley. Microwave harmonic generation by ferrimagnetic crystals—1905
Dow, W. G. (see Miller, M. H.)—274
Doyle, W. D., J. E. Rudisill, and S. Shtrikman. Angular dependence of torque in anisotropic permalloy films—1785(L)
Drougard, M. E. (see Schlosser, H.)—1227
Duncan, R. H. (see Ferguson, T. R.)—1385
Dunn, D. A. and R. E. Holaday. Electron trajectories in a nonuniform axially symmetric magnetic field—1612
Durelli, A. J. and W. F. Riley. Stress distribution on the boundary of an elliptical hole in a large plate during passage of a stress pulse of long duration (major axis normal to the wave front)—1255
Dwight, K. (see Kaplan, T. A.)—13S
Dymanus, A. and I. P. Kaminow. Ferromagnetic resonance in piezoelectric Ga$_{2-x}$Fe$_x$O$_3$—144S

Ebisuzaki, Yukiko. Preparation of monocrystalline cuprous oxide—2027
Eby, R. K. and K. M. Sinnott. Transitions and relaxations in polytetrafluoroethylene—1765
Eckstein, Yakov, A. W. Lawson, and Darrell H. Reneker. Elastic constants of bismuth—752(E)
Eddy, David S. (see Bockemuehl, Robert R.)—1324
Edgerton, H. E. (see Miles, P. A.)—740(L)
Edwards, David L. (see Horgan, James D.)—1784(L)
Egerton, L. (see Van Uitert, L. G.)—959(L)
Eggenberger, J. S. Influence of nearby conductors on thin-film switching—752(E)
Eggers, F. G. (see Rowen, J. H.)—313S

Ehrenreich, H. Band structure and transport properties of some 3–5 compounds—2155
Ehrlich, Gert. Kinetic and experimental basis of flash desorption—4
Eichenbaum, A. L. and K. G. Hernqvist. Space charge instabilities in synthesized plasmas—16
Eisner, R. L., R. Mazelsky, and W. A. Tiller. Growth of ZnSb single crystals—1833
Elbaum, C. (Howe, S.)—742(L)
Eldridge, Donald F. Quantitative determination of the interaction fields in aggregates of single-domain particles—247S
Ellet, M. R. (see Cuff, K. F.)—2179
Ellis, W. C. (see Greiner, E. S.)—2489(L)
Enz, U. Magnetization process of a helical spin configuration—22S
Epstein, D. J., B. Frackiewicz, and R. P. Hunt. Uniaxial anisotrophy in polycrystalline garnets—270S
Erkman, John O. Smooth spalls and the polymorphism of iron—939
Estle, T. L. (see Walters, G. K.)—1854

Fahlenbrach, H. (see Baran, W.)—199S
Falk, R. B. and G. D. Hooper. Elongated iron-cobalt: ferrite, a new, lightweight, permanent magnet material—190S
—— Properties of single-domain particles of cobalt-nickel—2536
Fan, H. Y. (see Becker, W. M.)—2094
Farnsworth, H. E. and Hannibal H. Madden, Jr. Mechanism of chemisorption, place exchange, and oxidation on a (100) nickel surface—1933
Farrall, G. A. and G. H. Reiling. Experimental study of arc stability. II. An investigation of mercury arc stability—1528
—— (see Cobine, J. D.)—328(E)
Fatuzzo, Ennio. Increase in dielectric constant switching in lithium selenite and triglycine sulfate—1571
—— **and Walter J. Merz.** Surface layer in $BaTiO_3$ single crystals—1685
Faucher, Joseph A. Extension of the Eyring-Ree theory of non-Newtonian flow—2336
Ferguson, R. T. and R. H. Duncan. Charged cylindrical tube—1385
Ferretti, A., R. J. Arnott, E. Delaney, and A. Wold. Cobalt ferrite single crystals—905
Ferro, A. (see Biorci, G.)—630
—— (see Bonfiglioli, G.)—2499
Ferry, John D. (see Birnboim, Meyer H.)—2305
Feucht, Donald L. and James B. Woodford, Jr. Superconductor-transition switching time measurements using a superconductive radio-frequency mixer—1882
Fine, M. E. (see Koppenaal, T. J.)—1781
Finn, M. C. (see Gatos, H. C.)—1174(L)
Fischler, A. S. (see Turner, W. J.)—2241
Fisher, Bertina and P. S. Rudman. X-ray diffraction study of interdiffusion in Cu-Ni powder compacts—1604
Fisher, J. C. and I. Giaever. Tunneling through thin insulating layers—172
Fitzgerald, Edwin R. (see Broadhurst, Martin G.)—972
Flanders, P. J. and F. R. L. Schoening. Precipitation in gold-nickel single crystals—344S
Fletcher, P. C. and Neal Silence. Subsidiary absorption above ferrimagnetic resonance—706
Fletcher, R. C. (see Suhl, H.)—281
Flom, D. G. Rolling friction of polymeric materials. II. Thermoplastics—1426
Folweiler, Robert C. Creep behavior of pore-free polycrystalline aluminum oxide—773
Foner, Simon. Antiferromagnetic resonance in $(Cr_2O_3)_{1-x}\cdot(Al_2O_3)_x$—63S
Forman, R. Electrical conduction and breakdown in high-pressure (0.25–300 mm) rare gases—1651
Forrester, P. A. and W. B. Mims. Seesaw maser operation—317
Fowler, C. A., Jr., E. M. Fryer, and D. Treves. Domain structures in iron whiskers as observed by the Kerr method—296S
Fowler, H. A., L. Marton, J. Arol Simpson, and J. A. Suddeth. Electron interferometer studies of iron whiskers—1153
Fowler, R. G. (see Seay, G. E.)—2439
Fowler, V. J. (see Zucker, J.)—2606
Fowles, G. R. Shock wave compression of hardened and annealed 2024 aluminum—1475
Frackiewicz, B. (see Epstein, D. J.)—270S
Francis, E. E. (see Pimbley, W. T.)—1729
Francombe, M. H. and A. H. Noreika. Some properties of uniaxial permalloy films prepared by cathodic sputtering—97S
Frank, G. R., Jr., D. L. Robinson, and G. Thomas. Precipitation sites in aluminum alloys—1763
Fray, S. J. (see Cochran, W.)—2102
Fredricks, R. W. Traveling wave analysis of a class of parametric amplifiers based upon the Hill equation—901
Fredericks, William J. (see Cook, C. J.)—860
Frederikse, H. P. R. Recent studies on rutile (TiO_2)—2211
Freeman, A. J. (see Watson, R. E.)—118S
Frei, E. H. (see Aharoni, A.)—1851
Freudenthal, A. M. Thermoelastic equations and Grueneisen's relation—1801(L)
Friauf, J. B. Thermodynamics of thermally regenerated fuel cells—616
Friedberg, S. A. (see Pierce, R. D.)—66S
Friedel, J., G. Leman, and S. Olszewski. On the nature of the magnetic couplings in transitional metals—325S
Froelich, H. (see Brannen, Eric)—1179(L)
—— (see Brannen, E.)—964(E)
Frosch, C. J., M. Gershenzon, and L. Derick. Presence of carbon in gallium phosphide crystals—2060(L)
Frost, L. S. Conductivity of seeded atmospheric pressure plasmas—2029
Fryer, E. M. (see Fowler, C. A., Jr.)—296S
Fujita, Hiroshi. (see Weissmann, Sigmund)—1156
Fuller, Harrison W., Harvey Rubinstein, and Donald L. Sullivan. Spiral walls in thin magnetic films—286S
Furutsu, K. and T. Ishida. On the theory of amplitude distribution of impulsive random noise—1206

Gabor, T. Anodic oxidation of germanium—1361
Garton, G. (see Ball, M.)—267S
Gatos, H. C., M. C. Finn, and M. C. Lavine. Antimony edge dislocations in InSb—1174(L)
—— Dangling bonds in III–V compounds—1232
——, **A. J. Strauss, M. C. Lavine and T. C. Harmon.** Impurity striations in unrotated crystals of InSb—2057(L)
Gazzara, Charles P. and Raymond M. Middleton. Temperature-compensated Debye temperature of carbonyl iron—1546
Geldmacher, R. C. On the macroscopic analysis of the conducting electromechanical solid with application to cylinders subjected to axial electric fields—143
Gerhardt, U. (see Gobrecht, H.)—2246
Germer, L. H., A. U. MacRae, and C. D. Hartman. (110) nickel surface—2432
Gershenzon, M. and R. M. Mikulyak. Electroluminescence at *p-n* junctions in gallium phosphide—1338
—— (see Frosch, C. J.)—2060(L)
Gerstner, Dieter and Eckart Kneller. High-temperature magnetic lag in iron-nickel alloys—364S

Geschwind, S. Anisotropy of YIG calculated from crystal field parameters Fe^{3+} in yttrium gallium garnet—263S
Giaever, I. (see Fisher, J. C.)—172
Gianola, U. F. Possibilities of all-magnetic logic—27S
Gibbs, P. (see Huber, R. J.)—2488(L)
—— (see Huber, R. J.)—2573
Gilbert, G. B., T. O. Poehler, and C. F. Miller. Study of electron bombardment of thin films—1597
Gilbert, J. F. (see Logan, R. A.)—1201
—— (see Logan, R. A.)—131(L)
Gilman, J. J. and B. W. Roberts. Elastic constants of TiC and TiB$_2$—1405(L)
—— Reduction of cohesion in ionic crystals by dislocations—738(L)
Gilvarry, J. J. Fracture of brittle solids. I. Distribution function for fragment size in single fracture (theoretical)—391
—— **and B. H. Bergstrom.** Fracture of brittle solids. II. Distribution function for fragment size in single fracture (experimental)—400
Gleichauf, P. H. and V. Ozarow. Electron-emission microscope and velocity distribution studies on silicon carbide p-n junction emitters—549(L)
Glenn, R. C. (see Michalak, J. T.)—1261
Gobrecht, H., U. Gerhardt, B. Peinemann, and A. Tausend. Electrical and optical properties of mercury selenide (HgSe)—2246
Godlove, Terry F. Nanosecond triggering of air gaps with intense ultraviolet light—1589
Goldberg, N. (see Matcovich, T.)—163S
Goldberg, Paul. Etch pits in electroluminescent zinc sulfide crystallites—1520
Goldfarb, Eli M. and Harry G. Heard. Full-voltage range spark-gap crowbar—326(L)
Goldsmid, H. J. Recent studies of bismuth telluride and its alloys—2198
Goldstein, B. and H. Keller. Diffusion of tin in gallium arsenide—1180(L)
Goldstein, H. L. (see Ollom, J. F.)—2059(L)
Goldstein, Y. Improved representation of calculated surface mobilities in semiconductors. II. Majority carriers—2540
—— (see Grover, N. B.)—2538
Goetzberger, A. and C. Stephens. Voltage dependence of microplasma density in p-n junctions in silicon—2646
Gooch, C. H., C. Hilsum and B. R. Holeman. Properties of semi-insulating GaAs—2069
Goodman, A. M. Short minority carrier diffusion lengths—2550
Goodman, S. R. (see Hu, Hsun)—1392
Goodwin, D. W. and R. H. Jones. Far infrared and microwave detector—2055
Goodwin, F. E. Maser action in emerald—1624(L)
Gordon, E. I. and A. Ashkin. Energy interchange between cyclotron and synchronous waves in quadrupolar pump fields—1137
—— (see Adler, R.)—672
Gottlieb, Milton (see Zollweg, R. J.)—890
Gould, R. W. and C. C. Johnson. Coupled mode theory of electron-beam parametric amplification—248
Gourley, L. E. (see Hughes, D. S.)—624
Gourley, Mary F. (see Hughes, D. S.)—624
Graham, C. D., Jr., and J. M. Lommel. Magnetic anisotropies of nickel films evaporated and measured at 10^{-8} mm Hg and below—83S
Graham, R. R. Piezoelectric behavior of impacted quartz—555(L)
Gran, B. E. (see Prosen, R. J.)—91S
Green, J. J. and E. Schlömann. Ferromagnetic relaxation at low microwave frequencies—168S
—— (see Saunders, J. H.)—161S
Green, Milton. Corbino disk—2047(L)
—— Corbino disk magnetoresistivity measurements on InSb—1286
Greenberg, J. Mayo, Norman E. Pedersen, and Jeanne C. Pedersen. Microwave analog to the scattering of light by nonspherical particles—233
Greener, E. H. and D. H. Whitmore. Nonohmic behavior in near-stoichiometric rutile (TiO$_2$)—1320
Greenfield, I. G. and H. G. F. Wilsdorf. Effect of neutron irradiation on the plastic deformation of copper single crystals—827
Greenler, Robert G. and Robert M. Kay. Electric breakdown strength of single and laminated films of vinyl chloride-acetate—1252
Greenwood, Allan (see Lee, T. H.)—916
—— (see Lee, T. H.)—2161(E)
Greifer, Aaron P., Yoshinao Nakada, and Howard Lessoff. Preparation and properties of low-loss ferrites—382S
Greiner, E. S., J. A. Gutowski, and W. C. Ellis. Preparation of silicon ribbons—2489(L)
Greiner, J. H., I. M. Croll, and M. Sulich. Unidirectional properties in the iron-iron sulfide system—188S
Grimmeiss, H. G. and A. Rabenau. Some properties of p-n junctions in GaP—2123
Grover, N. B., Y. Goldstein, and A. Many. Improved representation of calculated surface mobilities in semiconductors. I. Minority carriers—2538
—— (see Goldstein, Y.)—2540
Guggenheim, H. Growth of single-crystal calcium fluoride with rare-earth impurities—1337
Gutowski, J. A. (see Greiner, E. S.)—2489(L)
Gyorgy, E. M. (see Nesbitt, E. A.)—1305
—— (see Hagedorn, F. B.)—282S

Haas, C. (see Albers, W.)—2220
Haas, C. Warren and Herbert B. Callen. Ferromagnetic resonance linewidth in cobalt-substituted ferrites—157S
Haase, O. and R. D. Heidenreich. "Anamalous" electron double diffraction—1840
Hagedorn, F. B. and E. M. Gyorgy. Domain wall mobility in single-crystal yttrium iron garnet—282S
Hagelbarger, D. W. (see Kramer, H. P.)—764
Hagstrum, Homer D. Oxygen adsorption on silicon and germanium—1020
—— Effects of monolayer adsorption and bombardment damage or Auger electron ejection from germanium—1015
Hahan, E. L. (see Weger, M.)—124S
Hall, R. B. and Sanborn C. Brown. Reflection of an electron beam from high-frequency fields—1835
Hall, R. N. and J. H. Racette. Band structure parameter deduced from tunneling experiments—2078
—— **and J. H. Racette.** Distribution coefficients of impurities in gallium antimonide—856
Ham, F. S. (see Pell, E. M.)—1052
Hanlon, J. E. (see Wolf, J. D.)—2584
Harada, Roy (see McCaldin, J. O.)—557(L)
Hardy, Wilton A. Nuclear resonances in cubic, hexagonal, and mixed phase cobalt powders and thin films—122S
Hargreaves, C. M. On the growth of sapphire microcrystals—936
Harkins, P. A. (see Magnuson, G. D.)—369
—— (see Meckel, B. B.)—489
Harman, G. G. and R. L. Raybold. Measurement of minority carrier lifetime in SiC by a novel electroluminescent method—1168(L)
Harman, Theodore C. Angular dependence of magnetoresistance in HgSe—1800(L)
—— **and A. J. Strauss.** Band structure of HgSe and HgSe-HgTe alloys—2265
Harrick, N. J. Determination of the semiconductor surface potential under a metal contact—568

Harrison, Don E., Jr. Determination of the maximum lattice-chain energy from sputtering yield curves—924

Harrison, S. E. (see Kriessman, C. J.)—392S

Hartman, D. C. (see Germer, L. H.)—2432

Hartwick, T. S., E. R. Peressini, and M. T. Weiss. Subsidiary resonance in YIG—223S

Harumi, K. Scattering of plane waves by a rigid ribbon in a solid—1488

Hasiguti, Ryukiti R. (see Hiki, Yosio)—1647

Hassen, P. (see in der Schmitten, W.)—1790(L)

Hasty, Turner E. and Lee J. Boudreaux. Ferromagnetic resonance in thin magnetic films at radio frequencies—1807

Haszko, S. E. (see Wernick, J. H.)—2495(L)

—— (see McHugh, J. P.)—1785(L)

Hatch, Albert J. Electron bunching in the multipacting mechanism of high-frequency discharge—1086

Hatsopoulos, G. N. (see Carabateas, E. N.)—352

Haus, H. A. (see Bobroff, D. L.)—749(L)

—— Thermal noise in dissipative media—493

Hauser, J. J. (see Banerjee, B. R.)—556(L)

Healy, J. H. (see Uphoff, H. L.)—950

Heard, Harry G. (see Goldfarb, Eli M.)—326(L)

Heidenreich, R. D. (see Haase, O.)—1840

Heikes, R. R. (see Miller, R. C.)—2202

Heinecke, M. J. and S. Ing, Jr. Surface kinetics and physics investigation of the reaction between single-crystal germanium and iodine—1498

Heitmann, W. E. and R. W. Balluffi. Relative polygonization rates in copper and copper-zinc alloys—963(L)

Helfand, E. (see Reiss, H.)—228

Heller, G. S., J. J. Stickler, and J. B. Thaxter. Antiferromagnetic materials for millimeter and submillimeter devices—307S

Hensley, Eugene B. (see Stevenson, James R.)—166

—— Thermionic emission constants and their interpretation—301

Hernqvist, K. G. (see Eichenbaum, A. L.)—16

Hight, M. J. (see Teale, R. W.)—150S

—— (see Teale, R. W.)—140S

Hiki, Yosio and Ryukiti R. Hasiguti. Mosaic size in lead from x-ray measurements—1647

Hill, Robert M. and Robert S. Bergman. Nonlinear response of YIG—227S

Hillig, William B. Strength of bulk fused quartz—741(L)

—— **and R. J. Charles.** Concerning dislocations in glass—123(L)

Hilsum, C. (see Gooch, C. H.)—2069

Hines, R. L. and R. Wallor. Sputtering of vitreous silica by 20- to 60-kev Xe^+ ions—202

—— (see Arndt, R. A.)—1913

Hirabayashi, Makoto (see Weissmann, Sigmund)—1156

Hirsch, E. H. Flow of gas through porous media in the region between molecular and viscous condition—977

Hirschel, Louis R. and Louis F. Libelo. Nuclear magnetic resonance in flowing fluids—1404(L)

Hirth, J. P. On dislocation interactions in the fcc lattice—700

—— (see Banerjee, B. R.)—556(L)

Holaday, R. E. (see Dunn, D. A.)—1612

Holdaway, H. W. (see Carmichael, A. J.)—159

—— (see Carmichael, A. J.)—1724

Holeman, B. R. (see Gooch, C. H.)—2069

Hollander, Lewis E., Jr. Electrical conductivity and thermoelectric effect in single-crystal TiC—996

Holmen, J. O. (see Prosen, R. J.)—91S

Holonyak, Nick, Jr. Evidence for states (bands) in the forbidden gap of degenerate GaAS and InP—secondary tunnel currents and negative resistances—130(L)

Holroyd, Louis V. (see Srinivasan, Devanatha)—446

—— (see Macleay, Robert Q.)—449

Holscher, P. C. (see Trivelpiece, A. W.)—259

Hooper, G. D. (see Falk, R. B.)—190S

—— Properties of single-domain particles of cobalt-nickel—2536

Hooper, H. L. (see Culp, F. L.)—2480

Hopfield, J. J. Exciton states and band structure in CdS and CdSe—2277

—— (see Dietz, R. E.)—2282

Horgan, James D. and David L. Edwards. Forces in dielectric fluids—1784(L)

Hörl, E. and J. A. Suddeth. Electron energy loss at low temperatures—2521

Horn, F. H. Growth of single-crystal iron ferrites by the Czochralski method—900

Hornbogen, Erhard. Clustering in an alpha iron-molybdenum solid solution—132

Houde, A. L. Observations of cross-tie domain walls by the Faraday effect—1234

Howe, S. and C. Elbaum. Dislocation-free aluminum crystals—742(L)

Hsu, F. S. L. (see Buehler, E.)—325(L)

Hu, Hsun, R. S. Cline, and S. R. Goodman. Texture transition in high-purity silver and its correlation with stacking fault frequency—1392

—— **and R. S. Cline.** Temperature dependence of rolling texture in high-purity silver—760

Huber, R. J., G. S. Baker, and P. Gibbs. Damping effects of thin surface films—2488(L)

——**, G. S. Baker, and P. Gibbs.** High-temperature kilocycle internal friction—2573

Huffman, Fred N. Open circuit voltages in the cesium diode—1927

Hughes, D. S., L. E. Gourley, and Mary F. Gourley. Shock-wave compression of iron and bismuth—624

Hunt, Angus L., Charles C. Damm, and Earl C. Popp. Attainment of ultrahigh vacua, reduction in surface desorption, and the adsorption of hydrogen by evaporated molybdenum—1937

Hunt, R. P. (see Epstein, D. J.)—270S

Hurley, James. Drift velocity of a charged particle in an inhomogeneous magnetic field—2368

Hurwitz, H., Jr., R. W. Kilb, and G. W. Sutton. Influence of tensor conductivity on current distribution in a MHD generator—205

Hutson, A. R. Piezoelectric scattering and phonon drag in ZnO and CdS—2287

Ignatius, A. (see Trivelpiece, A. W.)—259

in der Schmitten, W. and P. Hassen. Dislocation density and flow stress of sodium chloride—1790(L)

Ing, S., Jr. (see Heinecke, W. J.)—1498

Ingold, John H. Calculation of the maximum efficiency of the thermionic converter—769

—— Thermionic properties of HfC—2651(L)

Ingraham, J. N. (see Swoboda, T. J.)—374S

Ingraham, R. L. Theory of the potential well produced by multipacting electrons. Part I. Very low pressure regime—2553

Ishida, T. (see Furutsu, K.)—1206

Ishii, Koryu (see Wang, Franklin F. Y.)—1621(L)

Ito, Kasuhiko. Thermorheological simplicity in extrusion flow curves of high polymers—1743

Ives, M. B. Orientation-dependent dissolution of lithium fluoride—1534

Jaccarino, V. NMR and the conduction electron polarization in rare-earth metals—102S

Jacobs, I. S. and J. S. Kouvel. Exchange anisotropy in mixed manganites with the hausmannite structure—274S

—— Spin-flopping in MnF_2 by high magnetic fields—61S

Jacobson, R. L. (see Mueller, R. K.)—1406(E)
—— (see Mueller, R. K.)—550(L)
Jahn, Robert G. (see Albini, Frank A.)—75
Jamerson, F. E. (see Luke, K. P.)—321(L)
—— (see Abrams, R. H., Jr.)—1783(L)
James, R. H., W. M. Overn, and C. W. Lundberg. Flux distribution in ferrite cores under various modes of partical switching—38S
James, W. J. (see Straumanis, M. E.)—1382
Janssen, K. (see Baran, W.)—199S
Jarrett, H. S., P. E. Bierstedt, F. J. Darnell, and M. Sparks. Magnetic anisotropy and electrical resistivity in exchange inversion compounds—57S
Jefferson, Clinton F. and Russell G. West. Ferrite system for application at lower microwave frequencies—390S
Jellinek, H. H. G. Liquidlike layers on ice—1793(L)
Jenkins, Alvin W., Jr. (see Tterlikkis, Lambros)—1293
Jenkins, R. J. (see Parker, W. J.)—1679
Jepsen, R. L. Harmonic generation and frequency mixing in ferromagnetic insulators—2627
—— Magnetically confined cold-cathode gas discharges at low pressures—2619
Johansen, I. J. T. (see Powers, D. A.)—1083
Johnson, C. C. (see Gould, R. W.)—248
Johnson, Clark, E., Jr., and William Fuller Brown, Jr. Theoretical magnetization curves for particles with cubic anisotropy—243S
Johnson, F. A. (see Cochran, W.)—2102
Johnson, Peter D. Dichroic color centers in calcium fluorophosphate—127(L)
Johnston, W. G. (see Nadeau, J. S.)—2563
Jones, R. H. (see Goodwin, D. W.)—2055(L)
Joseph, R. I. and E. Schlömann. Theory of magnetostatic modes in long, axially magnetized cylinders—1001
—— (see Schlömann, E.)—1006
—— (see Schlömann, E.)—165S
Jovanovic, Stanka and Cyril Stanley Smith. Elastic modulus of amorphous nickel films—121(L)
Judge, Jane T. and Richard S. Stein. Growth of crystals from molten crosslinked oriented polyethylene—2357
Julien, Carl A. (see Campbell, Robert B.)—192S
—— (see Campbell, Robert B.)—346S
Juretschke, H. J. (see Coren, R. L.)—292S

Kaiser, W. and C. D. Thurmond. Solubility of oxygen in germanium—115
Kaminow, I. P. (see Dymanus, A.)—144S
Kanai, Yasuo, Riro Nii, and Naozo Watanabe. Electrical properties of lead telluride—2146
Kane, Evan O. Theory of tunneling—83
Kaplan, Asa. Magnetic core losses resulting from a rotating flux—370S
Kaplan, Jerome I. Nonlinear effects of z-directed spin waves in thin films—1831
Kaplan, T. A., K. Dwight, D. Lyons, and N. Menyuk. Classical theory of the ground spin state in spinels—13S
Kaufman, I. (see Douthett, D. D.)—1905
Kauppila, James E. (see Bockemuehl, Robert R.)—1324
Kay, Eric. Magnetic thin films prepared by sputtering—99S
Kay, Robert M. (see Greenler, Robert G.)—1252
—— (see Wycklendt, Daniel A.)—368S
Keffer, F., A. H. Sievers, III, and M. Tinkham. Infrared antiferromagnetic resonance in MnO—65S
—— **and R. Loudon.** Simple physical theory of spin wave interactions—2S
Keiffer, David (see Primak, William)—660
Keller, H. (see Goldstein, B.)—1180(L)
Keller, Joseph B. (see Rubinow, S. I.)—814
Kelley, R. H. (see Kulp, B. A.)—1290
Kelly, J. C. Voids in resolidified drops of molten metal—1797(L)
Kerr, Nancy A. Determination of certain spectral distributions of soft x rays by theoretical analysis of absorption experiments—2465
Kilb, R. W. (see Hurwitz, H., Jr.)—205
Kingery, W. D. and G. E. Meiling. Transference number measurements for aluminum oxide—556(L)
Kirkpatrick, H. B. (see Delavignette, P.)—1098
Kleiner, W. H. (see Zwerdling, S.)—2118
Klüver, J. W. Parametric coupling between the transverse waves on O- and M-type beams—1111
—— (see Bobroff, D. L.)—749(L)
Kneller, Eckart (see Gerstner, Dieter)—364(S)
Knippenberg, W. F. (see van Daal, H. J.)—2225
Koehler, W. C. (see Wilkinson, M. K.)—48S
—— (see Cable, J. W.)—49S
—— Neutron diffraction by helical spin structures—20S
Koh, P. K. Cube texture in ultrathin molybdenum permalloy tape—358S
Kolm, Henry H. and Osman K. Mawardi. Hydromagnet: a self-generating liquid conductor electromagnet—1296
Komarek, K. (see Miller, E.)—2457
Koppenaal, T. J. and M. E. Fine. Acoustical study of quench-aging in α Cu-Al alloys—1781
Korostoff, E. (see Matcovich, T.)—93S
Koster, G. F. (see Statz, H.)—218S
—— **and H. Statz.** Probabilities for the neon laser transitions—2054(L)
Kostyk, B. M. (see Verderber, R. R.)—696
Kotik, J. and M. C. Newstein. Theory of laser oscillations in Fabry-Perot resonators—178
Kottenstette, James P. (see Murgai, Mahinder P.)—324(L)
Kouvel, J. S. and R. H. Wilson. Magnetocrystalline anisotropy of Fe-Si alloy crystals under hydrostatic pressure—276S
—— (see Jacobs, I. S.)—274S
—— **and R. H. Wilson.** Magnetization of iron-nickel alloys under hydrostatic pressure—435
Kovacs, A. J. (see Rabesiaka, J.)—2314
Kramer, H. P., B. P. Bogert, and D. W. Hagelbarger. Stability of pressure-supported molten zones in horizontal sheets—74
Kriessman, C. J. and S. E. Harrison. Cation distributions in magnesium-nickel ferrites—392S
Krimm, S. (see Onishi, T.)—2320
Kronenberg K. J. Crystal lattice investigation of the permanent magnet precipitate in various Alnico materials—196S
Ku, T. C. and W. T. Pimbley. Effect of temperature on the emission of electrons from abraded surfaces of beryllium, calcium, aluminum, and magnesium—124(L)
Kuglin, C. D. (see Cuff, K. F.)—2179
Kulp, B. A. Effect of electron bombardment of the near-infrared fluorescence of single crystal CdS—1966
—— **and R. H. Kelley.** p-type photoconductivity and infrared quenching in electron-bombarded CdS—1290
Kunz, William E. (see Sirkis, Murray D.)—2055(L)
Kurnick, S. W. (see Appel, J.)—2206
Kydd, P. H. (see Mullaney, G. J.)—668

Laegreid, Nils and G. K. Wehner. Sputtering yields of metals for Ar$^+$ and Ne$^+$ ions with energies from 50 to 600 ev—365
Lafferty, J. M. Hot-cathode magnetron ionization gauge for the measurement of ultrahigh vacua—424
Langenberg, D. N. (see Stiles, P. J.)—2174
Langer, G. and J. L. Radnik. Development and preliminary testing of a device for electrostatic classification of submicron airborne particles—955

Larrabee, Robert D. Majority carrier magneto-surface effect—2019
Larson, O. W. (see Reynolds, D. C.)—2250
Laukonis, J. V. and R. V. Coleman. Iron whisker surface rearrangements resulting from the hydrogen reduction of oxides and from thermal etching—242
Lauttman, R. G. (see Stein, M. N.)—2352
Lavik, Melvin T., T. Bruce Daniel, and A. Neal Abbott. Friction of molybdenum diselenide—1795(L)
Lavine, M. C. (see Gatos, H. C.)—1174(L)
Law, J. T. Some experiments using a vacuum-cleaned silicon *p-n* junction—848
—— Surface electrical changes caused by the adsorption of hydrogen and oxygen on silicon—600
Lawrence, Philip E. (see Luborsky, Fred E.)—231S
Lawson, A. W. (see Eckstein, Yakov)—752(E)
Lax, Benjamin and Yuichiro Nishina. Interband Faraday rotation in III–V compounds—2128
—— (see Wright, George B.)—2113
Leask, M. J. M. (see Ball, M.)—267S
LeCraw, R. C. and L. R. Walker. Temperature dependence of the spin-wave spectrum of yttrium iron garnet—167S
Lee, C. H. and R. Maddin. Effect of torsional deformation on self-diffusion in silver—1846
Lee, T. H. and Allan Greenwood. Theory for the cathode mechanism in metal vapor arcs—916
—— **and Allan Greenwood.** A theory for the cathode mechanism in metal vapor arcs—2161(E)
Lefever, R. A., Juanita W. Torpy, and A. B. Chase. Growth of single crystals of yttrium aluminum garnet from lead oxide-lead fluoride melts—962(L)
Legvold, Sam. (see Born, H. J.)—2543
Lemaire, Henry P. and William J. Croft. Ferrite thin films—46S
Leman, G. (see Friedel, J.)—325S
Lengyel, B. A. and K. M. Mitzner. Electromagnetic surface waves on a plane interface—1758
Lessoff, Howard (see Greifer, Aaron P.)—382S
Levengood, W. C. Defect mechanisms in a noncrystalline solid—2525
Levine, L. P. (see Targ, R.)—731
Lewis, T. J. and P. E. Secker. Influence of the cathode surface on arc velocity—54
Li, Che-Yu, A. L. Ruoff, and C. W. Spencer. Effect of pressure on the energy gap of Bi_2Te_3—1733
Li, James C. M. Cross slip and cross climb of dislocations induced by a locked dislocation—593
—— Energy of a cross grid of screw dislocations—1873
—— High-angle tilt boundary—a dislocation core model—525
Libelo, Louis F. (see Hirschel, Louis R.)—1404(L)
Lin, C. J. Behavior of ferro- or ferrimagnetic very fine particles—233S
Lin, S. T. Remanent magnetization of a synthetic hematite single crystal—394S
Linhart, J. G. Dynamic stability of a conducting, cylindrical shell in a magnetic field—500
Link, G. L. The motion of *c* domain centers in $BaTiO_3$—2566
Lipsitt, H. A. (see Marcinkowski, M. J.)—1238
Littman, Howard and Burton Davidson. Theoretical bound on the thermoelectric figure of merit from irreversible thermodynamics—217
Livingston, J. D. and C. P. Bean. Specific heat of superparamagnetic particles—1964
Lo, Y. T. On the theoretical limitation of a radio telescope in determining the sky temperature distribution—2052(L)
Logan, R. A., W. M. Augustyniak, and J. F. Gilbert. Electron bombardment damage in silicon Esaki diodes—1201
——**, J. F. Gilbert, and F. A. Trumbore.** Electron mobilities and tunneling currents in silicon—131(L)
—— (see Spitzer, W. G.)—1822
Loh, E. and R. Newman. Infrared properties of flame-fused MnO crystals—470
Lommel, J. M. (see Graham, C. D., Jr.)—83S
Long, Donald. Stress dependence of the piezoresistance effect—2050(L)
Loudon, R. (see Keffer, F.)—2S
Luborsky, Fred E. Development of elongated particle magnets—171S
—— **and Philip E. Lawrence.** Saturation magnetization and size of iron particles less than 100 A in diameter—231S
Ludeke, Carl A. Guidance and collimation of sputtered tungsten particles—1400(L)
Luke, K. P. and F. E. Jamerson. Low-frequency oscillations in a filamentary cathode cesium diode converter—321(L)
Lundberg, C. W. (see James, R. H.)—38S
Lyons, D. (see Kaplan, T. A.)—13S

McCaldin, J. O. and Roy Harada. Influence of arsenic pressure on the doping of gallium arsenide with germanium—557(L)
—— **and D. B. Wittry.** Germanium saturated with gallium antimonide—65
McCall, Gilbert (see Bady, Isidore)—146S
McCarroll, W. H. Crystal structure of photoelectric films of cesium antimonide—2054(L)
McEwan, William S. (see Mallory, H. Dean)—2421
McHugh, J. P. (see Cosgrove, G. J.)—621
——**, W. A. Tiller, S. E. Haszko, and J. H. Wernick.** Phase diagram for the pseudobinary system $Ag_2Te—Sb_2Te_3$—1785(L)
McIntyre, R. J. Theory of microplasma instability in silicon—983
McKelvey, J. P. Recombination of excess carriers at twin structures in germanium—442
McLachlan, Dan, Jr. Similarity function for pattern recognition—1795(L)
McMahon, H. O. (see Miles, J. L.)—1176(L)
McSkimin, H. J. (see Bateman, T.)—928
MacDonald, Harold E. (see Blanc, Joseph)—1666
Macdonald, J. Ross. Theory and application of a superposition model of internal friction and creep—2385
MacAvoy, T. C. (see Marley, J. A.)—2504
Machlup, S. and M. E. Christopher. Piezoelectricity of quartz for finite strain—1387
Macleay, Robert Q. and Louis V. Holroyd. Space-time analysis of the sonoluminescence emitted by cavitated water—449
MacRae, A. U. (see Germer, L. H.)—2432
Madden, Hannibal H., Jr. (see Farnsworth, H. E.)—1933
Maddin, R. (see Lee, C. H.)—1846
Madigan, John R. (see Reich, Allen D.)—294
—— (see Reich, A. D.)—2493(L)
—— (see Arai, Thomas T.)—609
Magnuson, G. D., B. B. Meckel, and P. A. Harkins. Etch effects from oblique-incidence ion bombardment—369
Maitland, A. New derivation of the vacuum breakdown equation relating breakdown voltage and electrode separation—2399
Malinofsky, W. W. and R. W. Babbitt. Fine-grained ferrites. I. Nickel ferrite—237S
Mallory, H. Dean and William S. McEwan. Transparency of glass and certain plastics under shock attack—2421
Mandelkern, L., A. S. Posner, A. F. Diorio, and D. E. Roberts. Low-angle x-ray diffraction of crystalline non-

oriented polyethylene and its relation to crystallization —1509

Many, A. (see Grover, N. B.)—2538

— (see Goldstein, Y.)—2540

Marcinkowski, M. J. and H. A. Lipsitt. Electrical resistivity of chromium in the vicinity of the Néel temperature—1238

—— **and N. Brown.** Transformation—disorder to order in Ni$_3$Mn—375

Marcuse, D. Stimulated emission from HCN gas maser observed at 88.6 kMc—743(L)

Maringer, R. E. Some effects of directional ordering in zone-melted iron—366S

Marley, J. A. and T. C. MacAvoy. Growth of stannic oxide crystals from the vapor phase—2504

Marple, D. T. F. (see Aven, M.)—2261

—— (see Piper, W. W.)—2237

Martius, U. M. and W. J. Bratina. Frequency dependence of ultrasonic wave attenuation in Armco iron and low-carbon steel—280S

Marton, L. (see Fowler, H. A.)—1153

Mason, Donald R. and J. Stanley Cook. Zone leveling and crystal growth of peritectic compounds—475

Mason, W. P. (see Bateman, T.)—928

Matcovich, T., Henry S. Belson, and N. Goldberg. Resonant frequency shift in ellipsoidal samples—163S

——, **E. Korostoff, and A. Schemeckenbecher.** Anisotropy rotation in thin permalloy films at room temperature—93S

Matsuoka, Shiro. Hypothesis of voids in semicrystalline polymers—2334

Matthias, B. T. (see Buehler, E.)—325(L)

Mawardi, Osman K. (see Kolm, Henry H.)—1296

Mazelsky, R. (see Eusner, R. L.)—1833

—— (see Miller, R. C.)—2202

Mead, C. A. Operation of tunnel-emission devices—646

Meckel, B. B. (see Magnuson, G. D.)—369

—— **and P. A. Harkins.** Production and analysis of a large-diameter plasma beam—489

Medicus, G. Theory of electron collection of spherical probes —2512

Meechan, C. J. Experimental study of intermetallic diffusion in large temperature gradients—945

Meikeljohn, W. H. Exchange anisotropy in stainless steel —274S

Meiling, G. E. (see Kingery, W. D.)—556(L)

Mendelson, S. Birefringence due to dislocations in glide bands of rocksalt single crystals—1999

—— Dislocation etch pit formation in sodium chloride—1579

Menyuk, N. (see Kaplan, T. A.)—13S

Meredith, Robert E. and Charles W. Tobias. Resistance to potential flow through a cubical array of spheres—132(E)

Merz, Walter J. (see Fatuzzo, Ennio)—1685

Messmer, J. H. (see Woodside, W.)—1688

—— (see Woodside, W.)—1699

Methfessel, S., S. Middelhoek, and H. Thomas. Nucleation processes in thin Permalloy films—294S

——, **S. Middelhoek, and H. Thomas.** Partial rotation in Permalloy films—1959

Meyer, A. J. P. and G. Asch. Experimental g' and g values of Fe, Co, Ni, and their alloys—330S

Michalak, J. T. and R. C. Glenn. Transmission electron microscope observations of magnetic domain walls—1261

Middelhoek, S. (see Methfessel, S.)—294S

—— (see Methfessel, S.)—1959

Middleton, F. H. Analytic hysteresis function—251S

Middleton, Raymond M. (see Charles P. Gassara)—1546

Mikulyak, R. M. (see Gershenzon, M.)—1338

Miles, J. L. and H. O. McMahon. Use of monomolecular layers in evaporated-film tunneling devices—1176(L)

Miles, P. A. and H. E. Edgerton. Optically efficient ruby laser pump—740(L)

Miller, C. F. (see G. B. Gilbert)—1597

Miller, D. S. (see Arajs, Sigurds)—857

Miller, E., K. Komarek and I. Cadoff. Interrelation of electronic properties and defect equilibria in PbTe—2457

Miller, H. C. (see Oppegard, A. L.)—184S

Miller, M. H. Quasi-Brillouin electron streams—1791(L)

—— **and W. G. Dow.** Experimental study of anomalous electron stream behavior—274

Miller, R. C., R. R. Heikes, and R. Mazelsky. Model for the electronic transport properties of mixed valency semiconductors—2202

—— (see Sagar, A.)—2073

Miller, Robert C. and Albert Savage. Motion of 180° domain walls in BaTiO$_3$ under the application of a train of voltage pulses—714

Milmoe, James O. (see Murgai, Mahinder P.)—324(L)

Mims, W. B. (see Forrester, P. A.)—317

Mitzner, K. M. (see Lengyel, B. A.)—1758

Miwa, Hirosi (see Yosida, Kei)—8S

Miyake, Kiyoshi. Measurement of the partial pressure of cesium over cesium antimonides—1132

Mojoni, A. (see Bonfiglioli, G.)—2499

Monforte, F. R., F. W. Swanekamp, and L. G. Van Uitert. Radio-frequency technique for pulling oxide crystals without employing a crucible susceptor—959(L)

Montalenti, G. (see Biorci, G.)—630

Montgomery, M. D. Excess noise in germanium and gallium-arsenide Esaki diodes in the negative resistance region—2408

Moore, D. B. (see Muller, G. M.)—1065

Moore, George E. Dissociation of adsorbed Co by slow electrons—1241

Moore, R. G., Jr. (see Clingman, W. H.)—675

Morin, F. J. Halides, oxides, and sulfides of the transition metals—2195

Morrish, A. H. (see Bonstrom, D. B.)—272S

Moruzzi, Victor L. Triangular moment arrangements in manganese-iron spinels—59S

Moser, F., D. C. Burnham, and H. H. Tippins. Zone refining of the silver halides—48

Moss, T. S. Optical absorption edge in GaAs and its dependence on electric field—2136

Mueller, R. K. and R. L. Jacobson. Growth twins in indium antimonide—1406(E)

—— **and R. L. Jacobson.** Growth twins in indium antimonide—550(L)

—— Current flow across grain boundaries in n-type germanium. I.—635

—— Current flow across grain boundaries in n-type germanium. II.—640

Mueller, W. M. Propagation in periodic electron beams—1349

Mullaney, G. J., P. H. Kydd, and N. R. Dibelius. Electrical conductivity in flame gases with large concentrations of potassium—668

Muller, Erwin W. and Russell D. Young. Determination of field strength for field evaporation and ionization in the field ion microscope—2425

—— (see Waclawski, B. J.)—1472

Muller, G. M., D. B. Moore, and D. Bernstein. Growth of explosion in electrically initiated RDX—1065

Muller, M. W. and A. Wehlau. Magnetization curve of an infinite cylinder—2448

—— **and C. R. Buffler.** Anisotropy of the spin-wave spectrum—152S

Mura, T., I. Tamura, and J. O. Brittain. On the internal friction of cold-worked and quenched martensitic iron and steel—92

Murgai, Mahinder P., James O. Milmoe, James P. Kottenstette, and Fred L. Smith. On a problem in the thermal stability of explosives—324(L)
Murray, G. T. Precipitation of helium along dislocations in aluminum—1045
Muss, D. R. and J. R. Townsend. Energy dependence of radiation damage in tungsten—189

Nadeau, J. S. and W. G. Johnston. Hardening of LiF crystals by irradiation—2563
Nagorsen, G. and B. L. Averbach. Small-angle scattering in gold-nickel alloys—688
Nakada, Yoshinao (see Greifer, Aaron P.)—382S
Naseledov, D. N. Energy of spectrum and scattering of current carriers in gallium arsenide—2140
Nassau, K. Application of the Czochralski method to divalent metal fluorides—1820
Nassenstein, H. Electrical control of the critical angle of total reflection—2488(L)
Nelson, C. M. and R. A. Weeks. Vacuum-ultraviolet absorption studies of irradiated silica and quartz—883
Nelson, D. F. and R. J. Collins. Spatial coherence in the output of an optical maser—739(L)
Nesbitt, E. A. and E. M. Gyorgy. Two-phase Permalloy for high-speed switching—1305
——, H. J. Williams, J. H. Wernick, and R. C. Sherwood. Magnetic moments of compounds of cobalt with rare-earth elements having a Cu_5Ca structure—342S
Newman, R. (see Loh, E.)—470
Newstein, M. C. (see Kotik, J.)—178
Niblett, D. H. Low-frequency measurements on the Bordoni internal friction peak in copper—895
Nii, Riro (see Kanai, Yasuo)—2146
Nickel, J. C. (see Wild, R. L.)—520
Nishina, Yuichiro (see Lax, Benjamin)—2128
Noble, F. E. and J. E. Thomas, Jr. Effect of gaseous ambients upon $1/f$ noise in germanium filaments—1709
Nomura, K. C. Analytic solution of the double-diffusion problem—1167(L)
—— (see Blakemore, J. S.)—745(L)
Noreika, A. H. (see Francombe, M. H.)—97S
Norwood, M. H. Theory and experiment of a thermoelectric cooler—2559

Ogawa, Tomoya. Measurement of the electrical conductivity and dielectric constant without contacting electrodes—583
Ogier, W. T. (see Wild, R. L.)—520
Okazaki, Susumu. Confirmation of lifetimes by noise and by Haynes-Shockley method—712
Ollom, J. F. and H. L. Goldstein. Effect of frequency modulation on subsidiary resonance in ferrites—2059(L)
Olsen, K. H. (see Sallo, J. S.)—203S
Olszewski, S. (see Friedel, J.)—325S
Onishi, T. and S. Krimm. Origins of characteristic bands in the infrared spectra of isotactic polystyrene and isotactic poly(ring-d_5 styrene)—2320
Oppegard, A. L., F. J. Darnell, and H. C. Miller. Magnetic properties of single-domain iron and iron-cobalt particles prepared by borohydride reduction—184S
—— (see Swoboda, T. J.)—374S
Otte, Henry M. Lattice parameter determinations with an x-ray spectrogoniometer by the Debye-Scherrer method and the effect of specimen condition—1536
Overmeyer, James. Microwave resonance in tetragonally distorted manganese-iron spinel—142S
Overn, W. M. (see James, R. H.)—38S
Owen, J. Paramagnetic resonance measurements of exchange interactions—213S
Ozarow, V. (see Gleichauf, P. H.)—549(L)

Pagel, B. R. and R. L. Petritz. Noise in InSb photodiodes—1901
Palik, E. D., S. Teitler, and R. F. Wallis. Free carrier cyclotron resonance, Faraday rotation, and Voigt double refraction in compound semiconductors—2132
Paoletti, A. and M. Vicentini-Missoni. Diffusion in a liquid indium-tin alloy at several concentrations—559
—— and M. Vicentini. Diffusion in a liquid indium-tin alloy at the eutectic concentration—22
Papadakis, Emmanuel P. and Everett L. Reed. Ultrasonic detection of changes in the elastic properties of a 70-30 iron-nickel alloy upon heat treatment—682
Papirno, Ralph. Stress and strain in thin films bulged over circular openings—1175(L)
Paré, Victor K. Study of the Bordoni internal friction peaks in copper—332
Parker, W. J., R. J. Jenkins, C. P. Butler, and G. L. Abbott. Flash method of determining thermal diffusivity, heat capacity, and thermal conductivity—1679
Parzen, Philip. Radiation from a modulated electron beam with a plasma background—2484
Paschke, F. Note on the mechanism of the multipactor effect—747(L)
Patrick, Lyle. Electron emission from reverse-biased p-n junctions in SiC—2047(L)
Paul, William. Band structure of the intermetallic semiconductors from pressure experiments—2082
Pavlik, Norman. High-temperature stability of magnetic materials—372S
Paxton, G. W. (see Rocard, J. M.)—1171(L)
Paxton, H. W. (see Cooper, H. W.)—2506
Pearson, R. F. and R. W. Cooper. Torque measurements on rare-earth doped yttrium iron garnet—265S
—— (see Teale, R. W.)—150S
Pease, M. C. Generalized coupled mode theory—1736
—— Transduction of noise. Theory of a generalized traveling-wave coupler—1145
Pedersen, Jeanne C. (see Greenberg, J. Mayo)—233
Pedersen, Norman E. (see Greenberg, J. Mayo)—233
Pedrotti, L. S. (see Reynolds, D. C.)—2250
Peinemann, B. (see Gobrecht, H.)—2246
Pell, E. M. Study of Li-O interaction in Si by ion drift—1048
—— and F. S. Ham. Recombination kinetics for thermally dissociated Li-B ion pairs in Si—1052
Penfield, Paul, Jr. Available power from a nonideal thermal source—1794(L)
Peressini, E. R. (see Hartwick, T. S.)—223S
Perry, R. L. Experimental evidence for the existence of two distinct field emission characteristics from silicon emitters—128(L)
Persson, K. B. A method for measuring the conductivity in a high electron density plasma—2631
Peter, Martin. Paramagnetic resonance of ^8S state ions in metals—338S
Petritz, R. L. (see Pagel, B. R.)—1901
Pezaris, S. D. (see Carabateas, E. N.)—352
Pfann, W. G. and R. N. Thurston. Semiconducting stress transducers utilizing the transverse and shear piezoresistance effects—2008
Phillips, R. L., R. G. DeLosh, and D. E. White. Microwave propagation through a magnetoplasma—1406(E)
——, R. G. DeLosh, and D. E. White. Microwave propagation through a magnetoplasma—551(L)
Phillips, W. L., Jr. Lattice parameter studies of impurity effects on plastic properties of lithium fluoride—751(L)
Pickard, William F. Experimental investigation of the Sumoto effect—1888
Piekoszewski, J. (see Czachor, A.)—1837
Pierce, J. R. Momentum and energy of waves—2580

Pierce, R. D. and S. A. Friedberg. Magnetic susceptibility of FeCl$_2$·4H$_2$O at low temperatures—66S
Pigon, Krzysztof. A graphical method for determination of mobility ratio in the semiconductors from Hall effect measurements only—2369
Pimbley, W. T. and E. E. Francis. Effect of temperature on the exoemission of electrons from abraded aluminum surfaces—1729
—— (see Ku, T. C.)—124(L)
Piper, W. W. and D. T. F. Marple. Optical properties of free electrons in CdS—2237
—— **and S. J. Polich.** Vapor-phase growth of single crystals of II–VI compounds—1278
Poehler, T. O. (see G. B. Gilbert)—1597
Pohl, Herbert A. Formation of liquid jets in nonuniform electric fields—1784(L)
Pohm, A. V. (see Daughton, J. M.)—36S
Polich, S. J. (see Piper, W. W.)—1278
Popp, Earl C. (see Hunt, Angus L.)—1937
Porter, John F., Jr. Use of PrCl$_3$ in a solid-state infrared quantum counter—1803(E)
—— Use of PrCl$_3$ in a solid state infrared quantum counter—825
Porter, Roger S. and Julian F. Johnson. Non-Newtonian viscosity of polymers—2326
Portis, A. M. (see Weger, M.)—124S
Posner, A. S. (see L. Mandelkern)—1509
Powers, D. A. and I. J. T. Johansen. Electric strength of rutile single crystals—1083
Preziosi, S. (see Van Uitert, G.)—1176(L)
Price, P. B. Nonbasal glide in dislocation-free cadmium crystals. I. The $(10\bar{1}1)$ $[1\bar{2}10]$ system—1746
—— Nonbasal glide in dislocation-free cadmium crystals. II. The $(11\bar{2}2)$ $[\bar{1}\bar{1}23]$ system—1750
Priest, J., C. Chiou, and H. L. Caswell. Characteristics of the annealing kinetics of tin films deposited at 88°K—1772
Primark, William, Herman Szymanski, and David Keiffer. Frequency factors for annealing fast-neutron induced density changes in vitreous silica—660
Prince, E. Structure of nickel chromite—68S
Prosen, R. J., J. O. Holmen, and B. E. Gran. Rotatable anisotropy in thin Permalloy films—91S
Prussin, S. Generation and distribution of dislocations by solute diffusion—1876
Pugh, E. W. and B. E. Argyle. Low-temperature pyromagnetic measurements on nickel—334S

Quarrington, J. E. (see Cochran, W.)—2102
Queisser, H. J. Slip patterns on boron-doped silicon surfaces—1776
—— (see Shockley, William)—510

Rabenau, A. (see Grimmeiss, H. G.)—2123
Rabesiaka, J. and A. J. Kovacs. Isothermal crystallization kinetics of polyethylene. III. Influences of the sample preparation—2314
Rabinowicz, E. Influence of surface energy on friction and wear phenomena—1440
Racette, J. H. (see Hall, R. N.)—2078
—— (see Hall, R. N.)—856
Radnik, J. L. (see Langer, G.)—955
Rado, George T. Report on ferromagnetic resonance at the 1960 conference on magnetism and magnetic materials—129S
Ramdas, A. K. (see Becker, W. M.)—2094
Ramsey, T. H., Jr. (see Abernethy, L. L.)—376S
Raybold, R. L. (see Harman, G. G.)—1168(L)
Raymo, C. T., C. W. Brands, and B. Schwartz. Surface potential of silicon—1165(L)
Read, A. A. (see Daughton, J. M.)—36S
Rediker, R. H. and A. R. Calawa. Magnetotunneling in lead telluride—2189
Reed, Everett L. (see Papadakis, Emmanuel P.)—682
Reed, Thomas B. Induction-coupled plasma torch—821
—— Growth of crystals using induction plasma torch—2534
Reese, W. E. (see Turner, W. J.)—2241
Reich, Allen D. and John R. Madigan. Transient response of a thermocouple circuit under steady currents—294
——**, T. Arai, and J. R. Madigan.** Transient effects in Peltier coolers—2493(L)
Reiling, G. H. (see Farrall, G. A.)—1528
Reiss, H. and E. Helfand. Analytical solutions for some zone melting problems—228
Reitz, John R. Peltier coefficient at high current levels—1623(L)
Remde, Harry F. Effect of cobalt oxide in porous nickel ferrites at very high frequency—384S
Reneker, Darrell H. (see Eckstein, Yakov)—752(E)
Reynolds, C. E. and G. E. Seay. Multiple shock wave structures in polycrystalline ferroelectrics—1401(L)
Reynolds, D. C., L. S. Pedrotti, and O. W. Larson. Edge emission in zinc selenide single crystals—2250
Rhodes, Marion B. and Richard S. Stein. Light scattering study of the annealing of drawn polyethylene—2344
Rich, J. A. Resistance heating in the arc cathode spot zone—1023
Richard, N. A. (see Austin, A. E.)—1462
Richards, L. M. (see Wild, R. L.)—520
Riederman, N. H. (see Banks, E.)—44S
Riley, W. F. (see Durelli, A. J.)—1255
Rimai, L. (see Statz, H.)—218S
Rinehart, John S. (see Auberger, Michel)—219
Riney, T. D. Residual thermoelastic stresses in bonded silicon wafers—454
Risley, A. S. (see Douthett, D. D.)—1905
Roberts, B. W. (see Gilman, J. J.)—1405(L)
Roberts, D. E. (see L. Mandelkern)—509
Roberts, M. W. (see Thomas, K.)—70
Roberts, Roy W. (see Barry, Don)—1405(L)
Robinson, D. L. (see Frank, G. R.)—1763
Rocard, J. M. and G. W. Paxton. Relaxation oscillations in a plasma diode—1171(L)
Rodot, H. (see Rodot, M.)—2245
Rodot, M., H. Rodot, and R. Triboulet. Some properties of HgSe-HgTe solid solutions—2254
Rohatgi, V. K. Electronic and ionic current at the cathode of a hollow-cathode discharge—1173(L)
Rollins, F. R., Jr. Use of graphite whiskers in a study of the atmosphere dependence of graphite friction—1454
Romanow, W. J. (see Wernick, J. H.)—2495(L)
Rosenbaum H. S. and M. M. Saffren. Dislocation etch pits on the basal plane of zinc crystals—1866
Rosenberg, D. (see Wehner, G. K.)—887
Rosenblatt, J. On three-dimensional space charge flow—1803(E)
Ross, John W. (see Abernethy, L. L.)—376S
Rowen, J. H., F. G. Eggers, and W. Strauss. Generation of microwave electromagnetic radiation in magnetic materials—313S
Rowley, J. J. Phase shift studies in ferrite-dielectric loaded coaxial lines at 2200 Mc—321S
Rubenstein, C. Lubrication of polymers—1445
Rubinow, S. I. and Joseph B. Keller. Shift of the shadow boundary and scattering cross section of an opaque object—814
Rubinstein, Harvey (see Fuller, Harrison W.)—286S
—— (see Spain, Robert J.)—288S
Rudisill, J. E. (see Doyle, W. D.)—1785(L)
Rudman, P. S. (see Bertina Fisher)—1604

Rudnick, Philip. Likelihood detection of small signals in stationary noise—140
Rueda, F. and W. Dekeyser. Charged dislocations in ionic crystals—1799(L)
Ruedl, E., P. Delavignette, and S. Amelinckx. Fission fragment damage to platinum—2492(L)
Ruoff, A. L. (see Butcher, B. M.)—2136
—— (see Li, Che-Yu)—1733
Ryan, D. (see Ball, M.)—267S

Sadler, M. S. (see Swoboda, T. J.)—374S
Saenz, A. W. Spin waves in complex exchange-coupled lattices and neutron scattering—752(E)
Saffren, M. M. (see Rosenbaum, H. S.)—1866
Sagar, A. and R. C. Miller. Study of band structures of intermetallic compounds by pressure experiments—2073
Salcedo, F. S. (see Bills, K. W. Jr.)—2364
Sallo, J. S. and K. H. Olsen. Studies of a high-coercivity electrodeposit having a lamellar structure—203S
Samelson, Harold. Vapor phase growth and properties of zinc sulfide single crystals—309
Sanders, Richard M. Stable-oscillation conditions for the magnetic-film parametron—478
Sato, Hiroshi. Remarks on the magnetic properties of Au-Mn system—53S
Sauer, J. A. (see Stein, M. N.)—2352
Saunders, J. H. and J. J. Green. High-power characteristics of low-magnetization garnets—161S
Savage, Albert (see Miller, Robert C.)—714
Scheidlinger, Z. (see Aharoni, A.)—1851
Schemeckenbecher, A. (see Matcovich, T.)—93S
Schieber, M. (see Aharoni, A.)—1851
Schleuning, H. W. (see Banks, E.)—44S
Schlömann, E. and R. I. Joseph. Instability of magnetostatic modes in a microwave magnetic field applied parallel to the dc field—165S
—— (see Joseph, R. I.)—1001
—— **and R. I. Joseph.** Instability of spin waves and magnetostatic modes in a microwave magnetic field applied parallel to the dc field—1006
—— (see Green, J. J.)—168S
Schlosser, H. and M. E. Drougard. Surface layers on barium titanate single crystals above the Curie point—1227
Schock, Alfred. Optimization of emission-limited thermionic generators—1564
Schoening, F. R. L. (see Flanders, P. J.)—344S
Schools, R. S. Recording and reproduction of NRZI signals —42S
Schroeder, J. B. Thermal conductivity in two-phase alloys —1798(L)
Schröder, K. Effect of magnetic clusters on the specific heat of Ni-Cu and Fe-V alloys—880
Schuele, W. J. and V. D. Deetscreek. Preparation, growth, and study of ultrafine ferrite particles—235S
Schwartz, B. (see Raymo, C. T.)—1165(L)
Seay, G. E., L. B. Seely, Jr., and R. G. Fowler. Production of high ion densities in helium by means of high explosives—2439
—— (see Reynolds, C. E.)—1401(L)
—— **and L. B. Seely, Jr.** Initiation of a low-density PETN pressing by a plane shock wave—1092
Secker, P. E. (see Lewis, T. J.)—54
Seely, L. B., Jr. (see Seay, G. E.)—1092
—— (see Seay, G. E.)—2439
Segall, B. (see Aven, M.)—2261
Segmuller, Armin. Annealing behavior and temperature dependence of the magnetic properties of thin Permalloy films—89S
Selwood, P. W. (see Abeledo, Carlos R.)—229S
Shaw, H. J. (see Auld, B. A.)—317S
Sherman, Christopher and J. M. Yos. Scaling laws for electric arcs subject to forced convection—744(L)
Sherwood, R. C. (see Nesbitt, E. A.)—342S
Shichijō, Yūzō, Noboru Tsuya, and Koki Suzuki. Initial permeability characteristics of vanadium-doped manganese-zinc ferrites—386S
Shmoys, J. Proposed diagnostic method for cylindrical plasmas—689
Shockley, W. Field-enhanced donor diffusion in degenerate semiconductor layers—1402(L)
—— **and Hans J. Queisser.** Detailed balance limit of efficiency of p-n junction solar cells—510
Shtrikman, S. (see Doyle, W. D.)—1785(L)
—— **and E. P. Wohlfarth.** Coherent and incoherent magnetization processes in powders—241S
Shull, Daniel S., Jr. Improved magnetic properties of high-purity iron-cobalt alloys containing 27-43% cobalt—356S
Shulman, R. G. Nuclear magnetic resonance in NiF_2 domain walls—126S
Sievers, A. J., III (see Keffer, F.)—65S
Silber, L. M. (see Banks, E.)—44S
Silberg, Paul A. On the question of ball lightning—30
Silence, Neal. (see Fletcher, P. C.)—706
Silsbee, Robert H. Electron spin resonance in neutron-irradiated quartz—1459
Simmons, Charles A. Influence of the Hall effect upon the transverse magnetoresistance in indium antimonide—1970
Simon, R., J. H. Cahn, and J. C. Bell. Uniformity of electrical current flow in cylindrical semiconductor specimens with cylindrical metallic end caps—46
Simpson, J. Arol (see Fowler, H. A.)—1153
Singer, J. R. (see Wang, S.)—1371
Sinha, P. P. and Paul A. Beck. Polygonization in bent zinc crystals—1222
Sinnott, K. M. (see Eby, R. K.)—1765
Sirkis, Murray D., Robert J. Strain, and William E. Kunz. Electron beam excitation of a Fabry-Perot interferometer—2055(L)
Slichter, W. P. Molecular motion in disordered regions of solid polyethylene—2339
Slonczewski, J. C. Anisotropy and magnetostriction in magnetic oxides—253S
Sloope, Billy W. and Calvin O. Tiller. Formation conditions and structure of thin epitaxial silver films on rock-salt—1331
Smay, T. A. (see Daughton, J. M.)—36S
Smith, Archibald W. and Akira Watanabe. Ferrimagnetic resonance in a single-crystal disk of yttrium iron garnet —155S
Smith, Cyril Stanley (see Jovanovic, Stanka)—121(L)
Smith, D. O. (see Weiss, G. P.)—85S
—— (see Cohen, M. S.)—1405(E)
—— Anisotropy in nickel-iron films—70S
Smith, F. P. (see Dale, Brian)—1377
Smith, Fred L. (see Murgai, Mahinder P.)—324(L)
Smy, P. R. Alternating current magnetohydrodynamic generator—1946
Snitzer, E. Proposed fiber cavities for optical masers—36
Soden, R. R. Effects of rare-earth substitutions on the fluorescence of terbium hexa-antipyrine tri-iodide—750(L)
Sodha, M. S. Thermionic emission from spherical metallic particles—2059(L)
Sommer, A. H. and W. E. Spicer. Bismuth-silver-oxygen-cesium photocathode—1036
Soohoo, R. F. Excitation and boundary effects in spin-wave resonance—148S
Spain, Robert J. and Harvey Rubinstein. Thin-film switching in the hard direction by wall motion—288S
Sparks, M. (see Jarrett, H. S.)—57S
Spedding, F. H. (see Born, H. J.)—2543

Spencer, C. W. (see Li, Che-Yu)—1733
Spicer, W. E. (see Sommer, A. H.)—1036
Spitzer, W. G. and M. Tanenbaum. Interference method for measuring the thickness of epitaxially grown films—744(L)
——, **F. A. Trumbore, and R. A. Logan.** Properties of heavily doped *n*-type germanium—1822
Sprague, G. Physical behavior of photographic grains—2410
Spurr, R. T. Frictional behavior of a simple rheological material—1450
Srinivasan, Devanatha and Louis V. Holroyd. Optical spectrum of the sonoluminescence emitted by cavitated water—446
Stanley, James and Charles Wert. Diffusion in a ferromagnetic alloy—267
Statton, W. O. Rate of recrystallization of polyethylene single crystals—2332
Statz, H. (see Koster, G. F.)—2054(L)
——, **L. Rimai, M. J. Weber, G. A. deMars, and G. F. Koster.** Chromium ion pair interactions in the paramagnetic resonance spectrum of ruby—218S
Steijn, R. P. On the wear of sapphire—1951.
Stein, M. N., R. G. Lauttman, J. A. Sauer, and A. E. Woodward. Dielectric loss in poly-(hexamethylene adipamide) and poly-(hexamethylene sebacamide) at low temperatures—2352
Stein, Richard S. (see Judge, Jane T.)—2357
—— Optical properties of oriented polystyrene—1280
—— (see Rhodes, Marion B.)—2344
Stephens, C. (see Goetzberger, A.)—2636
Stern, Ernest. Fine-wire ferrite limiter—315S
Stern, Frank. Optical properties of lead-salt and III-V semiconductors—2166
Stevenson, James R. and Eugene B. Hensley. Thermionic and photoelectric emission from magnesium oxide—166
Stewart, T. W. W. (see Brannen, E.)—964(E)
Stickler, J. J. (see Heller, G. S.)—307S
Stiles, P. J., E. Burstein, and D. N. Langenberg. de Haas-van Alphen effect in *p*-type PbTe and *n*-type PbS—2174
Stitch, Malcolm L. Power output characteristics of a ruby laser—1994
Stocker, Hans Juerg. Current-voltage characteristics of alloyed and diffused *p*-*n* junction diodes in InSb—322(L)
Strain, Robert J. (see Sirkis, Murray D.)—2055(L)
Strakna, R. E. (see Clark, A. E.)—1172(L)
Straumanis, M. E., P. Borgeaud, and W. J. James. Perfection of the lattice of dislocation-free silicon, studied by the lattice-constant and density method—1382
Strauss, A. J. (see Harman, T. C.)—2265
Strauss, W. (see Rowen, J. H.)—313S
Strumane, G. (see Amelinckx, S.)—1182(E)
Sucher, J. (see Day, T. B.)—1788(L)
Suddeth, J. A. (see Fowler, H. A.)—1153
—— (see Hörl, E.)—2521
Suhl, H. and R. C. Fletcher. Note on ferromagnetic relaxation equations—281
Sulich, M. (see Greiner, J. H.)—188S
Sullivan, Donald L. (see Fuller, Harrison W.)—286S
Surtees, Walter J. (see Wait, James R.)—557(L)
Sutera, S. P. and Harold Wayland. Quantitative analysis of two-dimensional flow by means of streaming birefringence—721
Sutton, G. W. (see Hurwitz, H., Jr.)—205
Suzuki, Kōki (see Shichijō, Yūzō)—386S
Swanekamp, F. W. (see Van Uitert, G.)—1176(L)
—— (see Monforte, F. R.)—959(L)
Swartz, D. Bruce. Compact uhf isolator—319S
Swartz, J. C. On the interpretation of internal friction experiments on strain aging of iron—2048(L)
—— **and J. Weertman.** Modification of the Koehler-Granato-Lucke dislocation damping theory—1860
Swihart, James C. Field solution for a thin-film superconducting strip transmission line—461
Swoboda, T. J. (see Cloud, W. H.)—55S
——, **Paul Arthur, Jr., N. L. Cox, J. N. Ingraham, A. L. Oppegard, and M. S. Sadler.** Synthesis and properties of ferromagnetic chromium oxide—374S
Szymanski, Herman (see Primak, William)—660

Takayanagi, Shigetoshi (see Teramoto, Iwao)—119(L)
Talley, Claude P. Preparation of single-crystal boron—1787(L)
Tamai, Yasukatsu. Friction of metals in reciprocating sliding—1437
Tamura, I. (see Mura, T.)—92
Tancrell, Roger H. Impulse selection for core logic—40S
Tanenbaum, M. (see Spitzer, W. G.)—744(L)
Targ, R. and L. P. Levine. Backward-wave microwave oscillations in a system composed of an electron beam and a hydrogen gas plasma—731
Taylor, Anthony. Low-temperature internal friction peaks in single crystals of NaCl and LiF—1799(L)
Taylor, C. R. (see Zollweg, R. J.)—1316
Taylor, Leonard S. Reflection of electromagnetic waves at electron density ramps—1796(L)
Taylor, P. F. and C. Wood. Thermoelectric properties of Ag_2Te—1
Teale, R. W. and M. J. Hight. Ferrimagnetic resonance in single crystals of cobalt-substituted manganese ferrite—140S
——, **R. F. Pearson, and M. J. Hight.** Ferrimagnetic resonance and torque measurements on ytterbium-substituted yttrium iron garnet—150S
Teitler, S. (see Palik, E. D.)—2132
Tennery, Victor J. and Russell G. West. New, thermally variable bead resistor—1402(L)
Teramoto, Iwao and Shigetoshi Takayanagi. Dislocation etch pits on bismuth telluride crystals—119(L)
Testardi, Louis R. Calculations of the thermoelectric parameters and the maximum figure of merit for acoustical scattering—1978
Teutonico, L. J. On the measurement of C_{13} in rhombohedral crystals—119(L)
Thaxter, J. B. (see Heller, G. S.)—307S
Theriault, J. P. (see Zwerdling, S.)—2118
Thomas, D. G. Excitons and band splitting produced by uniaxial stress in CdTe—2298
—— (see Dietz, R. E.)—2282
—— (see Frank, G. R.)—1763
Thomas, H. (see Middelhoek, S.)—294S
—— (see Methfessel, S.)—1959
Thomas, J. E., Jr. (see Noble, F. E.)—1709
Thomas, K. and M. W. Roberts. Direct observation in the electron microscope of oxide layers on aluminum—70
Thompson, D. O. (see Alers, G. A.)—283
Thompson, G. H. B. Backward waves in longitudinally magnetized ferrite rods—2491(L)
Thornton, W. A. Effects of phosphor powder dispersion in electroluminescent lamps—2379
Thurmond, C. D. (see Kaiser, W.)—115
Thurston, R. N. (see Pfann, W. G.)—2008
Tiedemann, K. J. Schmidt. Stress optical constants of germanium—2058(L)
Tiller, Calvin O. (see Sloope, Billy W.)—1331
Tiller, W. A. (see Cosgrove, G. J.)—621
—— (see Eisner, R. L.)—1833
—— (see Bolling, G. F.)—2587
—— (see McHugh, J. P.)—1785(L)
Tinkham, M. (see Keffer, F.)—65S

Tippins, H. H. (see Moser, F.)—48
Tobias, Charles W. (see Meredith, Robert E.)—132(E)
Tolman, E. M. Diffusion reactions in the aging of 4-79 molybdenum Permalloy—360S
Tomizuka, C. T. (see Darby, J. B., Jr.)—840
Torpy, Juanita W. (see Lefever, R. A.)—962(L)
Torre, E. Della (see Woodward, J. G.)—126(L)
Townsend, J. R. (see Muss, D. R.)—189
Treuting, R. G. (see Wagner, R. S.)—2490(L)
Treves, D. (see Fowler, C. A., Jr.)—296S
—— Limitations of the magneto-optic Kerr technique in the study of microscopic magnetic domain structures—358
Triboulet, D. (see Rodot, M.)—2254
Trivelpiece, A. W., A. Ignatius, and P. C. Holscher. Backward waves in longitudinally magnetized ferrite rods —259
Truell, Rohn. Influence of deformation and temperature on the cobalt gamma irradiation of sodium chloride, evidence for electrical interaction between dislocations and point defects—1601
Trumbore, F. A. (see Logan, R. A.)—131(L)
—— (see Spitzer, W. G.)—1822
Tsang, T. An approximate solution of Fick's diffusion equation—1518
Tschoegl, N. W. Equation of motion of the torsion pendulum and the complex modulus—1794(L)
Tsue, James B. Y. (see Wang, Franklin F. Y.)—1621(L)
Tsuya, Noboru (see Shichijō, Yūzō)—386S
Tterlikkis, Lambros and Alvin W. Jenkins, Jr. Magnetization of nickel single crystals—1293
Tucker, T. J. Behavior of exploding gold wires—1894
Tufts, C. (see Weinreich, O.)—1170(L)
Tuler, Floyd R. (see Birnbaum, Howard K.)—1403(L)
Turnbull, R. C. Reinterpretation of the reaction kinetics of nickel ferrite—380S
Turner, W. J., A. S. Fischler, and W. E. Reese. Electrical and optical properties of the II–V compounds—2241

Uphoff, H. L. and J. H. Healy. Semiconducting properties of inorganic amorphous materials—950

Van Bladel, J. (see Cristal, E. G.)—1715
van Daal, H. J., C. A. A. J. Breebe, W. F. Knippenberg, and H. J. Vink. Investigations on silicon carbide—2225
Van Uitert, G., F. W. Swanekamp, and S. Preziosi. Single-crystal molybdates for resonance and emission studies—1176(L)
—— **and L. Egerton.** Bismuth titanate. A ferroelectric—959(L)
—— (see Monforte, F. R.)—959(L)
Vassamillet, L. F. Stacking fault probability of noble metal-zinc alloys—778
Verderber, R. R. and B. M. Kostyk. Ni-Fe single-crystal films and their magnetic characteristics—696
Vicentini, M. (see Paoletti, A.)—22
Vicentini-Missoni, M. (see Paoletti, A.)—559
Vink, H. J. (see Albers, W.)—2220
—— (see van Daal, H. J.)—2225
Vook, Richard W. Single-crystal tin films—1557
—— Forbidden reflections in electron diffraction patterns of evaporated tin films—2474

Waclawski, B. J. and E. W. Muller. Operation of the field ion microscope with a dynamic gas supply—1472
Wade, Glen (see Comstock, R. L.)—227S
Wagner, R. S. and R. G. Treuting. Morphology and growth mechanism of silicon ribbons—2490(L)
Wagner, W. G. and G. Birnbaum. Theory of quantum oscillators in a multimode cavity—1185
Wahl, C. (see Buehler, E.)—325(L)
Wait, James R. and Walter J. Surtees. Impedance of a top-loaded antenna of arbitrary length over a circular grounded screen—557(L)
Walker, L. R. Magnetic anisotropy of yttrium iron garnet at 0°K—264S
—— (see LeCraw, R. C.)—167S
Wallace, W. E. (see Cherry, L. V.)—340S
Wallis, R. F. (see Palik, E. D.)—2132
Wallor, R. (see Hines, R. L.)—202
Walters, G. K. and T. L. Estle. Paramagnetic resonance of defects introduced near the surface of solids by mechanical damage—1854
Walters, K. Use of idealized relaxation spectra in the interpretation of experimental results concerning polymer solutions—1975
Wang, Franklin F. Y., Koryu Ishii, and James B. Y. Tsui. Ferrimagnetic resonance of single-crystal barium ferrite in the millimeter wave region—1621
Wang, S. and J. R. Singer. Paramagnetic maser oscillator analysis—1371
Warren, B. E. X-ray measurement of stacking fault widths in fcc metals—2428
Wasscher, J. D. (see Albers, W.)—2220
Watanabe, Akira (see Smith, Archibald W.)—155S
Watanabe, Naozo (see Kanai, Yasuo)—2146
Watson, R. E. and A. J. Freeman. On the contribution of the Fermi contact term to the magnetic field at the nucleus —118S
Watson, William H., Jr. Catalytic activity of p- and n-type germanium—120(L)
Watt, L. A. K. (see Bonstrom, D. B.)—272S
Wayland, Harold (see Sutera, S. P.)—721
Wayman, C. M. Observations on the growth of α-iron single crystals by halogen reduction—1844
Webb, W. W. (see Amelinckx, S.)—1182(E)
Weber, M. J. (see Statz, H.)—218S
Webster, H. F. Thermionic emission from a tantalum crystal in cesium or rubidium vapor—1802(L)
Weeks, R. A. (see Nelson, C. M.)—883
Weertman, J. (see Swartz, J. C.)—1860
Wegener, H. A. Richard (see Carlson, Henry A.)—125(L)
Weger, M., E. L. Hahn, and A. M. Portis. Transient excitation of nuclei in ferromagnetic metals—124S
Wehlau, A. (see Muller, M. W.)—2448
Wehner, G. K. and D. Rosenberg. Mercury ion beam sputtering of metals at energies 4–15 kev—887
—— (see Laegreid, Nils)—365
Weinreich, O., G. Dermit, and C. Tufts. Germanium films on germanium obtained by thermal evaporation in vacuum —1170(L)
Weiss, G. P. (see Cohen, M. S.)—1405(E)
—— **and D. O. Smith.** Annealing of oblique-incidence permalloy films—85S
Weiss, H. Galvanomagnetic properties of InSb—2064
Weiss, M. T. (see Hartwick, T. S.)—223S
Weissmann, Sigmund, Makoto Hirabayashi, and Hiroshi Fujita. On the mechanical and thermal stability of low-angle boundaries in zinc single crystals—1156
Weisz, R. S. Square-loop ferrites with temperature-independent properties and improved disturb ratio—1152
Wentink, Tunis, Jr. Properties of polyvinylidene fluoride. I. Dielectric measurements—1063
Wernick, J. H. and R. Wolfe. Semiconducting "compound" AgFeTe$_2$—749(L)
——, **S. E. Haszko, and W. J. Romanow.** New magnetic ternary compound with a high crystalline anisotropy—2495(L)
—— (see McHugh, J. P.)—1785(L)
Wernick, J. H. (see Nesbitt, E. A.)—342S
Wert, Charles (see Stanley, James)—267

Wertheim, G. K. Mössbauer effect: Applications to magnetism—110S
West, Forrest G. Magnetoresistive measurements on domain rotation and wall development in Ni-Fe alloy films—290S
—— General superparamagnetic behavior of an aligned assembly of uniaxially anisotropic particles—249S
West, Russell G. (see Tennery, Victor J.)—1402(L)
—— (see Jefferson, Clinton F.)—390S
Wetzel, Lewis. Wave interaction in plasma inhomogeneities —327(L)
Wheeler, R. G. (see Dimmock, J. O.)—2271
White, D. E. (see Phillips, R. L.)—1406(E)
—— (see Phillips, R. L.)—551(L)
White, David J. Models for switching in ferroelectrics—1169(L)
White, Robert L. Comment on the saturation magnetization of neodymium yttrium iron garnet—1178(L)
—— (see Carson, J. E.)—1787(L)
Whitmore, D. H. (see Greener, E. H.)—1320
Whitmore, R. W. (see Chou, Y. T.)—1920
Whitsett, Charles R. Righi-Leduc effect in mercuric selenide—2257
Wickersheim, Kenneth A. Optical and infrared spectra of the ferrites and garnets—205S
Wiese, J. R. (see Bennett, L. C.)—562
Wild, R. L., W. T. Ogier, L. M. Richards, and J. C. Nickel. Double Bragg x-ray scattering studies of polycrystalline metals—520
Wilkinson, M. K. (see Cable, J. W.)—49S
——, W. C. Koehler, E. O. Wollan, and J. W. Cable. Neutron diffraction investigation of magnetic ordering in dysprosium—48S
Williams, Albert J., III (see Danforth, W. E.)—1181(L)
Williams, H. J. (see Nesbitt, E. A.)—342S
Williams, Wendell S. Mondrian precipitation patterns in single crystals of titanium carbide—552(L)
Willis, A. H., J. M. Baugnet, and R. C. De Beukelaer. Stored energy in fuel-bearing graphites—1622(L)
Wilsdorf, H. G. F. (see Greenfield, I. G.)—827
Wilson, R. H. (see Kouvel, J. S.)—276S
—— (see Kouvel, J. S.)—435
Winogradoff, N. N. Photoconductivity of CdS-type photoconductors in the vicinity of the absorption edge—506
Winslow, D. K. (see Auld, B. A.)—317S
Wittry, D. B. (see McCaldin, J. O.)—65
Wohlfarth, E. P. (see Shtrikman, S.)—241S
Woisard, Edwin L. Pulse method for the measurement of thermal diffusivity of metals—40
Wold, A. (see Ferretti, A.)—905
Wolf, J. D. and J. E. Hanlon. Magnetic domain patterns in Cr-modified Mn_2Sb—2584
Wolf, Peter. Free oscillations of the magnetization in permalloy films—95S
Wolf, W. P. Ferromagnetic alignment by antiferromagnetic exchange interaction. Note on the magnetic behavior of neodymium garnet—742(L)
—— (see Ball, M.)—267S
Wolfe, R. (see Wernick, J. H.)—749(L)
Wollan, E. O. (see Cable, J. W.)—49S
—— (see Wilkinson, M. K.)—48S
Wolsky, S. P. and E. J. Zdanuk. Investigation of the sputtering of silicon—782
Wood, C. (see Taylor, P. F.)—1
Wood, C. G. (see Cole, H.)—1942
Woodside, W. and J. H. Messmer. Thermal conductivity of porous media. I. Unconsolidated sands—1688
—— and J. H. Messmer. Thermal conductivity of porous media. II. Consolidated rocks—1699
Woodward, A. E. (see Stein, M. N.)—2352
Woodward, J. G. and E. Della Torre. Particle interaction in magnetic recording tapes—126(L)
Wooten, Frederick O. (see Condas, George A.)—323(L)
—— Photovoltaic effects in Cs_3Sb films—1789(L)
Worlton, D. C. Experimental confirmation of Lamb waves at megacycle frequencies—967
Wright, George B. and Benjamin Lax. Magnetoreflection experiments in intermetallics—2113
Wycklendt, Daniel A. and Robert M. Kay. Losses in silicon iron at very low frequencies and high flux densities. —368S

Yamaguchi, S. Magnetic anisotropy of cobalt as revealed by electron diffraction—961(L)
Yamashita, Jiro. Heitler-London approach to electrical conductivity—2215
Yos, J. M. (see Sherman, Christopher)—744(L)
Yosida, Kei and Hirosi Miwa. Magnetic ordering in the ferromagnetic rare-earth metals—8S
Young, Charles E. Extended curves of the space charge, electric field, and free carrier concentration at the surface of a semiconductor, and curves of the electrostatic potential inside a semiconductor—329
Young, F. W., Jr. Elastic-plastic transition in copper crystals as determined by an etch-pit technique—1815
—— Etch pits at dislocations in copper—192
Young, Russell D. (see Muller, Erwin W.)—2425

Zdanuk, E. J. (see Wolsky, S. P.)—782
Zijlstra, H. Magnetic annealing of "ticonal" G magnet steel —194S
Zollweg, R. J. and C. R. Taylor. Temperature dependent bismuth-cesium photosurfaces—1316
—— and Milton Gottlieb. Oscillations and saturation current measurements in thermionic conversion cells—890
Zucker, J., V. J. Fowler, and E. M. Conwell. High-field conductivity in germanium and silicon at microwave frequencies—2606
Zwerdling, S., W. H. Kleiner, and J. P. Theriault. Oscillatory magnetoabsorption in InSb under high resolution—2118

JOURNAL OF APPLIED PHYSICS VOLUME 32, NUMBER 12 DECEMBER, 1961

Subject Index to Volume 32

References with (L) are to Letters to the Editor; (E) to Errata

Acoustics
- Acoustical study of quench-aging in α Cu-Al alloys. T. J. Koppenaal and M. E. Fine—1781
- Calculations of the thermoelectric parameters and the maximum figure of merit for acoustical scattering. Louis R. Testardi—1978
- Double phonon processes in cadmium sulfide. Minko Balkanski and Jean Michel Besson—2292
- Elastic constants of bismuth. Yakov Eckstein, A. W. Lawson, and Darrell H. Reneker—752(E)
- Elastic constants of single-crystal YIG. A. E. Clark and R. E. Strakna—1172(L)
- Elastic constants of TiC and TiB_2. J. J. Gilman and B. W. Roberts—1405(L)
- Experimental study of the interrelation between the theory of dislocations in polycrystalline media and finite amplitude wave propagation in solids. James F. Bell—1982
- Frequency dependence of ultrasonic wave attenuation in Armco iron and low-carbon steel. U. M. Martius and W. J. Bratina—280S
- On the measurement of C_{13} in rhombohedral crystals. L. J. Teutonico—119(L)
- Optical spectrum of sonoluminescence emitted by cavitated water. Devanatha Srinivasan and Louis V. Holroyd—446
- Parametric effects in magnetoacoustic resonance. R. L. Comstock, B. A. Auld, and Glen Wade—227S
- Piezoelectric scattering and phonon drag in ZnO and CdS. A. R. Hutson—2287
- Scattering of plane waves by a rigid ribbon in a solid. K. Harumi—1488
- Space-time analysis of the sonoluminescence emitted by cavitated water. Robert Q. Macleay and Louis V. Holroyd—449
- Third-order elastic moduli of germanium. T. Bateman, W. P. Mason, and H. J. McSkimin—928
- Ultrasonic detection of changes in the elastic properties of a 70–30 iron-nickel alloy upon heat treatment. Emmanuel P. Papadakis and Everett L. Reed—682

Astrophysics
- On the theoretical limitation of a radio telescope in determining the sky temperature distribution. Y. T. Lo—2052(L)
- Spiral walls in thin magnetic films. Harrison W. Fuller, Harvey Rubinstein, and Donald L. Sullivan—286S
- Thin-films switching in the hard direction by wall motion. Robert J. Spain and Harvey Rubinstein—288S

Ballistics
- Nonlinear effects of Z-directed spin waves in thin films. Jerome I. Kaplan—1831

Biophysics
- Thin-film switching in the hard direction by wall motion. Robert J. Spain and Harvey Rubinstein—288S

Crystal Growth
- Analytical solutions for some zone melting problems. H. Reiss and E. Helfand—228
- Application of the Czochralski method to divalent metal fluorides. K. Nassau—1820
- Characteristics of the annealing kinetics of tin films deposited at 88°K. J. Priest, C. Chiou, and H. L. Caswell—1772
- Cobalt ferrite single crystals. A. Ferretti, R. J. Arnott, E. Delaney, and A. Wold—905
- Dislocation-free aluminum crystals. S. Howe and C. Elbaum—742(L)
- Formation conditions and structure of thin epitaxial silver films on rocksalt—Billy W. Sloope and Calvin O. Tiller—1331
- Growth from the melt. III. Dendritic growth. C. F. Bolling and W. A. Tiller—2587
- Growth of crystals using induction plasma torch. T. B. Reed—2534
- Growth of single-crystal calcium fluoride with rare-earth impurities. H. Guggenheim—1337
- Growth of single-crystal iron ferrites by the Czochralski method. F. H. Horn—900
- Growth of single crystals of yttrium aluminum garnet from lead oxide-lead fluoride melts. R. A. Lefever, Juanita W. Torpy, and A. B. Chase—962(L)
- Growth of stannic oxide crystals from the vapor phase. J. A. Marley and T. C. MacAvoy—2504
- Growth of yttrium iron garnet single crystals by the floating zone technique. L. L. Abernethy, T. H. Ramsey, Jr., and John W. Ross—376S
- Growth of ZnSb single crystals. R. L. Eisner, R. Mazelsky, and W. A. Tiller—1833
- Iron whisker surface rearrangements resulting from the hydrogen reduction of oxides and from thermal etching. J. V. Laukonis and R. V. Coleman—242
- Isothermal crystallization kinetics of polyethylene. II. Influence of the sample preparation. J. Rabesiaka and A. J. Kovacs—2314
- Low-angle x-ray diffraction of crystalline nonoriented polyethylene and its relation to crystallization mechanisms. L. Mandelkern, A. S. Posner, A. F. Diorio, and D. E. Roberts—1509
- Morphology and growth mechanism of silicon ribbons. R. S. Wagner and R. G. Treuting—2490(L)
- Observations on the growth of α-iron single crystals by halogen reduction. C. M. Wayman—1844
- On the growth of sapphire microcrystals. C. M. Hargreaves—936
- Orientation-dependent dissolution of lithium fluoride. M. B. Ives—1534
- Preparation of monocrystalline cuprous oxide. Yukiko Ebisuzaki—2027
- Preparation of silicon ribbons. W. S. Greiner, J. A. Gutowski, and W. C. Ellis—2489(L)
- Preparation of single-crystal boron. Claude P. Talley—1787(L)
- Rate of recrystallization of polyethylene single crystals. W. O. Statton—2332
- Single-crystal molybdates for resonance and emission studies. G. Van Uitert, F. W. Swanekamp, and S. Preziosi—1176(L)
- Sintering crystalline solids. I. Intermediate and final state diffusion models. R. L. Coble—787
- Sintering crystalline solids. II. Experimental test of diffusion models in powder compacts. R. L. Coble—793
- Spiral walls in thin magnetic films. Harrison W. Fuller, Harvey Rubinstein, and Donald L. Sullivan—286S
- Stability of pressure-supported molten zones in horizontal sheets. H. P. Kramer, B. P. Bogert, and D. W. Hagelbarger—764
- Useful technique for growing large, single-crystal YIG. Don Barry and Roy W. Roberts—1405(L)
- Vapor-phase growth of single crystals of II–VI compounds. W. W. Piper and S. J. Polich—1278

Vapor phase growth and properties of zinc sulfide single crystals. Harold Samelson—309
Zone leveling and crystal growth of peritectic compounds. Donald R. Mason and J. Stanley Cook—475
Zone refining of the silver halides. F. Moser, D. C. Burnham, and H. H. Tippins—48

Crystal Properties and Behavior
Dangling bonds in III–V compounds. Harry C. Gatos—1232
Domain structures in iron whiskers as observed by the Kerr method. C. A. Fowler, Jr., E. M. Fryer, and D. Treves—296S
Effect of indium substitution in yttrium iron garnet: high permeability garnets. J. Richard Cunningham, Jr., and Elmer E. Anderson—388S
Elastic constants of single-crystal YIG. A. E. Clark and R. E. Strakna—1172(L)
Electron interferometer studies of iron whiskers. H. A. Fowler, L. Marton, J. Arol Simpson, and J. A. Suddeth—1153
Ferrimagnetic resonance of single-crystal barium ferrite in the millimeter wave region. Franklin F. Y. Wang, Koryu Ishii, and James B. Y. Tsui—1621(L)
Ferromagnetic nucleation sources on iron whiskers. R. E. De Blois—1561
Friction of molybdenum diselenide. Melvin T. Lavik, T. Bruce Daniel, and A. Neal Abbott—1795(L)
Grain-boundary diffusion. A. E. Austin and N. A. Richard—1462
Growth twins in indium antimonide. R. K. Mueller and R. L. Jacobson—550(L)
High-angle tilt boundary—a dislocation core model. James C. M. Li—525
Impurity striations in unrotated crystals of InSb. H. C. Gatos, A. J. Strauss, M. C. Lavine, and T. C. Harmon—2057(L)
Infrared properties of flame-fused MnO crystals. E. Loh and R. Newman—470
Interaction between vacancies and stacking fault ribbons in graphite. P. Delavignette and S. Amelinckx—554(L)
Low-temperature internal friction peaks in single crystals of NaCl and LiF. Anthony Taylor—1799(L)
Mechanism of chemisorption, place exchange, and oxidation of a (100) nickel surface. H. E. Farnsworth and Hannibal H. Madden, Jr.—1933
Magnetic moments of compounds of cobalt with rare-earth elements having a Cu_6Ca structure. E. A. Nesbitt, H. J. Williams, J. H. Wernick, and R. C. Sherwood—342S
Magnetization of nickel single crystals. Lambros Tterlikkis and Alvin W. Jenkins, Jr.—1293
Mondrian precipitation patterns in single crystals of titanium carbide. Wendell S. Williams—552(L)
Morphology and growth mechanism of silicon ribbons. R. S. Wagner and R. G. Treuting—2490(L)
Mosaic size in lead from x-ray measurements. Yosio Hiki and Ryukiti R. Hasiguti—1647
Ni-Fe single-crystal films and their magnetic characteristics. R. R. Verderber and B. M. Kostyk—696
On the mechanical and thermal stability of low-angle boundaries in zinc single crystals. Sigmund Wiessman, Makoto Hirabayashi, and Hiroshi Fujita—1156
On the wear of sapphire. R. P. Steijn—1951
Physical behavior of photographic grains. G. Sprague—2410
Precipitation in gold-nickel single crystals. P. J. Flanders and F. R. L. Schoening—344S
Preparation of silicon ribbons. E. S. Greiner. J. A. Gutowski, and W. C. Ellis—2489(L)
Remanent magnetization of a synthetic hematite single crystal. S. T. Lin—394S
Single and double pile-up dislocations in MgO crystals. Y. T. Chou and R. W. Whitmore—1920
Surface kinetics and physics investigation of the reaction between single-crystal germanium and iodine. W. J. Heinecke and S. Ing, Jr.—1498
Surface layer in $BaTiO_3$ single crystals. Ennio Fatuzzo and Walter J. Merz—1685
Surface layers on barium titanate single crystals above the Curie point. H. Schlosser and M. E. Drougard—1227
Temperature-compensated Debye temperature of carbonyl iron. Charles P. Gazzara and Raymond M. Middleton—1546
Transference number measurements for aluminum oxide. W. D. Kingery and G. E. Meiling—556(L)
Vapor phase growth and properties of zinc sulfide single crystals. Harold Samelson—309

Crystal Structure
Cation distributions in magnesium-nickel ferrites. C. J. Kriessman and S. E. Harrison—392S
Crystal lattice investigation of the permanent magnet precipitate in various Alnico materials. K. J. Kronenberg—196S
Crystal structure of photoelectric films of cesium antimonide. W. H. McCarroll—2051(L)
Growth twins in indium antimonide. R. K. Mueller and R. L. Jacobson—1406(E)
Lattice parameter determinations with an x-ray spectrogoniometer by the Debye-Scherrer method and the effect of specimen condition. Henry M. Otte—1536
Polygonization in bent zinc crystals. P. P. Sinha and Paul A. Beck—1222
Role of crystal structure in diffusion. I. Diffusion paths in closest-packed crystals. Leonid V. Azároff—1658
Role of crystal structure in diffusion. II. Activation energies for diffusion in closest-packed structure. Leonid V. Azároff—1663
Single-crystal tin films. Richard W. Vook—1557
Structure of Alnico V. Robert B. Campbell and Carl A. Julien—192S
Structure of nickel chromite. E. Prince—68S
Use of graphite whiskers in a study of the atmosphere dependence of graphite friction. F. R. Rollins, Jr.—1454

Defects in Solids, Point Defects
Cross-section ratios of sensitizing centers in photoconductors. Richard H. Bube—1707
Deformation-produced point defects. Howard K. Birnbaum and Floyd R. Tuler—1403(L)
Dichroic color centers in calcium fluorophosphate. Peter D. Johnson—127(L)
Distribution coefficients of impurities in gallium antimonide. R. N. Hall and J. H. Racette—856
Effect of reactor fast neutrons on electron-hole recombination in germanium. A. Czachor and J. Piekoszewski—1837
Generation and distribution of dislocation by solute diffusion. S. Prussin—1876
Germanium saturated with gallium antimonide. J. O. McCaldin and D. B. Wittry—65
Influence of arsenic pressure on the doping of gallium arsenide with germanium. J. O. McCaldin and Roy Harada—557(L)
Influence of deformation and temperature on the cobalt gamma irradiation of sodium chloride. Evidence for electrical interaction between dislocations and point defects. Rohn Truell—1601
Interaction between vacancies and stacking fault ribbons in graphite. P. Delavignette and S. Amelinckx—554(L)

Defects in Solids, Point Defects (*continued*)
  - Interrelation of electronic properties and defect equilibria in PbTe. E. Miller, K. Komarek, and I. Cadoff—2457
  - Monotonic trap distributions. Richard H. Bube—1621(L)
  - On additivity of imperfections as means for domain nucleation. A. Aharoni—245S
  - Paramagnetic resonance of defects introduced near the surface of solids by mechanical damage. G. W. Walters and T. L. Estle—1854
  - Precipitation sites in aluminum alloys. G. R. Frank, Jr., D. L. Robinson, and G. Thomas—1763
  - Presence of carbon in gallium phosphide crystals. C. J. Frosch, M. Gershenzon, and L. Derick—2060(L)
  - Properties of high-resistivity gallium arsenide compensated with diffused copper. Joseph Blanc, Richard H. Bube, and Harold E. MacDonald—1666
  - Recombination kinetics for thermally dissociated Li-B pairs in Si. E. M. Pell and F. S. Ham—1052
  - Solubility of oxygen in germanium. W. Kaiser and C. D. Thurmond—115
  - Stored energy in fuel-bearing graphites. A. H. Willis, J. M. Baugnet, and R. C. De Buekelaer—1622(L)

Defects in Solids, Dislocations and Stacking Faults
  - Antimony edge dislocations in InSb. H. C. Gatos, M. C. Finn, and M. C. Lavine—1174(L)
  - Birefringence due to dislocations in glide bands of rocksalt single crystals. S. Mendelson—1999
  - Charged dislocations in ionic crystals. F. Rueda and W. Dekeyser—1799(L)
  - Concerning dislocations in glass. W. B. Hillig and R. J. Charles—123(L)
  - Cross slip and cross climb of dislocations induced by a locked dislocation. James C. M. Li—593
  - Defect mechanisms in a noncrystalline solid. W. C. Levengood—2525
  - Dislocation contributions to the modulus and damping in copper at megacycle frequencies. G. A. Alers and D. O. Thompson—283
  - Dislocation density and flow stress of sodium chloride. W. in der Schmitten and P. Hassen—1790
  - Dislocation etch pit formation in sodium chloride. S. Mendelson—1579
  - Dislocation etch pits on bismuth telluride crystals. Iwao Teramoto and Shigetoshi Takayanagi—119(L)
  - Dislocation etch pits on the basal plane of zinc crystals. H. S. Rosenbaum and M. M. Saffren—1856
  - Dislocation etching solution for potassium chloride and other alkali halides. J. S. Cook—2492(L)
  - Dislocation relaxation phenomena in oxide crystals. Roger Chang—1127
  - Dislocation-free aluminum crystals. S. Howe and C. Elbaum—742(L)
  - Dislocation interaction in bcc stainless steel. B. R. Banerjee, J. M. Capenos, J. J. Hauser, and J. P. Hirth—556(L)
  - Dislocations and stacking faults in aluminum nitride. P. Delavignette, H. B. Kirkpatrick, and S. Amelinckx—1098
  - Dislocations in silicon carbide. S. Amelinckx, G. Strumane, and W. W. Webb—1182(E)
  - Effects of transition metal solutes on the electrical resistivity of copper and gold between 4° and 1200°K. C. A. Domenicali and E. L. Christenson—2450
  - Electron microscope observations of dislocations in talc. S. Amelinckx and P. Delavignette—341
  - Enantiomorphous character of etch pits in telliurium. J. S. Blakemore and K. C. Nornura—745(L)
  - Energy of a crossed grid of screw dislocations. James C. M. Li—1873
  - Etch pits at dislocations in copper. F. W. Young, Jr.—192
  - Experimental study of the interrelation between the theory of dislocations in polycrystalline media and finite amplitude wave propagation in solids. James F. Bell—1982
  - Generation and distribution of dislocation by solute diffusion. S. Prussin—1876
  - Growth twins in indium antimonide. R. K. Mueller and R. L. Jacobson—550(L)
  - Growth twins in indium antimonide. R. K. Mueller and R. L. Jacobson—1406(E)
  - High-angle tilt boundary—a dislocation core model. James C. M. Li—525
  - Influence of deformation and temperature on the cobalt gamma irradiation of sodium chloride. Evidence for electrical interaction between dislocations and point defects. Rohn Truell—1601
  - Interaction between vacancies and stacking fault ribbons in graphite. P. Delavignette and S. Amelinckx—554(L)
  - Modification of the Koehler-Granato-Lücke dislocation damping theory. J. C. Swartz and J. Weertman—1860
  - Nonbasal glide in dislocation-free cadmium crystals. I. The (10$\bar{1}$1) [1$\bar{2}$10] system. P. B. Price—1746
  - Nonbasal glide in dislocation-free cadmium crystals. II. The (1122) [1123] system. P. B. Price—1750
  - On dislocation interactions in the fcc lattice. J. P. Hirth—700
  - On the mechanical and thermal stability of low-angle boundaries in zinc single crystals. Sigmund Weissmann, Makoto Hirabayashi, and Hiroshi Fujita—1156
  - Perfection of the lattice of dislocation-free silicon, studied by the lattice-constant and density method. M. E. Straumanis, P. Borgeaud, and W. J. James—1382
  - Polygonization in bent zinc crystals. P. P. Sinha and Paul A. Beck—1222
  - Recombination of excess carriers at twin structures in germanium. J. P. McKelvey—442
  - Precipitation of helium along dislocations in aluminum. G. T. Murray—1045
  - Reduction of cohesion in ionic crystals by dislocations. John J. Gilman—738(L)
  - Relative polygonization rates in copper and copper-zinc alloys. W. E. Heitmann and R. W. Balluffi—963(L)
  - Single and double pile-up dislocations in MgO crystals. Y. T. Chou and R. W. Whitmore—1920
  - Stacking fault probability of noble metal-zinc alloys. L. F. Vassamillet—778
  - Temperature dependence of rolling textures in high-purity silver. Hsun Hu and R. S. Cline—760
  - Texture transition in high-purity silver and its correlation with stacking fault frequency. Hsun Hu, R. S. Cline, and S. R. Goodman—1392
  - Variant in technique for A. R. Lang's x-ray diffraction topography. Henry A. Carlson and H. A. Richard Wegener—125(L)
  - Voids in resolidified drops in molten metal. J. C. Kelly—1797(L)
  - X-ray measurement of stacking fault widths in fcc metals. B. E. Warren—2428

Dielectrics and Dielectric Properties (see also Ferroelectricity)
  - Dielectric loss in poly-(hexamethylene adipamide) and poly-(hexamethylene sebacamide) at low temperatures. M. N. Stein, R. G. Lauttman, J. A. Sauer, and A. E. Woodward—2352
  - Dielectric properties and side-chain crystallinity of polyvinyl stearate. Martin G. Broadhurst, Edwin R. Fitzgerald, and Anthony J. Bur—972
  - Experimental investigation of the Sumoto effect. William F. Pickard—1888

Forces in dielectric fluids. James D. Horgan and David L. Edwards—1784(L)
Increase in dielectric constant during switching in lithium selenite and triglycine sulfate. Ennio Fatuzzo—1571
Measurement of the electrical conductivity and dielectric constant without contacting electrodes. Tomoya Ogawa—583
Properties of polyvinylidene fluoride. I. Dielectric measurements. Tunis Wentink, Jr.—1063

Diffraction, Electron
"Anomalous" electron double diffraction. O. Hasse and R. D. Hiedenreich—1840
Forbidden reflections in electron diffraction patterns of evaporated thin films. Richard W. Vook—2474
(110) nickel surface. L. H. Germer, A. U. MacRae, and C. D. Hartman—2432
Magnetic anisotropy of cobalt as revealed by electron diffraction. S. Yamaguchi—961(L)

Diffraction, Neutron
Neutron diffraction by helical spin structures. W. C. Koehler—20S
Neutron diffraction investigation of magnetic ordering in dysprosium. M. K. Wilkinson, W. C. Koehler, E. O. Wollan, and J. W. Cable—48S
Neutron diffraction study of metallic erbium. J. W. Cable, E. O. Wollan, W. C. Koehler, and M. W. Wilkinson—49S

Diffraction, X-ray
Determination of crystallite size distributions from x-ray line broadening. Arthur Bienenstock—187
Double Bragg x-ray scattering studies of polycrystalline metals. R. L. Wild, W. T. Ogier, L. M. Richards, and J. C. Nickel—520
Imaginary part of x-ray scattering factor for germanium. Comparison of theory and experiment. Boris W. Batterman—998
Lattice parameter determinations with an x-ray spectrogoniometer by the Debye-Scherrer method and the effect of specimen condition. Henry M. Otte—1536
Lattice parameter studies of impurity effects on plastic properties of lithium fluoride. W. L. Phillips, Jr.—751(L)
Low-angle x-ray diffraction of crystalline nonoriented polyethylene and its relation to crystallization mechanisms. L. Mandelkern, A. S. Posner, A. F. Diorio, and D. E. Roberts—1509
Mosaic size in lead from x-ray measurements. Yosio Hiki and Ryukiti R. Hasiguti—1647
Perfection of the lattice of dislocation-free silicon, studied by the lattice-constant and density method. M. E. Straumanis, P. Borgeaud, and W. J. James—1382
Small-angle scattering in gold-nickel alloys. G. Nagorsen and B. L. Averbach—688
Variant in technique for A. R. Lang's x-ray diffraction topography. Henry A. Carlson and H. A. Richard Wegener—125(L)
X-ray diffraction study of interdiffusion in Cu-Ni powder compacts. Bertina Fisher and P. S. Rudman—1604
X-ray measurement of stacking fault widths in fcc metals. B. E. Warren—2428
X-ray polarizer. H. Cole, F. W. Chambers, and C. G. Wood—1942

Diffusion
Analysis of photojunctions formed by diffusing copper into insulating cadmium sulfide crystals. Robert R. Bockemuehl, James E. Kauppila, and David S. Eddy—1324
Analytic solution of the double-diffusion problem. K. C. Nomura—1167(L)
An approximate solution of Fick's diffusion equation. T. Tsang—1518
Diffusion in a ferromagnetic alloy. James Stanley and Charles Wert—267
Diffusion in a liquid indium-tin alloy at the eutectic concentration. A. Paoletti and M. Vicentini—22
Diffusion in a liquid indium-tin alloy at several concentrations. A. Paoletti and M. Vicentini-Missoni—559
Diffusion reactions in the aging of 4-79 molybdenum Permalloy. E. M. Tolman—360S
Diffusion of tin in gallium arsenide. B. Goldstein and H. Keller—1180(L)
Effect of torsional deformation on self-diffusion in silver. C. H. Lee and R. Maddin—1846
Experimental study of intermetallic diffusion in large temperature gradients. C. J. Meechan—945
Field-enhanced donor diffusion in degenerate semiconductor layers. W. Shockley—1402(L)
Generation and distribution of dislocation by solute diffusion. S. Prussin—1876
Grain-boundary diffusion. A. E. Austin and N. A. Richard—1462
Helium diffusion through glass. V. O. Altemose—1309
Mobility of radiation-induced defects in germanium. P. Baruch—653
Polarization and diffusion in a silicate glass. R. J. Charles—1115
Radiation enhancement of bulk diffusion in 10% Zn–90% Cu by 3-kev Ne$^+$ ion bombardment. R. A. Arndt and R. L. Hines—1913
Role of crystal structure in diffusion. I. Diffusion paths in closest-packed crystals. Leonid V. Azároff—1658
Role of crystal structure in diffusion. II. Activation energies for diffusion in closest-packed structures. Leonid V. Azároff—1663
Self-diffusion in silver during plastic deformation in torsion. J. B. Darby, Jr., C. T. Tomizuka, and R. W. Balluffi—840
Sintering crystalline solids. I. Intermediate and final state diffusion models. R. L. Coble—787
Sintering crystalline solids. II. Experimental test of diffusion models in powder compacts. R. L. Coble—793
X-ray diffraction study of interdiffusion in Cu-Ni powder compacts. Bertina Fisher and P. S. Ridman—1604

Elasticity and Anelasticity
Application of the three-parameter stress function to natural rubbers of widely different hardness. A. J. Carmichael and H. W. Holdaway—1724
Crack propagation in a strain-crystallizing elastomer. E. H. Andrews—452
Dislocation contributions to the modulus and damping in copper at megacycle frequencies. G. A. Alers and D. O. Thompson—283
Elastic constants of bismuth. Yakov Eckstein, A. W. Lawson, and Darrell H. Reneker—752(E)
Elastic constants of single crystals of the bcc transition elements V, Nb, and Ta. D. I. Bolef—100
Elastic constants of single-crystal YIG. A. E. Clark and R. E. Strakna—1172(L)
Elastic constants of TiC and TiB_2. J. J. Gilman and B. W. Roberts—1405(L)
Elastic modulus of amorphous nickel films. Stanka Jovanovic and Cyril Stanley Smith—121(L)
Experimental study of the interrelation between the theory of dislocations in polycrystalline media and finite amplitude wave propagation in solids. James F. Bell—1982
Influence of deformation and temperature on the cobalt gamma irradiation of sodium chloride. Evidence for electrical interaction between dislocations and point defects. Rohn Truell—1601

Elasticity and Anelasticity (*continued*)
- Low-frequency measurements on the Bordoni internal friction peak in copper. D. H. Niblett—895
- Low-temperature internal friction peaks in single crystals of NaCl and LiF. Anthony Taylor—1799 (L)
- Modification of the Koehler-Granato-Lucke dislocation damping theory. J. C. Swartz and J. Weertman—1860
- On the internal friction of cold-worked and quenched martensitic iron and steel. T. Mura, I. Tamura, and J. O. Brittain—92
- On the interpretation of internal friction experiments on strain aging of iron. J. C. Swartz—2048 (L)
- On the measurement of C_{13} in rhombohedral crystals. L. J. Teutonico—119 (L)
- Phenomenological elastomechanical behavior of rubbers over wide ranges of strain. A. J. Carmichael and H. W. Holdaway—159
- Residual thermoelastic stresses in bonded silicon wafers. T. D. Riney—454
- Scattering of plane waves by a rigid ribbon in a solid. K. Harumi—1488
- Semiconducting stress transducers utilizing the transverse and shear piezoresistance effects. W. G. Pfann and R. N. Thurston—2008
- Study of the Bordoni internal friction peaks in copper. Victor K. Paré—332
- Theory and application of a superposition model of internal friction and creep. J. Ross Macdonald—2385
- Thermoelastic equations and Grueneisen's relation. A. M. Freudenthal—1801 (L)
- Third-order elastic moduli of germanium. T. Bateman, W. P. Mason, and H. J. McSkimin—928
- Ultrasonic attenuation of longitudinal waves in plastics. Michel Auberger and John S. Rinehart—219
- Ultrasonic detection of changes in the elastic properties of a 70–30 iron-nickel alloy upon heat treatment. Emmanuel P. Papadakis and Everett L. Reed—682

Electrical Circuits and Networks
- Compact uhf isolator. D. Bruce Swartz—319S
- Energy interchange between cyclotron and synchronous waves in quadrupolar pump fields. E. I. Gordon and A. Ashkin—1137
- Field solution for a thin-films superconducting strip transmission line. James C. Swihart—461
- Generation of microwave electromagnetic radiation in magnetic materials. J. H. Rowen, F. C. Eggers, and W. Strauss—313S
- Impedance of a top-loaded antenna of arbitrary length over a circular grounded screen. James R. Wait and Walter J. Surtees—557 (L)
- Open circuit voltages in the cesium diode. Fred N. Huffman—1927
- Perturbation techniques for miniaturized coaxial *Y*-junction circulators. John Clark—323S
- Phase shift studies in ferrite-dielectric loaded coaxial lines at 2200 Mc. J. J. Rowley—321S
- Preliminary operation of a four-sector racetrack microtron. Eric Brannen and H. Froelich—1179 (L)
- Seesaw maser operation. P. A. Forrester and W. B. Mims—317

Electrical Conductivity (Galvanomagnetic Effects)
- A graphical method for determination of mobility ratio in the semiconductors from Hall effect measurements only. Krzysztof Pigoń—2369
- A method for measuring the conductivity in a high electron density plasma. K. B. Persson—2631
- Angular dependence of magnetoresistance in HgSe. Theodore C. Harman—1800 (L)
- Anodic oxidation of germanium. T. Gabor—1361
- Band structure and transport properties of some 3–5 compounds. H. Ehrenreich—2155
- Band structure of the intermetallic semiconductors from pressure experiments. William Paul—2082
- Conductivity of seeded atmospheric pressure plasmas. L. S. Frost—2029
- Corbino disk. Milton Green—2047 (L)
- Corbino disk magnetoresistivity measurements on InSb. Milton Green—1286
- Current flow across grain boundaries in *n*-type germanium. I. R. K. Mueller—635
- Current flow across grain boundaries in *n*-type germanium. II. R. K. Mueller—640
- Effects of transition metal solutes on the electrical resistivity of copper and gold between 4° and 1200°K. C. A. Comenicali and E. L. Christenson—2450
- Electrical and optical properties of mercury selenide (HgSe). H. Gobrecht, U. Gerhardt, B. Peinemann, and A. Tausend—2246
- Electrical and optical properties of the II–V compounds. W. J. Turner, A. S. Fischler, and W. E. Reese—2241
- Electrical conduction and breakdown in high-pressure (0.25–300 mm) rare gases. R. Forman—1651
- Electrical conductivity and thermoelectric effect in single-crystal TiC. Lewis E. Hollander, Jr.—996
- Electrical conductivity in flame gases with large concentrations of potassium. G. J. Mullaney, P. H. Kydd, and N. R. Dibelius—668
- Electrical conductivity of NaCl during high-temperature creep. R. W. Christy and W. E. Daniels, Jr.—1265
- Electrical properties of lead telluride. Yasuo Kanai, Riro Nii, and Naozo Watanabe—2146
- Electrical resistivity of chromium in the vicinity of the Néel temperature. M. J. Marcinkowski and H. A. Lipsitt—1238
- Electrical resistivities of nickel-niobium solid solutions. Sigurds Arajs—97
- Electron mobilities and tunneling currents in silicon. R. A. Logan, J. F. Gilbert, and F. A. Trumbore—131 (L)
- Energy band structure of gallium antimonide. W. M. Becker, A. K. Ramdas, and H. Y. Fan—2094
- Energy dependence of radiation damage in tungsten. D. R. Muss and J. R. Townsend—189
- Energy of spectrum and scattering of current carriers in gallium arsenide. D. N. Naseledov—2140
- Galvanomagnetic properties of InSb. H. Weiss—2064
- Galvanomagnetic effects in III–V compound semiconductors. A. C. Beer—2107
- Heitler-London approach to electrical conductivity. Jiro Yamashita—2215
- High-field conductivity in germanium and silicon at microwave frequencies. J. Zucker, V. J. Fowler, and E. M. Conwell—2606
- Impurity band conduction and the problem of excess current in tunnel diodes. T. P. Brody—746 (L)
- Influence of conductivity gradients on galvanomagnetic effects in semiconductors. R. T. Bate and A. C. Beer—800
- Influence of magnetoconductivity discontinuities on galvanomagnetic effects in indium antimonide. R. T. Bate, J. C. Bell, and A. C. Beer—806
- Influence of tensor conductivity on current distribution in a MHD generator. H. Hurwitz, Jr., R. W. Kilb, and G. W. Sutton—205
- Influence of the cathode surface on arc velocity. T. J. Lewis and P. E. Secker—54
- Influence of the Hall effect upon the transverse magnetoresistance in indium antimonide. Charles A. Simmons—1970

Interrelation of electronic properties and defect equilibria in PbTe. E. Miller, K. Komarek, and I. Cadoff—2457
Investigations on silicon carbide. H. J. van Daal, C. A. A. J. Greebe, W. F. Knippenberg, and H. J. Vink—2225
Investigations on SnS. W. Albers, C. Haas, H. J. Vink, and J. D. Wasscher—2220
Magnetoresistive measurements on domain rotation and wall development in Ni-Fe alloy films. Forrest G. West—290S
Magnetoresistance and magnetic switching in permalloy films. R. L. Coren and H. J. Juretschke—292S
Majority carrier magnetosurface effect. Robert D. Larrabee—2019
Measurement of the electrical conductivity and dielectric constant without contacting electrodes. Tomoya Ogawa—583
Model for the electronic transport properties of mixed valency semiconductors. R. C. Miller, R. R. Heikes, and R. Mazelsky—2202
Negative resistance and hot electrons. I. Adawi—1101
Nonohmic behavior in near-stoichiometric rutile (TiO_2). E. H. Greener and D. H. Whitmore—1320
Observations on the striation of electrically exploded copper foils. Eugene C. Cnare—1043
Oscillatory magnetoresistance in the conduction band of PbTe. K. F. Cuff, M. R. Ellett, and C. D. Kuglin—2179
Polaron band model and its application to Ce-S semiconductors. J. Appel and S. W. Kurnick—2206
Properties of semi-insulating GaAs. C. H. Gooch, C. Hilsum, and B. R. Holeman—2069
Recent studies of bismuth telluride and its alloys. H. J. Goldsmid—2198
Recent studies on rutile (TiO_2). H. P. R. Frederikse—2211
Resistance heating in the arc cathode spot zone. J. A. Rich—1023
Righi-Leduc effect in mercuric selenide. Charles R. Whitsett—2257
Some electrical and optical properties of ZnSe. M. Aven, D. T. F. Marple, and B. Segall—2261
Some properties of HgSe-HgTe solid solutions. M. Rodot, H. Rodot, and R. Triboulet—2254
Some properties of *p-n* junctions in GaP. H. G. Grimmeiss and A. Rabenau—2123
Study of band structure of intermetallic compounds by pressure experiments. A. Sagar and R. C. Miller—2073
Theory of microplasma instability in silicon. R. J. McIntyre—983
Theory of the potential well produced by multipacting electrons. Part I. Very low pressure regime. R. L. Ingraham—2553
Transference number measurements for aluminum oxide. W. D. Kingery and G. E. Meiling—556(L)
Tunneling through thin insulating layers. J. C. Fisher and I. Giaever—172
Uniformity of electrical current flow in cylindrical semiconductor specimens with cylindrical metallic end caps. R. Simon, J. H. Cahn, and J. C. Bell—46

Electromagnetic Waves
Backward-wave microwave oscillations in a system composed of an electron beam and a hydrogen gas plasma. R. Targ and L. P. Levine—731
Backward waves in longitudinally magnetized ferrite rods. G. H. B. Thompson—2491(L)
Backward waves in longitudinally magnetized ferrite rods. A. W. Trivelpiece, A. Ignatius, and P. C. Holscher—259
Calculation of x-ray intensities from electron probe specimens. L. S. Birks—387
Determination of field strength for field evaporation and ionization in the field ion microscope. Erwin W. Muller and Russell D. Young—2425
Effect of cobalt oxide in porous nickel ferrites at very high frequency. Harry F. Remde—384S
Electric breakdown strength of single and laminated films of vinyl chloride-acetate. Robert G. Greenler and Robert M. Kay—1252
Electromagnetic surface waves on a plane interface. B. A. Lengyel and K. M. Mitzner—1758
Energy interchange between cyclotron and synchronous waves in quadrupolar pump fields. E. I. Gordon and A. Ashkin—1137
Excitation and amplification of cyclotron waves and thermal orbits in the presence of space charge. R. Adler, A. Ashkin, and E. I. Gordon—672
Experimental confirmation of Lamb waves at megacycle frequencies. D. C. Worlton—967
Free carrier cyclotron resonance, Faraday rotation, and Voigt double refraction in compound semiconductors. E. D. Palik, S. Teitler, and R. F. Wallis—2132
Generalized coupled mode theory. M. C. Pease—1736
Generation of microwave electromagnetic radiation in magnetic materials. J. H. Rowen, F. G. Eggers, and W. Strauss—313S
Generation of millimeter waves by the electron beam of a microtron. E. Brannen, H. Froelich, and T. W. W. Stewart—964(E)
Harmonic generation and frequency mixing in ferromagnetic insulators. R. L. Jepsen—2627
Impedance of a top-loaded antenna of arbitrary length over a circular grounded screen. James R. Wait and Walter J. Surtees—557(L)
Microwave analog to the scattering of light by nonspherical particles. J. Mayo Greenberg, Norman E. Pedersen, and Jeanne C. Pedersen—233
Microwave harmonic generation by ferrimagnetic crystals. D. D. Douthett, I. Kaufman, and A. S. Risley—1905
Microwave measurements of the radiation temperature of plasmas. G. Bekefi and Sanborn C. Brown—25
Microwave propagation through a magnetoplasma. R. L. Phillips, R. G. DeLosh, and D. E. White—551(L)
Microwave propagation through a magnetoplasma. R. L. Phillips, R. G. DeLosh, and W. E. White—1406(E)
Momentum and energy of waves. J. R. Pierce—2580
Parametric coupling between the transverse waves on *O*- and *M*-type beams. J. W. Klüver—1111
Propagation in periodic electron beams. W. M. Mueller—1349
Proposed fiber cavities for optical masers. E. Snitzer—36
Radiation from a modulated electron beam with a plasma background. Philip Parzen—2484
Reflection and transmission of electromagnetic waves at electron density gradients. Frank A. Albini and Robert G. Jahn—75
Reflection of electromagnetic waves at electron density ramps. Leonard S. Taylor—1796(L)
Reflection of an electron beam from high-frequency fields. R. B. Hall and Sanborn C. Brown—1835
Theory of quantum oscillators in a multimode cavity. W. G. Wagner and G. Birnbaum—1185

Electrostatic Fields (see also Space Charge)
Charged cylindrical tube. T. R. Ferguson and R. H. Duncan—1385
Determination of field strength for field evaporation and ionization in the field ion microscope. Erwin W. Muller and Russell D. Young—2425
Discharge photocells for the detection of resonance radiation. W. E. Bell and A. L. Bloom—906

Electrostatic Fields (*continued*)
Electric strength of rutile single crystals. D. A. Powers and I. J. T. Johansen—1083
Experimental evidence for the existence of two distinct field emission characteristics from silicon emitters. R. L. Perry—128(L)
Experimental investigation of the Sumoto effect. William F. Pickard—1888
Experimental study of arc stability. II. An investigation of mercury arc stability. G. A. Farrall and G. H. Reiling—1528
Fields in cavity-excited accelerators. E. G. Cristal and J. Van Bladel—1715
Forces in dielectric fluids. James D. Horgan and David L. Edwards—1784(L)
Formation of liquid jets in nonuniform electric fields. Herbert A. Pohl—1784(L)
Influence of the cathode surface on arc velocity. T. J. Lewis and P. E. Secker—54
Nanosecond triggering of air gaps with intense ultraviolet light. Terry F. Godlove—1589
On the microscopic analysis of the conducting electromechanical solid with application to cylinders subjected to axial electric fields. R. C. Geldmacher—143
On the question of ball lightning. Paul A. Silberg—30
Electron and Ion Emission
Bismuth-silver-oxygen-cesium photocathode. A. H. Sommer and W. E. Spicer—1036
Effects of monolayer adsorption and bombardment damage or Auger Electron ejection from germanium. Homer D. Hagstrum—1015
Effect of temperature on the emission of electrons from abraded surfaces of beryllium, calcium, aluminum, and magnesium. T. C. Ku and W. T. Pimbley—124(L)
Effect of temperature on the exoemission of electrons from abraded aluminum surfaces. W. T. Pimbley and E. E. Francis—1729
Electron bunching in the multipacting mechanism of high-frequency discharge. Albert J. Hatch—1086
Electron emission from reverse-biased *p-n* junctions in SiC. Lyle Patrick—2047(L)
Electron trajectories in a nonuniform axially symmetric magnetic field. D. A. Dunn and R. E. Holaday—1612
Electronic and ionic current at the cathode of a hollow-cathode discharge. V. K. Rohatgi—1173(L)
Emission fluctuations of tungsten-based barium dispenser cathodes. I. Brodie—2039
Etch effects from oblique-incidence ion bombardment. G. D. Magnuson, B. B. Meckel, and P. A. Harkins—369
Experimental evidence for the existence of two distinct field emission characteristics from silicon emitters. R. L. Perry—128(L)
Mass spectrographic analysis of insulators using a vacuum spark positive ion source. A. J. Ahearn—1195
Mercury ion beam sputtering of metals at energies 4–15 kev. G. K. Wehner and D. Rosenberg—887
On the thermionic properties of ZrC, UC, and ZrC·UC mixture. W. E. Danforth and Albert J. Williams, III—1181(L)
Operation of tunnel-emission devices. C. A. Mead—646
Sputtering of vitreous silica by 20- to 60-kev Xe^+ ions. R. L. Hines and R. Wallor—202
Sputtering yields of metals for Ar^+ and Ne^+ ions with energies from 50–60 ev. Nils Laegreid and G. K. Wehner—365
Temperature-dependent bismuth-cesium photosurfaces. R. J. Zollweg and C. R. Taylor—1316
Thermionic and photoelectric emission from magnesium oxide. James R. Stevenson and Eugene B. Hensley—166
Thermionic emission constants and their interpretation. Eugene B. Hensley—301
Thermionic emission from a tantalum crystal in cesium or rubidium vapor. H. F. Webster—1802(L)
Thermionic emission from spherical metallic particles. M. S. Sodha—2059(L)
Thermionic emission of UC-Nb. R. H. Abrams, Jr., and F. E. Jamerson—1783(L)
Thermionic properties of HfC. John H. Ingold—2651(L)
Tunneling through thin insulating layers. J. C. Fisher and I. Giaever—172
Use of monomolecular layers in evaporated-film tunneling devices. J. L. Miles and H. O. McMahon—1176(L)
Electron and Ion Optics
Drift velocity of a charged particle in an inhomogeneous magnetic field. James Hurley—2368
Electron-emission microscope and velocity distribution studies on silicon carbide *p-n* junction emitters. P. H. Gleichauf and V. Ozarow—549(L)
Operation of the field ion microscope with a dynamic gas supply. B. J. Waclawski and E. W. Müller—1472
Study of Li-O interaction in Si by ion drift. E. M. Pell—1048
Electron Beams
Back scattering of electrons. G. D. Archard—1505
Backward-wave microwave oscillations in a system composed of an electron beam and a hydrogen gas plasma. R. Targ and L. P. Levine—731
Calculation of x-ray intensities from electron probe specimens. L. S. Birks—387
Coupled mode theory of electron-beam parametric amplification. R. W. Gould and C. C. Johnson—248
Dissociation of adsorbed CO by slow electrons. George E. Moore—1241
Electron beam excitation of a Fabry-Perot interferometer. Murray D. Sirkis, Robert J. Strain, and William E. Kunz—2055(L)
Electron interferometer studies of iron whiskers. H. A. Fowler, L. Marton, J. Arol Simpson, and J. A. Suddeth—1153
Energy interchange between cyclotron and synchronous waves in quadrupolar pump fields. E. I. Gordon and A. Ashkin—1137
Experimental study of anomalous electron stream behavior. M. H. Miller and W. G. Dow—274
Generation of millimeter waves by the electron beam of a microtron. E. Brannen, H. Froelich, and T. W. W. Stewart—964(E)
Interaction of slow electrons with insulating crystals. I. Absorption coefficient for cleaved alkali halides; experimental techniques. C. J. Cook and William J. Fredericks—860
On E. L. Chu's definition of small-signal rf power of electron beams. D. L. Bobroff, H. A. Haus, and J. W. Kluver—749(L)
Parametric coupling between the transverse waves on *O*- and *M*-type beams. J. W. Klüver—1111
Propagation in periodic electron beams. W. M. Mueller—1349
Quasi-Brillouin electron streams. M. H. Miller—1791(L)
Radiation from a modulated electron beam with a plasma background. Philip Parzen—2484
Reflection of an electron beam from high-frequency fields. R. B. Hall and Sanborn C. Brown—1835
Electron Microscopy
Direct observation in the electron microscope of oxide layers on aluminum. K. Thomas and M. W. Roberts—70
Electron-emission microscope and velocity distribution studies on silicon carbide *p-n* junction emitters. P. H. Gleichauf and V. Ozarow—549(L)

Electron microscope observation of dislocations in talc. S. Amelinckx and P. Delavignette—341
Electron microscope study of radiation damage in graphite. W. Bollmann—869
Nonbasal glide in dislocation-free cadmium crystals. I. The (10$\bar{1}$1) [1$\bar{2}$10] system. P. B. Price—1746
Nonbasal glide in dislocation-free cadmium crystals. II. The ($\bar{1}$122) [1123] system. P. B. Price—1750
Single-crystal tin films. Richard W. Vook—1557
Transmission electron microscope observations of magnetic domain walls. J. T. Michalak and R. C. Glenn—1261
Transmission electron microscopy of Alnico. V. J. M. Capenos and Bani R. Banerjee—323(L)

Electron Paramagnetic Resonance
Chromium ion pair interactions in the paramagnetic resonance spectrum of ruby. H. Statz, L. Rimai, M. J. Weber, G. A. deMars, and G. F. Koster—218S
Cross-doping agents for rutile masers. P. F. Chester—866
Electron spin resonance in powders. Gerald Burns—2048(L)
Electron spin resonance in neutron-irradiated quartz. Robert H. Silsbee—1459
Electron spin resonance in semiconducting rutile. P. F. Chester—2233
Paramagnetic resonance of defects introduced near the surface of solids by mechanical damage. G. K. Walters and T. L. Estle—1854
Paramagnetic resonance of *S* state ions in metals. Martin Peter—338S
Paramagnetic resonance measurements of exchange interactions. J. Owen—213S
Zero-field splitting of the Cr^{3+} ground state in YGa and YAl garnet. J. E. Carson and R. L. White—1787(L)

Electron Tubes
Emission fluctuations of tungsten-based barium dispenser cathodes. I. Brodie—2039

Energy Conversion
Alternating current magnetohydrodynamic generator. P. R. Smy—1946
Application of ferroelectricity to energy conversion processes. W. H. Clingman and R. G. Moore, Jr.—675
Available power from a nonideal thermal source. Paul Penfield, Jr.—1794(L)
Calculation of the maximum efficiency of the thermionic converter. John H. Ingold—769
Calculations of the thermoelectric parameters and the maximum figure of merit for acoustical scattering. Louis R. Testardi—1978
Detailed balance limit of efficiency of *p-n* junction solar cells. William Shockley and Hans J. Queisser—510
End effect losses in dc magnetohydrodynamic generators. Roland A. Boucher and Dennis B. Ames—755
Influence of tensor conductivity on current distribution in a MHD generator. H. Hurwitz, Jr., R. W. Kilb, and G. W. Sutton—205
Interpretation of experimental characteristics of cesium thermionic converters. E. N. Carabateas, S. D. Pezaris, and G. N. Hatsopoulos—352
Low-frequency oscillations in a filamentary cathode cesium diode converter. K. P. Luke and F. E. Jamerson—321(L)
On the thermionic properties of ZrC, UC, and ZrC·UC mixture. W. E. Danforth and Albert J. Williams, III—1181(L)
Open circuit voltages in the cesium diode. Fred N. Huffman—1927
Optimization of emission-limited thermionic generators. Alfred Schock—1564
Oscillations and saturation current measurements in thermionic conversion cells. R. J. Zollweg and Milton Gottlieb—890
Paramagnetic maser oscillator analysis. S. Wang and J. R. Singer—1371
Peltier coefficient at high current levels. John R. Reitz—1623(L)
Relaxation oscillations in a plasma diode. J. M. Rocard and G. W. Paxton—1171(L)
Response of a thermocouple circuit to nonsteady currents. Thomas T. Arai and John R. Madigan—609
Shock-wave compression of iron and bismuth. D. S. Hughes, L. E. Gourley, and Mary F. Gourley—624
Spectral response of solar cells. Brian Dale and F. P. Smith—1377
Theoretical bound on the thermoelectric figure of merit from irreversible thermodynamics. Howard Littmann and Burton Davidson—217
Thermionic emission from a tantalum crystal in cesium or rubidium vapor. H. F. Webster—1802(L)
Thermionic emission of UC-Nb. R. H. Abrams, Jr., and F. E. Jamerson—1783(L)
Thermionic properties of HfC. John H. Ingold—2651(L)
Thermodynamics of thermally regenerated fuel cells. J. B. Friauf—616
Transient effects in Peltier coolers. A. D. Reich, T. Arai, and J. R. Madigan—2493(L)
Transient response of a thermocouple circuit under steady currents. Allen D. Reich and John R. Madigan—294
Zero-, first-, and second-order theories of a general thermocouple. A. H. Boerdijk—1584

Experimental Techniques and Instruments
Calculation of x-ray intensities from electron probe specimens. L. S. Birks—387
Development and preliminary testing of a device for electrostatic classification of submicron airborne particles. G. Langer and J. L. Radnik—955
Discharge photocells for the detection of resonance radiation. W. E. Bell and A. L. Bloom—906
Electron beam excitation of a Fabry-Perot interferometer. Murray D. Sirkis, Robert J. Strain, and William E. Kunz—2055(L)
Electron interferometer studies of iron whiskers. H. A. Fowler, L. Marton, J. Arol Simpson, and J. A. Suddeth—1153
Equilibrium atmosphere schedules for the cooling of ferrites. John M. Blank—378S
Far infrared and microwave detector. D. W. Goodwin and R. H. Jones—2056(L)
Flash method of determining thermal diffusivity, heat capacity, and thermal conductivity. W. J. Parker, R. J. Jenkins, C. P. Butler and G. L. Abbott—1679
Hot-cathode magnetron ionization gauge for the measurement of ultrahigh vacua. J. M. Lafferty—424
Hydromagnet: a self-generating liquid conductor electromagnet. Henry H. Kolm and Osman K. Mawardi—1296
Induction-coupled plasma torch. Thomas B. Reed—821
Interaction of slow electrons with insulating crystals. I. Absorption coefficient for cleaved alkali halides; experimental techniques. C. J. Cook and William J. Fredericks—860
Interference method for measuring the thickness of epitaxially grown films. W. G. Spitzer and M. Tanenbaum—744(L)
Measurement of minority carrier lifetime in SiC by a novel electroluminescent method. G. G. Harman and R. L. Raybold—1168(L)
On the theoretical limitation of a radio telescope in determining the sky temperature distribution. Y. T. Lo—2052(L)

Experimental Techniques and Instruments (*continued*)

Particle interaction in magnetic recording tapes. J. G. Woodward and E. Della Torre—126(L)

Proposed method of measuring thermal diffusivity at high temperatures. Robert D. Cowan—1363

Pulse method for the measurement of thermal diffusivity of metals. Edwin L. Woisard—40

Radio-frequency technique for pulling oxide crystals without employing a crucible susceptor. F. R. Monforte, F. W. Swanekamp, and L. G. Van Uitert—959(L)

Semiconducting stress transducers utilizing the transverse and shear piexoresistance effects. W. G. Pfann and R. N. Thurston—2008

Spherical lenses for infrared and microwaves. G. Toraldo de Francia—2051(L)

Stability of pressure-supported molten zones in horizontal sheets. H. P. Kramer, B. P. Bogert, and D. W. Hagelbarger—764

Superconductor-transition switching time measurements using a superconductive radio-frequency mixer. Donald L. Feucht and James B. Woodford, Jr.—1882

Useful technique for growing large, single-crystal YIG. Don Barry and Roy W. Roberts—1405(L)

X-ray polarizer. H. Cole, F. W. Chambers, and C. G. Wood—1942

Explosions and Explosives

Behavior of exploding gold wires. T. J. Tucker—1894

Electrically imploded-exploded aluminum tube. Eugene C. Cnare—1275

Growth of explosion in electrically initiated RDX. G. M. Muller, D. B. Moore, and D. Bernstein—1065

Initiation of a low-density PETN pressing by a plane shock wave. G. E. Seay and L. B. Seely, Jr.—1092

Observations on the striation of electrically exploded copper foils. Eugene C. Cnare—1043

On a problem in the thermal stability of explosives. Mahinder P. Murgai, James O. Milmoe, James P. Kottenstette, and Fred L. Smith—324(L)

Production of high ion densities in helium by means of high explosives. G. E. Seay, L. B. Seely, Jr., and R. G. Fowler—2439

Transparency of glass and certain plastics under shock attack. H. Dean Mallory and William S. McEwan—2421

Ferroelectricity (see also Dielectrics)

Application of ferroelectricity to energy conversion processes. W. H. Clingman and R. G. Moore, Jr.—675

Bismuth titanate. A ferroelectric. L. G. Van Uitert and L. Egerton—959(L)

Ferromagnetic resonance in piezoelectric $Ga_{2-x}Fe_xO_3$. A. Dymanus and I. P. Kaminow—144S

Increase in dielectric constant during switching in lithium selenite and triglycine sulfate. Ennio Fatuzzo—1571

Models for switching in ferroelectrics. David J. White—1169(L)

Motion of 180° domain walls in $BaTiO_3$ under the application of a train of voltage pulses. Robert C. Miller and Albert Savage—714

Multiple shock wave structures in polycrystalline ferroelectrics. C. E. Reynolds and G. E. Seay—1401(L)

On the microscopic analysis of the conducting electromechanical solid with application to cylinders subjected to axial electric fields. R. C. Geldmacher—143

Piezoelectric behavior of impacted quartz. R. A. Graham—555(L)

Piezoelectricity of quartz for finite strain. S. Machlup and M. E. Christopher—1387

Piezoelectric scattering and phonon drag in ZnO and CdS. A. R. Hutson—2287

Stress dependence of the piezoresistance effect. Donald Long—2050(L)

Surface layer in $BaTiO_3$ single crystals. Ennio Fatuzzo and Walter J. Merz—1685

Surface layers on barium titanate single crystals above the Curie point. H. Schlosser and M. E. Drougard—1227

The motion of c domain centers in $BaTiO_3$. G. L. Link—2566

Variation of permittivity with electric field in perovskite-like ferroelectrics. Howard Diamond—909

Ferromagnetic Materials and Ferrites (see also Ferromagnetic Resonance, Magnetic Domain Wall Behavior, Magnetic Devices, Magnetization)

Angular variation of the magnetic properties of partially aligned γ-Fe_2O_3 particles. G. Bate—239S

Anisotropic Curie temperature. Earl R. Callen—221S

Anisotropy and magnetostriction in magnetic oxides. J. C. Slonczewski—253S

Anisotropy in permalloy films evaporated at grazing incidence. M. S. Cohen—87S

Anisotropy in nickel-iron films. D. O. Smith—70S

Anisotropy of YIG calculated from crystal field parameters Fe^{3+} in yttrium gallium garnet. S. Geschwind—263S

Anisotropy rotation in thin permalloy films at room temperature. T. Matcovich, E. Korostoff, and A. Schmeckenbecher—93S

Annealing behavior and temperature dependence of the magnetic properties of thin Permalloy films. Armin Segmüller—89S

Annealing of oblique-incidence permalloy films. G. P. Weiss and D. O. Smith—85S

Backward waves in longitudinally magnetized ferrite rods. G. H. B. Thompson—2491(L)

Backward waves in longitudinally magnetized ferrite rods. A. W. Trivelpiece, A. Ignatius, and P. C. Holscher—259

Behavior of ferro- or ferrimagnetic very fine particles. C. J. Lin—233S

Cation distributions in magnesium-nickel ferrites. C. J. Kriessman and S. E. Harrison—392S

Cobalt ferrite single crystals. A. Ferretti, R. J. Arnott, E. Delaney, and A. Wold—905

Comment on the saturation magnetization of neodymium yttrium iron garnet. Robert L. White—1178(L)

Crystal lattice investigation of the permanent magnet precipitate in various Alnico materials. K. J. Kronenberg—196S

Cube texture in ultrathin molybdenum Permalloy tape. P. K. Koh—358S

Curie temperature of some garnets by the differential thermal analysis technique. A. Aharoni, E. H. Frei, Z. Scheidlinger, and M. Schieber—1851

Determination of the directions of magnetization in polycrystalline ferrites. D. R. Callaby—298S

Diffusion in a ferromagnetic alloy. James Stanley and Charles Wert—267

Diffusion reactions in the aging of 4-79 molybdenum Permalloy. E. M. Tolman—360S

Domain structures in iron whiskers as observed by the Kerr method. C. A. Fowler, Jr., E. M. Fryer, and D. Treves—296S

Domain wall mobility in single-crystal yttrium iron garnet. F. B. Hagedorn and E. M. Gyorgy—282S

Effect of cobalt oxide in porous nickel ferrites at very high frequency. Harry F. Remde—384S

Effect of frequency modulation on subsidiary resonance in ferrites. J. F. Ollom and H. L. Goldstein—2059(L)

Effect of indium substitution in yttrium iron garnet: high permeability garnets. J. Richard Cunningham, Jr., and Elmer E. Anderson—388S

Effect of magnetic clusters on the specific heat of Ni-Cu and Fe-V alloys. K. Schröder—800
Elastic constants of single-crystal YIG. A. E. Clark and R. E. Strakna—1172(L)
Elongated iron-cobalt: ferrite, a new, lightweight, permanent magnet material. R. B. Falk and G. D. Hooper—190S
Epitaxial growth and magnetic properties of single-crystal films of iron, nickel, and Permalloy. Soshin Chikazumi—81S
Equilibrium atmosphere schedules for the cooling of ferrites. John M. Blank—378S
Exchange inversion in $Mn_{2-x}Cr_xSb$. W. H. Cloud, T. A. Bither, and T. J. Swoboda—55S
Exchange anisotropy in oxidized iron-cobalt particles. F. J. Darnell—186S
Experimental g' and g values of Fe, Co, Ni, and their alloys. A. J. P. Meyer, and G. Asch—330S
Ferrimagnetic resonance and torque measurements on ytterbium-substituted yttrium iron garnet. R. W. Teale, R. F. Pearson, and M. J. Hight—150S
Ferrimagnetic resonance in single crystals of cobalt-substituted manganese ferrite. R. W. Teale and M. J. Hight—140S
Ferrimagnetic resonance in a single-crystal disk of yttrium iron garnet. Archibald W. Smith and Akira Watanabe—155S
Ferrimagnetic resonance of single-crystal barium ferrite in the millimeter wave region. Franklin F. Y. Wang, Koryu Ishii, and James B. Y. Tsui—1621(L)
Ferrite system for application at lower microwave frequencies. Clinton F. Jefferson and Russell G. West—390S
Ferrite thin films. Henry P. Lemaire and William J. Croft—46S
Ferromagnetic alignment by antiferromagnetic exchange interaction. Note on the magnetic behavior of neodymium garnet. W. P. Wolf—742(L)
Ferromagnetic nucleation sources on iron whiskers. R. E. De Blois—1561
Ferromagnetic phase of Mn-Al. Robert B. Campbell and Carl A. Julien—346S
Ferromagnetic relaxation at low microwave frequencies. J. J. Green and E. Schlömann—168S
Ferromagnetic resonance in piezoelectric $Ga_{2-x}Fe_xO_3$. A. Dymanus and I. P. Kaminow—144S
Ferromagnetic resonance due to magnetic fields generated by displacement currents in ferrites. Isidore Bady and Gilbert McCall—146S
Ferromagnetic resonance linewidth in cobalt-substituted ferrites. C. Warren Haas and Herbert B. Callen—157S
Fine-grained ferrites. I. Nickel ferrite. W. W. Malinofsky and R. W. Babbitt—237S
Fine-wire ferrite limiter. Ernest Stern—315S
First magnetocrystalline anisotropy constants of some iron-silicon alloys. Sigurds Arajs, Henry Chessin, and D. S. Miller—857
Flux distribution in ferrite cores under various modes of partial switching. R. H. James, W. M. Overn, and C. W. Lundberg—38S
Free oscillations of the magnetization permalloy films. Peter Wolf—95S
Frequency dependence of ultrasonic wave attenuation in Armco iron and low-carbon steel. U. M. Martius and W. J. Bratina—280S
Generation of microwave electromagnetic radiation in magnetic materials. J. H. Rowen, F. G. Eggers, and W. Strauss—313S
Growth of single-crystal iron ferrites by the Czochralski method. F. H. Horn—900
Growth of yttrium iron garnet single crystals by the floating zone technique. L. L. Abernethy, T. H. Ramsey, Jr., and John W. Ross—376S
Harmonic generation and frequency mixing in ferromagnetic insulators. R. L. Jepsen—2627
High-power characteristics of low-magnetization garnets. J. H. Saunders and J. J. Green—161S
High-temperature magnetic lag in iron-nickel alloys. Dieter Gerstner and Eckart Kneller—364S
High-temperature stability of magnetic materials. Norman Pavlik—372S
Improved magnetic properties of high-purity iron-cobalt alloys containing 27–43% cobalt. Daniel S. Shull, Jr.—356S
Induced magnetic anisotropy created by magnetic or stress annealing of iron-aluminum alloys. H. J. Birkenbeil and R. W. Cahn—362S
Initial permeability characteristics of vanadium-doped manganese-zinc ferrites. Yūzō Shichijō, Noboru Tsuya, and Kōki Suzuki—386S
Losses in silicon iron at very low frequencies and high flux densities. Daniel A. Wycklendt and Robert M. Kay—368S
Low-temperature magnetic properties of some rare-earth garnet compounds. M. Ball, G. Garton, M. J. M. Leask, D. Ryan, and W. P. Wolf—267S
Low-temperature pyromagnetic measurements on nickel. E. W. Pugh and B. E. Argyle—334S
Magnetic anisotropy of cobalt as revealed by electron diffraction. S. Yamaguchi—961(L)
Magnetic anisotropies of nickel films evaporated and measured at 10^{-8} mm Hg and below. C. D. Graham, Jr., and J. M. Lommel—83S
Magnetic anisotropy of yttrium iron garnet at 0°K. L. R. Walker—264S
Magnetic annealing of "ticonal" G magnet steel. H. Zijlstra—194S
Magnetic characteristics of some intermetallic compounds between manganese and the lanthanide metals. L. V. Cherry and W. E. Wallace—340S
Magnetic core losses resulting from a rotating flux. Asa Kaplan—370S
Magnetic domain patterns in Cr-modified Mn_2Sb. J. D. Wolf and J. E. Hanlon—2584
Magnetic moments of compounds of cobalt with rare-earth elements having a Cu_5Ca structure. E. A. Nesbitt, H. J. Williams, J. H. Wernick, and R. C. Sherwood—342S
Magnetic ordering in the ferromagnetic rare-earth metals. Kei Yosida and Hirosi Miwa—8S
Magnetic properties of single-domain iron and iron-cobalt particles prepared by borohydride reduction. A. L. Oppegard, F. J. Darnell, and H. C. Miller—184S
Magnetic properties of the low-temperature form of magnetite. D. B. Bonstrom, A. H. Morrish, and L. A. K. Watt—272S
Magnetic thin films prepared by sputtering. Eric Kay—99S
Magnetization of iron-nickel alloys under hydrostatic pressure. J. S. Kouvel and R. H. Wilson—435
Magnetization of nickel single crystals. Lambros Tterlikkis and Alvin W. Jenkins, Jr.—1293
Magnetization process in small particles of CrO_2. F. J. Darnell—1269
Magnetocrystalline anisotropy of Fe-Si alloy crystals under hydrostatic pressure. J. S. Kouvel and R. H. Wilson—276S
Magnetoresistance and magnetic switching in Permalloy films. R. L. Coren and H. J. Juretschke—292S

Ferromagnetic Materials and Ferrites (*continued*)
- Magnetoresistive measurements on domain rotation and wall development in Ni-Fe alloy films. Forrest G. West—290S
- Metallurgy and magnetic properties of an Fe-Co-V alloy. C. W. Chen—348S
- Microwave harmonic generation by ferrimagnetic crystals. D. D. Douthett, I. Kaufman, and A. S. Risley—1905
- Microwave resonance in tetragonally distorted manganese-iron spinel. James Overmeyer—142S
- New characteristic in the temperature dependence of ferrimagnetic resonance linewidth in some rare-earth doped yttrium iron garnets. J. F Dillon, Jr.—159S
- New magnetic ternary compound with a high crystalline anisotropy. J. H. Wernick, S. E. Haszko, and W. J. Romanow—2495(L)
- Ni-Fe single-crystal films and their magnetic characteristics. R. R. Verderber and B. M. Kostyk—696
- Nonlinear damping losses in YIG. Robert L. Conger—1525
- Nonlinear response of YIG. Robert M. Hill and Robert S. Bergman—227S
- Nuclear magnetic resonance of Fe^{57} in unenriched Fe. J. I. Budnick, L. J. Bruner, R. J. Blume, and E. L. Boyd—120S
- Nuclear magnetic resonance in NiF_2 domain walls. R. G. Shulman—126S
- Nuclear resonances in cubic, hexagonal, and mixed phase cobalt powders and thin films. Wilton A. Hardy—122S
- Nucleation processes in thin Permalloy films. S. Methfessel, S. Middelhoek, and H. Thomas—294S
- Optical and infrared spectra of the ferrites and garnets. Kenneth A. Wickersheim—205S
- Partial rotation in Permalloy films. S. Methfessel, S. Middelhoek, and H. Thomas—1959
- Particle interaction in magnetic recording tapes. J. G. Woodward and E. Della Torre—126(L)
- Phase shift studies in ferrite-dielectric loaded coaxial lines at 2200 Mc. J. J. Rowley—321S
- Preparation and properties of low-loss ferrites. Aaron P. Greifer, Yoshinao Nakada, and Howard Lessoff—382S
- Preparation and properties of thin ferrite films. E. Banks, N. H. Riederman, H. W. Schleuning, and L. M. Silber—44S
- Preparation, growth, and study of ultrafine ferrite particles. W. J. Schuele and V. D. Deetscreek—235S
- Pressure and temperature dependence of the Fe^{57} nuclear magnetic resonance frequency in ferromagnetic iron. G. B. Benedek and J. Armstrong—106S
- Quantitative determination of the interaction fields in aggregates of single-domain particles. Donald F. Eldridge—247S
- Reinterpretation of the reaction kinetics of nickel ferrite. R. C. Turnbull—380S
- Remarks on the magnetic properties of Au-Mn system. Hiroshi Sato—53S
- Report on ferromagnetic resonance at the 1960 conference on magnetism and magnetic materials. George T. Rado—129S
- Rotatable anisotropy in thin Permalloy films. R. J. Prosen, J. O. Holmen, and B. E. Gran—91S
- Saturation magnetization and size of iron particles less than 100 A in diameter. Fred E. Luborsky and Philip E. Lawrence—231S
- Some effects of directional ordering in zone-melted iron. R. E. Maringer—366S
- Some investigations on iron-cobalt permanent magnet alloys of the Vicalloy II type. W. Baran, W. Breuer, H. Fahlenbrach, and K. Janssen—199S
- Some properties of uniaxial Permalloy films prepared by cathodic sputtering. M. H. Francombe and A. J. Noreika—97S
- Spin-flopping in MnF_2 by high magnetic fields. I. S. Jacobs—61S
- Square-loop ferrites with temperature-independent properties and improved disturb ratio. R. S. Weisz—1152
- Stable-oscillation conditions for the magnetic-film parametron. Richard M. Sanders—478
- Structure of Alnico V. Robert B. Campbell and Carl A. Julien—192S
- Structure of nickel chromite. E. Prince—68S
- Studies of a high-coercivity electrodeposit having a lamellar structure. J. S. Sallo and K. H. Olsen—203S
- Subsidiary resonance in YIG. T. S. Hartwick, E. R. Peressini, and M. T. Weiss—223S
- Synthesis and properties of ferromagnetic chromium oxide. T. J. Swoboda, Paul Arthur, Jr., N. L. Cox, J. N. Ingraham, A. L. Oppegard, and M. S. Sadler—374S
- Temperature dependence of magnetostriction and anisotropy in MnBi. P. A. Albert and W. J. Carr, Jr.—201S
- Temperature dependence of the spin-wave spectrum of yttrium iron garnet. R. C. LeCraw and L. R. Walker—167S
- Temperature dependence of spontaneous magnetization in superparamagnetic nickel. Carlos R. Abeledo and P. W. Selwood—229S
- Theoretical and experimental characteristics of a ferromagnetic amplifier using longitudinal pumping. R. T. Denton—300S
- Torque measurements on rare-earth doped yttrium iron garnet. R. F. Pearson and R. W. Cooper—265S
- Transient excitation of nuclei in ferromagnetic metals. M. Weger, E. L. Hahn, and A. M. Portis—124S
- Transmission electron microscopy of Alnico V. J. M. Capenos and Bani R. Banerjee—323(L)
- Traveling-wave frequency doubling in ferrites. B. A. Auld, H. J. Shaw, and D. K. Winslow—317S
- Triangular moment arrangements in manganese-iron spinels. Victor L. Moruzzi—59S
- Two-phase Permalloy for high-speed switching. E. A. Nesbitt and E. M. Gyorgy—1305
- Ultrasonic detection of changes in the elastic properties of a 70–30 iron-nickel alloy upon heat treatment. Emmanuel P. Papadakis and Everett L. Reed—682
- Uniaxial anisotropy in polycrystalline garnets. D. J. Epstein, B. Frackiewicz, and R. P. Hunt—270S
- Unidirectional properties in the iron-iron sulfide system. J. H. Greiner, I. M. Croll, and M. Sulich—188S
- Useful technique for growing large, single-crystal YIG. Don Barry and Roy W. Roberts—1405(L)

Ferromagnet Resonance, Ferri-G Antiferromagnetism
- Anisotropic Curie temperature. Earl R. Callen—221S
- Antiferromagnetic resonance in $(Cr_2O_3)_{1-x}\cdot(Al_2O_3)_x$ single crystals. Simon Foner—63S
- Effect of frequency modulation on subsidiary resonance in ferrites. J. F. Ollo and H. L. Goldstein—2050(L)
- Excitation and boundary effects in spin-wave resonance. R. F. Soohoo—148S
- Ferrimagnetic resonance and torque measurements on ytterbium-substituted yttrium iron garnet. R. W. Teale, R. F. Pearson, and M. J. Hight—150S
- Ferrimagnetic resonance in a single-crystal disk of yttrium iron garnet. Archibald W. Smith and Akira Watanabe—155S
- Ferrimagnetic resonance in single crystals of cobalt-substituted manganese ferrite. R. W. Teale and M. J. Hight—140S
- Ferromagnetic relaxation at low microwave frequencies. J. J. Green and E. Schlömann—168S

Ferromagnetic resonance due to magnetic fields generated by displacement currents in ferrites. Isidore Bady and Gilbert McCall—146S
Ferromagnetic resonance in piezoelectric $Ga_{2-x}Fe_xO_3$. A. Dymanus and I. P. Kaminow—144S
Ferromagnetic resonance in thin magnetic films at radio frequencies. Turner E. Hasty and Lee J. Boudreaux—1807
Ferromagnetic resonance linewidth in cobalt-substituted ferrites. C. Warren Haas and Herbert B. Callen—157S
Infrared antiferromagnetic resonance in MnO. F. Keffer, A. J. Sievers, III, and M. Tinkham—65S
Microwave harmonic generation by ferrimagnetic crystals. D. D. Douthett, I. Kaufman, and A. S. Risley—1905
Microwave resonance in tetragonally distorted manganese-iron spinel. James Overmeyer—142S
New characteristic in the temperature dependence of ferrimagnetic resonance linewidth in some rare-earth doped yttrium iron garnets. J. F. Dillon, Jr.—159S
Note on ferromagnetic relaxation equations. H. Suhl and R. C. Fletcher—281
Note on the back reaction term in ferromagnetic relaxation equations. Herbert Callen—738(L)
Parametric effects in magnetoacoustic resonance. R. L. Comstock, B. A. Auld, and Glen Wade—227S
Report on ferromagnetic resonance at the 1960 conference on magnetism and magnetic materials. George T. Rado—129S
Resonant frequency shift in ellipsoidal samples. T. Matcovich, Henry S. Belson, and N. Goldberg—163S
Subsidiary absorption above ferrimagnetic resonance. P. C. Fletcher and Neal Silence—706
Subsidiary resonance in YIG. T. S. Hartwick, E. R. Peressini, and M. T. Weiss—223S

Fluid Dynamics
Flow of gas through porous media in the region between molecular and viscous condition. E. H. Hirsch—977
Quantitative analysis of two-dimensional flow by means of streaming birefringence. S. P. Sutera and Harold Wayland—721
Resistance to potential flow through a cubical array of spheres. Robert E. Meredith and Charles W. Tobias—132(E)

Fluid Flow, Low Speed
Extension of the Eyring-Ree theory of non-Newtonian flow. Joseph A. Faucher—2336
Non-Newtonian viscosity of polymers. Roger S. Porter and Julian F. Johnson—2326
Nuclear magnetic resonance in flowing liquids. Louis R. Hirschel and Louis F. Libelo—1404(L)
Study of impact cratering in sand. F. L. Culp and H. L. Hooper—2480
Thermorheological simplicity in extrusion flow curves of high polymers. Katsuhiko Ito—1743

Fracture (see also Plastic Deformation)
Crack propagation in a strain-crystallizing elastomer. E. H. Andrews—452
Electrically imploded-exploded aluminum tube. Eugene C. Cnare—1275
Fracture of brittle solids. I. Distribution function for fragment size in single fracture (Theoretical). J. J. Gilvarry—391
Fracture of brittle solids. II. Distribution function for fragment size in single fracture (Experimental). J. J. Gilvarry and B. H. Bergstrom—400
Reduction of cohesion in ionic crystals by dislocations. John J. Gilman—738(L)

Friction and Wear
Frictional behavior of a simple rheological material. R. T. Spurr—1450
Friction and adhesion of clean and contaminated mica surfaces. Anita I. Bailey—1407
Friction of metals in reciprocating sliding. Yasukatsu Tamai—1437
Friction of molybdenum diselenide. Melvin T. Lavik, T. Bruce Daniel, and A. Neal Abbott—1795(L)
Influence of surface energy on friction and wear phenomena. E. Rabinowicz—1440
Lubrication of polymers. C. Rubenstein—1445
On the wear of sapphire. R. P. Steijn—1951
Preface to international conference on the nature of solid friction—1407
Recent work on solid friction at the Research Laboratory for the Physics and Chemistry of Solids. Anita I. Bailey—1413
Rolling friction of polymeric materials. II. Thermoplastics. D. G. Flom—1426
Single contacts and multiple encounters. J. F. Archard—1420
Use of graphite whiskers in a study of the atmosphere dependence of graphite friction. F. R. Rollins, Jr.—1454

Gaseous Electron Physics (see also Sputtering)
A theory for the cathode mechanism in metal vapor arcs. T. H. Lee and Allan Greenwood—2061(E)
Calculation of the maximum efficiency of the thermionic converter. John H. Ingold—769
Discharge photocells for the detection of resonance radiation. W. E. Bell and A. L. Bloom—906
Electrical conduction and breakdown in high-pressure (0.25–300 mm) rare gases. R. Forman—1651
Electrical conductivity in flame gases with large concentrations of potassium. G. J. Mullaney, P. H. Kydd, and N. R. Dibelius—668
Electron bunching in the multipacting mechanism of high-frequency discharge. Albert J. Hatch—1086
Electronic and ionic current at the cathode of a hollow-cathode discharge. V. K. Rohatgi—1173(L)
End effect losses in dc magnetohydrodynamic generators. Roland A. Boucher and Dennis B. Ames—755
Experimental study of arc stability. II. An investigation of mercury arc stability. G. A. Farrall and G. H. Reiling—1528
Magnetically confined cold-cathode gas discharges at low pressures. R. L. Jepsen—2619
New derivation of the vacuum breakdown equation relating breakdown voltage and electrode separation. A. Maitland—2399
Note on the mechanism of the multipactor effect. F. Paschke—747(L)
On the question of ball lightning. Paul A. Silberg—30
Relaxation oscillations in a plasma diode. J. M. Rocard and G. W. Paxton—1171(L)
Resistance heating in the arc cathode spot zone. J. A. Rich—1023
Scaling laws for electric arcs subject to forced convection. Christopher Sherman and J. M. Yos—744(L)
Space-charge instabilities in electron diodes and plasma converters. C. K. Birdsall and W. B. Bridges—2611
Theory for the cathode mechanism in metal vapor arcs. T. H. Lee and Allan Greenwood—916

Glasses and Amorphous Solids (see also Polymers)
Application of the three-parameter stress function to natural rubbers of widely different hardness. A. J. Carmichael and H. W. Holdaway—1724
Concerning dislocations in glass. W. B. Hillig and R. J. Charles—123(L)
Defect mechanisms in a noncrystalline solid. W. C. Levengood—2525

Glasses and Amorphous Solids (*continued*)
- Frequency factors for annealing fast-neutron induced density changes in vitreous silica. William Primak, Herman Szymanski, and David Keiffer—660
- Helium diffusion through glass. V. O. Altemose—1309
- Optical properties of oriented polystyrene. Richard S. Stein—1280
- Polarization and diffusion in a silicate glass. R. J. Charles—1115
- Semiconducting properties of inorganic amorphous materials. H. L. Uphoff and J. H. Healy—950
- Sputtering of vitreous silica by 20- to 60-kev Xe^+ ions. R. L. Hines and R. Wallor—202
- Strength of bulk fused quartz. William B. Hillig—741(L)
- Thermal conductivity of porous media. I. Unconsolidated sands. W. Woodside and J. H. Messmer—1688
- Thermal conductivity of porous media. II. Consolidated rocks. W. Woodside and J. H. Messmer—1699
- Transparency of glass and certain plastics under shock attack. H. Dean Mallory and William S. McEwan—2421
- Vacuum-ultraviolet absorption studies of irradiated silica and quartz. C. M. Nelson and R. A. Weeks—883

Liquids
- Diffusion in a liquid indium-tin alloy at several concentrations. A. Paoletti and M. Vicentini-Missoni—559
- Experimental investigation of the Sumoto effect. William F. Pickard—1888
- Formation of liquid jets in nonuniform electric fields. Herbert A. Pohl—1784(L)
- Hydromagnet: a self-generating liquid conductor electromagnet. Henry H. Kolm and Osman K. Mawardi—1296
- Liquidlike layers on ice. H. H. G. Jellinek—1793(L)
- Optical spectrum of the sonoluminescence emitted by cavitated water. Devanatha Srinivasan and Louis V. Holroyd—449
- Space-time analysis of the sonoluminescence emitted by cavitated water. Robert Q. Macleay and Louis V. Holroyd—449

Luminescence
- Edge emission in zinc selenide single crystals. D. C. Reynolds, L. S. Perdotti, and O. W. Larson—2250
- Effects of phosphor powder dispersion in electroluminescent lamps. W. A. Thornton—2379
- Effects of rare-earth substitutions on the fluorescence of terbium hexa-antipyrine tri-iodide. R. R. Soden—750(L)
- Effect of electron bombardment on the near-infrared fluorescence of single-crystal CdS. B. A. Kulp—1966
- Electroluminescence of *p-n* junctions in gallium phosphide. M. Gershenzon and R. M. Mikulyak—1338
- Etch pits in electroluminescent zinc sulfide crystallites. Paul Goldberg—1520
- Measurement of minority carrier lifetime in SiC by a novel electroluminescent method. G. G. Harman and R. L. Raybold—1168(L)
- Monotonic trap distributions. Richard H. Bube—1621(L)
- Optical spectrum of the sonoluminescence emitted by cavitated water. Devanatha Srinivasan and Louis V. Holroyd—449
- Space-time analysis of the sonoluminescence emitted by cavitated water. Robert Q. Macleay and Louis V. Holroyd—449
- Theory of microplasma instability in silicon. R. J. McIntyre—983
- Thermal tuning of ruby optical maser. I. D. Abella and H. Z. Cummins—1177(L)
- Use of $PrCl_3$ in a solid state infrared quantum counter. John F. Porter, Jr.—825
- Use of $PrCl_3$ in a solid-state infrared quantum counter. John F. Porter, Jr.—1803(E)
- Voltage dependence of microplasma density in *p-n* junctions in silicon. A. Goetzberger and C. Stephens—2646

Magnetic Anisotropy
- Acceleration of rigid, conducting, diamagnetic bodies by a magnetic field. R. U. Ayers—1549
- Angular dependence of torque in anisotropic permalloy films. W. D. Doyle, J. E. Rudisill, and S. Shtrikman—1785(L)
- Anisotropy and magnetostriction in magnetic oxides. J. C. Slonczewski—253S
- Anisotropy in nickel-iron films. D. O. Smith—70S
- Anisotropy in permalloy films evaporated at grazing incidence. M. S. Cohen—87S
- Anisotropy of the spin-wave spectrum. M. W. Muller and C. R. Buffler—152S
- Anisotropy of YIG calculated from crystal field parameters Fe^{3+} in yttrium gallium garnet. S. Geschwind—263S
- Anisotropy rotation in thin permalloy films at room temperature. T. Matcovich, E. Korostoff, and A. Schmeckenbecher—93S
- Exchange anisotropy in mixed manganites with the hausmannite structure. I. S. Jacobs and J. S. Kouvel—274S
- Exchange anisotropy in oxidized iron-cobalt particles. F. J. Darnell—186S
- Exchange anisotropy in stainless steel. W. H. Meiklejohn—274S
- First magnetocrystalline anisotropy constants of some iron-silicon alloys. Sigurds Arajs, Henry Chessin, and D. S. Miller—857
- General superparamagnetic behavior of an aligned assembly of uniaxially anisotropic particles. Forrest G. West—249S
- Induced magnetic anisotropy created by magnetic or stress annealing of iron-aluminum alloys. H. J. Birkenbeil and R. W. Cahn—362S
- Magnetic anisotropy and electrical resistivity in exchange inversion compounds. H. S. Jarrett, P. E. Bierstedt, F. J. Darnell, and M. Sparks—57S
- Magnetic anisotropy of cobalt as revealed by electron diffraction. S. Yamaguchi—961(L)
- Magnetic anisotropies of nickel films evaporated and measured at 10^{-8} mm Hg and below. C. D. Graham, Jr., and J. M. Lommel—83S
- Magnetic anisotropy of yttrium iron garnet at 0°K. L. R. Walker—264S
- Magnetocrystalline anisotropy of Fe-Si alloy crystals under hydrostatic pressure. J. S. Kouvel and R. H. Wilson—276S
- New magnetic ternary compound with a high crystalline anisotropy. J. H. Wernick, S. E. Haszko, and W. J. Romanow—2495(L)
- Oblique-incidence anisotropy in evaporated films. M. S. Cohen, D. O. Smith, and G. P. Weiss—1405(E)
- Rotatable anisotropy in thin permalloy films. R. J. Prosen, J. O. Holmen, and B. E. Gran—91S
- Some effects of directional ordering in zone-melted iron. R. E. Maringer—366S
- Temperature dependence of magnetostriction and anisotropy in MnBi. P. A. Albert and W. J. Carr, Jr.—201S
- Theoretical magnetization curves for particles with cubic anisotropy. Clark E. Johnson, Jr. and William Fuller Brown, Jr.—243S
- Torque measurements on rare-earth doped yttrium iron garnet. R. F. Pearson and R. W. Cooper—265S
- Uniaxial anisotropy in polycrystalline garnets. D. J. Epstein, B. Frackiewicz, and R. P. Hunt—270S

Magnetic Domain Wall Behavior
- Development of elongated particle magnets. Fred E. Luborsky—171S

Domains and extreme value statistics. William Fuller Brown, Jr.—278S
Domain structures in iron whiskers as observed by the Kerr method. C. A. Fowler, Jr., E. M. Fryer, and D. Treves—296S
Domain wall mobility in single-crystal yttrium iron garnet. F. B. Hagedorn and E. M. Gyorgy—282S
Limitations of the magneto-optic Kerr technique in the study of microscopic magnetic domain structures. D. Treves—358
Magnetic domain patterns in Cr-modified Mn_2Sb. J. D. Wolf and J. E. Hanlon—2584
Magnetic properties of single-domain iron and iron-cobalt particles prepared by borohydride reduction. A. L. Oppegard, F. J. Darnell, and H. C. Miller—184S
Magnetic viscosity due to solute atom pairs. Part II. Experimental results. G. Biorci, A. Ferro, and G. Montalenti—630
Magnetoresistive measurements on domain rotation and wall development in Ni-Fe alloy films. Forrest G. West—290S
Measurements of the domain wall area-mobility product during slow flux reversals. R. M. Brownell and R. C. Barker—284S
Nuclear magnetic resonance in NiF_2 domain walls. R. G. Shulman—126S
Observations of cross-tie domain walls by the Faraday effect. A. L. Houde—1234
On additivity of imperfections as means for domain nucleation. A. Aharoni—245S
Properties of single-domain particles of cobalt-nickel. R. B. Falk and G. D. Hooper—2536
Transmission electron microscope observations of magnetic domain walls. J. T. Michalak and R. C. Glenn—1261

Magnetic Devices
- Acceleration of rigid, conducting, diamagnetic bodies by a magnetic field. R. U. Ayers—1549
- Alternating current magnetohydrodynamic generator. P. R. Smy—1946
- Antiferromagnetic materials for millimeter and submillimeter devices. G. S. Heller, J. J. Stickler, and J. B. Thaxter—370S
- Compact uhf isolator. D. Bruce Swartz—319S
- Demagnetization of twistor bits. W. A. Barrett—35S
- Development of elongated particle magnets. Fred E. Luborsky—171S
- End effect losses in dc magnetohydrodynamic generators. Roland A. Boucher and Dennis B. Ames—755
- Ferrite system for application at lower microwave frequencies. Clinton F. Jefferson and Russell G. West—390S
- Fields in cavity-excited accelerators. E. G. Cristal and J. Van Bladel—1715
- Fine-wire ferrite limiter. Ernest Stern—315S
- High-power characteristics of low-magnetization garnets. J. H. Saunders and J. J. Green—161S
- Hydromagnet: a self-generating liquid conductor electromagnet. Henry H. Kolm and Osman K. Mawardi—1296
- Impulse selection for core logic. Roger H. Tancrell—40S
- Influence of nearby conductors on thin-film switching. J. S. Eggenberger—752(E)
- Influence of tensor conductivity on current distribution in a MHD generator. H. Hurwitz, Jr., R. W. Kilb, and G. W. Sutton—205
- Instability of magnetostatic modes in a microwave magnetic field applied parallel to the dc field. E. Schlömann and R. I. Joseph—165S
- Magnetically confined cold-cathode gas discharges at low pressures. R. L. Jepsen—2619
- Magnetic film devices using passive loading. J. M. Daughton, T. A. Smay, A. V. Pohm, and A. A. Read—36S
- Perturbation techniques for miniaturized coaxial *Y*-junction circulators. John Clark—323S
- Phase shift studies in ferrite-dielectric loaded coaxial lines at 2200 Mc. J. J. Rowley—321S
- Possibilities of all-magnetic logic. U. F. Gianola—27S
- Possibility of a spin wave magnetic-moment detector. T. B. Day and J. Sucher—1788(L)
- Preliminary operation of a four-sector racetrack microtron. Eric Brannen and H. Froelich—1179(L)
- Production of magnetic fields exceeding 15 kilogauss by a superconducting solenoid. J. E. Kunzler, E. Buehler, F. S. L. Hsu, B. T. Matthias, and C. Wahl—325(L)
- Recording and reproduction of NRZI signals. R. S. Schools—42S
- Theoretical and experimental characteristics of a ferromagnetic amplifier using longitudinal pumping. R. T. Denton—300S
- Traveling-wave frequency doubling in ferrites. B. A. Auld, H. J. Shaw, and D. K. Winslow—317S
- Two-phase permalloy for high-speed switching. E. A. Nesbitt and E. M. Gyorgy—1305

Magnetic Susceptibility
- Acceleration of rigid, conducting, diamagnetic bodies by a magnetic field. R. U. Ayers—1549
- de Haas-van Alphen effect in *p*-type PbTe and *n*-type PbS. P. J. Stiles, E. Burstein, and D. N. Langenberg—2174
- General superparamagnetic behavior of an aligned assembly of uniaxially anisotropic particles. Forrest G. West—249S
- Magnetic susceptibility of $FeCl_2 \cdot 4H_2O$ at low temperatures. R. D. Pierce and S. A. Friedberg—66S
- Paramagnetism of polycrystalline gadolinium, terbium, and dysprosium metals. Sigurds Arajs and R. V. Colvin—336S
- Some effects of directional ordering in zone-melted iron. R. E. Maringer—366S

Magnetic Structure (Spin Orientation, Antiferromagnetism, and Spin Waves)
- Anisotropy of the spin-wave spectrum. M. W. Muller and C. R. Buffler—152S
- Antiferromagnetic materials for millimeter and submillimeter devices. G. S. Heller, J. J. Stickler, and J. B. Thaxter—307S
- Antiferromagnetic resonance in $(Cr_2O_3)_{1-x} \cdot (Al_2O_3)_x$ single crystals. Simon Foner—63S
- Antiferromagnetism of α-Mn and its alloys. Anthony Arrott and B. R. Coles—51S
- Classical theory of the ground spin state in spinels. T. A. Kaplan, K. Dwight, D. Lyons, and N. Menyuk—13S
- Damping effects of thin surface films. R. J. Huber, G. S. Baker, and P. Gibb—2488(L)
- Electrical resistivity of chromium in the vicinity of the Néel temperature. M. J. Marcinkowski and H. A. Lipsitt—1238
- Exchange inversion in $Mn_{2-x}Cr_xSb$. W. H. Cloud, T. A. Bither, and T. J. Swoboda—55S
- Excitation and boundary effects in spin-wave resonance. R. F. Soohoo—148S
- Experimental g' and g values of Fe, Co, Ni, and their alloys. A. J. P. Meyer and G. Asch—330S
- Ferromagnetic alignment by antiferromagnetic exchange interaction. Note on the magnetic behavior of neodymium garnet. W. P. Wolf—742(L)
- Infrared antiferromagnetic resonance in MnO. F. Keffer, A. J. Sievers, III, and M. Tinkham—65S

Magnetic Structure (*continued*)
- Instability of magnetostatic modes in a microwave magnetic field applied parallel to the dc field. E. Schlömann and R. I. Joseph—165S
- Instability of spin waves and magnetostatic modes in a microwave magnetic field applied parallel to the dc field. E. Schlömann and R. I. Joseph—1006
- Low-temperature magnetic properties of some rare-earth garnet compounds. M. Ball, G. Garton, M. J. M. Leask, D. Ryan, and W. P. Wolf—267S
- Magnetic anisotropy and electrical resistivity in exchange inversion compounds. H. S. Jarrett, P. E. Bierstedt, F. J. Darnell, and M. Sparks—57S
- Magnetic investigation of pure manganese and of several of its alloys. H. W. Cooper, A. S. Arrott, and H. W. Paxton—2506
- Magnetic moments of compounds of cobalt with rare-earth elements having a Cu_6Ca structure. E. A. Nesbitt, H. J. Williams, J. H. Wernick, and R. C. Sherwood—342S
- Magnetic ordering in the ferromagnetic rare-earth metals. Kei Yosida and Hirosi Miwa—8S
- Magnetic properties of the low-temperature form of magnetite. D. B. Bonstrom, A. H. Morrish, and L. A. K. Watt—272S
- Magnetization process of a helical spin configuration. U. Enz—22S
- Neutron diffraction by helical spin structures. W. C. Koehler—20S
- Neutron diffraction investigation of magnetic ordering in dysprosium. M. K. Wilkinson, W. C. Koehler, E. O. Wollan, and J. W. Cable—48S
- Neutron diffraction study of metallic erbium. J. W. Cable, E. O. Wollan, W. C. Koehler, and M. K. Wilkinson—49S
- Nonlinear damping losses in YIG. Robert L. Conger—1525
- On the contribution of the Fermi contact term to the magnetic field at the nucleus. R. E. Watson and A. J. Freeman—118S
- On the nature of the magnetic couplings in transitional metals. J. Friedel, G. Leman, and S. Olszewski—325S
- Partial rotation in permalloy films. S. Methfessel, S. Middelhoek, and H. Thomas—1959
- Possibility of a spin wave magnetic-moment detector. T. B. Day and J. Sucher—1788(L)
- Remarks on the magnetic properties of Au-Mn system. Hiroshi Sato—53S
- Simple physical theory of spin wave interactions. F. Keffer and R. Loudon—2S
- Specific heat of superparamagnetic particles. J. D. Livingston and C. P. Bean—1964
- Spin-flopping in MnF_2 by high magnetic fields. I. S. Jacobs—61S
- Spin waves in complex exchange-coupled lattices and neutron scattering. A. W. Saenz—752(E)
- Temperature dependence of the spin-wave spectrum of yttrium iron garnet. R. C. LeCraw and L. R. Walker—167S
- Theory of magnetostatic modes in long, axially magnetized cylinders. R. I. Joseph and E. Schlömann—1001
- Triangular moment arrangements in manganese-iron spinels. Victor L. Moruzzi—59S

Magnetization
- Analytic hysteresis function. F. H. Middleton—251S
- Angular variation of the magnetic properties of partially aligned γ-Fe_2O_3 particles. G. Bate—239S
- Annealing behavior and temperature dependence of the magnetic properties of thin permalloy films. Armin Segmüller—89S
- Backward waves in longitudinally magnetized ferrite rods. G. H. B. Thompson—2491(L)
- Coherent and incoherent magnetization processes in powders. S. Shtrikman and E. P. Wohlfarth—241S
- Comment on the saturation magnetization of neodymium yttrium iron garnet. Robert L. White—1178(L)
- Demagnetization of twistor bits. W. A. Barrett—35S
- Determination of the directions of magnetization in polycrystalline ferrites. D. R. Callaby—298S
- Development of elongated particle magnets. Fred E. Luborsky—171S
- Domain wall mobility in single-crystal yttrium iron garnet. F. B. Hagedorn and E. M. Gyorgy—282S
- Dynamic stability of a conducting, cylindrical shell in magnetic field. J. G. Linhart—500
- Epitaxial growth and magnetic properties of single-crystal films of iron, nickel, and permalloy. Soshin Chikazumi—81S
- Ferromagnetic nucleation sources on iron whiskers. R. E. De Blois—1561
- Flux distribution in ferrite cores under various modes of partial switching. R. H. James, W. M. Overn, and C. W. Lundberg—38S
- Free carrier cyclotron resonance, Faraday rotation, and Voigt double refraction in compound semiconductors. E. D. Palik, S. Teitler, and R. F. Wallis—2132
- Free oscillations of the magnetization in permalloy films. Peter Wolf—95S
- High-temperature magnetic lag in iron-nickel alloys. Dieter Gerstner and Eckart Kneller—364S
- Losses in silicon iron at very low frequencies and high flux densities. Daniel A. Wycklendt and Robert M. Kay—368S
- Initial permeability characteristics of vanadium-doped manganese-zinc ferrites. Yūzō Shichijō, Noboru Tsuya, and Kōki Suzuki—386S
- Instability of spin waves and magnetostatic modes in a microwave magnetic field applied parallel to the dc field. E. Schlömann and R. I. Joseph—1006
- Low-temperature pyromagnetic measurements on nickel. E. W. Pugh and B. E. Argyle—334S
- Magnetic annealing of "ticonal" G magnet steel. H. Zijlstra—194S
- Magnetic core losses resulting from a rotating flux. Asa Kaplan—370S
- Magnetic viscosity due to solute atom pairs. Part II. Experimental results. G. Biorci, A. Ferro, and G. Montalenti—630
- Magnetization curve of an infinite cylinder. M. W. Muller and A. Wehlau—2448
- Magnetization of iron-nickel alloys under hydrostatic pressure. J. S. Kouvel and R. H. Wilson—435
- Magnetization of nickel single crystals. Lambros Tterlikkis and Alvin W. Jenkins, Jr.—1293
- Magnetization process in small particles of CrO_2. F. J. Darnell—1269
- Measurements of the domain wall area-mobility product during slow flux reversals. R. M. Brownell and R. C. Barker—284S
- Nonlinear response of YIG. Robert M. Hill and Robert S. Bergman—227S
- Production of magnetic fields exceeding 15 kilogauss by a superconducting solenoid. J. E. Kunzler, E. Buehler, F. S. L. Hsu, B. T. Matthias, and C. Wahl—325(L)
- Quantitative determination of the interaction fields in aggregates of single-domain particles. Donald F. Eldridge—247S
- Remanent magnetization of a synthetic hematite single crystal. S. T. Lin—394S
- Saturation magnetization and size of iron particles less than 100 A in diameter. Fred E. Luborsky and Philip E. Lawrence—231S

Square-loop ferrites with temperature-independent properties and improved disturb ratio. R. S. Weisz—1152
Studies of a high-coercivity electrodeposit having a lamellar structure. J. S. Sallo and K. H. Olsen—203S
Temperature dependence of spontaneous magnetization in superparamagnetic nickel. Carlos R. Abeledo and P. W. Selwood—229S
Theoretical magnetization curves for particles with cubic anisotropy. Clark E. Johnson, Jr., and William Fuller Brown, Jr.—243S
Theory of magnetostatic modes in long, axially magnetized cylinders. R. I. Joseph and E. Schlömann—1001
Torque measurements on rare-earth doped yttrium iron garnet. R. F. Pearson and R. W. Cooper—265S
Two-phase permalloy for high-speed switching. E. A. Nesbitt and E. M. Gyorgy—1305
Unidirectional properties in the iron-iron sulfide system. J. H. Greiner, I. M. Croll, and M. Sulich—188S

Masers and Lasers
Cross-doping agents for rutile masers. P. F. Chester—866
A cw solid state, push-pull maser in the 5- to 6-millimeter wavelength region. David L. Carter—2541
Electron beam excitation of a Fabry-Perot interferometer. Murray D. Sirkis, Robert J. Strain, and William E. Kunz—2055(L)
Growth of single-crystal calcium fluoride with rare-earth impurities. H. Guggenheim—1337
Maser action in emerald. F. E. Goodwin—1624(L)
Optically efficient ruby laser pump. P. A. Miles and H. E. Edgerton—740(L)
Paramagnetic maser oscillator analysis. S. Wang and J. R. Singer—1371
Power output characteristics of a ruby laser. Malcolm L. Stitch—1994
Probabilities for the neon laser transitions. G. F. Koster and H. Statz—2054(L)
Proposed fiber cavities for optical masers. E. Snitzer—36
Seesaw maser operation. P. A. Forrester and W. B. Mims—317
Single-crystal molybdates for resonance and emission studies. G. Van Uitert, F. W. Swanekamp, and S. Preziosi—1176(L)
Thermal tuning of ruby optical maser. I. D. Abella and H. Z. Cummins—1177(L)
Spatial coherence in the output of an optical maser. D. F. Nelson and R. J. Collins—739(L)
Stimulated emission from HCN gas maser observed at 88.6 kMc. D. Marcuse—743(L)
Theory of laser oscillations in Fabry-Perot resonators. J. Kotik and M. C. Newstein—178
Use of PrCl$_3$ in a solid-state infrared quantum counter. John F. Porter, Jr.—825
Use of PrCl$_3$ in a solid-state infrared quantum counter. John F. Porter, Jr.—1803(E)
Zero-field splitting of the Cr^{3+} ground state in YGa and YAl garnet. J. E. Carson and R. L. White—1787(L)

Mass Spectrometry
Mass spectrographic analysis of insulators using a vacuum spark positive ion source. A. J. Ahearn—1195
Mass spectrographic detection of impurities in liquids. A. J. Ahearn—1197
Reactions of oxygen with pure tungsten and tungsten containing carbon. J. A. Becker, E. J. Becker, and R. G. Brandes—411

Mathematics
Analysis of a nonlinear first-order system with a white noise input. T. K. Caughey and J. K. Dienes—2476
Analytic solution of the double-diffusion problem. K. C. Nomura—1167(L)
An approximate solution of Fick's diffusion equation. T. Tsang—1518
Equation of motion of the torsion pendulum and the complex modulus. N. W. Tschoegl—1794(L)
Instability of spin waves and magnetostatic modes in a microwave magnetic field applied parallel to the dc field. E. Schlömann and R. I. Joseph—1006
Measurement of noise power spectra by Fourier analysis. A. Ziya Akcasu—565
Resistance as dissipation into many reactive circuits: Landau damping and Nyquist's noise theorem. O. Buneman—1783(L)
Scattering of plane waves by a rigid ribbon in a solid. K. Harumi—1488
Similarity function for pattern recognition. Dan McLachlan, Jr.—1795(L)
Theory of magnetostatic modes in long, axially magnetized cylinders. R. I. Joseph and E. Schlömann—1001
Theory of quantum oscillators in a multimode cavity. W. G. Wagner and G. Birnbaum—1185
Thermoelastic equations and Grueneisen's relation. A. M. Freudenthal—1801(L)
Transduction of noise. Theory of a generalized traveling-wave coupler. M. C. Pease—1145

Metallurgical Processes (Precipitation, Order-Disorder, Phase Transformations)
Acoustical study of quench-aging in α Cu-Al alloys. T. J. Koppenaal and M. E. Fine—1781
Characteristics of the annealing kinetics of tin films deposited at 88°K. J. Priest, C. Chiou, and H. L. Caswell—1772
Clustering in an alpha iron-molybdenum solid solution. Erhard Hornbogen—132
Crystal lattice investigation of the permanent magnet precipitate in various Alnico materials. K. J. Kronenberg—196S
Diffusion in a liquid indium-tin alloy at the eutectic concentration. A. Paoletti and M. Vicentini—22
Diffusion reactions in the aging of 4-79 molybdenum permalloy. E. M. Tolman—360S
Electrical resistivities of nickel-niobium solid solutions. Sigurds Arajs—97
Metallurgy and magnetic properties of an Fe-Co-V alloy. C. W. Chen—348S
Mondrian precipitation patterns in single crystals of titanium carbide. Wendell S. Williams—552(L)
On the internal friction of cold-worked and quenched martensitic iron and steel. T. Mura, I. Tamura, and J. O. Brittain—92
On the interpretation of internal friction experiments on strain aging of iron. J. C. Swartz—2048(L)
On the possibility of detecting shock-induced second-order phase transitions in solids. The equation of state of Invar. D. R. Curran—1811
Phase diagram for the pseudobinary system Ag$_2$Te-Sb$_2$Te$_3$. J. P. McHugh, W. A. Tiller, S. E. Haszko, and J. H. Wernick—1785(L)
Precipitation in gold-nickel single crystals. P. J. Flanders and F. R. L. Schoening—344S
Precipitation of helium along dislocations in aluminum. G. T. Murray—1045
Precipitation sites in aluminum alloys. G. R. Frank, Jr., D. L. Robinson, and G. Thomas—1763
Reinterpretation of the reaction kinetics of nickel ferrite. R. C. Turnbull—380S
Shock wave compression of hardened and annealed 2024 aluminum. G. R. Fowles—1475
Smooth spalls and the polymorphism of iron. John O. Erkman—939

Metallurgical Processes (*continued*)
Thermal conductivity in two-phase alloys. J. B. Schroeder—1798(L)
Transformation—disorder to order in Ni_3Mn. M. J. Marcinkowski and N. Brown—375
Transitions and relaxations in polytetrafluoroethylene. R. K. Eby and K. M. Sinnott—1765
Voids in resolidified drops of molten metal. J. C. Kelly—1797(L)
Molecular Beams (see also Mass Spectrometry)
Guidance and collimation of sputtered tungsten particles. Carl A. Ludeke—1400(L)

Noise
Analysis of a nonlinear first-order system with a white noise input. T. K. Caughey and J. K. Dienes—2476
Confirmation of lifetimes by noise and by Haynes-Shockley method. Susumu Okazaki—712
Effect of gaseous ambients upon $1/f$ noise in germanium filaments. F. E. Noble and J. E. Thomas, Jr.—1709
Excess noise in germanium and gallium-arsenide Esaki diodes in the negative resistance region. M. D. Montgomery—2408
Likelihood detection of small signals in stationary noise. Philip Rudnick—140
Measurement of noise power spectra by Fourier analysis. A. Ziya Akcasu—565
Noise in InSb photodiodes. B. R. Pagel and R. L. Petritz—1901
On the theory of amplitude distribution of impulsive random noise. K. Furutsu and T. Ishida—1206
Production and analysis of a large-diameter plasma beam. B. B. Meckel and P. A. Harkins—489
Thermal noise in dissipative media. H. A. Haus—493
Transduction of noise. Theory of a generalized traveling-wave coupler. M. C. Pease—1145
Nuclear Magnetic Resonance
NMR and the conduction electron polarization in rare-earth metals. V. Jaccarino—102S
Nuclear magnetic resonance in flowing fluids. Louis R. Hirschel and Louis F. Libelo—1404(L)
Nuclear magnetic resonance in NiF_2 domain walls. R. G. Shulman—126S
Nuclear magnetic resonance of Fe^{57} in unenriched Fe. J. I. Budnick, L. J. Bruner, R. J. Blume, and E. L. Boyd—120S
Nuclear resonances in cubic, hexagonal, and mixed phase cobalt powders and thin films. Wilton A. Hardy—122S
Pressure and temperature dependence of the Fe^{57} nuclear magnetic resonance frequency in ferromagnetic iron. G. B. Benedek and J. Armstrong—106S
Transient excitation of nuclei in ferromagnetic metals. M. Weger, E. L. Hahn, and A. M. Portis—124S
Nuclear Physics
Mössbauer effect: Applications to magnetism. G. K. Wertheim—110S

Optical Properties
Birefringence due to dislocations in glide bands of rock-salt single crystals. S. Mendelson—1999
Dichroic color centers in calcium fluorophosphate. Peter D. Johnson—127(L)
Domain structures in iron whiskers as observed by the Kerr method. C. A. Fowler, Jr., E. M. Fryer, and D. Treves—296S
Effect of electron bombardment on the near-infrared fluorescence of single-crystal CdS. B. A. Kulp—1966
Electrical and optical properties of mercury selenide (HgSe). H. Gobrecht, U. Gerhardt, B. Peinemann, and A. Tausend—2246
Electrical and optical properties of the II–V compounds. W. J. Turner, A. S. Fischler, and W. E. Reese—2241
Electrical control of the critical angle of total reflection. H. Nassenstein—2488(L)
Energy band structure of gallium antimonide. W. M. Becker, A. K. Ramdas, and H. Y. Fan—2094
Excitons and band splitting produced by uniaxial stress in CdTe. D. G. Thomas—2298
Excitons and the absorption edge of ZnO. R. E. Dietz, J. J. Hopfield, and D. G. Thomas—2282
Exciton states and band structure in CdS and CdSe. J. J. Hopfield—2277
Exciton structure and Zeeman effects in cadmium selenide. J. O. Dimmock and R. G. Wheeler—2271
Far infrared and microwave detector. D. W. Goodwin and R. H. Jones—2056(L)
Free carrier cyclotron resonance, Faraday rotation, and Voigt double refraction in compound semiconductors. E. D. Palid, S. Teitler, and R. F. Wallis—2132
Fundamental reflectivity spectrum of semiconductors with zinc-blende structure. Manuel Cardona—2151
Infrared antiferromagnetic resonance in MnO. F. Keffer, A. J. Sievers, III, and M. Tinkham—65S
Infrared properties of flame-fused MnO crystals. E. Loh and R. Newman—470
Interband Faraday rotation in III–V compounds. Benjamin Lax and Yuichiro Nishina—2128
Investigations on SnS. W. Albers, C. Haas, H. J. Vink, and J. D. Wasscher—2220
Lattice absorption in gallium arsenide. W. Cochran, S. J. Fray, F. A. Johnson, J. E. Quarrington, and N. Williams—2102
Limitations of the magneto-optic Kerr technique in the study of microscopic magnetic domain structures. D. Treves—358
Magnetoreflection experiments in intermetallics. George B. Wright and Benjamin Lax—2113
Observations of cross-tie domain walls by the Faraday effect. A. L. Houde—1234
Optical absorption edge in GaAs and its dependence on electric field. T. S. Moss—2136
Optically efficient ruby laser pump. P. A. Miles and H. E. Edgerton—740(L)
Optical properties of free electrons in CdS. W. W. Piper and D. T. F. Marple—2237
Optical properties of lead-salt and III–V semiconductors. Frank Stern—2166
Optical properties of oriented polystyrene. Richard S. Stein—1280
Optical studies of the band structure of InP. Manuel Cardona—958(L)
Oscillatory magnetoabsorption in InSb under high resolution. S. Zwerdling, W. H. Kleiner, and J. P. Theriault—2118
Photoconductivity of CdS-type photoconductors in the vicinity of the absorption edge. N. N. Winogradoff—506
p-type photoconductivity and infrared quenching in electron-bombarded CdS. B. A. Kulp and R. H. Kelley—1290
Single-crystal molybdates for resonance and emission studies. G. Van Uitert, F. W. Swanekamp, and S. Preziosi—1176(L)
Some electrical and optical properties of ZnSe. M. Aven, D. T. F. Marple, and B. Segall—2261
Spatial coherence in the output of an optical maser. D. F. Nelson and R. J. Collins—739(L)
Spherical lenses for infrared and microwaves. G. Toraldo de Francia—2051(L)
Stimulated emission from HCN gas maser observed at 88.6 kMc. D. Marcuse—743(L)

- Stress optical constants of germanium. K. J. Schmidt-Tiedemann—2058(L)
- Theory of laser oscillations in Fabry-Perot resonators. J. Kotik and M. C. Newstein—178
- Thermal tuning of ruby optical maser. I. D. Abella and H. Z. Cummins—1177(L)
- Transparency of glass and certain plastics under shock attack. H. Dean Mallory and William S. McEwan—2421
- Use of $PrCl_3$ in a solid-state infrared quantum counter. John F. Porter, Jr.—825
- Use of $PrCl_3$ in a solid-state infrared quantum counter. John F. Porter—1803(E)
- Vacuum-ultraviolet absorption studies of irradiated silica and quartz. C. M. Nelson and R. A. Weeks—883

Paramagnetic Amplifiers
- Coupled mode theory of electron-beam parametric amplification. R. W. Gould and C. C. Johnson—248
- Generalized coupled mode theory. M. C. Pease—1736
- Parametric coupling between the transverse waves on *O*- and *M*-type beams. J. W. Klüver—1111
- Stable-oscillation conditions for the magnetic-film parametron. Richard M. Sanders—478
- Traveling wave analysis of a class of parametric amplifiers based upon the Hill equation. R. W. Fredricks—901

Photoconductivity and Photovoltaic Effects
- Analysis of photojunctions formed by diffusing copper into insulating cadmium sulfide crystals. Robert R. Bockemuehl, James E. Kauppila, and David S. Eddy—1324
- Confirmation of lifetimes by noise and by Haynes-Shockley method. Susumu Okazaki—712
- Cross-section ratios of sensitizing centers in photoconductors. Richard H. Bube—1707
- Crystal structure of photoelectric films of cesium antimonide. W. H. McCarroll—2051(L)
- Detailed balance limit of efficiency of *p-n* junction solar cells. William Shockley and Hans J. Queisser—510
- Effects of phosphor powder dispersion in electroluminescent lamps. W. A. Thornton—2379
- Light scattering study of the annealing of drawn polyethylene. Marion B. Rhodes and Richard S. Stein—2344
- Photoconductivity of CdS-type photoconductors in the vicinity of the absorption edge. N. N. Winogradoff—506
- Photovoltaic effects in Cs_3Sb films. Frederick Wooten—1789(L)
- Physical behavior of photographic grains. G. Sprague—2410
- *p*-type photoconductivity and infrared quenching in electron-bombarded CdS. B. A. Kulp and R. H. Kelley—1290
- Spectral response of solar cells. Brian Dale and F. P. Smith—1377
- Temperature-dependent bismuth-cesium photosurfaces. R. J. Zollweg and C. R. Taylor—1316

Plasma Physics
- A method for measuring the conductivity in a high electron density plasma. K. B. Persson—2631
- Backward-wave microwave oscillations in a system composed of an electron beam and a hydrogen gas plasma. R. Targ and L. P. Levine—731
- Conductivity of seeded atmospheric pressure plasmas. L. S. Frost—2029
- Dynamic stability of a conducting, cylindrical shell in a magnetic field. J. G. Linhart—500
- Excitation and amplification of cyclotron waves and thermal orbits in the presence of space charge. R. Adler, A. Ashkin, and E. I. Gordon—672
- Experimental study of arc stability. I. J. D. Cobine and G. A. Farrall—328(E)
- Fields in cavity-excited accelerators. E. G. Cristal and J. Van Bladel—1715
- Induction-coupled plasma torch. Thomas B. Reed—821
- Influence of the cathode surface on arc velocity. T. J. Lewis and P. E. Secker—54
- Interpretation of experimental characteristics of cesium thermionic converters. E. N. Carabateas, S. D. Pezaris, and G. N. Hatsopoulos—352
- Low-frequency oscillations in a filamentary cathode cesium. diode converter. K. P. Luke and F. E. Jamerson—321(L)
- Microwave measurements of the radiation temperature of plasmas. G. Bekefi and Sanborn C. Brown—25
- Microwave propagation through a magnetoplasma. R. L. Phillips, R. G. DeLosh, and D. E. White—551(L)
- Microwave propagation through a magnetoplasma. R. L. Phillips, R. G. DeLosh, and D. E. White—1406(E)
- Note on the mechanism of the multipactor effect. F. Paschke—747(L)
- Oscillations and saturation current measurements in thermionic conversion cells. R. J. Zollweg and Milton Gottlieb—890
- Production of high ions densities in helium by means of high explosives. G. E. Seay, L. B. Seely, Jr., and R. G. Fowler—2439
- Propagation in a plasma. P. A. Clavier—578
- Proposed diagnostic method for cylindrical plasmas. J. Shmoys—689
- Radiation from a modulated electron beam with a plasma background. Philip Parzen—2484
- Relaxation oscillations in a plasma diode. J. M. Rochard and G. W. Paxton—1171(L)
- Resistance as dissipation into many reactive circuits: Landau damping and Nyquist's noise theorem. O. Buneman—1783(L)
- Space-charge instabilities in electron diodes and plasma converters. C. K. Birdsall and W. B. Bridges—2611
- Space charge instabilities in synthesized plasmas. A. L. Eichenbaum and K. G. Hernqvist—16
- Theory of electron collection of spheric probes. G. Medicus—2512
- Theory of microplasma instability in silicon. R. J. McIntyre—983
- Wave interaction in plasma inhomogeneities. Lewis Wetzel—327(L)

Plastic Deformation (see also Defects in Solids-Dislocations)
- Birefringence due to dislocations in glide bands of rocksalt single crystals. S. Mendelson—1999
- Creep behavior of pore-free polycrystalline aluminum oxide. Robert C. Folweiler—773
- Cross slip and cross climb of dislocations induced by a locked dislocation. James C. M. Li—593
- Deformation-produced point defects. Howard K. Birnbaum and Floyd R. Tuler—1403(L)
- Dislocation density and flow stress of sodium chloride. W. in der Schmitten and P. Hassen—1790
- Effect of hydrostatic pressure on the high-temperature steady-state creep of lead. B. M. Butcher and A. L. Ruoff—2036
- Effect of neutron irradiation on the plastic deformation of copper single crystals. I. G. Greenfield and H. G. F. Wilsdorf—827
- Effect of torsional deformation on self-diffusion in silver. C. H. Lee and R. Maddin—1846
- Elastic-plastic transition in copper crystals as determined by an etch-pit technique. F. W. Young, Jr.—1815
- Electrical conductivity of NaCl during high-temperature creep. R. W. Christy and W. E. Daniels, Jr.—1265

Plastic Deformation (*continued*)
Electrically imploded-exploded aluminum tube. Eugene C. Cnare—1275
High-temperature kilocycle internal friction. R. J. Huber, G. S. Baker, and P. Gibbs—2573
Influence of deformation and temperature on the cobalt gamma irradiation of sodium chloride. Evidence for electrical interaction between dislocations and point defects. Rohn Truell—1601
Lattice parameter studies of impurity effects on plastic properties of lithium fluoride. W. L. Phillips, Jr.—751(L)
Nonbasal glide in dislocation-free cadmium crystals. I. The $(10\bar{1}1)$ $[1\bar{2}10]$ system. P. B. Price—1746
Nonbasal glide in dislocation-free cadmium crystals. II. The $(\bar{1}122)$ [1123] system. P. B. Price—1750
On the internal friction of cold-worked and quenched martensitic iron and steel. T. Mura, I. Tamura, and J. O. Brittain—92
On the interpretation of internal friction experiments on strain aging of iron. J. C. Swartz—2048(L)
On the mechanical and thermal stability of low-angle boundaries in zinc single crystals. Sigmund Weissman, Makoto Hirabayashi, and Hiroshi Fujita—1156
Piezoelectricity of quartz for finite strain. S. Machlup and M. E. Christopher—1387
Polygonization in bent zinc crystals. P. P. Sinha and Paul A. Beck—1222
Relative polygonization rates in copper and copper-zinc alloys. W. E. Heitmann and R. W. Balluffi—963(L)
Self-diffusion in silver during plastic deformation in torsion. J. B. Darby, Jr., C. T. Tomizuka, and R. W. Balluffi—840
Shock wave compression of hardened and annealed 2024 aluminum. G. R. Fowles—1475
Slip patterns on boron-doped silicon surfaces. H. J. Queisser—1776
Strength of bulk fused quartz. William B. Hillig—741(L)
Stress distribution on the boundary of an elliptical hole in a large plate during passage of a stress pulse on long duration (major axis normal to the wave front). A. J. Durelli and W. F. Riley—1255
Stress and strain in thin films bulged over circular openings. Ralph Papirno—1175(L)
Temperature dependence of rolling textures in high-purity silver. Hsun Hu and R. S. Cline—760
Theory and application of a superposition model of internal friction and creep. J. Ross MacDonald—2385

Polymers (see also Glasses and Amorphous Solids)
Application of the three-parameter stress function to natural rubbers of widely different hardness. A. J. Carmichael and H. W. Holdaway—1724
Crack propagation in a strain-crystallizing elastomer. E. H. Andrews—452
Dielectric loss in poly-(hexamethylene adipamide) and poly-(hexamethylene sebacamide) at low temperatures. M. N. Stein, R. G. Lauttman, J. A. Sauer, and A. E. Woodward—2352
Dielectric properties and side-chain crystallinity of polyvinyl stearate. Martin G. Broadhurst, Edwin R. Fitzgerald, and Anthony J. Bur—972
Electric breakdown strength of single and laminated films of vinyl chloride-acetate. Robert G. Greenler and Robert M. Kay—1252
Extension of the Eyring-Ree theory of non-Newtonian flow. Joseph A. Faucher—2336
Frictional behavior of a simple rheological material. R. T. Spurr—1450
Growth of crystals from molten cross-linked oriented polyethylene. Jane T. Judge and Richard S. Stein—2357
Hypothesis of voids in semicrystalline polymers. Shiro Matsuoka—2334
Isothermal crystallization kinetics of polyethylene. II. Influence of the sample preparation. J. Rabesiaka and A. J. Kovacs—2314
Light scattering study of the annealing of drawn polyethylene. Marion B. Rhodes and Richard S. Stein—2344
Low-angle x-ray diffraction of crystalline nonoriented polyethylene and its relation to crystallization mechanisms. L. Mandelkern, A. S. Posner, A. F. Diorio, and D. E. Roberts—1509
Lubrication of polymers. C. Rubenstein—1445
Method for measuring dynamic mechanical properties of viscoelastic liquids and gels; the gelation of polyvinyl chloride. Meyer H. Birnboim and John D. Ferry—2305
Non-Newtonian viscosity of polymers. Roger S. Porter and Julian F. Johnson—2326
Origins of characteristic bands in the infrared spectra of isotactic polystyrene and isotactic poly (ring-d_5 styrene). T. Onishi and S. Krimm—2320
Phenomenological elastomechanical behavior of rubbers over wide ranges of strain. A. J. Carmichael and H. W. Holdaway—159
Properties of polyvinylidene fluoride. I. Dielectric measurements. Tunis Wentink, Jr.—1063
Rate of recrystallization of polyethylene single crystals. W. O. Statton—2332
Rolling friction of polymeric materials. II. Thermoplastics. D. G. Flom—1426
The swelling of unfilled and highly filled polymers. K. W. Bills, Jr., and F. S. Salcedo—2364
Thermorheological simplicity in extrusion flow curves of high ploymers. Katsuhiko Ito—1743
Transitions and relaxations in polytetrafluoroethylene. R. K. Eby and K. M. Sinnott—1765
Transparency of glass and certain plastics under shock attack. H. Dean Mallory and William S. McEwan—2421
Ultrasonic attenuation of longitudinal waves in plastics. Michel Auberger and John S. Rinehart—219
Use of idealized relaxation spectra in the interpretation of experimental results concerning polymer solutions. K. Walters—1975

Radiation Effects
Determination of the maximum lattice-chain energy from sputtering yield curves. Don E. Harrison, Jr.—924
Effect of electron bombardment on the near-infrared fluorescence of single-crystal CdS. B. A. Kulp—1966
Effect of neutron irradiation on the plastic deformation of copper single crystals. I. G. Greenfield and H. G. F. Wilsdorf—827
Effect of reactor fast neutrons on electron-hole recombination in germanium. A. Czachor and J. Piekoszewski—1837
Effects of monolayer adsorption and bombardment damage or Auger electron ejection from germanium. Homer D. Hagstrum—1015
Electron bombardment damage in silicon Esaki diodes. R. A. Logan, W. M. Augustyniak, and J. F. Gilbert—1201
Electron microscope study of radiation damage in graphite. W. Bollmann—869
Electron spin resonance in neutron-irradiated quartz. Robert H. Silsbee—1459
Energy dependence of radiation damage in tungsten. D. R. Muss and J. R. Townsend—189
Fission fragment damage to platinum. E. Reudl, P. Delavignette, and S. Amelinckx—2492(L)

Frequency factors for annealing fast-neutron induced density changes in vitreous silica. William Primak, Herman Szymanski, and David Keiffer—660
Hardening of LiF crystals by irradiation. J. S. Nadeau and W. G. Johston—2563
Influence of deformation and temperature on the cobalt gamma irradiation of sodium chloride. Evidence for electrical interaction between dislocations and points defects. Rohn Truell—1601
Mobility of radiation-induced defects in germanium. P. Baruch—653
p-type photoconductivity and infrared quenching in electron-bombarded CdS. B. A. Kulp and R. H. Kelley—1290
Radiation enhancement of bulk diffusion in 10% Zn–90% Cu by 30-kev Ne^+ ion bombardment. R. A. Arndt and R. L. Hines—1913
Stored energy in fuel-bearing graphites. A. H. Willis, J. M. Baugnet, and R. C. De Buekelaer—1622(L)
Study of electron bombardment of thin films. G. B. Gilbert, T. O. Poehler, and C. F. Miller—1597
Vacuum-ultraviolet absorption studies of irradiated silica and quartz. C. M. Nelson and R. A. Weeks—883

Scattering of Electromagnetic Waves
Electrical control of the critical angle of total reflection. H. Nassenstein—2488(L)
Imaginary part of x-ray scattering factor for germanium, comparison of theory and experiment. Boris W. Batterman—998
Infrared properties of flame-fused MnO crystals. E. Loh and R. Newman—470
Microwave analog to the scattering of light by nonspherical particles. J. Mayo Greenberg, Norman E. Pedersen, and Jeanne C. Pedersen—233
Shift of the shadow boundary and scattering cross section of an opaque object. S. I. Rubinow and Joseph B. Keller—814
Small-angle scattering in gold-nickel alloys. G. Nagorsen and B. L. Averbach—688
Wave interaction in plasma inhomogeneities. Lewis Wetzel—327(L)

Scattering of Particles
Back scattering of electrons. G. D. Archard—1505
Electron energy loss at low temperatures. E. Hörl and J. A. Suddeth—2521
Electron microscope investigation on the nature of tracks of fission products in mica. G. Bonfiglioli, A. Ferro, and A. Mojoni—2499
Interaction of slow electrons with insulating crystals. I. Absorption coefficient for cleaved alkali halides; Experimental techniques. C. J. Cook and William J. Fredericks—860
Spin waves in complex exchange-coupled lattices and neutron scattering. A. W. Saenz—752(E)

Semiconducting Devices (*p-n* Junctions)
Band structure parameters deduced from tunneling experiments. R. N. Hall and J. H. Racette—2078
Current-voltage characteristics of alloyed and diffused *p-n* junction diodes in InSb. Hans Juerg Stocker—322(L)
Detailed balance limit of efficiency of *p-n* junction solar cells. William Shockley and Hans J. Queisser—510
Determination of the semiconductor surface potential under a metal contact. N. J. Harrick—568
Effect of gaseous ambients upon 1/*f* noise in germanium filaments. F. E. Noble and J. E. Thomas, Jr.—1709
Electroluminescence at *p-n* junctions in gallium phosphide. M. Gershenzon and R. M. Mikulyak—1338
Electron bombardment damage in silicon Esaki diodes. R. A. Logan, W. M. Augustyniak, and J. F. Gilbert—1201
Electron emission from reverse-biased *p-n* junctions in SiC. Lyle Patrick—2047(L)
Electron-emission microscope and velocity distribution studies on silicon carbide *p-n* junction emitters. P. H. Gleichauf and V. Ozarow—549(L)
Electron mobilities and tunneling currents in silicon. R. A. Logan, J. F. Gilbert, and F. A. Trumbore—131(L)
Evidence for states (bands) in the forbidden gap of degenerate GaAs and InP—secondary tunnel currents and negative resistances. Nick Holonyak, Jr.—130(L)
Excess and hump current in Esaki diodes. Richard S. Claasen—2372
Extended curves of the space charge, electric field, and free carrier concentration at the surface of a semiconductor, and curves of the electrostatic potential inside a semiconductor. Charles E. Young—329
Excess noise in germanium and gallium-arsenide Esaki diodes in the negative resistance region. M. D. Montgomery—2408
Fast-risetime excitation scheme to achieve nonequilibrium and amplifying carrier distributions. George C. Dousmanis—2005
Gallium arsenide Esaki diodes for high-frequency applications. C. A. Burrus—1031
High-frequency silicon varactor diodes. C. A. Burrus—1166(L)
Impurity band conduction and the problem of excess current in tunnel diodes. T. P. Brody—746(L)
Negative resistance and hot electrons. I. Adawi—1101
New, thermally variable bead resistor. Victor J. Tennery and Russell G. West—1402(L)
Noise in InSb photodiodes. B. R. Pagel and R. L. Petritz—1901
Semiconducting stress transducers utilizing the transverse and shear piezoresistance effects. W. G. Pfann and R. N. Thurston—2008
Some electrical properties of zinc telluride—cadmium sulfide heterojunctions. M. Aven and D. M. Cook—960(L)
Some experiments using a vacuum-cleaned silicon *p-n* junction. J. T. Law—848
Some properties of *p-n* junctions in GaP. H. G. Grimmeiss and A. Rabenau—2123
Theory of tunneling. Evan O. Kane—83
Thermoelectric behavior of *p-n* junctions. Melvin Cutler—222
Uniformity of electrical current flow in cylindrical semiconductor specimens with cylindrical metallic end caps. R. Simon, J. H. Cahn, and J. C. Bell—46
Voltage dependence of microplasma density in *p-n* junctions in silicon. A. Goetzberger and C. Stephens—2646

Semiconductors, Compound
Analysis of photojunctions formed by diffusing copper into insulating cadmium sulfide crystals. Robert R. Bockemuehl, James E. Kauppila, and David S. Eddy—1324
Antimony edge dislocations in InSb. H. C. Gatos, M. C. Finn, and M. C. Lavine—1174(L)
Band structure of HgSe and HgSe-HgTe alloys. T. C. Harman and A. J. Strauss—2265
Band structure of the intermetallic semiconductors from pressure experiments. William Paul—2082
Band structure parameters deduced from tunneling experiments. R. N. Hall and J. H. Racette—2078
Bismuth-silver-oxygen-cesium photocathode. A. H. Sommer and W. E. Spicer—1036
Corbino disk. Milton Green—2047(L)
Corbino disk magnetoresistivity measurements on InSb. Milton Green—1286

Semiconductors, Compound (*continued*)
- Current-voltage characteristics of alloyed and diffused *p-n* junction diodes in InSb. Hans Juerg Stocker—322(L)
- Dangling bonds in III-V compounds. Harry C. Gatos—1232
- de Haas-van Alphen effect in *p*-type PbTe and *n*-type PbS. P. J. Stiles, E. Burstein, and D. N. Langenberg—2174
- Distribution coefficients of impurities in gallium antimonide. R. N. Hall and J. H. Racette—856
- Diffusion of tin in gallium arsenide. B. Goldstein and H. Keller—1180(L)
- Dislocation etch pits on bismuth telluride crystals. Iwao Teramoto and Shigetoshi Takayanagi—119(L)
- Dislocations and stacking faults in aluminum nitride. P. Delavignette, H. B. Kirkpatrick, and S. Amelinckx—1098
- Dislocations in silicon carbide. S. Amelinckx, G. Strumane, and W. W. Webb—1182(E)
- Double phonon processes in cadmium sulfide. Minko Balkanski and Jean Michel Besson—2292
- Edge emission in zinc selenide single crystals. D. C. Reynolds, L. S. Perdotti, and O. W. Larson—2250
- Effect of freezing conditions on the thermoelectric properties of BiSbTe$_3$ crystals. G. J. Cosgrove, J. P. McHugh, and W. A. Tiller—621
- Effect of pressure on the energy gap of Bi$_2$Te$_3$. Che-Yu Li, A. L. Ruoff, and C. W. Spencer—1733
- Effects of doping additions on the thermoelectric properties of the intrinsic semiconductor Bi$_2$Te$_{2.1}$Se$_{0.9}$. L. C. Bennett and J. R. Wiese—562
- Electrical and optical properties of mercury selenide (HgSe). H. Gobrecht, U. Gerhardt, B. Peinemann, and A. Tausend—2246
- Electrical and optical properties of the II-V compounds. W. J. Turner, A. S. Fischler, and W. E. Reese—2241
- Electrical properties of lead telluride. Yasuo Kanai, Riro Nii, and Naozo Watanabe—2146
- Electron emission from reverse-biased *p-n* junctions in SiC. Lyle Patrick—2047(L)
- Electron-emission microscope and velocity distribution studies on silicon carbide *p-n* junction emitters. P. H. Gleichauf and V. Ozarow—549(L)
- Electron spin resonance in semiconducting rutile. P. F. Chester—2233
- Energy of spectrum and scattering of current carriers in gallium arsenide. D. N. Naseledov—2140
- Energy band structure of gallium antimonide. W. M. Becker, A. K. Ramdas, and H. Y. Fan—2094
- Evidence for states (bands) in the forbidden gap of degenerate GaAs and InP—secondary tunnel currents and negative resistances. Nick Holonyak, Jr.—130(L)
- Excess noise in germanium and gallium-arsenide Esaki diodes in the negative resistance region. M. D. Montgomery—2408
- Exciton states and band structure in CdS and CdSe. J. J. Hopfield—2277
- Exciton structure and Zeeman effects in cadmium selenide. J. O. Dimmock and R. G. Wheeler—2271
- Excitons and band splitting produced by uniaxial stress in CdTe. D. G. Thomas—2298
- Excitons and the absorption edge of ZnO. R. E. Dietz, J. J. Hopfield, and D. G. Thomas—2282
- Field-enhanced donor diffusion in degenerate semiconductor layers. W. Shockley—1402(L)
- Free carrier cyclotron resonance, Faraday rotation, and Voigt double refraction in compound semiconductors. E. D. Palik, S. Teitler, and R. F. Wallis—2132
- Fundamental reflectivity spectrum of semiconductors with zinc-blende structure. Manuel Cardona—2151
- Gallium arsenide Esaki diodes for high-frequency applications. C. A. Burrus—1031
- Galvanomagnetic effects in III-V compound semiconductors. A. C. Beer—2107
- Galvanomagnetic properties of InSb. H. Weiss—2064
- Germanium saturated with gallium antimonide. J. O. McCaldin and D. B. Wittry—65
- Growth of ZnSb single crystals. R. L. Eisner, R. Mazelsky, and W. A. Tiller—1833
- Growth twins in indium antimonide. R. K. Mueller and R. L. Jacobson—550(L)
- Growth twins in indium antimonide. R. K. Mueller and R. L. Jacobson—1406(E)
- Impurity striations in unrotated crystals of InSb. H. C. Gatos, A. J. Strauss, M. C. Lavine, and T. C. Harmon—2057(L)
- Influence of arsenic pressure on the doping of gallium arsenide with germanium. J. O. McCaldin and Roy Harada—557(L)
- Influence of the Hall effect upon the transverse magnetoresistance in indium antimonide. Charles A. Simmons—1970
- Influence of magnetoconductivity discontinuities on galvanomagnetic effects in indium antimonide. R. T. Bate, J. C. Bell, and A. C. Beer—806
- Interband Faraday rotation in III-V compounds. Benjamin Lax and Yuichiro Nishina—2128
- Interrelation of electronic properties and defect equilibria in PbTe. E. Miller, K. Komarek, and I. Cadoff—2457
- Investigations on silicon carbide. H. J. van Daal, C. A. A. J. Greebe, W. F. Knippenberg, and H. J. Vink—2225
- Investigations on SnS. W. Albers, C. Haas, H. J. Vink, and J. D. Wasscher—2220
- Halides, oxides, and sulfides of the transition metals. F. J. Morin—2195
- Heitler-London approach to electrical conductivity. Jiro Yamashita—2215
- Lattice absorption in gallium arsenide. W. Cochran, S. J. Fray, F. A. Johnson, J. E. Quarrington, and N. Williams—2102
- Magnetoreflection experiments in intermetallics. George B. Wright and Benjamin Lax—2113
- Magnetotunneling in lead telluride. R. H. Rediker and A. R. Calawa—2189
- Measurement of minority carrier lifetime in SiC by a novel electroluminescent method. G. G. Harman and R. L. Raybold—1168(L)
- Model for the electronic transport properties of mixed valency semiconductors. R. C. Miller, R. R. Heikes, and R. Mazelsky—2202
- Nonohmic behavior in near-stoichiometric rutile (TiO$_2$). E. H. Greener and D. H. Whitmore—1320
- Optical absorption edge in GaAs and its dependence on electric field. T. S. Moss—2136
- Optical properties of free electrons in CdS. W. W. Piper and D. T. F. Marple—2237
- Optical properties of lead-salt and III-V semiconductors. Frank Stern—2166
- Optical studies of the band structure of InP. Manuel Cardona—958(L)
- Oscillatory magnetoabsorption in InSb under high resolution. S. Zwerdling, W. H. Kleiner, and J. P. Theriault—2118
- Oscillatory magnetoresistance in the conduction band of PbTe. K. F. Cuff, M. R. Ellett, and C. D. Kuglin—2179
- Phase diagram for the pseudobinary system Ag$_2$Te-Sb$_2$Te$_3$. J. P. McHugh, W. A. Tiller, S. E. Haszko, and J. H. Wernick—1785(L)

Photoconductivity of CdS-type photoconductors in the vicinity of the absorption edge. N. N. Winogradoff—506
Piezoelectric scattering and phonon drag in ZnO and CdS. A. R. Hutson—2287
Polaron band model and its application to Ce-S semiconductors. J. Appel and S. W. Kurnick—2206
Preparation of monocrystalline cuprous oxide. Yukiko Ebisuzaki—2027
Properties of high-resistivity gallium arsenide compensated with diffused copper. Joseph Blanc, Richard H. Bube, and Harold E. MacDonald—1666
Properties of semi-insulating GaAs. C. H. Gooch, C. Hilsum, and B. R. Holeman—2069
Presence of carbon in gallium phosphide crystals. C. J. Frosch, M. Gershenzon, and L. Derick—2060 (L)
p-type photoconductivity and infrared quenching in electron-bombarded CdS. B. A. Kulp and R. H. Kelley—1290
Recent studies of bismuth telluride and its alloys. H. J. Goldsmid—2198
Recent studies on rutile (TiO_2). H. P. R. Frederikse—2211
Righi-Leduc effect in mercuric selenide. Charles R. Whitsett—2257
Semiconducting "compound" $AgFeTe_2$. J. H. Wernick and R. Wolfe—749 (L)
Semiconducting properties of inorganic amorphous materials. H. L. Uphoff and J. H. Healy—950
Some electrical and optical properties of ZnSe. M. Aven, D. T. F. Marple, and B. Segall—2261
Some electrical properties of zinc telluride—cadmium sulfide heterojunctions. M. Aven and D. M. Cook—960 (L)
Some properties of HgSe-HgTe solid solutions. M. Rodot, H. Rodot, and R. Triboulet—2254
Some properties of *p*-*n* junctions in GaP. H. G. Grimmeiss and A. Rabenau—2123
Study of band structure of intermetallic compounds by pressure experiments. A. Sagar and R. C. Miller—2073
Thermal expansion and related bonding problems of some III-V compound semiconductors. Leonard Bernstein and Robert J. Beals—122 (L)
Thermoelectric properties of Ag_2Te. P. F. Taylor and C. Wood—1
Valence bands in lead telluride. R. S. Allgaier—2185
Vapor phase growth and properties of zinc sulfide single crystals. Harold Samelson—309
Vapor-phase growth of single crystals of II-VI compounds. W. W. Piper and S. J. Polich—1278

Semiconductors, Elemental
Anodic oxidation of germanium. T. Gabor—1361
Band structure and transport properties of some 3–5 compounds. H. Ehrenreich—2155
Catalytic activity of *p*- and *n*- type germanium. William H. Watson, Jr.—120 (L)
Current flow across grain boundaries in *n*-type germanium. I. R. K. Mueller—635
Current flow across grain boundaries in *n*-type germanium. II. R. K. Mueller—640
Effects of monolayer adsorption and bombardment damage or Auger electron ejection from germanium. Homer D. Hagstrum—1015
Effect of reactor fast neutrons on electron-hole recombination in germanium. A. Czachor and J. Piekoszewski—1837
Electron bombardment damage in silicon Esaki diodes. R. A. Logan, W. M. Augustyniak, and J. F. Gilbert—1201
Electron mobilities and tunneling currents in silicon. R. A. Logan, J. F. Gilbert, and F. A. Trumbore—131 (L)
Enantiomorphous character of etch pits in tellurium. J. S. Blakemore and K. C. Nomura—745 (L)
Excess noise in germanium and gallium-arsenide Esaki diodes in the negative resistance region. M. D. Montgomery—2408
Germanium films on germanium obtained by thermal evaporation in vacuum. O. Weinreich, G. Dermit, and C. Tufts—1170 (L)
Germanium saturated with gallium antimonide. J. O. McCaldin and D. B. Wittry—65
High-field conductivity in germanium and silicon at microwave frequencies. J. Zucker, V. J. Fowler, and E. M. Conwell—2606
High-frequency silicon varactor diodes. C. A. Burrus—1166 (L)
Imaginary part of x-ray scattering factor for germanium. Comparison of theory and experiment. Boris W. Batterman—998
Influence of conductivity gradients on galvanomagnetic effects in semiconductors. R. T. Bate and A. C. Beer—800
Investigation of the sputtering of silicon. S. P. Wolsky and E. J. Zdanuk—782
Majority carrier magnetosurface effect. Robert D. Larrabee—2019
Morphology and growth mechanism of silicon ribbons. R. S. Wagner and R. G. Treuting—2490 (L)
Oxygen adsorption on silicon and germanium. Homer D. Hagstrum—1020
Perfection of the lattice of dislocation-free silicon, studied by the lattice-constant and density method. M. E. Straumanis, P. Borgeaud, and W. J. James—1382
Preparation of silicon ribbons. E. S. Greiner, J. A. Gutowski, and W. C. Ellis—2489 (L)
Preparation of single-crystal boron. Claude P. Talley—1787 (L)
Properties of heavily doped *n*-type germanium. W. G. Spitzer, F. A. Trumbore, and R. A. Logan—1822
Recombination kinetics for thermally dissociated Li-B pairs in Si. E. M. Pell and F. S. Ham—1052
Recombination of excess carriers at twin structures in germanium. J. P. McKelvey—442
Residual thermoelastic stresses in bonded silicon wafers. T. D. Riney—454
Short minority carrier diffusion lengths. A. M. Goodman—2550
Slip patterns on boron-doped silicon surfaces. H. J. Queisser—1776
Solubility of oxygen in germanium. W. Kaiser and C. D. Thurmond—115
Stress optical constants of germanium. K. J. Schmidt-Tiedemann—2058 (L)
Study of Li-O interaction in Si by ion drift. E. M. Pell—1048
Surface electrical changes caused by the adsorption of hydrogen and oxygen on silicon. J. T. Law—600
Surface kinetics and physics investigation of the reaction between single-crystal germanium and iodine. W. J. Heinecke and S. Ing, Jr.—1498
Surface potential of silicon. C. T. Raymo, C. W. Brands, and B. Schwartz—1165 (L)
Textural properties of germanium films. John E. Davey—877
Theory of microplasma instability in silicon. R. J. McIntyre—983
Third-order elastic moduli of germanium. T. Bateman, W. P. Mason, and H. J. McSkimin—928
Voltage dependence of microplasma density in *p*-*n* junctions in silicon. A. Goetzberger and C. Stephens—2646

Shock Waves (see also Explosions)
Initiation of a low-density PETN pressing by a plane shock wave. G. E. Seay and L. B. Seely, Jr.—1092
Multiple shock wave structures in polycrystalline ferroelectrics. C. E. Reynolds and G. E. Seay—1401(L)
On the possibility of detecting shock-induced second-order phase transitions in solids. The equation of state of invar. D. R. Curran—1811
Production of high ion densities in helium by means of high explosives. G. E. Seay, L. B. Seely, Jr, and R. G. Fowler—2439
Shock wave compression of hardened and annealed 2024 aluminum. G. R. Fowles—1475
Shock-wave compression of iron and bismuth. D. S. Hughes, L. E. Gourley, and Mary F. Gourley—624
Smooth spalls and the polymorphism of iron. John O. Erkman—939
Study of impact cratering in sand. F. L. Culp and H. L. Hooper—2480

Space Charge (see also Electrostatic Fields)
Charged cylindrical tube. T. R. Ferguson and R. H. Duncan—1385
Determination of the semiconductor surface potential under a metal contact. N. J. Harrick—568
Effects of phosphor powder dispersion in electroluminescent lamps. W. A. Thornton—2379
Electrical conduction and breakdown in high pressure (0125–300 mm) rare gases. R. Forman—1651
Electric strength of rutile single crystals. D. A. Powers and I. J. T. Johansen—1083
Electroluminescence at *p-n* junctions in gallium phosphide. M. Gershenzon and R. M. Mikulyak—1338
Excitation and amplification of cyclotron waves and thermal orbits in the presence of space charge. R. Adler, A. Ashkin, and E. I. Gordon—672
Experimental study of arc stability. I. J. D. Cobine and G. A. Farrall—328(E)
Extended curves of the space charge, electric field, and free carrier concentration at the surface of a semiconductor, and curves of the electrostatic potential inside a semiconductor. Charles E. Young—329
Field-enhanced donor diffusion in degenerate semiconductor layers. W. Shockley—1402(L)
Full-voltage range spark-gap crowbar. Eli M. Goldfarb and Harry G. Heard—326(L)
On three-dimensional space charge flow. J. Rosenblatt—1803(E)
Polarization and diffusion in a silicate glass. R. J. Charles—1115
Reflection of electromagnetic waves at electron density ramps. Leonard S. Taylor—1796(L)
Space-charge instabilities in electron diodes and plasma converters. C. K. Birdsall and W. B. Bridges—2611
Space charge instabilities in synthesized plasmas. A. L. Eichenbaum and K. G. Hernqvist—16
Stress distribution on the boundary of an elliptical hole in a large plate during passage of a stress pulse of long duration (major axis normal to the wave front). A. J. Durelli and W. F. Riley—1255
Surface potential of silicon. C. T. Raymo, C. W. Brands, and B. Schwartz—1165(L)

Space Physics
Man-made heating and ionization of the upper atmosphere. P. A. Clavier—570
Man-made heating and ionization of the upper atmosphere. P. A. Clavier—2651(E)
Surface electrical changes caused by the adsorption of hydrogen and oxygen on silicon. J. T. Law—600

Spectra and Spectroscopy
Determination of certain spectral distributions of soft x-rays by theoretical analysis of absorption experiments. Nancy A. Kerr—2465
Optical and infrared spectra of the ferrites and garnets. Kenneth A. Wickersheim—205S
Origins of characteristic bands in the infrared spectra of isotactic polystyrene and isotactic poly (ring-d_8 styrene). T. Onishi and S. Krimm—2320
Spectral response of solar cells. Brian Dale and F. P. Smith—1377

Sputtering
Determination of the maximum lattice-chain energy from sputtering yield curves. Don E. Harrison, Jr.—924
Etch effects from oblique-incidence ion bombardment. G. D. Magnuson, B. B. Meckel, and P. A. Harkins—369
Guidance and collimation of sputtered tungsten particles. Carl A. Ludeke—1400(L)
Investigation of the sputtering of silicon. S. P. Wolsky and E. J. Zdanuk—782
Magnetic thin films prepared by sputtering. Eric Kay—99S
Mercury ion beam sputtering of metals at energies 4–15 kev. G. K. Wehner and D. Rosenberg—887
Sputtering of vitreous silica by 20- to 60-kev Xe^+ ions. R. L. Hines and R. Wallor—202
Sputtering yields of metals for Ar^+ and Ne^+ ions with energies from 50 to 600 ev. Nils Laegreid and G. K. Wehner—365
Some properties of uniaxial permalloy films prepared by cathodic sputtering. M. H. Francombe and A. J. Noreika—97S

Superconductivity, Superconductors
Effect of residual gases on superconducting characteristics of tin films. Hollis L. Caswell—105
Field solution for a thin-film superconducting strip transmission line. James C. Swihart—461
Production of magnetic fields exceeding 15 kilogauss by a superconducting solenoid. J. E. Kunzler, E. Buehler, F. S. L. Hsu, B. T. Matthias, and C. Wahl—325(L)
Superconductor-transition switching time measurements using a superconductive radio-frequency mixer. Donald L. Feucht and James B. Woodford, Jr.—1882

Surface Properties (Etching) (see also Sputtering)
Anodic oxidation of germanium. T. Gabor—1361
Attainment of ultrahigh vacua, reduction in surface desorption, and the adsorption of hydrogen by evaporated molybdenum. Angus L. Hunt, Charles C. Damm, and Earl C. Popp—1937
Catalytic activity of *p*- and *n*-type germanium. William H. Watson, Jr.—120(L)
Dangling bonds in III-V compounds. Harry C. Gatos—1232
Direct observation in the electron microscope of oxide layers on aluminum. K. Thomas and M. W. Roberts—70
Dislocation etching solution for potassium chloride and other alkali halides. J. S. Cook—2492(L)
Dislocation etch pits on the basal plane of zinc crystals. H. S. Rosenbaum and M. M. Saffren—1856
Dissociation of adsorbed CO by slow electrons. George E. Moore—1241
Effect of residual gases on the properties of indium films. H. L. Caswell—2641
Effect of temperature on the emission of electrons from abraded surfaces of beryllium, calcium, aluminum, and magnesium. T. C. Ku and W. T. Pimbley—124(L)

Effect of temperature on the exoemission of electrons from abraded aluminum surfaces. W. T. Pimbley and E. E. Francis—1729
Effects of monolayer adsorption and bombardment damage or Auger electron ejection from germanium. Homer D. Hagstrum—1015
Elastic-plastic transition in copper crystals as determined by an etch-pit technique. F. W. Young, Jr.—1815
Etch effects from oblique-incidence ion bombardment. G. D. Magnuson, B. B. Meckel, and P. A. Harkins—369
Etch pits in electroluminescent zinc sulfide crystallites. Paul Goldberg—1520
Friction and adhesion of clean and contaminated mica surfaces. Anita I. Bailey—1407
Improved representation of calculated surface mobilities in semiconductors. I. Minority carriers. N. B. Grover, Y. Goldstein, and A. Many—2538
Improved representation of calculated surface mobilities in semiconductors. II. Majority carriers. Y. Goldstein, N. B. Grover, and A. Many—2540
Influence of surface energy on friction and wear phenomena. E. Rabinowicz—1440
Iron whisker surface rearrangements resulting from the hydrogen reduction of oxides and from thermal etching. J. V. Laukonis and R. V. Coleman—242
Kinetic and experimental basis of flash desorption. Gert Ehrlich—4
Liquidlike layers on ice. H. H. G. Jellinek—1793(L)
Mechanism of chemisorption, place exchange, and oxidation on a (100) nickel surface. H. E. Farmsworth and Hannibal H. Madden, Jr.—1933
(110) nickel surface. L. H. Germer, A. U. MacRae, and C. D. Hartman—2432
Orientation-dependent dissolution of lithium fluoride. M. B. Ives—1534
Oxygen adsorption on silicon and germanium. Homer D. Hagstrum—1020
Reactions of oxygen with pure tungsten and tungsten containing carbon. J. A. Becker, E. J. Becker, and R. G. Brandes—411
Slip patterns on boron-doped silicon surfaces. H. J. Queisser—1776
Some experiments using a vacuum-cleaned silicon *p-n* junction. J. T. Law—848
Surface electrical changes caused by the adsorption of hydrogen and oxygen on silicon. J. T. Law—600
Surface kinetics and physics investigation of the reaction between single-crystal germanium and iodine. W. J. Heinecke and S. Ing, Jr.—1498
Surface layer in $BaTiO_3$ single crystals. Ennio Fatuzzo and Walter J. Merz—1685
Surface layers on barium titanate single crystals above the Curie point. H. Schlosser and M. E. Drougard—1227
Textural properties of germanium films. John E. Davey—877

Thermal Conductivity and Diffusivity
Experimental study of intermetallic diffusion in large temperature gradients. C. J. Meechan—945
Flash method of determining thermal diffusivity, heat capacity, and thermal conductivity. W. J. Parker, R. J. Jenkins, C. P. Butler, and G. L. Abbott—1679
Proposed method of measuring thermal diffusivity at high temperatures. Robert D. Cowan—1363
Pulse method for the measurement of thermal diffusivity of metals. Edwin L. Woisard—40
Thermal conductivity in two-phase alloys. J. B. Schroeder—1798(L)
Thermal conductivity of porous media. I. Unconsolidated sands. W. Woodside and J. H. Messmer—1688
Thermal conductivity of porous media. II. Consolidated rocks. W. Woodside and J. H. Messmer—1699
Thermodynamic Properties
Available power from a nonideal thermal source. Paul Penfield, Jr.—1794(L)
Curie temperature of some garnets by the differential thermal analysis technique. A. Aharoni, E. H. Frei, Z. Scheidlinger, and M. Schieber—1851
Effect of magnetic clusters on the specific heat of Ni-Cu and Fe-V alloys. K. Schröder—880
Electrical resistivity of chromium in the vicinity of the Néel temperature. M. J. Marcinkowski and H. A. Lipsitt—1238
Flash method of determining thermal diffusivity, heat capacity, and thermal conductivity. W. J. Parker, R. J. Jenkins, C. P. Butler, and G. L. Abbott—1679
Measurement of the partial pressure of cesium over cesium antimonides. Kiyoshi Miyake—1132
Monotonic trap distributions. Richard H. Bube—1621(L)
Specific heat of superparamagnetic particles. J. D. Livingston and C. P. Bean—1964
Stored energy in fuel-bearing graphites. A. H. Willis, J. M. Baugnet, and R. C. De Buekelaer—1622(L)
Temperature-compensated Debye temperature of carbonyl iron. Charles P. Gazzara and Raymond M. Middleton—1546
Theoretical bound on the thermoelectric figure of merit from irreversible thermodynamics. Howard Littman and Burton Davidson—217
Thermal expansion and related bonding problems of some III-V compound semiconductors. Leonard Bernstein and Robert J. Beals—122(L)
Thermodynamics of thermally regenerated fuel cells. J. B. Friauf—616
Thermoelectricity
Effect of pressure on emf of thermocouples. F. P. Bundy—483
Effects of doping additions on the thermoelectric properties of the intrinsic semiconductor $Bi_2Te_{2.1}Se_{0.9}$. L. C. Bennett and J. R. Wiese—562
Effect of freezing conditions on the thermoelectric properties of $BiSbTe_3$ crystals. G. J. Cosgrove, J. P. McHugh, and W. A. Tiller—621
Calculations of the thermoelectric parameters and the maximum figure of merit for acoustical scattering. Louis R. Testardi—1978
Electrical conductivity and thermoelectric effect in single-crystal TiC. Lewis E. Hollander, Jr.—996
Low temperature thermoelectric power of the rare-earth metals. H. J. Born, Sam Legvold, and F. H. Spedding—2543
Peltier coefficient at high current levels. John R. Reitz—1623(L)
Recent studies of bismuth telluride and its alloys. H. J. Goldsmid—2198
Response of a thermocouple circuit to nonsteady currents. Thomas T. Arai and John R. Madigan—609
Theoretical bound on the thermoelectric figure of merit from irreversible thermodynamics. Howard Littman and Burton Davidson—217
Theory and experiment of a thermoelectric cooler. M. H. Norwood—2559
Thermoelectric behavior of *p-n* junctions. Melvin Cutler—222
Thermoelectric measurements at small-area contacts. M. Cutler—1075
Thermoelectric properties of Ag_2Te. P. F. Taylor and C. Wood—1

Thermoelectricity (*continued*)
  Transient response of a thermocouple circuit under steady currents. Allen D. Reich and John R. Madigan—294
  Zero-, first-, and second-order theories of a general thermocouple. A. H. Boerdijk—1584

Thin Films
  Angular dependence of torque in anisotropic permalloy films. W. D. Doyle, J. E. Rudisill, and S. Shtrikman—1785(L)
  Anisotropy in nickel-iron films. D. O. Smith—70S
  Anisotropy in permalloy films evaporated at grazing incidence. M. S. Cohen—87S
  Anisotropy rotation in thin permalloy films at room temperature. T. Matcovich, E. Korostoff, and A. Schmeckenbecher—93S
  Annealing behavior and temperature dependence of the magnetic properties of thin permalloy films. Armin Segmüller—89S
  Annealing of oblique-incidence permalloy films. G. P. Weiss and D. O. Smith—85S
  Characteristics of the annealing kinetics of tin films deposited at 88°K. J. Priest, C. Chiou, and H. L. Caswell—1772
  Crystal structure of photoelectric films of cesium antimonide. W. H. McCarroll—2051(L)
  Cube texture in ultrathin molybdenum permalloy tape. P. K. Koh—358S
  Damping effects of thin surface films. R. J. Huber, G. S. Baker, and P. Gibb—2488(L)
  Effect of residual gases on superconducting characteristics of tin films. Hollis L. Caswell—105
  Effect of residual gases on the properties of indium films. H. L. Caswell—2641
  Elastic modulus of amorphous nickel films. Stanko Jovanovic and Cyril Stanley Smith—121(L)
  Electric breakdown strength of single and laminated films of vinyl chloride-acetate. Robert G. Greenler and Robert M. Kay—1252
  Epitaxial growth and magnetic properties of single-crystal films of iron, nickel, and permalloy. Soshin Chikazumi—81S
  Ferrite thin films. Henry P. Lemaire and William J. Croft—46S
  Ferromagnetic resonance in thin magnetic films at radio frequencies. Turner E. Hasty and Lee J. Boudreaux—1807
  Field solution for a thin-film superconducting strip transmission line. James C. Swihart—461
  Forbidden reflections in electron diffraction patterns of evaporated tin films. Richard W. Vook—2474
  Formation conditions and structure of thin epitaxial silver films on rocksalt. Billy W. Sloope and Calvin O. Tiller—1331
  Free oscillations of the magnetization in permalloy films. Peter Wolf—95S
  Germanium films on germanium obtained by thermal evaporation in vacuum. O. Weinreich, G. Dermit, and C. Tufts—1170(L)
  Influence of nearby conductors on thin-film switching. J. S. Eggenberger—752(E)
  Interference method for measuring the thickness of epitaxially grown films. W. G. Spitzer and M. Tanenbaum—744(L)
  Magnetic anisotropies of nickel films evaporated and measured at 10^{-8} mm Hg and below. C. D. Graham, Jr., and J. M. Lommel—83S
  Magnetic film devices using passive loading. J. M. Daughton, T. A. Smay, A. V. Pohm, and A. A. Read—36S
  Magnetic thin films prepared by sputtering. Eric Kay—99S
  Magnetoresistance and magnetic switching in permalloy films. R. L. Coren and H. J. Juretschke—292S
  Ni-Fe single-crystal films and their magnetic characteristics. R. R. Verderber and B. M. Kostyk—696
  Nonlinear effects of Z-directed spin waves in thin films. Jerome I. Kaplan—1831
  Nucleation processes in thin permalloy films. S. Methfessel, S. Middelhoek, and H. Thomas—294S
  Nuclear resonances in cubic, hexagonal, and mixed phase cobalt powders and thin films. Wilton A. Hardy—122S
  Oblique-incidence anisotropy in evaporated films. M. S. Cohen, D. O. Smith, and G. P. Weiss—1405(E)
  Partial rotation in permalloy films. S. Methfessel, S. Middelhoek, and H. Thomas—1959
  Photovoltaic effects in Cs_3Sb films. Frederick Wooten—1789(L)
  Preparation and properties of thin ferrite films. E. Banks, N. H. Riederman, H. W. Schleuning, and L. M. Silber—44S
  Properties of thin antimony films deposited in high vacuum. George A. Condas and Frederick O. Wooten—323(L)
  Rotatable anisotropy in thin permalloy films. R. J. Prosen, J. O. Holmen, and B. E. Gran—91S
  Single-crystal tin films. Richard W. Vook—1557
  Some properties of uniaxial permalloy films prepared by cathodic sputtering. M. H. Francombe and A. J. Noreika—97S
  Spiral walls in thin magnetic films. Harrison W. Fuller, Harvey Rubinstein, and Donald L. Sullivan—286S
  Stress and strain in thin films bulged over circular openings. Ralph Papirno—1175(L)
  Study of electron bombardment of thin films. G. B. Gilbert, T. O. Poehler, and C. F. Miller—1597
  Textural properties of germanium films. John E. Davey—877
  Thin-film switching in the hard direction by wall motion. Robert J. Spain and Harvey Rubinstein—288S
  Transient effects in Peltier coolers. A. D. Reich, T. Arai, and J. R. Madigan—2493(L)
  Use of monomolecular layers in evaporated-film tunneling devices. J. L. Miles and H. O. McMahon—1176(L)

Vacuum Techniques
  Attainment of ultrahigh vacua, reduction in surface desorption, and the adsorption of hydrogen by evaporated molybdenum. Angus L. Hunt, Charles C. Damm, and Earl C. Popp—1937
  Germanium films on germanium obtained by thermal evaporation in vacuum. O. Weinreich, G. Dermit, and C. Tufts—1170(L)
  Hot-cathode magnetron ionization gauge for the measurement of ultrahigh vacua. J. M. Lafferty—424
  Kinetic and experimental basis of flash desorption. Gert Ehrlich—4
  Properties of thin antimony films deposited in high vacuum. George A. Condas and Frederick O. Wooten—323(L)
  Some experiments using a vacuum-cleaned silicon p-n junction. J. T. Law—848

Viscosity and Viscoelasticity
  Flow of gas through porous media in the region between molecular and viscous condition. E. H. Hirsch—977
  Method for measuring dynamic mechanical properties of viscoelastic liquids and gels; the gelation of polyvinyl chloride. Meyer H. Birnboim and John D. Ferry—2305
  Non-Newtonian viscosity of polymers. Roger S. Porter and Julian F. Johnson—2326
  Thermorheological simplicity in extrusion flow curves of high polymers. Katsuhiko Ito—1743
  Use of idealized relaxation spectra in the interpretation of experimental results concerning polymer solutions. K. Walters—1975

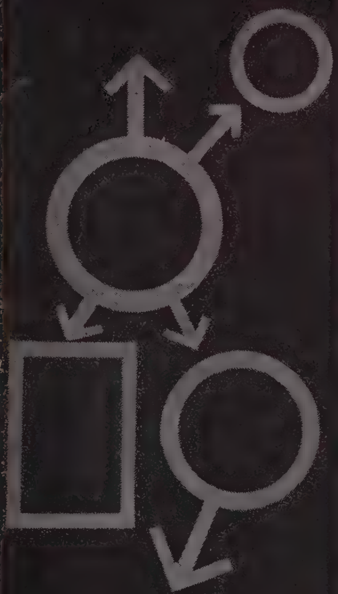

ENGINEERS
PHYSICISTS

Professional Assignments now available in the NUCLEONICS LABORATORY at HUGHES-FULLERTON in Southern California

Hughes-Fullerton Nucleonics Laboratory has major R&D interest in the fields of radiation systems (source generators, linacs and cyclotrons); radiation effects on materials, components, subsystems and systems; radiation environments of weapons; remote handling systems for hazardous or repetitive applications (undersea, nuclear, automated and space applications). Challenging positions now open in the following areas:

■ Circuit Design — High Voltage & High Power Electronic Systems ■ Accelerator Research & Development ■ Particle Dynamics and Beam Analysis Studies ■ Control Systems ■ Radiation Environments & Effects ■ Weapon Environments ■ Electro-magnetic Fields ■ Electronic Circuitry ■ Nuclear Instrumentation.

Applicants must have PhD or MS in EE or Physics (or equivalent: BSEE or Physics plus 2-5 years' experience).

For full information on these outstanding professional assignments, call Southern California collect:

TRojan 1-4080, ext. 3741.

or, send complete resume to:

Mr. B. P. RAMSTACK
HUGHES-FULLERTON R & D,
P. O. Box 2097, Fullerton, California

HUGHES

HUGHES AIRCRAFT COMPANY

An equal opportunity employer.

Cenco's new compact

VACUUM SYSTEM

for thin-film coating, component testing and other research and limited production tasks requiring vacuum 2×10^{-6} mm of Hg

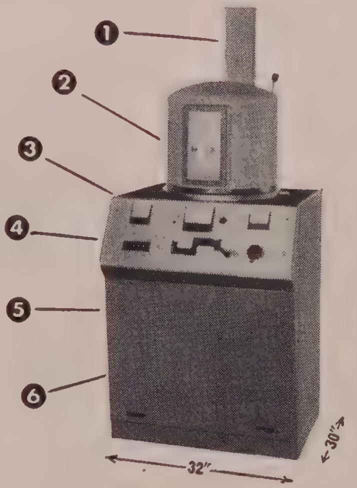

① **SAFETY HOIST** spring-loaded hoist raises and lowers bell jar quickly and easily; locks solidly in any position.

② **ALUMINUM BELL JAR** light-weight, implosion-proof—large window provides unimpeded view of the pump plate area.

③ **TWO BUILT-IN ELECTRONIC VACUUM GAGES** read directly from front panel—thermocouple gauge (1000 to 1 microns) connected into foreline discharge gage (20 to .001 micron) connected directly to pump plate.

④ **THREE-WAY VALVE** exclusive, single-lever valve permits immediate change-over and eliminates costly mistakes.

⑤ **PUMPS** a Cenco 14 Hyvac Pump backing a fast 6″ oil diffusion pump for rapid bell jar evacuation.

⑥ **POWER SUPPLIES** the 19″ pump plate contains 9 electrodes fed from either of two built-in power supplies—12 volt DC, 100 amps and 5000 volts AC, 30 ma, or conveniently fed from any external source.

The Cenco Vacuum System can evacuate to 0.1 micron in eight minutes using less than 1 pint of cooling water per minute. Input power required 30 amps at 115 volts. Dimensions, height 71″, width 30″, depth 32″, only 960 sq. in. of floor space used. For further information contact the Cenco branch office nearest you, or write direct.

No. 94700, Cenco Vacuum System complete...... $3,950.00

cenco

CENTRAL SCIENTIFIC
a division of Cenco Instruments Corporation
1700 Irving Park Road • Chicago 13, Illinois
Mountainside, N. J. Montreal Santa Clara
Somerville, Mass. Toronto Los Angeles
Birmingham, Ala. Ottawa Vancouver Houston
Cenco S.A., Breda, The Netherlands Tulsa

Scientists and Engineers in Research

CAREER IN RESEARCH IN A NEW FIELD

SEMICONDUCTOR TECHNOLOGIES

IBM THOMAS J. WATSON RESEARCH CENTER

The new IBM Thomas J. Watson Research Center in Yorktown, N.Y. is undertaking important new long-range projects requiring scientists and engineers with experience in, or relating to, various aspects of semiconductor research. Research projects under way are directed toward purely scientific goals . . . as well as toward developing technology for engineering advanced information handling systems.

SEMICONDUCTOR COMPOUND CHEMISTRY

Several openings exist for physical and inorganic chemists to conduct research on the preparation and purification of materials, and to study their physical properties. This is a unique opportunity to work in advanced areas to open exciting new fields for research. Experience is highly desirable, but not necessary.

SEMICONDUCTOR VAPOR GROWTH

Applicants should be familiar with studies of vapor growth reactions in general as well as vapor grown junction technologies. This is a unique opportunity to work in advanced areas of semiconductor research, to open exciting new fields for research. An advanced degree in physical chemistry, metallergy or physics is desirable, but a B.S. with a strong background in relevant experiences will be considered.

SEMICONDUCTOR CIRCUITS

The position involves the preparing, experimental exploration, and evaluation of circuits which have a high degree of probaability of lending themselves to fabrication into integrated circuitry by means of advanced semiconductor technologies including expitaxial crystal growth from the vapor phase. The work will be done in close cooperation with device fabrication scientists and the ultimate aims include consideration of integrated of preconnected computer circuits wherein transmission lines are treated as integral pasts. An advanced degree or equivalent in E.R. or Physics is desirable. We prefer experience in circuits using semiconductor devices as applied to large high-speed computers.

The Thomas J. Watson Research Center at Yorktown, N.Y., in located in pleasant, rural Westchester County countryside just 35 miles from New York City. The Research Center was designed to provide the best possible working environment for scientists and engineers engaged in advanced research studies. The location provides excellent schools and housing. IBM offers a fully paid benefits program that is meeting the pace for industry today. All qualified applicants will receive consideration for employment without regard to race, creed, color, or national origin.

Please write, outlining your education and experience, to:

Mr. J. B. Farrington, Dept. 579M
Thomas J. Watson Research Center
P. O. Box 218
Yorktown Heights, New York

IBM®

INTERNATIONAL BUSINESS MACHINES CORPORATION

OPTICAL CRYSTALS

SODIUM HALIDES
POTASSIUM HALIDES
CESIUM HALIDES
THALLIUM HALIDES

Special crystals grown to order, optical blanks cut to specifications, finish polishing as required.

123 WOODLAND
AVENUE
WESTWOOD
NEW JERSEY

CRYSTALS DIVISION
ISOTOPES, INC.

SCIENTISTS
ENGINEERS
CALIFORNIA

offers you and your family

- A world center of the electronics-missile-space industries for CAREER ADVANCEMENT
- The High Sierra and the Pacific Ocean for RECREATION
- And for your children some of the nation's FINEST PUBLIC SCHOOLS
- World Famous Universities for ADVANCED STUDY
- MAJOR CULTURAL CENTERS

while living in such places as
Exciting San Francisco
Fabulous Southern California
Cultural Palo Alto

Companies pay interview, relocation and agency expenses

Submit resume in confidence to:

PROFESSIONAL and TECHNICAL
RECRUITING ASSOCIATES
(a Division of the Permanent Employment Agency)
Suite A
825 San Antonio Road
Palo Alto, Calif.

For ULTRA-HIGH VACUUM or ULTRA-CLEAN SYSTEMS

All-metal bakeable valves • Elbows, tees, crosses, nipples • Variable leaks
Flanged metal to glass seals • Bakeable capacitance manometers • Flanged bellows assemblies

AVAILABLE FROM STOCK

At right are some of the standard Granville-Phillips components available from stock. None contain organic materials. All are bakeable to 450°C and useful at 10^{-10} mm Hg or lower. Right-angle valves presently available in ½", 1", 2", 4", and 6" sizes, straight-through valves in ½", 1", 2½", and 4" sizes. Complete line of demountable plumbing. Custom designs on request.

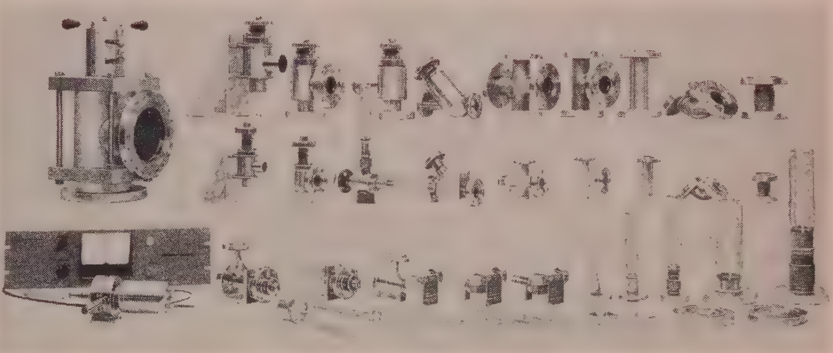

WRITE OR TELEPHONE FOR COMPLETE CATALOG

Granville-Phillips Company
P. O. Box J-198 Pullman, Washington • telephone LOgan 4-1130

COMPUTER RESEARCH

RCA Laboratories has openings for professional engineers and scientists to work on advanced computer systems through the application of new solid state devices and modern mathematical techniques.

The areas of work include cryogenic devices, nanosecond switching circuits, large capacity and ultra-fast memories, and the theory of computers including advanced logic design, and learning machines.

Applicants with a master's or higher degree or equivalent research experience are invited to contact:

Dr. S. G. Ellis, Dept. RL-9A
Radio Corporation of America
RCA Laboratories
Princeton, New Jersey

An Equal Opportunity Employer

RADIO CORPORATION OF AMERICA

An equal opportunity employer.

Optical Engineers

Require additional personnel with a background in optics. Prefer several years as an optical engineer and/or physicist. Should be familiar with the design & application of interferometers. Other experience in spectroscopy, astronomical or telescopic equipment helpful. Challenging work in an expanding laser program.

Please refer all
correspondence to
or call:
H. C. Stafford

TRG
Incorporated
Two Aerial Way
Syosset, New York
Phone
OVerbrook 1-6900

An Equal/Opportunity Employer

TRG INC
TECHNICAL RESEARCH GROUP

laser physicists

Hughes' broad experimental program in the development of new LASER techniques, components and systems is being enlarged. With the unusually varied and significant applications of LASERS, the opportunities created through this expansion will be professionally rewarding and exciting and of long range promise. Three of the several openings are indicated below. We invite your inquiry.

1 PHYSICISTS
A background in experimental techniques (optical spectroscopy, flash photometry, etc.) involving phenomenon at optical frequencies, an advanced degree or compensating experience and demonstrated ability will be preferred. We will also consider Physical Chemists with strong backgrounds in optical physical techniques.

2 ELECTRONIC ENGINEERS or PHYSICISTS
Pulse circuit techniques experience is required.

3 SYSTEMS ENGINEER
About five years of experience, preferably in radar systems, and a physical, as opposed to a mathematical, orientation are required.

Airmail your resume to:
Mr. Robert A. Martin, Supervisor of Employment, Hughes Aircraft Company, Culver City 64, California.

CREATING A NEW WORLD WITH ELECTRONICS

HUGHES

HUGHES AIRCRAFT COMPANY
AEROSPACE DIVISIONS

WE PROMISE YOU A REPLY WITHIN ONE WEEK

new books in the International Series in Pure and Applied Physics

PARTICLE ACCELERATORS

By STANLEY LIVINGSTON, Massachusetts Institute of Technology; and JOHN P. BLEWETT, Brookhaven National Laboratory. Available January, 1962

This textbook provides a descriptive and comparative study of the electronuclear machines used for accelerating beams of charged particles. Each class of accelerator is discussed in a separate chapter, with emphasis on the physical principles of acceleration and focusing. The major technical problems and limitations are discussed and the original contributions and sequence of development are described. The overall purpose is to explain the basic principles of particle accelerating and to show how the several types of accelerators complement each other as tools for nuclear research.

SUPERFLUID PHYSICS

By CECIL T. LANE, Yale University. Available February, 1962

A senior-graduate text which gives an updated survey of research in the field of superfluidity. Aimed at acquainting newcomers to the field with the most important advances of the last 20 years, it embraces both superfluid helium and superconductivity. The treatment is both theoretical and experimental; the level of mathematical treatment is elementary with the main emphasis on the physical principles involved.

ELEMENTARY QUANTUM FIELD THEORY

By ERNEST M. HENLEY, University of Washington; and WALTER THIRRING, University of Vienna. Available April, 1962

This second-year graduate book presents an extension and expansion of the material covered in the last third of Schiff's QUANTUM MECHANICS. The important features of quantum field theory are examined on a level students can follow after a standard quantum mechanics course.

Send for approval copies

McGraw-Hill Book Company, Inc.

330 West 42nd Street New York 36, N. Y.

TECH NEWS

FOR SCIENTISTS, MATHEMATICIANS
OPERATIONS EVALUATION GROUP, M.I.T.

In its research and analysis for the Chief of Naval Operations and Fleet Commanders, the Operations Evaluation Group, M.I.T., pursues knowledge in virtually every sphere of naval interest.

Consider OEG study 644, for example, entitled "Echo Variability and the Formulation of a Radar Theory." OEG's analysts found that blaming radar operators and poor radar maintenance for variability of signal presentation on radar scopes (all other things supposedly being equal) was convenient but erroneous. New culprits will have to be isolated and bested. OEG thinks it has found some of them for the Navy.

When is a sea not a sea? When it's a swell. Seriously. Seas and swells, ramp-to-touchdown distances, vertical velocities, wave-to-wave amplitude variations, and similarly specialized factors enter into "The Effect of Ship Motion and Flight Deck Geometry upon Carrier Air Operations." This is Naval Warfare Analysis Group Study No. 20 (NAVWAG being the long-range studies division of OEG). One interesting conclusion: Position of the touchdown point has a greater effect on precluded flying time than does ship length. And on the subject of ship length, the minimum recommended (for an angled-deck carrier) is 800 feet.

Would you like to have a hand in similar research, knowing that you would be contributing importantly to the national defense? Well paid career appointments in Washington, D.C., and Cambridge are available to scientists, mathematicians and engineers with advanced degrees. Direct your inquiry to the Director, Dr. Jacinto Steinhardt, either in Washington or in Cambridge.

OEG
OPERATIONS EVALUATION GROUP
Box 6196, Apex Station, Washington 4, D. C.
or 292 Main St., Cambridge, Mass.
An equal opportunity employer.

10th ANNUAL

PHYSICS SHOW

January 24–27, 1962 **Statler Hilton Hotel, N. Y.**

The meeting will bring together five thousand top level physicists—members of the American Physical Society and The American Association of Physics Teachers. Over five hundred technical papers will be presented.

An exhibit of scientific instruments, apparatus, components and technical books. Join the 72 companies who have reserved space, including:

Academic Press, Inc.—Johnson Reprint Co.
Addison-Wesley Publishing Co.
Allyn and Bacon, Inc.
Alpha Scientific Labs., Inc.
American Tradair Corp.
Baird-Atomic Inc.
W. A. Benjamin, Inc.
Charles Beseler Company
Cambridge Communications Corp.
Cambridge University Press
Central Scientific Company
The Conference Book Service
Consolidated Vacuum Corp.
Consultants Bureau
F. A. Davis Company
E-H Research Labs.
The Ealing Corporation
Elion Instruments Inc.
The Gaertner Scientific Co.
General Radio Company
Hamner Electronics Co., Inc.
Harvey-Wells Corp.
High Voltage Engineering
Holt, Rinehart, and Winston, Inc.
Ilikon Corp.
Interscience Publishers, Inc.
Isomet Corporation
Keithley Instruments
Kinney Vacuum Div.—New York Air Brake Co.
J. Klinger Scientific Apparatus
Laboratory for Science
La Pine Scientific Corp.
Macalaster Bicknell Corp.
The Macmillan Company
Magnion, Inc.
McGraw-Hill Book Co., Inc.
Mettler Instruments Corp.
Modern Learning Aids
N.R.C. Equipment Corp.
Nuclear Industries, Inc.
Oak Ridge Technical Enterprises
Office of Naval Research
Ophthos Instrument Co.
Pacific Electric Motor Co.
Pergamon Press, Inc.
Perkin-Elmer Corp.
Philips Electronic Instruments
Prentice-Hall, Inc.
Publishers' Authorized Bindery Service
Radiation Dynamics Inc.
Radiation Instrument Development Lab., Inc.
John F. Rider Publisher, Inc.
Semi-Elements Inc.
Solid State Radiations, Inc.
Space Technology Labs., Inc.
Spectromagnetic Industries
Technical Measurement Corp.
Vacuum-Electronics Corp.
Vacuum Instrument Corp.
D. Van Nostrand Company
Vactronic Lab. Equipment, Inc.
Varian Associates
Victoreen Instrument Co.
The Welch Scientific Co.
John Wiley and Sons, Inc.

Also . . .

Americana Corp.
Appleton-Century-Crofts, Inc.
Harshaw Chemical Co.
Itek Corp.
Oxford University Press
Samson Associates
Trident Manufacturing Corp.

Inquiries should be addressed to:

Mr. T. Vorburger, Exhibit Manager
American Institute of Physics
335 East 45th Street
New York 17, N. Y.

new CRYO-BAFFLES
REDUCE VACUUM CONTAMINATION

The new NRC Series 0315 Cryo-Baffle design provides the most effective solution for preventing backstreaming oil vapors from entering and contaminating vacuum chambers.

UNIQUE FEATURES AND ADVANTAGES:

- *Circular* chevron around a large *central* reservoir provides more condensation area than straight surfaces
- "Optically Opaque" baffles prevent gas molecules from entering vacuum chamber
- No external cooling required
- Internal cooling by liquid nitrogen, water or mechanical refrigeration
- Chevron surfaces more *evenly* cooled by connecting fins
- Long, high-impedance path between chevron and outer shell, shielding oil molecules from room temperature surfaces
- Lower over-all height than other baffles available
- 4″ – 6″ and 10″ models available to fit all standard 150 lb. drillings

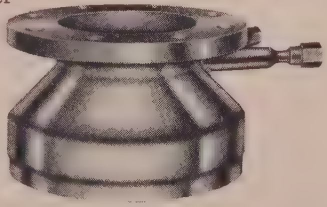

Write today for technical details on the Series 0315 line.

A Subsidiary of National Research Corp.
160 Charlemont Street, Dept. 20L
Newton 61, Massachusetts

NRC
NRC
EQUIPMENT
CORPORATION

MANUFACTURING PLANTS AT NEWTON, MASSACHUSETTS AND PALO ALTO, CALIFORNIA

Soviet Physics—SOLID STATE

Monthly. A cover to cover translation of the USSR Academy of Sciences journal, "Fizika Tverdogo Tela."

Soviet Physics—TECHNICAL PHYSICS

Monthly. A cover to cover translation of the USSR Academy of Sciences journal, "Zhurnal Tekhnicheskoi Fiziki."

Soviet Physics—CRYSTALLOGRAPHY

Bimonthly. A cover to cover translation of the USSR Academy of Sciences journal, "Kristallografiya."

Please address orders and inquiries to the publisher:

AMERICAN INSTITUTE OF PHYSICS
335 East 45th Street, New York 17, N. Y.

A MESSAGE FROM KEARFOTT
TO EMINENT SCIENTISTS

who have received their Doctorates, are specialists in Radiation Theory and Techniques and have spent 8–10 years in industrial, academic or government research.

ANNOUNCING A NEW RESEARCH CENTER FOR THE AEROSPACE SCIENCES

Your interest is enlisted in a new scientific community entirely concerned with scientific and technical investigations; totally divorced from administrative or development duties.

Studies will be related as closely as possible to urgent needs of government agencies, determined through personal consultation with their representatives. Particular (but not exclusive) emphasis will be placed on problems bearing on navigation, guidance and control of upper atmosphere, space and undersea vehicles, areas where Kearfott has long held a leadership position in the development of systems and components.

A PRINCIPAL STAFF SCIENTIST IS SOUGHT *who will initiate and guide his own research and whose experience is sufficiently broad to provide technical direction to other men in a plurality of the following areas:*

- INFRARED TECHNIQUES, SOURCES & THEORY
- ATMOSPHERIC TRANSMISSION (Intensities, Attenuation Studies)
- SCANNING TECHNIQUES (Space Applications)
- ENERGY CONVERSION (Thermo Cooling, Power Generation)
- WAVE PROPAGATION (In Various Media)
- KINETIC THEORY OF IONIZED GASES (Including Multiple Fluid Models of Plasmas, Magneto Hydrodynamic Flow)

▶ If you are interested in being one of the outstanding scientists from many fields of science who will form the nucleus of the new Research Center, write in confidence to Dr. R. C. Langford, Director of Research.

GP
KEARFOTT DIVISION
GENERAL PRECISION, INC.

Dept. 6C / 1150 McBride Ave. / Little Falls, N. J.
An Equal Opportunity Employer

INDEX TO ADVERTISERS

Name *Page*

AMPEREX ELECTRONIC CORP., NUCLEAR PRODUCTS DEPT. .. xvii

AMPEX CORPORATION xix

ARNOLD ENGINEERING CO. xiii

BELL TELEPHONE LABORATORIES iii

CBS LABORATORIES; DIV. OF COLUMBIA BROADCASTING SYSTEM, INC. .... Cover 2

CENTRAL SCIENTIFIC CO. xxi
Manufacturers of Cenco physical apparatus and instruments to meet all requirements of University, College and High School Physics Laboratories. Specializing in high vacuum pumps and development of instruments and apparatus for various sciences.

ERB & GRAY SCIENTIFIC, INC. .. xvi

GAERTNER SCIENTIFIC CORP. .. xxx
Spectroscopes, spectrometers, spectrographs, spectrophotometers, heliostats, measuring microscopes, comparators, cathetometers, reading telescopes, interferometers, chronographs, driving machines, etc.

GENERAL ELECTRIC. CO. xii

GENERAL RADIO CO. .... Cover 3
Manufacturers of electronic measuring instruments; vacuum-tube voltmeters, amplifiers, and oscillators; wave analyzers, noise meters and analyzers, stroboscopes, laboratory standards of capacitance; inductance and frequency; impedance bridges, decade resistors and condensers, air condenser and variable inductors; rheostats, variacs, transformers; other laboratory accessories.

Name *Page*

GRANVILLE–PHILLIPS CO. xxiii

HUGHES AIRCRAFT CO. .... xxi, xxiv

IBM CORPORATION .... vi, xxii

ILIKON CORPORATION ..... xviii, xix

ISOTOPES, INC. CRYSTALS DIVISION xxii

KEARFOTT DIVISION, GENERAL PRECISION, INC. ... xxvii

KEITHLEY INSTRUMENTS, INC. viii
Vacuum tube electrometers, microammeters, kilovoltmeters, static detectors, meg-meg-ohm-meters, high gain dc amplifiers, dc vacuum tube voltmeters, high input impedance ac isolation amplifiers.

KEUFFEL & ESSER COMPANY .. vii

LOS ALAMOS, SCIENTIFIC LABORATORY ix

McGRAW–HILL BOOK CO., INC. . xxv

MATERIAL RESEARCH CORP., ADVANCED MATERIALS DIV. xxx

NRC EQUIPMENT CORP. xxvii
Manufacturers of standard and special high vacuum components, equipment, and systems including mechanical booster, and diffusion pumps; gauges; valves; seals; connectors; melting and heat-treating furnaces; coaters; impregnators; gas in metal analyzers; driers and freeze driers; altitude chambers and leak detectors.

OPERATIONS EVALUATION GROUP xxv

PERMANENT EMPLOYMENT AGENCY xxii

INDEX—*Continued*

Name *Page*

PHILCO RESEARCH CENTER ... xxx

PHILIPS ELECTRONIC INSTRUMENTS .... x, xi

RADIO CORP. OF AMERICA xxiii

RAMO–WOOLDRIDGE LABS. .. Cover 4
Research, development, and manufacture in the field of electronic systems for commercial and military applications, and in the field of guided missiles.

S. A. M. E. S. xiv

SPERRY RAND RESEARCH CENTER iv

SYLVANIA ELECTRONIC SYSTEMS, AMHERST LABORATORIES xv

TRG INC. xxiv

TEKTRONIX, INC. v
Manufacturers of Cathode-Ray Oscilloscopes, Auxiliary amplifiers, square-wave generators, vacuum-tube characteristic-curve tracers, L.C. Meters, constant-amplitude generators, operational accessories.

WELCH SCIENTIFIC CO., W. M. .. xx
Manufacturers of high-vacuum pumps, both mechanical and diffusion; vacuum gauges; electrical measuring instruments; physics equipment; and other items for the physical and chemical laboratories.

TUBULAR SLIDE CONTACT RHEOSTATS
RESISTORS
Toroidal Winding Machines
REX RHEOSTAT CO.
149-a Babylon Tpke. Roosevelt, L. I., N. Y.

POSITIONS OPEN

Position available. Aerospace science. Senior academic position. A physicist with an interest in teaching and research in the aeronautical and astronautical sciences is needed in the Aerospace Engineering Department of a large state university. A Ph.D. is required; some experience in the field is desirable but not mandatory. Salary and rank from assistant professor to full professor will depend on preparation and experience. Location Southeast. Address inquiries to Box 1261A, American Institute of Physics, 335 E. 45th Street, New York 17, N. Y.

FELLOWSHIPS AND ASSISTANTSHIPS available for students interested in the field of the behavior and properties of materials (metals, ceramics, semiconductors, etc.). Summer employment between academic years is assured. Research performed as an assistant can be used for a thesis. A new Materials Research Center provides exceptional facilities for basic research and advanced studies in kinetics, physical ceramics and metallurgy, imperfections in solids, electronic and magnetic behavior, thermodynamics, x-ray diffraction and electron microscopy. Applicants with degrees in mathematics, the physical sciences or engineering and an interest in this field will be considered. Because of the quarter system, it is possible to start graduate studies at several times during the year. Department of Materials Science, The Technological Institute, Northwestern University, Evanston, Illinois.

SCIENTISTS AND ENGINEERS FOR JPL'S LUNAR AND PLANETARY PROGRAMS

with experience in any of the following areas: Celestial Mechanics, Orbit Determination, Space Navigation Theory, Trajectory Studies, and Systems Analysis. A new technology, based on celestial mechanics, mathematical statistics, and engineering systems analysis, is evolving in the space exploration program. Both theoretical and project positions are available for experienced people in this expanding field. Send resume to A. P. Locke, JET PROPULSION LABORATORY, California Institute of Technology, 4800 Oak Grove Drive, Pasadena, California. "An equal opportunity employer."

Gaertner Precision Optical Bench Assembly

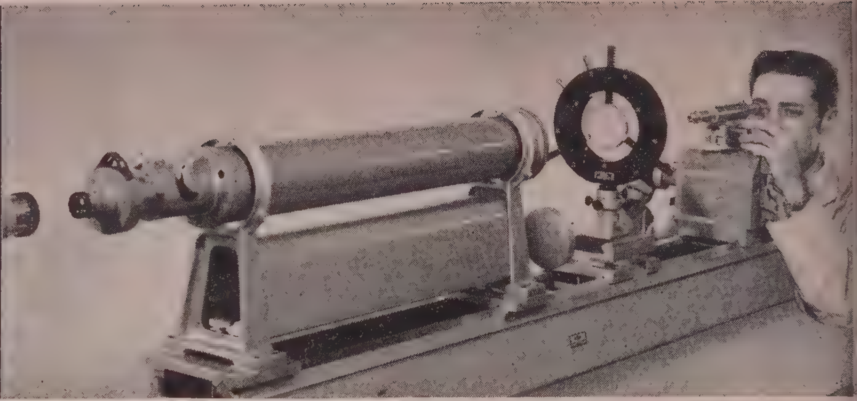

Useful in checking optics and for experimental instrumentation setups

The Precision Optical Bench is a versatile measuring instrument consisting of a lathe-bed-type base, light source, collimator with interchangeable filters and targets, nodal slide and microscope with three-dimensional adjustment. Focal lengths, resolving power and the various aberrations of optical parts and systems can be measured.

The several components can be used independently for special test setups, mock-ups and experimental instrumentation—providing linear and angular motions and measurements, alignment and stable support.

Double and single rod benches and a large selection of carriages, holders and supports provide a complete selection from which to choose.

Gaertner offers a wide range of optical and measuring instruments, including special modifications, design and manufacture of special instruments and optical systems, and manufacture of subassemblies and instruments from customer sketches and drawings.

Send for bulletin 156-59

Designed and manufactured in the U.S.A. by

Gaertner
SCIENTIFIC CORPORATION
1246 Wrightwood Ave., Chicago 14, Illinois • BU 1-5335

SUPER-PURE MATERIALS

Item: Single crystal nickel, tungsten, tantalum, niobium and molybdenum with interstitial impurity levels of less than 25 ppm in stock.

SPECIAL ALLOYS

Item: Homogeneous alloys of aluminum-3% boron, indium-3% aluminum, eutectic gold alloys and many others available.

PRECISION SHAPES

Item: Large diameter spheres (greater than .040); super-pure refractory metal foil and wire; strip, discs, buttons, special castings.

The research know-how that produced these breakthroughs can be put to work for your special materials needs. All items available in production and experimental quantities. Write us for full details.

mrc
Advanced Materials Division
MATERIALS RESEARCH CORP.
47 Buena Vista Ave., Yonkers, N.Y.

RESEARCH POSITIONS AVAILABLE

Professional staff positions have been created at Philco's new Research Center in suburban Philadelphia in such areas as Physics of Materials, Semiconductor Electrochemistry, Radiation Effects on Solids, Solid State Devices, Applied Radiochemistry, Thin Film and Tunneling Phenomena, and Fuel Cells. In general, the nature of these programs is such that the Ph.D. is required. Benefits of association with the Research Center include the opportunity for independent research, well-equipped laboratories, knowledgeable associates, and competitive salaries. Additional information may be obtained by writing Mr. R. A. Ruth, Philco Research Center, Blue Bell, Penna.

RESEARCH CENTER
PHILCO®
Famous for Quality the World Over
"An equal opportunity employer."

The Counter with a Memory *also writes*

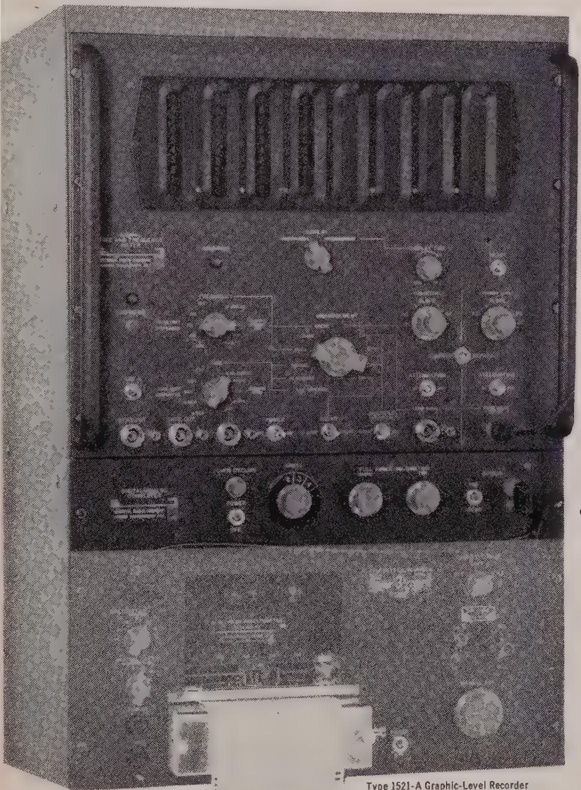

Type 1521-A Graphic-Level Recorder

The G-R Counter's unique storage circuits vastly simplify graphic analog recording. To decode the Counter's output to a d-c analog voltage you simply add G-R's all electronic Digital-to-Analog Converter.

For those desiring tabulated digital data, a Data Printer is available which connects directly to the Counter (no modifications or adaptor kits required).

◀ 1130-A Digital Time and Frequency Meter

Measurement Ranges:
Frequency: dc to 10 Mc
Period: 10μsec to 10^7 sec
Time Interval: 1μsec to 10^7 sec
Also measures 10 periods, frequency ratios, phase shifts, pulse characteristics, and counts random events.

Display: 8 digits intermittent; 4 digits continuous readout (previous count displayed continuously during counting interval; changes to new value when count is completed).

Sensitivity: 0.25v rms

Accuracy: ±1 count ± time-base stability. A variety of plug-in time-base generators are available with short-term stabilities ranging from 1 part in 10^8/min to 1 part in 10^9/min.

Price: From $2,585 to $2,950 depending on time-base generator desired.

◀ 1134-A Digital-to-Analog Converter $595

Will drive any standard 1 ma (or 100 mv) recorder

- High Accuracy —
  Linearity: ±0.05% of full scale
  Stability: ±0.02% for ±15% line voltage variations; ±0.03% for ambient temperature changes over the range from 0 to 50 C.
- All Electronic — No mechanical data printer required to convert counter output to steady analog signal. Operates directly from the G-R Counter's internal storage system.
- Either 1 ma or 100 mv output. Connects readily to most d-c strip-chart recorders.
- Records first 3, last 3, or last 2 digits of the G-R Counter's 4-digit continuous display which may be set to read any four consecutive digits of count over the range from dc to 10 Mc.

1132-A DATA PRINTER, $1450, for unattended measurements

Provides permanent printed records on adding machine tape. The printer has a 12-column register capacity, eight of which are used to print counter output. The remaining four columns can be used to display additional data such as time from a digital clock. Printing rate is adjustable from one print every twenty seconds to three prints per second. A keyboard and print-command bar allow numbers to be typed manually between automatic prints. An output for driving an IBM summary punch is available as a special option.

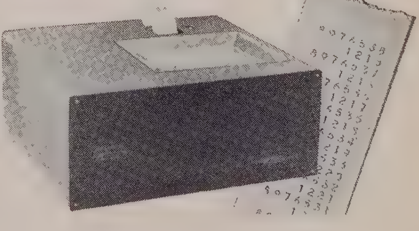

GENERAL RADIO COMPANY
WEST CONCORD, MASSACHUSETTS

NEW YORK, WOrth 4-2722
District Office in Ridgefield, N. J.
WHitney 3-3140

CHICAGO
Oak Park
Village 8-9400

PHILADELPHIA
Abington
HAncock 4-7419

WASHINGTON, D. C.
Silver Spring
JUniper 5-1088

SYRACUSE
Syracuse
GLenview 4-9323

SAN FRANCISCO
Los Altos
WHitecliff 8-8233

LOS ANGELES
Los Angeles
HOllywood 9-6201

ORLANDO, FLA.
Orlando
GArden 5-4671

IN CANADA
Toronto
CHerry 6-2171

Research is the
investigation of natural phenomena,
motivated
by a desire for basic understanding

Anyone actually doing research can easily define the term. Unfortunately, ever since research became an institutional status symbol, the word has rapidly been losing most of its meaning as a descriptive noun. Nowadays we see the word—along with its prestigious modifiers "basic" and "fundamental"—being applied to such unlike pursuits as the study of strange particle decays and the improvement of deodorants.

All of this poses more than just an interesting problem in semantics to the serious researcher—trained for, skilled in and devoted to understanding the first principles of natural phenomena—who is looking for a situation in which he can make a significant contribution to his chosen scientific field.

Where can he find such a situation?

To be sure, much of the basic research in the United States today is being carried on in universities and allied quasi-academic institutions. Another large fraction of it is done in certain research and development companies where the "development" activities are so advanced, and are being done by such competent technical people, that they could easily pass for research in most other companies. There are perhaps half a dozen firms like this in the entire country—places where basic research has always been considered a vital part of the technical program, enjoying the understanding, the support and the general environment required for creative work of high quality. We respectfully submit that Ramo-Wooldridge is one of these organizations.

During the past five years the Research Laboratory in R-W (and in its sister corporation, Space Technology Laboratories) has made notable contributions in such diverse fields as superconductivity, plasma physics and magnetohydrodynamics, millimeter waves and nuclear reactor kinetics. This breadth of activities reflects the varied interests of members of the Laboratory staff, and illustrates Ramo-Wooldridge's guiding principle that a necessary (although not sufficient) condition for worthwhile research is the definition and selection of problems by the scientists who are to work on them.

Ramo-Wooldridge's technical efforts are now directed toward the broad and challenging new field of extending man's intellectual powers. Basic research to support these activities ranges from problems of pure mathematics to studies in advanced areas of current experimental and theoretical physics.

We would be glad to discuss details of our programs with research scientists holding PhD degrees. Address Dr. Burton D. Fried, Director, Research Laboratory, or Mr. Theodore Coburn at

RAMO-WOOLDRIDGE

A DIVISION OF

Thompson Ramo Wooldridge Inc.

8433 FALLBROOK AVENUE • CANOGA PARK, CALIFORNIA

10-1

An Equal Opportunity Employer

No Renewal

DATE DUE

~~UIC 3-DAYS~~

APR 2 5 1998

UIC-REC'D APR 24 '98

~~MAR 0 4 2004~~

SCI LIB REC'D

UIC SCI LIB

NOV 1 3 2003

Reserve/Periodical Materials
must be returned to the
Reserve/Periodical Desk Only

GAYLORD

PRINTED IN U.S.A.